Amphibolite-Tonalite Relationships: Part I. Experimental Investigation of the Phase Relationships and Textural Development of Amphibolite Dehydration-Melting; Part II. The Geology, Petrology and Geochronology of a Tonalitic and Mafic Dike Swarm (Southwestern Foothills Terrane, California).

Thesis by

Michael Bennett Wolf

In Partial Fulfillment of the Requirements

for the Degree of

Doctor of Philosophy

California Institute of Technology

Pasadena, California

1992

(Defended November 26, 1991)

On Owens Mountain –
Seeking knowledge along a
dirty cattle path

Outcrops, hidden by
Summer's golden bounty, seen
again in Autumn

Deep rock, lab revealed:
What happened then, Mother Earth?
Show me secrets sealed

Universal Truths,
shorts, black socks and Birkenstocks:
at the Leading Edge

— M.B. Wolf 1985-1992

ACKNOWLEDGMENTS

I dedicate this thesis to my parents, Neil and Susan, who have nutured and inspired me and have given me the opportunity to pursue a fascinating career. I thank my parents, Neil, Susan, Bery, and Pat, for helping me throughout graduate school and for trying to prepare me for what comes after. Don Potter and Barb Tewksbury's enthusiasm and inspiration propelled me into geology. I thank my advisors, Peter Wyllie and Jason Saleeby, for their guidance and support. I learned most of my piston cylinder techniques from Dana Johnston. Dana Johnston, Michael Baker and Sieger van der Laan also aided in my developing understanding of experimental petrology. My office mates, Diane Clemens Knott and Yigal Erel, provided inestimable encouragement and scientific discussions that kept me going. The Chester House mates, David Pickett, Phil Ihinger, Mark Fahnestock, and Gloria, made the early years both highly enjoyable and intellectually stimulating. I thank Mark Fahnestock for his continued, unhesitating assistance in all matters of life, especially with the microprobe modal analysis program. Sally Newman and Yigal Erel taught me how to run the DCP spectrometer. In large part, John Armstrong taught me the intricacies of SEM and microprobe procedures. I learned U-Pb zircon geochronological techniques from Mahmood Chaudhry (mineral separation) and Jason Saleeby and Charlie Rubin (picking, clean room and mass spectrometry). Joe Kirschvink helped deconvolute the apparent polar wander data from the literature. The field work could not have been done without the permission of the many ranch owners around Owens Mountain, but I am especially indebted to Morgan Blasingame, who unhesitatingly opened his land and home to me and made me feel like family. Research grants from the Sigma Xi Society and the Geological Society of America (Penrose) eased the costs of field work. I thank all of the people of the Division of Geological and Planetary Sciences who have made my time at Caltech a mostly positive and wholly worthwhile experience. Most of all, I thank my love, Susan, for her unwavering encouragement and support.

THESIS OVERVIEW

The original intent of this thesis was to study the physicochemical relationships of amphibolites and tonalites. The amphibolite-tonalite relationship may be one of the most important in the continuing evolution of continental crust. One process by which tonalites are thought to be derived is by partial melting of hydrated basaltic (amphibolitic) crust. Instead of experimentally studying the melting relationships of many different compositions of amphibolite at many different pressures, I have approached this problem on two fronts using both experimentally and field-based methods. There are many studies of tonalites and basalts that employ either method, but I believe that there are benefits to using both. Eventually, a deeper level of understanding may be gained with this dual approach – the combination of experimental and field observations may more clearly discern some of the actual processes governing continental crustal evolution.

The first part of the thesis is an experimental study (conducted under the supervision of Professor Peter J. Wyllie) of the dehydration-melting of one natural amphibolite at one pressure (10 kbar). Because of these self-imposed limitations, this study focuses on the details of the physicochemical behavior of amphibolite dehydration-melting. The attainment of equilibrium is difficult in a complex system such as this one, so in one set of experiments, I used a finely-ground powder of the amphibolite to study the near-equilibrium phase relationships, reaction kinetics and mineral and liquid compositional changes during dehydration-melting. In another set of complimentary experiments, I used solid, cylindrical cores of the amphibolite to study the nature of the reactions and the effect of texture and time on reaction progress, disequilibrium reaction kinetics and phase morphologies. These solid experiments are an attempt to bridge the results from the powder experiments with observations on natural, relatively coarse-grained rocks.

The second part of the thesis is a field-based study (conducted under the supervision of Professor Jason B. Saleeby) of an area predominantly composed of

metatonalites and metabasites, in the western Foothills terrane of the Sierra Nevada batholith, just northeast of Fresno, California. Previous reconnaissance work suggested some relationship through partial melting between the metatonalites and amphibolites (MacDonald 1941; Primrose 1980; Powers, unpublished data). However, it soon became clear to me that there is little field evidence for extensive partial melting of the mafic layers at the levels of exposure of the rocks. In fact, I have identified a felsic and mafic dike swarm/shear zone within the field area. The goals of this project were reassessed, and I focussed on the tectonic significance of the metatonalitic and mafic layers. Although an extensive geochemical study of the REE and isotopic signatures of the rocks would have been interesting and useful (and possibly more compatible with the petrological bent of the experiments), I deemed a geochronological study of the area to be of greater importance. Thus, this field-based study encompasses structural, petrographic, geochemical, and U-Pb (zircon) geochronologic work to better understand the nature of the tonalitic and mafic dikes in a local and regional context.

SHORT ABSTRACT (PARTS I AND II)

PART I: Phase relationships have been determined for the dehydration-melting of a (powdered and solid) calcic, low-K, olivine tholeiitic amphibolite (hornblende 70%, plagioclase 30%), in runs at 10 kbar, 750 to 1000°C, $f_{O_2} \equiv$ Ni-NiO, and for 1 to 21 days. Hornblende is involved in a sliding reaction: hornblende + anorthitic plagioclase → clinopyroxene + liquid + aluminous hornblende + calcic hornblende + orthopyroxene + garnet. The liquid fraction varies from <1% at 750°C to ~47% at 1000°C, with the big increase occurring above 875°C. Liquids are tonalitic but have very high Al_2O_3 contents (18-21 wt.%). At high liquid fractions (~0.5), liquids are high-alumina basaltic. Liquids become more sodic with increasing temperature, but the compositional trends reverse direction, and liquids become more calcic above 975°C, where garnet is unstable. The water contents of liquids range from over 7 wt.% at low liquid fractions to 2 wt.% at high liquid fractions. In the solid amphibolite runs, liquid interconnectivity may be attained at 875°C with only 2 vol.% liquid and dihedral angles less than 60°. The removal of water-rich tonalitic liquids from a substantially melted amphibolitic source could help generate a relatively dry mafic granulite terrane, with densities up to 3.5 gm/cm^3. Delamination of this dense lower crust is possible.

PART II: A cogenetic and coeval tonalitic and mafic dike swarm has been identified within a southern fragment (the Owens Mountain area) of the western Foothills terrane (Sierra Nevada, California). The swarm was mylonitized and transposed during emplacement, from 155 to 148 m.y. (U-Pb zircon data), at an estimated depth of 10 km. Steeply SE-plunging fold axes and S-fold geometries indicate a left-lateral sense of shear. The Late Jurassic Nevadan orogeny is a manifestation of dramatic changes in magnitude and direction of North American motion. The Cordilleran dike swarms record a complex pattern of sinistral-sense transtension-transpression that developed during this period of change, at the J2 (~150 m.y.) apparent polar wander cusp, and during subsequent, rapid northwestward acceleration of North America.

EXTENDED ABSTRACT (PART I)

Phase relationships and morphologies and reaction kinetics have been determined for the dehydration-melting of a natural amphibolite (mode: hornblende 70%, plagioclase 30%) with no added water, at 10 kbar and 750 to 1000°C, and for durations of 1 to 21 days, using both finely-powdered and solid starting materials. The amphibolite composition is equivalent to a calcic, low-K, olivine tholeiite. Experimental conditions simulated the dehydration-melting of deep mafic continental crust and hot, subducted oceanic crust. Experiments were conducted in unbuffered Au capsules at oxygen fugacities probably just above the Ni-NiO buffer.

Hornblende is involved in the following sliding reaction (the order of the product phases represents the order of appearance with increasing temperature): hornblende + anorthitic plagioclase → clinopyroxene + liquid + aluminous hornblende + calcic hornblende + orthopyroxene + garnet. The liquid fraction ranges from <1% at 750°C to ~47% at 1000°C, with most of the increase occurring above 875°C. The liquids are generally tonalitic but have very high Al_2O_3 contents (18-21 wt.%). At high liquid fractions (~0.5), the liquids have a composition of high-alumina basalt. Fractionation of the plagioclase would be necessary to reduce both the CaO and Al_2O_3 contents of the liquids to calc-alkaline compositions. The liquid compositions become more sodic with increasing temperature, but the compositional trends reverse direction, and the liquid compositions become more calcic above 975°C, as garnet disappears. The water contents of the liquids range from over 7 wt.% at low liquid fractions to 2 wt.% at high liquid fractions. The high-temperature mineral assemblage that coexists with the liquid is clinopyroxene, orthopyroxene and plagioclase ± garnet ± aluminous hornblende. Thus, dehydration-melting of the amphibolite can reproduce natural granulite and garnet pyroxenite mineral assemblages. The removal of the water-rich tonalitic liquids from a substantially melted amphibolitic source would help generate a relatively dry granulite

terrane. The stability of garnet plays a major role in determining the REE composition of the liquids. Garnet modes from these runs are consistent with REE patterns of Archean tonalites. Delamination of the garnet clinopyroxenite restite is possible due to the very high densities (up to 3.5 gm/cm^3) of these assemblages after liquid segregation. Garnet phenocrysts show syn-growth compositional zoning. The total alumina in hornblende geobarometer appears to work for this mafic mineral assemblage.

The solid amphibolite runs indicate that anisotropic crystal structures and rock texture control liquid morphology and distribution during dehydration-melting. The shapes of most liquid pockets are crystallographically-controlled, with many corners having angles greater than 60°. Few crystal/liquid triple-junctions develop the interfacial energy-controlled dihedral angles (θ), which form in experiments using finely-ground powders of minerals with poor cleavage. Liquid interconnectivity probably is attained at 875°C with only 2 vol.% liquid, indicating that dihedral angles less than 60° may not be necessary to achieve interconnectivity in partially melted metamorphic rocks. The surfaces between elongated grains in lineated rocks can become pathways for the migration of liquid or the diffusion of components.

EXTENDED ABSTRACT (PART II)

The geology, petrology and geochronology (U-Pb zircon) of a southern fragment of the western Foothills terrane has been studied (the Owens Mountain area of the western Sierra Nevada foothills, northeast of Fresno, California). A previously unrecognized dike swarm/shear zone is identified within the steeply dipping, Callovian to Kimmeridgian metavolcanic and metasedimentary strata. The dike swarm consists predominantly of cogenetic tonalitic and mafic dikes and tonalitic tabular bodies. Mutually cross-cutting relationships indicate that the tonalitic and mafic dikes also were coeval. Some of the tonalitic dikes range up to ~100 m in thickness, and individual dikes of both tonalitic and basaltic composition can be followed for up to 3 km. The dike swarm is sheeted in places, comprising almost 100% of some outcrops. Textures and fabrics within the dike swarm range from partially recrystallized igneous to strongly deformed S and L metamorphic tectonites, implying that dike emplacement occurred during ductile deformation. Hot subsolidus mylonitization has transposed layering parallel to foliation and has greatly thinned many of the dikes to centimeter to meter thicknesses. Layering and parallel foliation dip subvertically and strike NNW-SSE. Post-tectonic annealing has destroyed most microscopic shear indicators, but macroscopic intrafolial folds are common and have steeply SE-plunging fold axes and S-fold geometries that indicate a left-lateral sense of shear. The geochronological data on the tonalite dikes reveal that emplacement and crystallization of the coeval tonalitic and mafic magmas at Owens Mountain occurred over an 8 m.y. period, from 155 to 148 Ma, at an estimated depth of 10 km. Thus the beginning of intrusion occurred within 5 m.y. of deposition of the metavolcanic and metasedimentary strata into which the dikes were emplaced. A correlation between age and degree of deformation and recrystallization of the tonalites implies syntectonic dike emplacement. Undeformed granitic dikes that cut the strata are younger than 124 Ma.

The regional tectonics of the Owens Mountain and other Cordilleran dike swarms can be related in a broad dynamic sense to the absolute motion of North America by using the apparent polar wander (APW) analysis of May and Butler (1986). The Late Jurassic Nevadan orogeny is the manifestation of the drastic changes in magnitude and direction of North American motion (from ~45 km/m.y. to the NNE to ~200 km/m.y. to the NW; May and Butler, 1986). The Late Jurassic dike swarms record a complex pattern of sinistral-sense transtension-transpression that developed at the J2 (~150 Ma) APW cusp and during subsequent, rapid northwestward acceleration of North America.

TABLE OF CONTENTS

LIST OF TABLES AND FIGURES (PART I)

LIST OF TABLES AND FIGURES (PART II)

CHAPTER 1. INTRODUCTION

1.1 Preface

The generation of silicic magmas is a fundamental problem in continental crustal evolution. The magmas that contribute to the growth of batholiths are produced by either differentiation of mantle-derived magmas, anatexis of crustal rocks or a combination of both of these processes. Less extensive anatexis of crustal rocks produces migmatites. Regardless of the nature of melting, H_2O plays a critical role in the production of most magmas. Under H_2O-saturated conditions melting begins at 600-700°C (at pressures greater than a few kilobars) in both felsic and mafic systems (e.g., Tuttle and Bowen 1958; Yoder and Tilley 1962; Merrill et al. 1970). The beginning of melting (the solidus) shifts to higher temperatures as the H_2O content in the system decreases. The role of CO_2, though secondary to H_2O, also influences the location of the solidi in P-T space. The fluxing of CO_2 may be an important mechanism for crustal dehydration, granulite formation and anatexis (Newton et al. 1980; Powell 1983). Early H_2O-CO_2-rock studies demonstrated that an increase in CO_2 shifts solidi to higher temperatures by decreasing the activity of H_2O in the fluid (e.g., Holloway and Burnham 1972). However, recent work suggests that under certain conditions the addition of some CO_2 to H_2O-rich fluids may actually lower the solidi and enhance melting in mafic systems by increasing the solubility of $MgCO_3$ in the liquid (Peterson and Newton 1990). Residuum mineralogies produced during partial melting of a wide variety of rocks are characteristic of granulite-facies metamorphism (quartz, garnet, clinopyroxene, orthopyroxene, and plagioclase), so anatexis ($\pm H_2O \pm CO_2$) and liquid removal have been considered possible granulite-forming processes (e.g., Fyfe 1973; Powell 1983).

In contrast to conditions in the upper continental crust, vapor-absent conditions probably exist in the lower crust, so any H_2O that is present is located in hydrous minerals

(Burnham 1979; Vielzeuf and Holloway 1988). Seismic and geochemical studies indicate that much of the lower continental crust may be mafic (Jackson and Arculus 1984; Rudnick and Taylor 1986; Griffin and O'Reilly 1987; Kempton et al. 1990). Anatexis of this hydrated crust occurs by dehydration-melting, during which H_2O released by the breakdown of the hydrous minerals dissolves directly into the silicate liquid. Thus an understanding of the phase relationships of hydrous mafic rocks – amphibolites – is important for modelling the anatexis of lower continental crust.

Experimental petrologists have been studying H_2O-rock systems at near-solidus conditions to learn which parameters influence anatexis. Until recently, only Brown and Fyfe (1970) and Huang and Wyllie (1973, 1981) had determined solidus curves for the vapor-absent melting of rocks containing hydrous minerals. Robertson and Wyllie (1971) and Lambert and Wyllie (1972) correlated the solidi in H_2O-deficient rock systems with the beginning of hydrous mineral breakdown reactions. Burnham (1979) presented a detailed experimentally-based theoretical analysis of melting in vapor-absent, biotite and hornblende gneisses. These studies placed the solidi at relatively high temperatures, so the generation of large amounts of liquid within nonthickened continental crust with a normal geothermal gradient or within relatively old, cool, oceanic crust was difficult to envision.

Some processes that may elevate the lower crustal isotherms and form partial melts and granulites include continental collision followed by erosional or extensional thinning, magmatic underplating, magmatic arc or hot spot activity, or crustal delamination (Thompson 1990; Bohlen 1991). An elevated geothermal gradient is characteristic of continental environments undergoing extension (Kay and Kay 1980). During continental rifting, asthenospheric upwelling adds heat to the region. Thus, conditions necessary for anatexis (and granulite formation) may be achieved in lower continental crust.

High temperature (750-1000°C) melting experiments are appropriate for simulating conditions of lower continental crustal amphibolite anatexis and granulite formation, because these temperatures can be attained in the lower crust. Pressure-temperature

conditions deduced for regional Archean granulites require geothermal gradients greater than 35°C km^{-1} (Bohlen 1991) – gradients that result in temperatures ≥1000°C at a pressure of 10 kbar. Temperatures during granulite-facies regional metamorphism are estimated to have approached or exceeded 1000°C at pressures of 7 to 10 kbar in many localities such as Antarctica (e.g., Ellis 1983; Sandiford 1985; Sandiford and Powell 1986), Canada (e.g., Morse and Talley 1971), India (e.g., Kamineni and Rao 1988; Dasgupta et al. 1991), Uganda (e.g., Sandiford et al. 1987), Norway (e.g., Kars et al. 1980), and Scotland (e.g., Barnicoat and O'Hara 1979). A granulite-silicate liquid association possibly is indicated by the mineralogy of these granulites and the compositional and field relationships of the crystallized partial melts.

Crustal temperatures in the Archean were higher than at the present (e.g., Martin 1986). Thus, anatexis and granulite formation occurred more readily. Most of the Archean tonalitic, trondhjemitic and granodioritic granulites and gneisses may have been derived by the anatexis of amphibolites or eclogites (Arth and Hanson 1972; Hanson 1981; Jahn et al. 1984). Most (>70%) of the present continental crustal material was separated from the mantle during the Archean (Reymer and Schubert 1984; Dewey 1986). Thus, anatexis of amphibolite may have been one of the fundamental processes for generating much of the continental crust. In addition, granulite-facies metamorphism may be occurring even at the present time (Hayob et al. 1989; Clemens 1989).

Oceanic crust has a higher normal temperature gradient than continental crust, and it is possible that anatexis may be induced by frictional heating along low-angle shear zones within hydrated oceanic crust (e.g., Flagler and Spray 1991). More extensive anatexis of the oceanic crust may occur during subduction. The subduction and subsequent dehydration and possible partial melting of hydrated basaltic crust has been the dominant process of continental crustal growth since the Archean (Drummond and Defant 1990). Mantle-derived magmas originate either in the subducted slab or the mantle wedge. In both cases, though, fluids or liquids from the dehydrating and dehydration-melting oceanic crust

are critical in the production of these magmas. Thus an understanding of the phase relationships of hydrous mafic rocks – amphibolites – also is important for modelling the anatexis of hot, subducted oceanic crust.

Subduction zone wedges and much of the upper and middle continental crust are composed of pelitic sediments and their metamorphic equivalents (Taylor and McLennan 1985), and due to tectonic processes, these materials may be incorporated into an anatectic source region. Dehydration and anatexis of these felsic rocks can produce massive quantities of granitoid magma (White and Chappell 1977). Experimentalists have simulated this melting process to generate granitic liquids (e.g., Thompson 1982; Le Breton and Thompson 1988; Vielzeuf and Holloway 1988; Patiño Douce and Johnston 1991).

However, because much of the lower crust may be mafic, an understanding of the phase relationships of amphibolites is an important part of the modelling of crustal anatexis. Amphibolites have a very large compositional variability, which reflects the variability of their protoliths (both igneous and sedimentary), the processes which formed them, and the environments in which they formed. By comparison, the number of amphibolite melting experiments is small. Melting of amphibolite was simulated in basalt-H_2O experiments (e.g., Yoder and Tilley 1962; Holloway and Burnham 1972; Helz 1973, 1976). Ellis and Thompson (1986) studied glasses, oxides and synthesized mineral mixes in the CMASH system (CaO-MgO-Al_2O_3-SiO_2-H_2O).

The presence of amphibole in the starting material is important because the initial mineralogy, not just bulk composition, influences the reactions and subsequent liquid and mineral compositions. Rushmer (1987), Beard and Lofgren (1989, 1991) and Rapp (1990) studied the melting of a few natural amphibolites at elevated temperatures (>900°C), different pressures and P_{H_2O}. Winther et al. (1989), Wolf and Wyllie (1989), Beard and Rushmer (1990), Rushmer (1991), and Beard and Lofgren (1991) extended the temperature range down toward the respective solidi. These studies show that the liquid

trends and mineral reactions can neither be accurately predicted nor extrapolated from past or present experimental data, due to the diversity of natural amphibolite compositions and the complexities of amphibole mineralogy, nonequilibrium effects and analysis of H_2O- and alkali-rich glasses.

The origin and evolution of granitoid magmas involves three major processes: (1) magma generation, (2) magma segregation, separation and ascent, and (3) differentiation and contamination during ascent, intrusion and eruption. The conditions for mobilization of silicic liquid or magma, once generated, have received much attention recently, but they remain rather uncertain (McKenzie 1985; Wickham 1987; Clemens and Vielzeuf 1987; Patiño Douce and Johnston 1991). Important factors include the solid-liquid-solid interfacial angle geometry which controls the interconnectivity of liquids at low liquid fractions (Watson 1982), and the critical melt fraction which demarcates a rapid decrease in rock strength and effective viscosity at higher liquid fractions (Van der Molen and Paterson 1979). Experiments designed to study the interfacial angle parameters also have concentrated on measuring liquid interconnectivity in partially fused, structurally near-isotropic mineral powders (e.g., Jurewicz and Watson 1984; Toramaru and Fujii 1986). It has been determined that, for small liquid fractions, both granitic and basaltic liquids may be interconnected and possibly able to migrate (Watson 1982; Waff and Bulau 1982; Jurewicz and Watson 1984, 1985; Toramaru and Fujii 1986).

The ability of a silicate liquid to segregate depends upon how that liquid is distributed within the matrix of a partially melted rock, as well as its viscosity and composition, and the stress field and duration of anatexis. The mechanism by which partial melt segregates from its host controls the formation of migmatites and larger bodies of magma. Deformation prior to anatexis may be important in imparting a lineated texture to the rock that, during or after anatexis, is conducive to liquid interconnectivity and possible subsequent liquid segregation. All of the phase equilibrium experiments cited above used finely-ground mineral powders, because this form gives the best prospect of attaining

equilibrium. The partial melt textures produced in these fine-grained powder experiments, however, are not necessarily applicable to the study of coarser-grained crustal rocks (Spry 1969). There have been a few experiments in which solid pieces of felsic rocks were used to study anatexis (e.g., Mehnert et al. 1973; Büsch et al. 1974; Arzi 1978; Van der Molen and Paterson 1979; Brearley 1987; Rubie and Brearley 1987; Hacker 1990). Prior to the present work, the combination of solid and powder experiments had not been conducted; however, comparisons of the run products give insights into kinetic factors such as crystal nucleation and growth that may influence the compositional evolution of the whole, crystal + liquid, system.

1.2 Previous Experiments on H_2O-Mafic Rock Systems

Early studies of H_2O-mafic rock systems were conducted using powders with basaltic mineral assemblages or glasses, under H_2O-saturated and H_2O-undersaturated conditions. Because of the importance of vapor-absent, crustal anatexis, more recent work focused on dehydration-melting experiments in general and then on dehydration-melting experiments with amphibolitic starting assemblages.

1.2.1 Vapor-Present Experiments

Yoder and Tilley (1962) measured the wet solidus temperature of three basalt compositions in a gas apparatus. At P_{H_2O} = 10 kbar, the alkali basalt and olivine tholeiite solidi are located at 620°C, and the high-alumina basalt solidus is at 720°C. Amphibolites with these compositions would begin to melt at these temperatures at 10 kbar, in the presence of excess H_2O. No experiments were done on vapor-absent, dehydration-melting of hydrated basalts. Plagioclase disappears at relatively low temperatures in the H_2O-oversaturated runs (675-825°C, depending on composition). Liquid compositions were not analyzed.

In piston-cylinder experiments, Green and Ringwood (1968) used both dry and wet glasses with compositions corresponding to six members of the calc-alkaline series, ranging from high-alumina olivine tholeiite to rhyodacite. Run conditions for runs with dry glasses were 9-36 kbar, 1000-1400°C and very short durations, from 10 minutes to 4 hours. In the wet runs, the quantity of H_2O added was not controlled but was assumed to result in $P_{H_2O} < P_{Total}$. Run conditions were 9, 10 and 27 kbar, 880-1320°C and <1 to 8 hour durations. Iron loss to the platinum capsule was a serious problem. In the wet basalt experiments (9 and 10 kbar), there are large fields of clinopyroxene, amphibole and minor orthopyroxene, with plagioclase and garnet absent. Plagioclase or garnet become liquidus phases in more silicic compositions or at higher pressure (27 kbar), respectively. For low degrees of partial melting of hydrous basalt at 9 and 10 kbar, the residuums consist of amphibole, pyroxenes and plagioclase, and the liquid compositions are dacitic to rhyodacitic.

Holloway and Burnham (1972) studied the melting relationships of an olivine tholeiite up to 8 kbar at $P_{H_2O} < P_{Total}$, 800-1100°C, and an fO_2 buffered by Ni-NiO. The projected 10 kbar solidus is at 730°C for vapor-present conditions with X_{H_2O}= 0.6. The calculated 8 kbar modes show a gradual increase in the quantity of liquid until the amphibole stability field is exceeded (1060°C). Above this point there is a sharp increase in the amount of liquid (35 to 95% in less than 50°C). Runs were performed only above 800°C at 8 kbar, so the beginning of melting was not investigated, and modes were calculated only at and above 995°C. Plagioclase disappears at about 875°C at 10 kbar (projected). The 8 kbar liquid compositions at 995-1050°C are aluminous (~20 wt.% Al_2O_3) in the presence of amphibole. Small compositional and modal changes in amphibole slightly affect the composition of the coexisting liquid. A large change in liquid composition occurs with the breakdown of amphibole (SiO_2, Al_2O_3, Na_2O, and K_2O decrease, and TiO_2, FeO, MgO, and CaO increase).

Lambert and Wyllie (1972) studied the phase relationships olivine tholeiite with excess H_2O up to 35 kbar. The importance to the present study is that they anticipated that the beginning of melting under H_2O-deficient conditions should correspond with the beginning of amphibole reaction, not with the amphibole-out curve. However, this solidus still was located 250-400°C higher than the H_2O-saturated solidus between 5-10 kbar.

Helz (1973,1976) studied the phase relationships of three basalts (quartz tholeiite, olivine tholeiite and alkali basalt) under H_2O-oversaturated conditions at 5 kbar, from 680-1050°C and at the fO_2 of the quartz-fayalite-magnetite (QFM) and hematite-magnetite (HM) buffers. The solidi for all three compositions and both fO_2s are located at about 690°C. Plagioclase disappears between 800 and 860°C. The upper stability limit of amphibole is fO_2-dependent, decreasing with increasing fO_2. Amphibole disappears above 960°C at fO_2 = HM and above 1050°C at fO_2 = QFM. The amount of liquid increases steadily throughout the melting interval until very high temperature are reached (~1000°C). The compositions of the liquids are enriched in SiO_2 (75-55 wt.%) and Al_2O_3 (14-24 wt.%) with increasing temperature, although many compositions had to be corrected due to the growth of quench phases and the loss of iron to the capsule. In general, SiO_2 and K_2O decrease and all the other oxides increase in the liquid as the temperature increases and amphibole breaks down.

In basalt-H_2O-CO_2 experiments, Allen and Boettcher (1978) showed that amphiboles are stable to temperatures over 1000°C for most values of fH_2O at 10 kbar. This study focused on the high-temperature phase relationships and did not address problems regarding low degrees of melting. Liquids produced from the melting of basalt (>960°C) were silicic (59-67 wt.%) and aluminous (19-23 wt.%).

Spulber and Rutherford (1983) studied the melting relationships of two tholeiites under H_2O-saturated conditions at 1-3 kbar, from 800-1075°C and at the very low fO_2 of the graphite-methane (G-CH) buffer. One of the starting compositions (DO8) is similar to the amphibolite composition in the present study. The liquids produced are more enriched

in SiO_2 (68-50 wt.%) and Al_2O_3 (14-19 wt.%) than anhydrous liquids. The generation of rhyolitic or plagiogranitic (trondhjemitic) liquid compositions, an expression of the Na_2O:K_2O ratio, depends on the starting bulk composition.

1.2.2 Vapor-Absent Experiments

The dehydration-melting process was studied by Brown and Fyfe (1970). They melted granite and diorite, plus hornblende or biotite (with no free H_2O added) to study the effect of H_2O (from the hydrous minerals) on the location of the solidi and the compositions of the liquids. The solidi of hornblende-bearing mixtures appear to be located at about 950°C at 10 kbar. Few liquid compositions are given from diorite-hornblende (50:50) melting experiments (2-4 kbar); relative to the bulk starting compositions, the granitoid liquid compositions are strongly enriched in SiO_2, Na_2O and K_2O, strongly depleted in FeO, MgO and CaO, and similar in Al_2O_3.

Ellis and Thompson (1986) studied the stability of amphibole up to 10 kbar in the CMASH system under H_2O-undersaturated and H_2O-saturated conditions. At 10 kbar, all the amphibole breaks down between 900-925°C at the solidus. In contrast to the H_2O-saturated peraluminous liquids, the liquids produced by dehydration-melting are only marginally metaluminous. The direct applicability of these results to natural systems is limited by the lack of iron and sodium in the CMASH system, which have important effects on both mineral stabilities (and thus reaction boundary locations) and liquid compositions.

Rutter and Wyllie (1988) melted a natural biotite- and hornblende-bearing tonalite at 10 kbar with no H_2O added. The solidus lies between 800-850°C. Melting began with the breakdown of biotite followed at higher temperatures by the breakdown of hornblende. The bimineralic nature of the hydrous minerals resulted in a step-like pattern in the degree of melting as a function of temperature.

Recently, experimentalists have been studying the dehydration-melting of natural amphibolites, as briefly mentioned in the introduction (e.g., Rushmer 1987, 1991; Beard

and Lofgren 1989, 1991; Winther et al. 1989; Wolf and Wyllie 1989, 1990; Rapp 1990; Winther and Newton 1990).

Beard and Lofgren (1991) studied the H_2O-saturated melting and the dehydration-melting relationships of natural greenstones and amphibolites at 1, 3 and 6.9 kbar, 800-1000°C, and at an fO_2 about 1-2 log units above the Ni-NiO buffer. In the H_2O-saturated experiments, liquids are formed above 750°C, are enriched in Al_2O_3 and CaO, relative to most natural silicic igneous rocks, and coexist with amphibole. In the dehydration-melting experiments, the breakdown of amphibole and quartz defines the solidus between 800-850°C at 6.9 kbar. The starting bulk compositions all are more aluminous, but the liquids are all less aluminous, relative to the rock and liquid compositions in the present study. The dehydration liquids are similar to natural silicic are rocks.

Winther and Newton (1990) studied the melting relationships of a natural, high-alumina basalt and the average Archean tholeiite (AAT) composition with different amounts of H_2O, at 5-30 kbar, 750-1000°C, and fO_2 = QFM. Melting the high-Al basalt produces liquids very high in Al_2O_3 (17-24 wt.%). The AAT melting experiments did produce liquids similar to natural tonalites and trondhjemites above the 850°C solidus (5-20 kbar), however, there is evidence of plagioclase disequilibrium (zoning on initial anorthite crystals [D. Sykes, pers. comm., 1991]), which may have been the cause of the elevated sodium content in the trondhjemitic liquids.

Hacker (1990) melted and deformed solid pieces of amphibolite $\pm H_2O$ at temperatures of 700-1000°C and confining pressures of 5-15 kbar. Under H_2O-undersaturated conditions, the liquid compositions that formed above the 900°C solidus are silicic (66-80 wt.%) and aluminous (13-19 wt.%).

Rushmer (1991) investigated the dehydration-melting of two coarsely-ground, natural amphibolites (compositionally an alkali basalt and a tholeiite) and mechanically mixed amphibolitic compositions at 8 kbar, in talc and pyrex assemblies. The fO_2 was assumed to be close to the QFM buffer. The solidi are located at 925°C for the alkali basalt

and 800°C for the tholeiite. The low solidus temperature of the tholeiite is due mainly to the breakdown of biotite and cummingtonite. In one mechanically mixed amphibolite, composed of 54 wt.% hornblende and 46 wt.% anorthitic plagioclase (An_{90-96}), only 5 vol.% liquid was generated at 975°C. Most of the liquids appear to be corundum-normative, although few data on compositions are given. Run durations are generally ≤4 days.

1.3 Scope of the Present Work

In order to determine some of the possible products of anatexis in deep mafic crust, I have studied dehydration-melting of an amphibolite at 10 kbar (with no H_2O added to the system other than that which is structurally bound in the hydrous mineral, hornblende). This study consists of two parts: a study of the phase relationships and compositions of the powdered amphibolite, and a study of the textural development of the solid amphibolite.

When I started this study, there were no published studies on the dehydration-melting of amphibolites in which the compositions of the new mineral phases as well as the liquid phase were extensively documented. Thus one of my goals in the powdered amphibolite study was to determine the mineral and melting reactions, and to analyze the compositions of all minerals and glasses (quenched liquids) in order to obtain liquid compositional trends during melting. An analysis of the modal data helps constrain which reactions may have occurred, but a textural analysis is also important. The amount of liquid generated as a function of temperature is critical for modelling liquid segregation. Modal data are used in mass balance calculations that yield estimates of parameters such as the H_2O content of the liquids (and thus liquid viscosities) and the densities of the residual mineral assemblage.

A comparative study between the powder and solid amphibolite studies may help bridge the gap between experimental results and the natural world. There is an obvious difference in the reaction times of experiments and nature. A detailed comparative look at

the mineral morphologies gives some insight into the kinetics of nucleation and growth in this complex, partially melted amphibolite. The morphology of the liquid is explored to see how the textures of structurally anisotropic minerals (hornblendes) affect solid-liquid-solid interfacial angles and the interconnectivity of liquids. I have determined where and how liquid forms along grain boundaries. The geometry of the liquid pockets influences the manner in which the liquid collects and possibly its ability to move and segregate.

The attainment of equilibrium is generally the implicit though unprovable goal of experimentalists. Reaching equilibrium is especially problematic in experiments in natural amphibolite systems at temperatures <1000°C; experimental durations of at least a week appear to be necessary, even for very fine-grained materials. However, non-equilibrium experiments may shed light on geochemical consequences of non-equilibrium and kinetic processes that are not observed in experiments in which equilibrium has been achieved. I have used the combination of powder and solid experiments to study the effects of temperature, time and texture on the progressive physicochemical nature of the reactions. Studying these effects allows me to chart the approach toward equilibrium.

This study of the partial melting of amphibolite has many petrologic applications – the anatexis of amphibolite in hot subducted oceanic or lower continental crust being the most obvious. The experimental results have implications for liquid segregation and the concomitant formation of granulitic or garnet clinopyroxenitic restite. These ideas are further developed and may lead to a better understanding of the generation and differentiation of hydrous granitoid liquids, and of some tectonic and geochemical implications of anatexis and restite formation. The initial role and subsequent behavior of H_2O in this system have further physicochemical applications. The combination of powder and solid experiments also may lead to a better understanding of mineral reactions that may be useful in geobarothermometric and textural development studies.

CHAPTER 2. EXPERIMENTAL METHODS

2.1 Starting Material

Fresh amphibolite was collected from the west central Foothills Metamorphic Belt of the Sierra Nevada Batholith, California. The chemical analysis in Table 2.1 reveals 1.7 wt.% Na_2O and 0.2 wt.% K_2O, corresponding to an alkali basalt, though the composition lies close to the plane of critical undersaturation of Yoder and Tilley (1962). Amphibolites with similar low values of Na_2O are common in association with tonalites (e.g., Barker et al. 1979a; Barker et al. 1979b). Low-K rocks also are common in oceanic and arc environments (Gill 1981). The rock mode is 67.4% hornblende (Hb) and 32.5% plagioclase (Pl) with minor sphene (0.1%), determined by electron microprobe (EMP) partial analysis of 1063 points from a thin-section of the rock (EMP-ARP technique discussed below). None of the minerals shows any signs of alteration.

Table 2.2 lists the plagioclase compositions from the thin-section, analyzed with a scanning electron microscope (SEM) using an energy dispersive spectrometer (EDS) and mineral standards. Table 2.1 lists both the average from these 6 SEM analyses (Table 2.2) and the average from 283 EMP analyses, determined during measurement of the initial mode. The amount of Na_2O in the EMP average is calculated by difference, and it agrees closely with the measured SEM value. The plagioclase composition, as determined from the 6 complete SEM analyses is An_{89}, and as determined from the 283 partial EMP analyses is An_{90}. Thus the initial composition of the plagioclase in the amphibolite is taken to be An_{90} – having a formula of $Na_{0.1}Ca_{0.9}Al_{1.8}Si_{2.1}O_8$ with only a trace of K, plus some Ti, Fe and Mg impurities. Table 2.1 also lists the compositions of the only two sodic plagioclases found in a thin section of the rock. These two grains were less than 10 μm in diameter. Figure 2.1 shows the compositional variation of the anorthitic plagioclase throughout the thin-section of the amphibolite, from the EMP-ARP analyses.

Table 2.3 lists the hornblende compositions (SEM-EDS) from the thin-section, which also are plotted in Fig. 2.2a,b. The simplified hornblende formula from Table 2.3 is $X_{2.0}Y_{5.2}Z_8O_{22}(OH)_2$, where X = Ca + Na + K, Y = Mg + Fe + Al^{VI} + Ti + Mn + Cr and Z = Si + Al^{IV} (after Deer et al. 1983). Figure 2.3 shows the compositional variation of the hornblende from a thin section of the amphibolite, from the electron microprobe analyses determined during measurement of the initial mode. The abundance of data in a central location indicates that the range in composition is not due to mixing of compositionally distinct hornblende populations (e.g., separated by a miscibility gap). Most of the data fall within a fairly narrow range: SiO_2 – 47.5 - 50.5 wt.%; Al_2O_3 – 6.5 - 9.0 wt.%; FeO – 10.5 - 12.5 wt.%; MgO – 14.0 - 16.0 wt.%; CaO – 12.0 - 13.0 wt.%.

The amphibolite has no foliation, but a strong mineral lineation. Grain size ranges from 0.1 to 1.0 mm. In a two dimensional view, isolated groups of plagioclase crystals, 50-500 μm long, are surrounded by hornblende crystals, 100-1000 μm long (Fig. 2.4). Many groups of small plagioclase grains are optically continuous, indicating that these groups comprise a single, larger plagioclase crystal, and thus are interconnected in three dimensions. The aspect ratio of the plagioclase grains, measured in planes containing the mineral lineation, ranges from 1:1 to 1:8. The hornblende aspect ratios appear to be similar to the plagioclase ratios.

2.2 Experimental Procedure

2.2.1 Powder Experiments

The outer, dirty surfaces were cut off of a hand sample-sized, fine-grained, homogeneous amphibolite. The amphibolite first was broken into flakes and then hand-ground in an agate mortar and pestle, but many of the grains still were larger than 30 μm in diameter. A better and faster grain-size reduction method used a shatterbox. Approximately 250 cm^2 of rock were run through a tungsten carbide shatterbox mill (with ring and puck) for eight minutes, and the resulting powder was reground by hand and

optically inspected. Fifty percent of the volume of the grains is <5 μm in diameter. Forty percent of the remaining powder volume is composed of grains <20 μm, and very few grains are >50 μm in diameter. This powder was not sieved to remove the larger pieces so as not to alter the bulk composition. The powder was dried in a 110°C vacuum oven overnight and then stored in a sealed desiccator. Approximately 30 mg of powder were pressed into gold capsules and welded shut, without adding any water. The problem of iron loss from the sample was avoided by using gold capsules. The gold capsule walls were analyzed by SEM after some runs, and no Fe peak was detected.

In a few of the experiments, the glasses contain a few spherical dimples which were vapor bubbles within the liquids. However, the presence of these bubbles does not indicate water-oversaturated conditions during the experiments. Since all of the experiments were quenched at a sustained 10 kbar pressure, the formation of bubbles during decompression did not occur. The bubbles probably are the result of minute air pockets left between grains in the amphibolite powder. Although an attempt was made to reduce the amount of air by compacting the powder within the capsule, complete powder compaction is very difficult to achieve (e.g., Helz 1982). The implied ever-presence of air space within the starting powder means that the dehydration-melting reactions technically are not vapor-absent. However, neither the phase relationships nor the liquid compositions are affected by these few bubbles, so their presence is considered to be inconsequential.

2.2.2 Solid Experiments

Samples of amphibolite were prepared by drilling cylindrical cores (2 mm diameter; 5 mm long) perpendicular to the lineation of a single rock slab (2x4x1 cm), using a diamond core drill bit. The edges of the rock cylinders were smoothed by grinding to minimize to chance of puncturing the capsule walls during the runs. The amphibolite was submerged in H_2O for a few minutes during the coring process, so the cores were redried in a 110°C vacuum oven for a week. The dried, solid amphibolite cylinders were sealed

within gold capsules, with no H_2O added, and the capsules were embedded in a horizontal position within the furnace assemblies, with inclinations less than 30°, which ensured that vertical temperature gradients through the capsules were minimized.

2.2.3 Run Procedure

The powder experiments were run at a pressure of 10 kbar and temperatures ranging from 750-1000°C. The solid experiments were run at a pressure of 10 kbar and temperatures ranging from 850-1000°C. At temperatures lower than 975°C, the gold capsules were embedded into half-inch NaCl-C-NaCl furnace assemblies, but at higher temperatures, near the melting point of NaCl (1000°C at 10 kbar), half-inch CaF_2-C-NaCl, CaF_2-C-CaF_2, or pyrex/CaF_2-C-NaCl assemblies were used (Fig. 2.5). The use of the CaF_2 assemblies solved a problem of sodium infiltration/contamination into a few of the higher temperature NaCl-assembly runs. The oxygen fugacity in these experiments is about 0.5-1.0 log f_{O_2} above the Ni-NiO buffer, based on the measured compositions of coexisting Fe-Ti oxides from other experiments run in these furnace assemblies (Carroll and Wyllie 1990; Wolf and Wyllie 1986, unpub. data). The duration of experiments ranged from one to twenty one days. Rapid quenching at pressure reduced any prospect that the liquid might move during the quench. I assume that all liquids quenched in place. There is no visible growth of quench crystals in any of the glasses. The regular distribution of glass throughout the samples indicates that there probably was no diffusion of H_2O from the furnace assembly. Robertson and Wyllie (1971) found that diffusion of H_2O through gold into partially melted, vapor-absent granite produced an outer, glass-rich zone. The use of gold capsules minimized iron loss; scanning electron microscope measurements of the gold capsules indicated no iron diffusion into the walls.

Although reversed runs are desirable to determine the attainment of equilibrium, no reversal runs were attempted because of the complexities of natural amphibole reactions, especially in the absence of a free vapor phase. The sluggishness of the approach to

equilibrium in the amphibolite system, in fact, can be used to the advantage of studying how reactions actually may proceed in nature under vapor-absent conditions. An understanding of the short duration kinetics may serve as a guide to slow reactions occurring over longer, geological periods of time.

2.2.4 Apparatus

The furnace assemblies were run in a piston-cylinder apparatus with a half-inch diameter tungsten carbide piston and hardened steel chamber (Boyd and England 1960). Run conditions were attained using a hot piston-out technique, modified after Boyd et al. (1967), described as follows: [1] pressure on the cold sample was increased to a few kbar below run pressure (10 kbar); the power to the graphite resistance furnace was brought up to the run temperature, which also increased the pressure to just above 10 kbar; the pressure usually continued to rise 1-2 kbar over the next 30-60 minutes, during which time careful adjustments of the pressure controls settled the pressure back down to 10 kbar. The nominal pressure is considered accurate to ±5%. No friction correction was applied. Temperatures, recorded by welded W-Re_5/W-Re_{26} thermocouples, were precise to ±5°C and accurate to ±15°C. No significant long-term temperature drift occurred in the thermocouples, as shown by the constant power output throughout the experiments.

2.3 Analytical Methods

Microscopic observations were made using both reflected light and SEM backscattered electron imagery (BE). Textures were studied from photomicrographs taken in BE mode. The experiments were analyzed on a Camscan scanning electron microscope (SEM) with energy dispersive spectrometers (EDS) and a Jeol 733 electron microprobe (EMP) with wavelength dispersive spectrometers (WDS), both utilizing Tracor Northern software for quantitative mineral analysis. The software employs mineral and oxide

standards and Bence-Albee and Armstrong correction procedures (Bence and Albee 1968; Armstrong 1988). The SEM results are normalized to 100%.

The beam parameters on the EMP were 15 kV, 15 nA and spot mode for minerals and 15 kV, 5 nA and 10 μm diameter for glasses. The beam parameters on the SEM were 15 kV, 0.1 nA and spot mode for minerals or full-field, high magnification for glasses (approximately 5 μm diameter). Counting times for both machines were 60 or 100 seconds. Comparison of analyses of the same glasses shows that the results from both instruments are in excellent agreement with one another (Appendix 1). A similar positive correlation between the results of the EDS and WDS techniques was determined by Hollister et al. (1987). The low alkali content of the bulk rock and constituent phases and the low beam currents and unfocused beams solved any potential problem of alkali mobilization during analysis. Glass analyses were done in the centers of glass areas >20 μm^2 to eliminate adjacent phase fluorescence.

Eight phases were identified in the capsules: the two initial minerals, hornblende and anorthite, two new amphiboles, two pyroxenes, garnet, and glass. Identification of all the phases is based on SEM and EMP analyses.

Several methods were tried to obtain modes in order to record the progression of mineral reactions as a function of time and temperature. Mass balance calculations using phase analyses were attempted but did not correspond at all with the actual modes that can be determined visually, probably due to the similarities in compositions of the five pyriboles. Four-oxide, X-ray mapping using the SEM also did not work well in distinguishing between the different pyriboles.

Modes were determined by point counting using the electron microprobe. The electron microprobe was set up to give automated, rapid, partial analyses (herein designated as EMP-ARP analyses). Five oxides were analyzed: SiO_2, Al_2O_3, FeO, MgO, and CaO. Background readings were taken at the beginning and end of the entire probe run but not before and after each analysis. In every experiment 250 points were analyzed, each for

only five seconds. Phase discrimination was possible by using this technique. Since only five oxides were analyzed, low totals were expected, but the totals obtained are generally quite good, with amphibole totals summing to greater than 94% and the other mineral totals summing to greater than 98%. Liquid totals are somewhat lower (~90%), but this low total is normal for analyses of hydrous glasses. In future work, a combination of this EMP-ARP technique and the x-ray mapping technique (limited to the discrimination of a few very distinct phases) probably would yield the most accurate results.

A thin-section of the fine-grained amphibolite rock also was probed to determine original mineral modes and compositions. The EMP-ARP procedure was used on a 1 cm^2 grid containing 1063 points. The mode is within 3% of the approximate, optically determined mode, and the calculated mass balance also roughly agrees with the bulk composition determined by both XRF and DCP (Table 2.1).

The automated probe is necessary for obtaining quick, unbiased EMP modal analyses, but the major drawback with using the EMP-ARP method is that many of the analyses from the experiments do not represent single phases, but are mixtures of two or more proximal phases. This problem arises because the electron beam excites electrons and their resulting X-rays from a volume, not a point. In the very fine-grained experimental capsules, the sampling volume of the beam may be larger than the volume of a single crystal. This mixing problem is minimized in relatively coarse-grained natural rocks such as the thin-section of the amphibolite.

Phase identification from these partial EMP-ARP analyses is based upon the ranges in chemistry obtained by the full, quantitative SEM and EMP analyses (Appendix 2). All five oxides of each EMP-ARP analysis must fall within the respective oxide range of a pure phase to be considered a single phase and not a mixture. Each phase has its own set of oxide ranges, although considerable overlap results if an EMP-ARP analysis represents a combination of two similar phases. The prevalence of some particular phase mixtures probably is due to grain size and not to reaction relationships between the phases. The

results of the EMP-ARP technique are discussed below. Appendix 3 lists additional analyses of most of the phases from EMP-WDS for comparison with EMP-ARP and SEM-EDS.

Table 2.1. Amphibolite chemistry and mineralogy

Amphibolite starting composition			
Method	XRF	DCP	EMP-ARP*
SiO2	48.4	48.5	47.8
TiO2	0.4	0.4	n.d.
Al2O3	14.6	14.4	16.7
FeO	8.4	8.5	7.8
MnO	0.2	0.2	n.d.
MgO	10.7	10.8	10.0
CaO	14.3	14.8	14.3
Na2O	1.0	1.7	n.d.
K2O	0.1	0.2	n.d.
Total	98.1	99.5	96.6
		n = 2	

CIPW Norm from DCP	
Q	0.0
or	1.2
ab	12.6
an	31.2
ne	1.0
C	0.0
di	34.6
hy	0.0
ol	18.6
il	0.8

Mode from EMP-ARP	
Hornblende	67.4
Plagioclase	32.5
Sphene	0.1

Hornblende:

	SEM	sdm:23	EMP-ARP	sdm:669
SiO2	50.39	0.28	48.87	0.05
TiO2	0.36	0.03	n.d.	--
Al2O3	7.92	0.25	7.80	0.04
FeO	12.33	0.16	11.42	0.02
MnO	0.27	0.02	n.d.	--
MgO	15.32	0.17	14.86	0.03
CaO	13.10	0.04	12.45	0.01
Na2O	0.12	0.05	n.d.	--
K2O	0.12	0.02	n.d.	--
Total	100.00		95.40	0.05

Plagioclase:

	SEM	sdm:6	EMP-ARP	sdm:283
SiO2	45.55	0.23	45.42	0.06
TiO2	0.00	0.00	n.d.	--
Al2O3	34.60	0.14	35.06	0.04
FeO	0.25	0.06	0.19	0.01
MnO	0.00	0.00	n.d.	--
MgO	0.00	0.00	0.04	0.01
CaO	18.40	0.18	18.21	0.04
Na2O	1.19	0.10	1.09^	--
K2O	0.02	0.01	n.d.	--
Total	100.00		98.91	0.04

* determined by mass balance

n.d. = not determined

EMP-ARP = Electron MicroProbe - Automated, Rapid, Partial Analysis

sdm:#= standard deviation of the mean of n=# analyses.

^ = determined by difference

Table 2.2. Plagioclase compositions from amphibolite thin-section, normalized to 100 (SEM-EDS).

							Average	sdm:6	Very rare Plagioclase	
SiO2	44.97	45.35	45.65	46.16	46.34	44.84	45.55	0.23	50.47	66.97
TiO2	0.00	0.00	0.00	0.00	0.00	0.00	0.00	0.00	0.00	0.00
Al2O3	35.02	35.04	34.26	34.34	34.19	34.76	34.60	0.14	31.19	20.61
FeO	0.26	0.00	0.27	0.17	0.32	0.45	0.25	0.06	0.29	0.22
MnO	0.00	0.00	0.00	0.00	0.00	0.00	0.00	0.00	0.00	0.00
MgO	0.00	0.00	0.00	0.00	0.00	0.00	0.00	0.00	0.00	0.00
CaO	18.82	18.75	18.68	17.93	17.68	18.51	18.40	0.18	14.33	1.33
Na2O	0.96	0.79	1.16	1.43	1.50	1.30	1.19	0.10	3.65	10.90
K2O	0.00	0.09	0.00	0.00	0.00	0.00	0.02	0.01	0.09	0.00
Ions per 32 oxygens										
Si	8.310	8.361	8.433	8.501	8.533	8.313	8.409		9.215	11.739
Ti	0.000	0.000	0.000	0.000	0.000	0.000	0.000		0.000	0.000
Al	7.628	7.615	7.459	7.453	7.420	7.596	7.528		6.712	4.258
Fe	0.040	0.000	0.042	0.026	0.049	0.070	0.038		0.044	0.032
Mn	0.000	0.000	0.000	0.000	0.000	0.000	0.000		0.000	0.000
Mg	0.000	0.000	0.000	0.000	0.000	0.000	0.000		0.000	0.000
Ca	3.726	3.704	3.697	3.538	3.488	3.677	3.638		2.803	0.250
Na	0.344	0.282	0.415	0.511	0.536	0.467	0.426		1.292	3.705
K	0.000	0.021	0.000	0.000	0.000	0.000	0.004		0.021	0.000
sdm:6 = standard deviation of the mean of n=6 anayses.							An89		An68	An6

Table 2.3. Hornblende compositions from amphibolite thin-section, normalized to 100 (SEM-EDS).

SiO2	50.08	49.87	50.67	51.62	50.17	53.32	50.04	51.05	48.86	50.80	50.50	50.93	51.76
TiO2	0.49	0.43	0.44	0.00	0.25	0.00	0.41	0.37	0.48	0.46	0.35	0.30	0.25
Al2O3	8.45	7.92	8.05	7.08	8.69	5.04	7.84	7.57	9.73	7.76	7.96	8.05	6.78
Cr2O3	0.00	0.00	0.20	0.15	0.00	0.00	0.19	0.00	0.16	0.17	0.00	0.00	0.00
FeO	12.51	12.88	11.96	11.65	12.65	10.44	12.58	12.27	13.08	12.01	12.39	11.87	11.32
MnO	0.22	0.18	0.27	0.00	0.30	0.30	0.31	0.16	0.43	0.30	0.21	0.30	0.26
MgO	14.94	15.24	15.08	15.99	14.67	17.38	15.37	15.55	13.94	15.47	15.68	15.35	16.70
CaO	13.22	12.92	13.28	13.13	13.30	13.41	13.32	12.97	12.78	13.07	12.95	13.09	12.87
Na2O	0.00	0.45	0.00	0.42	0.00	0.00	0.00	0.00	0.48	0.00	0.00	0.00	0.00
K2O	0.14	0.15	0.10	0.00	0.00	0.15	0.00	0.10	0.09	0.00	0.00	0.15	0.12
Ions per 23 oxygens													
Si	7.068	7.064	7.131	7.241	7.078	7.438	7.074	7.179	6.932	7.144	7.110	7.155	7.247
Al4	0.932	0.936	0.870	0.759	0.922	0.562	0.926	0.821	1.068	0.856	0.890	0.845	0.753
Al6	0.472	0.385	0.465	0.411	0.523	0.265	0.379	0.433	0.559	0.430	0.430	0.488	0.364
Ti	0.051	0.045	0.046	0.000	0.027	0.000	0.043	0.039	0.051	0.048	0.037	0.032	0.026
Fe	1.477	1.526	1.407	1.366	1.492	1.217	1.487	1.442	1.552	1.412	1.458	1.395	1.325
Mn	0.025	0.022	0.032	0.000	0.036	0.035	0.036	0.018	0.051	0.035	0.024	0.035	0.030
Mg	3.142	3.218	3.164	3.343	3.085	3.613	3.238	3.260	2.947	3.243	3.291	3.214	3.484
Cr	0.000	0.000	0.021	0.016	0.000	0.000	0.021	0.000	0.018	0.018	0.000	0.000	0.000
Ca	1.999	1.961	2.002	1.974	2.010	2.004	2.017	1.954	1.943	1.970	1.953	1.970	1.930
Na	0.000	0.122	0.000	0.113	0.000	0.000	0.000	0.000	0.132	0.000	0.000	0.000	0.000
K	0.025	0.026	0.017	0.000	0.000	0.025	0.000	0.018	0.015	0.000	0.000	0.026	0.020
X	2.023	2.109	2.019	2.087	2.010	2.030	2.017	1.972	2.090	1.970	1.953	1.996	1.950
Y	5.168	5.196	5.135	5.136	5.162	5.131	5.204	5.192	5.178	5.186	5.240	5.163	5.229
Mol.%													
Mg#	68.0	67.8	69.2	71.0	67.4	74.8	68.5	69.3	65.5	69.7	69.3	69.7	72.5
Ca	30.2	29.2	30.5	29.5	30.5	29.3	29.9	29.4	30.2	29.7	29.1	29.9	28.6
Mg	47.5	48.0	48.1	50.0	46.8	52.9	48.0	49.0	45.8	49.0	49.1	48.9	51.7
Fe	22.3	22.8	21.4	20.4	22.7	17.8	22.1	21.7	24.1	21.3	21.8	21.2	19.7

X = Ca+Na+K; Y = Mg+Fe+Al6+Ti+Mn+Cr; Z = Si+Al4

sdm:23 = standard deviation of the mean of the 23 analyses.

Table 2.3 (cont.). Hornblende compositions (SEM-EDS).											Hb avg.	sdm:23
SiO2	47.89	49.96	51.04	50.35	50.45	51.82	51.02	50.05	50.41	46.34	50.39	0.28
TiO2	0.57	0.57	0.18	0.40	0.46	0.47	0.22	0.43	0.23	0.52	0.36	0.03
Al2O3	10.14	7.95	7.27	7.83	7.96	6.50	7.05	7.76	7.85	10.99	7.92	0.25
Cr2O3	0.00	0.00	0.00	0.13	0.00	0.00	0.00	0.37	0.00	0.00	0.06	0.02
FeO	12.89	12.65	12.00	12.64	12.19	11.75	12.30	12.47	12.26	14.83	12.33	0.16
MnO	0.29	0.23	0.35	0.33	0.40	0.32	0.15	0.40	0.26	0.27	0.27	0.02
MgO	14.11	15.22	15.43	15.24	15.32	15.92	15.85	15.15	15.29	13.37	15.32	0.17
CaO	13.12	13.12	13.36	12.90	13.09	13.16	13.09	13.20	13.21	12.75	13.10	0.04
Na2O	0.93	0.00	0.00	0.00	0.00	0.00	0.00	0.00	0.00	0.45	0.12	0.05
K2O	0.10	0.19	0.16	0.22	0.17	0.10	0.16	0.22	0.18	0.33	0.12	0.02
Ions per 23 oxygens												
Si	6.815	7.065	7.192	7.114	7.113	7.276	7.190	7.084	7.115	6.663	7.108	
Al4	1.185	0.935	0.808	0.887	0.887	0.724	0.810	0.916	0.885	1.337	0.892	
Al6	0.515	0.390	0.399	0.416	0.435	0.351	0.361	0.377	0.420	0.525	0.426	
Ti	0.061	0.060	0.019	0.042	0.048	0.049	0.022	0.045	0.024	0.056	0.038	
Fe	1.534	1.496	1.414	1.494	1.437	1.379	1.450	1.476	1.446	1.783	1.455	
Mn	0.035	0.028	0.041	0.039	0.048	0.038	0.018	0.048	0.030	0.032	0.032	
Mg	2.992	3.208	3.240	3.208	3.218	3.332	3.329	3.195	3.217	2.866	3.219	
Cr	0.000	0.000	0.000	0.015	0.000	0.000	0.000	0.041	0.000	0.000	0.007	
Ca	2.001	1.989	2.017	1.952	1.977	1.979	1.976	2.002	1.998	1.964	1.980	
Na	0.256	0.000	0.000	0.000	0.000	0.000	0.000	0.000	0.000	0.123	0.032	
K	0.017	0.034	0.028	0.039	0.029	0.016	0.028	0.039	0.031	0.060	0.021	
X	2.274	2.023	2.045	1.991	2.006	1.995	2.003	2.041	2.029	2.148	2.034	
Y	5.137	5.181	5.112	5.213	5.186	5.150	5.180	5.182	5.137	5.262	5.176	
Mol.%												
Mg#	66.1	68.2	69.6	68.2	69.1	70.7	69.7	68.4	69.0	61.6	68.8	
Ca	30.6	29.7	30.2	29.3	29.8	29.6	29.3	30.0	30.0	29.7	29.8	
Mg	45.9	47.9	48.6	48.2	48.5	49.8	49.3	47.9	48.3	43.3	48.4	
Fe	23.5	22.4	21.2	22.4	21.7	20.6	21.5	22.1	21.7	27.0	21.9	

X = Ca+Na+K; Y = Mg+Fe+Al6+Ti+Mn+Cr; Z = Si+Al4

sdm:23 = standard deviation of the mean of the 23 analyses.

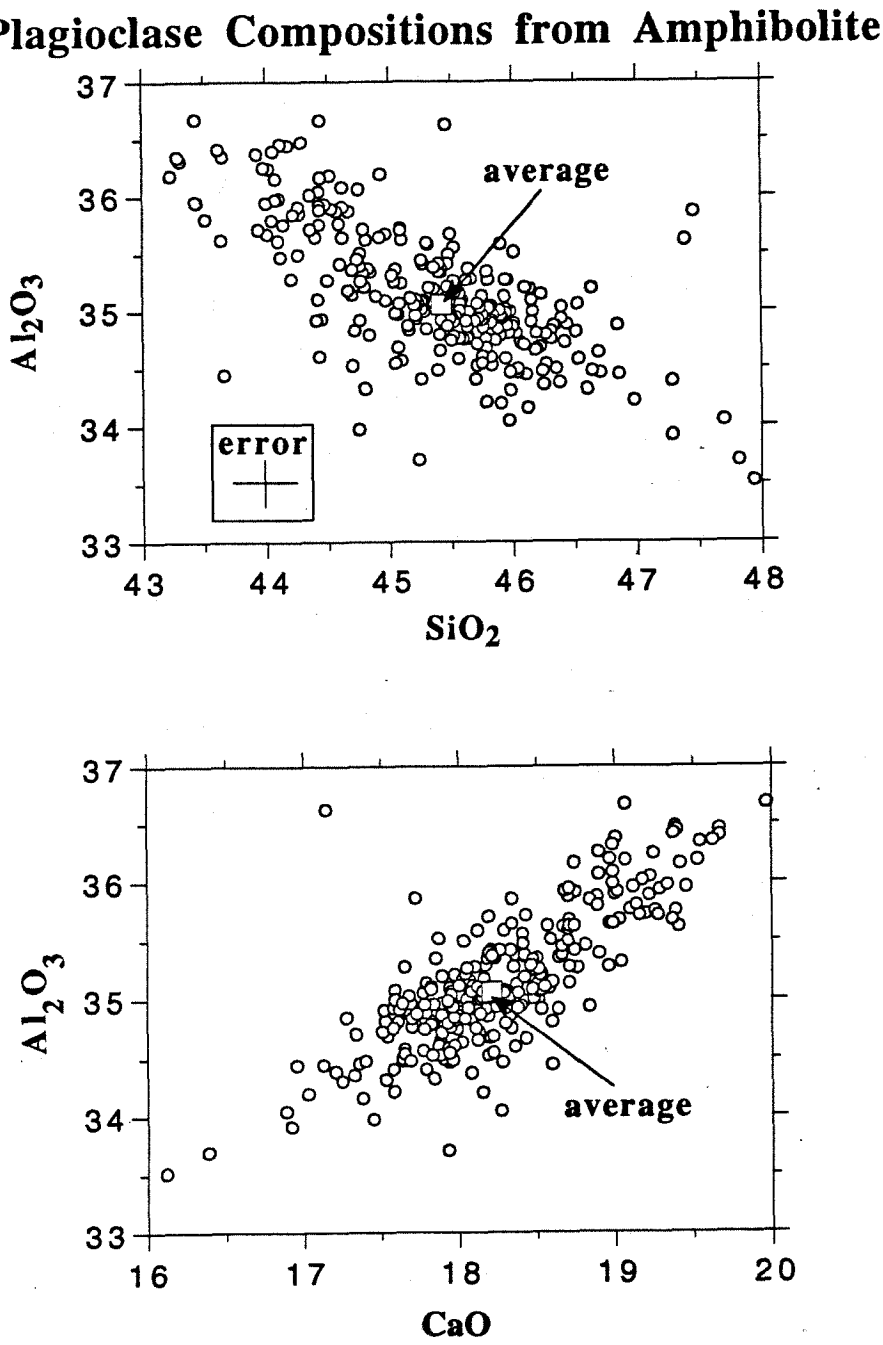

Fig. 2.1. The compositional variation of the anorthitic plagioclase from a thin-section of the amphibolite, from 283 EMP-ARP (electron microprobe-automated, rapid, partial) analyses (see text for explanation). The averages of these analyses (large squares) are listed in Table 2.1. Standard deviation of the means of the average analyses are 0.06 or better.

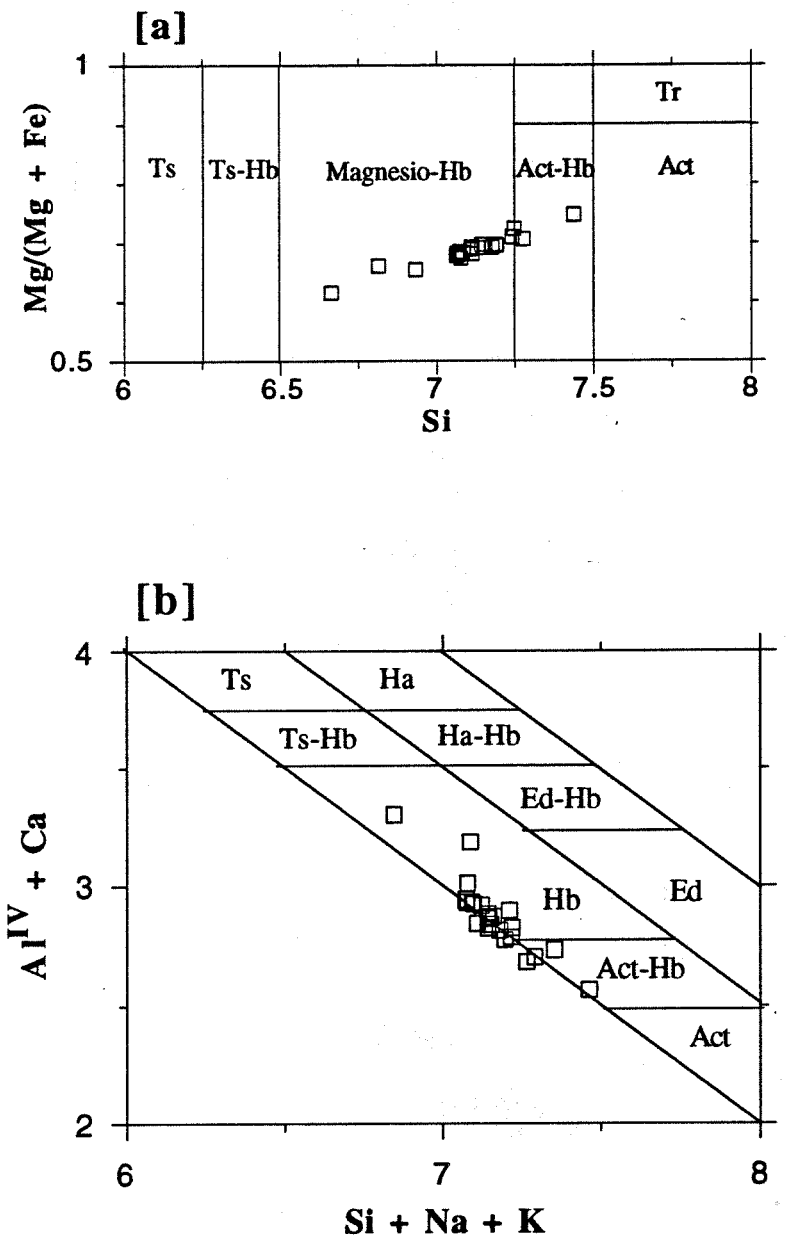

Fig. 2.2. Classification schemes for amphiboles from SEM-EDS analyses Table 2.3, after: [a] Rock and Leake (1984) and [b] Giret et al. (1980). Amphibole is magnesio-hornblende. Hb: hornblende; Act: actinolite; Ed: edenite; Ha: hastingsite; Ts: tschermakite; Tr: tremolite.

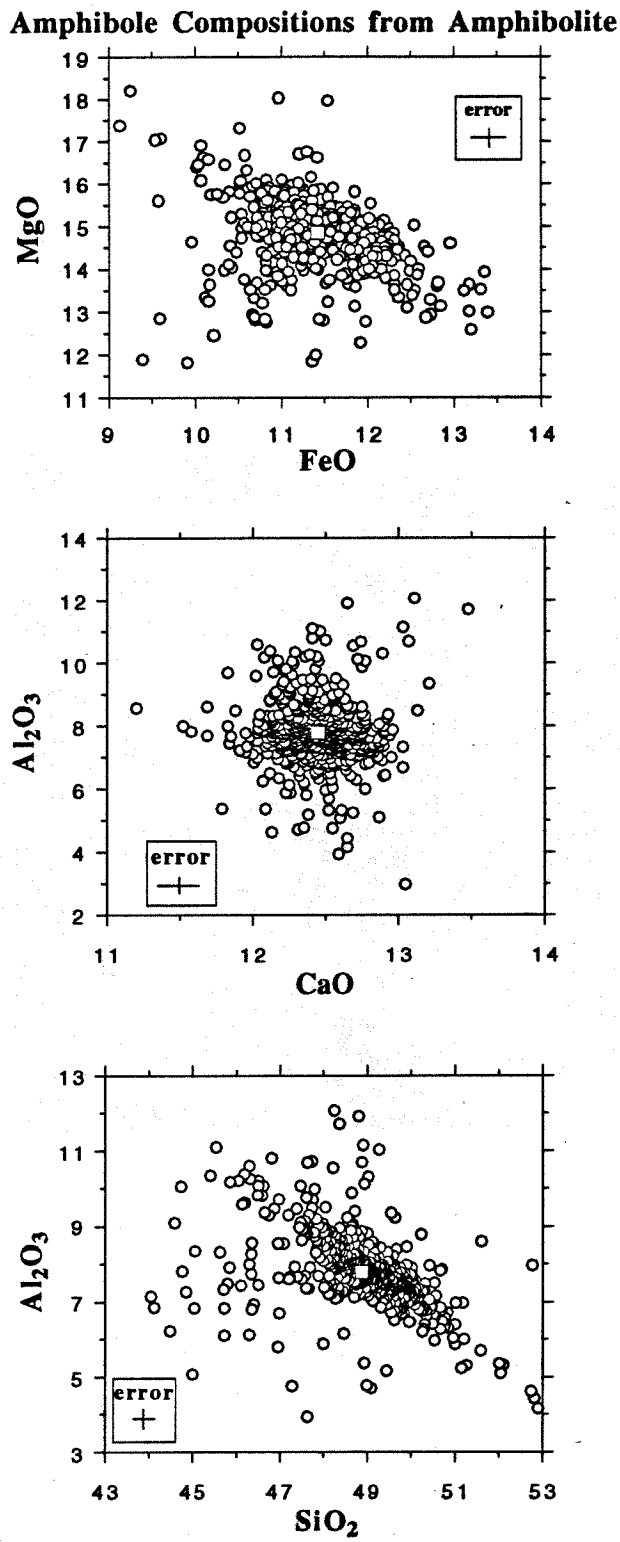

Fig. 2.3. The compositional variation of the hornblende from a thin-section of the amphibolite, from 669 EMP-ARP analyses. The averages of these analyses (large squares) are listed in Table 2.1. Standard deviation of the means of the average analyses are 0.05 or better.

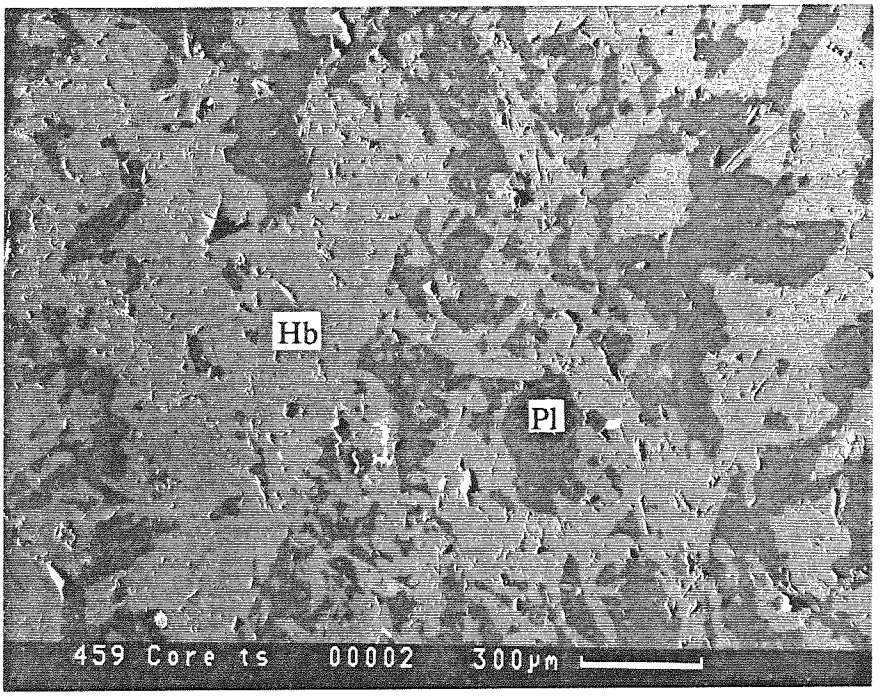

Fig. 2.4. Backscattered electron SEM photomicrograph of a thin-section of the amphibolite starting material. Hb: hornblende; Pl: plagioclase.

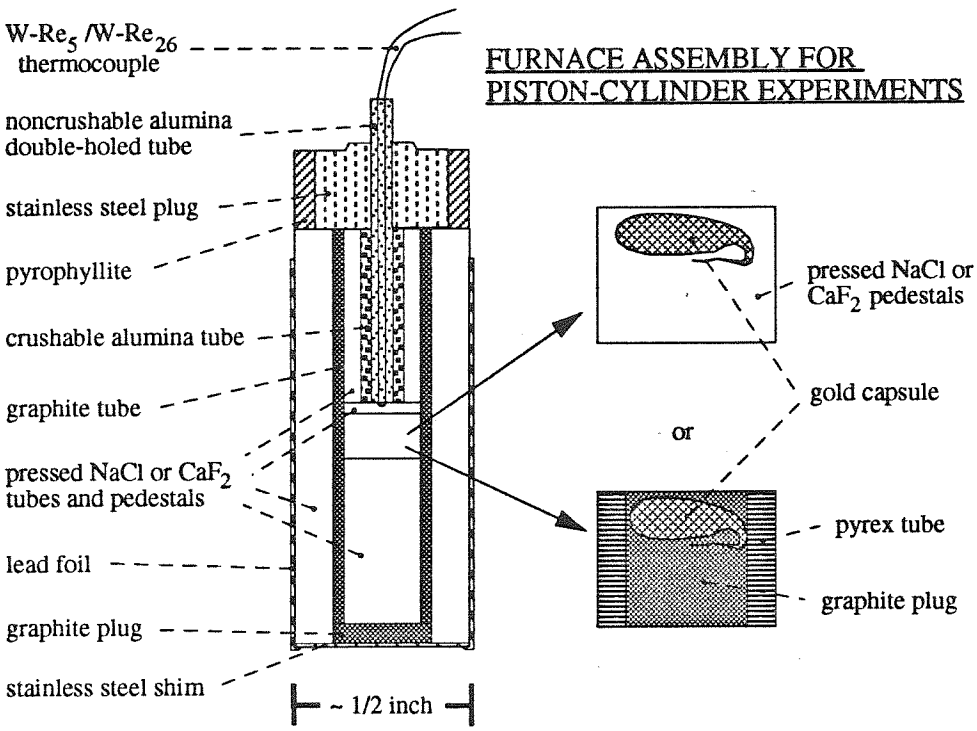

Fig. 2.5. Furnace assembly design for piston-cylinder experiments.

CHAPTER 3. EXPERIMENTAL RESULTS

3.1 Powder Experiments

3.1.1 Phase Relationships and Modes

Figure 3.1 is a temperature-time phase diagram of the powdered amphibolite experiments and displays the phase assemblages and the phase boundaries that separate them, based on run data summarized in Table 3.1. The positions of runs using solid amphibolite also are shown, but these runs reacted differently, as discussed below. The locations of the boundaries were determined using optical and scanning electron microscopes.

Many of the experiments done in the past and at the present were and still are being run for relatively short durations of a few minutes to a few days. It is clear from Fig. 3.1 that in this complex, natural system, the position of the reaction boundaries is time-dependent. More accurate reaction temperatures (i.e., those closer to equilibrium) are attained only after run durations of at least a week at temperatures throughout most of the melting interval of this amphibolite. The reaction sequence in these longer-duration runs is described below, followed by a comparison with the shorter-duration runs.

At the lowest temperatures of the longer duration experiments, the assemblage hornblende and plagioclase reacts to form clinopyroxene and liquid. Dehydration-melting of the amphibolite produces silicic liquids with compositions similar to tonalite or quartz diorite, although with higher alumina contents. With increasing temperature, many of the hornblendes have higher CaO or Al_2O_3 contents than the range in initial hornblende compositions. At still higher temperatures, orthopyroxene and garnet appear (Fig. 3.1). The calcic hornblende disappears between 925°C and 950°C.

High temperature runs (>950°C) tended to fail (e.g., capsule leaks, thermocouple breaks) in the longer duration runs. Runs with durations shorter than 8 days help constrain

many of the mineral-out reaction boundaries at these high temperatures. There appears to be a cross-over in the initial and Ca-rich hornblende-out reaction boundaries at ~950°C after ~5 days. The Al-rich hornblende, probably the stable, high-temperature hornblende, disappears at approximately 980°C. Although present as a minor mineral at 990°C for 1 day, garnet disappears above 975°C in the 4-day run. At the highest run temperature (1000°C), the assemblage is liquid, clinopyroxene, orthopyroxene, and plagioclase. This high-temperature liquid composition is high-alumina basaltic.

Modal analyses (determined by automated, rapid, partial electron microprobe analysis: EMP-ARP) are reported in Table 3.1. Phases that were identified by scanning electron microscope using an energy dispersive spectrometer (SEM-EDS) but not by EMP-ARP are listed with an "X" in Table 3.1. The errors associated with the modes could be rather large, because of the variability in the percent of volume mixing in EMP-ARP analyses in the runs; because 10-60% of the 250 EMP-ARP analyses of each run are mixtures of phases, and these mixed analyses are not used in the mode, the number of good analyses varies from 90-40% of 250, or 225-100. However, the modes of the lowest temperature experiments do approximate the rock mode, so the rest of the modal analyses are considered accurate (to ±5% absolute error). One exception is that the EMP-ARP technique cannot accurately determine the phase boundary locations due to the small quantity of the new phase. The minerals in the powdered runs are assumed to have no preferred orientation, so the slices through the capsules reveal an average amount of each phase. Thus, modal proportions from these cut surfaces are taken to be the volume percentages of the phases throughout the capsules.

Figure 3.2 is a graphical representation of the modal data from Table 3.1. This figure shows the phase modes of all of the powder experiments as histograms that are positioned with temperature versus time. The columns within the individual histograms are arranged so that the reactants are to the left and the products are to the right: hornblende, plagioclase, Ca-rich hornblende, Al-rich hornblende, orthopyroxene, garnet,

clinopyroxene, liquid. The products are generally ordered so that phases that are present at higher temperatures are placed farther to the right. With this arrangement of phases, the reaction progress can be visualized as the changes in column heights sweep across the histograms from left to right as both temperature and time increase. Hornblende and plagioclase are the predominant low temperature phases. Garnet, clinopyroxene, plagioclase, and liquid are the predominant phases in the higher temperature runs (both short and long durations). Clinopyroxene and liquid (±garnet) are the major phases at the highest temperatures.

Figure 3.3 is a graphical representation of the eight-day and four-day modal data from Table 3.1 and focuses on the modal effects of temperature. The highest temperature 8-day run is at 925°C, so at higher temperatures the data from 4-day runs are used. Figure 3.3 is slightly modified from Table 3.1 to show more accurately the temperature at which the new phases appear. For instance, instead of a smooth extrapolation for the modal increase of garnet between 800°C and 850°C, the garnet-in area in Fig. 3.3 (8-day runs) was modified to correspond with the 825°C garnet-in boundary from Fig. 3.1. In general, with increasing temperature, as hornblende and anorthite decrease in quantity, liquid and clinopyroxene increase to ~47 and ~46 vol.%, respectively. The combined amounts of new hornblende increase to about 15 vol.% but decrease above 925°C. Orthopyroxene is a minor mineral throughout most of the melting interval. The large modal increase in garnet at 875°C may be due to the position of this run near the middle of the garnet stability field. The 4- and 8-day data overlap between 900°C and 925°C in Fig. 3.3 and can be directly compared. The changes in the relative amounts of the phases throughout this temperature interval are similar for runs of both durations.

The solidus was not located, as a small amount of liquid is present in the lowest temperature run at 750°C. The percentage of liquid generated as a function of temperature and time is shown in Figs. 3.4a,b. In Fig. 3.4a, the amount of liquid in the 8-day runs increases from 1% to ~9% with increasing temperature from 750°C to 875°C. Above

875°C, the liquid fraction increases rapidly with temperature; the amount of liquid increases from ~9% to 30% in the 50°C interval from 875°C to 925°C. The increase in liquid fraction in the 900-1000°C 4-day runs parallels the 8-day increase. The 2-day runs also show this same trend. The 8-, 4- and 2-day runs yield the expected trend of increasing liquid fraction with increasing temperature. The 1-day runs do not conform to the trend because the runs at 925°C and 950°C contain too much liquid – about twice as much as predicted from the longer duration trends (clearly illustrated by Fig. 3.4b). The inconsistency in the 1-day runs may be explained by the lack of equilibrium in experiments of this duration.

Time does not have as strong an effect as temperature does on the percent of liquid generated, but, in general, longer duration experiments contain more liquid than shorter ones at a given temperature. Taken as a whole, the data in Fig. 3.4a show that the volume of liquid increases from about 1% to 47% with increasing temperature from 750°C to 1000°C.

Figure 3.4b shows that in general, the amount of liquid increases as the run duration lengthens. The parallelism of the 875°C, 925°C and 975°C trends indicates that the rate of liquid production may be a constant that is temperature-independent. Based on the slopes of the other temperature trends, the 900°C, 9-day run should have ~20% liquid, but has only 2%. This inconsistency also shows up as modal differences in Figs. 3.2 and 3.3. The result from the 900°C, 9-day run cannot be easily explained and may indicate a problem with this run (#106), such as the misplacement of the capsule outside of the furnace hotspot. However, all of the 900°C runs (Table 3.1) are consistent with each other in having low amounts of liquid (and garnet) relative to the runs at 875°C and 925°C. Thus, it is possible that these modal differences (apparent discrepancies) are due to the complexities of the dehydration-melting reactions within the natural amphibolite.

Because the trends in Fig. 3.4b are not perpendicular, the equilibrium values of liquid fractions have not be attained for any of these temperatures. Presumably, at some time longer than that of the runs, equilibrium is achieved and a further increase in run

duration will not result in the production of more liquid, and the liquid trends will become vertical, as shown by the theoretical nonequilibrium liquid fraction curves in Fig. 3.4c.

3.1.2 Crystal Morphology

3.1.2.1 Hornblende and Orthopyroxene

Differences in SEM back-scattered (BE) imaging reflectivity accompany compositional changes in the new hornblendes, but the morphology of the new hornblendes is not different than that of the initial hornblende. The boundaries between different hornblende compositions are generally diffuse and anastomosing. At all but the highest temperatures anhedral orthopyroxene also shows only subtle differences with the hornblendes in BE imaging mode. The orthopyroxene is euhedral and easily recognizable only at 1000°C, in the absence of hornblende.

3.1.2.2 Clinopyroxene

The shapes of the clinopyroxene crystals are both time- and temperature-dependent. The shorter duration and lower temperature runs preserve small, euhedral, acicular (needle-like) crystals with aspect ratios over 1:5 (Figs. 3.5 and 3.6). It is possible that these crystals really have aspect ratios more similar to pancakes rather than needles, and that the two-dimensional photomicrographs never reveal the true morphology but only show needle-like slices cut perpendicular through the plane of the pancake. However, it is more likely that the photomicrographs would show some clinopyroxene crystals to have the pancake shape if indeed they really had that shape. Thus the observed acicular morphology is assumed to be real and not an artifact of the view. The crystals grow more blocky (aspect ratio ~1:2) and subhedral with increasing run duration and temperature (Fig. 3.7). Figure 3.8 illustrates this morphological time-temperature relationship. The morphological change from acicular to blocky occurs gradually across the boundary, as can be seen in the fairly continuous changes in Figs. 3.5-3.7.

Most of the early-forming acicular crystals are located at the boundaries of hornblende grains, which may be bounded by plagioclase, liquid or, most commonly, other hornblende grains. The long axes of the clinopyroxenes are oriented along (parallel to) these boundaries. Thus, the orientations of the clinopyroxene crystals are controlled initially by the orientations of the hornblende grain boundaries. These hornblende-hornblende boundaries initially contain a very fine mixture of sub-micron hornblende ± plagioclase. Most clinopyroxene crystals nucleate along these gouge-filled hornblende-hornblende boundaries rather than along hornblende-plagioclase boundaries. Liquid generally is not associated with the clinopyroxenes wholly surrounded by large hornblende grains but may be present at clinopyroxene, hornblende and plagioclase junctions. In the higher temperature and/or longer duration runs, the clinopyroxenes are either small, separate, blocky crystals or are patches within larger hornblende grains. Liquid generally surrounds the smaller clinopyroxene crystals but rarely is found along the clinopyroxene-hornblende interfaces within the larger patches.

3.1.2.3 Garnet

Garnet grow very rapidly and to very large sizes in the powdered amphibolite experiments. The garnets grow as euhedral, trapezohedron-modified dodecahedrons. The size and number of garnets generally increase as the duration and temperature increase (Figs. 3.6, 3.7, and 3.9-3.11). Enlargement mostly is due to single grain growth, not the aggregation of multiple small grains. At high temperatures garnets appear within a day.

As they rapidly grow, the garnets engulf the other minerals, forming relatively large (0.1-0.7 mm) poikiloblasts. A comparison of the EMP-ARP garnet mode with a cursory glance of the photomicrographs appears to give very different results (Table 3.1 and Figs. 3.6, 3.7, 3.9, and 3.10). In some of the higher temperature, longer duration runs, visual estimates based on garnet crystal boundaries indicate that ~60% of the capsule volume is garnet – much higher than the quantitative analyses. This difference is due to the

poikiloblastic nature of the garnet phenocrysts, with the included phases comprising up to 40% of the volume within the boundaries of the garnet crystals.

The modes of the included phases were approximated by visual inspection of photomicrographs. The modes of phases inside and outside of the garnets are similar, except that liquid is not found in the poikiloblasts. There is little correlation between the volume percent of inclusions and the temperature, however, there is a slight increase in the number of tiny, 5 μm, included grains with increasing temperature. Thus the inclusion size within the garnets is slightly temperature dependent. At higher temperatures the faster growth of garnet traps more small hornblende grains before they disappear, although some of the hornblendes are replaced by pyroxenes before entrapment. The distribution of small grains does not decrease toward the perimeter of the garnet poikiloblasts, indicating either that the garnet growth rate may be more rapid than the hornblende decomposition rate or that the reaction of hornblende to pyroxene may preserve the small grains.

Fast crystal growth often results in crystal geometries conducive to liquid entrapment, such as skeletal, dendritic and hopper structures (Lofgren 1980, 1983; Cashman and Marsh 1988), but the garnets do not have these features. Garnet growth was too slow to engulf any pockets of liquid. Since liquid is not trapped, a record of its compositional evolution within a given run is not available.

3.1.3 Mineral Compositions

3.1.3.1 Clinopyroxene

Clinopyroxene (Cpx: diopsidic augite) occurs in every run. It is the first mineral product of the hornblende breakdown (Fig. 1), and in the highest temperature run at 1000°C, it also coexists with liquid, orthopyroxene and plagioclase. The clinopyroxene compositions, listed in Table 3 and plotted in Fig. 5, exhibit no detectable trend.

3.1.3.2 New Hornblendes

The breakdown of the initial hornblende (Hb) at higher temperatures produces two new, compositionally distinct amphiboles as well as clinopyroxene and liquid (Fig. 3.1). The compositions of all of the amphiboles from the powder experiments are listed in Table 3.3 and plotted in Figs. 3.12 and 3.13a,b. The amphibole compositions are plotted twice in Fig. 3.13 to show different relationships (compare with Figs. 2.2a,b). In Fig. 3.13a the initial hornblende compositions fall mostly in the magnesio-hornblende field but extend into the actinolitic hornblende field, plotted as Mg/(Mg + Fe) versus Si (after Rock and Leake 1984). One of the new amphiboles fills the tschermakitic hornblende field. The other new amphibole is not distinguishable from the initial composition in Fig. 3.13a. However, in Fig. 3.13b all three compositions have been separated in Al^{IV} + Ca versus Si + Na + K space (after Giret et al. 1980). In this figure, the new minerals are still hornblendes, although they plot near the tschermakitic end of the hornblende field. Both new hornblendes contain more Al^{IV} + Ca than the initial hornblende. Relative to each other and the initial hornblende, the tschermakitic hornblende contains more Al^{IV}, and the other new hornblende contains more Ca. Since no one plotting scheme adequately describes these hornblendes, they are labelled as follows: the initial hornblende as (Hb), the new aluminous, tschermakitic hornblende as (Al-Hb), and the new calcic hornblende as (Ca-Hb).

3.1.3.3 Orthopyroxene

Moving to temperatures above the new hornblende-in curves in Fig. 3.1, orthopyroxene (Opx) and garnet (Ga) both appear within the same temperature intervals. Orthopyroxene is not abundant at any temperature. Orthopyroxene compositions are listed in Table 3.4 and plotted also in Fig. 3.12. The chemical similarities between orthopyroxene and Fe-Mg amphibole (cummingtonite) do not allow definitive mineral identification based upon microprobe analysis. Optical identification of the very fine-

grained experimental products also is not definitive. I consider the Fe-Mg pyriboles to be pyroxenes because experimental data shows that cummingtonite breaks down to orthopyroxene above 700°C under water-deficient conditions (Robinson 1982). The orthopyroxene is bronzite, based on its $En_{71.4}$ composition [100*Mg/(Mg + Fe + Mn)].

3.1.3.4 Garnet

The averaged compositions of the garnets are listed in Table 3.5 and plotted in Fig. 3.14a. Averages include both core and rim analyses from one or more crystals from each run. The garnet compositions vary from $pyrope_{35}$-$grossular_{23}$-$(almandine+spessartine)_{42}$ to $pyrope_{50}$-$grossular_{21}$-$(almandine+spessartine)_{29}$ with increasing temperature. The grossular component does not change much throughout the temperature range. Huang and Wyllie (1986) and Carroll and Wyllie (1990) report similar increases in the pyrope component with increasing temperature, but the garnets in their 15 kbar gabbro and tonalite melting experiments varied more in the grossular component. Green and Adam (1991) found that the grossular component is affected much more by pressure changes than by temperature changes, an effect that I am not able to assess in my isobaric study. The EMP-ARP garnet data plotted in Fig. 3.14a are listed in Appendix 4.

Most of the garnets are zoned. Figure 3.14b shows the variation in pyrope content in some garnet cores and rims of individual crystals as a function of run temperature and duration. The grossular component is taken to be an almost constant ~22 mol.% (Fig. 3.14a), so that the variation in pyrope content in Fig. 3.14b adequately defines the compositional zoning within the garnets. Together, Figs. 3.14b and 3.14a show that the compositional variation between cores and rims within zoned garnets at a single temperature (tie-lines; Fig. 3.14b) is generally less than the variation of averaged garnet compositions at different temperatures (circles; Fig. 3.14a). Figure 3.14b also reveals a reversal in the garnet compositional trend above 975°C (to pyrope-poorer values).

Compositional profiles of representative zoned garnets are shown in Fig. 3.15. The zoning spans the entire crystals from cores to edges, regardless of the duration or temperature. The compositional range is less than three weight percent in any oxide. The greatest zoning is in FeO. In general, cores have more FeO and MnO, and less SiO_2, Al_2O_3, and MgO than rims. The core-to-edge CaO compositional trends are not well defined, but the compositional trends of MgO and CaO are mirror images in the 925°C garnet profile.

The variation in core and edge compositions as a function of temperature can be seen by comparing the oxide profile locations in the three garnets. The SiO_2 profile is located at higher values of SiO_2 at higher temperatures, and thus total SiO_2 in the garnet is greater at higher temperatures. Likewise, Al_2O_3 and MgO profiles increase and FeO, and marginally, CaO, TiO_2 and MnO profiles decrease with increasing temperatures.

The core-to-edge oxide profiles of garnets that grew at 925°C are plotted as a function of time in Fig. 3.16. The temperature and time parameters can be compared by studying Figs. 3.15 and 3.16. In Fig. 3.16, Al_2O_3 increases and FeO decreases throughout the entire garnet crystal with increasing experimental duration, but in Fig. 3.15, Al_2O_3 decreases and FeO increases in the cooler, longer experiments. Thus, the profile changes in Fig. 3.15 are clearly a function of changes in temperature, not duration. In Fig. 3.16, the lengths of the profiles show that the garnets grow larger in the longer duration experiments. For the most part, these profiles agree with the Fig. 3.15 profiles in that the cores contain more FeO, MnO and TiO_2 and less SiO_2 and Al_2O_3. If the two day experiment is discounted, the cores generally also contain more CaO and less MgO than the edges.

It is instructive to view each profile as a time curve (with forward in time to the left in Fig. 3.16), because each garnet grew outward as a single crystal through time. It is clear that the compositions of the garnets continually evolved through time. Each set of oxide profiles also shows the compositional evolution of the garnets through time. Within each

set, a profile should look like the next longer duration profile after the specified passage of time, and each profile should have looked like the last shorter duration profile before the specified passage of time. For example, taking the FeO set, after another day at 925°C, the one-day profile should look like the two-day profile and, after six more days, like the eight-day profile. What is now the eight-day profile looked like the one-day profile after one day. A direct comparison now can be made between the profile termini, i.e., the core and edge compositions in different duration experiments (Fig. 3.16). The SiO_2, FeO and MnO contents at the cores generally decrease through time [$(\partial C_c/\partial t)$ is negative], but the TiO_2, Al_2O_3 and CaO contents at the cores generally increase through time [$(\partial C_c/\partial t)$ is positive], from one to eight days, where ∂C_c is the change in composition ($_c$ = in the core), and ∂t is the change in time. The MgO content at the cores does not vary through time. At the edges of the garnet crystals, most of the time-dependent compositional trends are equivocal; however, FeO clearly decreases, and Al_2O_3 clearly increases through time. In each of these two sets of profiles, the slopes of the profiles are parallel to one another. In Fig. 3.16, the slopes of the core compositional trends (dashed lines) also can be compared with the slopes of the edge-to-core profiles (solid lines). Al_2O_3 in the cores increases through time, but the Al_2O_3 compositional gradients decrease from the edges to the cores, i.e., $(\partial C_c/\partial t)$ is positive, but $(\partial C/\partial X_{e\text{-}c})$ is negative, where $\partial X_{e\text{-}c}$ is the change in distance from the edge to the core. In contrast, for FeO and MnO, $(\partial C_c/\partial t)$ is negative, but $(\partial C/\partial X_{e\text{-}c})$ is positive. In contrast to these oxides, for SiO_2, $(\partial C_c/\partial t)$ is negative, and $(\partial C/\partial X_{e\text{-}c})$ also is negative. For TiO_2, $(\partial C_c/\partial t)$ is positive, and $(\partial C/\partial X_{e\text{-}c})$ also is positive. Thus, the intracrystalline behavior of these elements may be very different from one another. One potential problem, though, is whether the garnet crystals were truly bisected and thus had their cores exposed for analysis. The composition of the measured "core" would have been different than that of the true core. For instance, it is possible that some of the decrease in FeO through time is due to an off-centered core measurement. Analysis of the largest

garnets in the runs helped to minimize this problem, as these garnets were more likely to represent bisected crystals than were smaller ones.

3.1.3.5 Plagioclase

Table 3.6 lists the compositions of 16 plagioclases from the powder experiments. The average composition is An_{92}, which is slightly higher than the An_{90} composition of the initial plagioclase – the average of 283 EMP-ARP analyses. Although the direction of the compositional shift (to higher An content) is consistent with the increased temperatures of the runs, this difference probably has no real significance. Thus no obvious change in composition of the starting anorthitic plagioclase could be detected by either SEM or EMP analysis of the experimental products (compare Tables 2.1, 2.2 and 3.6). No trace of marginal zoning is detected in any of the plagioclase crystals. Modal analyses show that the amount of plagioclase decreases with increased temperature, confirming that it does participate in some reaction.

3.1.4 Liquid Compositions

3.1.4.1 Compositional Trends

Glass, quenched silicate liquid (Liq), occurs in all runs. The dehydration-melting produces calcium- and alumina-rich silicate liquids that are similar to quartz diorites and high-alumina tonalites (Table 3.7 and Fig. 3.17a). In the An-Ab-Or system of Fig. 3.17a, all liquids plot in the tonalite field, but they vary as a function of temperature and time, as shown in the expanded Fig. 3.17b. With progressive fusion the liquid compositions become richer in the albite component, until approximately 975°C is reached. However, at temperatures near and above 975°C, the liquid trends reverse direction, as the liquid compositions become richer in the anorthite component.

Trends for different experimental durations coincide reasonably well and indicate that the liquids may be in equilibrium with the mineral assemblage that produced them,

although the system as a whole may not have attained equilibrium. The four day, garnet-absent trend reverses its direction above 975°C and heads back toward the anorthite apex. The 990°C one day experiment has only a minute amount of garnet, so the one day trend does not have as large a reversal in liquid composition as the four day trend, but it does turn back. The liquid compositions are strongly dependent on temperatures. The weaker, time-composition correlation, however, may be due to the time-dependent nature of the interplay between mineral growth and destruction. In other words, the rapid and continued growth of garnet counterbalances liquid-producing reactions by consuming components of the hornblende breakdown that otherwise would remain in the silicate liquid.

The liquid compositional trends, plotted in Fig. 3.18 as anorthite (An) percent versus temperature, clearly show the temperature dependent nature of the reversals. The decrease in An content with increasing temperature below 975°C is caused by the growth of calcic minerals such as clinopyroxene and garnet. Within the stability field of garnet, as hornblendes breakdown, the calcium – but not the sodium – is incorporated into the garnet or clinopyroxene, which increases the albite component in the liquids. The garnet-out curve lies between 975-1000°C, which corresponds with the trend reversals, indicating that the stability of garnet may control the liquid compositional trend. The increase in the ratio above 975°C is caused by the lack of growth or resorption of garnet; with little or no garnet present, much of the calcium from the hornblende breakdown enters the liquid, which increases the anorthite component in the liquids. The absence of garnet results in the generation of liquids with more tonalitic compositions at these higher temperatures.

The liquid compositions also are plotted in a CaO - FeO+MgO - 1/4SiO_2 triangle in Fig. 3.19. The mineral compositions, the amphibolite starting composition and the average calc-alkaline rock trend are shown as well. The liquid compositional trend diverges from the calc-alkaline rock trend. Similar non-calc-alkaline trends were observed by Huang and Wyllie (1986) for a gabbro and tonalite at 15 kbar (both with 5 wt.% H_2O added), Carroll

and Wyllie (1990) for a tonalite at 15 kbar (with 2.5-10 wt.% H_2O added), and Stern and Wyllie (1978) for a basalt at 30 kbar (with 5 wt.% H_2O added).

The phase assemblage at 1000°C contains liquid, clinopyroxene, orthopyroxene, and anorthite. Figure 3.19 clearly shows that during near-liquidus crystallization, orthopyroxene controls the liquid trend away from the bulk rock composition, although both clinopyroxene and anorthite are more abundant. The Ca/(Mg+Fe) ratio of the liquids decreases slightly at lower temperatures. The liquid trend at these temperatures is controlled by a combination of garnet, clinopyroxene and hornblende crystallization. Green and Ringwood (1968) determined that subsilicic hornblende and clinopyroxene controlled the silica content of the liquid. In these experiments, silica enrichment of the liquid is controlled mainly by garnet growth, because of its much lower silica content, relative to both hornblende and clinopyroxene.

Assigning specific mineralogical controls on the liquid compositional trend is much more difficult for melting than it is for crystallization, because the reaction of one mineral, such as the initial hornblende, forms other minerals in addition to liquid. The dehydration-melting of amphibolite must drive the liquid from the 850°C composition toward the hornblende composition (Fig. 3.19). The growth of clinopyroxene, garnet, orthopyroxene, and Ca- and Al-rich hornblende modifies the shape of the liquid compositional trend.

The evolution of all of the liquid compositions during progressive fusion is shown in Fig. 3.20 as weight percent oxides versus temperature. The compositional axes scales of all of the oxides are the same, although the ranges in compositions vary. In general, the liquid trends of different durations coincide with each other, except for a few 1-day data points (975°C and 990°C). The higher temperature liquids dissolve more of the non-quartzofeldspathic components, especially Al_2O_3, FeO, MgO and CaO (e.g., Thompson 1988). The silica content of the liquids remains at approximately 65 wt.% until the percent of liquid increases rapidly above 875°C (Figs. 3.4 and 3.20). The amount of Al_2O_3 jumps

from 19 to 21 wt% between 900-925°C, possibly due to a modal decrease in plagioclase. FeO steadily increases from 2 to 7 wt%. Increases in both MgO and CaO are small until temperatures over 975°C are reached. Na_2O increases slightly above 900°C. The amounts of TiO_2 and K_2O do not change noticeably.

The liquid compositions as well as all of the minerals are plotted in ACF-deluxe coordinates in Fig. 3.21 (after O'Hara 1976; Thompson 1988). The diagram is not strictly legal since none of the liquids are quartz- or water-saturated. This projection is useful nevertheless, because it displays the divergence from the quartz-feldspar minimum composition in the granite system as non-quartzofeldspathic components dissolve in the evolving liquid (Ellis and Thompson 1986; Thompson 1988). Most of the liquids are corundum-normative, i.e., most of the liquids produced by dehydration-melting of this metaluminous amphibolite are mildly peraluminous (e.g., Zen 1986). At the highest temperature the liquids are diopside-normative (metaluminous).

Figure 3.22 shows the liquid compositional fields, as Al_2O_3 versus SiO_2, from the present study as well as from Helz (1976), Winther and Newton (1990), Beard and Lofgren (1991) and Rapp et al. (1991). The fields for natural arc tonalites (from Beard and Lofgren 1991) and natural rocks (from Winther and Newton 1990) are also shown. Most natural tonalites contain between 12-19 wt.% Al_2O_3 (Barker 1979), but the liquids produced in the present study contain 18-22 wt.% Al_2O_3. These liquid compositions fall on the high alumina side of natural arc tonalite compositions but within the larger range of natural rock compositions gathered by Winther and Newton (1990) (Fig. 3.22).

3.1.4.2 Water Content

The amount of H_2O in the liquids was calculated by mass balance using the modal data from Table 3.1 and assuming that the amphiboles contain 2 wt.% H_2O. The amount of H_2O that enters the silicate liquid is proportional to the amount of initial hornblende that reacts out minus the amounts of Ca-Hb and Al-Hb that appear, since these are the only

hydrous minerals present. Figure 3.23 shows the relationship between the calculated weight percent of water dissolved in the liquids and the percentage of liquid present in runs of different duration. The calculated amount of H_2O in the liquid is highly dependent on the hornblende and liquid modes, and the errors are large at low liquid fractions (shown by the bars through the data). The initial, lowest temperature liquids (<875°C) are not the most H_2O-rich because the hornblende has not reacted substantially. At ~875°C, considerable hornblende breakdown occurs, and the H_2O content of the liquid (<10 vol.%) rises to ~7-8 wt.%. With increasing temperature, the H_2O content of the liquid drops to approximately 2 wt.% as the amount of liquid increases to ~47 vol.%.

3.1.5 Distribution of Major Elements Among Coexisting Phases

Figures 3.24a-f graphically show the major element differences between the product phases and the initial hornblende (in weight percent). The vertical axis is calculated as the oxide in the phase minus the oxide in the initial hornblende so that positive columns (rising above zero) show the amount of oxide gained by the growth of the new phase, relative to initial hornblende. For instance, in Fig. 3.24a the average clinopyroxene only contains more CaO than the average initial hornblende. The increase in CaO in the Ca-rich hornblendes is accompanied by decreases in SiO_2 and FeO (Fig. 3.24b). Increases in Al_2O_3, Na_2O and TiO_2 in the Al-rich hornblende are accompanied by decreases in SiO_2, FeO and CaO (Fig. 3.24c). In orthopyroxene gains in MgO and FeO are balanced by losses in CaO and Al_2O_3 (Fig. 3.24d). Garnet contains more Al_2O_3 and FeO and less SiO_2, MgO and CaO than the initial hornblende (Fig. 3.24e). The silicate liquids contain more SiO_2, Al_2O_3 and Na_2O and less FeO, MgO and CaO than the hornblende (Fig. 3.24f).

Figures 3.24e,f are embellished to show the influence of temperature on garnet and liquid compositions. Each oxide column is split into two subcolumns. The solid

subcolumns on the left are the compositions at a low temperature. The hatchured subcolumns on the right are the high temperature compositions. In Fig. 3.24e, the solid, low temperature subcolumns display the relatively iron-rich garnet composition, and the hatchured subcolumns display the relatively magnesium-rich composition. The temperature limits in this garnet diagram are 850-975°C. FeO and MgO are the only oxides that vary much in the garnets, so the other oxides actually are averages of all of the garnets from the entire temperature range. Thus the only variations in this diagram are in the FeO and MgO columns.

In contrast with the other product mineral oxides, most oxides which make up the liquids vary as a function of temperature. The range in liquid compositions lies between the low (850°C) and high (1000°C) temperature limits represented by the low and high temperature subcolumns in Fig. 3.24f. These results are discussed in section 4.1.

The approximately linear variation in the molecular Mg/(Mg+Fe) ratio (the Mg#) of the garnet rims as a function of temperature is shown in Fig. 3.25 (solid line). The ratios of the other mafic minerals are shown as points since they do not vary much with temperature. The garnet rim Mg#s range from a minimum of 0.47 at 850°C to a maximum of 0.65 at 975°C, which is less than the 0.70 - 0.75 values for the pyriboles. The garnet data are from the longer duration experiments; at a given temperature, the shorter duration experiments have Mg#s about 0.01 - 0.05 lower. Figure 3.25 also shows that the Mg#s of the longer duration, experimental liquids vary with temperature, increasing from a minimum of 0.37 at 850°C to a maximum of 0.62 at 1000°C (dashed line). The liquid Mg#s average about 0.05 lower than the garnet rim values at any given temperature.

Figure 3.26 shows how the distribution of Fe and Mg between liquid and garnet varies as a function of time. Runs of 1- and 2-day duration between 900°C and 950°C show large changes in K_D, but runs of 4 days and longer appear more systematic. The leveling-off of the change in K_D's through time is taken to be an indication of the approach

to equilibrium. In short duration runs, the compositional differences may be due to differences in metastable reactions and reaction rates.

Given enough time, the compositional zoning in the garnets will homogenize through intracrystalline diffusion. The final MgO and FeO contents in the homogenized crystal, however, will not be the average of the early core and edge compositions but will be nearer to the edge composition, because this is the garnet composition in equilibrium with the liquid. Instead of resulting in a decrease in garnet Mg#, this homogenization will result in a net addition of MgO from the liquid to the garnet, with a slight readjustment to a final K_D (distribution coefficient) value.

3.2 Solid Experiments

In the present study, I investigated the textures produced during dehydration-melting of solid pieces of fine-grained, lineated amphibolite. The objective is to explore the liquid morphology under more natural conditions, with control exerted by the textures of oriented, anisotropic minerals in their natural geometries, to see how this control affects interfacial angles and the interconnectivity of liquids. I have determined where and how liquid forms along natural grain boundaries.

The back-scattered electron image of a thin-section of the fine-grained amphibolite (Fig. 2.4) provides a textural reference standard, showing an equilibrated, cleavage-dominated, metamorphic texture, with no low temperature mineral or textural alteration. The lineated texture of the original amphibolite and the partially melted rocks contrasts with the granoblastic texture of annealed powder specimens which are composed of subspherical, sieved mineral grains (e.g., Watson 1982; Jurewicz and Watson 1984). The 120° junctions separating different grains after annealing in the latter experiments are rarely found in the original amphibolite (Fig. 2.4) or in the partially melted rock cylinders. Grain junctions other than 120° are common in metamorphic rocks composed of anisotropic minerals. In a textural study that included hornblende- and plagioclase-bearing gneisses

and an amphibolite, Kretz (1966) found that boundary angles are far from 120° if the grain boundary orientation depends on the crystallographic orientation of the grains, as it does with anisotropic minerals. Cleavage planes of anisotropic minerals tend to dominate rock textures (Vernon 1976). The angular shape of plagioclase grains also results in boundary configurations markedly different from those in the powder mineral experiments. The plagioclase grains protrude into or are embedded within hornblende grains (Fig. 2.4), and their edges are scalloped outward, making them less stable than straight boundaries under higher temperature conditions (Bulau et al. 1979). The relatively smooth scalloping is interrupted by deeper embayments of hornblende into the plagioclase. These small hornblende embayments are sites of initial liquid formation, as discussed below. Before discussing the morphology of the liquid, I will briefly discuss the phase relationships in the solid experiments because of their direct effect on the liquid composition, location and morphology.

3.2.1 Phase Relationships and Modes

3.2.1.1 850°C Run

In the lowest temperature solid amphibolite run (Figs. 3.27a,b and 3.28a), approximately 5 vol.% of the large, blocky hornblende grains (100-1000 μm) have been replaced by very small acicular grains (10x50 μm) of clinopyroxene (Cpx). About 1 vol.% liquid (L) is present, predominantly along hornblende/plagioclase (Hb/Pl) boundaries but not along all of these boundaries (Figs. 3.27a and 3.28a); a smaller amount of liquid in isolated pockets within hornblende grains is likely associated with Hb/Pl boundaries in three dimensions. The number of original small hornblende embayments into the plagioclase grains has decreased, along with the concomitant appearance of liquid blebs along the boundaries at the embayment locations (compare Figs. 2.4 and 3.27a). Clinopyroxene is generally not in contact with liquid and plagioclase. Some change in amphibole composition marginal to the clinopyroxenes is expected, but no new,

compositionally distinct amphibole or other mineral was detected. Although the initial hornblende grains are compositionally slightly heterogeneous, the observed compositional variations, however, are not geometrically concentric, relative to the hornblende centers and grain boundaries. The locations of clinopyroxene nucleation sites also appear to be independent of the hornblende compositional heterogeneities.

3.2.1.2 875°C Run

Figures 3.29a,b shows that approximately 40 vol.% of the original hornblende is replaced by blocky clinopyroxene grains. These are concentrated in the central parts of hornblendes, remaining essentially isolated from the liquid (Figs. 3.28b and 3.29b). There is 2 vol.% liquid present that almost surrounds the plagioclase grains (Figs. 3.28b and 3.29a). This liquid is calculated to be H_2O-saturated, by mass balance.

3.2.1.3 900°C Run

Figures 3.28c and 3.30a,b show that although clinopyroxene (40 vol.%) has replaced more than 60 vol.% of the original hornblende, it is not commonly found in contact with either plagioclase or liquid. Liquid comprises about 5 vol.% of the rock. This liquid is calculated to be H_2O-saturated, by mass balance. Approximately 60% of the liquid is associated with Hb/Pl boundaries, and the remainder within the hornblende grains is commonly in approximately linear extensions of Hb/Pl liquid pockets.

3.2.1.4 1000°C Run

Figures 3.4, 3.28d and 3.31 show that by 1000°C, approximately 50 vol.% of the sample forms large liquid pockets (100-500 μm diameters) comparable in size to the clinopyroxene grains, which amount to 40 vol.% of the sample. Hornblende is rare, and plagioclase is reduced to below 5 vol.%; these minerals are always inside clinopyroxene and never surrounded by liquid. Rare orthopyroxene is located along clinopyroxene/liquid

boundaries. The liquid is H_2O-undersaturated, with 3 wt.% H_2O calculated from the mode, compared with about 10-12 wt.% required for saturation under these conditions (Silver and Stolper 1985).

3.2.2 Liquid Morphology

3.2.2.1 850°C Run

The liquid forms irregular-shaped polygonal pockets ranging in size from 5 to 20 μm. Many have corners with angles that range from approximately 30° to 120°, with most apparent angles >60° (Figs. 3.27a and 3.28a). Many of the pocket edges are straight, from corner to corner. Some of the edges near the corners have curved boundaries, but classical dihedral angles are not common.

3.2.2.2 875°C Run

The 2 vol.% of H_2O-saturated liquid present almost surrounds the plagioclase grains (Figs. 3.28b and 3.29a). As seen in the photomicrograph, the liquid at Hb/Pl boundaries is interconnected along the lengths of the plagioclase grains in two dimensions, and it appears to make inroads along the cleavages of hornblendes (Fig. 3.29a). Between 850°C and 875°C, individual liquid pockets within hornblende grains and along Hb/Pl boundaries grow larger (30-100 μm lengths), and the pocket edges lose their straightness. They are more curved than at 850°C, with longer edges of the pockets typically scalloped by many cusps protruding along possible cleavage traces into the hornblende (Figs. 3.28b and 3.29a). The smaller pockets (<20 μm), however, have corners bounded by straight edges. The majority of these angles are greater than 60° (Figs. 3.29a,b).

3.2.2.3 900°C Run

Approximately 60% of the liquid is associated with Hb/Pl boundaries, and the remainder within the hornblende grains is commonly in approximately linear extensions of

Hb/Pl liquid pockets. The shapes of the liquid pockets are flat-faced, irregular polyhedra, regardless of pocket size (10-70 μm lengths). The liquid pocket corners follow prism faces of the hornblende (Figs. 3.28c and 3.30a,b). Liquid penetrates into the Hb/Hb corners in small projections <5 μm in length (Figs. 3.30a,b).

3.2.2.4 1000°C Run

Figures 3.4, 3.28d and 3.31 show that by 1000°C, approximately 50 vol.% of the sample forms large liquid pockets (100-500 μm diameters) comparable in size to the clinopyroxene grains, which amount to 40 vol.% of the sample. The critical melt fraction has been exceeded, and the minerals are effectively suspended in the liquid (e.g., von Bargen and Waff 1986; Wickham 1987; Miller et al. 1988).

3.2.3 Analysis of Glass (Liquid) Compositions

Glasses from the 14-day runs at 875°C and 900°C contained 8.5 wt.% and 7.0 wt.% Na_2O, respectively, compared with 1.1 wt.% Na_2O found in the other runs at 850°C and 1000°C (Table 4.2). A visual comparison between the uncontaminated 850°C run and the contaminated 875°C run reveals similar crystal and liquid textures. Sodium contamination would have been a serious problem in a phase equilibrium study with powdered samples, but its occurrence in these solid samples appears to have little effect on melt textures. Indeed, it proves to be a useful indicator for liquid interconnectivity at low liquid fractions, as discussed below.

Table 3.1. The conditions for and results of the dehydration-melting of a natural (powder and solid) amphibolite at 10 kbar

Run #	Temp. (°C)	Time (days)	Phases Identified (with modes) Hb	Pl	L	Cpx	Ca-Hb	Al-Hb	Opx	Ga
Powder										
132	750	8	61	37	X	2	--	--	--	--
135	800	8	68	26	X	5	1	X	--	--
105	850	2	X	X	X	X	--	--	--	--
120	850	8	43	20	8	12	6	8	3	X
118	875	8	22	14	7	23	1	7	X	26
126	875	14	X	X	X	X	--	X	X	--
102	900	1	X	X	X	X	--	--	--	X
115	900	4	38	20	3	13	4	18	--	4
106	900	9	41	24	2	11	10	2	2	8
108	925	1	5	21	11	25	5	16	16	X
109	925	2	20	24	9	15	6	17	5	6
110	925	4	X	14	16	23	2	19	2	24
113	925	8	4	9	30	37	--	5	--	15
117	950	1	1	5	34	37	4	1	1	18
103	950	2	1	6	20	32	3	5	--	32
141	945	5	X	X	X	X	X	X	X	--
121	975	1	6	21	29	26	14	--	--	4
119	975	4	--	X	39	43	2	--	--	16
138	990	1	--	X	X	X	--	X	X	X
134	1000	4	--	8	47	45	--	--	X	--
Solid										
124s	850	21	X	X	X	X	--	--	--	--
125s	875	14	X	X	X^n	X	--	--	--	--
123s	900	14	X	X	X^n	X	--	--	--	--
127s	925	8	X	X	X^n	X	--	--	--	--
122s	950	8	X	X	X^n	X	--	--	--	--
133s	1000	4	--	X	X	X	--	--	X	--

Hb = hornblende; Pl = plagioclase; L = liquid; Cpx = clinopyroxene; Ca-Hb = calcic hornblende; Al-Hb = aluminous hornblende; Opx = orthopyroxene; Ga = garnet. Modes from electron microprobe, automated, rapid, partial analyses (EMP-ARP, see text). X = identified with SEM, but no modal analysis made or phase missed by EMP-ARP. -- = not identified, though not necessarily absent from run. X^n indicates a high Na_2O content. Leaked powder runs with high Na_2O not shown.

Table 3.2. Clinopyroxene compositions from powder runs, normalized to 100 (SEM-EDS).

Run #	105-7	105-6	120-12	120-9	118-10	126-6	102-3	102-2	115-7	115-4	108-3	110-10	113-8	113-11	141-1	141-6
Temp (°C)	850	850	850	850	875	875	900	900	900	900	925	925	925	925	945	945
Time (d)	2	2	8	8	8	14	1	1	4	4	1	4	8	8	5	5
SiO2	49.24	48.94	49.76	48.96	50.19	48.72	49.37	48.54	51.31	51.95	50.07	48.67	50.16	51.83	49.01	49.38
TiO2	0.39	0.53	0.26	0.38	0.34	0.51	0.43	0.54	0.20	0.19	0.32	0.55	0.45	0.30	0.19	0.35
Al2O3	6.46	6.56	5.03	6.52	5.68	6.61	7.80	8.33	3.72	3.94	6.29	8.41	7.66	5.51	6.33	6.37
FeO	9.37	8.78	10.09	9.40	8.73	8.45	9.60	9.34	8.19	7.69	9.13	8.48	5.23	5.51	9.94	8.35
MnO	0.00	0.41	0.51	0.00	0.17	0.34	0.15	0.20	0.35	0.00	0.24	0.25	0.00	0.21	0.50	0.78
MgO	12.02	11.86	14.17	13.32	13.56	12.78	12.82	12.69	15.53	15.65	14.56	13.07	14.15	14.57	14.13	14.00
CaO	22.53	22.92	20.18	21.42	21.34	22.37	19.83	20.27	20.64	20.58	19.39	20.57	22.26	22.07	19.94	20.80
Na2O	0.00	0.00	0.00	0.00	0.00	0.00	0.00	0.00	0.00	0.00	0.00	0.00	0.00	0.00	0.00	0.00
K2O	0.00	0.00	0.00	0.00	0.00	0.12	0.00	0.09	0.07	0.00	0.00	0.00	0.09	0.00	0.00	0.00
Ions per 6 oxygens																
Si	1.842	1.837	1.862	1.825	1.865	1.822	1.834	1.808	1.905	1.913	1.856	1.807	1.836	1.899	1.831	1.836
Al 4	0.158	0.163	0.138	0.175	0.135	0.178	0.166	0.192	0.095	0.087	0.144	0.193	0.164	0.101	0.169	0.164
Al 6	0.127	0.127	0.083	0.112	0.113	0.113	0.175	0.173	0.067	0.084	0.131	0.174	0.166	0.136	0.109	0.115
Ti	0.011	0.015	0.007	0.011	0.009	0.014	0.012	0.015	0.005	0.005	0.009	0.015	0.012	0.008	0.005	0.010
Fe	0.293	0.276	0.316	0.293	0.271	0.264	0.298	0.291	0.254	0.237	0.283	0.263	0.160	0.168	0.310	0.260
Mn	--	--	0.016	0.000	--	0.010	--	--	--	--	--	--	--	--	0.016	0.024
Mg	0.670	0.663	0.790	0.740	0.750	0.712	0.710	0.705	0.859	0.858	0.805	0.723	0.773	0.796	0.787	0.776
Ca	0.903	0.922	0.809	0.855	0.849	0.896	0.789	0.809	0.821	0.812	0.770	0.818	0.873	0.866	0.798	0.829
Na	0.000	0.000	0.000	0.000	0.000	0.000	0.000	0.000	0.000	0.000	0.000	0.000	0.000	0.000	0.000	0.000
K	0.000	0.000	0.000	0.000	0.000	0.005	0.000	0.004	0.003	0.000	0.000	0.000	0.004	0.000	0.000	0.000
mole. %																
Ca	48.38	49.53	42.24	45.29	45.38	47.85	43.92	44.83	42.43	42.57	41.45	45.33	48.36	47.32	42.10	44.45
Mg	35.91	35.66	41.27	39.19	40.12	38.04	39.49	39.05	44.43	45.02	43.32	40.09	42.78	43.47	41.51	41.63
Fe	15.71	14.81	16.49	15.52	14.49	14.11	16.60	16.12	13.14	12.41	15.23	14.58	8.86	9.21	16.38	13.93

-- MnO determined from K-ratio, but Mn not given or calculated

Table 3.2 (cont.). Clinopyroxene compositions (SEM-EDS).

Run #	141-7a	141-7b	117-12	117-10	117-11	103-6	119-4	119-6	138-8	138-9	138-11	134-3	134-4	134-9	Average	sdm
Temp (°C)	945	945	950	950	950	950	975	975	990	990	990	1000	1000	1000		
Time (d)	5	5	1	1	1	2	4	4	1	1	1	4	4	4		
SiO2	48.85	49.37	49.01	48.40	49.01	50.60	50.22	48.11	48.31	47.43	47.97	49.19	48.28	50.55	49.38	0.20
TiO2	0.63	0.56	0.45	0.46	0.30	0.27	0.15	0.39	0.44	0.21	0.51	0.46	0.43	0.20	0.38	0.02
Al2O3	7.88	7.49	9.76	9.97	9.43	5.84	7.61	8.36	7.84	9.52	8.61	8.30	8.92	6.99	7.26	0.29
FeO	7.30	8.03	6.53	7.21	6.90	9.51	6.27	8.32	9.22	9.44	8.68	5.66	8.20	6.44	8.13	0.25
MnO	0.42	0.00	0.00	0.39	0.16	0.35	0.14	0.37	0.44	0.18	0.00	0.16	0.38	0.00	0.24	0.04
MgO	13.41	13.95	13.61	13.71	14.55	14.42	14.47	13.87	13.06	13.17	13.18	14.97	14.63	15.86	13.86	0.18
CaO	21.54	20.63	20.64	19.87	19.65	19.01	21.04	20.59	20.64	20.07	21.07	20.83	18.93	19.74	20.71	0.18
Na2O	0.00	0.00	0.00	0.00	0.00	0.00	0.00	0.00	0.00	0.00	0.00	0.00	0.00	0.00	0.00	0.00
K2O	0.00	0.00	0.00	0.00	0.00	0.00	0.10	0.00	0.10	0.00	0.00	0.00	0.08	0.07	0.02	0.01
Ions per 6 oxygens																
Si	1.808	1.824	1.795	1.783	1.795	1.877	1.843	1.787	1.802	1.766	1.783	1.803	1.783	1.847		
Al 4	0.192	0.176	0.205	0.217	0.205	0.123	0.157	0.213	0.198	0.234	0.217	0.197	0.217	0.153		
Al 6	0.152	0.150	0.216	0.216	0.202	0.132	0.172	0.152	0.147	0.184	0.160	0.161	0.171	0.148		
Ti	0.017	0.015	0.012	0.125	0.008	0.008	0.004	0.011	0.012	0.006	0.014	0.013	0.012	0.005		
Fe	0.226	0.248	0.200	0.222	0.211	0.295	0.192	0.258	0.287	0.294	0.270	0.173	0.253	0.197		
Mn	0.013	0.000	--	--	--	--	--	0.012	0.014	0.005	0.000	0.005	0.012	0.000		
Mg	0.740	0.000	0.743	0.753	0.795	0.797	0.792	0.767	0.726	0.731	0.730	0.818	0.805	0.863		
Ca	0.854	0.768	0.810	0.784	0.772	0.756	0.827	0.819	0.825	0.801	0.839	0.818	0.749	0.773		
Na	0.000	0.000	0.000	0.000	0.000	0.000	0.000	0.000	0.000	0.000	0.000	0.000	0.000	0.000		
K	0.000	0.000	0.000	0.000	0.000	0.000	0.004	0.000	0.004	0.000	0.000	0.000	0.004	0.003		
mole. %																
Ca	46.93	44.55	46.20	44.57	43.40	40.88	45.67	44.39	44.86	43.86	45.62	45.21	41.43	42.15	44.71	0.40
Mg	40.65	41.92	42.40	42.80	44.71	43.14	43.71	41.61	39.50	40.04	39.71	45.21	44.56	47.12	41.60	0.48
Fe	12.41	13.54	11.40	12.63	11.89	15.97	10.62	14.00	15.64	16.10	14.67	9.59	14.01	10.73	13.69	0.41

Table 3.3. Hornblende compositions from powder runs, normalized to 100 (SEM-EDS).

Run #	105-2	105-1	105-3	120-10	120-11	118-8	118-9	102-5	102-6	102-4	115-3	115-6	106-7	109-4	Average	sdm
Temp (°C)	850	850	850	850	850	875	875	900	900	900	900	900	900	925		
Time (d)	2	2	2	8	8	8	8	1	1	1	4	4	9	2		
SiO2	53.57	50.68	50.19	51.77	51.04	49.19	49.88	53.23	50.40	50.55	51.75	49.23	50.22	51.93	50.97	0.34
TiO2	0.00	0.38	0.23	0.00	0.31	0.47	0.48	0.26	0.33	0.30	0.23	0.40	0.25	0.19	0.27	0.04
Al2O3	4.98	8.09	8.71	6.64	7.51	8.73	8.51	5.16	8.42	8.54	6.99	9.01	8.80	7.23	7.66	0.34
FeO	10.78	12.34	12.98	11.72	11.92	12.96	12.15	10.61	11.65	11.99	11.47	13.33	12.73	11.20	11.99	0.21
MnO	0.23	0.25	0.24	0.31	0.20	0.00	0.00	0.25	0.00	0.18	0.00	0.00	0.00	0.37	0.14	0.04
MgO	17.16	15.00	15.06	16.51	15.55	14.95	15.67	17.38	16.25	15.77	16.23	14.86	14.80	16.33	15.82	0.22
CaO	13.29	13.14	12.52	12.95	13.26	13.02	12.71	13.01	12.78	12.48	13.24	13.05	13.05	12.67	12.94	0.07
Na2O	0.00	0.00	0.00	0.00	0.00	0.44	0.33	0.00	0.00	0.00	0.00	0.00	0.00	0.00	0.05	0.04
K2O	0.00	0.12	0.07	0.10	0.21	0.23	0.27	0.11	0.17	0.19	0.10	0.14	0.16	0.08	0.14	0.02
Ions per 23 oxygens																
Si	7.469	7.139	7.079	7.265	7.180	6.976	7.031	7.421	7.070	7.097	7.248	6.974	7.080	7.257	7.164	
Al 4	0.531	0.861	0.921	0.735	0.820	1.024	0.969	0.579	0.930	0.903	0.752	1.026	0.920	0.743	0.836	
Al 6	0.287	0.482	0.526	0.363	0.426	0.435	0.444	0.268	0.462	0.510	0.402	0.479	0.542	0.448	0.434	
Ti	0.000	0.040	0.024	0.000	0.033	0.050	0.051	0.027	0.035	0.032	0.024	0.043	0.026	0.020	0.029	
Fe	1.257	1.453	1.531	1.375	1.402	1.538	1.433	1.237	1.366	1.408	1.343	1.579	1.500	1.309	1.409	
Mn	0.027	0.030	0.029	0.037	0.024	0.000	0.000	0.029	0.000	0.021	0.000	0.000	0.000	0.044	0.017	
Mg	3.566	3.150	3.166	3.455	3.261	3.162	3.294	3.612	3.399	3.300	3.387	3.138	3.109	3.403	3.315	
Ca	1.985	1.984	1.891	1.947	1.999	1.979	1.920	1.944	1.922	1.878	1.986	1.980	1.970	1.897	1.949	
Na	0.000	0.000	0.000	0.000	0.000	0.121	0.090	0.000	0.000	0.000	0.000	0.000	0.000	0.000	0.015	
K	0.000	0.022	0.013	0.018	0.038	0.042	0.049	0.020	0.030	0.034	0.018	0.025	0.029	0.014	0.025	
mole. %																
Ca	29.15	30.12	28.70	28.73	30.01	29.63	28.89	28.61	28.74	28.51	29.57	29.57	29.95	28.70	29.21	0.15
Mg	52.38	47.82	48.05	50.98	48.94	47.34	49.55	53.18	50.83	50.10	50.43	46.85	47.25	51.49	49.66	0.52
Fe	18.47	22.06	23.24	20.29	21.05	23.02	21.56	18.21	20.43	21.38	20.00	23.58	22.80	19.81	21.14	0.44

Table 3.3 (cont.). Alumina-rich hornblendes (Al-Hb) from powder runs, normalized to 100 (SEM-EDS).

Run #	118-11	126-8	108-5	109-9	110-5	113-9	113-10	141-9	141-7a	141-7b	141-5	103-5	138-7	Average	sdm
Temp (°C)	875	875	925	925	925	925	925	945	945	945	945	950	990		
Time (d)	8	14	1	2	4	8	8	5	5	5	5	2	1		
SiO2	47.47	45.02	44.95	47.68	44.79	47.15	46.99	45.44	45.47	44.83	44.74	44.56	43.44	45.58	0.35
TiO2	0.91	1.18	1.10	0.72	1.11	0.96	0.63	1.00	0.92	0.85	1.35	1.03	1.26	1.00	0.05
Al2O3	14.52	14.81	16.01	14.32	15.39	15.29	15.66	15.11	15.94	15.01	15.17	15.82	16.25	15.33	0.16
FeO	9.39	11.86	10.67	10.00	11.03	7.38	7.68	10.63	9.69	11.33	10.93	11.78	11.40	10.29	0.38
MnO	0.00	0.00	0.15	0.19	0.20	0.00	0.00	0.29	0.00	0.58	0.35	0.16	0.60	0.19	0.06
MgO	15.23	14.60	15.00	15.56	14.94	16.72	16.08	14.44	14.80	14.92	14.45	14.66	14.42	15.06	0.18
CaO	11.75	11.89	10.85	10.81	11.17	11.68	11.80	11.91	12.27	11.36	12.01	10.81	11.65	11.54	0.13
Na2O	0.59	0.56	1.27	0.73	1.16	0.67	1.03	1.05	0.93	0.84	1.03	0.99	0.82	0.90	0.06
K2O	0.14	0.12	0.00	0.00	0.21	0.15	0.13	0.17	0.00	0.33	0.00	0.21	0.21	0.13	0.03
Ions per 23 oxygens															
Si	6.587	6.352	6.304	6.623	6.314	6.490	6.484	6.388	6.350	6.332	6.307	6.289	6.152	6.382	
Al 4	1.413	1.648	1.696	1.377	1.686	1.510	1.516	1.612	1.650	1.668	1.693	1.711	1.848	1.618	
Al 6	0.961	0.814	0.952	0.967	0.871	0.970	1.030	0.891	0.974	0.830	0.827	0.920	0.864	0.913	
Ti	0.095	0.125	0.115	0.074	0.116	0.098	0.064	0.105	0.096	0.089	0.143	0.108	0.134	0.105	
Fe	1.088	1.399	1.251	1.161	1.300	0.849	0.885	1.249	1.132	1.338	1.289	1.390	1.350	1.206	
Mn	0.000	0.000	0.018	0.022	0.024	0.000	0.000	0.034	0.000	0.069	0.041	0.019	0.071	0.023	
Mg	3.150	3.071	3.137	3.223	3.140	3.430	3.308	3.026	3.080	3.140	3.037	3.083	3.043	3.144	
Ca	1.747	1.798	1.630	1.608	1.687	1.722	1.743	1.793	1.836	1.719	1.814	1.634	1.768	1.731	
Na	0.157	0.151	0.343	0.194	0.315	0.176	0.275	0.285	0.251	0.228	0.280	0.268	0.223	0.242	
K	0.024	0.020	0.000	0.000	0.038	0.026	0.022	0.030	0.000	0.060	0.000	0.036	0.037	0.023	
mole. %															
Ca	29.19	28.68	27.09	26.84	27.53	28.70	29.37	29.55	30.35	27.73	29.55	26.75	28.69	28.46	0.31
Mg	52.63	49.00	52.12	53.78	51.24	57.15	55.72	49.86	50.94	50.68	49.46	50.49	49.40	51.73	0.67
Fe	18.19	22.33	20.79	19.38	21.22	14.14	14.92	20.59	18.71	21.59	20.99	22.75	21.91	19.81	0.72

Table 3.3 (cont.). Calcium-rich hornblendes (Ca-Hb).

Run #	110-4	141-7a	103-4	121-7	121-5	Average	sdm
Temp (°C)	925	945	950	975	975		
Time (d)	4	5	2	1	1		
SiO2	49.45	50.44	50.02	47.39	48.98	49.26	0.47
TiO2	0.16	0.00	0.34	0.47	0.21	0.24	0.07
Al2O3	7.64	7.49	6.72	10.10	7.94	7.98	0.51
FeO	10.15	9.98	11.06	9.98	11.20	10.47	0.24
MnO	0.55	0.43	0.00	0.00	0.29	0.25	0.10
MgO	15.56	15.88	15.09	14.41	15.53	15.29	0.23
CaO	16.42	15.80	16.77	17.56	15.72	16.46	0.30
Na2O	0.00	0.00	0.00	0.00	0.00	0.00	0.00
K2O	0.07	0.00	0.00	0.10	0.13	0.06	0.02
Ions per 23 oxygens							
Si	7.023	7.099	7.097	6.727	6.955	6.980	
Al 4	0.977	0.901	0.903	1.273	1.045	1.020	
Al 6	0.302	0.341	0.219	0.416	0.283	0.312	
Ti	0.016	0.000	0.036	0.050	0.022	0.025	
Fe	1.205	1.174	1.312	1.185	1.329	1.241	
Mn	0.065	0.051	0.000	0.000	0.034	0.030	
Mg	3.294	3.332	3.189	3.048	3.287	3.230	
Ca	2.498	2.383	2.550	2.672	2.392	2.499	
Na	0.000	0.000	0.000	0.000	0.000	0.000	
K	0.013	0.000	0.000	0.018	0.022	0.011	
mole. %							
Ca	35.71	34.58	36.16	38.69	34.13	35.85	0.71
Mg	47.07	48.36	45.24	44.15	46.91	46.35	0.66
Fe	17.23	17.05	18.60	17.15	18.97	17.80	0.36

Table 3.4. Orthopyroxene compositions from powder runs, normalized to 100 (SEM-EDS).

Run #	126-9	106-4	106-6	108-4	109-10	109-5	110-7	141-4	141-8	141-10	141-7a	138-10	134-5	134-6	134-7	Average	sdm
Temp (°C)	875	900	900	925	925	925	925	945	945	945	945	990	1000	1000	1000		
Time (d)	14	9	9	1	2	2	4	5	5	5	5	1	4	4	4		
SiO2	49.38	52.53	51.10	50.30	50.48	50.30	49.00	50.16	51.76	50.21	52.70	48.89	50.13	49.68	50.48	50.47	0.28
TiO2	0.00	0.00	0.22	0.31	0.00	0.01	0.37	0.16	0.00	0.00	0.00	0.00	0.00	0.00	0.00	0.07	0.03
Al2O3	6.97	2.52	4.63	5.80	6.74	6.92	7.38	6.16	7.02	6.78	6.38	9.12	8.94	9.03	8.75	6.88	0.44
FeO	18.06	18.58	18.09	15.40	16.89	16.55	17.63	17.49	16.29	17.53	13.47	17.72	13.27	13.31	12.63	16.19	0.51
MnO	0.34	0.43	0.65	0.22	0.28	0.62	0.30	0.18	0.43	0.39	0.00	0.22	0.49	0.23	0.35	0.34	0.04
MgO	24.09	24.68	24.08	26.82	24.39	24.29	23.62	24.25	23.01	23.57	26.21	22.61	25.57	25.95	25.68	24.59	0.30
CaO	1.11	1.13	1.24	1.15	1.23	1.30	1.70	1.63	1.39	1.54	1.04	1.40	1.62	1.56	1.76	1.39	0.06
Na2O	0.00	0.00	0.00	0.00	0.00	0.00	0.00	0.00	0.00	0.00	0.00	0.00	0.00	0.00	0.00	0.00	0.00
K2O	0.09	0.12	0.00	0.00	0.00	0.00	0.00	0.00	0.13	0.00	0.24	0.07	0.00	0.00	0.00	0.04	0.02
Ions per 6 oxygens																	
Si	1.811	1.932	1.880	1.825	1.840	1.837	1.800	1.834	1.873	1.835	1.879	1.787	1.796	1.781	1.804	1.834	
Al 4	0.189	0.068	0.120	0.175	0.160	0.163	0.200	0.166	0.127	0.165	0.121	0.213	0.204	0.219	0.196	0.166	
Al 6	0.112	0.041	0.081	0.073	0.129	0.135	0.119	0.099	0.172	0.127	0.147	0.180	0.174	0.162	0.368	0.141	
Ti	0.000	0.000	0.006	0.008	0.000	0.000	0.010	0.004	0.000	0.000	0.000	0.000	0.000	0.000	0.000	0.002	
Fe	0.554	0.571	0.556	0.467	0.515	0.506	0.542	0.534	0.493	0.528	0.401	0.542	0.398	0.399	0.377	0.492	
Mn	0.010	--	--	--	--	--	--	0.005	0.013	0.012	0.000	0.007	0.015	0.007	0.010	0.009	
Mg	1.317	1.353	1.321	1.451	1.324	1.320	1.293	1.322	1.241	1.284	1.393	1.232	1.366	1.387	1.368	1.331	
Ca	0.043	0.045	0.049	0.044	0.048	0.051	0.067	0.064	0.054	0.060	0.040	0.055	0.062	0.060	0.067	0.054	
Na	0.000	0.000	0.000	0.000	0.000	0.000	0.000	0.000	0.000	0.000	0.000	0.000	0.000	0.000	0.000	0.000	
K	0.004	0.005	0.000	0.000	0.000	0.000	0.000	0.000	0.006	0.000	0.010	0.003	0.000	0.000	0.000	0.002	
mole. %																	
Ca	2.28	2.27	2.54	2.27	2.54	2.71	3.53	3.32	3.01	3.21	2.17	3.00	3.41	3.25	3.72	2.88	0.13
Mg	68.79	68.71	68.57	73.92	70.19	70.39	68.00	68.83	69.42	68.30	75.94	67.38	74.81	75.14	75.46	70.92	0.78
Fe	28.93	29.02	28.89	23.81	27.27	26.90	28.47	27.85	27.57	28.50	21.89	29.62	21.78	21.62	20.82	26.20	0.80
Mg#	0.70	0.70	0.70	0.76	0.72	0.72	0.70	0.71	0.72	0.71	0.78	0.69	0.77	0.78	0.78	0.73	

-- = wt.% MnO determined from K-ratio

Table 3.5. Garnet compositions from powder runs, normalized to 100 (SEM-EDS).

Run #	120-1	120-2	120-3	120-4	120-5	Avg.	sdm	118-1b	118-1a	118-2	118-9a
core/rim	r	-	-	-	r	120	120				
Temp (°C)	850	850	850	850	850	850	850	875	875	875	875
Time (d)	8	8	8	8	8	8	8	8	8	8	8
SiO2	38.77	38.96	38.60	38.94	39.54	38.96	0.14	39.66	39.53	39.18	39.19
TiO2	0.62	0.75	0.78	0.87	0.77	0.76	0.04	0.64	0.47	0.72	0.42
Al2O3	21.46	21.36	21.10	21.50	21.26	21.34	0.06	21.70	21.95	21.81	21.87
FeO	19.08	19.57	20.02	19.36	18.46	19.30	0.23	17.19	17.36	18.16	17.40
MnO	0.81	1.27	1.14	0.99	1.13	1.07	0.07	0.51	0.51	0.57	0.61
MgO	9.82	9.22	9.42	9.83	9.56	9.57	0.10	11.17	10.95	10.91	11.42
CaO	9.28	8.91	8.91	8.56	9.11	8.95	0.11	9.14	9.28	8.61	9.12
Ions per 24 oxygens											
Si	5.903	5.935	5.902	5.913	5.997	5.930		5.953	5.937	5.908	5.896
Ti	0.071	0.086	0.090	0.099	0.088	0.087		0.072	0.053	0.082	0.048
Al	3.851	3.835	3.802	3.848	3.801	3.827		3.839	3.886	3.876	3.878
Fe	2.429	2.493	2.560	2.459	2.342	2.456		2.158	2.181	2.290	2.189
Mn	0.104	0.164	0.148	0.127	0.145	0.138		0.065	0.065	0.073	0.078
Mg	2.229	2.094	2.147	2.225	2.162	2.171		2.499	2.452	2.453	2.561
Ca	1.514	1.454	1.460	1.393	1.480	1.460		1.470	1.493	1.391	1.470
mole. %											
Alm-Sps	40.37	42.82	42.88	41.68	40.57	41.67		35.90	36.27	38.07	35.99
Pyr	35.51	33.74	34.00	35.87	35.27	34.88		40.37	39.61	39.52	40.67
Gross	24.12	23.44	23.12	22.45	24.16	23.45		23.74	24.12	22.41	23.34

Run #	118-9b	Avg.	sdm	102	102-9a	102-9b	102-9c	102-9d	Avg.	sdm	115-14
core/rim		118	118						102	102	r
Temp (°C)	875	875	875	900	900	900	900	900	900	900	900
Time (d)	8	8	8	1	1	1	1	1	1	1	4
SiO2	39.75	39.46	0.11	39.26	38.75	39.05	38.95	39.04	39.01	0.07	39.55
TiO2	0.49	0.55	0.05	0.92	0.74	0.73	0.67	0.76	0.76	0.04	0.44
Al2O3	21.86	21.84	0.04	21.22	21.25	20.79	21.37	21.24	21.17	0.09	21.91
FeO	17.59	17.54	0.15	18.33	18.60	19.65	19.45	19.19	19.04	0.22	16.88
MnO	0.58	0.56	0.02	1.15	1.15	1.02	0.98	0.54	0.97	0.10	0.80
MgO	11.37	11.16	0.09	9.87	10.48	10.21	10.28	10.20	10.21	0.09	11.49
CaO	8.40	8.91	0.15	9.29	9.06	8.59	8.26	9.01	8.84	0.16	8.93
Ions per 24 oxygens											
Si	5.961	5.931		5.949	5.885	5.944	5.918	5.925	5.924		5.933
Ti	0.055	0.062		0.105	0.085	0.084	0.077	0.087	0.087		0.050
Al	3.864	3.868		3.790	3.803	3.730	3.827	3.799	3.790		3.874
Fe	2.206	2.205		2.323	2.362	2.501	2.471	2.436	2.419		2.118
Mn	0.074	0.071		0.148	0.148	0.132	0.126	0.069	0.125		0.102
Mg	2.542	2.501		2.230	2.373	2.317	2.328	2.308	2.311		2.570
Ca	1.350	1.435		1.508	1.474	1.401	1.345	1.465	1.439		1.435
mole. %											
Alm-Sps	36.94	36.63		39.79	39.49	41.46	41.42	39.90	40.41		35.66
Pyr	41.19	40.27		35.91	37.32	36.48	37.13	36.76	36.72		41.28
Gross	21.87	23.10		24.29	23.19	22.06	21.44	23.34	22.86		23.06

($Na_2O + K_2O < 0.1$ for all garnets)

Consecutive dashes between core (c) or rim (r) analysis indicates a profile across the same crystal.

Table 3.5 (cont.). Garnet compositions (SEM-EDS).

Run #	115-13	115-12	115-8a	115-8b	115-9b	115-9a	115-10	115-11	Avg.	sdm	106-5	106-8
core/rim	-	-	c	c	-	-	-	r	115	115		
Temp (°C)	900	900	900	900	900	900	900	900	900	900	900	900
Time (d)	4	4	4	4	4	4	4	4	4	4	9	9
SiO2	39.41	39.14	39.25	39.75	40.35	38.89	39.59	40.14	39.56	0.15	39.97	39.44
TiO2	0.47	0.67	0.65	0.50	0.69	0.62	0.42	0.35	0.53	0.04	0.42	0.42
Al2O3	22.15	21.99	21.18	20.93	21.53	21.61	22.08	22.15	21.73	0.14	21.54	21.69
FeO	17.95	18.85	19.21	18.35	18.53	19.15	17.69	17.83	18.27	0.24	18.01	19.18
MnO	0.87	0.91	1.18	1.13	0.61	1.04	0.89	0.53	0.88	0.07	1.01	0.72
MgO	10.87	10.57	10.14	10.23	10.17	10.02	10.84	10.95	10.59	0.15	10.71	10.04
CaO	8.39	7.92	8.15	9.14	8.15	8.74	8.53	8.68	8.51	0.13	8.35	8.44
Ions per 24 oxygens												
Si	5.925	5.910	5.968	6.015	6.064	5.903	5.950	5.986	5.962		6.015	5.971
Ti	0.053	0.076	0.074	0.057	0.078	0.071	0.047	0.039	0.061		0.048	0.048
Al	3.925	3.914	3.796	3.733	3.813	3.866	3.911	3.893	3.859		3.821	3.871
Fe	2.257	2.380	2.443	2.322	2.329	2.431	2.223	2.223	2.302		2.267	2.429
Mn	0.111	0.116	0.152	0.145	0.078	0.134	0.113	0.067	0.113		0.129	0.092
Mg	2.436	2.379	2.299	2.308	2.278	2.267	2.429	2.434	2.378		2.403	2.266
Ca	1.352	1.281	1.328	1.482	1.312	1.421	1.374	1.387	1.375		1.346	1.369
mole. %												
Alm-Sps	38.46	40.55	41.71	39.43	40.13	41.01	38.06	37.48	39.16		38.98	40.95
Pyr	39.58	38.64	36.95	36.88	37.99	36.26	39.56	39.83	38.56		39.10	36.81
Gross	21.96	20.81	21.34	23.68	21.88	22.73	22.37	22.69	22.29		21.91	22.24

Run #	106-9a	106-9b	106-9c	Avg.	sdm	108-10	108-9	108-9a	108-9b	108-9c	Avg.	sdm
core/rim				106	106	r	c				108	108
Temp (°C)	900	900	900	900	900	925	925	925	925	925	925	925
Time (d)	9	9	9	9	9	1	1	1	1	1	1	1
SiO2	39.35	39.67	39.15	39.52	0.13	39.86	39.73	38.87	39.01	38.73	39.24	0.21
TiO2	0.51	0.49	0.69	0.51	0.04	0.52	0.55	0.73	0.56	0.74	0.62	0.04
Al2O3	21.21	20.76	21.62	21.36	0.15	22.08	21.44	21.56	21.30	21.41	21.56	0.12
FeO	19.50	18.50	19.39	18.92	0.26	17.15	17.93	18.07	18.44	18.75	18.07	0.24
MnO	1.11	1.01	1.33	1.04	0.09	0.53	0.81	1.04	0.96	0.77	0.82	0.08
MgO	9.72	10.36	9.79	10.12	0.17	11.82	11.43	10.74	11.32	11.05	11.27	0.16
CaO	8.63	9.24	8.07	8.55	0.17	8.08	8.17	9.04	8.44	8.51	8.45	0.15
Ions per 24 oxygens												
Si	5.979	6.009	5.942	5.983		5.956	5.972	5.880	5.901	5.870	5.916	
Ti	0.058	0.056	0.079	0.058		0.058	0.062	0.083	0.064	0.084	0.070	
Al	3.799	3.706	3.867	3.813		3.889	3.798	3.844	3.797	3.825	3.831	
Fe	2.478	2.343	2.461	2.395		2.143	2.254	2.286	2.333	2.377	2.278	
Mn	0.143	0.130	0.171	0.133		0.067	0.103	0.133	0.123	0.099	0.105	
Mg	2.202	2.339	2.215	2.285		2.633	2.561	2.422	2.553	2.497	2.533	
Ca	1.405	1.500	1.312	1.386		1.294	1.316	1.465	1.368	1.382	1.365	
mole. %												
Alm-Sps	42.08	39.18	42.73	40.78		36.02	37.81	38.36	38.51	38.96	37.94	
Pyr	35.36	37.06	35.96	36.86		42.91	41.08	38.41	40.03	39.29	40.33	
Gross	22.56	23.76	21.31	22.36		21.08	21.11	23.23	21.45	21.75	21.73	

Table 3.5 (cont.). Garnet compositions (SEM-EDS).

Run #	109-8	109-7	109-6	109-12	109-11	109-13	109-14	Avg.	sdm	110-9	110-8
core/rim	r			c			r	109	109	r	c
Temp (°C)	925	925	925	925	925	925	925	925	925	925	925
Time (d)	2	2	2	2	2	2	2	2	2	4	4
SiO2	40.37	40.56	40.09	39.50	39.80	39.89	39.76	40.00	0.13	40.49	39.45
TiO2	0.55	0.34	0.69	0.67	0.62	0.53	0.63	0.58	0.04	0.44	0.57
Al2O3	22.39	21.89	21.65	21.27	21.61	21.84	22.35	21.86	0.14	22.46	21.84
FeO	16.01	16.83	17.25	17.81	17.83	17.42	17.11	17.18	0.22	14.97	17.31
MnO	0.34	0.68	0.77	1.23	0.75	0.36	0.31	0.63	0.12	0.34	0.81
MgO	11.78	10.61	10.55	11.66	11.01	11.24	11.88	11.25	0.19	13.53	11.56
CaO	8.58	8.99	9.01	7.75	8.38	8.72	7.96	8.48	0.17	7.77	8.38
Ions per 24 oxygens											
Si	5.996	6.068	6.015	5.954	5.982	5.978	5.935	5.990		5.975	5.927
Ti	0.061	0.038	0.078	0.076	0.070	0.060	0.071	0.065		0.049	0.064
Al	3.920	3.860	3.829	3.779	3.828	3.857	3.932	3.858		3.906	3.867
Fe	1.989	2.106	2.165	2.245	2.241	2.183	2.136	2.152		1.847	2.175
Mn	0.043	0.086	0.098	0.157	0.095	0.046	0.039	0.080		0.042	0.103
Mg	2.608	2.366	2.360	2.620	2.467	2.511	2.643	2.511		2.976	2.589
Ca	1.365	1.441	1.448	1.252	1.350	1.400	1.273	1.361		1.228	1.349
mole. %											
Alm-Sps	33.83	36.54	37.27	38.29	37.98	36.30	35.71	36.57		31.01	36.65
Pyr	43.44	39.44	38.87	41.76	40.09	40.90	43.40	41.13		48.84	41.65
Gross	22.74	24.02	23.86	19.95	21.93	22.80	20.90	22.30		20.16	21.70

Run #	110-9a	110-9b	110-9c	Avg.	sdm	113-14	113-13	113-12	113-1	113-3	Avg.
core/rim				110	110	r	-	c			113
Temp (°C)	925	925	925	925	925	925	925	925	925	925	925
Time (d)	4	4	4	4	4	8	8	8	8	8	8
SiO2	38.86	38.98	39.78	23.57	0.18	40.13	39.92	39.28	39.77	40.31	39.88
TiO2	0.66	0.59	0.48	0.35	0.03	0.37	0.57	0.77	0.36	0.46	0.51
Al2O3	21.46	21.49	21.79	12.97	0.09	22.83	22.25	21.89	21.66	22.94	22.31
FeO	18.41	18.63	17.10	10.88	0.33	14.51	15.95	17.14	17.54	14.99	16.03
MnO	0.91	0.75	0.52	0.45	0.07	0.42	0.55	0.60	0.39	0.32	0.46
MgO	11.24	11.27	11.94	6.92	0.14	12.70	11.59	11.54	11.55	12.14	11.90
CaO	8.49	8.33	8.43	5.08	0.03	8.97	9.19	8.76	8.77	8.82	8.90
Ions per 24 oxygens											
Si	5.878	5.892	5.953	5.925		5.937	5.952	5.898	5.966	5.964	5.943
Ti	0.075	0.067	0.054	0.062		0.041	0.064	0.087	0.041	0.051	0.057
Al	3.826	3.829	3.843	3.854		3.981	3.910	3.874	3.830	4.000	3.919
Fe	2.329	2.355	2.140	2.168		1.795	1.989	2.152	2.200	1.855	1.997
Mn	0.117	0.096	0.066	0.085		0.053	0.069	0.076	0.050	0.040	0.058
Mg	2.534	2.540	2.664	2.662		2.801	2.576	2.583	2.583	2.678	2.645
Ca	1.376	1.349	1.352	1.330		1.422	1.468	1.409	1.410	1.398	1.421
mole. %											
Alm-Sps	38.47	38.66	35.46	37.32		30.44	33.73	35.82	36.04	31.74	33.57
Pyr	39.88	40.06	42.82	41.09		46.14	42.21	41.52	41.38	44.85	43.21
Gross	21.65	21.28	21.73	21.59		23.42	24.06	22.65	22.58	23.42	23.22

Table 3.5 (cont.). Garnet compositions (SEM-EDS).

Run #	sdm	117-6	117-5	117-4	117-7	117-8	Avg.	sdm	103-13	103-12	103-11
core/rim	113	r	-	c	r	c	117	117	r	-	c
Temp (°C)	925	950	950	950	950	950	950	950	950	950	950
Time (d)	8	1	1	1	1	1	1	1	2	2	2
SiO2	0.16	40.48	39.91	40.06	39.93	39.59	39.99	0.13	39.80	40.08	40.12
TiO2	0.07	0.20	0.79	0.42	0.22	0.71	0.47	0.11	0.51	0.81	0.48
Al2O3	0.23	22.83	21.91	22.06	22.82	21.97	22.32	0.19	23.03	21.79	21.51
FeO	0.53	13.52	15.77	15.38	15.23	16.14	15.21	0.40	13.96	15.67	16.51
MnO	0.05	0.31	0.44	0.46	0.33	0.45	0.40	0.03	0.26	0.34	0.83
MgO	0.20	14.51	12.69	13.18	13.44	12.56	13.28	0.31	14.53	12.38	12.05
CaO	0.07	8.21	8.52	8.46	8.05	8.62	8.37	0.09	7.94	8.51	8.54
Ions per 24 oxygens											
Si		5.938	5.936	5.945	5.908	5.904	5.926		5.855	5.980	5.995
Ti		0.022	0.088	0.047	0.024	0.080	0.052		0.056	0.091	0.054
Al		3.947	3.841	3.859	3.979	3.862	3.898		3.993	3.832	3.788
Fe		1.658	1.962	1.909	1.884	2.013	1.885		1.717	1.955	2.063
Mn		0.039	0.055	0.058	0.041	0.057	0.050		0.032	0.043	0.105
Mg		3.173	2.814	2.916	2.964	2.792	2.933		3.187	2.753	2.684
Ca		1.290	1.358	1.345	1.276	1.377	1.329		1.251	1.360	1.367
mole. %											
Alm-Sps		27.55	32.59	31.58	31.23	33.17	31.22		28.28	32.69	34.86
Pyr		51.51	45.47	46.82	48.07	44.75	47.33		51.50	45.05	43.16
Gross		20.95	21.94	21.60	20.69	22.07	21.45		20.22	22.26	21.98

Run #	103-10	103-9	103-8	103-7	Avg.	sdm	121-3	121-4	121-9a	121-9b	Avg.
core/rim	r	-	-	c	103	103	r	c			121
Temp (°C)	950	950	950	950	950	950	975	975	975	975	975
Time (d)	2	2	2	2	2	2	1	1	1	1	1
SiO2	39.96	40.21	39.80	39.52	39.93	0.08	39.94	40.13	38.83	39.67	39.64
TiO2	0.39	0.65	0.67	0.53	0.58	0.05	0.37	0.57	0.80	0.56	0.58
Al2O3	22.32	22.36	22.38	21.88	22.18	0.18	22.32	21.52	21.20	21.45	21.62
FeO	13.89	15.23	15.65	16.85	15.39	0.40	15.01	15.62	17.27	16.02	15.98
MnO	0.32	0.39	0.61	0.44	0.46	0.07	0.53	0.54	0.66	0.59	0.58
MgO	13.92	12.33	11.96	12.08	12.75	0.36	13.44	13.53	12.93	13.52	13.36
CaO	8.23	8.77	8.96	8.73	8.53	0.12	8.11	8.13	8.35	8.21	8.20
Ions per 24 oxygens											
Si	5.941	5.965	5.925	5.915	5.939		5.931	5.961	5.840	5.915	5.912
Ti	0.044	0.073	0.075	0.060	0.065		0.041	0.064	0.090	0.063	0.064
Al	3.911	3.910	3.927	3.860	3.889		3.906	3.768	3.758	3.770	3.801
Fe	1.727	1.890	1.948	2.109	1.915		1.864	1.940	2.172	1.998	1.993
Mn	0.040	0.049	0.077	0.056	0.057		0.067	0.068	0.084	0.075	0.073
Mg	3.085	2.727	2.654	2.695	2.827		2.975	2.996	2.899	3.005	2.969
Ca	1.311	1.394	1.429	1.400	1.359		1.290	1.294	1.346	1.312	1.310
mole. %											
Alm-Sps	28.67	31.99	33.15	34.58	32.03		31.16	31.89	34.71	32.43	32.56
Pyr	50.06	45.00	43.45	43.06	45.91		48.02	47.57	44.59	47.04	46.79
Gross	21.27	23.01	23.39	22.36	22.06		20.82	20.54	20.70	20.53	20.65

Table 3.5 (cont.). Garnet compositions (SEM-EDS).

Run #	sdm	119-5	119-9a	119-9b	119-9c	119-9d	Avg.	sdm	138-1	138-2	138-3
core/rim	121						119	119	r	c	r
Temp (°C)	975	975	975	975	975	975	975	975	990	990	990
Time (d)	1	4	4	4	4	4	4	4	1	1	1
SiO2	0.25	39.85	40.61	40.42	40.68	40.75	40.46	0.15	40.07	39.96	39.56
TiO2	0.08	0.61	0.20	0.56	0.31	0.29	0.39	0.07	0.51	0.51	0.58
Al2O3	0.21	22.22	22.88	21.99	22.35	22.88	22.46	0.16	21.56	21.79	21.87
FeO	0.41	14.59	13.55	14.54	14.36	13.55	14.12	0.21	16.71	16.72	16.42
MnO	0.03	0.36	0.36	0.51	0.44	0.49	0.43	0.03	0.85	0.66	0.82
MgO	0.12	14.41	14.95	13.55	13.67	14.57	14.23	0.24	11.96	11.59	11.82
CaO	0.05	7.99	7.48	8.46	8.13	7.51	7.91	0.17	8.38	8.81	8.95
Ions per 24 oxygens											
Si		5.887	5.946	5.973	5.997	5.967	5.954		5.991	5.977	5.923
Ti		0.068	0.022	0.062	0.034	0.032	0.044		0.057	0.057	0.065
Al		3.869	3.949	3.830	3.883	3.949	3.896		3.799	3.841	3.859
Fe		1.803	1.659	1.797	1.770	1.659	1.737		2.089	2.091	2.056
Mn		0.045	0.045	0.064	0.055	0.061	0.054		0.108	0.084	0.104
Mg		3.174	3.263	2.985	3.004	3.181	3.122		2.666	2.584	2.638
Ca		1.265	1.173	1.339	1.284	1.178	1.248		1.342	1.412	1.436
mole. %											
Alm-Sps		29.39	27.75	30.08	29.86	28.30	29.08		35.41	35.25	34.65
Pyr		50.49	53.14	48.26	49.14	52.32	50.67		42.96	41.88	42.32
Gross		20.12	19.11	21.66	21.00	19.38	20.25		21.63	22.88	23.03

Run #	Avg.	sdm
core/rim	138	
Temp (°C)	990	
Time (d)	1	
SiO2	39.86	0.13
TiO2	0.53	0.02
Al2O3	21.74	0.08
FeO	16.62	0.08
MnO	0.78	0.05
MgO	11.79	0.09
CaO	8.71	0.14
Ions per 24 oxygens		
Si	5.964	
Ti	0.060	
Al	3.833	
Fe	2.079	
Mn	0.098	
Mg	2.629	
Ca	1.397	
mole. %		
Alm-Sps	35.10	0.19
Pyr	42.39	0.26
Gross	22.51	0.36

Table 3.6. Plagioclase compositions from powder runs (SEM-EDS).

Run #	105	105	120	118	102	115	106	108	108
Temp.(°C)	850	850	850	875	900	900	900	925	925
time (d)	2	2	8	8	1	4	9	1	1
SiO2	44.89	45.87	45.73	45.81	45.85	45.84	44.70	45.43	45.42
TiO2	0.00	0.00	0.18	0.19	0.00	0.00	0.00	0.11	0.12
Al2O3	34.79	34.36	34.52	34.50	34.93	34.79	35.19	34.71	34.64
FeO	0.36	0.32	0.24	0.24	0.26	0.28	0.52	0.45	0.41
MgO	0.15	0.00	0.00	0.00	0.00	0.00	0.00	0.00	0.00
CaO	19.37	18.14	17.97	18.31	17.76	18.04	18.77	18.16	17.87
Na2O	0.47	1.33	1.19	0.98	1.21	1.07	0.84	1.17	1.57
K2O	0.00	0.00	0.00	0.00	0.00	0.00	0.00	0.00	0.00
Ions per 32 oxygens									
Si	8.303	8.461	8.441	8.441	8.438	8.441	8.270	8.386	8.388
Ti	0.000	0.000	0.025	0.026	0.000	0.000	0.000	0.015	0.017
Al	7.584	7.470	7.510	7.493	7.577	7.550	7.673	7.552	7.540
Fe	0.056	0.049	0.037	0.037	0.040	0.043	0.080	0.069	0.063
Mg	0.041	0.000	0.000	0.000	0.000	0.000	0.000	0.000	0.000
Ca	3.838	3.585	3.554	3.615	3.502	3.559	3.720	3.592	3.536
Na	0.169	0.476	0.426	0.350	0.432	0.382	0.301	0.419	0.562
K	0.000	0.000	0.000	0.000	0.000	0.000	0.000	0.000	0.000

Run #	109	110	113	117	103	121	119	Average	sdm:16
Temp.(°C)	925	925	925	950	950	975	975		
time (d)	2	4	8	1	2	1	4		
SiO2	43.75	45.54	43.35	43.14	45.29	44.02	44.24	44.93	0.23
TiO2	0.00	0.00	0.00	0.00	0.00	0.17	0.00	0.05	0.02
Al2O3	35.77	34.51	35.70	36.05	34.35	35.52	35.29	34.98	0.13
FeO	0.27	0.50	0.40	0.41	0.00	0.29	0.00	0.31	0.04
MgO	0.18	0.00	0.19	0.00	0.00	0.00	0.00	0.03	0.02
CaO	19.60	18.41	20.12	19.87	18.71	19.36	19.85	18.77	0.19
Na2O	0.46	1.07	0.27	0.47	1.60	0.61	0.49	0.93	0.10
K2O	0.00	0.00	0.00	0.09	0.07	0.07	0.00	0.01	0.01
Ions per 32 oxygens									
Si	8.092	8.400	8.002	7.949	8.335	8.106	8.185	8.294	
Ti	0.000	0.000	0.000	0.000	0.000	0.024	0.000	0.007	
Al	7.798	7.503	7.767	7.829	7.451	7.709	7.695	7.610	
Fe	0.042	0.077	0.062	0.063	0.000	0.045	0.000	0.048	
Mg	0.050	0.000	0.052	0.000	0.000	0.000	0.000	0.009	
Ca	3.884	3.638	3.979	3.923	3.689	3.819	3.935	3.712	
Na	0.165	0.383	0.097	0.168	0.571	0.218	0.176	0.331	
K	0.000	0.000	0.000	0.021	0.016	0.016	0.000	0.003	

sdm:16 = standard deviation of the mean of the16 analyses An92

Table 3.7. Averaged, normalized liquid (glass) compositions from 10 kbar, powder experiments (SEM-EDS).

Run #	120	sdm:3	118	sdm:4	126	sdm:4	102	sdm:6	115	sdm:4	106	sdm:5	108	sdm:3	109	sdm:4	110	sdm:3
Temp (°C)	850		875		875		900		900		900		925		925		925	
Time (d)	8		8		14		1		4		9		1		2		4	
SiO2	64.79	0.26	65.09	0.10	61.46	0.08	63.97	0.25	63.79	0.30	66.34	0.17	62.47	0.29	63.51	0.27	61.72	0.14
TiO2	0.43	0.05	0.30	0.04	0.28	0.06	0.35	0.03	0.31	0.08	0.33	0.04	0.42	0.04	0.32	0.03	0.33	0.04
Al2O3	19.07	0.09	19.27	0.17	18.73	0.11	19.21	0.15	20.33	0.13	18.95	0.20	20.93	0.06	19.79	0.09	21.06	0.25
FeO	4.51	0.14	3.69	0.09	7.23	0.10	4.64	0.32	4.56	0.22	3.99	0.29	4.93	0.18	4.41	0.17	4.59	0.11
MnO	0.18	0.08	n.a.	--	0.17	0.05	0.12	0.07	0.00	0.00	0.05	0.03	n.a.	--	0.18	0.09	n.a.	--
MgO	1.51	0.13	1.99	0.08	1.97	0.04	2.06	0.10	1.70	0.08	1.36	0.09	1.33	0.15	1.97	0.07	2.47	0.10
CaO	7.95	0.03	7.91	0.09	8.52	0.10	8.54	0.31	8.27	0.16	7.50	0.06	8.53	0.05	8.28	0.28	7.88	0.08
Na2O	1.25	0.15	1.36	0.09	1.01	0.16	0.90	0.12	0.84	0.15	1.13	0.17	1.13	0.04	1.32	0.07	1.72	0.22
K2O	0.29	0.06	0.38	0.01	0.33	0.03	0.32	0.04	0.24	0.03	0.40	0.02	0.28	0.04	0.36	0.02	0.37	0.04
CIPW Norms																		
Q	33.5		33.0		27.2		32.4		34.2		37.0		30.8		30.2		26.1	
or	1.7		2.2		2.0		1.9		1.4		2.4		1.6		2.1		2.2	
ab	10.6		11.5		8.6		7.6		7.1		9.6		9.6		11.2		14.6	
an	39.4		39.2		42.4		42.4		41.0		37.2		42.3		41.1		39.1	
C	2.2		2.2		1.2		1.9		3.6		3.0		3.3		2.2		3.5	
di	0.0		0.0		0.0		0.0		0.0		0.0		0.0		0.0		0.0	
hy	11.7		11.2		18.1		13.3		12.1		10.3		11.7		12.8		14.0	
il	0.8		0.6		0.5		0.7		0.6		0.6		0.8		0.6		0.6	
ASI	1.1		1.1		1.1		1.1		1.2		1.2		1.2		1.1		1.2	

sdm:# = standard deviation of the mean of n=# analyses.

n.a. = not analyzed

ASI = alumina saturation index (after Zen, 1986).

Table 3.7 (cont.). Averaged, normalized liquid (glass) compositions from 10 kbar, powder experiments (SEM-EDS).

Run #	113	sdm:6	141	sdm:5	117	sdm:3	103	sdm:3	121	sdm:3	119	sdm:3	138	sdm:3	134	sdm:3
Temp (°C)	925		945		950		950		975		975		990		1000	
Time (d)	8		5		1		2		1		4		1		4	
SiO2	63.64	0.10	58.11	0.29	60.92	0.28	62.76	0.26	57.73	0.09	57.54	0.08	58.26	0.21	51.77	0.30
TiO2	0.40	0.06	0.39	0.11	0.39	0.07	0.38	0.02	0.46	0.01	0.47	0.03	0.48	0.10	0.51	0.01
Al2O3	20.33	0.04	21.23	0.18	20.97	0.02	20.56	0.12	21.78	0.02	20.93	0.21	22.39	0.06	20.95	0.07
FeO	3.27	0.10	6.99	0.31	4.76	0.14	3.62	0.14	6.25	0.03	5.99	0.11	6.19	0.22	7.09	0.15
MnO	0.14	0.06	0.10	0.05	n.a.	--	0.00	0.00	0.00	0.00	n.a.	--	0.15	0.06	0.23	0.09
MgO	2.11	0.06	2.45	0.19	2.46	0.04	2.68	0.09	2.86	0.09	3.48	0.09	1.55	0.13	6.36	0.08
CaO	7.93	0.09	9.17	0.13	8.18	0.12	7.50	0.11	7.62	0.09	9.24	0.13	9.21	0.14	11.50	0.16
Na2O	2.00	0.10	1.32	0.09	2.03	0.02	2.20	0.14	2.69	0.03	2.07	0.06	1.48	0.18	1.40	0.13
K2O	0.31	0.02	0.28	0.04	0.33	0.03	0.36	0.04	0.44	0.01	0.28	0.04	0.31	0.04	0.17	0.03
CIPW Norms																
Q	28.1		20.4		23.0		25.8		14.9		14.8		21.5		4.6	
or	1.8		1.6		2.0		2.1		2.6		1.6		1.8		1.0	
ab	16.9		11.2		17.2		18.6		22.8		17.5		12.5		11.8	
an	39.3		45.5		40.6		37.2		37.8		45.8		45.7		50.4	
C	2.3		2.1		2.4		2.9		3.0		0.4		2.9		0.0	
di	0.0		0.0		0.0		0.0		0.0		0.0		0.0		5.5	
hy	10.9		18.5		14.2		12.7		17.8		18.9		14.7		25.8	
il	0.8		0.7		0.7		0.7		0.9		0.9		0.9		1.0	
ASI	1.1		1.1		1.1		1.2		1.2		1.0		1.1		0.9	

sdm:# = standard deviation of the mean of n=# analyses.

n.a. = not analyzed

ASI = alumina saturation index (after Zen, 1986).

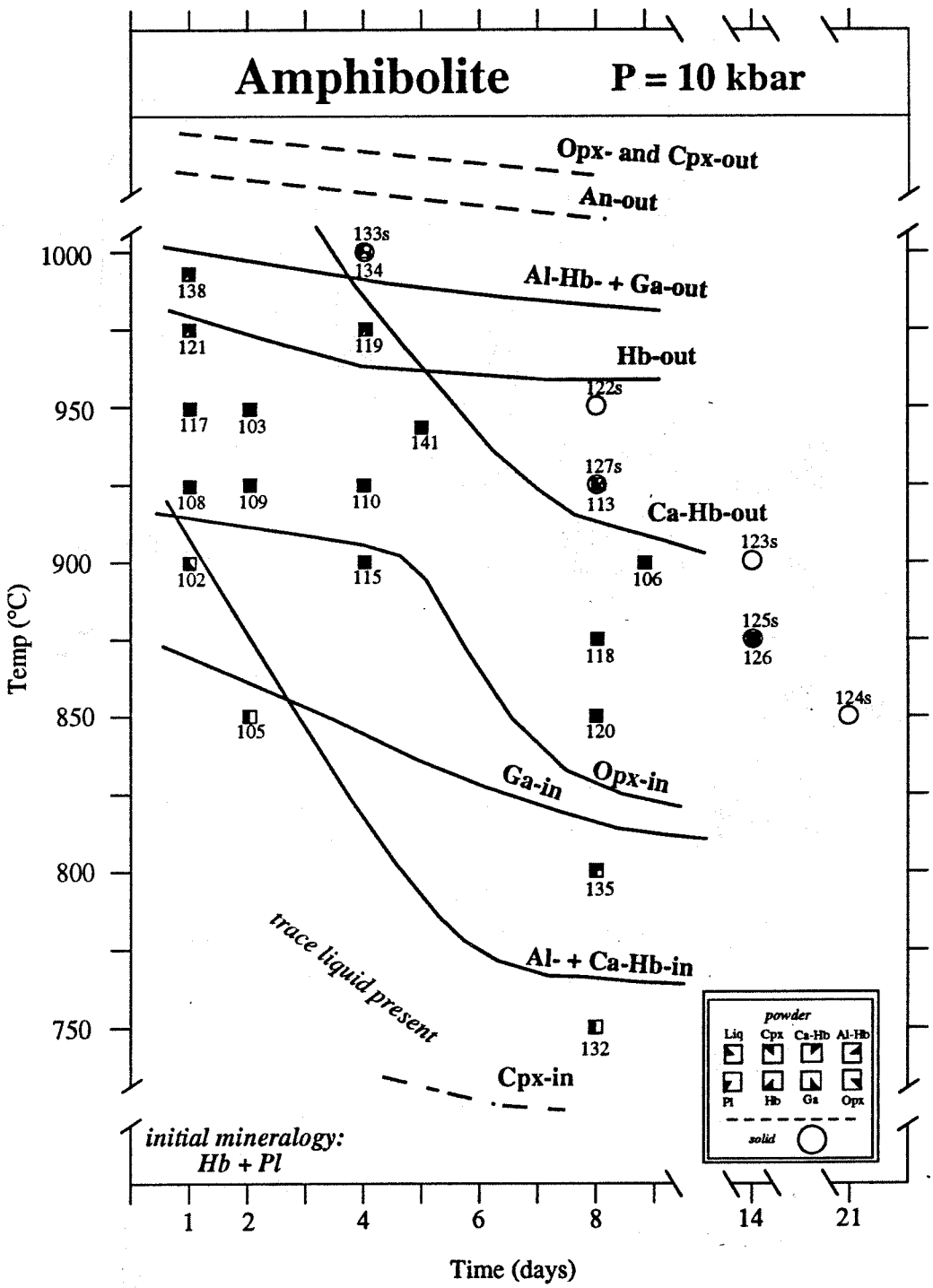

Fig. 3.1. Temperature-time diagram showing phase assemblages and time-dependent reaction boundaries determined from the 10 kbar amphibolite dehydration-melting powder runs (squares). The positions of solid amphibolite runs are identified by the circles.

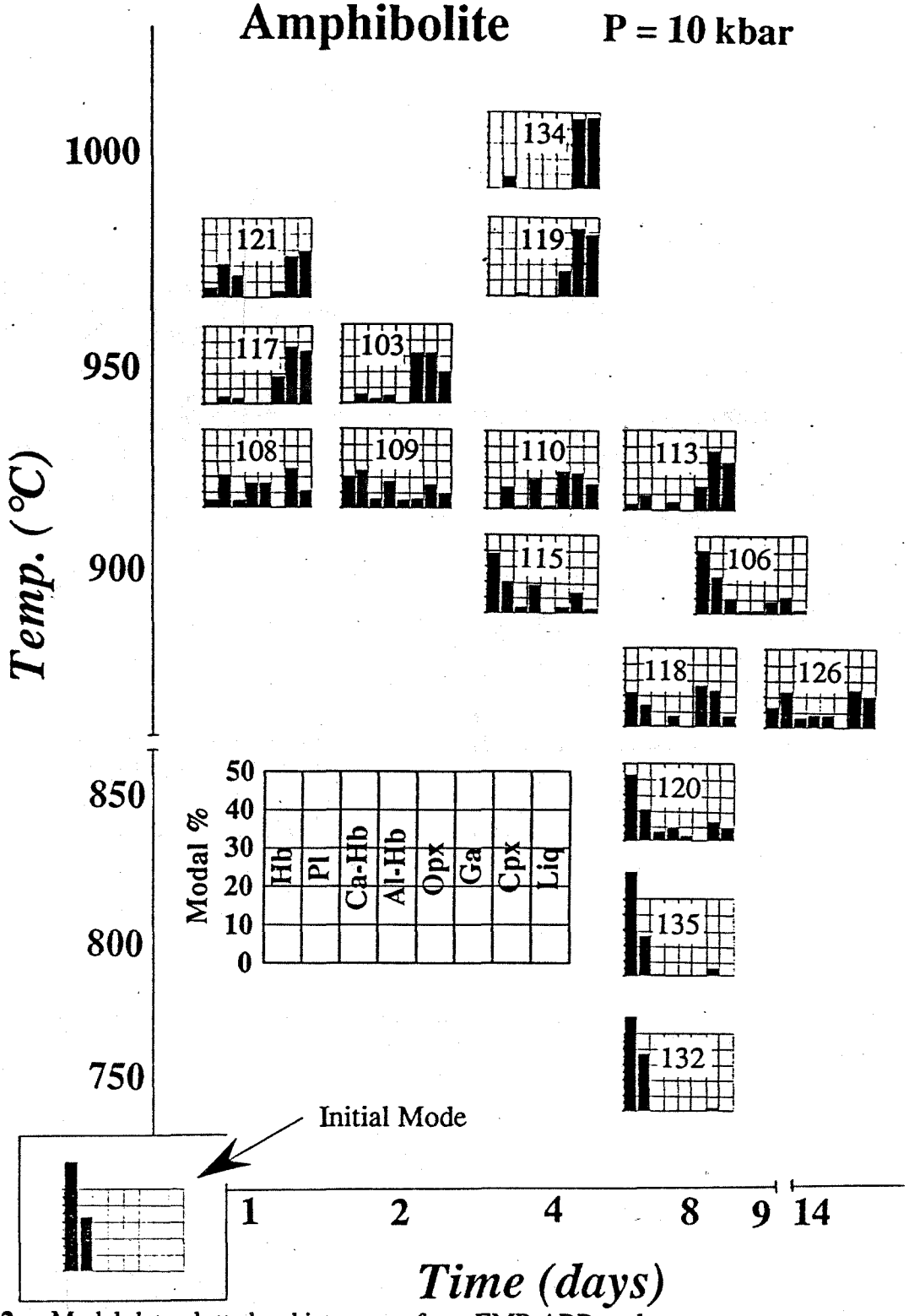

Fig. 3.2. Modal data plotted as histograms from EMP-ARP analyses versus temperature and time (see Fig. 3.1). Bars arranged with phase reactants to the left and phase products to the right, with the phases present at higher temperatures located farther to the right. An increase in the height of the phase bars (modes) generally sweeps across the histograms, from left to right, with increasing time or temperature. Errors on modes about ±5% absolute. Also see modal data in Fig. 3.3.

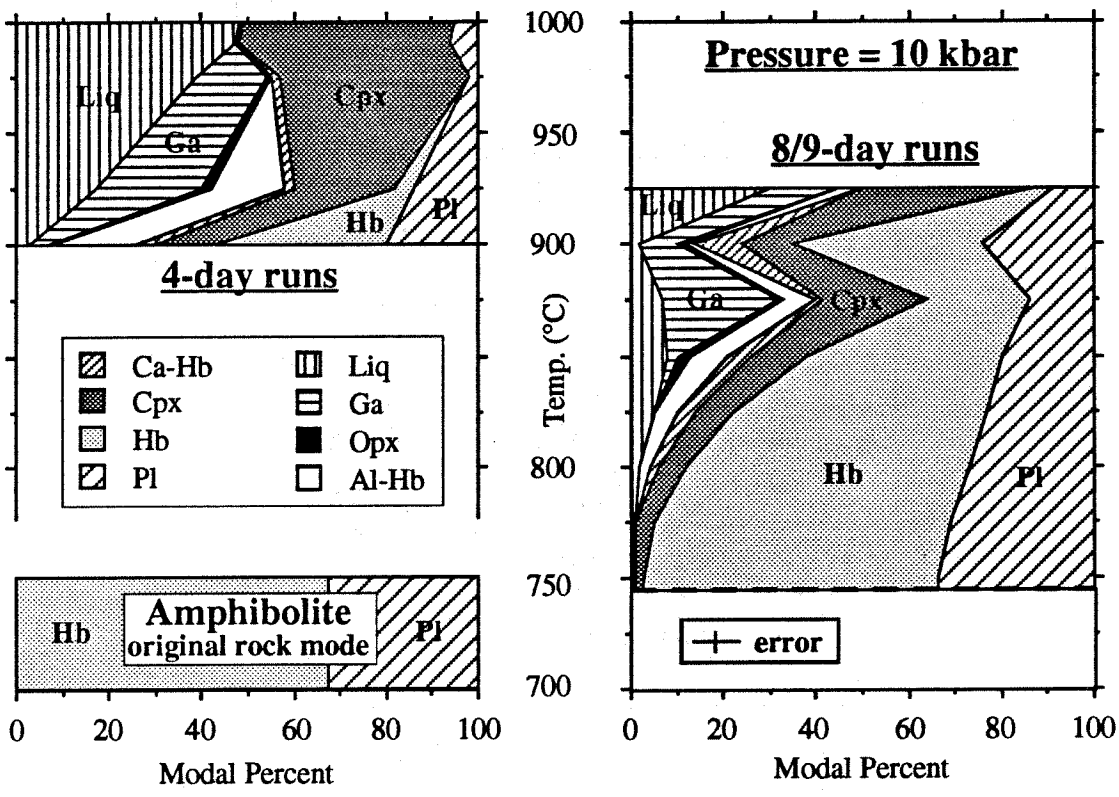

Fig. 3.3. Modal data from EMP-ARP analyses versus temperature for 4-, 8- and 9-day runs at 10 kbar (see Table 3.1). Initial amphibolite mode is 67.4% hornblende, 32.5% plagioclase, shown at bottom. See Fig. 3.2 for modes of all runs versus run duration.

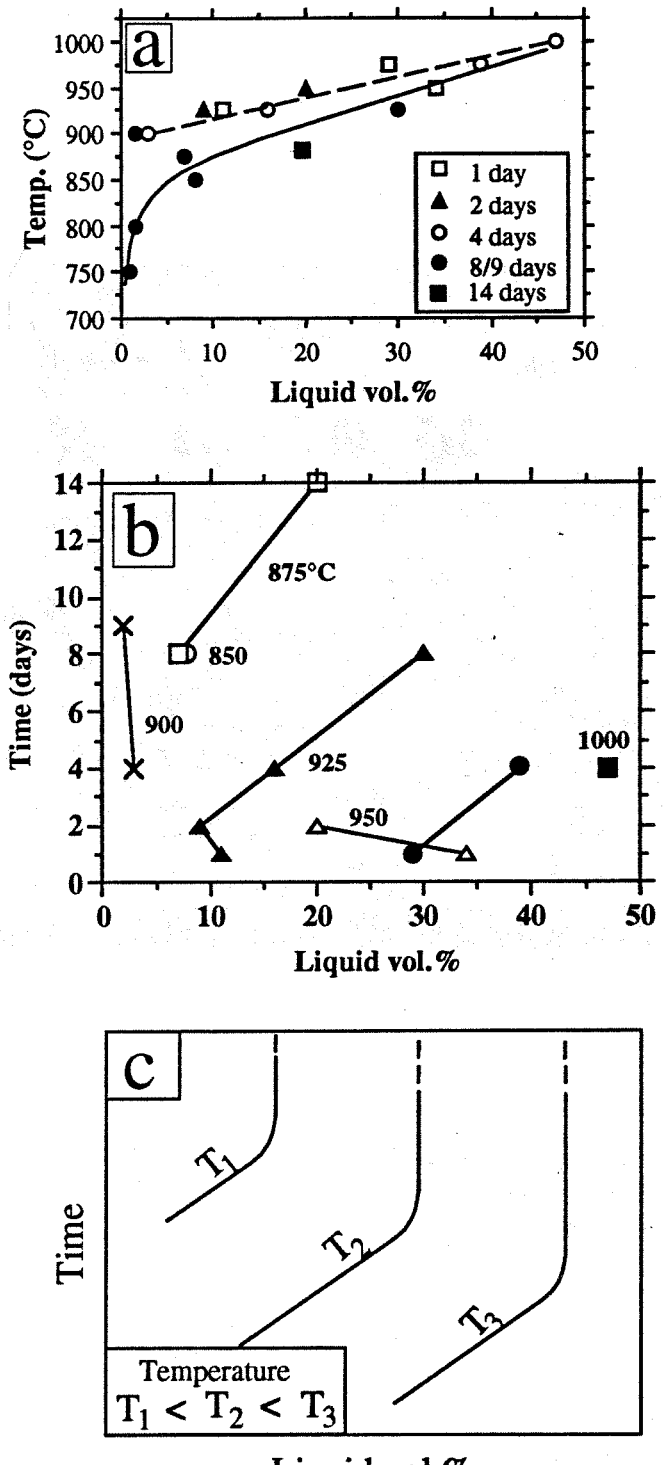

Fig. 3.4a-c. [a] Volume percentage of liquid generated during partial melting of amphibolite at 10 kbar as a function of temperature for four different run durations. Until temperatures above 875°C are reached, less than 10% liquid is generated. At 1000°C, ~47 vol.% liquid is produced. [b] Volume percentage of liquid as a function of time for runs at different temperatures. In general, more liquid is produced in the longer runs. [c] Theoretical shape of liquid fraction curves. Lower, inclined portions generalized from Fig. 3.4b. Theoretical vertical portions indicate that equilibrium has been attained, and further increases in run duration will yield no more liquid.

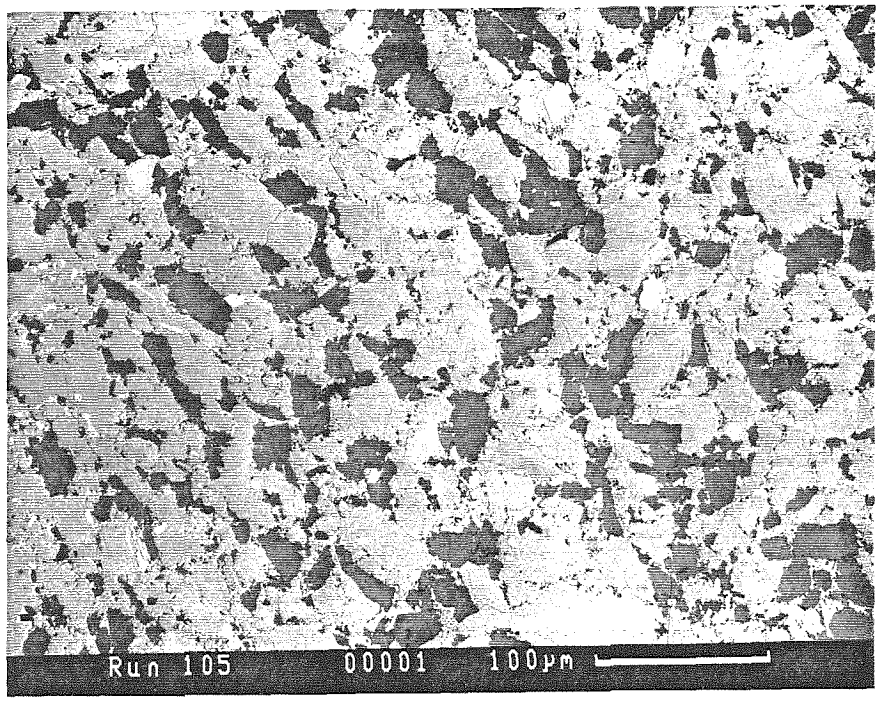

Fig. 3.5. Backscattered electron, SEM photomicrograph of powder amphibolite run #105 (850°C, 2 days). By brightness, from light to dark, the phases are clinopyroxene, hornblendes, plagioclase, glass. Note the early acicular growth of clinopyroxene needles (aspect ratio ~1:5).

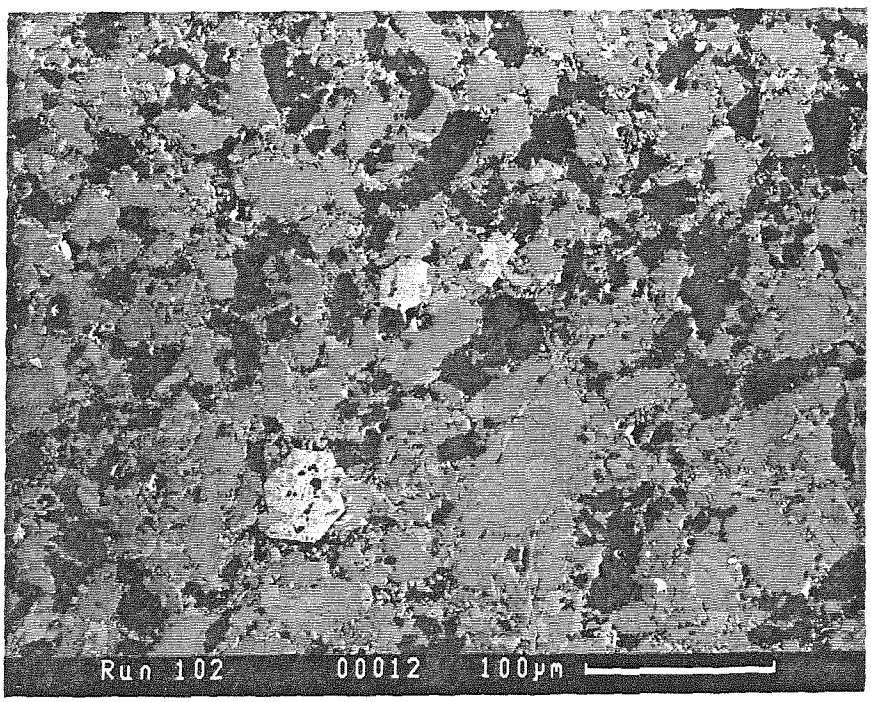

Fig. 3.6. Backscattered electron, SEM photomicrograph of powder amphibolite run #102 (900°C, 1 day). By brightness, from light to dark, the phases are clinopyroxene, hornblendes, plagioclase, glass.

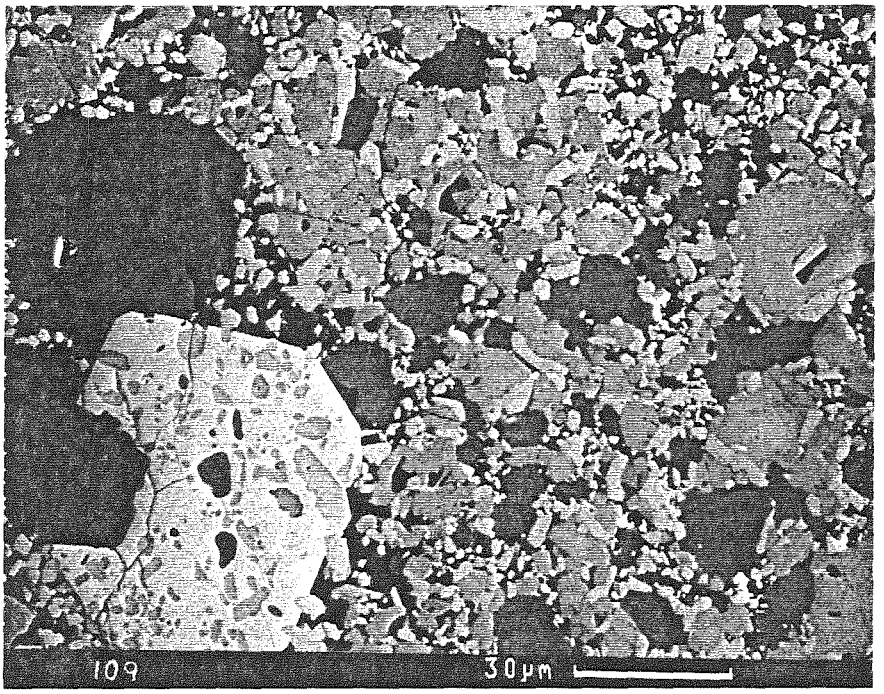

Fig. 3.7. Backscattered electron, SEM photomicrograph of powder amphibolite run #109 (925°C, 2 days). By brightness, from light to dark, the phases are clinopyroxene, hornblendes, plagioclase, glass. These higher-temperature clinopyroxene crystals are more blocky than the lower-temperature crystals in other runs (lower aspect ratio of ~1:2).

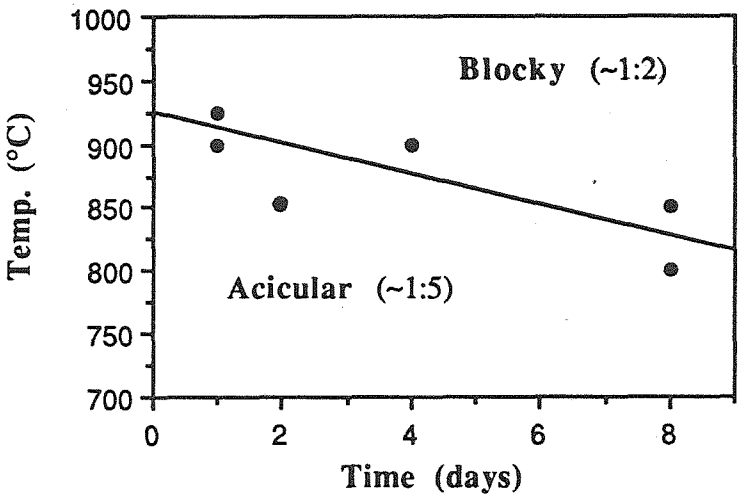

Fig. 3.8. Morphological changes in clinopyroxene as a function of temperature and time. Clinopyroxene nucleates and initially grows as acicular crystals, with large aspect ratios (~1:5). Crystals become more blocky with increasing temperature and/or time (lower aspect ratio of ~1:2). Changes are gradual across the boundary.

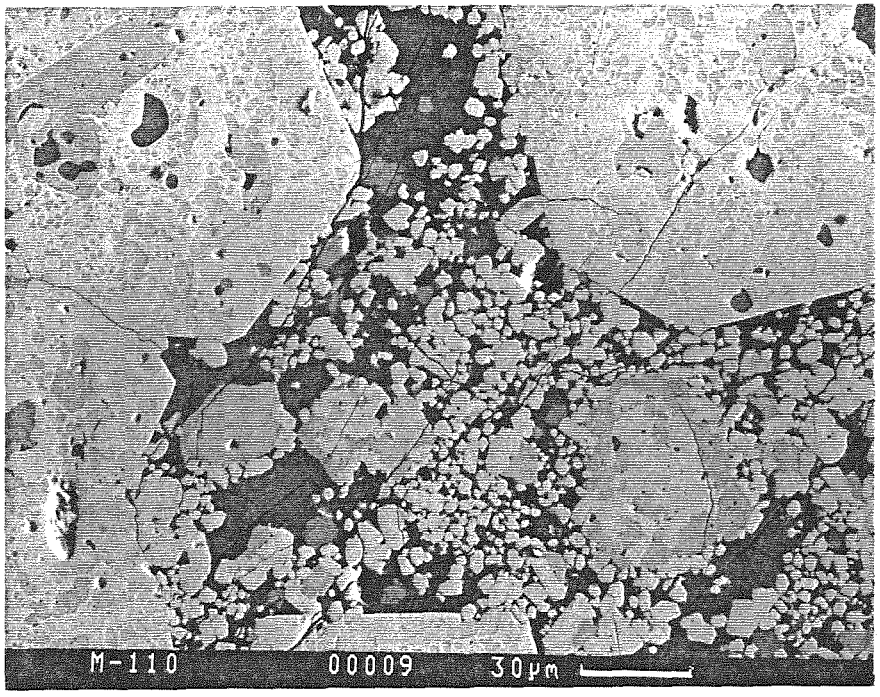

Fig. 3.9. Backscattered electron, SEM photomicrograph of powder amphibolite run #110 (925°C, 4 days). By brightness, from light to dark, the phases are clinopyroxene, hornblendes, plagioclase, glass.

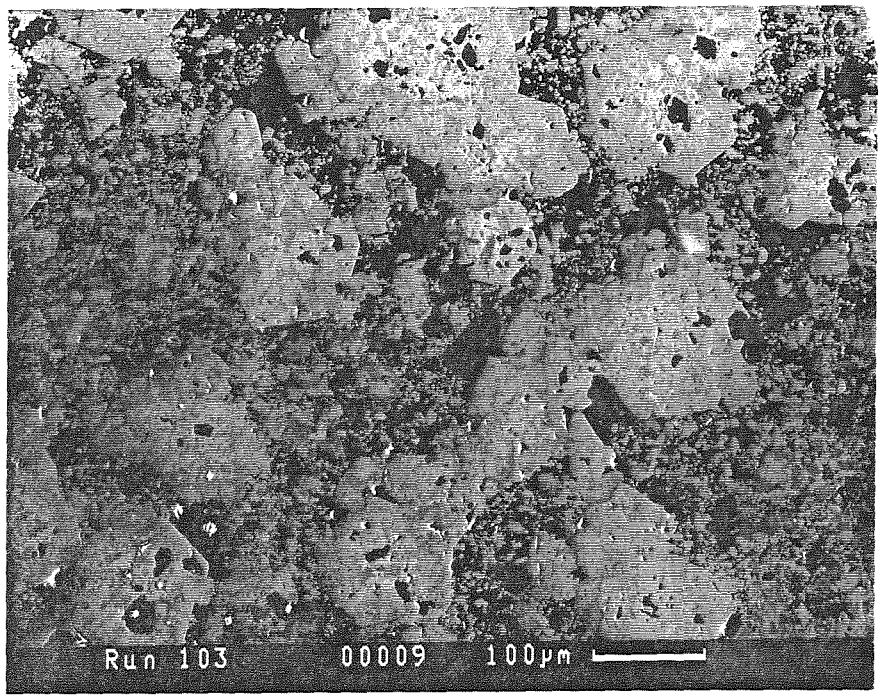

Fig. 3.10. Backscattered electron, SEM photomicrograph of powder amphibolite run #103 (950°C, 2 days). By brightness, from light to dark, the phases are clinopyroxene, hornblendes, plagioclase, glass.

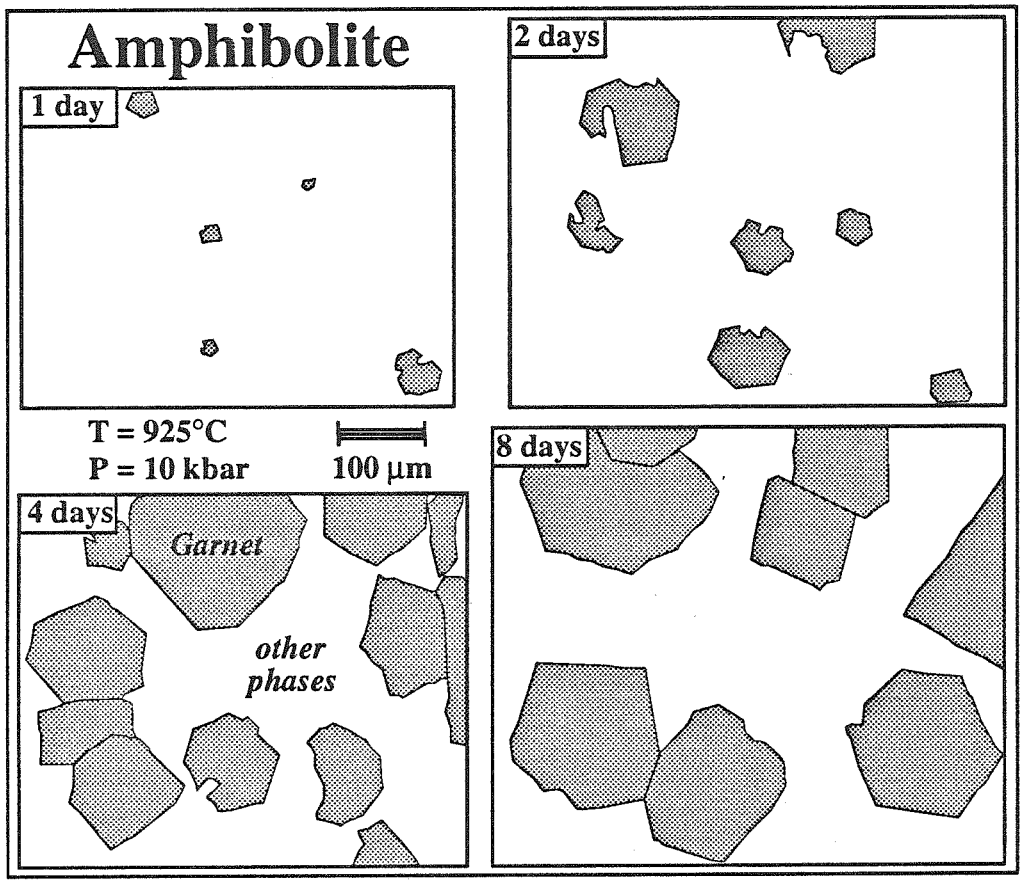

Fig. 3.11. Garnets grown in the partially melted amphibolite at 925°C, 10 kbar. Tracings of garnets show nucleation locations, spatial relationships and crystal sizes for four different durations (1, 2, 4, 8 days), drawn to the same scale.

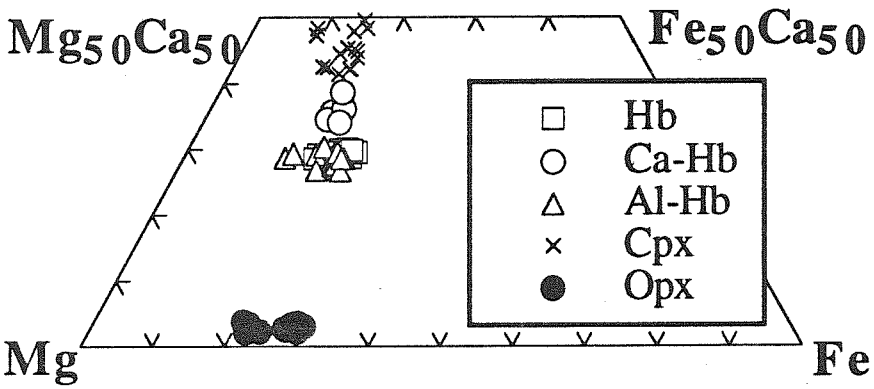

Fig. 3.12. Pyroxene Ca-Mg-Fe quadrilateral (mol. basis), showing initial hornblende (Hb), calcium-rich hornblende (Ca-Hb), alumina-rich hornblende (Al-Hb), clinopyroxene (Cpx), and orthopyroxene (Opx) (see Tables 3.2-3.4).

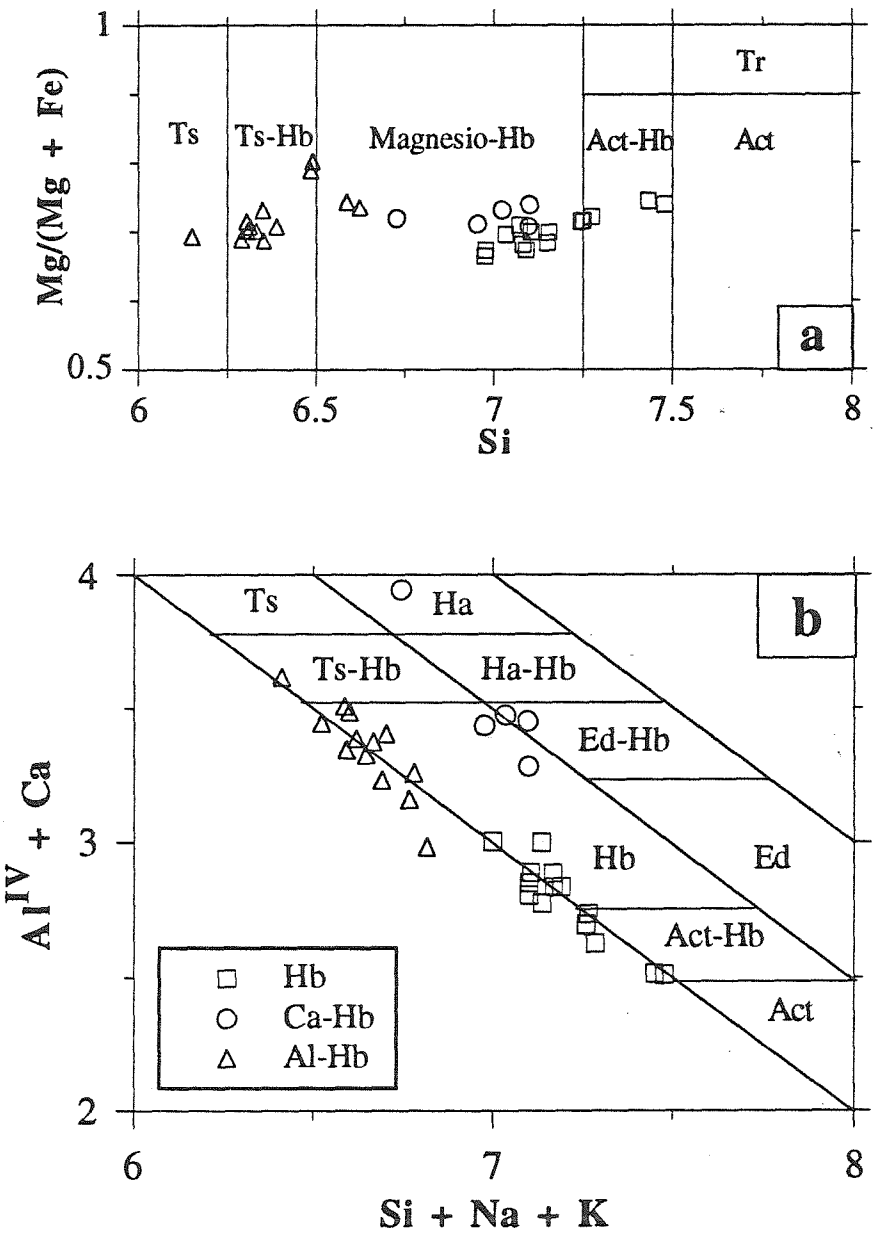

Fig. 3.13a,b. Classification schemes for amphiboles after: [a] Rock and Leake (1984) and [b] Giret et al. (1980). Initial amphibole is magnesio-hornblende [squares]. Two new hornblende compositions appear in the 10 kbar amphibolite melting experiments; calcium-rich hornblendes (Ca-Hb) [circles] and alumina-rich hornblendes (Al-Hb) [triangles] are due to $Al_2(Fe,Mg)_{-1}Si_{-1}$, $CaAlNa_{-1}Si_{-1}$, $NaAlSi_{-1}$, and $CaMg_{-1}$ substitutions (see Table 3.3). See Fig. 2.2 for amphibole abbreviations.

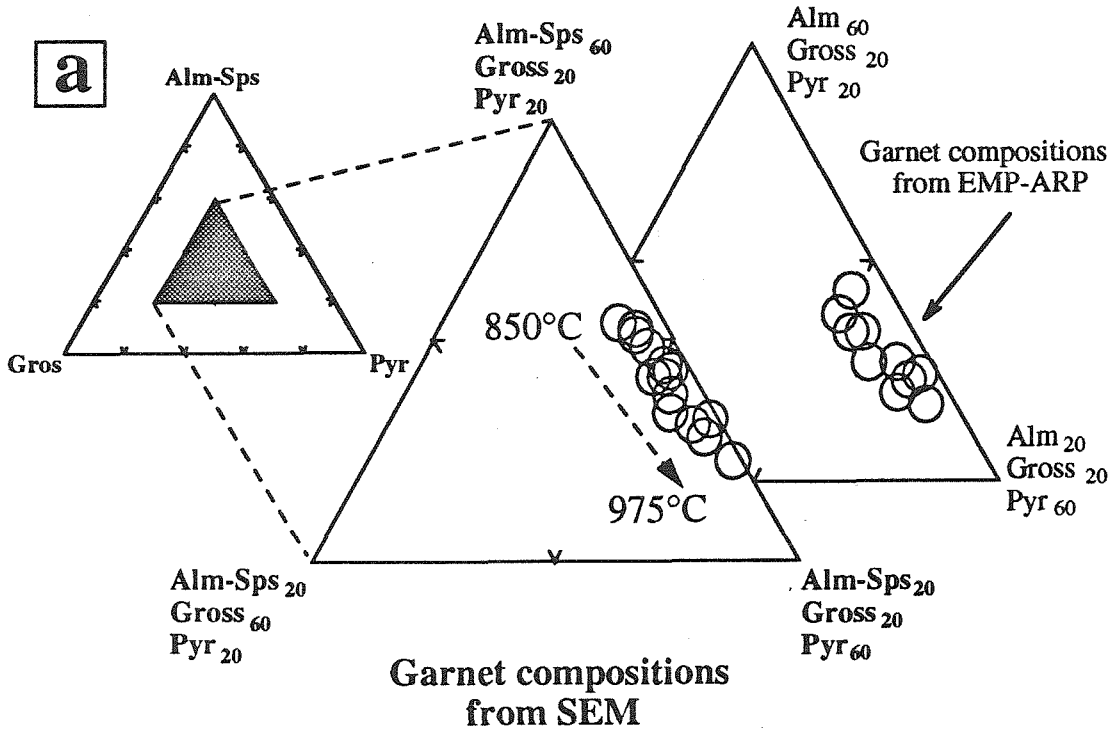

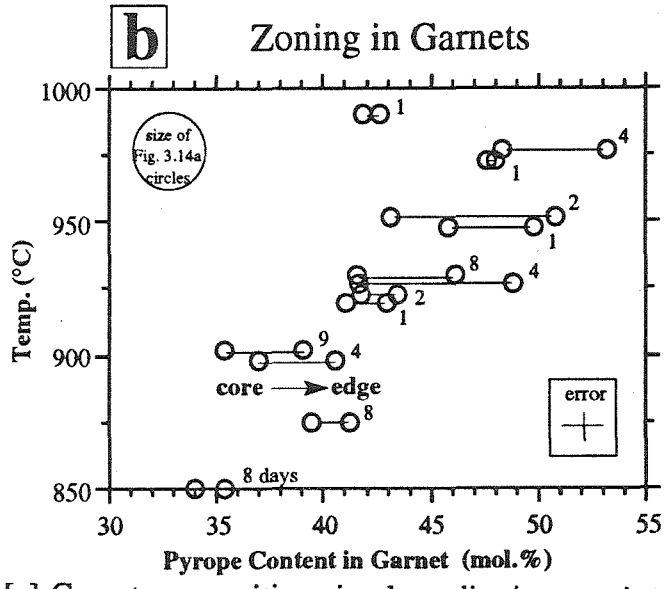

Fig. 3.14a,b. [a] Garnet compositions in almandine/spessartine (Alm-Sps) - grossular (Gross) - pyrope (Pyr) compositional space (mol. basis), from both SEM and EMP-ARP analyses. Each circle is an average from one or more garnets from a single run (see Table 3.5). The amount of grossular component does not vary much, but the amount of pyrope component generally increases with increasing run temperature (dashed arrow). [b] Variations in core and edge pyrope compositions as a function of temperature and time. Polythermal variations generally are larger than isothermal ones. Rims consistently contain more pyrope than the corresponding cores. Size of the big circle is scaled to those in [a].

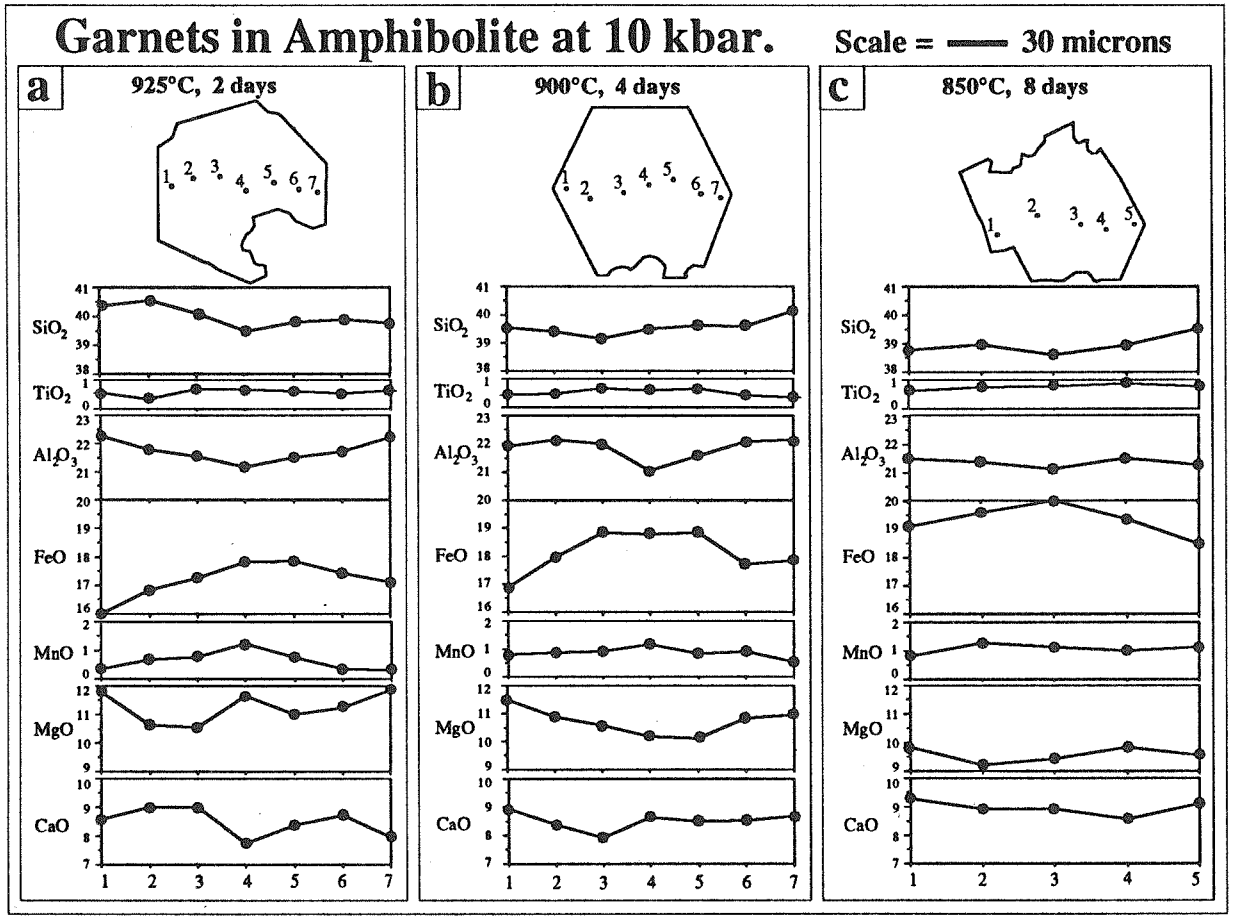

Fig. 3.15. Traced garnet outlines and locations of SEM analyses from three different runs with corresponding oxide profiles beneath each point. Profiles show that the garnets are compositionally zoned to varying degrees for different oxides. Note the shifts in the relative profile locations between each run. Analytical errors are about the size of the circles.

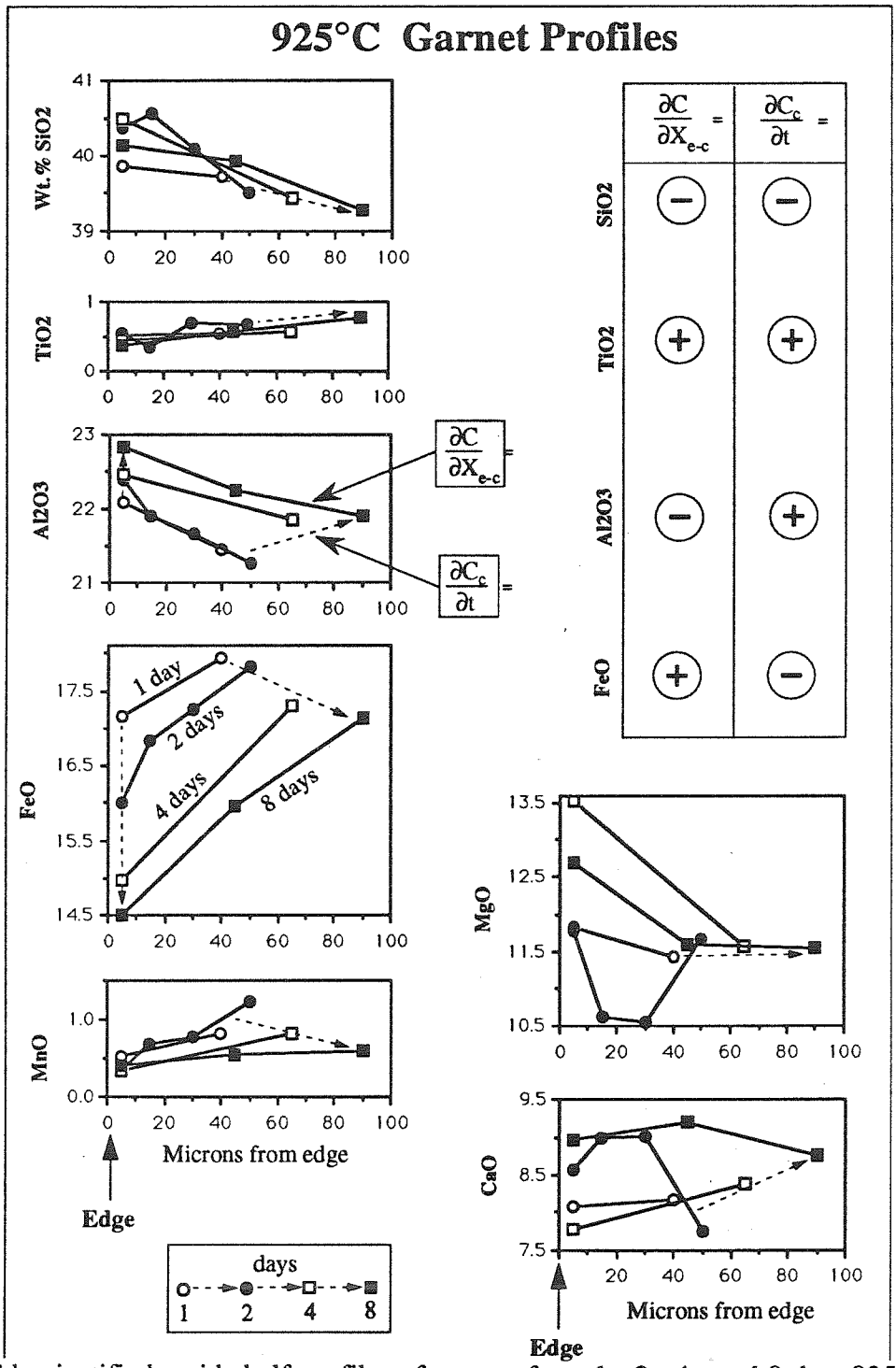

Fig. 3.16. Edge justified, oxide half-profiles of garnets from 1-, 2-, 4-, and 8-day, 925°C runs. Dashed arrows point in the direction of increasing time and show time-dependent changes in compositions of the cores and rims. $\frac{\partial C}{\partial X_{e\text{-}c}}$ refers to the change in composition with a change in distance from the edge to the core (solid lines). $\frac{\partial C_c}{\partial t}$ refers to the change in core composition with a change in time (dashed lines with arrows). The plus and minus symbols refer to the slope (positive or negative) of the solid and dashed lines.

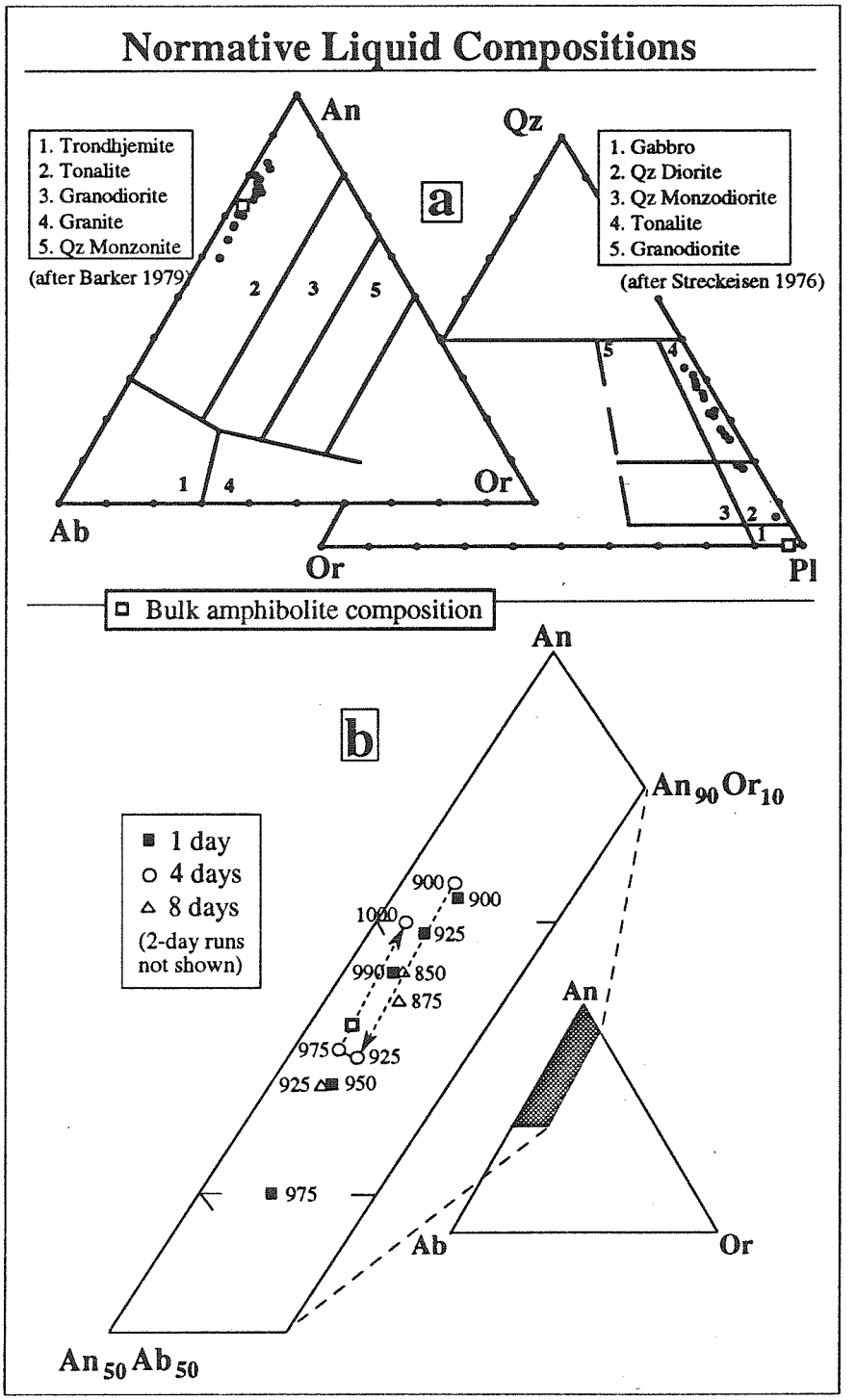

Fig. 3.17a,b. Liquid (glass) compositions from powder amphibolite runs: [a] plotted in anorthite (An)-albite (Ab)-orthoclase (Or) and quartz (Qz)-orthoclase (Or)-plagioclase (Pl) CIPW normative triangles. Liquids generally plot as tonalites. [b] expanded view of the An-Ab-Or triangle showing temperatures for some 1-, 4-, and 8-day runs. Dashed arrow shows the compositional reversal in the 4-day liquid trend above the garnet-out reaction boundary (>975°C; Fig. 3.1). This reversal also occurs in the 1-day trend above 975°C (arrow omitted for clarity). Bulk amphibolite composition shown by open square.

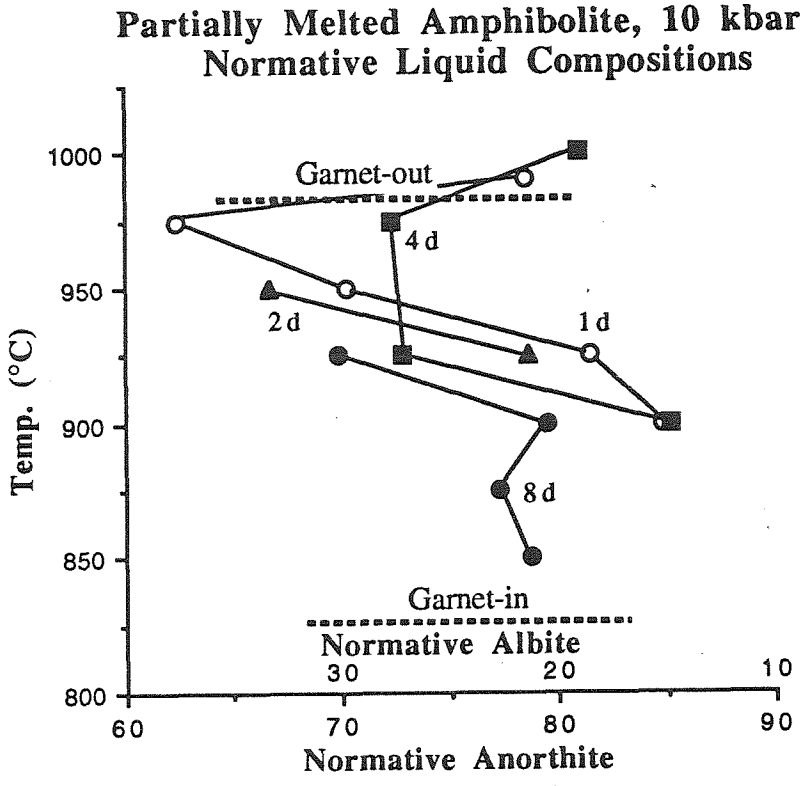

Fig. 3.18. Liquid compositions for 1-, 2-, 4-, and 8-day runs as a function of temperature and anorthite (or albite) content, showing the compositional reversal above 975°C, near the garnet-out reaction boundary.

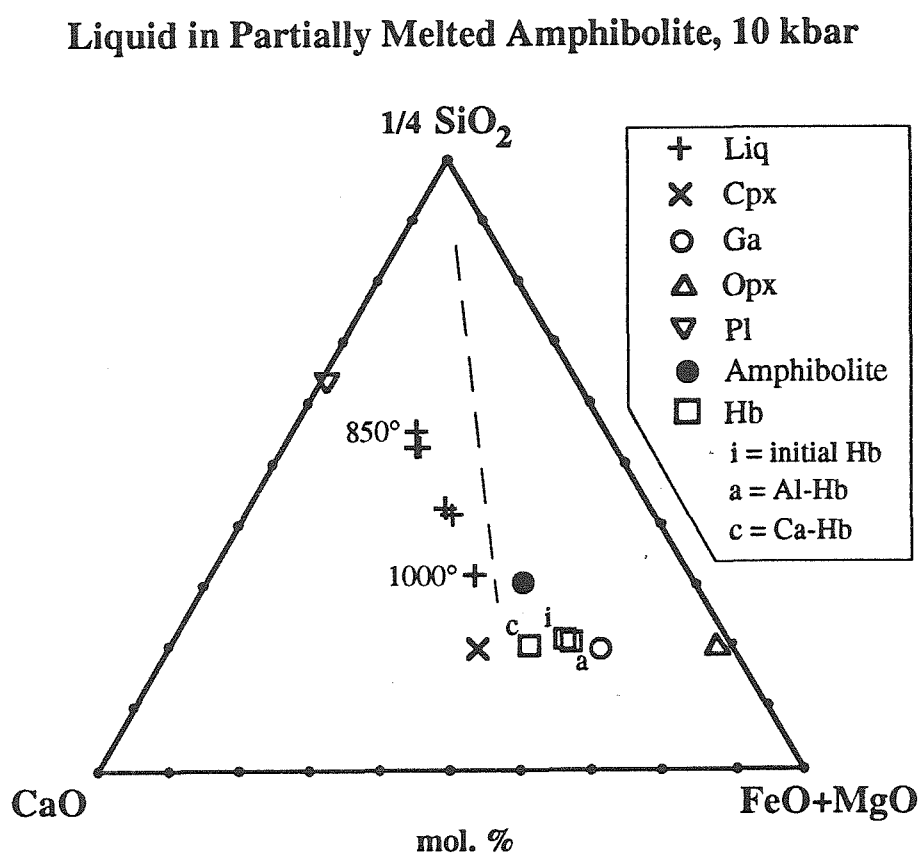

Fig. 3.19. Liquid and mineral compositions in $^{1}/_{4}SiO_2$-CaO-(FeO+MgO) triangle. Black circle is the bulk amphibolite composition. Dashed line shows the average calc-alkaline rock trend (after Stern and Wyllie 1978). Liquid compositions deviate from the calc-alkaline trend.

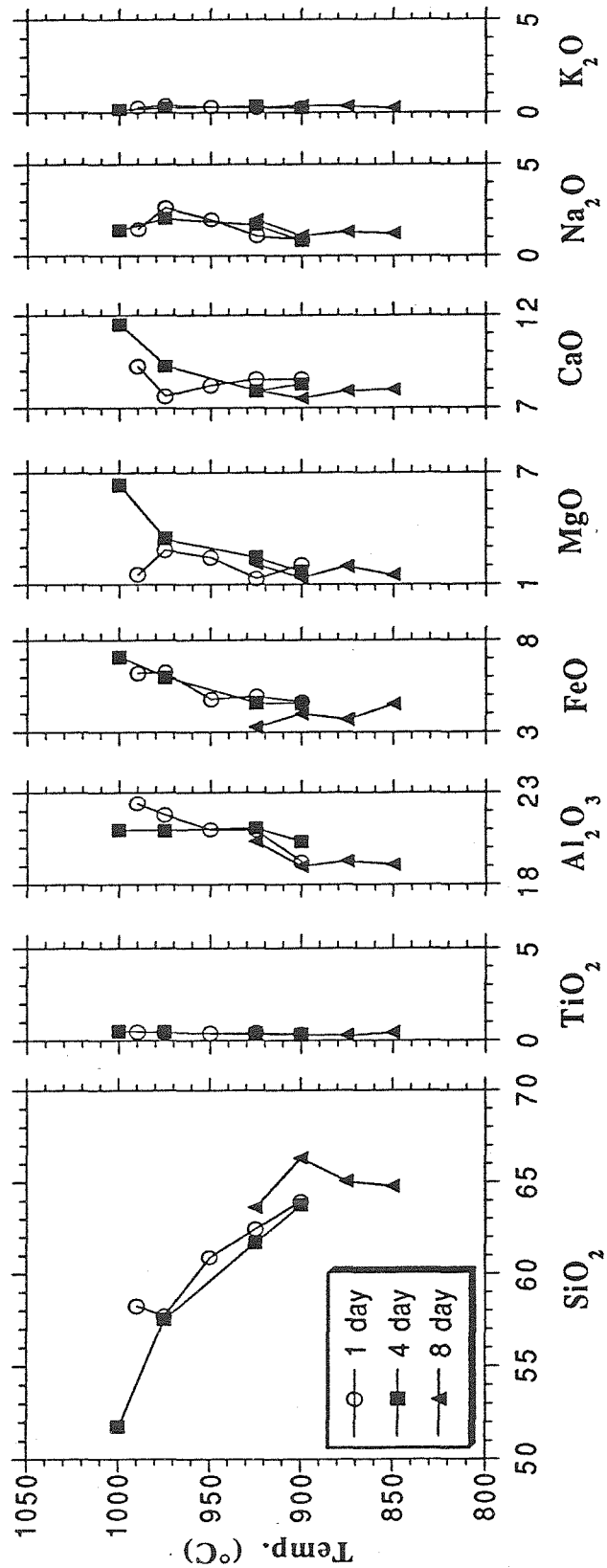

Fig. 3.20. Variations in the oxide components of the liquid compositions in partially melted amphibolite as a function of temperature and time (1-, 4- and 8/9-day runs).

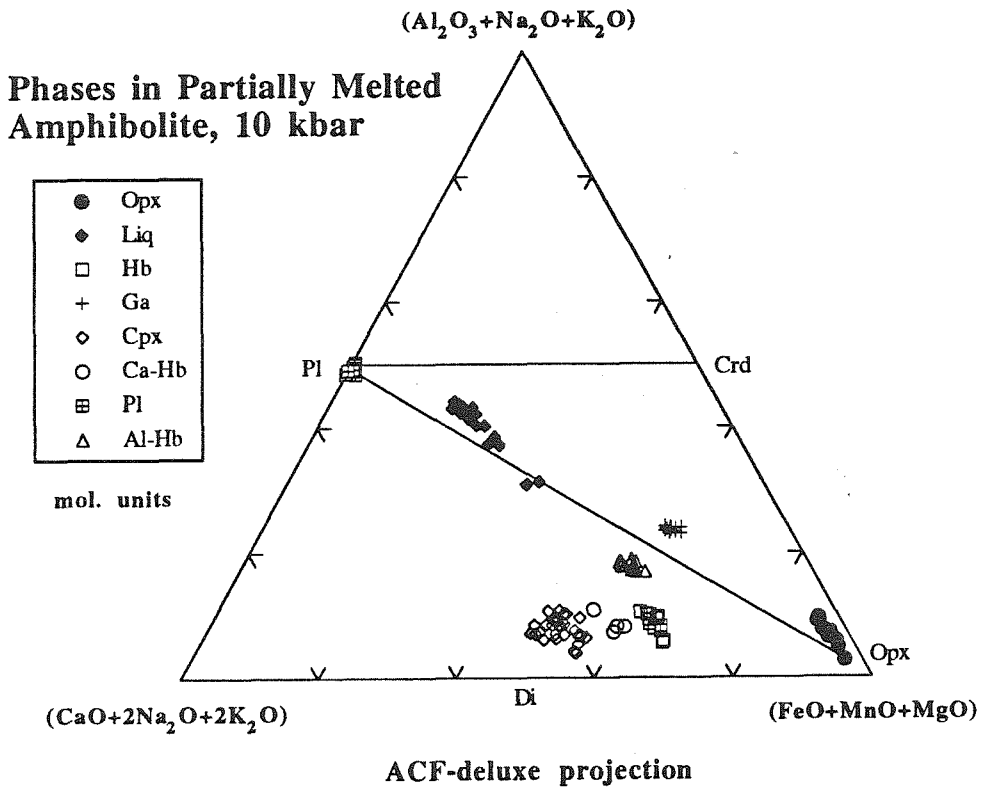

Fig. 3.21. An ACF-deluxe projection of the liquid and mineral compositions from the powder runs (after Thompson 1982, 1988; Ellis and Thompson 1986). Most of the liquids are mildly peraluminous, but high-temperature liquids are metaluminous (as defined by Zen 1986). Crd: corundum; Di: diopside; Pl: plagioclase; Opx: orthopyroxene.

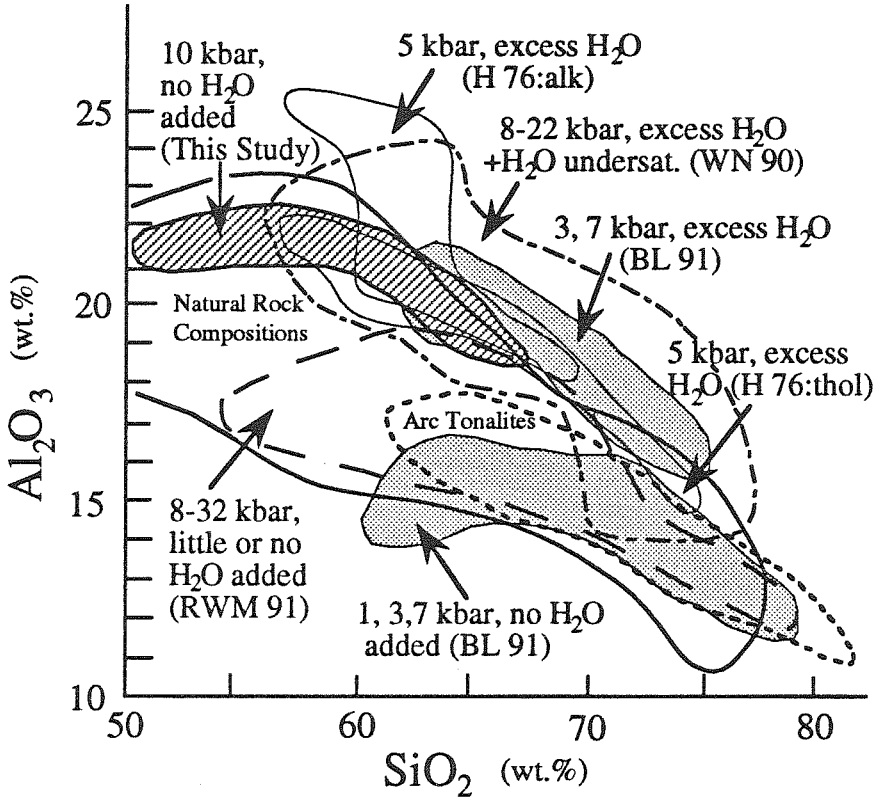

Fig. 3.22. Compositions of liquids (Al_2O_3 vs. SiO_2) from the dehydration-melting of amphibolite at 10 kbar (this study, Table 3.7, ruled field) compared with other amphibolite and basalt experimental results and natural rock compositions. Beard and Lofgren (1989, 1991) [BL91] results are from H_2O-saturated melting and dehydration-melting of amphibolite, 1-7 kbar (shaded fields). Rapp et al. (1991) [RWM91] results are from vapor-absent runs, 8-32 kbar. Winther and Newton (1990) results are from both vapor-present and -absent runs, 8-22 kbar. Helz (1976) [H76] results are from H_2O-saturated melting of basalts, 5 kbar. Natural rock compositions tabulated by Winther and Newton (1990), and natural arc tonalite compositions compiled by Beard and Lofgren (1989). In general, higher H_2O contents lead to higher amounts of Al_2O_3 in the liquids, although high-Al liquids can be produced during amphibolite dehydration-melting.

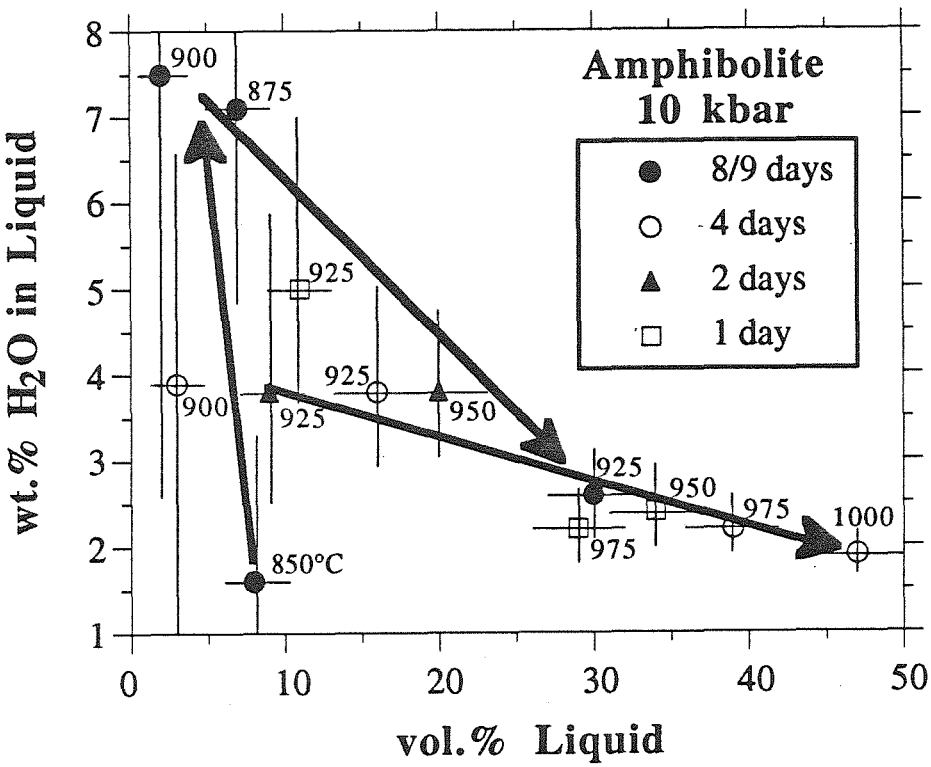

Fig. 3.23. Wt.% H_2O in liquid versus vol.% liquid for the 10 kbar amphibolite dehydration-melting runs (calculated by mass balance assuming all hornblendes contain 2 wt.% H_2O). Initial liquids contain ~2 wt.% H_2O. At 875°C, with wide-spread breakdown of hornblende and little increase in liquid fraction, the amount H_2O in the liquid rises to ~7.5 wt.% (thick arrow pointing up). With liquid fractions caused by increasing temperatures, the amounts of dissolved H_2O decrease to ~2 wt.% at X_L ~ 47 vol.%, 1000°C (thick arrows pointing down).

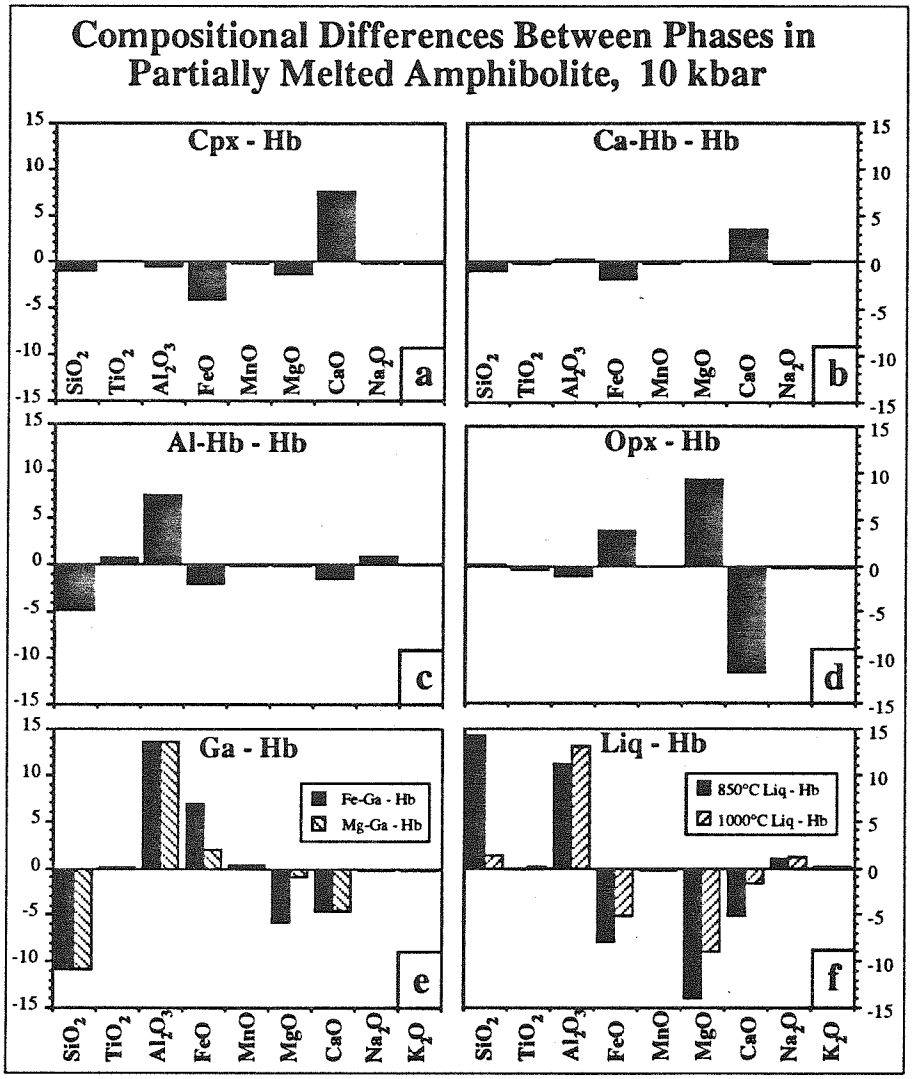

Fig. 3.24a-f. Compositional difference diagrams for the phases from amphibolite melting experiments, 10 kbar. The ordinates show the compositions of new phases minus that of the original hornblende, with the results expressed as histograms showing the differences in weight percent of oxides between the new phases and original hornblende. Positive values mean that the new phase contains more of the oxide than the initial hornblende. Conversely, negative values mean that the new phase contains less of the oxide than the initial hornblende. In [e], Fe-Ga: iron-rich garnet.

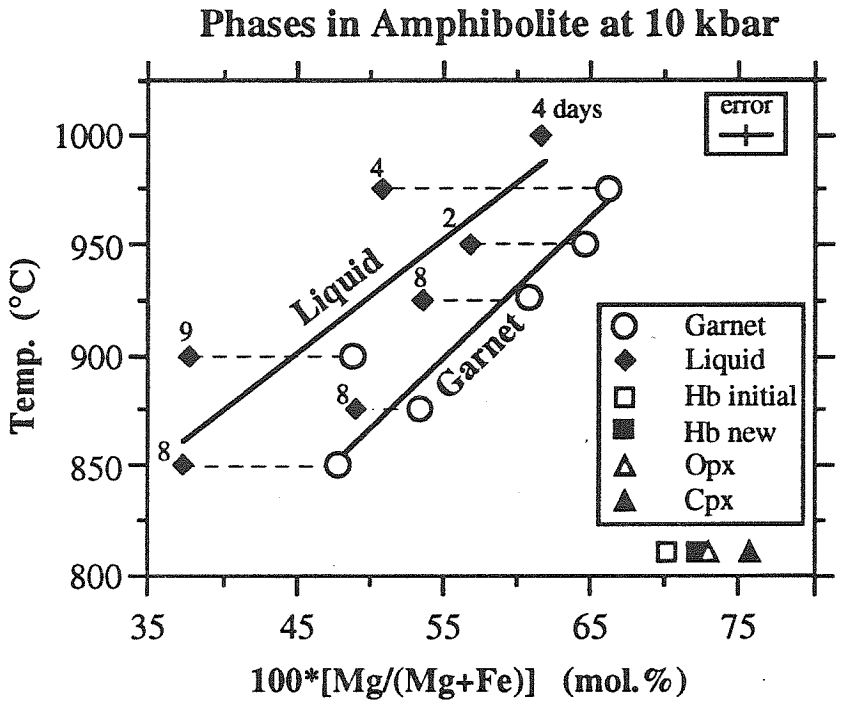

Fig. 3.25. Variation in molecular Mg/(Mg+Fe) ratios (Mg#) of garnet and liquid versus temperature, in amphibolite at 10 kbar. The numbers give run durations in days. Solid line fit to garnet data; dashed line fit to liquid data. Pyroxenes and hornblendes show no temperature-dependent variation but are plotted at 810°C for reference (both new hornblendes have similar Mg#s). Garnet, pyroxenes and hornblendes are consistently more Mg-rich than coexisting liquid at all temperatures.

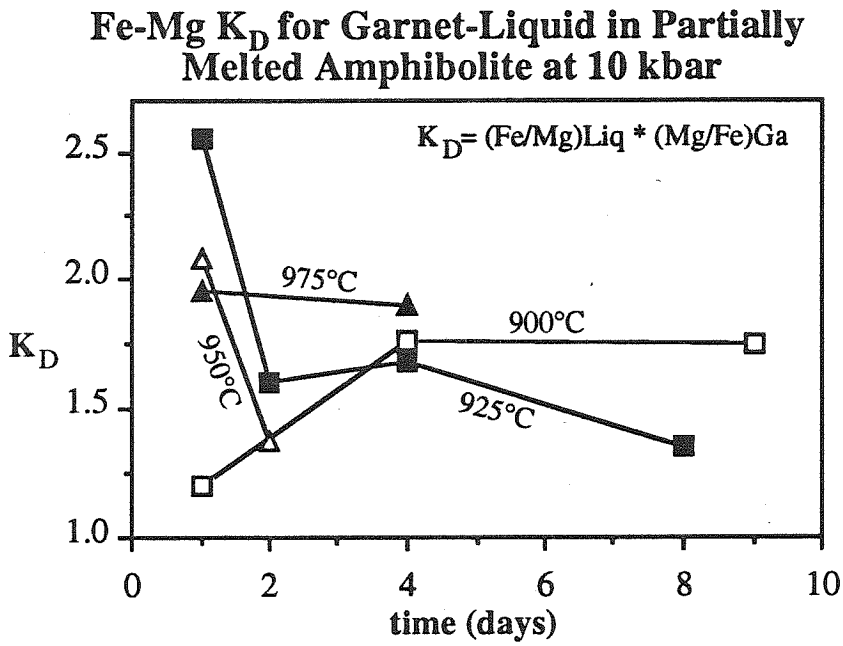

Fig. 3.26. Garnet-liquid Fe-Mg distribution coefficients (K_D) versus time for runs from 900-975°C. Complexity of the multiple reactions in the natural amphibolite melting experiments is illustrated by the initial changes in K_D (for the first two days of the runs).

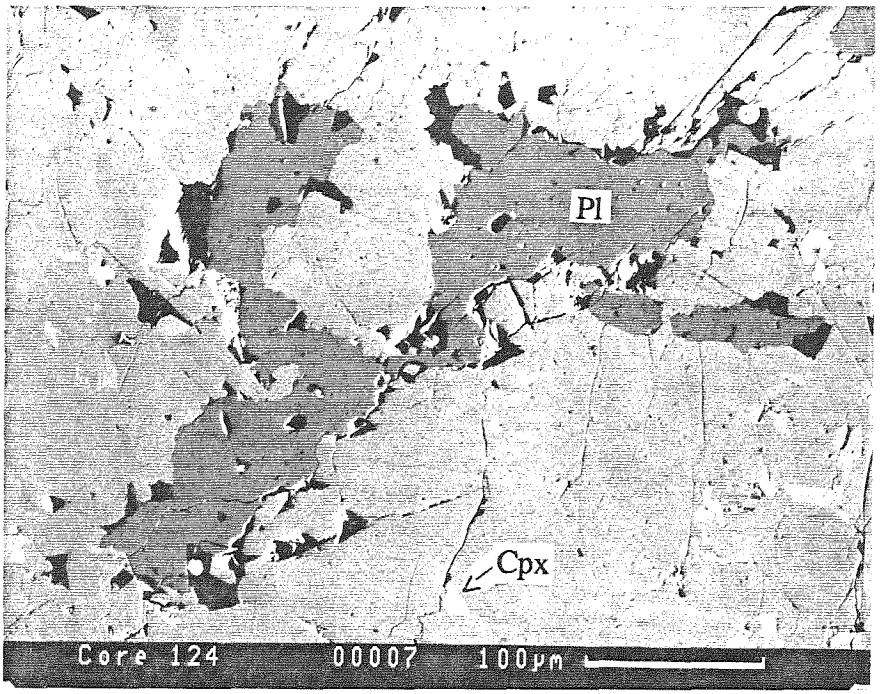

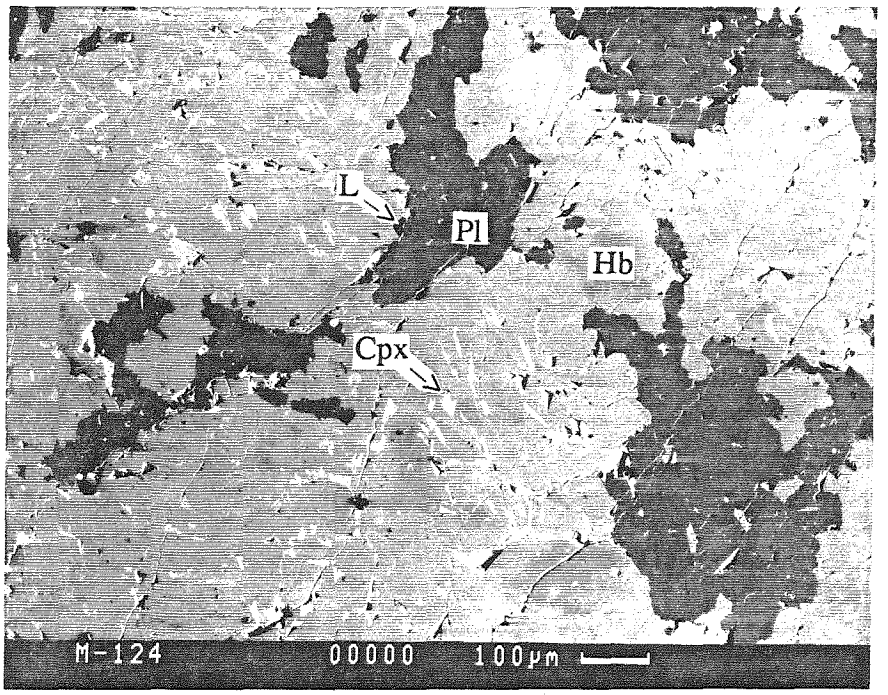

Fig. 3.27a,b. Backscattered electron, SEM photomicrograph of solid amphibolite run #124s (850°C, 21 days). View is oblique to the lineation. Phase identification is as follows: Hb - hornblende; Pl - plagioclase; Cpx - clinopyroxene; L - liquid (glass). Phase identification based on reflectivity is as follows: hornblende - medium grey; plagioclase - dark grey; clinopyroxene - light grey; liquid (glass) - black. [a] higher magnification shows details of liquid morphology; [b] lower magnification shows clinopyroxene replacement texture.

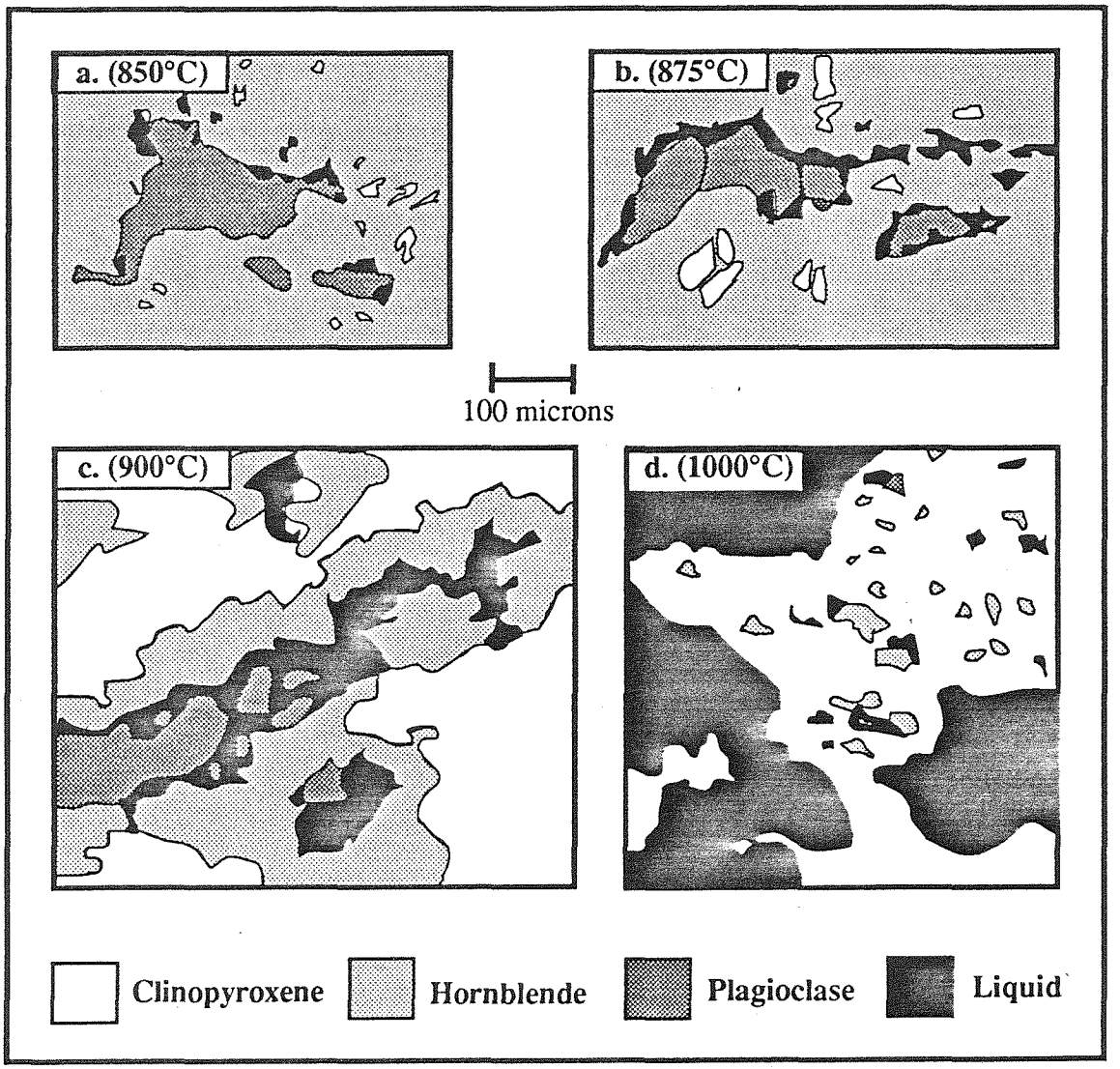

Fig. 3.28a-d. Representative morphologies of liquid pockets and mineral relationships, taken from photomicrographs. [a] Liquid is generated along Hb/Pl boundaries, commonly at embayments within the plagioclase grains. Acicular clinopyroxene grains grow within hornblende. [b] Liquid becomes interconnected along the Hb/Pl boundaries. [c] More liquid is produced. Clinopyroxene has replaced most of the hornblende, yet Cpx/L contact is still not common. [d] Liquid and clinopyroxene dominate the charge and are in intimate contact with each other.

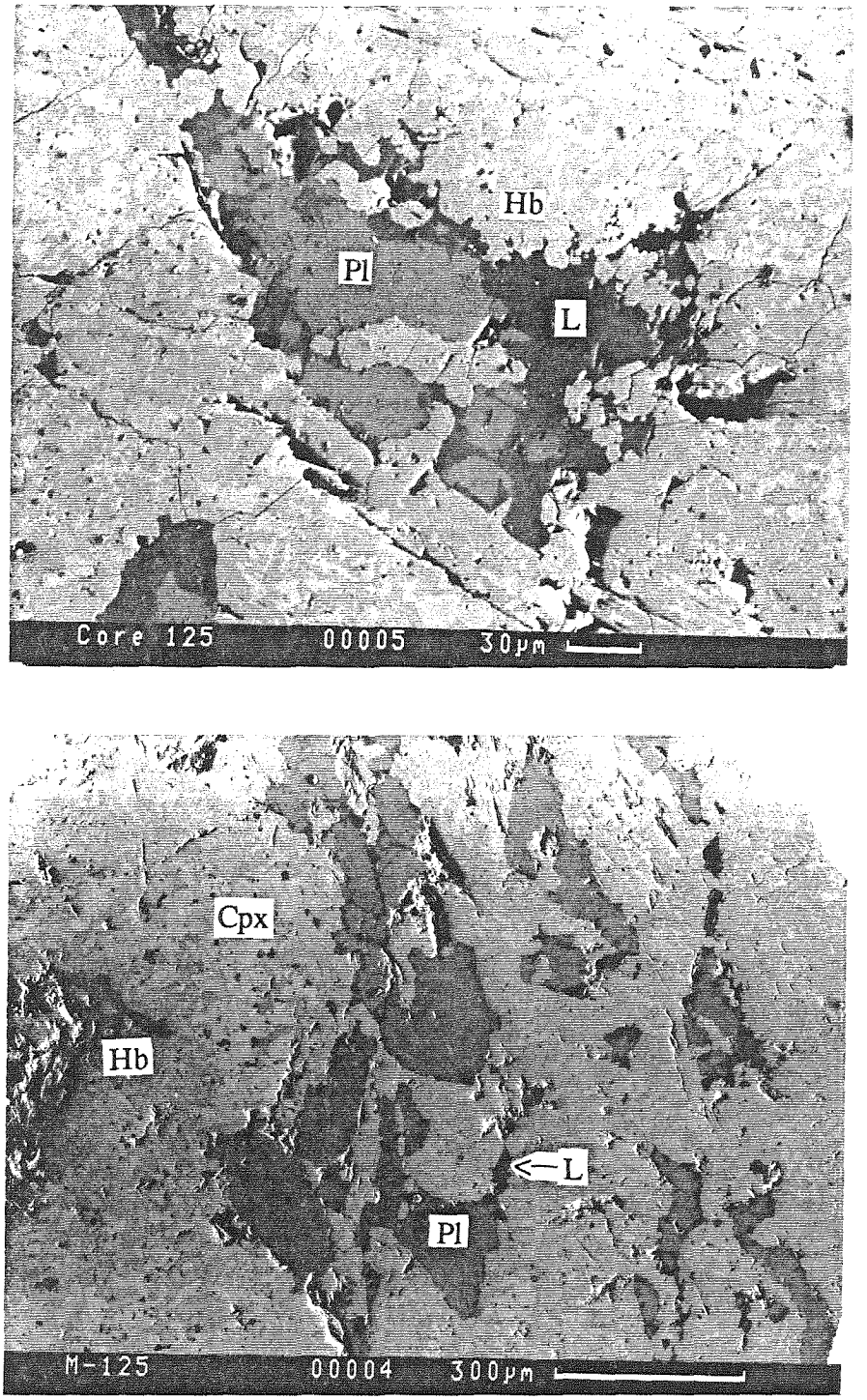

Fig. 3.29a,b. Backscattered electron, SEM photomicrograph of solid amphibolite run #125s (875°C, 14 days). View is oblique to the lineation. [a] higher magnification shows details of liquid morphology; [b] lower magnification shows clinopyroxene replacement texture.

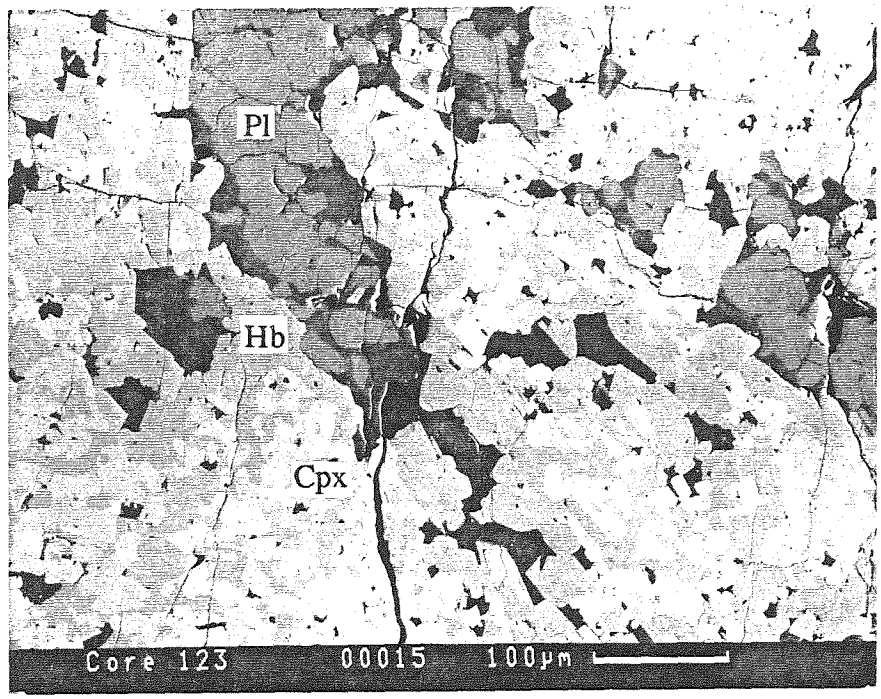

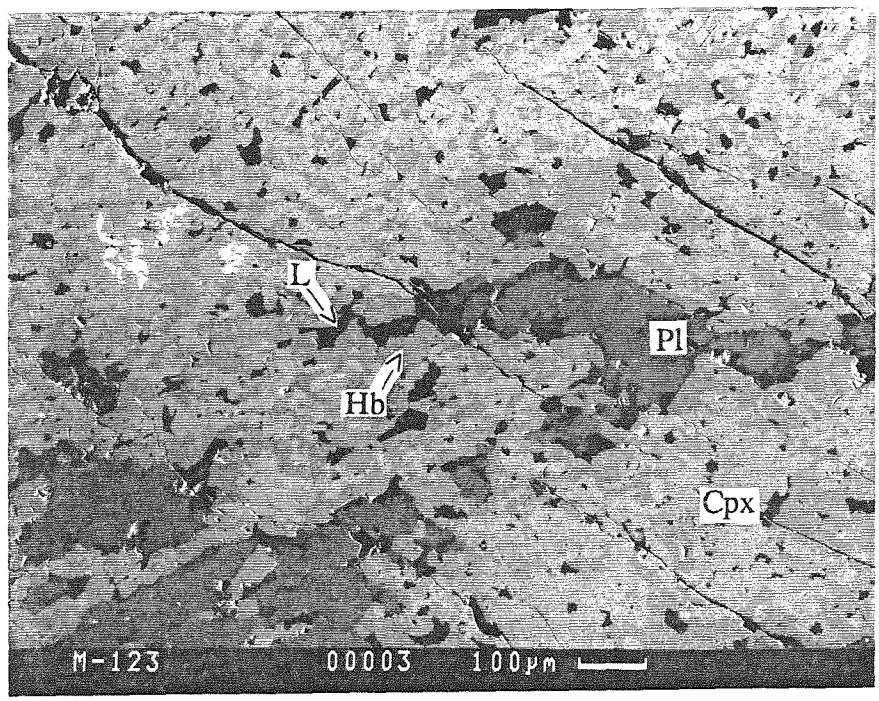

Fig. 3.30a,b. Backscattered electron, SEM photomicrograph of solid amphibolite run #123s (900°C, 14 days). View is oblique to the lineation. [a] higher magnification shows details of liquid morphology; [b] lower magnification shows clinopyroxene replacement texture.

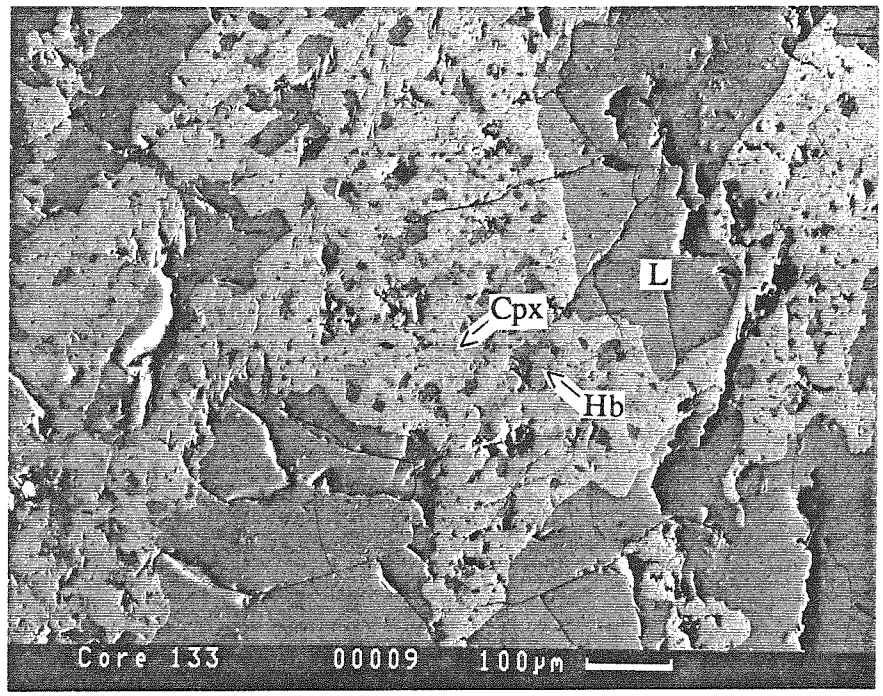

Fig. 3.31. Backscattered electron, SEM photomicrograph of solid amphibolite run #133s (1000°C, 4 days). View is oblique to the lineation.

CHAPTER 4. DISCUSSION OF EXPERIMENTAL RESULTS

4.1 Phase Relationships and Reactions in Powder and Solid Runs

The phase relationships and reactions in the powder and solid experiments are discussed together, because of the obvious similarities. In addition, the visual identification of particular physical phase relationships in the coarse-grained solid runs helps distinguish and substantiate reactions that may have occurred in the powder runs. A summary of the sequence of reaction determined from the powder runs is as follows. Dehydration-melting of hornblende plus plagioclase yields clinopyroxene plus a trace of liquid at the lowest temperature of the experiments (750°C). With increasing temperature, two new compositionally distinct hornblendes are formed – one with higher Al_2O_3 and the other with higher CaO than the initial hornblende composition – followed by orthopyroxene and garnet. All of the hornblendes, followed by garnet, disappear at still higher temperatures. At 1000°C, an aluminous tonalite-like liquid coexists with mostly clinopyroxene and minor orthopyroxene and plagioclase.

In the powder experiments, it took run durations of eight days to bring reaction temperatures down to those probably approaching equilibrium temperatures. Given the occurrence of time-dependent, metastable reactions using finely crushed rock with minerals in intimate contact, I did not expect to reach equilibrium in the relatively coarse-grained, solid cylindrical cores. In both sets of experiments, the reactions are similar in the sense that clinopyroxene and liquid are generated from hornblende and plagioclase at low temperatures. However, neither the two new hornblendes nor garnet are produced in any of the solid runs. Minor orthopyroxene and a trace of euhedral spinel have been found in the 1000°C solid run.

Figure 3.21 is an ACF-deluxe projection of all of the minerals from the powder runs that coexist with the silicate liquids. In Figs. 4.1a-c, the Fig. 3.21 overview is broken

down into a series of conventional ACF diagrams, arranged to show the changes in mineral assemblages as a function of temperature.

4.1.1 Clinopyroxene- and Liquid-Producing Reactions

Hornblende, clinopyroxene and plagioclase comprise the lowest temperature (750°C) assemblage (Fig. 4.1a). A liquid is present but in too small a quantity to be analyzed, but the probable composition is dashed in this diagram. Thus, one or more clinopyroxene- and/or liquid-producing reactions could have occurred:

hornblende → clinopyroxene + vapor [1]

hornblende + plagioclase + vapor → liquid [2]

hornblende + plagioclase → liquid [3]

hornblende + plagioclase → clinopyroxene + liquid [4]

hornblende → clinopyroxene + liquid [5]

hornblende → liquid [6]

Because the relatively high run temperatures are rapidly achieved, the occurrence of multiple reactions – some metastable – is possible. Without careful inspection of the physical relationships between phases, the presence of hornblende, plagioclase, clinopyroxene, and liquid may lead one to surmise that reaction [4] took place. It may well be that both clinopyroxene and liquid are produced by this reaction, but not necessarily to the exclusion of the other reactions. Much of the newly grown clinopyroxene in both the low temperature powder and solid runs is not in contact with the newly formed liquid, which indicates that separate reactions may be responsible for the production of these phases at these conditions. These results differ from those of Hacker (1990), who found clinopyroxene growing only in contact with liquid and only at and above 925°C in his solid amphibolite melting experiments done at 10 kbar.

The nucleation of clinopyroxenes isolated within hornblende hosts is suggestive of the occurrence of the subsolidus reaction [1]. Although visually observed in the powder

runs, this relationship is more clear in the coarse hornblende grains of the solid runs. No new amphibole or other mineral was detected, and although not observed, some change in amphibole composition marginal to the clinopyroxenes is expected. The initial hornblende grains are compositionally slightly heterogeneous, and this compositional variability may account for the early breakdown of the hornblende grain centers in the solid runs. The observed compositional variations, however, are not geometrically concentric, relative to the hornblende centers and grain boundaries. In addition, the locations of clinopyroxene nucleation sites appear to be independent of the hornblende compositional heterogeneities.

Reaction [2] begins between 620°C and 720°C at 10 kbar but produces only a small amount of liquid (Yoder and Tilley 1962). The vapor-absent dehydration-melting reaction [3] at 10 kbar was estimated from vapor-present experiments to be near 1000°C by Wyllie (1977), calculated to be at 1000°C by Burnham (1979), and measured at 925°C in experiments by Rushmer (1987). Wolf and Wyllie (1989, this study) found liquid in their dried, finely-ground, vapor-absent amphibolite in experiments at much lower temperatures (750°C). Because of the tenacity of adsorbed H_2O, it is impossible to remove all H_2O from solid or powder without dehydrating the amphibole as well, so part of the liquid produced by reaction [2] at 750°C could be due to traces of adsorbed H_2O. The trace of intergranular H_2O persisting in the dried rock core ensures some low-temperature liquid formation by reaction [2], as indicated in Fig. 4.2a. Thus, melting first occurs under vapor-saturated conditions, but vapor-absent conditions quickly prevail as reaction [3] begins.

The physical differences between the powder and solid runs appear to influence which reaction will proceed through time. Because grinding breaks up the large hornblende grains and intersperses plagioclase between the hornblende grains, reaction [2] is much more enhanced than reaction [1] in the powder runs, relative to the solid runs. Clinopyroxene is more commonly found associated with liquid in the powders as a result of reduced grain size. Although much of the clinopyroxene may have formed through the subsolidus reaction [1], the more complex dehydration reactions [4] and [5] also may have

taken place where clinopyroxene is in contact with liquid. These reactions are more possible in the powder runs above 900°C in which liquid is abundant. There is little conclusive evidence for the congruent melting of hornblende (reaction [6]). An analysis of the model A-H_2O system suggests that this reaction should not occur in the presence of other peritectic reactions (e.g., Eggler 1973).

The clinopyroxene- and liquid-forming reactions appear to have proceeded independently, although presumably linked by the transient vapor phase being released through reaction [1]. This vapor phase should dissolve in more liquid as reaction [3] proceeds isothermally with time. However, when vapor is released in dehydration reaction [1], as indicated in Fig. 4.2b, more H_2O becomes available than that required to saturate the liquid (mass balance calculation from modes), indicating that the liquid and rock become saturated with vapor. This H_2O-saturation does not occur at 850°C but does occur at 875°C and 900°C in the solid runs. H_2O-saturation does not occur in the powder runs because the fine-grained mix is conducive to reaction [3], the vapor-absent, dehydration-melting reaction.

How can an H_2O-saturated liquid be produced – however transiently – during the supposed dehydration-melting of the solid amphibolite? Figures 3.29a,b show that, in the 875°C solid run, approximately 40% of the original hornblende is replaced by blocky clinopyroxene grains. These are concentrated in the central parts of hornblendes, remaining essentially isolated from the liquid (Figs. 3.28c and 3.29b). This geometry confirms the continuation of dehydration reaction [1], and migration of H_2O to liquid pockets maintains melting reaction [2] instead of the vapor-absent melting reactions [3] or [4]. Figures 4.2c,d represent relatively early and later stages at 875°C of the reaction and advance of the hornblende/clinopyroxene dehydration front toward the margin of the hornblende grains.

Figures 3.28c and 3.30a,b show that although clinopyroxene has replaced more than 60% of the original hornblende, in the 900°C solid run, it still is not commonly found

in contact with either plagioclase or liquid. The continued nucleation of most of the clinopyroxene within hornblende crystals, away from liquid and plagioclase, rather than at the margins indicates that reactions [4] and [5] may not begin until temperatures above 900°C are reached in the solid runs.

Figures 3.4, 3.28d and 3.31 show that by 1000°C, approximately 50% of the sample forms large liquid pockets comparable in size to the clinopyroxene grains, which amount to 40% of the sample. Hornblende is rare, and plagioclase is reduced to below 5%; these minerals are always inside clinopyroxene and never surrounded by liquid. This texture may indicate that the subsolidus dehydration of hornblende, reaction [1], is replaced by dehydration-melting reaction [5], and probably by reaction [4] as well. However, the reaction rate of [1] appears to be quite rapid, and it may control the replacement of hornblende by clinopyroxene in coarse-grained rocks, even under hypersolidus conditions.

I have already discussed, in general terms, the dehydration of hornblende and concomitant growth of clinopyroxene. The stoichiometry of this and the other liquid-present reactions has not been quantified because of the complexity of and interrelationships between all of the solid solution hornblende reactions, the hornblende-plagioclase dehydration-melting reaction, and the clinopyroxene-, orthopyroxene- and garnet-producing reactions. However, the replacement of hornblende by clinopyroxene warrants further attention, because the dual, powder and solid, observations may bridge a gap between reactions in experiments and in natural systems. Eggler (1972) has experimentally demonstrated the existence of a metastable amphibole dehydration reaction in the presence of a silicate liquid. Mazzone et al. (1987) have found features in xenoliths within a natural andesite flow that are indicative of a similar dehydration reaction. Both of these studies postulate a reaction open only to H_2O – all other species are incorporated directly into the new minerals that replace the amphibole ($+SiO_2$): amph + SiO_2 → Cpx + Pl + Opx + Kspar + Opq + H_2O. In contrast, in the reaction that occurs in the present experiments, the dehydration of hornblende is locally an open system, with other species

leaving the reaction site along with the H_2O. In Fig. 3.24 the 'Cpx - Hb' histogram graphically shows the changes in oxide content during the dehydration reaction (Cpx: clinopyroxene; Hb: hornblende). Relative to hornblende, the new clinopyroxene gains CaO and loses SiO_2, FeO, MgO (and H_2O). Qualitatively, the reaction is $CaO + Hb \rightarrow Cpx + SiO_2 + FeO + MgO + H_2O$. The excess species end up in the silicate liquid and do not directly produce new minerals or compositionally distinct reaction halos during the dehydration process. Thus, mass transfer from the reaction site must have occurred.

The pressure is the major difference in reaction conditions between the previous experimental-based (Eggler 1972) and field-based (Mazzone et al 1987) studies (<2 kbar) and the present 10 kbar solid amphibolite experiments. The solubility of species dissolved in H_2O is greatly enhanced at elevated pressures. Fluids can carry several percent of silicate solutes at these high pressures (Holloway 1971). Selverstone et al. (1990) have documented the high solubility of Al, Ca, Mg Fe, Ti, and P in vein-forming brines at high pressures (20 kbar) in mafic rocks. The solubility may be high enough to leach the Si, Fe, and Mg from the hornblende and to inhibit mineral growth. Calcium is interesting in that it appears to be added to the hornblende to form clinopyroxene. The are no calcium-poor hornblende reaction halos around the clinopyroxene crystals, which would have indicated a localized calcium source. The anorthitic plagioclase is not directly involved in the clinopyroxene-forming reaction because the two minerals are rarely in contact in the solid runs. The plagioclase probably is indirectly involved in clinopyroxene growth, because it is the ultimate source of the calcium in the liquid. Calcium moves toward the site of the clinopyroxene growth reaction instead of away from it. Even though there is little liquid present in the low temperature (high pressure) runs in which hornblende is dehydrating, the presence of this liquid is critical to prevent the growth of the other minerals found in the low pressure experiments of Eggler (1972) and observed in nature by Mazzone et al. (1987).

4.1.2 New Hornblende-Producing Reactions

At 900°C all of the phases are present in the powder runs (Fig. 4.1b). Four new reactions have taken place. Two of the reactions involve substitutions in the hornblende structure:

hornblende → Ca-hornblende [7]

hornblende → Al-hornblende [8]

The formation of clinopyroxene is the first mineralogical indication of hornblende reaction, followed by the growth of the Ca- and Al-hornblendes. According to Putnis and McConnell (1980), a compositional change in the hornblende might be expected first because this involves a smaller change in the free energy of the mineral assemblage (Putnis and McConnell 1980). However, Rubie and Brearley (1987) have shown that, according to the Ostwald Step Rule, the most favorable path for mineral growth is not controlled necessarily by thermodynamic principles but by kinetic ones. The growth of clinopyroxene before Ca- and Al-hornblendes in the experiments probably is a consequence of favorable kinetics in the high temperature, liquid-producing experiments. These experiments may aid in distinguishing between time-dependent (kinetic) growth processes that normally cannot be separated by examining mineral assemblages in nature or in time-independent experiments. One important consequence of the early hornblende replacement by clinopyroxene, instead of just an Al- or Ca-shift in composition, is that clinopyroxene growth prevents the retention of H_2O in the crystalline structure and thus accelerates the dehydration-melting process. I emphasize that this kinetically favorable pathway probably will not occur in the absence of a liquid phase and cannot be called upon to accelerate the lower temperature, liquid-absent, dehydration process.

Ellis and Thompson (1986) have shown that in H_2O-excess experiments, amphibole coexists with liquid over a wide temperature interval above the solidus, but that the dehydration melting of amphibole defines the solidus in the vapor-absent system. In their dehydration melting experiments, Beard and Lofgren (1989) found that the amphibole

disappeared directly above the solidus (J. Beard, pers. comm., 11/1988). In contrast, the exchange reactions of the amphiboles in this study smear out the dehydration melting reactions and result in the persistence of amphibole well above the solidus.

4.1.3 Orthopyroxene- and Garnet-Producing Reactions

The growth of the Ca- and Al-hornblendes may concentrate the excess mafic hornblende components in the liquid and thus may facilitate orthopyroxene production. Thus, the abundance of orthopyroxene in the powder runs, relative to the solid runs, may be a consequence of the abundance of Ca- and Al-hornblendes in these runs. In the powder runs, the location of the orthopyroxene relative to these hornblendes is not well known, because of the subtle reflectivity differences in SEM-BE mode. The rare, euhedral orthopyroxenes in the 1000°C solid run are located along clinopyroxene/liquid boundaries.

It is clear from the crystal morphology that garnet grows from the alumina-rich liquid. The low temperature garnet-in boundary in the powder experiments lies at about 825°C. No garnet has been detected in any of the solid runs, and possible reasons are discussed below.

4.1.4 Kinetics

Qualitative reaction progress within the partially melted amphibolite can be visualized in the series of ACF diagrams arranged by temperature. Figures 4.1a-c may represent changes in the mineral assemblage of the calcic amphibolite under prograde conditions through ultrametamorphism and migmatization. Even though a silicate liquid is present in all of the runs, the changes in mineralogy that take place in the experiments can be described by the metamorphic reactions that separate the amphibolite facies from the pyroxene granulite facies (+ liquid). Figures 4.3a-c depict the amphibolite facies-pyroxene granulite facies transition in ACF space, showing the breakdown of hornblende and expansion of the orthopyroxene field (from Robinson 1982). Figure 4.3d shows the effect

that solid-solution minerals have in these types of composition-paragenesis diagrams (from Miyashiro 1978). Figure 4.3e combines the effects of solid-solutions (Fig. 4.3d) with the amphibolite facies-to-pyroxene granulite facies diagrams (Figs. 4.3b,c) to show the mineral assemblage present in most of the amphibolite melting experiments; hornblendes of different compositions coexisting with plagioclase, clinopyroxene, orthopyroxene and garnet (+ liquid).

The presence of a silicate melt should have a profound affect on the composition and mode of the minerals in equilibrium with it, and presumably these parameters would be different from the liquid-absent, metamorphic assemblages. Although the mineralogy of the liquid-present assemblages mimics the phase diagrams of the liquid-absent assemblages, a compositional comparison is not possible, in the absence of subsolidus experiments. Reaction rate may be the parameter that is the most different between the two assemblages if they are both closed systems.

The delineation of phase boundaries was made by comparing the mineral modes of the runs as plotted in Fig. 3.3. Distinct phases, for the most part, can be separated from each other, and, even with mixed-grain boundary-effects, reaction progress can be assessed clearly. In Fig. 3.1, the runs are plotted on a time-temperature phase diagram and are divided into separate phase assemblages. The lines represent reaction boundaries – the appearance or disappearance of mineral phases. The gentle negative slopes ($\partial T/\partial t$) of most of the curves indicate that the reactions are time-dependent (where T: temperature; t: time).

In depth explanations for the shapes of the reaction boundaries are given by Putnis and McConnell (1980) and Rubie and Brearley (1987). Simplified time-temperature-transformation (TTT) diagrams are useful in illustrating the results from kinetic studies. In Fig. 4.4a, the curve labelled "start" indicates the beginning of reaction above the equilibrium temperature (T_e) of the reaction (Putnis and McConnell, 1980). The curve labelled "finish" indicates the ending of the reaction. The space to the left of the "start"

curve, therefore, contains only reactants. The swath between the two curves contains both reactants and products, and the space to the right of the "finish" curve contains only products. The equilibrium assemblage, products-only, can be reached more quickly if the temperature interval above T_e is increased.

Figure 3.1 is redrawn with a logarithmic time scale in Fig. 4.5 to compare the repositioned phase boundaries with the simplified TTT diagram (Fig. 4.4a). The reaction boundaries in Fig. 4.5 can be described as a collective series of "start" and "finish" curves. This diagram is more complex than Fig. 4.4a, because the "start" and "finish" curves for a particular reaction are separated by "start" curves for other reactions. For instance, the garnet-in and -out curves are separated by orthopyroxene-in and Ca-hornblende- and hornblende-out curves.

Although the shapes of the curves are not rigorously constrained, the slopes of all of the curves probably flatten out with time (Fig. 4.5). The continuation of the boundaries may not have completely horizontal slopes past eight days, but the temperature dependence upon run duration is lessened. The eight day data have a considerable influence on the overall shapes of the reaction boundaries that would not have been apparent from short duration experiments. The Ca- and Al-hornblende-in curve drops over 100°C from one to eight day runs. Most of the other boundaries are flatter. The hornblende- and garnet-out curves are almost horizontal. However, the Ca-hornblende-out curve is relatively steep sloped.

The shapes of some reaction boundaries may be modified by the occurrence of metastable reactions, as shown in Fig. 4.4b (after Rubie and Brearley 1987). The growth of metastable phases above metastable reaction T_e' actually inhibits the attainment of the equilibrium assemblage, resulting in kinked reaction boundaries. The steepness of the Ca-hornblende-out curve may indicate the metastability of the Ca-hornblende through time (Fig. 4.5). It may be possible that the Ca-hornblende-in and -out curves are linked and form a kinked shape, as in a portion of Fig. 4.4b. The occurrence of this metastable phase

is different than that described by Rubie and Brearley (1987), because the growth of their metastable phase (muscovite) delayed the appearance of the stable mineral assemblage; in the present experiments, no phases are inhibited by the growth of Ca-hornblende.

4.2 Crystal Morphology

The morphology of crystals and the changes in morphology (as a function of numerous parameters, e.g., time, temperature, bulk composition, mineralogy) may be important in understanding the behavior of geological systems. Cashman (1990) used textures to constrain the kinetics of crystallization of igneous rocks. Likewise, it may be possible to do the same for melting processes, but quantitative analysis may be more difficult due to the complications of the breakdown of pre-existing minerals and the formation of liquid as well as new minerals. Thus, as a first cut, I have not attempted to quantify the results but instead have described the qualitative aspects of the kinetics of nucleation and growth during partial melting of the amphibolite. Clinopyroxene and garnet are the minerals examined in detail.

4.2.1 Clinopyroxene Morphology

Most clinopyroxenes probably nucleate as acicular crystals along hornblende-hornblende grain boundaries that initially contain very finely-ground, sub-micron particles of hornblende ± plagioclase. Nucleation is kinetically favorable along these boundaries possibly because they are pathways for H_2O being released during hornblende breakdown (e.g., Putnis and McConnell 1980) and because of the presence of the nucleation-enhancing grain boundary gouge. Clinopyroxenes with this acicular morphology are found in relatively lower temperature and shorter duration runs, which is an indication that this is an early – possibly nucleation – morphology (Figs. 3.5-3.8). In the higher temperature and/or longer duration runs, the clinopyroxenes are either small, separate, blocky crystals or are patches of larger hornblende grains. These patches appear to be subhedral

intergrowths of clinopyroxene in hornblende, probably represent the replacement of hornblende by clinopyroxene, and may result in clinopyroxene pseudomorphs after hornblende. Liquid generally surrounds the smaller clinopyroxene crystals but rarely is found along the clinopyroxene-hornblende interfaces within the larger patches. The small, separate, blocky crystals may have nucleated and grown along former hornblende-hornblende boundaries.

Clinopyroxene nucleation is heterogeneous in that it mostly occurs along grain boundaries (Putnis and McConnell 1980). The locations of the clinopyroxene crystals along hornblende surfaces appear to be independent of the morphology of the hornblende grains, i.e., clinopyroxenes grow along all hornblende surfaces, regardless of whether those surfaces are the relatively smooth crystal faces (parallel to the long axis of the grain) or the truncated ends (parallel to the short axis of the grain). Thus the degree of coherency (or structural match) of the interface does not seem to control clinopyroxene nucleation. In general, nucleation along a coherent interface has a lower activation energy than nucleation along an incoherent interface (Putnis and McConnell 1980). The presence of a grain boundary gouge in the experiments may influence the nucleation activation energy more than interface coherency.

The free energy of activation for nucleation, at the transformation temperature, is equal to the sum of the surface and strain energies. Clinopyroxene will grow "such that for any given volume formed, the total surface energy is minimized by preferential growth of those surfaces with minimum energy" (Putnis and McConnell 1980). The growth of acicular clinopyroxene crystals along hornblende-hornblende interfaces minimizes the free energy even though the acicular morphology tends to maximize the surface energy. Thus the strain energy probably is low due to the incoherence of these interfaces.

The morphology of the clinopyroxene crystals changes with growth because the conditions during growth change. On the higher temperature, longer duration side of the line in Fig. 3.8, acicular clinopyroxene crystals do not separate hornblende grains along

relatively dry boundaries. The progression of melting reactions has increased the amount of liquid in these runs to the point at which liquid-free boundaries do not exist between physically different grains. Hornblende interfaces do not impinge upon the clinopyroxene crystal faces. The clinopyroxene crystals are able to grow in thickness as well as length and thus become more blocky, with lower aspect ratios than the initial clinopyroxene nuclei.

Clinopyroxene-hornblende pairs (or patches) are found within the physical boundaries of single grains and thus probably represent clinopyroxene replacement of hornblende. In lower temperatures and shorter duration runs, some acicular clinopyroxene crystals are found within single hornblende grains, not associated with grain boundaries. At higher temperatures and/or for longer durations, these acicular crystals are not preserved. The clinopyroxene replacement morphology within these larger grains is similar to the blockiness of the smaller, physically separated clinopyroxene crystals. The replacement texture is more obvious in these larger grains because of the incompleteness of this process.

4.2.2 Comparison of the Clinopyroxene Morphologies From Both Powder and Solid Amphibolite Experiments

The shapes of clinopyroxene crystals are time- and temperature-dependent in both the powder and solid amphibolite experiments, and the changes in shape as a function of time and temperature also are similar. In both sets of experiments the clinopyroxenes nucleate in the short duration runs as small, euhedral, acicular crystals (aspect ratios up to 1:10). The crystals grow more blocky (aspect ratios ~1:2) and subhedral with increasing time and temperature. There is no systematic change in the compositions to match this morphological change. The morphological and compositional similarities are somewhat surprising given the apparent physicochemical differences in nucleation and growth sites.

In the powder experiments, the acicular clinopyroxenes mostly nucleate in the very fine-grained gouge along the outer surfaces between hornblende grains. These sites are the most incoherent and thus have the lowest strain energy associated with them, relative to sites within hornblende grains. In the solid experiments, the acicular clinopyroxenes mostly nucleate within the relatively large hornblende grains, at internal lattice defect points with low strain energy (e.g., Putnis and McConnell 1980), since hornblende-hornblende interfaces are relatively rare, compared to the fine-grained powder. Clinopyroxene nucleation or growth does not occur at the hornblende grain edges that are in contact with plagioclase. At these edge locations, a liquid-forming reaction takes place at low temperatures. The lower temperature clinopyroxene-forming reaction is sub-solidus, and thus the plagioclase- and liquid-absent internal grain sites generally are preferred.

In higher temperature and longer duration powder runs, clinopyroxene growth results in a blocky morphology, but the physical integrity of the crystalline mass is disrupted by the large increase in the amount of liquid produced. Most crystals are surrounded by liquid and thus have free, nonimpinged surfaces. In the analogous solid runs, liquid is only sparsely distributed throughout the rock, but the clinopyroxene crystals also have grown more blocky. The growth process is evident in some of these runs; parallel acicular clinopyroxene crystals appear to have grown along the cleavage within hornblende grains. At some point, non-cleavage-bound growth dominates the lateral growth along cleavage, and the clinopyroxene morphology becomes blocky. Brearley (1987), using a solid, garnet-biotite-plagioclase-quartz gneiss, and Hacker (1990), using a solid, quartz-bearing amphibolite, also investigated transformation kinetics and mechanisms. They also noticed morphological and distributional changes during nucleation and growth.

The morphological similarities in the two sets of experiments are an indication that the change in clinopyroxene morphology is the natural progression, at least under similar conditions of relatively rapid growth. The relevant clinopyroxene-forming reaction is sub-

solidus, which implies the need for only relatively low temperature conditions. The critical temperature of nucleation may have been greatly exceeded in the experiments, and this overstepping may affect the nucleation and growth morphology. Additional experiments at lower temperatures are needed to resolve this uncertainty.

The physical differences between nucleation sites in the powder and solid experiments may be comparable at low temperatures. The finely-ground amphibolite powder was not sieved in order to preserve the original composition. As much care as possible was taken to produce small, uniformly sized grains, but a Gaussian size distribution was inevitable nevertheless. During a run, the powder is compacted but not sintered by application of the confining pressure just before heating. The gouge between hornblende grains and the interfaces themselves become ideal defect sites surrounding relatively structurally coherent, defect-free, hornblende grains. In effect, the powdering technique adds defects and thus nucleation sites to the hornblende grains, thereby enhancing clinopyroxene nucleation and growth, although the nature of these processes resembles those in natural, solid rocks.

At higher temperatures, the blockiness of the clinopyroxenes in the powder experiments may be a consequence of free, clinopyroxene-liquid surfaces that do not impede clinopyroxene growth. However, in the solid experiments, with the absence or scarcity of liquid, clinopyroxene morphology also becomes blocky at higher temperatures, and this may be a consequence of the rapid breakdown of hornblende and the structural similarities between hornblende and clinopyroxene.

4.3 Garnet Nucleation and Growth

The appearance of a few garnet crystals marks the garnet-in reaction in the powder experiments (Fig. 3.1), but wide-spread garnet growth occurs at higher temperatures. This increase corresponds to an increase in the percentage of liquid, to approximately 10 vol.% liquid. At these higher temperatures, the number and size of garnet crystals increase

rapidly, within 25°C of the garnet-in reaction boundary (Figs. 3.7 and 3.9-3.11). There is no clear evidence that may indicate the cause of nucleation at a particular location and not somewhere else. The nucleation process also is not preserved, because once nucleation occurs, rapid growth quickly alters the nucleation morphology. Nucleation of new garnet continues throughout the runs, as shown by the crystal size distribution, and thus indicates late-site saturation (Rubie and Thompson 1985). The garnet-producing reaction appears only to depend on liquid as a reactant: L $\rightarrow$ Ga. Garnets grow from the liquid in pockets previously filled with liquid. In the lower temperature runs, these pockets may not be large enough to sustain garnet nucleation and growth, so crystal enlargement may be inhibited. Because the liquid encompasses most of the mineral grains in the capsules, rapid garnet growth and infiltration along the liquid paths result in garnet poikilitic phenocrysts. At the higher temperatures, with more liquid present, the garnet crystals generally have free surfaces and thus assume their true, euhedral crystal form – trapezohedron-modified dodecahedrons.

Crystal enlargement at low temperatures is due to single grain growth, not the aggregation of many small grains. In higher temperature, longer duration runs, most garnets still are not aggregates but a few clearly are doublets. As the garnets continue to grow and occupy more space, the chances increase for aggregation. The chances of aggregation also depend on the initial and subsequent nucleation density, which depends on grain size.

The grain size of the powder experiments is too fine compared to natural rocks, even mylonites. Thus, a comparison between the powder and solid experimental results is the next step in understanding garnet nucleation and growth in natural rocks. Unfortunately, there is not much to compare, because garnet did not nucleate in any of the solid amphibolite experiments.

What conditions necessary for garnet nucleation in the powder experiments are different in the solid experiments? The compositions of the two sets of liquids are different

from one another but not much different. There are greater compositional changes within each set than between sets. The most obvious difference is in the grain size, and this parameter controls the possible nucleation density by controlling where liquid is produced. The powder, with ~10 μm^3 diameter grains, has approximately five times the intergranular surface area of the rock, with ~100 μm^3 diameter grains. Thus, garnet nucleation is five times less likely to occur in the solid experiments than in the powder experiments, per unit volume. Grain size also controls how much and how fast liquid is generated. In the powder experiments, nucleation only is abundant in runs with more than about 10 vol.% liquid. The absence of garnet in the solid experiments may be due, in part, to the lack of runs, within the garnet stability field, with liquid percentages above 10 vol.%. The finely-ground minerals in the powder experiments may have acted as seeds for the nucleation of garnet. The absence of these seeds in the solid experiments may have inhibited garnet nucleation.

4.4 Mineral Compositions in Both Powder and Solid Experiments

4.4.1 Clinopyroxene

Table 4.1 lists the clinopyroxene compositions from both the solid and powder amphibolite experiments. The comparison shows that the minerals growing in the centers of hornblendes in the solid runs are clinopyroxenes with similar compositions (diopsidic augite) to those grown in the powder experiments. The clinopyroxene composition from the powder experiments is an average, since neither temperature- nor time-dependent compositional trends were detected.

4.4.2 Hornblendes

The amphibole compositions from the powder experiments are plotted twice in Fig. 3.13 to show different relationships (compare with Fig. 2.2). In Fig. 3.13a the initial hornblende compositions fall mostly in the magnesio-hornblende field but extend into the

actinolitic hornblende field, in Mg/(Mg + Fe) versus Si space (after Rock and Leake 1984). The Al-rich hornblende fills the tschermakitic hornblende field. The Ca-rich hornblende is not distinguishable from the initial composition in Fig. 3.13a. However, in Fig. 3.13b all three compositions have been separated in Al^{IV} + Ca versus Si + Na + K space (after Giret et al. 1980). In this figure the new minerals are still hornblendes, although they plot near the tschermakitic end of the hornblende field. The new hornblendes are the result of the tschermakitic substitution $Al_2(Fe,Mg)_{-1}Si_{-1}$, plus a combination of the $CaAlNa_{-1}Si_{-1}$, $NaAlSi_{-1}$ and $CaMg_{-1}$ substitutions. These substitutions have been documented in regional studies (Laird 1980; Spear 1982) and experimentally verified by Spear (1981). Both new hornblendes contain more Al^{IV} + Ca than the initial hornblende. Relative to each other and the initial hornblende, the tschermakitic (Al-Hb) hornblende contains more Al^{IV}, and the other new (Ca-Hb) hornblende contains more Ca. The formation of the two new hornblende compositions may be a consequence of the wide range in initial hornblende composition. These new hornblendes may have developed from different ends of the initial hornblende compositional spectrum.

The average TiO_2 content of the starting hornblende is 0.4 wt.%. TiO_2 is exchanged during the growth of the new hornblendes. The Ca-Hb contains 0.2 wt.%, and the Al-Hb contains 1.0 wt.% TiO_2. The amount of TiO_2 in hornblendes is a function of temperature – the higher the temperature of formation, the higher the TiO_2 content (Spear 1981). The increase in TiO_2 in the Al-Hb probably is due to the $TiSi_{-1}$ and/or $TiAl_2Mg_{-1}Si_{-2}$ substitutions (e.g., Giret et al. 1980; Helz 1982).

The $NaAlSi_{-1}$ substitution is important in the formation of the aluminous hornblende since this mineral contains more sodium than the other hornblendes (approximately 1%). The sodium enrichment of the Al-rich hornblende is not apparent from its location in Fig. 3.13b, because it has the least amount of Si + Na + K. However, its position is not due to a lack in Na but to a lack in Si, relative to the other hornblendes. A major effect of Na_2O is to stabilize hornblende through the $NaAlSi_{-1}$ exchange

(Thompson et al. 1982). This exchange increases hornblende stability under the experimental conditions.

Sodium is an important component in hornblendes that is not accounted for in the ACF diagrams (Figs. 4.1a-c and 4.3a-e). However, the coexistence of multiple hornblendes can be explained best by the use of a three dimensional ACFN diagram, in which N represents sodium (Robinson 1982). With the addition of the Na_2O component the two dimensional triangular hornblende field becomes a three dimensional hornblende tetrahedron (shaded in Fig. 4.6; from Robinson 1982). At each corner of this volume is a compositionally distinct hornblende in equilibrium with three other phases. Thus each distinct hornblende composition is in equilibrium with a different mineral assemblage. For instance, the most calcic hornblende is in equilibrium with clinopyroxene, anorthite and garnet, but the most mafic hornblende is in equilibrium with clinopyroxene, anorthite and orthopyroxene. The complete mineral assemblage, therefore, would consist of the several coexisting hornblendes and their own sub-set of assemblages (also see Fig. 4.3e). The apices of the hornblende tetrahedron can move independently of one another. According to Robinson (1982), progressive reaction will lower the Al content of the aluminous hornblende in equilibrium with plagioclase and orthopyroxene, but will increase the Al content of hornblendes in equilibrium with plagioclase and clinopyroxene (± orthopyroxene). The separate reaction volumes merge as the corners of the shrinking hornblende tetrahedron merge to a single, ultimate, hornblende composition (Robinson 1982).

Much of the initial magnesio-hornblende in the powder experiments underwent tschermakitic substitution, $Al_2(Fe,Mg)_{-1}Si_{-1}$, to form Al-hornblende (Fig. 3.13a). Similar, though much more subtle, compositional shifts were detected in the solid experiments. In his solid amphibolite melting experiments, Hacker (1990) found that the initial tschermakitic hornblendes were altered to magnesio-hornblende compositions through the $Al_{-2}MgSi$ substitution – the opposite trend observed in the present experiments. The liquid

compositions are more iron- and magnesium-rich than those of Hacker (1990), so most of the iron and magnesium lost from the magnesio-hornblendes during the reaction initially ends up in the liquid. This comparison indicates that the ultimate, high temperature hornblende composition is very much dependent on the initial hornblende composition, the bulk rock composition, the particular reactions that occur, and the compositions of the product phases. There is no single ultimate hornblende composition.

4.4.3 Plagioclase

No obvious change in composition of the starting anorthitic plagioclase (An_{90}) could be detected by either SEM or EMP analysis of the experimental products (Tables 2.1, 2.2 and 3.6). No trace of marginal zoning is detected in any of the plagioclase crystals. Marsh et al. (1990) have shown that An_{92-95} plagioclase is in equilibrium with H_2O-rich liquids of high-alumina basaltic and andesitic compositions. Modal analyses show that the amount of plagioclase decreases with increased temperature, confirming that it does react. Its composition does not change as a function of temperature, and this constancy is attributed to its An_{90} composition, i.e., the steepness of the lower limb of the plagioclase binary loop prohibits major compositional changes in anorthitic plagioclases through a large temperature interval. The anorthite reacts directly to produce the high-alumina character of the liquid.

4.4.4 Garnet Zoning

The garnets exhibit compositional growth-zoning even though they grew under isobaric and isothermal conditions. The fact that growth zoning can occur in garnets at constant pressure and temperature may have serious consequences for P-T history calculations that assume that growth zoning is due solely to changes in P-T conditions (e.g., Selverstone et al. 1984). The coexisting garnet and liquid always should be in local equilibrium. Thus, the garnet zoning reflects the compositional changes that occurred in the

liquid through time, as a result of the evolution of dehydration-melting reactions, not of changes in P-T conditions. However, the zoning in these experimentally grown garnets clearly was not produced under capsule-wide, equilibrium conditions.

The development of growth-zoning possibly may occur in response to a number of different conditions, but the zoning may be modified after growth if the garnet is exposed to high temperatures for a long enough durations. This post-growth, compositional homogenization could lead to erroneous thermometric results (Yardley 1977). Another question then is, given enough time, would the garnets become compositionally homogenized even as they continue to grow (syn-growth homogenization). The answer depends on the relative growth and intracrystalline diffusion rates of garnet, as noted by Jiang and Lasaga (1990).

The composition of newly growing garnet has a large effect on compositional gradients within the entire garnet crystal and thus on intracrystalline diffusion. In turn, the new garnet composition depends on the other phases' stabilities and reactions in the rock and the relative mineral growth rates. The garnet compositional profiles in Figs. 3.15 and 3.16 may vary in rocks with different compositions, e.g., the maintenance of compositional gradients may not occur if the components needed for changing the garnet composition are not released by other mineral reactions. The growth rate of garnet relative to other growing minerals also determines the availability of components.

As other reactions occur in the capsule, less iron is available to the garnet, so, through time, the new garnet that grows is relatively poorer in iron. The initial concentration of FeO in the core should remain constant through time (~18 wt.%) if no solid state transport (diffusion) is occurring within the garnet. In Fig. 3.15, the dashed line connecting the cores would be horizontal. Since this line has a non-zero slope, intracrystalline diffusion must have occurred during garnet growth. However, the zoning continued to develop in the garnets that grew in the longer duration experiments.

The slopes of the oxide profiles should rotate through time due to diffusion, as growth-zoned garnets become compositionally homogenized by post-growth thermal effects (Yardley 1977; Jiang and Lasaga 1990), i.e., the slopes of the compositional profiles rotate to the horizontal. In Fig. 3.15, the Al_2O_3 and FeO sets of profiles are the most unambiguous of the oxides. It is clear from these two oxides that the slopes do not rotate but are parallel to one another. The cores are losing FeO and gaining Al_2O_3 through time, but these oxides are not simply being redistributed within the garnet crystals. The picture is made complex by the growth of FeO-poorer and Al_2O_3-richer edges. In effect, the compositional changes occurring in the edges contribute to lowering the FeO and raising the Al_2O_3 contents in the cores by maintaining the compositional gradients within the garnet crystals during growth. When the garnet stops growing, the compositional profiles then should rotate to horizontal through time (e.g., Jiang and Lasaga 1990). Figure 4.7 illustrates the possible effects of growth heterogeneities (a-d) and post-growth homogenization (e-h) on the compositional profile of garnet through time. These profiles are juxtaposed in Fig. 4.7i to show the relative positional and slope changes through time.

Fick's Second Law of Diffusion states that:

$$\frac{\partial C}{\partial t} = D\frac{\partial^2 C}{\partial X^2}$$

where C is the oxide concentration, t is the time, X is the distance, and D is the diffusion coefficient. The slopes of the oxide profiles in figure GG are parallel to each other (most clearly seen in Al_2O_3 and FeO), thus $\partial C/\partial X$ does not vary with time [$(\partial^2 C/\partial X^2) = 0$]; however, $\partial C/\partial t$ does vary (e.g., positive for Al_2O_3, negative for FeO), which leads to an inequality in the diffusion law. This apparent conflict possibly can be resolved by calling upon growth-induced 'transient' steady-state diffusion which is due to the addition of edge garnet of ever-different composition. The diffusion may be considered steady-state because $(\partial^2 C/\partial X^2) = 0$ while the garnet continues to grow, yet this situation lasts only as long as the garnet grows. When growth stops, $\partial C/\partial X$ varies through time, i.e., the slopes of the oxide profiles rotate to horizontal [$(\partial^2 C/\partial X^2) \neq 0$].

Thus, diffusion passes through a syn-growth, 'transient' steady-state mode and a post-growth, time-dependent mode. The garnets do not exhibit post-growth compositional homogenization since they were still growing when the experiments were quenched.

The compositions of the cores change due to syn-growth diffusion [$(\partial C_c/\partial t)$ in Fig. 3.15], but the slopes of some of the oxide profiles ($\partial C/\partial X_{e\text{-}c}$) are not consistent with the direction of compositional change. In Fig. 3.15, the cores become more aluminous through time because ($\partial C/\partial X_{e\text{-}c}$) is negative, i.e., the edges are richer in Al_2O_3, so there is a flux of alumina to the cores. The opposite holds for FeO; ($\partial C/\partial X_{e\text{-}c}$) is positive, i.e., the cores are richer in FeO, so there is a flux of iron to the edges. MnO may behave like FeO, but the evidence is not as clear. However, the SiO_2 and TiO_2 trends appear to conflict with these composition-time correlations. SiO_2 in the cores decreases through time although ($\partial C/\partial X_{e\text{-}c}$) is negative, i.e., silica is diffusing out of the cores even though the edges are richer in SiO_2. TiO_2 in the cores increases slightly through time although ($\partial C/\partial X_{e\text{-}c}$) is positive, i.e., titanium is diffusing into the cores even though the cores are richer in TiO_2. Diffusion appears to be in the direction opposite to the normal, down-the-potential-gradient, flux direction for SiO_2 and TiO_2, so uphill diffusion may be occurring during garnet growth.

The MgO and CaO oxide profiles in Fig. 3.15 do not show as clear-cut trends as the other profiles, mainly because of the non-linear 2-day profiles. Compared with each other, though, they show opposite trends. The ($\partial C/\partial X_{e\text{-}c}$) of the 1-, 4- and 8-day profiles is negative for MgO and positive for CaO. The ($\partial C/\partial X_{e\text{-}c}$) of the 2-day profiles is concave up for MgO and concave down for CaO. This mirror image effect probably is due to the coupled substitution of Mg and Ca. The slopes of ($\partial C/\partial X_{e\text{-}c}$) are greater for MgO than CaO, so there is not a one-to-one coupling; the slope differences may indicate non-ideality of the Mg-Ca interactions.

The Mg-Ca interactions affect the Fe-Mg coupling (Harley 1984). In Fig. 3.15, ($\partial C/\partial X_{e\text{-}c}$) is opposite for FeO and MgO, since Fe and Mg substitute for each other.

($\partial C/\partial t$) also should be opposite, and in general it is. However, the 2- and 8-day MgO profiles are not mirror images of the FeO profiles, as are the 1- and 4-day profiles. The lack of symmetry between the FeO and MgO profiles is due to the curved and elevated 2-day and elevated 8-day CaO profiles.

In Fig. 4.8, the shape of the garnet radius versus time curve suggests that garnet growth is determined by the parabolic rate law, which holds for diffusion-controlled processes. Thus, garnet growth appears to be controlled by the diffusion of the necessary components through the silicate liquid, not by interface-controlled processes at the edges. However, it is possible that the initial garnet growth rate is linear but changes to parabolic as the size of the garnet increases (after ~4 days in these experiments). Aggregation of multiple grains would increase the overall growth rate and add to the composition complexity of the aggregate grain. Intraliquid diffusion, and thus garnet growth, is much faster than intracrystalline diffusion, so growth zoning is preserved; the presence of a liquid phase may be necessary to achieve this condition. The eventual lack of availability of components may limit the size or slow down the growth rate of the garnets, at which time homogenization may occur. However, rapid heating and cooling events, such as dike emplacements, may result in growth zoning with a lack of homogenization.

4.5 Garnet-Liquid Fe-Mg Equilibria

Many of the amphibolite experiments were run for different durations at similar temperatures to study the effect of time on reaction progress and phase compositions. One aspect of the compositional evolution of both liquid and garnet rims can be seen in Figs. 3.25 and 3.26. The molecular Mg/(Mg+Fe) ratio (the Mg number or Mg#) of the garnet rims as a function of temperature is shown in Fig. 3.25. The liquid Mg#s comprise the same approximate Mg# range (0.37-0.62) that natural andesite and MORB glasses comprise (Wilkinson 1982; Ellis 1986). There is no cross-over in relative Mg content between the liquids and coexisting garnets, i.e., the 'normal' relative iron enrichment in

liquid exists throughout the melting interval (Yoder 1976). In Fig. 3.26, the changes in K_D as a function of time reveal that Fe-Mg equilibrium between garnet and liquid is approached only for experimental durations longer than a few days at temperatures less than 975°C. The greatest changes in K_D's occur at the beginning of the experiments. The leveling-off of the change in K_D's through time is taken to be an indication of the approach to equilibrium.

In contrast with the results from this study (Fig. 3.25), in experiments using synthetic mineral mixes and glasses (in the FMAS system), Ellis (1986) found that below 900°C liquid is Mg-richer than coexisting garnet, but above 900°C garnet is Mg-richer than liquid. Ellis (1986) argued that this cross-over at 900°C necessitates a switch from peritectic to eutectic reactions under H_2O-saturated conditions. However, Ellis (1986) also states that this switch will not occur in dehydration-melting reactions (see Thompson 1982). In both the peritectic and eutectic H_2O-saturated reactions, garnet is always a reactant. In the present dehydration-melting experiments, both garnet and liquid are products, so the reaction cannot be eutectic, and the liquid does not have to be Mg-richer than the coexisting garnet.

Figure 4.9 shows the Fe-Mg distribution coefficients (K_D) between garnet rims and liquid from this study as a function of temperature ($10^4 * 1/T$ K) and also from Ellis (1986). The dashed line labelled "This study" is the best fit line through all of the data points; however, for reasons discussed previously, the solid line runs through the more reliable data. The conclusions are unchanged, whichever line is used. Compared with Ellis' (1986) data, the slopes of the curves from this study are shallower, and the curves are displaced to higher values. Because of the shallowness of the slopes, the curves cross $\ln (K_D) = 0$ at about 750°C and not 900°C. Therefore, it is possible that the liquid can be Mg-richer than garnet only below 750°C. However, 750°C is close to the solidus of this amphibolite and below the garnet-in reaction boundary, so that even if a liquid is formed

below this temperature, there is no garnet to coexist with it. No Fe-Mg liquid-garnet compositional cross-over is present in this amphibolite system.

In pelite melting experiments, Green (1977) and Vielzeuf and Holloway (1988) both find a reversal in the Fe-Mg partitioning between garnet and liquid. The cross-over is determined to be at 950°C by Green (1977) and between 950-1050°C by Vielzuef and Holloway (1988), with little pressure dependence. The ranges in Mg# for both liquids and garnets are narrower than the ranges in the present study. In both of these studies the garnets and liquids are relatively Mg-poor, due to the pelitic starting compositions. Thus, small changes in MgO contents in the phases may have a large effect on the relative garnet-liquid Mg#s.

The relative Mg contents of garnet and liquid do not depend solely on the garnet-liquid Fe-Mg equilibria. The presence of Mg-rich product minerals (Cpx, Opx, new Hb) forces the liquid to be Mg-poor but should not constrain the K_D's between garnet and liquid, because the garnet composition depends on the liquid composition. If it were to occur, the garnet-liquid Mg# cross-over is an interesting process to enrich the liquid in Mg. However, the pyriboles probably play a more important role than garnet in determining the low Mg# of the liquid, because their Mg#'s are so high (Fig. 3.25), so even with a cross-over, the liquids would still be relatively Mg-poor.

The liquids produced by partial melting of the natural amphibolite are Ca-rich, and the garnets contain about 20 mol.% of the grossular component. The presence of calcium may affect the Fe-Mg equilibrium in the garnet (Harley 1984). Ellis (1986) investigated a Ca-free system and thus did not see this possible influence. It is not clear whether the occurrence of dehydration-melting reactions and the presence of calcium are solely responsible for the lack of a garnet-liquid Mg# cross-over. Nevertheless, the continuous, Mg-poor nature of the liquid (relative to garnet and all the other mafic minerals) has important implications for the compositional evolution of amphibolite-derived liquids and possible interactions with mantle material, as discussed below.

4.6 Liquid Compositional Trends

The bulk composition of a rock influences the liquid composition, but the liquid trend is controlled by the initial rock mineralogy and the subsequent mineral assemblages. The partial melting of the amphibolite bulk composition used in this study results in liquids that are similar to tonalites but more calcic and aluminous. Amphibolites having more sodic bulk compositions may produce more trondhjemitic liquids when partially melted (e.g., Winther and Newton 1990). However, amphibolites having similar bulk compositions also may produce more sodic liquids if the plagioclase is more sodic and the hornblende is more calcic. For example, in a rock containing 30% plagioclase, the difference in the total Al_2O_3 content as a result of the presence of either anorthite or andesine is about 3%. The total CaO difference is 4%, and the total Na_2O difference is 2%. Even though the bulk composition may be only slightly different, the differences in the stabilities of the plagioclases (and hornblendes) may lead to relatively large differences in liquid composition. The bulk composition of the rock, therefore, may not be as important as the relative compositions and reactivities of the minerals in determining liquid compositions during small to moderate degrees of melting.

In Fig. 4.10 the normative liquid compositions from this study are plotted in An-Ab-Or space along with liquid compositions from other basalt and amphibolite melting experiments. The position of these liquids near the anorthite apex is a result of the high anorthite content of the plagioclase in the amphibolite. The initial liquid trends of these experiments head in the opposite direction from the liquid trends produced in Helz's (1976) 5 kbar, H_2O-oversaturated experiments (Figs. 3.17b and 4.10). With progressive melting, Helz's liquid compositions become enriched in the anorthite component, but the liquids in the present study become enriched in the albite component. Winther et al. (1989) also found a trondhjemitic to leucotonalitic liquid trend in their 8-22 kbar, H_2O-oversaturated melting experiments of a high-Al, low-K tholeiite.

The compositions of the minerals have an large effect on the evolution of the liquid compositions (Thompson 1988). The compositions of intermediate plagioclases, and the liquids produced from their reaction, vary considerably as a function of temperature. The starting mineral assemblages in Helz's (1976) study contain plagioclases of intermediate compositions which can change composition to a greater extent than the anorthite in the amphibolite used in this study. In the simple binary plagioclase system, both the residual plagioclase crystals and the new liquid become richer in the anorthite component with increasing temperature. Helz's (1976) liquid compositions follow trends which mimic trends governed by the liquid/crystal plagioclase binary relationships. The reaction of intermediate plagioclases contributes to the resulting trondhjemite to tonalite liquid compositional trend, even though hornblende is more important in controlling the liquid composition (Helz 1976). Not only does the amphibole composition control the liquid composition, but through the $CaAlNa_{-1}Si_{-1}$ exchange, it also affects the plagioclase composition (Thompson 1988).

The plagioclase composition in the amphibolite of the present study is so calcic that its composition shifts little. The reversed tonalitic to trondhjemitic liquid trends in these experiments are not due to the relatively minor compositional changes in the anorthitic plagioclase but to the breakdown of hornblende. Both sodium and calcium enter the liquid as hornblende breaks down, but the growth of calcic phases containing little sodium, such as clinopyroxene and garnet, forces a decrease in the anorthite content of the liquid (Fig. 3.18).

Not only do these trends run in the opposite direction from Helz's (1976) trends, but they also reverse their directions at high temperature. Figure 3.17b shows the reversals in the liquid composition trends. The dramatic changes are due to the disappearance or absence of garnet above 975°C. Direct comparison with Helz (1973) is not possible because garnet does not appear in any of her experiments.

It is clear from the experiments that the liquids are very sodium-poor (Table 3.7, Figs. 3.17a, 3.18). In An-Ab-Or space, the tonalitic liquids plot with the cumulate gabbros, far away from the oceanic plagiogranite, continental trondhjemite and granophyre fields (Coleman and Peterman 1975). The partial melting of this particular anorthite-bearing amphibolite cannot produce these more sodic rocks. The presence of anorthite may give the liquids their high CaO/Na_2O values. Thus alteration of this amphibolite (by alkali metasomatism or sea-water exchange) must occur to produce these sodic granitoids (e.g., Taylor 1980; DeVore 1981, 1982). Spulber and Rutherford (1983) reached this same conclusion based on their hydrothermal melting experiments on a tholeiite of similar though slightly more sodic composition (2.27 wt.% Na_2O; DO8). However, it is not known whether their tholeiite contained phenocrysts of anorthite.

There is field evidence that amphibolite anatexis produced plagiogranite in an ophiolite (Pedersen and Malpas 1984) and in oceanic shear zones (Flagler and Spray 1991). Flagler and Spray (1991) reported a gabbro, with a composition roughly equivalent to the amphibolite used in this study, and an amphibolite and plagiogranites with compositions enriched in sodium. They concluded that hydrothermal alteration was responsible for the formation of the sodium-enriched amphibolite, which subsequently underwent anatexis along low-angle shear zones in ocean crust to produce plagiogranite. Pedersen and Malpas (1984) also concluded that the compositions of the plagiogranites are in part due to metasomatic effects.

4.7 Peraluminous Nature of the Liquids

Helz's (1976) 5 kbar experiments produced liquids that are practically all peraluminous, which led her to surmise that excess Al_2O_3 may be a characteristic of liquids generated at high P_{H_2O}. Kushiro and Yoder (1972) found that liquids that formed in the presence of H_2O in the CaO-MgO-Al_2O_3-SiO_2-H_2O (CMASH) system at 10 kbar also are peraluminous. Ellis and Thompson (1986), also working in the CMASH system,

determined that liquids produced under water-saturated conditions at 5 and 10 kbar are peraluminous. However, under vapor-absent conditions the CMASH liquids are only marginally metaluminous (Ellis and Thompson 1986). Working with natural greenstones and amphibolites, Beard and Lofgren (1989) showed that water-saturated melting at 1 and 3 kbar produces liquids with too much Al_2O_3 to be considered real tonalites, but dehydration-melting produces liquids with "correct," natural tonalite compositions.

From these previous studies it would appear that water-saturation is an essential condition for the formation of peraluminous liquids. However, in the present study almost all of the liquids generated by dehydration-melting at 10 kbar are peraluminous, in that [Al/(Ca + Na + K)] > 1 (Table 3.7). In ACF-deluxe space, the cross-over from corundum-normative to diopside-normative liquids at 1000°C parallels the trend of Helz's (1976) water-saturated liquids (Fig. 3.21). From an analysis of model basalt systems, Ellis and Thompson (1986) concluded that the generation of peraluminous liquids from the melting of basalts must be influenced by water and/or pressure. A conclusion from the present study is that in at least this case, water alone does not necessarily control the peraluminousity of liquid compositions (Fig. 3.22). Studying a suite of gabbroic enclaves, Beard and Borgia (1989) postulated that alumina-rich magmas might stabilize anorthite. The corollary to this proposal is that the partial melting of an anorthite-bearing rock will produce high-alumina liquids (Al_2O_3 >15 wt.%), even if the bulk composition of the rock is not particularly aluminous, such as the amphibolite used in this study (Al_2O_3 <15 wt.%).

Peraluminousity of granitoids has long been considered a characteristic of a partially melted, aluminous metasedimentary source (e.g., White and Chappell 1977; Le Breton and Thompson 1988; Vielzeuf and Holloway 1988; Patiño Douce et al. 1990). Petrological arguments against the derivation of peraluminous liquids from more mafic (amphibolitic) sources include the necessity for a free H_2O-vapor phase and the occurrence of only small liquid fractions produced under the appropriate P-T conditions (Ellis and Thompson 1986; Beard and Lofgren 1989; Patiño Douce et al. 1990; Patiño Douce and Johnston 1991).

However, it is evident from the present experiments that the presence of sediments or abnormally hot or wet amphibolites is not necessary to generate relatively large quantities of peraluminous liquid during anatexis under lower crustal conditions.

Much of the lower crust may be mafic (Taylor and McLennan 1985; Rudnick and Taylor 1987; Kempton et al. 1990), so the anatexis of amphibolite may be responsible for a large part of the liquids that could form in this region. From the preceding discussion, it appears that the presence or absence of anorthite in a partially melted amphibolitic source plays a pivotal role in the development of the aluminous character of the liquid. Marsh et al. (1990) and Beard and Lofgren (1991) have determined that the An-content in plagioclase increases slightly with increasing P_{H_2O}. Thus, calcic plagioclase and hornblende amphibolites may form in H_2O-rich environments, conducive to melting. The anorthite-hornblende association has been found in xenoliths from the lower crust beneath Japan (Fukuyama 1985; Kushiro 1990), from basalt dredged from near the Aleutian Trench (Fournelle, unpub. data), as well as in plutons and dikes within the Sierra Nevada Batholith of western North America (Mack et al. 1986; Wolf and Saleeby 1990). Fournelle and Marsh (1991) suggest that An-rich xenoliths (An_{90-95}) in high-alumina basalts could have come from a slab source beneath an arc. The presence of An-rich plagioclase in arc lavas is common (Fournelle and Marsh 1991). Plagioclase with An_{90} composition is common in the gabbroic parts of many ophiolites (e.g., Malpas 1977; Morgan 1977; Aldiss 1978). Some mafic xenoliths have Al_2O_3 contents over 19 wt.% (Rudnick and Taylor 1987). Rudnick and Taylor (1987) suggested that this enrichment is due to the preferential accumulation of calcic plagioclase by cumulate or partial melting processes in the lower mafic crust. Infiltration of the liquid produced by partial melting of the amphibolite used in the present study would elevate the Al_2O_3 content of the infiltrated rock.

4.8 Water Contents and Activities of the Liquids

4.8.1 Water Contents

Since only one hydrous and one anhydrous mineral comprises the initial amphibolite, the model system A-H_2O can be used to describe the phase relationships and liquid compositions in an isobaric T-$X_{(H_2O)}$ diagram. Figure 4.11 schematically illustrates that the incongruent melting of a hydrate (in this case, hornblende) produces a silicate liquid that contains more H_2O than does the hydrate (Robertson and Wyllie 1971; Eggler 1973; Ellis and Thompson 1986; Thompson 1988). If anhydrous minerals are present in the mineral assemblage, the liquids will always remain H_2O-undersaturated, unless an invariant point is crossed fortuitously in P-T space; if this happens the topology of the T-$X_{(H_2O)}$ diagram will change. In the simple A-H_2O model system, the percentage of water in a dehydration melt-produced silicate liquid is at a maximum at the initial stage of the peritectic melting reaction (Fig. 4.11). As fusion progresses, the total amount of H_2O dissolved in the liquid increases, but the percentage of dissolved H_2O decreases, because the amount of liquid increases. The calculated H_2O content of the liquids agree with this simple model. The initial liquids contain approximately 7 wt.% H_2O. There is a steady decrease to 2 wt.% H_2O as the percentage of liquid increases to ~50 vol.%.

Rushmer (1991) calculates the H_2O content of an amphibolite-derived liquid to be a constant 2 wt.% over almost the entire melting interval in which hornblende is stable, even though the amount of liquid increases from from ~5 vol.% to 46 vol.%. This constancy is attributed to the buffering of the activity of H_2O in the liquid during dehydration-melting (Clemens and Vielzeuf 1987; Rushmer 1991). Thus, if the amount of H_2O in the liquid is not to increase over 2 wt.%, the reaction of hornblende must be limited at the solidus. However, Rushmer (1991) also reports relatively narrow hornblende reaction intervals, which necessitates a rapid $\partial X_L/\partial T$ – not a gradual increase (where X_L = liquid fraction; T = time).

The 7 wt.% H_2O content of the initial liquid produced in this study is essentially the same as that determined by Clemens (1984) and Clemens and Vielzeuf (1987) for mafic rocks (amphibolites) at 10 kbar. Mass balance calculations force the initial liquid to be H_2O-rich. The occurrence of hornblende sliding reactions (Hb → Ca- and Al-Hb) actually tends to reduce the release of H_2O into the liquid by increasing the stability of the hornblende. These sliding reactions tend to increase the hornblende melting interval. In systems in which these reactions are not observed, and the hornblende melting interval is narrower, the breakdown of hornblende should produce even more liquid at low temperatures than the amounts produced in the more complex systems.

4.8.2 Water Activities

On an isobaric T-$a_{(H_2O)}$ plane, in which $a_{(H_2O)}$ is the activity of water, the amount of liquid that is produced is buffered along the vapor-present solidus curve but not at the dehydration-melting invariant point (Powell 1983). Conversely, the $a_{(H_2O)}$ changes along the vapor-present solidus curve but is buffered at the dehydration-melting invariant point. Figures 4.12 - 4.14 illustrate some of the details of P-T-$a_{(H_2O)}$ space (P = pressure; T = temperature), of which the basics were clearly developed by Powell (1983) and enhanced by Pattison (1991). The earlier ideas were developed and visualized as two-dimensional slices [T-$a_{(H_2O)}$ planes], but I have found them much easier to understand by constructing three-dimensional P-T-$a_{(H_2O)}$ spaces and then taking T-$a_{(H_2O)}$ or P-$a_{(H_2O)}$ slices from these spaces. These figures are purely schematic, and in detail may not be rigorously correct due to the dearth of P-T-$a_{(H_2O)}$ data and to my own artistic limitations. Figure 4.12a shows that the intersection of the dehydration ($\mathbb{D}$) and vapor-present melting ($\mathbb{M}$) surfaces defines a curve in P-T-$a_{(H_2O)}$ space. Dehydration-melting occurs along this curve (thick, solid curves). For any given $a_{(H_2O)}$, the P-T plane is intersected by the ($\mathbb{D}$) and ($\mathbb{M}$) surfaces (the P-T plane at $a_{(H_2O)} = 1$ is shown), but the dehydration-melting curve (thick, dashed curve) must be projected onto it (horizontal arrows). In the particular case of hornblende

dehydration, with increasing pressure, the slope of the dehydration surface changes from positive to negative (as shown) as hornblende breaks down to form denser minerals (e.g., garnet and jadeite-rich amphiboles).

Figure 4.12b extends Fig. 4.12a to lower $a_{(H_2O)}$ values. The lining on the surfaces is only intended to aid in the visualization of the three dimensionality of the surfaces. The separation of the two (𝔻) and (𝕄) surfaces at low $a_{(H_2O)}$ can be seen in this figure. The four strait arrows with conical tips represent different heating scenarios. The three which are numbered also are illustrated in the isobaric T-$a_{(H_2O)}$ plane of Fig. 4.12c (even though the arrows are not strictly all at the same pressure). Paths 1 and 2 represent internally-buffered systems, in which the fluid:rock ratio is very small. Path 3 represents externally-buffered systems, in which the fluid:rock ratio is large. Path 1 hits the vapor-present solidus as the temperature rises (the vapor-present melting curve (𝕄) in Fig. 4.12c). The liquid-producing reaction buffers the $a_{(H_2O)}$ to lower values until the dehydration-melting invariant point is reached. A large amount of liquid is produced at this point, until a reactant is exhausted. Path 2 hits the dehydration curve (𝔻) and heads for higher $a_{(H_2O)}$, until the dehydration-melting invariant point is reached, at which point melting begins. Path 3 is externally-buffered by a large quantity of fixed-$a_{(H_2O)}$ fluid. This path pierces any reaction surface it encounters, in this case the dehydration reaction. Figure 4.12d is the projection of the occurrence of dehydration-melting onto the P-$a_{(H_2O)}$ plane, showing the minimum in $a_{(H_2O)}$ at moderate pressures. Figure 4.12e is a P-T slice that intersects the dehydration and vapor-present melting surfaces, with the projection of the dehydration-melting curve. The arrows point in the direction of decreasing $a_{(H_2O)}$ along this projection (also see Percival 1983).

Waters (1988) and Pattison (1991) have used the isobaric, T-$a_{(H_2O)}$ diagrams to analyze the role of H_2O in the evolution of natural rocks. Pattison (1991) determined that a limited amount of external fluid probably had driven the $a_{(H_2O)}$ of the mafic system to lower values until the dehydration curve was intersected (a path perpendicular to the

isoactivity part of the three paths shown in Figs. 4.12b,c). Anatexis occurred at higher temperatures. Conversely, Waters (1988) found that dehydration-melting and the formation of granulite-facies assemblages occurred without the addition of external fluids. Although widespread melting took place, large-scale extraction of the silicate liquid did not occur. The rocks textures and mineralogies indicated that local gradients in $a_{(H_2O)}$ may have been present during melting, with the liquid segregations acting as sinks for the volatiles (Waters 1988). Different $a_{(H_2O)}$ buffers may have been operating in liquid-present and liquid-absent domains within the rocks (Waters 1988). The evidence for the existence of these gradients implies that non-equilibrium conditions were sustained for geologically relevant durations and subsequently preserved in the rock records.

It is possible that these solid experiments also contain textural and mineralogical evidence that records similar $a_{(H_2O)}$ gradients but on a microscopic scale. Figure 4.13a is a T-$a_{(H_2O)}$ section that illustrates what might have occurred during the experiments and, more tenuously, during anatexis of some natural rocks (e.g., Waters 1988). With increasing temperature, the dehydration curve (𝔻) is hit, and H_2O is liberated in the generalized dehydration reaction, Hb $\rightarrow$ Cpx + H_2O, that occurs in the cores of the hornblende grains (Fig. 4.2). This transient H_2O diffuses into and along the hornblende-plagioclase boundaries and triggers or enhances melting along the vapor-present melting curve (𝕄). This is a non-equilibrium process, because at equilibrium, the $a_{(H_2O)}$ must be the same throughout the system. Continued melting along 𝕄 with no decrease in $a_{(H_2O)}$ may be sustained by the continued dehydration of hornblende. The equilibrium dehydration-melting invariant point may be reached if the appropriate temperature is reached (T_2). The approach to this point depends on the compositionally-dependent stability of the hornblendes in the system. Figure 4.13b illustrates some of the added complexity in the presence of minerals exhibiting solid-solution. As compositions of minerals change during reaction, the location of reaction boundaries will shift. This evolution is schematically illustrated by the series of parallel reaction curves. Rock types shown in relation to the

increasing grade of the reaction boundaries; amphibolite, pyroxene granulite, and garnet pyroxenite. Granulites may be formed without anatexis if the $a_{(H_2O)}$ of the system remains low enough so that dehydration-melting never occurs (path 3 in Fig. 4.12c).

The shapes of the preceding $a_{(H_2O)}$ diagrams (Figs. 4.12a-e and 4.13a,b) were based on the simplifying assumption that there is a negligible CO_2 solubility in the silicate liquid, in which case the stability field of the liquid shrinks as $a_{(H_2O)}$ decreases. However, Peterson and Newton (1990) have shown that CO_2 may have a non-negligible solubility in Mg-bearing silicate liquids. Thus, the stability field of the liquid may grow as $a_{(H_2O)}$ decreases. Figures 4.14a-d show most of the same features that Figs. 4.12b-e show, but, in addition, show what the effects of non-negligible CO_2 solubility may have on reaction boundaries in P-T-$a_{(H_2O)}$ space. Instead of monotonically decreasing with decreasing $a_{(H_2O)}$, as in Figs. 4.12a,b, the intersected volume bulges out and then decreases with decreasing $a_{(H_2O)}$ (Fig. 4.14a). The low temperature point of the bulge corresponds to an $H_2O/(H_2O+CO_2) = 0.6$ (molar basis) in the KMASH-CO_2 system at 6 kbar (Peterson and Newton 1990). Figure 4.14b shows this bulge in a P-$a_{(H_2O)}$ projection. Figures 4.14c,d are isobaric T-$a_{(H_2O)}$ slices at different pressures through the bulge, corresponding to P_2 and P_1 in Fig. 4.14a. At both pressures and relatively low $a_{(H_2O)}$, melting or dehydration proceeds as in Figs. 4.12b,c. At both pressures and relatively high $a_{(H_2O)}$, the $a_{(H_2O)}$ increases during melting. With internal-buffering, the $a_{(H_2O)}$ does not necessarily have to be driven to lower values with increasing temperatures (Powell 1983). The initial $a_{(H_2O)}$ of the system will determine the path taken, either to higher or lower values of $a_{(H_2O)}$. At P_1, another dehydration-melting invariant point is reached at the intersection of the vapor-present melting curve (𝕄) and the dehydration curve (𝔻) (Fig. 4.14d). This topology occurs over a very limited pressure range and depends on how soluble CO_2 is in the liquid. At P_1 and very high $a_{(H_2O)}$, the dehydration curve is hit first instead of the vapor-present melting curve, with increasing temperature. The addition of CO_2 to the system will cause melting.

4.9 Liquid Volumes in Powder Experiments

The amount of liquid that can be derived from a rock at a given temperature is a very important parameter (liquid fraction X_L) because it controls the rheological behavior, the transfer of heat, and chemical evolution in the solid-liquid systems (Bergantz 1990). In a system containing less than ~30-50% liquid (the critical melt fraction), the solid mass is a grain-supported framework, and large-scale, convective, movement of solid and liquid will not occur (Arzi 1978; Van der Molen and Paterson 1979; Wickham 1987; Miller et al. 1988), although liquid segregation still is possible through porous media flow.

Figure 3.4a shows the percentage of liquid generated as a function of temperature and time in the powder amphibolite experiments. Figure 4.15 is a compilation of the liquid percent versus temperature data from the present study, and the experimental data on different hornblende-bearing rocks from Helz (1976) [5 kbar, H_2O-saturated], Rushmer (1991) [8 kbar] and Beard and Lofgren (1991) [6.9 kbar]. Note that the liquid quantity is in volume percent. The liquid volumes in the present study were directly measured by point counting (isotropic liquid pocket geometry assumed for powder runs). Studies in which the modes are calculated indirectly by mass balance, and not point counting, almost invariably report the percentages of phases as weight percent. This method is fine except when the volume is the needed parameter, such as in an analysis of liquid fractions. Figure 4.15 shows the data of Helz (1976) and Beard and Lofgren (1991), that have been converted from weight percent to volume percent by calculating the compositionally-dependent phase densities from the relevant data sets (Rushmer (1991) reported data in vol.%). I use Nelson and Carmichael's (1979) partial molar volume data for all of the oxides except H_2O, for which I use Silver and Stolper's (1985) estimate. The percentage difference due to this conversion becomes more pronounced with an increasing amount of liquid. The conversion to volume percent increases the amount of liquid because the liquids' lower densities, relative to all the crystalline phases. The increase can amount to ~10% near critical melt fraction values, and thus this conversion is not a frivolous exercise.

The results of melting experiments containing subordinate amounts of muscovite, biotite and hornblende reveal step-like melting patterns, corresponding to the temperature-buffering effect of the breakdown of hydrous minerals (e.g., Vielzeuf and Holloway 1988; Rutter and Wyllie 1988). However, in a pelitic system, Patiño Douce and Johnston (1991) found that liquid fraction smoothly increased with increasing temperature. The partial melting of amphibolites generates relatively smoothly increasing amounts of liquid through the melting interval, as shown in Fig. 4.15. The liquid fractions for most of the amphibolites converge to 40-50 vol.% at 1000°C. More liquid is produced at lower temperatures in the H_2O-saturated experiments of Helz (1976) than in the H_2O-undersaturated experiments, even though in two of her three experiments, 40-50 vol.% liquid also is produced at 1000°C. Not shown in Fig. 4.15 are 1 kbar and 3 kbar, H_2O-saturated curves from Beard and Lofgren (1991) that fall within the area defined by the H_2O-saturated curves of Helz (1976). The data from the present study fall in the middle of the field defined by the H_2O-undersaturated melting experiments of Rushmer (1991) and Beard and Lofgren (1991). Rushmer (1991) makes a fundamental distinction between her H_2O-undersaturated ABA data and Helz's (1976) 1921 H_2O-saturated data, stating that Helz's data show a smooth increase but her data show a step-like increase, with increasing temperature. However, her step is smoothed by the wt.% to vol.% conversion and could completely disappear if she has located the solidus at too high a temperature. She has created a step by expanding the limited 900-1000°C temperature interval and by constraining her curves by very narrow error bars. Vielzeuf and Holloway (1988) demonstrate that melting in the pelitic system (with subordinate amounts of biotite and muscovite) results in a step-like melting pattern, regardless of the H_2O content of the system. Thus, the shapes of melting curves are functions of the amounts of hydrous phases in the rock and not a function of the H_2O content. Minor amounts of hydrous phases yield step-like patterns, whereas major amounts yield smoother patterns. Amphibolite, composed mostly of hydrous amphiboles, have smooth melting curves.

In their pelite melting experiments, Vielzeuf and Holloway (1988) produce a large quantity of liquid over a narrow temperature interval – a step (or plateau, depending on the axes' orientations). They propose that this voluminous melting process would buffer the temperature at about 850°C and prevent higher-grade metamorphism from occurring. They consider that the presence of previously melted, relatively infertile, recycled crust is necessary for the formation of high-temperature granulites (Vielzeuf and Holloway 1988). An alternative process, however, would be the partial melting of nonrecycled amphibolitic crust. Figure 4.15 shows that the melting of amphibolites does not produce step-like patterns but smoothly increasing liquid fraction with increasing temperature. Thus, the buffering effect of a jump in liquid fraction is diminished, or shifted to very high temperatures, in amphibolitic crust.

The preceding discussion does not mean that the rate of liquid production is necessarily constant through the temperature interval. Most of the melting curves in Fig. 4.15 are nearly linear (within ±5 vol.% error). In contrast, the curve from the present study has a pronounced bend at 850°C, with the liquid production rate increasing above this temperature to a rate matching those in the other experiments. This change is even sharper if the 900°C data are taken into account, as shown in Fig. 3.4a. The other vapor-absent curves do not have this shape because either (1) additional H_2O was added to the present runs, (2) the actual solidus was not located in the other experiments, or (3) the different rock compositions produce distinctly different melting curves.

4.10 Hornblende Breakdown Interval

Figure 4.16 is a pressure-temperature diagram showing some details (solidi, Hb-out and Ga-out curves) of the experimentally-determined phase relationships of amphibolites, compiled from this study, Holloway and Burnham (1972), Green (1982), Winther and Newton (1990), Beard and Lofgren (1991), Rushmer (1991), and Rapp et al. (1991). Geotherms from various environments are also shown in order to place the

experimental results in a geological context (from Boyd and Gurney 1986; Martin 1986, 1987). Peacock's (1990) PTt path for young subducting lithosphere is also shown.

The ~200°C difference in solidi temperatures (~750-950°C) at 8-10 kbar is most striking. At pressures of 8 kbar and less, the vapor-absent solidi lie between 850°C and 925°C. In experiments with no H_2O added, the lowest temperature solidus was found in the present study (below but probably near 750°C at 10 kbar) – close to the solidus determined by Holloway and Burnham (1972) in a basalt-H_2O system with a fixed a_{H_2O} ~0.6. Beard and Rushmer (1990) extrapolated the position of their vapor-absent solidus above 7 kbar to be approximately 750°C at 10 kbar (J. Beard, pers. comm. 11/1990). Rushmer (1991) found a wide range in solidi temperatures at 8 kbar (800-925°C). Rapp et al. (1991) reported relatively high solidi temperatures (950-975°C) at pressures of 8 kbar and higher.

Ellis and Thompson (1986) have shown that in H_2O-excess experiments, amphibole coexists with liquid over a wide temperature interval above the solidus, but that the dehydration-melting of amphibole defines the solidus in the vapor-absent system. In their dehydration-melting experiments, Beard and Lofgren (1989, 1991) found that the amphibole disappeared directly above the solidus. In contrast, the exchange reactions of the amphiboles in the present study smear out the dehydration-melting reactions, which results in a persistence of amphibole well above the solidus.

Rushmer (1991) also found hornblende to coexist with a liquid in her 8 kbar experiments. The temperature interval for hornblende melting is 75°C wide – from 925°C to 1000°C – for her alkalic basaltic amphibolite, and 125°C wide – from 825°C to 950°C – for her island arc tholeiitic amphibolite. Pressure, as well as composition, influences the melting interval width. As shown in Fig. 4.16, the temperature interval in which hornblende coexists with liquid expands from lower to higher pressures [compare Wolf and Wyllie (1989) with Beard and Rushmer (1990)]. This interval widens from 50°C to

125°C between 3 and 8 kbar (Beard and Rushmer 1990) and to 250°C at 10 kbar (Wolf and Wyllie 1989, this study).

There is an important implicit difference in the relative widths of the hornblende-present melting intervals. The breakdown of hornblende may occur along a univariant curve which also corresponds to the solidus (Beard and Lofgren 1989). In the present study the breakdown of hornblende clearly occurs throughout a divariant field. The upper limit of this hornblende plus liquid field lies well above the solidus (Fig. 4.16). In this case, hornblende could play an important role in differentiation processes.

4.11 Comparison of Liquid Compositions: Powder and Solid Runs

Table 4.2 lists two sets of liquid compositions for comparison. Each set contains two averaged liquid compositions – one from a solid amphibolite experiment and one from a powder experiment – run under as similar conditions as possible (note the difference in duration in the 850°C runs). A more extensive comparison is not possible due to the probable leaks and sodium contamination in the other solid runs. Considering the differences in reactivity between the solid and powder media and resulting differences in mineralogies and modes, the compositional differences of the liquids are small. The 1000°C runs have similar mineralogies (L, Cpx, An, and Opx), and their liquid compositions are very similar. The compositional differences in the 850°C runs are largest in SiO_2 and FeO, though only 2.65% and 0.86%, respectively – even with Ca-Hb, Al-Hb, Opx, and Ga absent from the solid run and present in the powder run.

4.12 High-Sodium Glasses

Some of the powder and solid runs end up with liquids having very high Na_2O contents (7-9 wt.%). Great care was taken to insure that a compositionally homogeneous powder was produced and used in all of the powder runs. Thus the high-Na_2O liquids in some of the powder runs probably had sodium introduced into the system during the run.

The low-Na_2O composition of the starting powder was directly measured twice by DCP spectroscopy, which can measure sodium reasonably well. The obvious source of sodium contamination is from the NaCl pressure medium into which the capsules were pressed prior to the experiment.

Glasses from the 14-day runs at 875°C and 900°C contained 8.5 wt.% and 7.0 wt.% Na_2O, respectively, compared with 1.1 wt.% Na_2O found in the other solid runs at 850°C and 1000°C. The source of sodium in the high-Na_2O liquids from solid runs is less certain. The possibility of sodium-contamination is not just academic, because the presence of a homogeneous, high-Na_2O liquid in these solid runs is one piece of evidence for supporting liquid interconnectivity. There are three possible sources of sodium: the external NaCl pressure medium, sodic trace phases and sodic major phases. If a major phase is sodium-rich, then the possibility of interconnectivity cannot be supported by the presence of a homogeneous, high-Na_2O liquid.

There is a much wider range in compositional variability in the amphibole than in the Na_2O-poor, anorthitic plagioclase. Compositional heterogeneities may exist in the nonpowdered media, but a comparison of amphiboles from the thin-section, powder runs and solid runs show the same range in compositions. However, in the runs with sodium-rich liquids, there may be a greater amount of hornblende with higher sodium contents. It is possible that compositional differences exist between the amphibolite slab used for coring these solid rock cylinders, the slab used for making the thin-section, and the pieces ground up for the powder, but large differences would be surprising, considering the close agreement between the thin-section and powder run hornblende compositions. All of the cores were drilled from the same rock blank, along a 2 cm strip. It is unlikely that the amphibole compositions would be so different so close together in such a sodium-poor rock. For future work using solid rock, better compositional characterization of the rock blank from which the cores are drilled would be very useful.

This anomalously high quantity of sodium in both the powder and solid run liquids may have come from undetected, sodium-rich, trace phases. Table 2.2 lists the only two sodic plagioclases found in an extensive search of the entire thin section of the starting material. There probably is not enough of these rare, sodic plagioclases to drastically enrich the liquid in sodium. Alternatively, sodium may have entered the liquid from the NaCl pressure medium, possibly through leaks in the gold capsules. No chlorine was detected in the glasses within the SEM-EDS detectability limit (~0.5 wt.%). The amounts of Na_2O in powder-filled capsules that leaked (7-9 wt.%) and did not leak (1-2 wt.%) are comparable to the amounts of Na_2O in the solid-filled capsules. The increase in sodium in the glasses of both types of starting material supports the case for external contamination rather than internal phase disequilibrium, analytical problems or large variations in initial hornblende compositions in different cored cylinders.

4.13 Liquid Morphology in the Solid Experiments

4.13.1 Interfacial Energy Theory and Previous Experiments

The interfacial energy theory developed in materials science for the equilibrium distribution of liquid in a solid matrix applies to nearly-isotropic grains only – isotropic with respect to structure or surface energy. Earth scientists experimenting with natural minerals such as olivine and quartz have used this theory to explain liquid distribution (e.g., Watson 1982; Jurewicz and Watson 1984). The equilibrium relationship between solid/solid and solid/liquid surface energies is characterized by the dihedral angle, (θ) (Bulau et al. 1979; Waff and Bulau 1982; Jurewicz and Watson 1985; von Bargen and Waff 1986). Figure 4.17a shows the contacts between three phases, 1, 2, and 3, and the interfacial angles between the phases. The relationship between surface energies and angles is given by the equation:

$$\frac{\gamma_{23}}{\sin\theta_1} = \frac{\gamma_{13}}{\sin\theta_2} = \frac{\gamma_{12}}{\sin\theta_3}$$

where γ_{ij} is the interfacial energy and θ_k is the dihedral angle (Smith 1964).

In systems consisting of one solid and one liquid phase, as illustrated in Fig. 4.17b, the interfacial angle is described as the wetting angle separating the two solid/liquid interfaces of a solid/liquid/solid triple junction. The equation reduces to:

$$2 \cos \frac{\theta}{2} = \frac{\gamma_{ss}}{\gamma_{sl}}$$

The equilibrium distribution of liquid can be predicted from the dihedral angle of the system. Interfacial energies depend on the liquid and mineral compositions. For small liquid fractions (<5%), if $\theta < 60°$, then the liquid will be interconnected through a series of channels along grain edges, forming a continuous network, but if $\theta > 60°$, then the liquid will remain isolated at grain corners. In multicomponent systems different crystal boundaries have different dihedral angles in contact with liquids (Spry 1969; Vernon 1970; Fujii et al. 1986; Jurewicz and Jurewicz 1986). The proportions of the phases and the corresponding proportions of junctions with different θs influences liquid interconnectivity (Toramaru and Fujii 1986). Measured θs in felsic systems are about 44-60°, in contrast to slightly lower values of θ in mafic systems (40-50°) (Watson 1982; Waff and Bulau 1982; Jurewicz and Watson 1984, 1985; Toramaru and Fujii 1986).

The interfacial energy equations are applicable only if the surface energy is solely a function of the interfacial angle (Spry 1969). Moment and Gordon (1964) found the equations to be invalid if the surface energies or angles depended on the boundary orientation of any of the grains. The invalidity stems from the addition of angular forces, torque term effects, that rotate the boundary into a lower energy crystallographic orientation (Herring 1951; Moment and Gordon 1964; Spry 1969; Swalin 1972). Moment and Gordon (1964) found that significant torque forces exist even in relatively isotropic NaCl.

Although some rock-forming minerals such as quartz and olivine are nearly structurally isotropic, most of them are anisotropic (e.g., mica, pyroxene, amphibole, and feldspar). The interfacial energy theory requires modification for minerals with low symmetry and significant structural anisotropy, because surface energy strongly depends on the specific crystallographic planes forming the interface, i.e., the crystal orientation

(Spry 1969; Swalin 1972). Figure 4.17c illustrates schematically the geometry of many liquid pockets found in the solid amphibolite experiments, showing the strong control that a mineral, S, may have on liquid morphology if the mineral has a high degree of structural anisotropy and a strong cleavage. The term "crystallographically-controlled angles" is used in this paper to distinguish the anisotropic liquid pocket angles (angles α and β in Fig. 4.17c) from the isotropic, torque-free dihedral angle, θ in Fig. 4.17b.

4.13.2 Liquid Morphology

At 850°C, the liquid forms irregular-shaped polygonal pockets ranging in size from 5 to 20 μm. Many have crystallographically-controlled corners with angles that range from approximately 30° to 120°, with most apparent angles >60° (Figs. 3.27a and 3.28a). Many of the pocket edges are straight, from corner to corner (Fig. 4.17c), showing little of the curvature which is typically found along the lengths of liquid pocket edges with simple dihedral angles (Fig. 4.17b) as in partial melting experiments using powders (Bulau et al. 1979; Jurewicz and Watson 1984). Some of the corners have curved boundaries, but classical dihedral angles are not common. Whether these angles would develop in longer runs remains to be determined. LaPorte and Watson, although using biotite- and amphibole-rich powders, found textural features similar to my flat crystal/liquid surfaces (B.Watson, pers. comm., 1/1991).

At 875°C, the 2 vol.% of H_2O-saturated liquid present almost surrounds the plagioclase grains (Figs. 3.28b and 3.29a). As seen in the photomicrograph, the liquid at Hb/Pl boundaries is interconnected along the lengths of the plagioclase grains in two dimensions, and it appears to make inroads along the cleavages of hornblendes (Fig. 3.29a). Between 850°C and 875°C, individual liquid pockets within hornblende grains and along Hb/Pl boundaries grow larger (30-100 μm lengths), and the pocket edges lose their straightness. They are more curved than at 850°C, with longer edges of the pockets typically scalloped by many cusps protruding along possible cleavage traces into the

hornblende (Figs. 3.28b and 3.29a). The smaller pockets (<20 μm), however, have corners bounded by straight edges, as illustrated in Fig. 4.17c, rather than dihedral angles as in Fig. 4.17b. The majority of crystallographically-controlled angles are greater than 60° (Figs. 3.29a,b).

At 900°C, the shapes of the liquid pockets are flat-faced, irregular polyhedra, regardless of pocket size (10-70 μm lengths). The liquid pocket corners follow prism faces of the hornblende (Figs. 3.28c and 3.30a,b), according to the model of Fig. 4.17c, but at 900°C some of these angular corners are modified as illustrated schematically in Fig. 4.18. Liquid penetrates into the Hb/Hb corners in small projections <5 μm in length (Figs. 3.30a,b), with one side being a continuation of a straight Hb/L boundary corresponding to a mineral face (edges 'b' or 'e' in Fig. 4.18). The other side may also be straight (edge 'df'), apparently controlled by crystallographic structure, but examples occur where the other side developed curvature (edge 'ac'), with interfacial energy tending to develop dihedral angles (Fig. 4.17b). Thus, because of the structural immobility of one of the faces, 'b' or 'e,' the value of some corner angles between coarse-grained amphiboles may approach one-half of the theoretical dihedral angle.

Figures 3.4, 3.28d and 3.31 show that by 1000°C, approximately 50 vol.% of the sample forms large liquid pockets (100-500 μm diameters) comparable in size to the clinopyroxene grains, which amount to 40 vol.% of the sample. The critical melt fraction has been exceeded, and the minerals are effectively suspended in the liquid (von Bargen and Waff 1986; Wickham 1987; Miller et al. 1988).

4.13.3 Liquid Interconnectivity

One of the objectives of the solid rock experiments was to observe the process of melt generation, and in particular the geometry of the melt. In each run, the liquid fractions and the associated measuring errors were estimated both by point counting and visual inspection of the area of glass present in the photomicrographs, with results shown in Fig.

4.19. The area fractions of glass in the photomicrographs are assumed to be approximately equal to the volume fractions of liquid in the capsules. The photomicrograph views, cut oblique to the mineral lineation, minimize errors due to possible liquid distribution anisotropies. The liquid fractions increase from approximately 1 vol.% at 850°C to 5 vol.% at 900°C and to approximately 50 vol.% at 1000°C (Figs. 3.27-3.31). The liquid fractions of 5 vol.% and greater were determined by point counting (n = 200) on the photomicrographs. The estimation of low liquid fractions <2 vol.% was made more accurate by comparisons with runs containing higher liquid fractions, e.g., the liquid fraction of 2 vol.% (875°C) was estimated by a comparison with the run containing 5 vol.% liquid (900°C), and the liquid fraction of 1 vol.% (850°C) was estimated by a comparison with the run containing 2 vol.% liquid (875°C). The dashed line in Fig. 4.19 shows the percentage of liquid formed in the eight-day, powder amphibolite melting experiments, determined by point counting (also see Fig. 3.4a). This percentage is considerably higher than that formed in the solid rock experiments for runs of comparable duration (7 vol.% compared with 1 vol.% at 850°C; 12 vol.% compared with 2 vol.% at 875°C; and 19 vol.% compared with 5 vol.% at 900°C). Therefore, given time, the percentage of melting in the solid rock experiments may increase until the amount of liquid generated approaches that of the powder experiments.

In Fig. 4.19, at any given temperature, liquid fraction (X_L^P) in the powder experiments (dashed curve) is greater than the liquid fraction (X_L^S) in the solid experiments (solid curve). The 8-day powder experiments may not have achieved equilibrium, yet they probably closely approached it. Thus X_L^P probably lies close to the equilibrium liquid fraction, which is the maximum amount of liquid possible to generate at a certain condition. However, the amount of liquid produced in a natural rock during partial melting may not necessarily attain this maximum equilibrium liquid fraction, i.e., there may be a characteristic X_L^S that is a function of grain size. This relationship may be akin to the grain size- and grain shape variation-dependence of the critical melt fraction (e.g., Van der Molen

and Paterson 1979). The X_L^S in the experiments may never reach X_L^P because the liquid fraction in relatively coarse-grained rocks may be kinetically-controlled, e.g., metastable growth, armoring, and grain-size-related disequilibrium effects. In the experiments, X_L^S may depend on the relative reaction rates of dehydration and dehydration-melting, i.e., if most of the hornblende dehydrates to clinopyroxene instead of melting, then less liquid will be produced. These effects would not be noticeably in powder experiments due to pervasive dehydration-melting. During anatexis of natural rocks, the liquid fraction attained lies between X_L^S and X_L^P, and possibly may lie closer to X_L^S, regardless of the duration of anatexis. Thus, the values of X_L^S from these solid amphibolite melting experiments may be geologically useful. However, experiments of much longer duration are needed to determine whether or not equilibrium liquid fractions for coarse-grained, solid rocks tend toward X_L^P or a grain-size-dependent X_L^S.

In the present study, I investigated the textures produced during dehydration-melting of solid pieces of fine-grained, lineated amphibolite. The objective is to explore the liquid morphology under more natural conditions, with control exerted by the textures of oriented, anisotropic minerals in their natural geometries, to see how this control affects interfacial angles and the interconnectivity of liquids. I have determined where and how liquid forms along natural grain boundaries. The results differ from those of powder experiments in that liquid interconnectivity, although achieved just as in the powder experiments, is controlled more by crystal structure than by interfacial energies. The presence of relatively coarse-grained, structurally anisotropic minerals such as hornblende plays a crucial role in the distribution and interconnectivity of liquid, at least in the short term. The geometrical differences between the solid and powder experiments influence the manner in which the liquid collects and possibly its ability to move.

At 875°C, liquid almost surrounds the plagioclase grains (Figs. 3.28b and 3.29a). The liquid at Hb/Pl boundaries is interconnected along the lengths of the plagioclase grains

in two dimensions. The optical continuity of many small plagioclase grains indicates that these grains comprise a single, larger plagioclase crystal and thus are interconnected in three dimensions. Therefore, the liquid that is present along the boundaries of these grains probably also is interconnected.

The compositions of glasses both along Hb/Pl boundaries and enclosed within hornblendes are the same in each experiment (within the analytical error), but the compositions change from experiment to experiment, as expected. In the runs at 875°C and 900°C, the glasses contained distinctively large quantities of sodium (7-9 wt.% Na_2O), not just near the capsule walls but in pockets throughout the rock cores. Mass balance calculations do not permit this enrichment simply as the result of small degrees of partial melting of the rock because there is not enough sodium in the rock. Therefore, unless trace amounts of an undetected sodic phase are present in these two runs, these samples suffered sodium contamination. The only source appears to be from the external NaCl pressure medium. This is a problem that requires more attention. However, regardless of the external or internal origin of the sodium, the homogeneous character of the liquid composition may indicate the presence of an interconnected liquid network. If the sodium migrated from the capsule wall to the center of the rock cylinder through a liquid network, a calculated minimum diffusivity is approximately 10^{-8} cm^2s^{-1}, which is consistent with the extrapolated values of sodium diffusion in basaltic and andesitic liquids at 875°C (e.g., Smith 1974). These textural and chemical data support the notion that the apparently isolated liquids inside hornblende grains were in fact interconnected with liquids at Hb/Pl boundaries throughout the capsules at 875°C, even with only 2 vol.% liquid present.

Bulau et al. (1979) considered the changes in liquid distribution in a partially melted polycrystalline aggregate as textural equilibrium is approached. They concluded that liquid will be "forced out of the flat intergranular faces" and will collect along the edges as the interfaces adjust to constant curvature. However, they added that this textural adjustment occurs only in the absence of anisotropic minerals. In samples with liquid located only at

grain edges and corners, most liquid pockets appear isolated at three-grain junctions in two-dimensional views (e.g., Waff and Bulau 1979; Watson 1982; Jurewicz and Watson 1985; Fujii et al. 1986; Watson and Brenan 1987).

The solid amphibolite begins to melt where hornblende and plagioclase are in contact, and liquid continues to form at this location until one of the reactants is consumed, in this case, plagioclase. There is no evidence in the partially melted amphibolite that the liquid is moving from its sites of generation. At 875°C and 900°C, liquid is produced along the entire boundary surfaces between hornblende and plagioclase grains (Figs. 3.28b,c), forming an extensive network of interconnected liquid layers. The interconnectivity depends upon the geometries of the liquid pockets. These appear to be influenced more by hornblende-plagioclase locations and the hornblende crystallography than by dihedral angles. At low degrees of partial melting, the pockets of liquid are interconnected even though many of the the corners have angles greater than 60°. This conclusion from the solid rock experiments differs from the results of previous experiments using rock and mineral powders, in that those experiments determined that a θ less than 60° is necessary for interconnectivity. It appears that the phase equilibrium constraints and structural anisotropy of the minerals dominate over the surface energy effects, at least in experiments with durations of two weeks. Any driving force to move liquid to grain edges and corners is not effective in these experiments (contrast with Bulau et al. 1979). Thus the liquid that is formed between mineral faces tends to remain there. Experiments with much longer durations are required to determine equilibrium textural relationships in systems composed of structurally anisotropic minerals.

Phase equilibrium has not been reached in the amphibolite cores, as shown by the comparison of the liquid fractions of the solid experiments with those of powder experiments in Fig. 4.19. Johannes (1983) estimated that equilibrium is achieved in plagioclase-H_2O melting reactions in a few months at 875°C. If this rate is relevant to my hornblende-plagioclase experiments, then the system will reach equilibrium

instantaneously, relative to any geologically reasonable melt separation time at 875°C. During anatexis of natural rocks, however, the liquid fraction attained lies between X_L^S and X_L^P, and possibly may lie closer to X_L^S, regardless of the duration of anatexis or the amount of time needed to reach equilibrium. Much longer duration experiments on solid rocks with different grain sizes are needed to address this possibility.

These experiments have not attained textural equilibrium, so the textures probably will continue to develop through time. Miller et al. (1988) proposed a continual "microstoping" of grains in a partly molten rock, leading to the upward displacement and migration of liquid. A similar process may occur in the amphibolite. Depending upon the relative plagioclase-liquid density contrast, the plagioclase suspended within pockets of liquid will either sink or float. Regardless of which occurs, the overall effect will be to consolidate many small pockets of liquid into fewer, enlarged pockets of liquid, still interconnected. This would increase the permeability of the system and the prospects for segregation of the liquid from the rock matrix. The growth of minerals as poikiloblastic phenocrysts (e.g., garnet) may affect the permeability, but I have no data on this problem.

4.14 Liquid Viscosity

Table 4.3 lists the viscosities of some of the liquids from both the solid and powder amphibolite experiments, as a function of composition, H_2O content and temperature, calculated according to Shaw (1972). Viscosities are calculated for 800°C even though there are no runs at this temperature. The left column in the top part of Table 4.3 is the measured composition of the glass (anhydrous basis) from the 850°C solid amphibolite experiment. In the columns to the right, various amounts of H_2O have been added to this anhydrous glass composition and the viscosities recalculated. These calculated viscosities are combined with information about the H_2O content in the 875°C run to estimate the 875°C liquid viscosity. This method was used instead of using the 875°C glass composition (suspect because of the sodium-contamination) and is justified since the H_2O

content presumably has more of an effect on viscosity than the anhydrous compositional differences between the 850°C and 875°C runs. Based on mass balance calculations, the partial dehydration of hornblende at 875°C releases enough transient H_2O to saturate the 2% liquid present (with 10-12 wt.% H_2O). No influx of additional H_2O is needed to generate the H_2O-saturated liquid. The viscosity of this liquid is estimated to be between 81 and 21 Pa s at 875°C (Table 4.3).

In the bottom part of Table 4.3 are the liquid viscosities calculated from powder amphibolite experiments. The modes listed were obtained by point counting. In the powder experiments, the large decrease in viscosity from 850°C to 875°C, with little change in the percentage of liquid, is due to the significant increase in dissolved H_2O associated with the wide-spread dehydration of hornblende (compare Figs. 3.27 and 3.29). The liquid viscosity from the 875°C powder run is about 900 Pa s. Thus, the liquid viscosities calculated from the powder amphibolite experiments are only about one order of magnitude higher than the values from the solid amphibolite experiments.

The liquid fraction (X_L) that could be generated from this amphibolite during deep crustal anatexis lies between the solid (X_L^S) and dashed (X_L^P) [powder] curves in Fig. 4.19. The liquid fraction will increase from (X_L^S) toward (X_L^P) through time. The maximum amount of liquid possible to generate at 875°C is about 12 vol.% (Fig. 4.20). If X_L^S reaches X_L^P at 875°C during melting of solid amphibolite, the H_2O activity will decrease, and the H_2O-undersaturated liquid will contain about 6 wt.% H_2O (calculated by mass balance). The liquid viscosity should be about 900 Pa s, but the estimate from Table 4.3 yields a viscosity of about 2900 Pa s. However, if X_L^S does not reach X_L^P, then the smaller amount of liquid generated will have more dissolved H_2O and thus a lower viscosity than 2900 Pa s. In addition, during melting, hornblende will continue to dehydrate and add H_2O to the liquid, thereby also decreasing the liquid viscosity. These factors, along with errors in modal estimates, may account for the discrepancy between the calculated (875°C, 12 vol.% liquid) viscosities from the powder run (900 Pa s) and the solid run (2900 Pa s).

Thus, during melting at 875°C, the liquid viscosity may increase from about 50 Pa s to probably less than 900 Pa s near equilibrium.

Even if the liquid viscosities rise to the levels calculated for the powder runs (bottom of Table 4.3), these values are still quite low. Figure 4.20 illustrates these calculations and shows the rapid decrease in viscosity from 850°C to 875°C due to the wide-spread breakdown of hornblende and with little change in the liquid fraction. The viscosity increases at 925°C as the liquid fraction increases and the percentage of H_2O dissolved in this liquid decreases. Above 925°C, the viscosity drops again mostly due to the effect of increasing temperature.

Table 4.1. Normalized and averaged clinopyroxene compositions from powder and solid experiments.

Temp. (°C)	850	875	900	1000	Powder
SiO_2	49.35	48.89	48.17	48.29	49.38
TiO_2	0.28	0.35	0.19	0.13	0.38
Al_2O_3	4.96	5.15	6.97	7.67	7.26
FeO*	9.56	10.22	9.33	8.56	8.13
MgO	13.41	15.22	13.51	16.24	13.86
CaO	21.90	19.43	20.93	18.32	20.71
Na_2O	0.54	0.74	0.88	0.79	0.00
K_2O	0.00	0.00	0.02	0.00	0.02

The temperature-specified columns are from the solid experiments, n = 3 for each average. The powder average is from the entire temperature range (850-1000°C), n = 30.

Table 4.2. Comparison of the liquid compositions from powder and solid (s) amphibolite dehydration-melting experiments at 10 kbar.

Run #	120	sdm:3	124s	sdm:5	134	sdm:3	133s	sdm:3
Temp (°C)	850		850		1000		1000	
Time (d)	8		21		4		4	
SiO2	64.79	0.26	67.44	0.12	51.77	0.30	51.33	0.14
TiO2	0.43	0.05	0.14	0.06	0.51	0.01	0.39	0.05
Al2O3	19.07	0.09	18.50	0.10	20.95	0.07	21.27	0.08
FeO	4.51	0.14	3.65	0.02	7.09	0.15	8.49	0.17
MnO	0.18	0.08	0.19	0.08	0.23	0.09	0.30	0.14
MgO	1.51	0.13	1.20	0.04	6.36	0.08	5.86	0.04
CaO	7.95	0.03	7.43	0.05	11.50	0.16	10.95	0.04
Na2O	1.25	0.15	1.08	0.06	1.40	0.13	1.08	0.07
K2O	0.29	0.06	0.41	0.03	0.17	0.03	0.24	0.02
CIPW Norms								
Q	33.5		38.8		4.6		5.3	
or	1.7		2.4		1.0		1.4	
ab	10.6		9.1		11.8		9.2	
an	39.4		36.8		50.4		52.5	
C	2.2		2.8		0.0		0.0	
di	0.0		0.0		5.5		1.5	
hy	11.7		9.8		25.8		29.4	
il	0.8		0.3		1.0		0.7	

sdm:# = standard deviation of the mean of n=# analyses

Table 4.3 Calculated liquid compositions using measured composition from 21 day, 850°C solid rock experiment and various H_2O contents, normalized to 100.

SiO_2	67.39	66.04	64.69	63.35	62.00	60.65	59.30
TiO_2	0.15	0.15	0.14	0.14	0.14	0.14	0.13
Al_2O_3	18.50	18.13	17.76	17.39	17.02	16.65	16.28
FeO	3.65	3.58	3.50	3.43	3.36	3.29	3.21
MnO	0.19	0.19	0.18	0.18	0.17	0.17	0.17
MgO	1.20	1.18	1.15	1.13	1.10	1.08	1.06
CaO	7.43	7.28	7.13	6.98	6.84	6.69	6.54
Na_2O	1.08	1.06	1.04	1.02	0.99	0.97	0.95
K_2O	0.41	0.40	0.39	0.39	0.38	0.37	0.36
H_2O	0.00	2.00	4.00	6.00	8.00	10.00	12.00
Viscosity (Pa s), calculated after Shaw (1972).						H_2O-saturated .	
at 900°C:	$2.6*10^7$	$4.4*10^5$	$2.1*10^4$	$1.9*10^3$	$2.8*10^2$	$5.8*10^1$	$1.6*10^1$
at 875°C:	$5.1*10^7$	$7.8*10^5$	$3.4*10^4$	$2.9*10^3$	$4.1*10^2$	$8.1*10^1$	$2.1*10^1$
at 850°C:	$1.0*10^8$	$1.4*10^6$	$5.6*10^4$	$4.5*10^3$	$6.0*10^2$	$1.2*10^2$	$2.9*10^1$
at 800°C:	$4.8*10^8$	$5.1*10^6$	$1.7*10^5$	$1.2*10^4$	$1.4*10^3$	$2.4*10^2$	$5.7*10^1$

Calculated liquid compositions from powder experiments. Wt.% H_2O in liquids from mass balance, assuming 2 wt.% H_2O in the hornblende (Hb) and the Hb initially comprised 67% of the amphibolite. Final modes from point counting.

Temp. (°C)	850	875	900	925	950	975	1000
Time (days)	8	8	9	8	2	4	4
SiO_2	63.79	60.80	61.68	61.95	60.44	56.30	50.81
TiO_2	0.42	0.28	0.31	0.39	0.36	0.46	0.50
Al_2O_3	18.78	18.00	17.62	19.79	19.80	20.48	20.56
FeO	4.44	3.44	3.71	3.18	3.48	5.86	6.96
MnO	0.17	0.00	0.05	0.14	0.00	0.00	0.22
MgO	1.49	1.85	1.26	2.06	2.58	3.40	6.24
CaO	7.82	7.38	6.97	7.72	7.22	9.04	11.29
Na_2O	1.23	1.27	1.05	1.95	2.12	2.03	1.38
K_2O	0.28	0.35	0.37	0.30	0.34	0.28	0.17
H_2O	1.58	6.63	6.97	2.53	3.66	2.15	1.86
Final mode							
Total Hb	57	30	53	9	9	2	0
Liquid	8	7	2	30	20	39	47
Visc(Pa s)	$1.1*10^6$	$9.0*10^2$	$6.0*10^2$	$3.0*10^4$	$3.0*10^3$	$2.0*10^3$	$2.2*10^2$

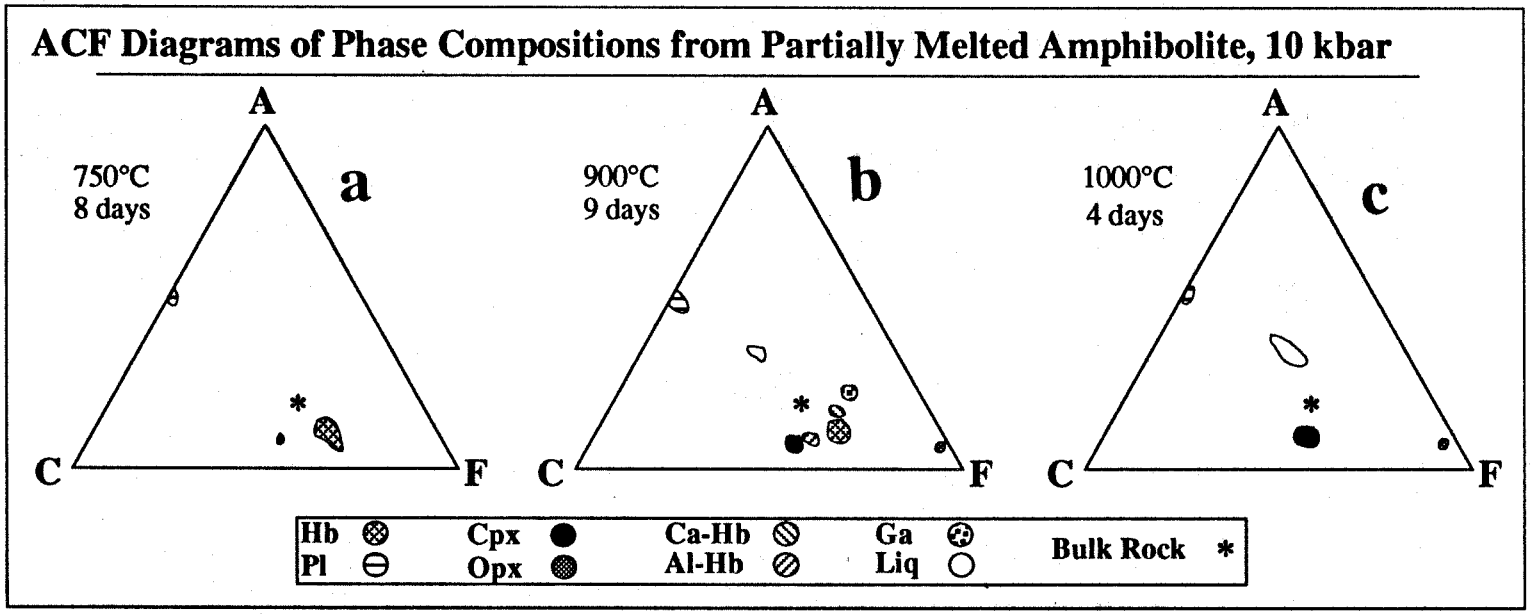

Fig. 4.1a-c. Compositions of phases in partially melted amphibolite at 10 kbar, plotted in a series of conventional ACF diagrams arranged in order of increasing temperature. The bulk amphibolite composition is located at the asterisk (*). See Fig. 4.3 for comparison with high-grade metamorphic phase assemblages.

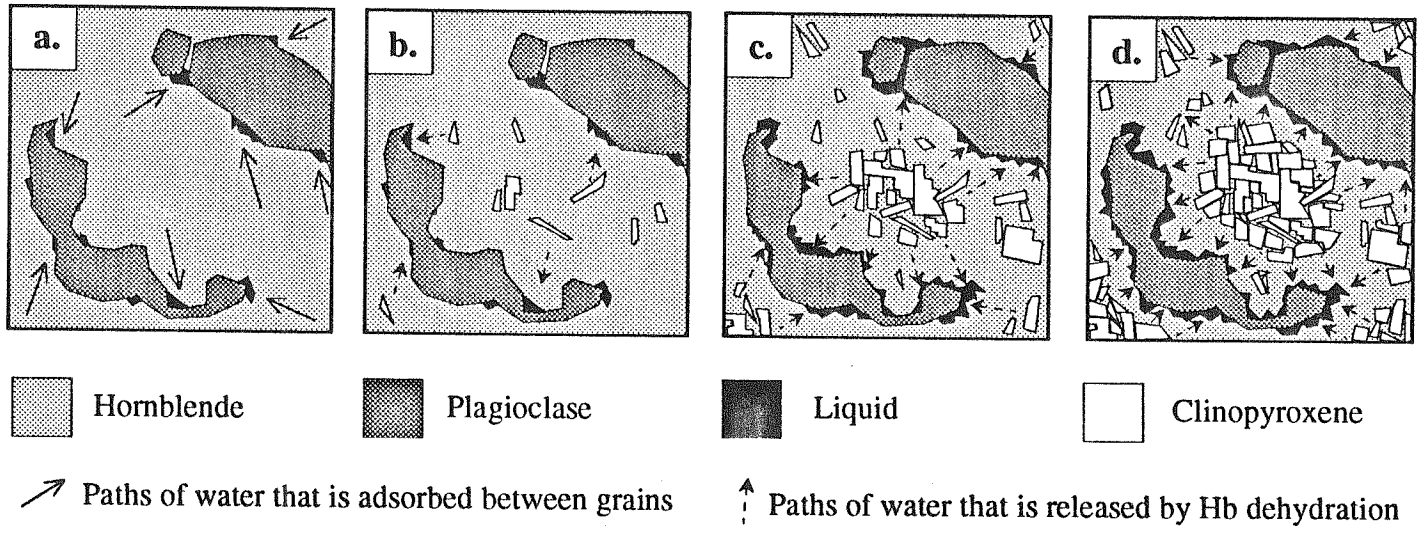

Fig. 4.2a-d. Schematic representation of dehydration sequences which may simulate the changes that occur either through time at constant temperature or at progressively higher temperatures. [a] A trace of adsorbed, intergranular water causes the formation of liquid through reaction [2] (see text). [b] The partial dehydration of hornblende and replacement by clinopyroxene, through reaction [1], gives rise to a transient vapor phase which H_2O-saturates the system. [c] As more clinopyroxene grows, more liquid is produced. Preferential dehydration of hornblende grain interiors results in clinopyroxene-rich centers and hornblende-rich margins. H_2O-rich liquids possibly may buffer and sustain hornblende along Hb/L boundaries. [d] Continued dehydration leads to apparent outward displacement of dehydration reaction front.

ACF Diagrams of High-grade Metamorphic Iron-rich Rocks

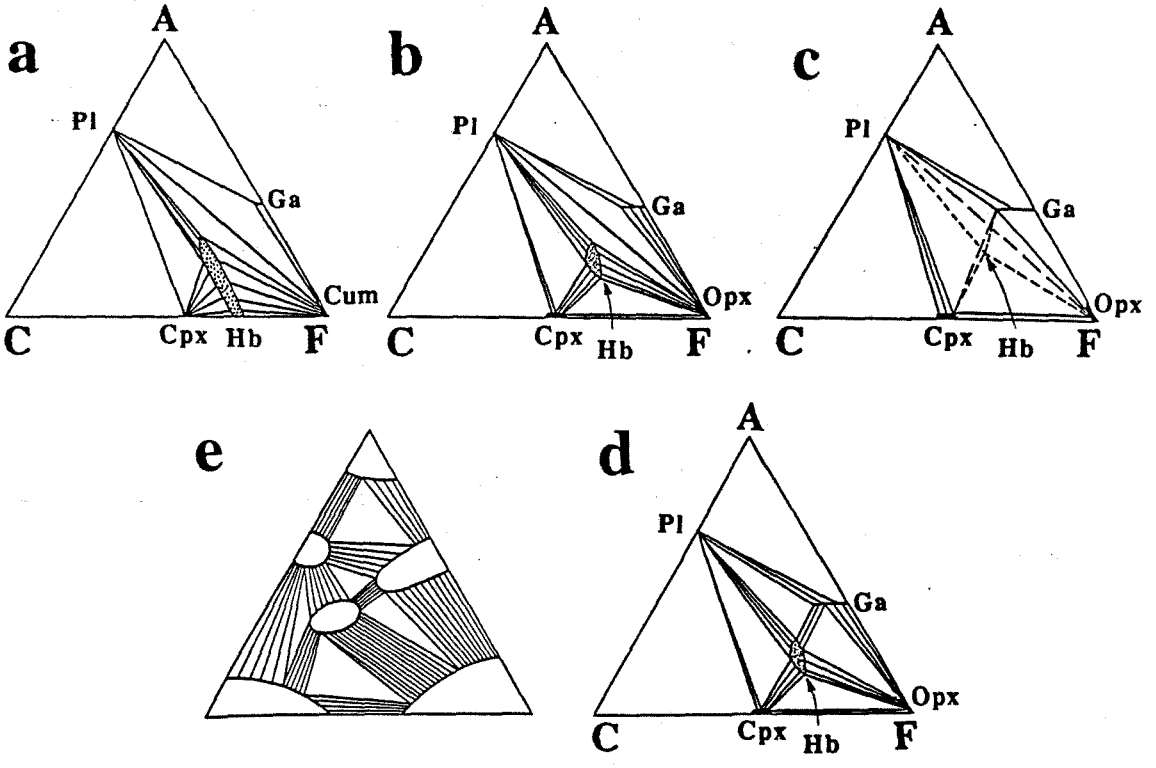

Fig. 4.3a-e. ACF diagrams show typical phase relationships (iron-rich systems) in the [a] amphibolite facies (Cum: cummingtonite), [b] the amphibolite facies-pyroxene granulite facies transition, and [c] the pyroxene granulite facies (after Robinson 1982). [d] Generalized triangular diagram shows the possible phase relationships of minerals with ternary solid-solutions (after Miyashiro 1973). [e] The liquid-present experimental results from Fig. 4.1 are portrayed in the ACF framework of subsolidus phase relationships, using tie-lines from Fig. 4.3a-d.

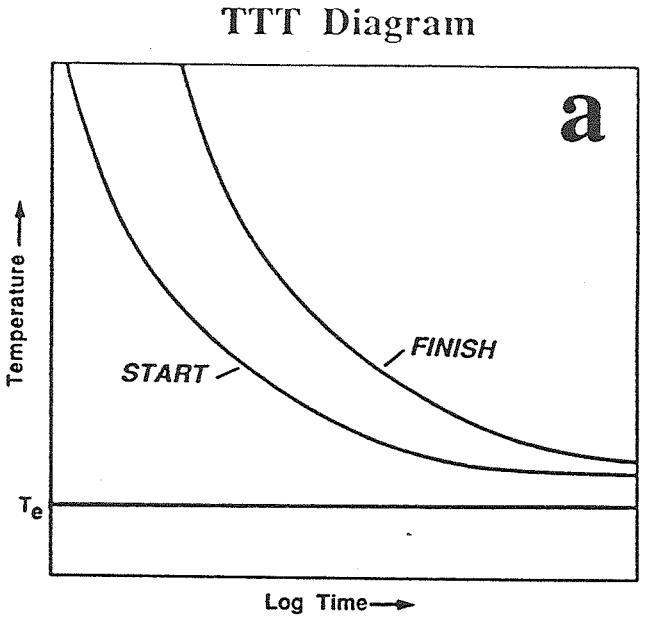

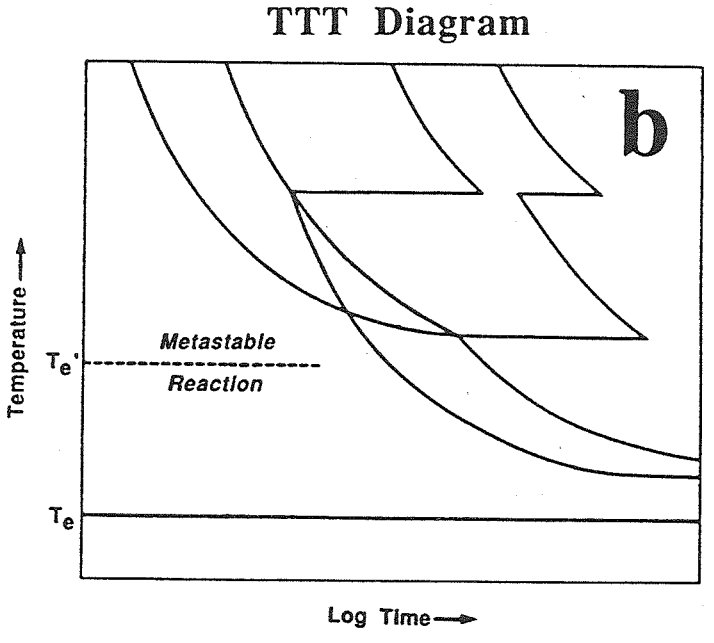

Fig. 4.4a,b. Schematic temperature-time-transformation (TTT) diagrams (after Putnis and McConnell (1980) and Rubie and Brearley (1987)). [a] TTT diagram for a simple reaction. [b] more complex TTT diagram with metastable phases.

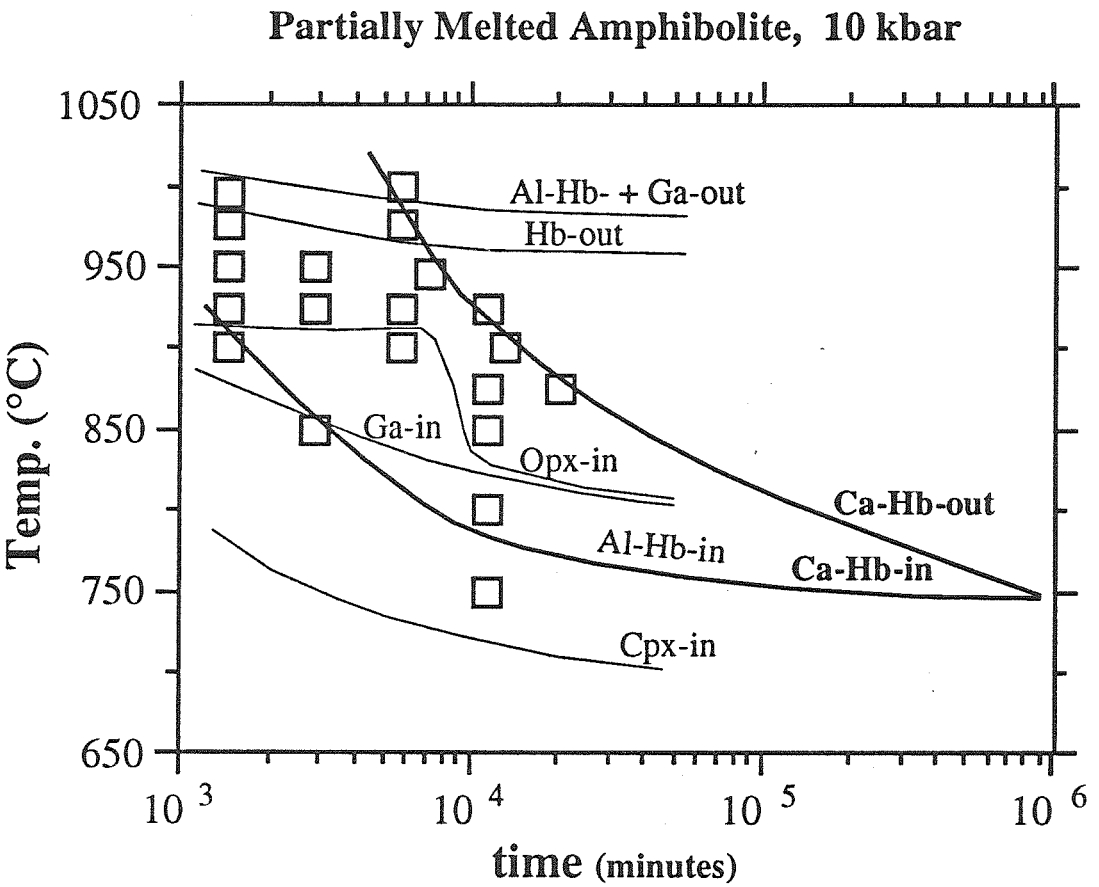

Fig. 4.5. Results from dehydration-melting of amphibolite at 10 kbar from Fig. 3.1, with the time axis replotted on a log scale. This reconfiguration converts the figure into a temperature-time-transformation (TTT) diagram (see Fig. 4.4).

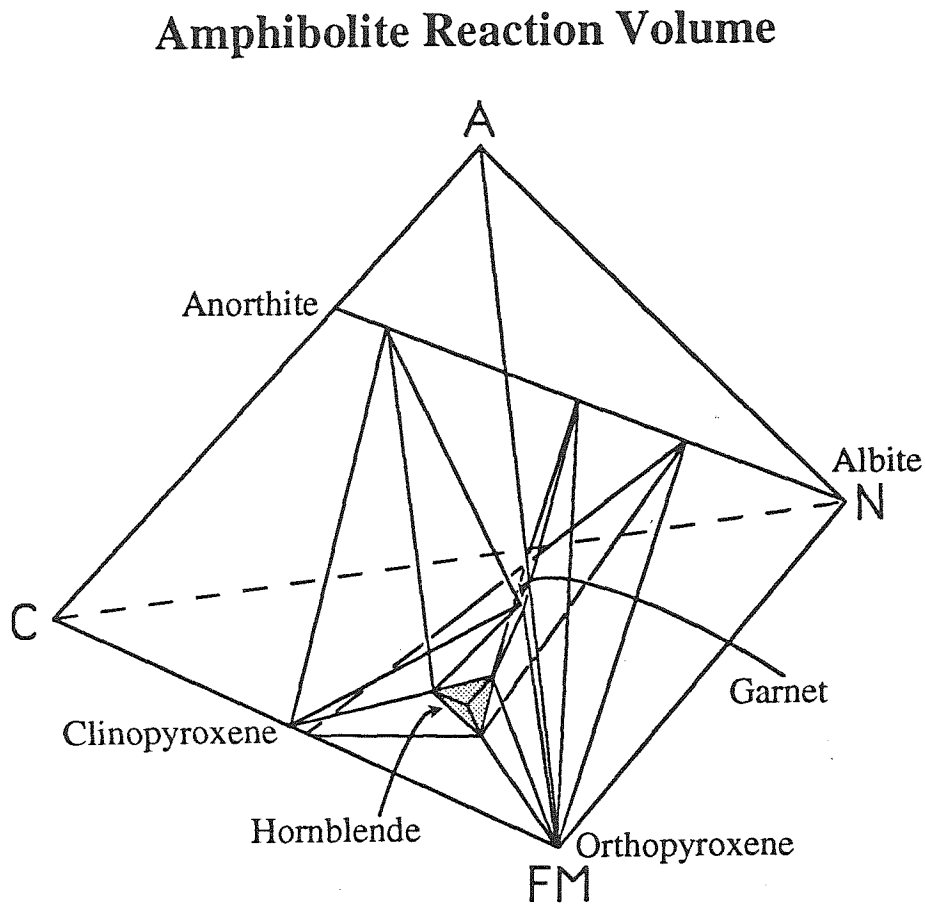

Fig. 4.6. A schematic ACFN tetrahedron (Al_2O_3, CaO, FeO+MgO, Na_2O) showing the liquid-absent amphibolite phase relationships near the high-temperature breakdown of hornblende (from Robinson 1982). Hornblendes with distinct compositions, at the different corners of the the small, shaded hornblende tetrahedron, coexist with different mineral assemblages, represented by the other clear tetrahedrons (also see Fig. 4.3e).

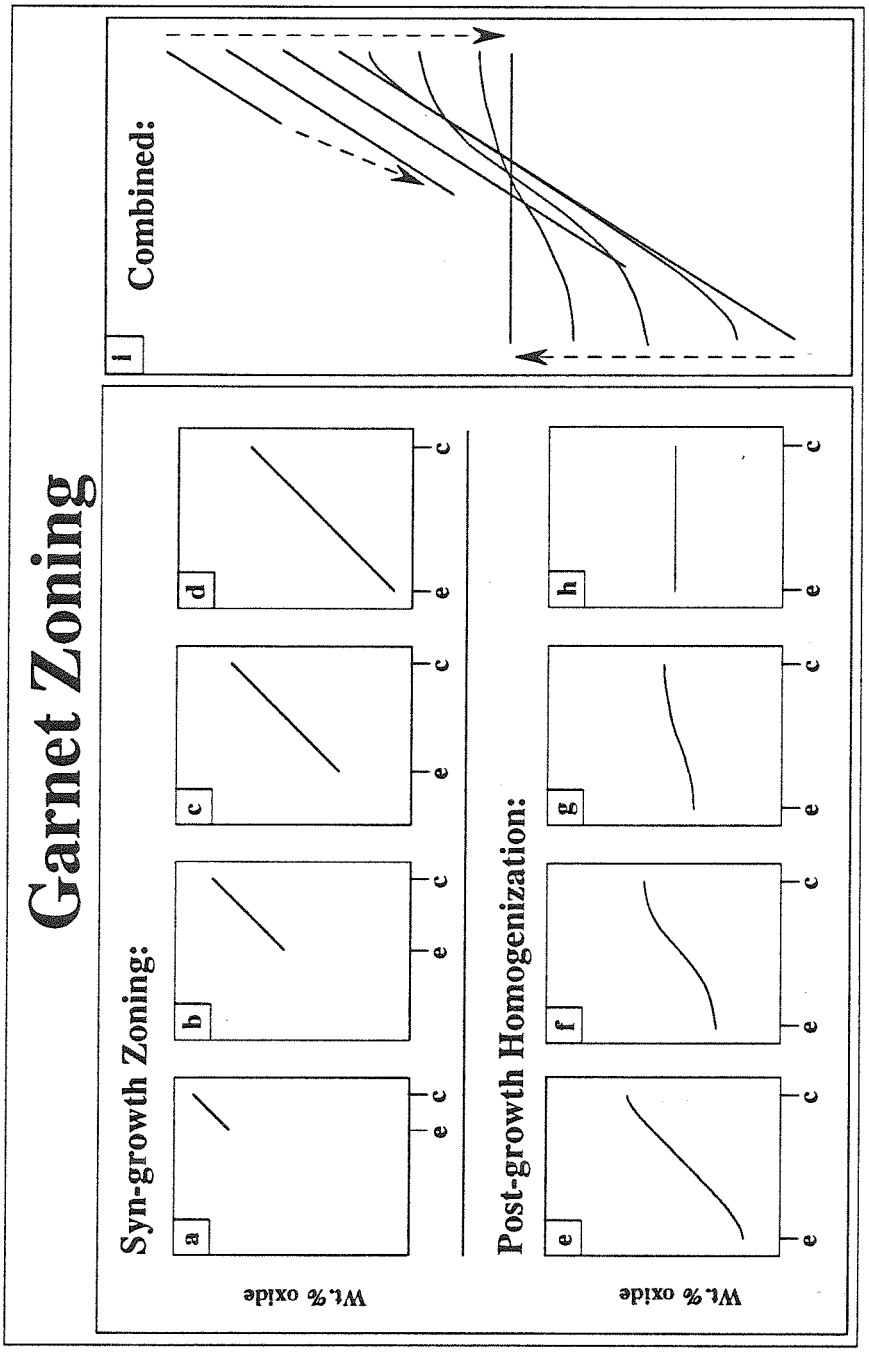

Fig. 4.7a-i. Garnet compositional profile history. [a-d] actual syn-growth zoning as exhibited by the garnets in the 10 kbar amphibolite melting experiments. [e-h] post-growth homogenization determined and modelled by Yardley (1977) and Jiang and Lasaga (1990). [i] compiled measured syn- and post-growth profiles revealing one possible zoning history in garnets.

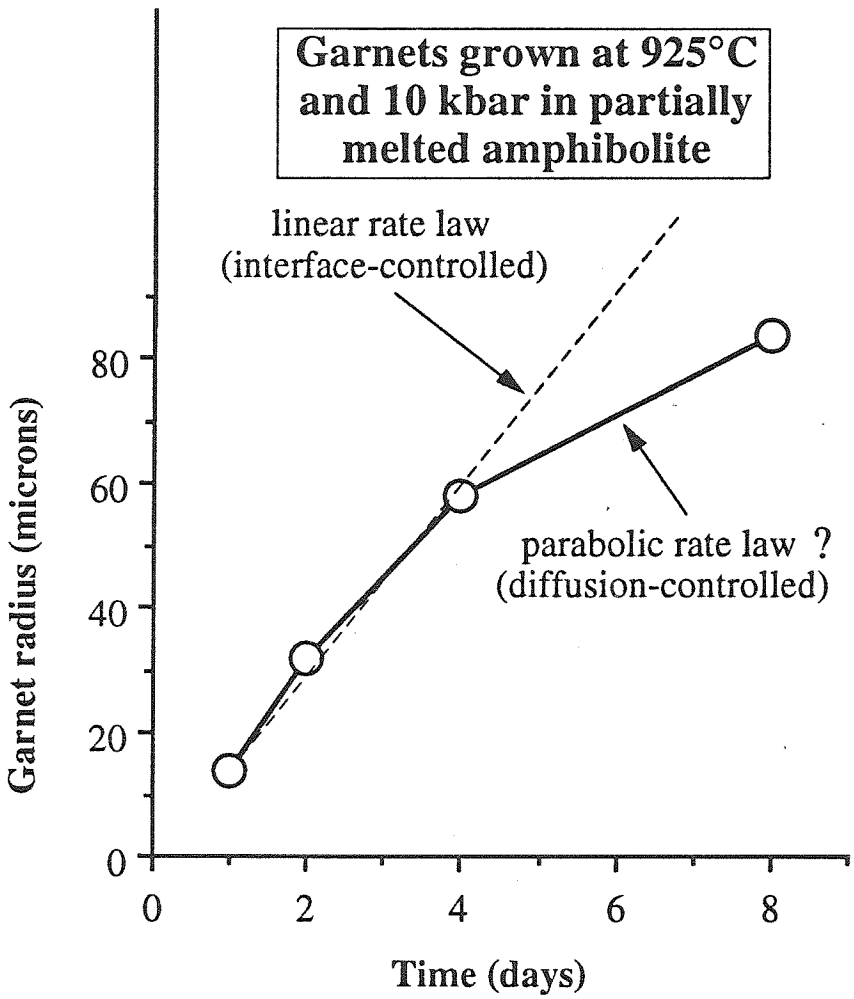

Fig. 4.8. Measured average garnet radii from 925°C runs as a function of time. Growth appears to follow the parabolic rate law (growth controlled by the diffusion rate of necessary components through the silicate liquid). If included nature of poikilitic garnets is taken into account, radii would be smaller at longer durations and would more clearly not fit the linear rate law.

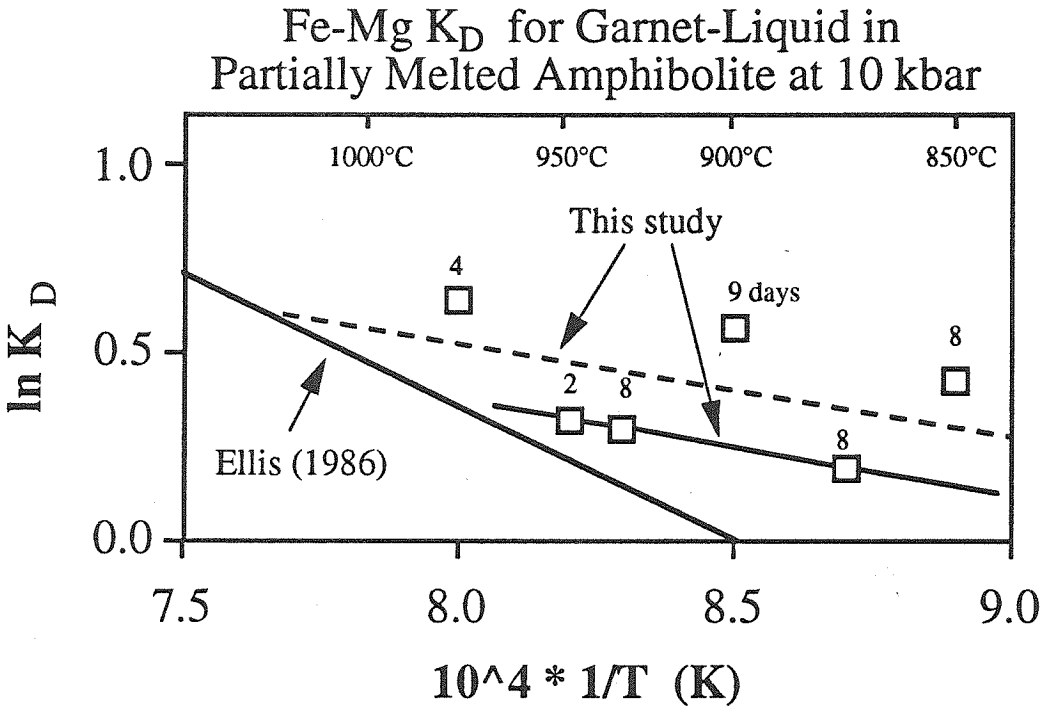

Fig. 4.9. Garnet-liquid Fe-Mg distribution coefficients (K_D) versus inverse temperature. The numbers give run durations in days. The regression lines fit to experimental data from the present study cross zero at ~750°C, below the stability field of garnet (solid line passes through most reliable data). The line from Ellis (1986) crosses zero at 900°C because the low temperature liquids are Mg-richer than coexisting garnets in the FMAS system.

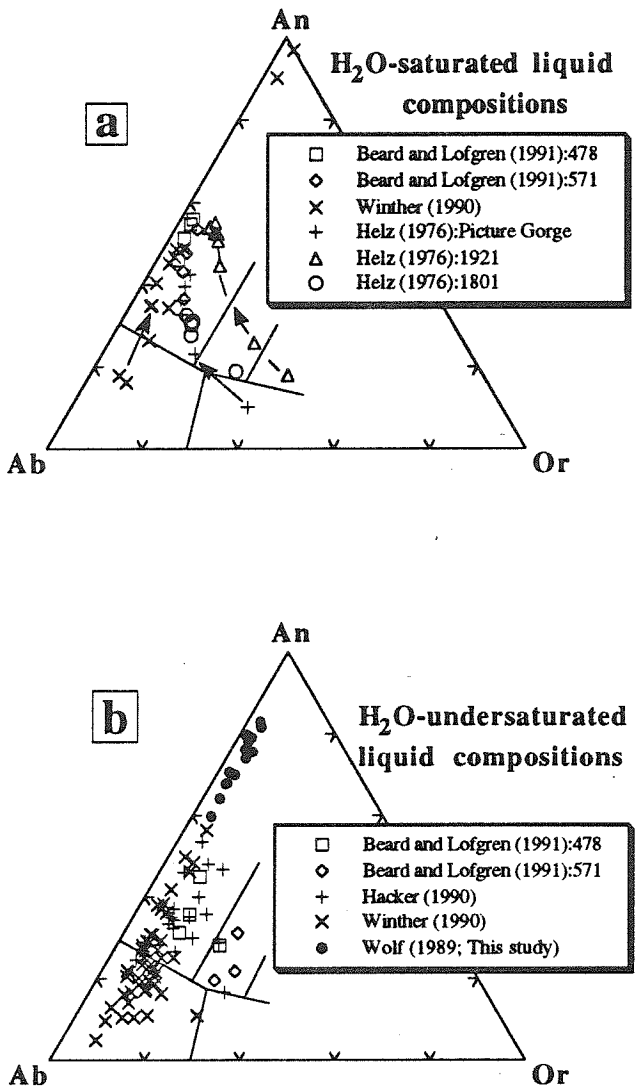

Fig. 4.10a,b. Liquid compositions from amphibolite and basalt experiments plotted in the anorthite (An) - albite (Ab) - orthoclase (Or) compositional triangle. Pressure range: 5-30 kbar (see section 1.2.2). [a] H_2O-saturated liquid compositions (excess H_2O added to runs). Arrows show some of the liquid compositional trends during progressive fusion (increasing temperature). Contrast these trends with the trends from the present experiments in Fig. 3.17b. [b] H_2O-undersaturated liquid compositions, including data from this study (from Table 3.7).

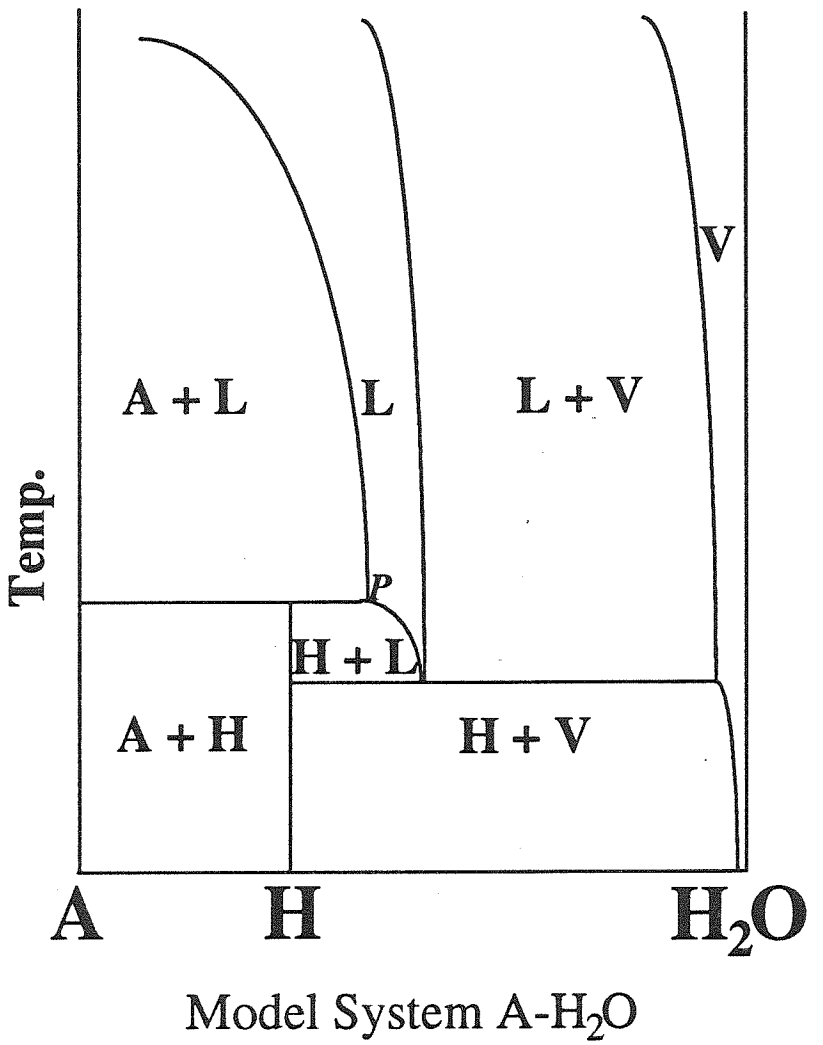

Fig. 4.11. Schematic drawing of the anhydrous mineral (A) - H_2O model system, with intermediate hydrous mineral (H). In a system containing anhydrous and hydrous phases, the first liquid to be produced at the peritectic, P, is vapor-undersaturated. All subsequent liquids also will be vapor-undersaturated.

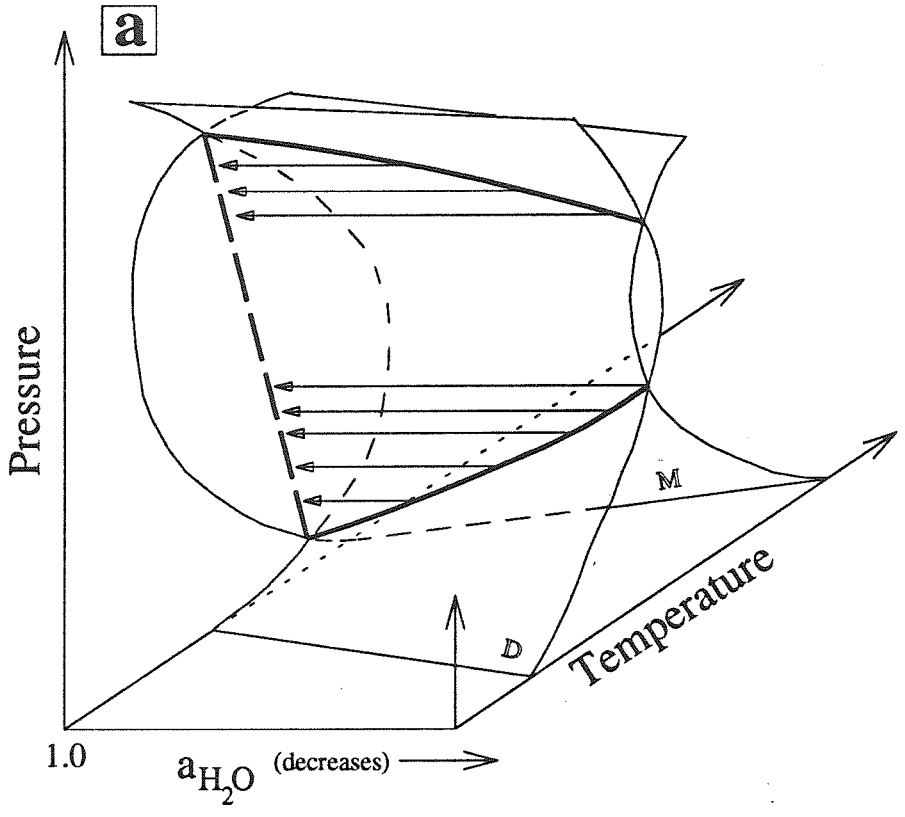

Fig. 4.12a-e. Schematic diagrams of the dehydration (𝔻) and vapor-present melting (𝕄) surfaces and their intersection along loci of dehydration-melting in P-T-H_2O activity ($a_{(H_2O)}$) space and on T-$a_{(H_2O)}$, P-$a_{(H_2O)}$ and P-T planes (see text for details). [a] In P-T-$a_{(H_2O)}$ space, dehydration-melting occurs along the intersection (thick, solid curves) of the dehydration and vapor-present melting surfaces. These surfaces intersect P-T planes as curves (P-T plane at $a_{(H_2O)}$ = 1 shown), but the dehydration-melting reaction (thick, solid curves) projects onto them (horizontal projection arrows pointing to thick dashed projection line). The $a_{(H_2O)}$ along this projection varies as a function of pressure, with a minimum at moderate pressures. [b] P-T-$a_{(H_2O)}$ space is expanded to lower $a_{(H_2O)}$ values at which the dehydration and vapor-present melting surfaces no longer intersect. Four possible paths that can be taken during metamorphism and anatexis are shown (three numbered paths further described). The dashed projection of a constant $a_{(H_2O)}$ slice of the dehydration surface at low-$a_{(H_2O)}$ is referred to in Fig. 4.18 [c] An isobaric T-$a_{(H_2O)}$ plane cuts the dehydration (𝔻) and vapor-present melting (𝕄) surfaces and shows the three numbered paths from [b]. [d] The P-$a_{(H_2O)}$ projection of the intersection of the dehydration and vapor-present melting surfaces defines where dehydration-melting occurs. [e] a P-T plane with dehydration (𝔻) and vapor-present melting (𝕄) curves of constant $a_{(H_2O)}$, along with the projected dehydration-melting curve, which has an $a_{(H_2O)}$ that decreases toward the center (two converging arrows).

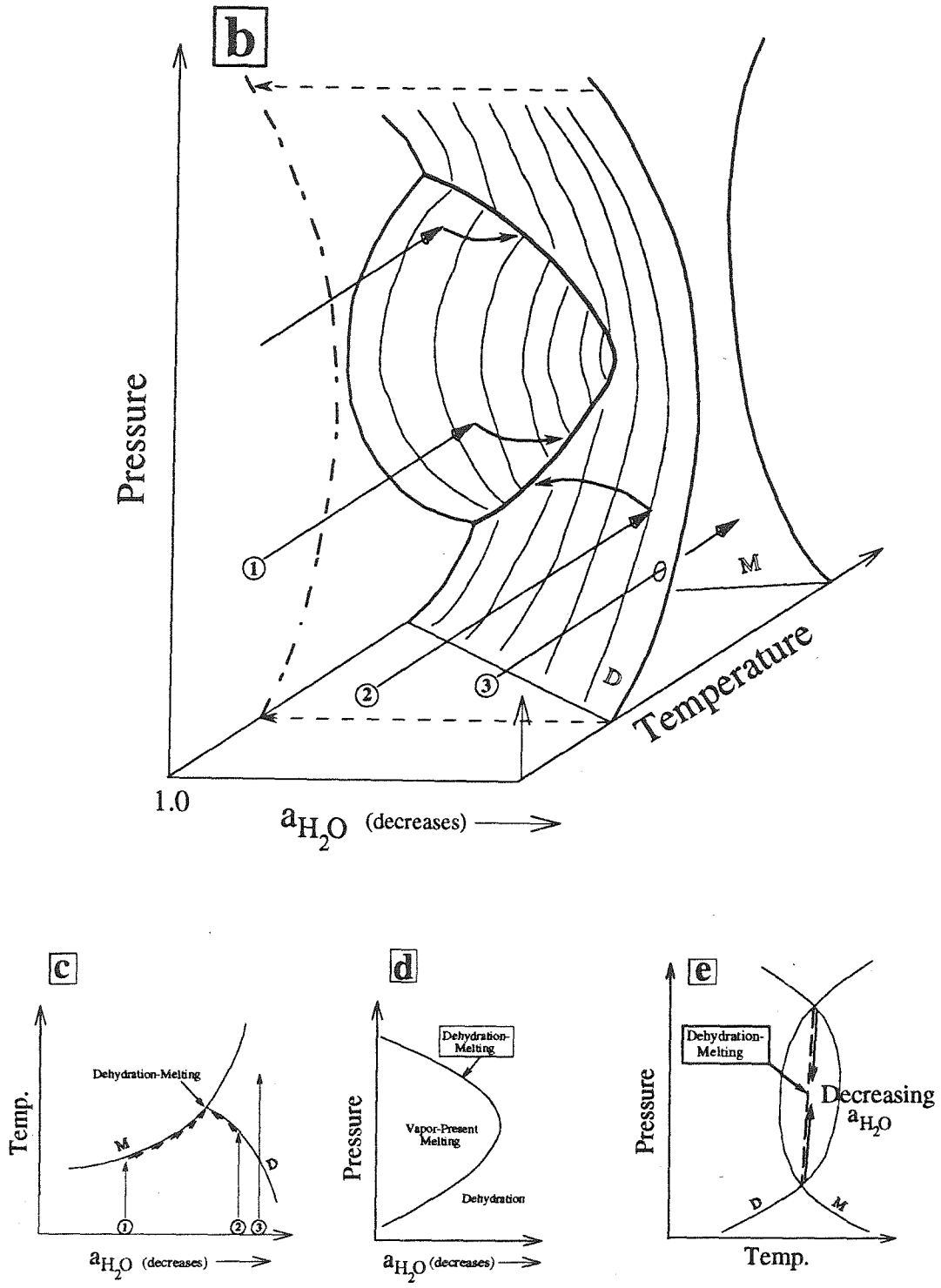
b
Pressure
Temperature
1.0
a_{H_2O} (decreases)
M
D
1
2
3
c
Temp.
Dehydration-Melting
M
D
a_{H_2O} (decreases)
d
Pressure
Dehydration-Melting
Vapor-Present Melting
Dehydration
a_{H_2O} (decreases)
e
Pressure
Dehydration-Melting
Decreasing a_{H_2O}
D
M
Temp.

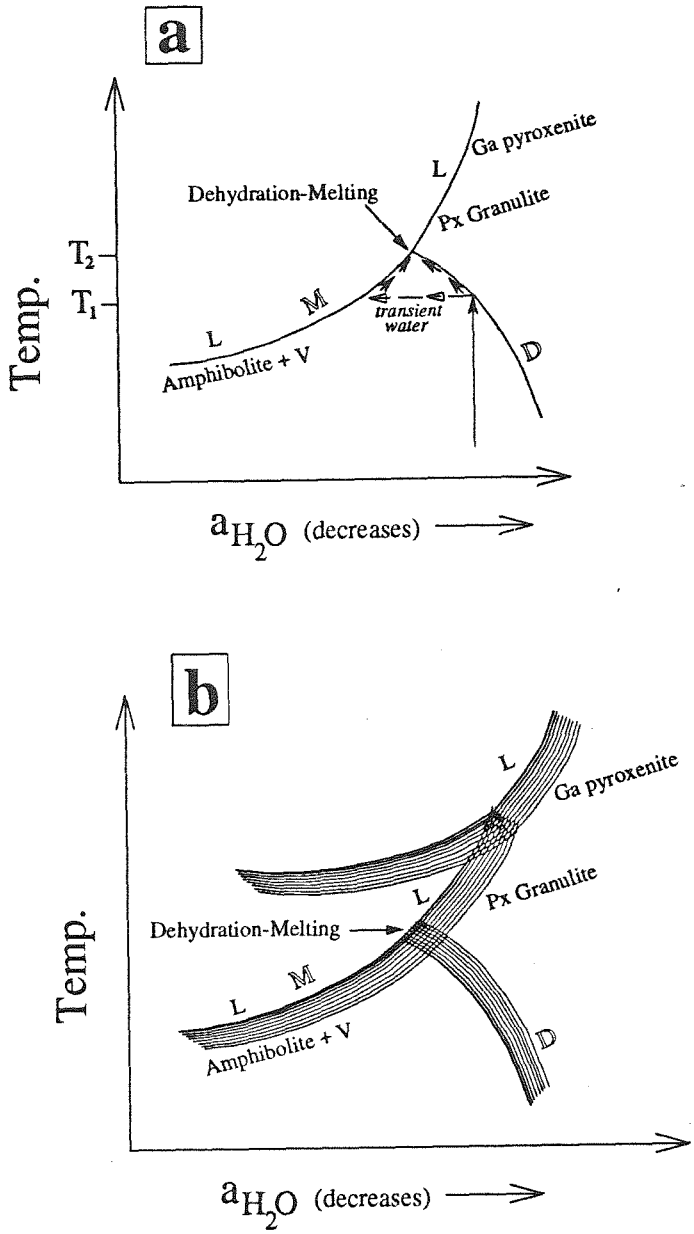

Fig. 4.13a,b. [a] A T-$a_{(H_2O)}$ plane illustrating a possible explanation for the non-equilibrium effects of simultaneous dehydration (reaction [1]) and vapor-present melting (reaction [2]) in the solid amphibolite experiments. [b] a T-$a_{(H_2O)}$ plane with the added complexity of mineral solid-solutions. As compositions of minerals change during reaction, location of reaction boundaries will shift. Rock types shown in relation to the increasing grade of the reaction boundaries; amphibolite, pyroxene granulite, and garnet pyroxenite.

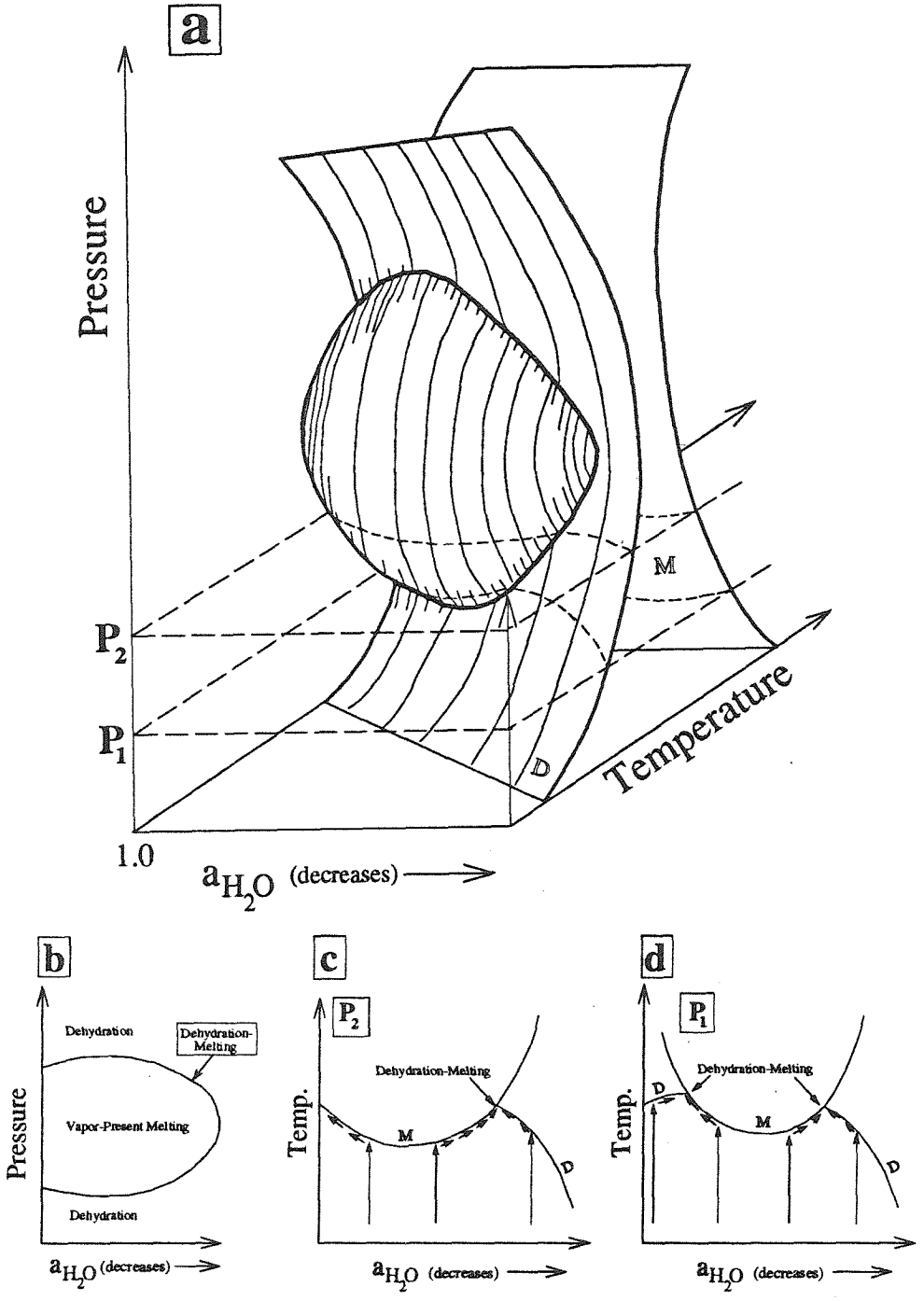

Fig. 4.14a-d. Schematic diagrams of the dehydration (𝔻) and vapor-present melting (𝕄) surfaces and their intersection along loci of dehydration-melting in P-T-H_2O activity ($a_{(H_2O)}$) space and on T-$a_{(H_2O)}$, P-$a_{(H_2O)}$ and P-T planes. These diagrams differ from Figs. 4.12a-c in that the solubility of CO_2 in Mg-bearing liquids may be non-negligible (determined by Peterson and Newton 1990). Non-negligible CO_2 solubility results in a bulge in the intersection of the dehydration and vapor-present melting surfaces.

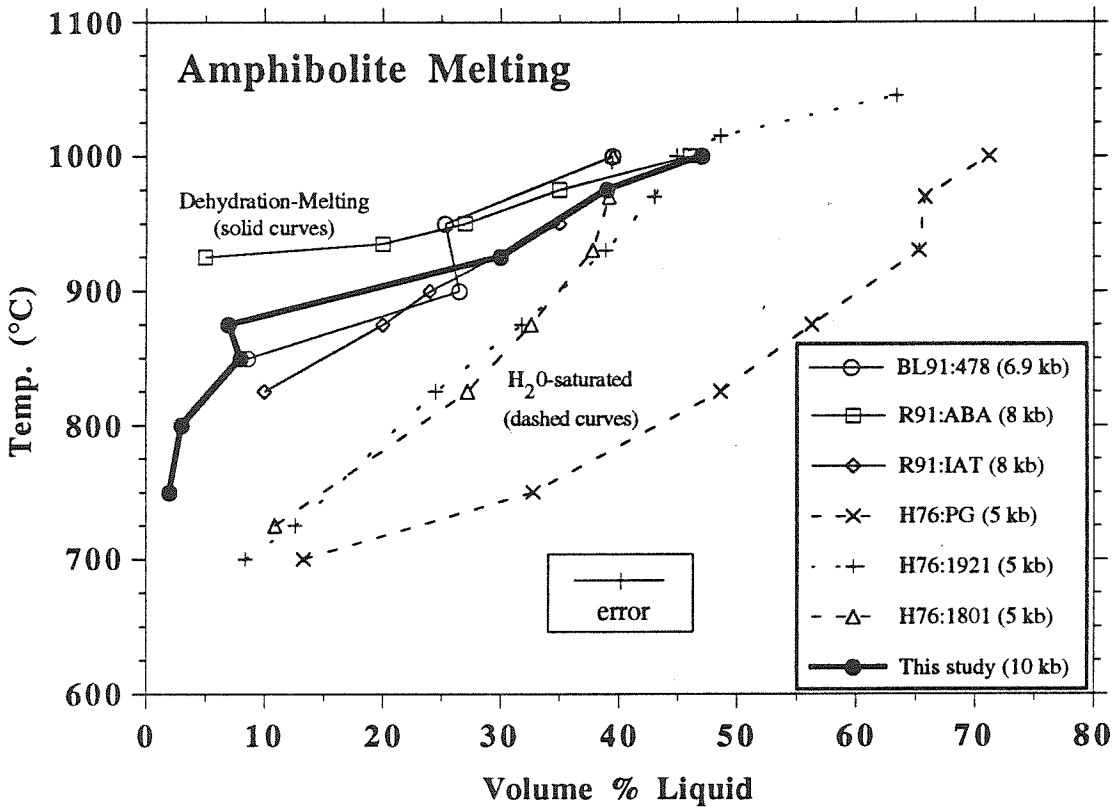

Fig. 4.15. Volume percents of liquids produced in various amphibolite melting experiments as a function of temperature. Data from literature converted from wt.% to vol.% liquid. This conversion increases the percent of liquid by ~10% at the high end of the range. Dehydration-melting results (solid curves) are fairly consistent with each other and distinct from H_2O-saturated melting results (dashed curves). Sources: BL91: Beard and Lofgren (1991), 6.9 kbar; R91: Rushmer (1991), 8 kbar; H76: Helz (1976) (H_2O-saturated), 5 kbar; This study: 8- and 4-day runs, 10 kbar, data from Fig. 3.4a.

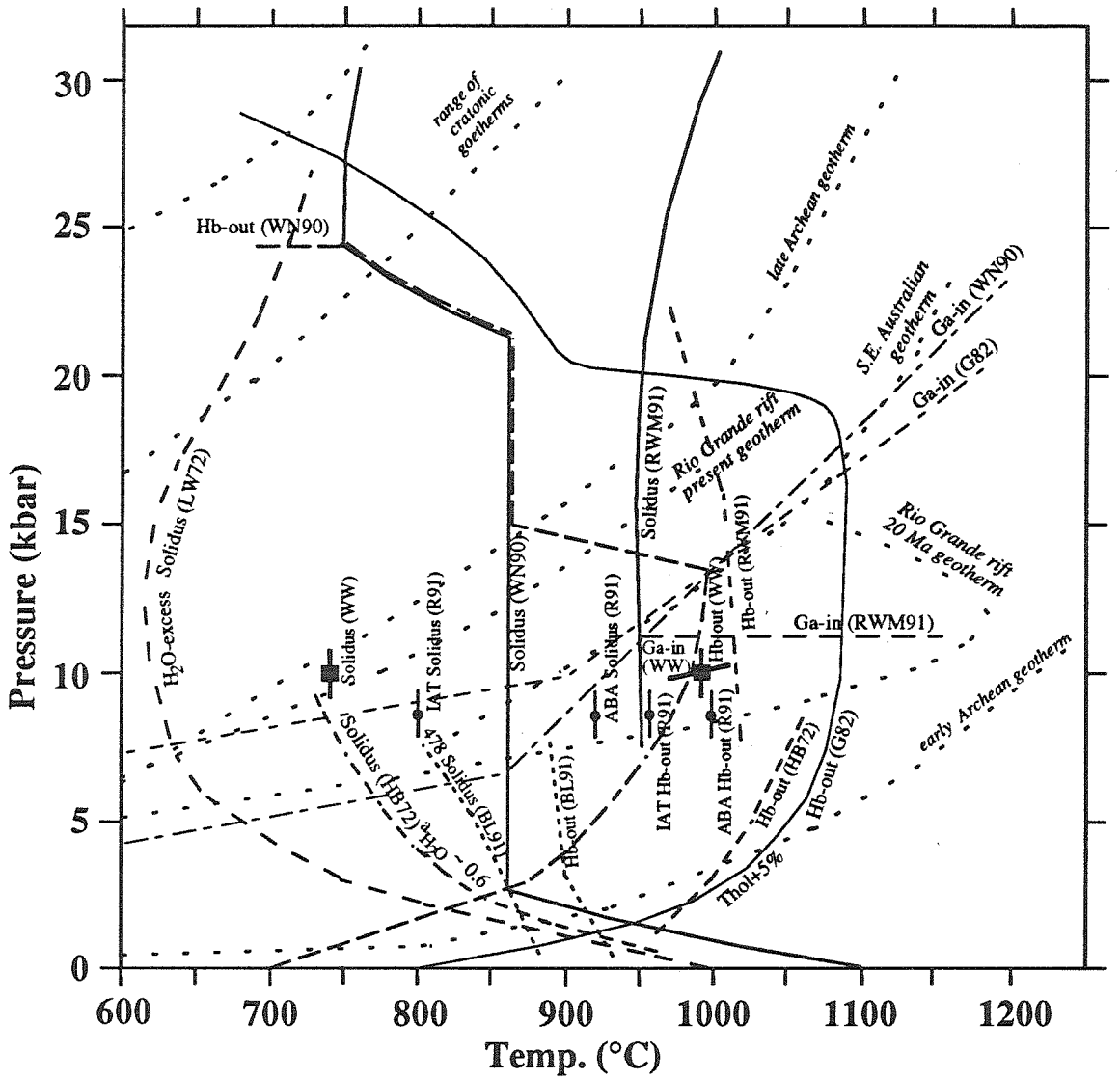

Fig. 4.16. Pressure-temperature diagram showing some of the details of the phase relationships of amphibolites (solidus, Hb- and Ga-out curves). Note the ~200°C range in solidi temperatures (~750-950°C) and the ~125°C range in the location of Hb-out curves, at 8-10 kbar. Data from this study: (WW); Holloway and Burnham (1972): (HB72); Green (1982): tholeiitic basalt + 5 wt.% H_2O (G82); Winther and Newton (1990): (WN90); Beard and Lofgren (1991): (BL91); Rushmer (1991): (R91); and Rapp et al. (1991): (RWM91). Cratonic geotherms from Boyd and Gurney (1986) and Martin (1986), Archean geotherms from Martin (1987), SE Australian geotherm from O'Reilly and Griffin (1985), Rio Grande rift geotherms from Bussod and Williams (1991).

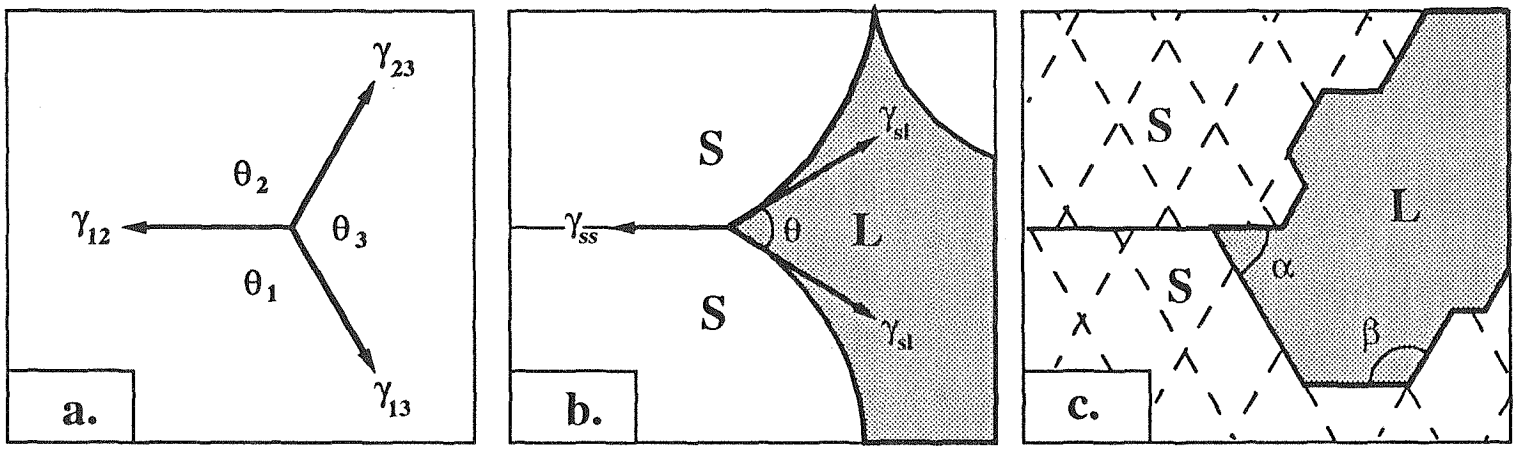

Fig. 4.17a-c. Schematic diagrams of grain boundary geometries pertinent to interfacial energy theory, where θ is the dihedral angle, γ is the interfacial energy, S is solid, and L is liquid. [a] the geometry described by equation [1]; [b] the geometry described by equation [2]; [c] possible geometry of anisotropic, crystallographically-controlled angles, α and β.

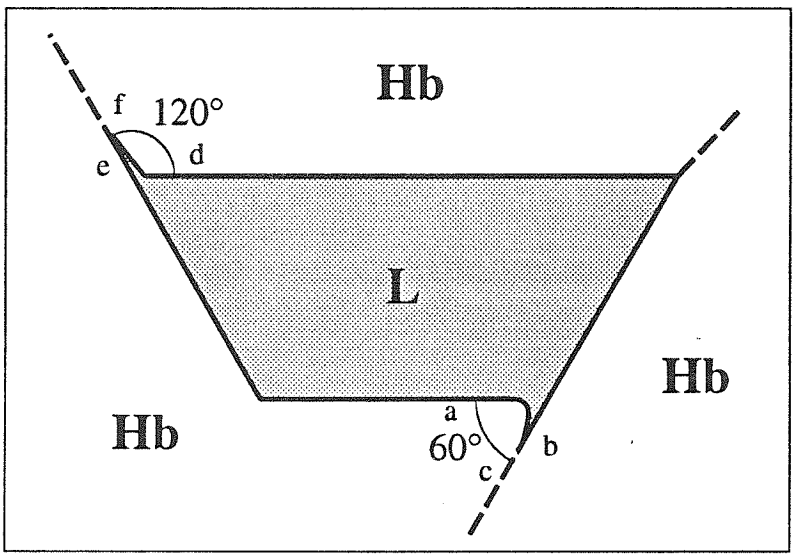

Fig. 4.18. Schematic representation of a liquid pocket with crystallographically-controlled corner angles, at 900°C. Liquid projections at some corners cut into hornblende grains along 60°/120° crystallographically-controlled grain boundaries. Crystal faces 'c' and 'f' may dissolve and peel away from their opposing faces, 'b' and 'e,' as the system attempts to reach equilibrium.

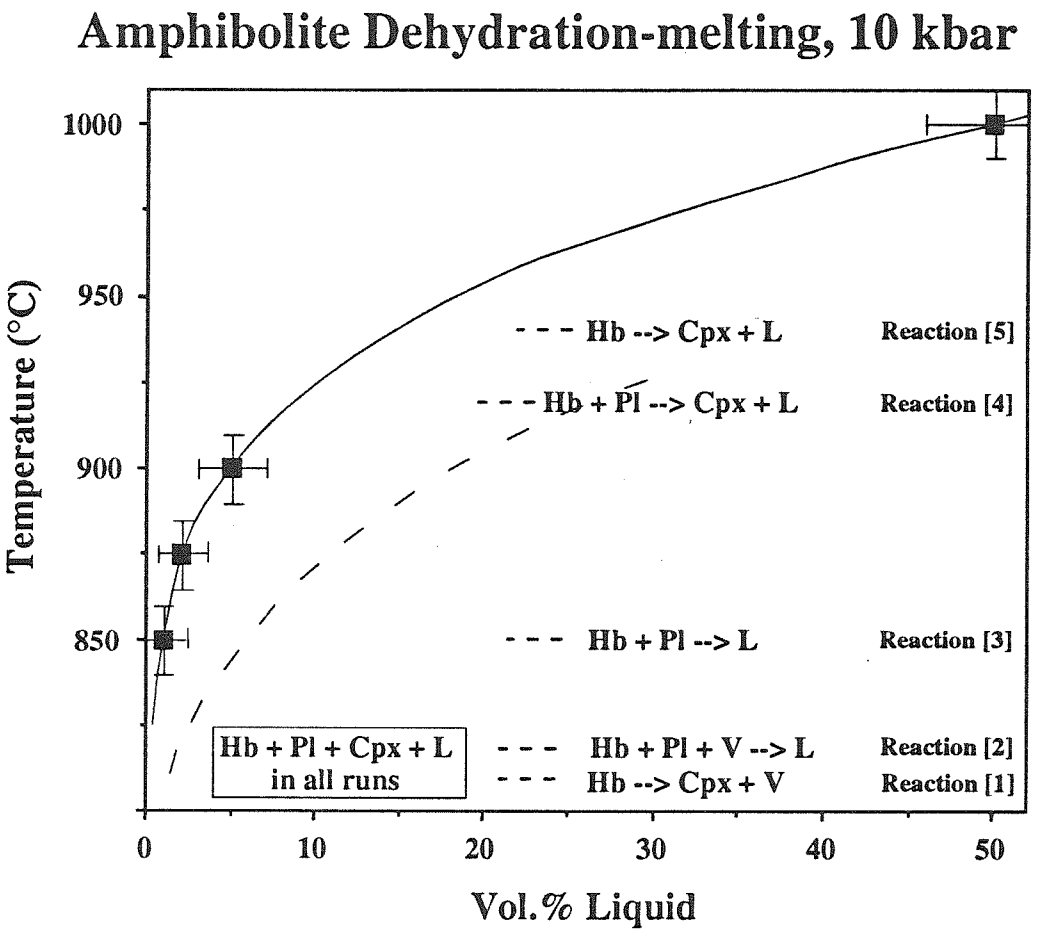

Fig. 4.19. Percentage of liquid produced by dehydration-melting of solid amphibolite as a function of temperature (solid curve) at 10 kbar. The liquid fractions were determined by point counting in runs with 5% and 50% liquid and were estimated in runs with 1% and 2% liquid (by comparison with the 5% liquid run). Errors are approximated. The dashed curve is the near-equilibrium liquid fraction determined from 8- and 4-day, powdered-amphibolite experiments (Fig. 3.4a). The temperatures of the reactions were determined by textural analysis and are schematically represented: reactions [1], [2] and [3] begin below 850°C (Yoder and Tilley 1962); reactions [4] and [5] begin between 900°C and 950°C.

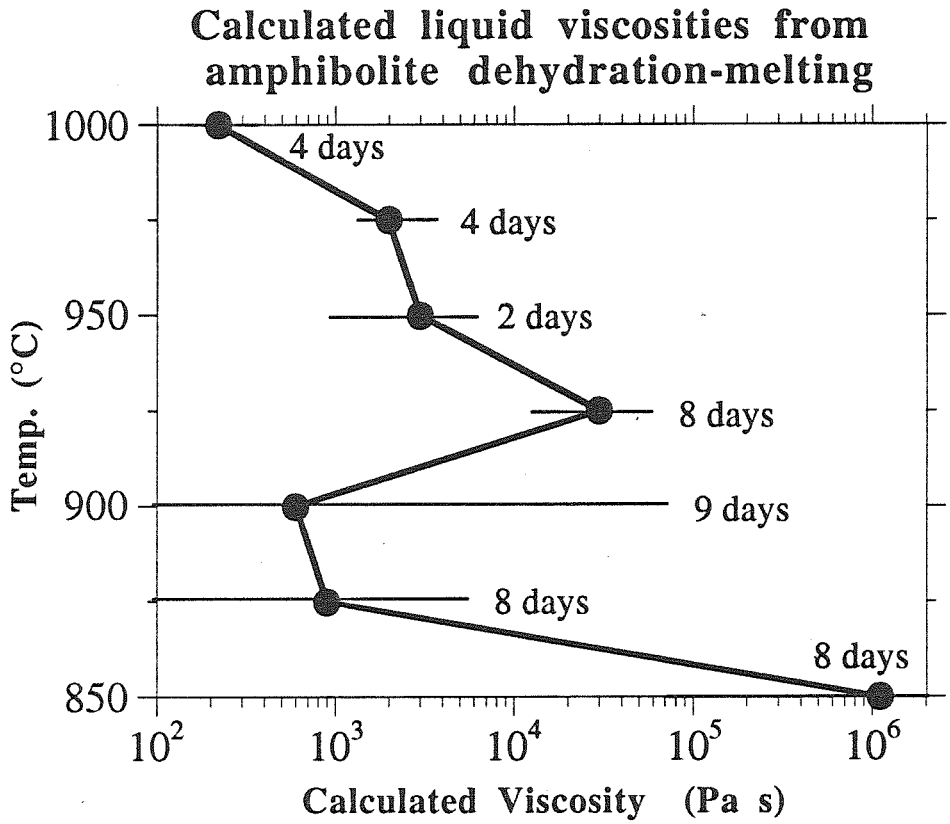

Fig. 4.20. Calculated liquid viscosity as a function of temperature. The main controls on viscosity are the relative amounts of liquid and amphibole (the two sinks for H_2O). Also see Fig. 3.23.

CHAPTER 5. PETROLOGIC APPLICATIONS

A pressure of 10 kbar is attained at a depth of about 33-38 km. Thus my results are applicable to magmatic processes that occur in the deep crust of non-orogenic regions, in the middle crust of thickened orogenic belts, in continental environments undergoing extension (Kay and Kay 1980; Bussod and Williams 1991), in Archean crust (Martin 1986; Rapp 1991), or in hot, young, subducted oceanic crust (Peacock 1990a,b; Defant and Drummond 1990). The experimentally determined phase equilibria and compositions provide a basis for understanding the differentiation of slightly hydrated, basaltic magmas and the vapor-absent anatexis of amphibolite in the lower crust (Fig. 4.16).

My experiments generate silicic liquids with highly aluminous compositions rarely found in the crust, although the conditions and bulk composition of the experiments simulate natural conditions. A number of possibilities may account for the scarcity: [1] the mafic plutons and buried mafic metavolcanic strata with similar high values of calcium and alumina to the amphibolite either are not very abundant in the lower crust or [2] do not participate to a great extent in crustal anatexis; [3] the primary aluminous liquids are always subsequently modified through crystal fractionation or assimilation.

Possibility [1] may be discounted. The amphibolite in this study is similar in mineralogy and bulk composition to mantle-derived, cumulate-rich, mafic plutons such as those that are exposed in the Sierra Nevada foothills of California. Plutons of this composition possibly reside at all levels within the crust and may represent a significant portion of the lower and middle crust (e.g., DeBari and Sleep 1991).

It is well known that rocks more felsic than the amphibolite should begin to melt at lower temperatures, if all other parameters are held equal. My experiments show, however, that metastable dehydration of hornblende can provide H_2O for melting reactions at very low temperature (below 750°C). Thus, amphibolite anatexis may be fairly extensive

at relatively low temperatures, and possibility [2] may not apply. The third possibility of liquid composition modification is discussed below.

5.1 Anatexis

5.1.1 Melting Interval

The lower continental crust generally is thought to be predominantly composed of hydrated mafic rocks. However, a free vapor-phase probably does not exist under lower crustal P-T conditions (Burnham 1979). The water present is structurally bound in hydrous minerals such as amphiboles. Thus, much of the lower continental crust may be amphibolite. Dehydration-melting of the amphibolite is the mode of anatexis under these conditions. Anatexis can occur at 10 kbar if the temperature exceeds about 750°C. Extensive liquid generation takes place at temperatures above 900°C (Fig. 3.4a). For large-scale anatexis of amphibolite, the crust must be thickened or the geotherm must be elevated, such as beneath volcanic arcs, above regions underplated with basaltic magma, and within subducted, hot, young, oceanic crust. The addition of CO_2-rich fluids from an external source, however, may induce widespread melting at lower temperatures (Peterson and Newton 1990).

Figure 4.15 shows the generalized phase relationships of amphibolite in P-T space and the fundamental differences in shape between the solidi for wet basalt (H_2O-saturated) and for amphibolite (H_2O-undersaturated). The shape of the amphibolite dehydration-melting solidus prevents low temperature anatexis in the upper and middle crust. The anatexis of amphibolites is limited to hotter, deeper crustal regions, except along the margins of hot, shallow plutons. However, my solid amphibolite melting experiments show that the dehydration of the interior of coarse hornblende grains, and the concomitant generation of transient H_2O may temporarily saturate the liquid and can significantly lower the solidus temperature (below the <750°C solidus found in the powder runs). At low pressure the solidus and Hb-out curves nearly coincide (Beard and Rushmer 1990).

Dehydration-melting will not occur until relatively high temperatures (Fig. 4.16). If it does occur it will produce a large amount of liquid in a narrow temperature interval. The melting interval widens as the solidus and Hb-out curves diverge at higher pressures, so dehydration-melting at higher pressures will produce a smaller amount of liquid for any given temperature increment. Thus, within a limited temperature interval above the solidus, segregation of the liquid may occur more readily at lower pressures. At higher pressures, the dehydration-melting solidus bends back to lower temperatures ($\partial T/\partial P$ becomes negative), so regardless of the wide melting interval and small increase in liquid volume with temperature, significant quantities of liquid can be generated at relatively low temperatures, compared with lower pressure anatexis.

5.1.2 Liquid Compositions

Commonly of very large size, peraluminous granitoids are present in most igneous provinces, in both cratons and orogenic belts (Zen 1986). They are economically important because they can contain valuable ore deposits, and are geologically important because they are an end-member of crustal evolution. Models for the generation of peraluminous granitoid liquids include near solidus melting of hydrous spinel lherzolite, partial melting of a peraluminous source, sediment contamination, fractional crystallization of subaluminous phases, and metasomatic alkali loss (Kushiro and Yoder 1972; Zen 1986). It is evident from my experiments that peraluminous granitoid liquids also can be produced by the dehydration-melting of metaluminous amphibolite.

The liquid compositions produced in the experiments are much more aluminous than the bulk rock composition from which they were produced because of the initial presence and subsequent reaction of anorthite in the starting material. Low-alumina liquids probably cannot be generated from anorthite-bearing rocks. Very high-alumina tonalite can be generated by the dehydration-melting of calcic plagioclase-bearing amphibolite, regardless of the presence or absence of garnet in the residue. Plagioclase can remain in the

residue. The absence or only minor appearance of natural silicic rocks with very high Al_2O_3 contents (>18 wt.%) implies that either most anatectic liquids form without anorthite present or that crystallization of anorthite after partial melting is common in initially highly aluminous liquids.

The presence of calcic plagioclase is the norm in basaltic and gabbroic rocks comprising the oceanic crust. This crust eventually is involved in subduction zone anatexis, but, because of the preceding argument, the melting reactions may not involve anorthite. Hydrothermal and seawater alteration converts some proportion of the basaltic clinopyroxene to amphibole on the crust's journey from ridge to trench. Another important aspect of this alteration process is the possible conversion of calcic plagioclase to a more sodic composition (e.g., Marsh et al. 1990). Thus both H_2O- and Na-alteration processes strongly influence the composition of the subduction zone anatectic liquids (e.g., Spulber and Rutherford 1983; Flagler and Spray 1991).

If anorthite is involved in the melting reactions, then fractionation of anorthite must subsequently take place (as discussed in section 5.2 Differentiation, below). Tonalite is the predominant Archean silicic rock type, but Archean anorthosite complexes also are common. The formation of highly aluminous liquids from the dehydration-melting of anorthite-bearing amphibolites would be conducive to the formation of these plagioclase-rich complexes in the lower crust.

If the sodium in the amphibolite is held predominantly in the hornblende and not the plagioclase, then the liquids will have low Na_2O contents until hornblende breaks down at high temperatures (in the absence of Na-metasomatism). During anatexis, the formation of more-sodic liquids does not have to precede more-calcic liquid formation, and my results show that the opposite is possible. This calcic to sodic liquid anatectic trend generally mimics the liquid line-of-descent trend produced by fractional crystallization. Thus, the use of general chemical trends to deduce specific lower crustal processes may be even more difficult than envisioned by Helz (1976).

5.1.3 Liquid Mg# and Reaction with Mantle Wedge

Ellis (1986) proposed that subduction zone melting of hydrated oceanic basalt (amphibolite) will yield liquid more Mg-rich than the residual garnet, based on his H_2O-saturated experiments using Ca-free, synthetic mineral mixes and glasses. Both my starting material and run conditions are closer to what is present and what occurs in subduction zones. My dehydration-melting experiments on a natural amphibolite yield the opposite results, i.e., the liquid Mg# is always less than the garnet Mg#. The liquid compositions become Mg-richer at higher temperatures, but no garnet-liquid Mg# cross-over exists. Thus, in contrast to Ellis' (1986) proposal, these Mg-poor liquids may undergo considerable modification in the overlying mantle peridotite wedge (Nicholls 1974).

5.2 Differentiation

Differentiation of this slightly hydrated, basaltic magma at 10 kbar involves the fractionation of orthopyroxene, clinopyroxene and anorthite near the liquidus and hornblende and garnet at lower temperatures. The near-liquidus crystallization of clinopyroxene and orthopyroxene with high Mg/(Mg+Fe) values results in an iron-enrichment in the liquid. This iron-enrichment trend is partially offset predominantly by the crystallization of garnet with lower Mg/(Mg+Fe) values at lower temperatures (Fig. 4.8). Precipitation of orthopyroxene displaces the liquid composition to a higher Ca/(Fe+Mg) ratio than the calc-alkaline trend (Fig. 3.19). At lower temperatures, coprecipitation of garnet, hornblende and especially clinopyroxene reduces the Ca/(Fe+Mg) ratios of the liquids somewhat, but not enough to reach calc-alkaline compositions. Huang and Wyllie (1986) observed a similar displaced liquid trend for a partially melted gabbro. In addition to having more CaO than calc-alkaline compositions, the liquids also have more Al_2O_3 (Fig. 3.22).

Fractionation of anorthite would greatly reduce both the CaO and the Al_2O_3 contents of the liquids. This process could drive the liquid back to calc-alkaline compositions and leave behind an anorthositic restite (e.g., Rudnick and Taylor 1987). Fractionation of 20% anorthite from the liquids would produce a residual liquid with about 70 wt.% SiO_2, 15 wt.% Al_2O_3 and 5 wt.% CaO, but the alkali content cannot be raised much without an influx of alkalis. The presence of anorthite phenocrysts in many arc lavas (Fournelle and Marsh 1991) may indicate that this anorthite fractionation process is still occurring at the present time, though possibly on a much reduced scale. However, fractionation of anorthite alone is unlikely, as the liquid is multiply saturated with respect to the other phases.

Huang and Wyllie (1986) reviewed the role that amphibole fractionation may play in the genesis of calc-alkaline rocks. Many experimentalists have tried to determine whether amphibole fractionation can inhibit iron-enrichment of basaltic to andesitic liquids during differentiation (e.g., Boettcher 1973; Ringwood 1974; Cawthorn and O'Hara 1976; Allen and Boettcher 1978, 1983; Green 1982; Carroll and Wyllie 1990). Figure 4.8 shows that the hornblendes and pyroxenes in my 10 kbar experiments have much higher Mg/(Mg+Fe) ratios than the liquids, which suggests that neither hornblende nor pyroxene fractionation is effective in inhibiting iron-enrichment in basaltic and more evolved liquids under these experimental conditions. Fractionation of garnets with relatively low Mg/(Mg+Fe) ratios also would not be very effective in inhibiting iron-enrichment of the liquids, because the liquids still are enriched in iron relative to garnet and all of the mafic minerals. Similar conclusions have been reached by Allen and Boettcher (1983), Huang and Wyllie (1986) and Carroll and Wyllie (1990), based on basalt and tonalite melting experiments.

Once again, Fig. 4.16 shows the phase relationships of amphibolite in P-T space. At low pressure the solidus and Hb-out curves nearly coincide (Beard and Rushmer 1990). The solidus and Hb-out curves diverge at higher pressures. The effectiveness of crystal

fractionation processes may be inhibited by the narrower, crystal plus liquid zone at low pressures, during cooling of hydrous, basaltic magma.

5.3 A Possible Origin for High-Alumina Basalt

Much debate has been directed at the relative roles of subducted oceanic crust and the overlying mantle wedge in the genesis of andesites (e.g., Gill 1981). Experimental petrologists, as well as geochemists and geologists, have attempted to deduce the composition and origin of the parental magma. The principle parental magma may be high-alumina basalt (Gill 1981). One process involves the partial melting of hydrous peridotite in the mantle wedge (Kushiro 1974; Mysen 1982). Another process relies on melting of the slab with little or no mantle interaction (Green and Ringwood 1968; Brophy and Marsh 1986; Johnston 1986; Myers 1988). Johnston (1986) reviews in detail the petrochemical arguments against a peridotitic mantle origin and for a basaltic or eclogitic crustal origin for the generation of primary high-alumina basalt. However, DeBari and Sleep (1991) have shown that the mass influx of magma to island arc crust may be Mg-rich and Al-poor. They derive high-alumina basalt through crystal fractionation of Al-poor phases in differentiating crustal magma chambers that encompass most of the thickness of the arc crust. Although it is possible to enrich liquids in Al_2O_3 by crystal fractionation of low-alumina phases (e.g., DeBari and Sleep 1991), Marsh et al. (1990) have demonstrated that, because of the presence of An-rich plagioclase, the high-alumina character of arc rocks probably is a primitive feature.

Table 5.1 lists the compositions of some high-alumina basalts as well as that of the liquid generated at 1000°C in this powder study (run #134). The similarity between this liquid composition and high-alumina basalt is clear. My experimentally-derived, primary liquid has a high-alumina basaltic composition and is rich in normative plagioclase. The aluminous character is derived by partial melting of an anorthite-bearing source. Thus, dehydration-melting of amphibolite at 10 kbar can produce high-alumina basalt if the

temperature is high enough to induce about 50 vol.% melting. At 10 kbar, a temperature of 1000°C can be reached in hot, young subducting oceanic crust or at the base of hot, thickened arc or continental crust. Higher pressure experiments are needed to determine the phase relationships and compositions that would occur in a cooler, older subducting slab.

Rocks in the high-alumina basalt-andesite series typically have flat (chondrite-normalized) rare earth element (REE) patterns, indicative of the absence of HREE-enriched garnet in the residue from which the magmas were extracted (Gill 1981). In contrast, rocks of the high-alumina tonalite-trondhjemite series typically have HREE-depleted patterns, indicative of the possible presence of HREE-enriched garnet in the residue (Barker and Arth 1976; Arth 1979). In my experiments, aluminous tonalitic liquids are formed in the presence of garnet below about 1000°C, whereas a high-alumina basaltic liquid is formed in the absence of garnet at 1000°C. Thus, the liquids formed by amphibolite dehydration-melting at 10 kbar may be parental to both rock series, depending on the presence or absence of garnet. The silica content of the liquids increases as the temperature decreases and the amount of liquid formed decreases. Johnston (1986) found these phase and compositional relationships to hold for high pressure melting (30 kbar) of high-alumina basalt. In contrast, Brophy (1989) argues for a lower pressure (8-12 kbar) origin for high-alumina basalt.

Hornblende gabbros with similar mineralogy and compositions to my amphibolite composition comprise a significant portion of the crust of island arcs (e.g., Kay and Kay 1985; Burns 1985; DeBari and Sleep 1991). The temperature and pressure regime for this thickened crust is similar to my experimental conditions. Thus, the formation of high-alumina basalt and more silicic liquids could proceed due to remelting of this hydrated, lower crust due to temperature-elevating magma intrusion. Evolution of these liquids could occur in second-generation, deep-seated magma chambers at the base of thickened crust.

Johnston (1986) argues for extensive, high temperature melting (1325-1400°C) of the upper few hundred meters of the subducted crust to generate primary high-alumina

basalt. However, in his preliminary anhydrous MORB melting experiments, the Al_2O_3 content of the liquids is not elevated to high-alumina basalt levels (> 17 wt.%) above 1400°C. It is unlikely that the liquids below 1400°C will be more aluminous in the presence of garnet, which is stable in his lowest temperature (1433°C) run (Johnston 1986).

A high degree (~50 vol.%) of partial melting of a high-alumina basalt source is called for by Johnston (1986) to totally consume garnet, and I reach the same conclusion based on my amphibolite melting experiments. However, the temperature needed to generate this amount of liquid from amphibolite is considerably lower (300-400°C) than the temperature needed for melting anhydrous MORB. The top of the subducted crust is the most likely part to be hydrated, and thus hydrous, not anhydrous, melting may more closely simulate the melting process, although dehydration prior to melting is possible. My amphibolite composition is that of the gabbros in the lower oceanic crust (layer 3). These lower levels within hot, young subducted crust can reach temperatures of 1000°C at ~30-35 km (10 kbar) (Peacock 1990b). This crust must be hydrated, though, to attain the high degrees of melting. If the entire crust were hydrated, extensive melting would generate an enormous quantity of liquid – much more than what appears to have been erupted.

5.4 Partial Melting Along Shear Zones in Deep Mafic Crust

Localized hydration and subsequent partial melting of portions the deeper levels of subducted oceanic or deep continental mafic crust is proposed as one mechanism for the generation of high-alumina basalt. The localization could occur as a result of the increase in permeability along hydrating shear zones (Rutter and Brodie 1985; Newton 1990) (Fig. 5.1a). Franz et al. (1989) and Selverstone et al. (1990) argue for localized rather than pervasive fluid flow in the subducted slab. Paquet and Francois (1980) observed fault-localized liquids in deformation experiments. Flagler and Spray (1991) found evidence for melting along hydrated, low-angle shear zones within the layer 3 gabbros in oceanic crust.

They postulated that these shear zones are the consequence of asthenospheric shear extending up into layer 3. Subducted crust would be affected by this asthenospheric shear along both its top and bottom, so the shearing may increase during subduction. Subducted crust that is young and hot has reached the subduction zone relatively quickly either because it is generated near the subduction zone or it is moving at a faster rate. Young, hot crust may subduct at a faster rate than old, cold crust, and consequently may induce higher shear stresses. Thus extensive melting of amphibolitized shear zones may occur in a largely anhydrous gabbroic subducted crust (Fig. 5.1b). Hydration and subsequent melting also may occur along deep, vertical fracture zones. The stress regimes in subducted crust enhance the formation of shear zones, but this process may also occur in deep continental crust (Newton 1990).

This model has a few geophysical ramifications for the deformation of the subducted slab. Continued asthenosphere-coupled shearing along the liquid-filled shear zones within the slab could cause a delamination of the oceanic crust of the slab. In effect, the crust structure would evolve from a continuous, thick, solid mass to thin, discontinuous, solid masses separated by crystal mush regions (Fig. 5.1b). This geometry may be conducive to oceanic crustal delamination or imbrication, which may initiate crustal underplating. The liquid in these crystal mush regions can readily segregate because the liquid fraction exceeds the critical melt fraction (X_L ~0.5) (e.g., Van der Molen and Paterson 1979; Wickham 1987; Miller et al. 1988). Because of a large solid-liquid density contrast, gravitational instabilities may result in the liquid layers forming diapirs. The ascent of these diapirs would further disrupt the solid crustal masses (Fig. 5.1c). Ascent could more easily occur along previously hydrated, vertically oriented fracture zones. The liquids could mix with the liquids being generated along the hotter, upper portion of the crust. Thus, the crust would first lose coherency along its length and then along its thickness. Regardless of whether the lower oceanic crust is a source for high-alumina

basalts, the geophysical implications for the structural evolution (destruction) of oceanic crust still may be valid.

5.5 The Restite: Formation of Granulites and Consequences

Granulites comprise a substantial portion of Archean crust and probably are continuing to be formed during the present. Granulites can be produced by the separation of hydrous liquid from amphibolites (Fyfe 1973; White and Chappell 1977; Powell 1983). My experimentally-determined refractory mineral assemblage consists of clinopyroxene, orthopyroxene and plagioclase at 1000°C and of clinopyroxene, garnet, plagioclase, orthopyroxene, and hornblende at lower temperatures. Dehydration-melting of the amphibolite also generates hydrous liquids. The water content ranges from 6 wt.% in the earlier liquids to 2 wt.% in the later liquids (Fig. 3.23). Thus, the dehydration-melting experiments reproduce natural granulite mineral assemblages along with the generation of water-rich yet vapor-absent liquids. This process may help form relatively dry granulite terrains. The partial melting of deep crustal amphibolite can leave a granulitic assemblage containing abundant garnet and only minor amount of plagioclase.

Defant and Drummond (1990) give evidence for subducted oceanic crust-derived magmas in the Aleutian Islands. As already discussed, amphibolitic gabbro cumulates containing calcic plagioclase are a predominant rock type found as xenoliths in Japanese lavas and may comprise a significant portion of Japan's lower crust (Fukuyama 1985; Kushiro 1990). Although Kushiro (1990) argues for a mostly mantle source for the silicic magmas, the lower crustal amphibolites constitute another possible source. My experimental results can be applied to the Japanese setting because of the mineralogical and compositional similarities between my starting material and the xenoliths.

I have examined the mineralogy and composition of the crystalline restite left behind after an initial liquid segregation process. Green and Ringwood (1968) determine that the

restite left by slightly melting a wet, high-alumina basalt at 9-10 kbar contains amphibole, plagioclase, pyroxene, and possibly minor garnet. At higher degrees of melting, amphibole and subordinate pyroxene remain, and with even more melting, equal proportions of amphibole and pyroxene remain. The results from my powder experiments differ somewhat from those of Green and Ringwood (1968). The low temperature runs are similar in that they contain hornblende, plagioclase and pyroxene, but garnet also is an important phase. At higher temperatures, clinopyroxene and garnet comprise most of the restite, and hornblende is subordinate. At the highest temperature, clinopyroxene, comprising most of the restite, coexists with a liquid of high-alumina basaltic composition.

Table 5.2 lists the calculated bulk restite composition for five powder runs. These compositions were calculated using mineral compositions from the runs and modal data slightly modified from Table 3.1 to be more mineralogically consistent, based on phase relationship considerations. Two statements can be made relating mineralogy to bulk composition. The Al_2O_3 content of the restite generally decreases with increasing melting temperature, although the decrease is not steady. The trend is due to a monotonic decrease in plagioclase and a concomitant increase then decrease in garnet. The CaO content of the restite generally increases to quite high values, although the garnetiferous nature of the 950°C run results in a relatively low value. Above 900°C the restite is classified as garnet clinopyroxenite – at 1000°C it is clinopyroxenite.

Garnet clinopyroxenites may be very abundant within the lower crust. In a compilation of xenolith studies, Griffin and O'Reilly (1987) found that garnet clinopyroxenites comprise part of the mafic granulite suite that comprises the lower crust. Mukhopadhyay (1991) emphasized the distinction between these low-Na (quadrilateral-component enrichment) clinopyroxene-bearing garnet clinopyroxenites and omphacitic clinopyroxene-bearing eclogites, and documented the occurrence of garnet clinopyroxenite xenoliths throughout the world. Konnikov et al. (1990) have found garnet clinopyroxenite

masses associated with gabbros and relate the two rock types through ultrametamorphic processes.

The calculated densities of the restites also are listed in Table 5.2. The densities are quite high, with the maximum of 3.5 g/cm^3 corresponding to the most garnet-rich restite. The restite density depends on the mineralogy, which depends on the melting relationships. Note that this most dense restite is not the most infertile, high temperature residue but an intermediate one. If this garnet-rich restite comprises a large portion of the lower crust, it is a prime candidate to decouple from the region of anatexis and to sink into the mantle or subcontinental lithosphere (e.g., Ringwood and Green 1966; Bird 1979; Sun 1984). Restite and liquid should separate because the critical melt fraction is attained, and the solid-liquid density contrast is large. The density of this sinking mass would decrease as it heated up and garnet reacted out, and thus it may founder in the subcontinental lithosphere or mantle. In effect, the initially higher density may act to overcome the viscous forces keeping the mass attached to the lower crust but may not aid in its continued descent.

Conditions necessary for granulite formation appear to be commonly achieved in the lower crust. However, the occurrence of granulites at the surface is restricted (Thompson 1990). The rarity of exposure of garnet-rich, mafic granulite may be due to the elevated density, which may not only inhibit exhumation but may even induce sinking. The formation of a garnet-rich restite in the lower continental crust may help maintain isostatic equilibrium of thickened crust (Bohlen and Mezger 1989). This dense material may control the uplift, erosional and cooling rates of granulite terranes (Bohlen 1991). Delamination of this dense root may not necessarily occur during the initial anatectic and granulite-forming event. After a period of time during which the restite density increases by continued garnet growth, later tectonic activity may trigger basal delamination and subsequent uplift of the granulite terrane (Ellis 1987; Harley 1989; Thompson 1990; Bohlen 1991).

Some processes that may elevate the lower crustal isotherms and form granulites include continental collision followed by erosional or extensional thinning, magmatic underplating, magmatic arc or hot spot activity, or crustal delamination (Thompson 1990; Bohlen 1991). During continental rifting, asthenospheric upwelling adds heat to the region. Isotherms within the subcontinental lithosphere shift upwards during this process (e.g., Wyllie 1987) and could induce substantial garnet growth in the mafic rocks at the base of the crust. This dense crust could delaminate and sink, and would cause crustal thinning concurrently with the thinning of the subcontinental lithosphere (Fig. 5.2). The crust could be thinned not only by plastic flow but also by this rifting-induced, lower crustal delamination. Thus, the process of continental rifting could proceed not only by erosion at the base of the lithosphere but also by material transport away from the base of the crust.

There are other geophysical consequences of the restite density changes. Figure 5.3 schematically illustrates, in P-T space, some possible paths that could be followed during density-induced settling of the garnet-rich restite. These paths are superimposed on the garnet stability curve for rocks of basaltic composition. Each path is labelled with the volume percent of garnet in the restite and the resultant density of the restitic body. Assuming a subcontinental lithospheric and mantle density of 3.3 g/cm^3, the relative restite density and its overall size govern which path is taken. Larger restite bodies would sink more rapidly and heat up more slowly than smaller bodies, and thus may sink to greater depths before encountering the garnet-out reaction boundary. Then the density of the restite decreases as the garnet reacts out. The descent would stop and the body would stagnate at that particular depth, because its density is equal to or less than that of the surrounding rock. If the body was large enough, it could overcome the viscous drag forces and begin to rise.

In an open system, the garnetiferous material could be lost from the restite body as it melts, and high densities could not be reestablished by recrossing the garnet-in boundary.

If the restite body acts as a closed system, the potential exists for the density-induced oscillation of the body; it could "yo-yo" up and down across its garnet-out and -in boundary, changing its density from lower to higher than the surrounding mantle density (Fig. 5.3). Along the proper geotherm this process could be stable. The oscillations eventually would be dampened, and the body would sit astride the reaction boundary. If the body were large enough, garnet could grow in the upper, slightly cooler regions while reacting out in the lower, slightly warmer regions. These reactions would lead to a gravitationally unstable body (having a denser top than bottom) that would overturn. The process could repeat itself until the initial geotherm is reestablished.

5.6 Other Tectonic Implications of Garnet-rich Restite

Oblique subduction and non-linearity of the continental shelf coastline of microcontinents or crustal slivers may lead to contrasting styles of deformation along the collisional front (M. McGroeder, pers. comm., 5/1991). Differences in deformation may be attributed to differences in crustal thickness as well as the lateral variations. The presence of deep, sediment-filled basins above thinned crust along the collision front tends to weaken the crust-crust coupling across the front (Figs. 5.4a,b) (M. McGroeder, pers. comm., 5/1991). This coupling could also be weakened by density-induced lower crustal delamination of garnet-rich restite, prior to or during collision (Figs. 5.4c,d).

The presence of garnet does not necessarily lead to a weakening or delamination of crust. Garnet has a very high creep strength (Wang et al. 1991), and a garnet-rich layer would also have a high creep strength. Thus, a garnet-rich layer may strengthen the lower crust, until delamination actually occurs.

Trench-trench-ridge (TTR) triple junction migration may lead to a lateral shift in the isotherms in the mantle wedge and at the base of the continental crust. The base of the overriding plate may heat up because the hot, near-ridge subducted crust will not chill the mantle wedge as much as cooler, older crust (Fig. 5.5). The hot upwelling asthenosphere

below the subducted ridge also may temporarily elevate basal temperatures. The appropriate thermal regime may be imposed upon the base of amphibolitic crust such that abundant garnet growth ensues, followed by restite delamination. Thus TTR triple junction migration may erode the base of the overriding plate.

The style of deformation during collision of continental crust may be influenced by the location of the crustal blocks, relative to the ridge axis. The collision of a crustal block (darkly shaded mass in Fig. 5.5) subsequent to ridge subduction (post-ridge collision) may occur against thinned (delaminated) continental crust. The collision of a crustal block prior to ridge subduction (pre-ridge collision) would occur against thicker continental crust (Fig. 5.5).

The increased lower crustal density and possible subsequent delamination may influence the degree of subduction zone coupling between the two convergent plates. A dense lower crust in the overriding plate would cause it to subside slightly and may increase the coupling between it and the subducted plate. If delamination occurred, the upper plate would rebound upwards slightly, and the plate-plate coupling might weaken. However, these effects would be opposed and possibly cancelled by the topographical differences within the subducted oceanic crust (hotter crust; higher topography; stronger coupling).

5.7 REE Behavior

Garnet has the most profound affect of any major silicate mineral upon the rare earth element (REE) signature of the coexisting silicate liquid (Hanson 1980). The heavy REE are greatly concentrated in the garnet structure, relative to the light REE, so the coexisting liquid has a depleted HREE pattern. Although the HREE also can be concentrated in hornblende, the HREE-to-LREE partitioning in garnet is about 20 times greater than in hornblende (Arth and Barker 1976).

The positions of the garnet reaction boundaries in Fig. 3.1 are time-dependent but do flatten out with time ($\partial T/\partial t$). At equilibrium the garnet-in and garnet-out curves may lie close to 825°C and 980°C, respectively. Therefore, the liquids that are generated by partially melting the amphibolite form in the absence of garnet below 825°C and in the presence of garnet above 825°C. Since the composition of the liquids also changes with temperature, the lower temperature liquids (garnet-absent) are more tonalitic and the higher temperature liquids (garnet-present) more trondhjemitic.

In a region of deep, mafic crust undergoing progressive anatexis, the earlier liquids will be tonalitic and will have a relatively flatter REE pattern. Later, more trondhjemitic liquids will have a relatively steeper REE pattern, being depleted in HREE. The concomitant, garnet-bearing, refractory mineral assemblage will contain the HREE (Hanson 1980; Weber et al. 1985). The REE K_D for garnets varies as a function of the garnet and coexisting liquid composition, so the concentration of REE changes slightly throughout the garnet-present melting interval (Rudnick and Taylor 1986). If an external heat source drives temperatures to 1000°C or higher, these late stage, high-alumina basaltic liquids will have a flatter REE pattern (or even HREE enriched) due to the break down of garnet in the source region. The REE patterns of Archean tonalitic-trondhjemitic rocks generated by the partial melting of mafic crust necessitates the presence of at least 20 vol.% garnet in the source region (Rudnick and Taylor 1986). This condition is achieved in my experiments between about 825°C and 980°C at 10 kbar.

Garnet is a significant restite phase through much of the amphibolite melting interval, so the segregated liquids would have a HREE-depleted signature. This garnet-rich, lower crustal material becomes, in effect, a storage zone for HREE. If hot magmas (> 1000°C) later intrude this crust, they will directly incorporate some of the garnet-rich material into the melt. Depending on the relative temperatures, they also may elevate the temperature of the intruded crust above 1000°C, causing the garnet to react out and possibly to add substantial amounts of HREE into the anatectic liquids, which may mix into the

intruding magma. Thus, the modification of the trace element signatures of through-going magmas may be temperature-dependent. These signatures also may be time-dependent, because continued passage through the same conduits may eventually break down all of the nearby garnet. A change in the deep level plumbing system or in the location of intrusion to another garnet-rich area could result in another influx of HREE-enriched liquid into the ascending magma.

5.8 Geobarothermometry and Mineral Metastabilities

5.8.1 Total Alumina in Hornblende Barometer

The hornblende and plagioclase assemblage used in the melting experiments does not contain most of the phases necessary to rigorously apply the total alumina (Al_T) in hornblende barometers proposed by Hammarstrom and Zen (1986) and developed by Hollister et al. (1987), Johnson and Rutherford (1989) and Rutter et al. (1989). The phases absent are quartz, orthoclase and biotite. Nevertheless, in Fig. 5.6, the plot of pressure versus Al_T for the hornblendes from the experiments indicates that this barometer may hold even for this assemblage. The pressure at which the amphibolite initially equilibrated is unknown but close to 2.5 kbar, based on the geology of the area from which the amphibolite was taken and more extensive hornblende geobarometry on other rocks in the area. The Al_T in the initial hornblende is compatible with this pressure estimate. In Fig. 5.6, the Al_T of this hornblende is plotted at 2.5 kbar, and the Al_T of the two new hornblendes (Ca-Hb and Al-Hb) is plotted at 10 kbar. The errors in composition and pressure of these hornblendes are about the size of the symbols. The Al_T in the Ca-Hb is the same as in the initial Hb, but the Al_T in the Al-Hb increases two-fold, which places it in line with the barometry curve of Hollister et al. (1987). This alignment may be fortuitous or it may mean that the Al_T barometer is fairly robust and not necessarily invalid with the absence of one or more of the "critical" phases. Earlier researchers recognized the pressure dependence of Al^{VI} in hornblendes within regional metamorphic terranes (Leake 1971;

Raase 1974). These metamorphic rocks covered a wide range of lithologies and may have included rocks not containing the complete mineral assemblage needed for Al_T geobarometry.

Regardless of whether or not this barometer holds up for these mineralogical conditions (or lack thereof), if the growth of Al-Hb is a consequence of the high pressure, then the relatively Al-poor composition of the Ca-Hb may indicate its metastability. There is always modally less Ca-Hb than Al-Hb in the experiments. The Al-Hb probably grows readily due to the high alumina content of the sample and especially the liquid. This available supply of alumina, though, does not affect the Al_T of the Ca-Hb composition, relative to the initial hornblende. The Ca-Hb may be the intermediate step between breakdown of the initial hornblende and the nucleation of clinopyroxene. Hornblende compositions around clinopyroxene grains, however, are not more calcic, which could have indicated preferential clinopyroxene nucleation sites within these Ca-Hb patches. The Ca-Hb probably is not the intermediate, metastable phase between Hb and Cpx, because it appears after Cpx (or at higher temperatures) – not before it (or at lower temperatures) (Fig. 3.1).

5.8.2 Amphibole-Calcic Plagioclase Thermometer

The metastability of the Ca-Hb is also suggested by the application of the amphibole-plagioclase thermometer of Blundy and Holland (1990). Table 5.3 lists the results from the three different hornblende compositions. The An_{90} plagioclase composition of the experiments lies within the recommended limit (An_{92}) for the thermometer. Compare the actual temperatures (T) of the experiments with the calculated temperatures (T_c) of the thermometer in Table 5.3. The T and T_c for Al-Hb agree very well, considering the errors of the measurements and thermometer (±80°C). The T and T_c for Ca-Hb, however, do not agree at all. It appears that the thermometer does work for the Al-Hb but not for the Ca-Hb. This dichotomy may be the result of Ca-Hb metastability and

its lack of equilibrium with the plagioclase. The temperature determined for the initial hornblende also is reasonable.

5.8.3 Other Thermometers

Other geothermometers can be applied because of the presence of clinopyroxene, orthopyroxene and garnet in many of the experiments. Table 5.4 lists the results of T and T_c comparisons for garnet-orthopyroxene pairs (Harley 1984), garnet-clinopyroxene pairs (Ellis and Green 1979; Powell 1985; Ganguly and Bhattacharya 1987), garnet-hornblende pairs (Powell 1985), and clinopyroxene-orthopyroxene pairs (Kretz 1982). Garnet analyses are from the crystal edges. The small pyroxenes crystals are compositionally homogeneous. The hornblendes measured are the new, aluminous compositions. The results of Table 5.4 are striking in the lack of correlation between T and T_c for all of these thermometers. T_c is generally much larger than T. Differences between T and T_c reach hundreds of degrees, and the trends in T_c also are not consistent, i.e., as T increases, T_c may increase or decrease.

If the thermometer of Blundy and Holland (1990) seems to work so well, then why do these other thermometers not give the actual experimental temperatures? The actual temperatures and pressure of the experiments and the measured mineral compositions are the best known of the variables affecting T_c. Possible reasons for the inconsistencies include compositional and metastability factors in the experiments and problems associated with the thermometers. The clinopyroxene compositions vary little throughout the experiments; the values of [Ca/(Ca+Mg+Fe)] for clinopyroxene range from 0.42 to 0.48 with no temperature-dependent trend. The grossular component in the garnets also appears to be temperature-insensitive. The compositional invariability of the mineral components clearly has an adverse effect on the geothermometric estimates. The pyroxenes are quite aluminous (>7 wt.% Al_2O_3), so the poor thermometry results support Lindley's (1983)

finding that aluminous pyroxenes yield high T_c – temperatures that increase as the amounts of Al_2O_3 in pyroxenes increase.

The possible metastability of Ca-Hb may account for the discrepancy between T and T_c with the Blundy and Holland (1990) thermometer. It is possible that the pyroxenes are metastable and thus also may record anomalous calculated temperatures. The constancy of pyroxene compositions and their continued presence and abundance in runs at all temperatures and for all durations, however, seems to indicate that they are stable phases. However, a phase may be metastable, but its composition nonetheless should be governed by the same chemical partitioning that occurs between stable phases and the rest of the system. Thus, the presence of metastable phases should not necessarily be a problem for thermometric calculations.

Much of the discrepancies between T and T_c probably is associated with the limitations of application of the thermometers. The thermometers are empirical fits to various data sets and thus may be very pressure- and/or compositionally-dependent, i.e., they may only "work" for rocks with similar bulk compositions and mineralogies under similar conditions, and should not be liberally applied to all rocks. A case in point is the Ellis and Green (1979) garnet-clinopyroxene Fe-Mg thermometer, which, when applied to my data, overestimates the run temperatures by 75-200°C (Table 5.4). This thermometer was derived from high pressure (30 kbar) data. Green and Adam (1991) recently reassessed Ellis and Green's thermometer and found that the pressure correction and possibly the grossular content correction are not appropriate for lower pressure conditions; it overestimated their experimental run temperatures by ~150°C at 10 kbar. Thus, based on this reevaluation, my thermometric results from garnet-clinopyroxene Fe-Mg exchange are generally within the error (±50°C) of the true run temperatures.

5.9 Dehydration Textures in Natural Rocks

These experiments have applications to the amphibolite-facies to granulite-facies transition, and to the generation of magmas during ultrametamorphism. The results indicate that in a solid piece of amphibolite, clinopyroxene may be produced initially not in a dehydration-melting reaction, but through a subsolidus dehydration reaction occurring within hornblende crystals, independently of reactions elsewhere in the rock. Melting proceeds simultaneously at hornblende/plagioclase contacts. At 850°C, clinopyroxene nucleates throughout most of the hornblende, and at a slightly higher temperature, 875°C, clinopyroxene growth is concentrated in the center of hornblende grains, producing a texture containing clusters of clinopyroxene crystals surrounded by rims of hornblende (Fig. 4.2). It is possible that the 875°C texture may be produced at lower temperatures if the reaction time is lengthened. Subsolidus experiments are needed to determine whether clinopyroxene nucleation occurs within or along the boundaries of hornblende grains in the metamorphic regime. A change in the nucleation location may coincide with the formation of a liquid, if the liquid is an integral part of the clinopyroxene-forming, hornblende-buffering reactions.

The textural relationships between amphibole and clinopyroxene have been used to deduce processes and histories of rock formation (Spry 1969; Vernon 1976; Mason 1978). The occurrence of hornblende rims on clinopyroxenes in metamorphic rocks is commonly interpreted in terms of the progressive alteration and hydration of basalts, with hornblende replacing clinopyroxene from its outer margins. However, my experiments indicate the possibility that a similar texture may be produced in an amphibolite during a higher temperature dehydration event. In the absence of fluids in the retrograde environment, this texture would record high-temperature H_2O losses, not low-temperature H_2O infiltration and gains.

Mazzone et al. (1987) reported intra-clot clinopyroxenes within amphibole precursors in an andesite. They deduced that the subsolidus dehydration of the amphibole

occurred as a result of heating by the andesitic magma. Their amphibole breakdown reaction consumes quartz and, in addition to clinopyroxene, also produces plagioclase, orthopyroxene and minor K feldspar and opaque minerals. In my experiments, the extra components not incorporated into the clinopyroxene structure during hornblende breakdown do not form other minerals but leave the hornblende grain and probably enter the silicate liquid dissolved in the previously structurally-bound H_2O.

5.10 Liquid Segregation

The solid amphibolite begins to melt below 850°C, a temperature considerably lower than the values of 925-1000°C deduced, calculated, or measured previously (Wyllie 1977; Burnham 1979; Rushmer 1987; Rapp 1990). In the powder amphibolite runs, liquid is present at much lower temperatures (750°C). This is because the multicomponent amphibole begins to break down about 200°C below its upper temperature stability limit, releasing vapor to cause H_2O-saturated melting elsewhere in the rock. Interconnectivity is facilitated if the plagioclase grains are long enough and oriented so that they touch other plagioclase grains. These criteria are naturally fulfilled in lineated rocks such as amphibolites. The boundaries between elongated grains in lineated amphibolites can become pathways for the migration of liquid or the diffusion of components during partial melting. Deformation prior to anatexis may be important in imparting a lineated texture to the rock that, during or after anatexis, is conducive to liquid interconnectivity and possible subsequent liquid segregation.

McKenzie (1985), Wickham (1987) and Miller et al. (1988) reviewed in detail the conditions necessary for liquid migration and segregation from its host rock. The most important determinants are interconnectivity, time, viscosity, liquid fraction, and strain rate. The time to reach textural equilibrium, the "equilibrium adjustment time" of McKenzie (1984), is an important parameter in the compaction of partially melted systems, since the

compaction time is a function of the adjustment time. The adjustment time depends on grain size and composition.

McKenzie (1985) has calculated diagrams as a basis for discussion of the evolution of partially molten regions within the earth. These show the time taken for liquids of various viscosities to become separated from columns of rock of various thicknesses. He concluded that granitic liquids would only be able to move with respect to their matrices if they were sufficiently rich in dissolved volatile components for their viscosity to become less than about 100 Pa s. In contrast, mafic liquids can easily separate from their matrices McKenzie (1985). The behavior of liquids of intermediate compositions (e.g., diorites and mafic tonalites) probably lies between these two bounds.

Liquid segregation depends on the permeability of the system and the viscosity of the liquid (McKenzie 1985). The crystallographically-controlled liquid morphology widens liquid channels, enhances the rock permeability and may promote liquid separation. For a given liquid fraction, the channels connecting pockets of liquid between mineral faces in anisotropic rock systems have larger cross-sectional areas relative to dihedral angle-controlled liquid channels, due to the absence of the concave channels necessary for interconnectivity in θ-controlled systems (Fig. 4.16) (e.g., Bulau et al. 1979; von Bargen and Waff 1986). Movement of liquid through such crystallographically-controlled pathways is enhanced due to the increased permeability, k (k for tube- or dike-like channels > k for channels in a medium composed of close-packed spheres). Faul et al. (1990) also found that permeability may be enhanced by the presence of faceted faces in a partially melted olivine-basalt system. The partial dehydration of hornblende, at sites away from the Hb/Pl boundaries where liquid is generated, temporarily creates H_2O-saturated conditions, lowering the viscosity of the hydrous liquid.

The extraction of liquid is controlled not only by its viscosity and the permeability of the rock, but also by the rate of rock matrix deformation (Sleep 1974; McKenzie 1984). The strongly lineated textures of amphibolites are developed during regional deformation,

and the associated metamorphism may progress to anatexis; if it does, then the deformation will produce the mineral geometry conducive to liquid interconnectivity and will become the driving force for the extraction of the liquid through matrix compaction (e.g., Cooper and Kohlstedt 1984; Richter and McKenzie 1984; McKenzie 1984, 1987). Hacker (1990) partially melted and deformed solid amphibolite but did not reach conclusions on liquid interconnectivity.

I use McKenzie's (1985) graphs and my experimental results to explore the possible behavior of the granitoid liquid during dehydration-melting of amphibolite. However, there are too may complexities in the application of my short-duration laboratory experiments to long-duration natural processes for McKenzie's equations to be directly applicable. Application of the results cannot take into account many of the changes that may occur in the liquid quantity and morphology, and H_2O content as a function of time and temperature for an amphibolite in the crust. In addition, the calculated values and subsequent results from Table 4.3 should not be freely used for all amphibolites because of the strong compositional dependence of the critical dehydration and dehydration-melting reactions.

Furthermore, McKenzie's (1985) calculations were based on compaction of structurally isotropic rocks, whereas I am dealing with lineated amphibolite. The lineation may direct the flow of liquid more effectively than gravity, and the direction of lineation may not be vertical. Deformation can occur during regional metamorphism of amphibolites and also during subduction of hydrated oceanic crust. In a subducting slab, the state of stress at the depths of partial melting can be extensional in the down-dip direction (Isacks et al. 1968). Rocks strained in this stress field may develop mineral lineations which would plunge down-dip. In a steeply dipping, melting slab, the lineations could become pathways for the migration of liquid back up the slab dip. During hydrous melting, liquid pockets are more likely to be oriented normal to σ_1, due to slight orientation-dependent pressure differences (George 1977). This effect may aid in liquid migration through

porous flow. Boudier and Nicolas (1977) have observed dikes normal to the mineral lineation in a peridotite. Dikes oriented normal to the mineral lineation (σ_3) in subducted crust may enable liquid to migrate directly to the upper portions of the crust.

With full realization of the uncertainties in these applications, I apply McKenzie's (1985) results to the experimental system as determined in the solid amphibolite at 875°C. Given a constant 2 vol.%, H_2O-saturated liquid (10-12 wt.% H_2O), if compaction were the only force operating, the calculations indicate that the liquid could separate from 100 m of partially melted amphibolite in 10^5 years, or from 1 km in 10^6 years. However, the parameters change through time. Segregation is enhanced as the liquid fraction increases, because the liquid remains H_2O-saturated until about 6 vol.%. This H_2O-saturated liquid could separate from 100 m of partially melted amphibolite in 10^4 years, or from 1 km in 10^5 years. The liquid fraction may continue to increase through time, up to a maximum of about 12 vol.%. The decrease in the liquid's H_2O content would tend to increase extraction time, but the increase in liquid fraction would tend to decrease extraction time. Using McKenzie's (1985) graphs, the calculated extraction time for this 12 vol.% of liquid is 10^5 years for 100 m or 10^6 years for 1 km of amphibolite, similar to the time for the initial 2 vol.%. Thus the integrated rate of liquid segregation may not decrease to a halt during anatexis at about 875°C. The maximum duration of a metamorphic-anatectic event is 10^6 - 10^7 years (Wickham 1987). In 10^6 years about a 100 m thick layer of liquid could be produced by the partial dehydration-melting and compaction of a 1 km thick region of amphibolite remaining at a temperature near 875°C. Therefore, despite the uncertainty in the numbers, I qualitatively conclude that bodies of H_2O-saturated granitoid liquid might be generated and separated from a source of amphibolite experiencing dehydration-melting at 875°C.

For amphibolite at temperatures higher than 875-900°C, the reduced H_2O content of the increased liquid fraction increases its viscosity (Table 4.3). This precludes escape of the liquid from the rock matrix. Only when the system reaches the critical melt fraction of

> 30 vol.% liquid, near 975°C does the rock mass become mobile. At temperatures lower than 850°C, not enough hornblende would dehydrate to saturate the liquid with H_2O, even at low liquid fractions. Under these conditions, the liquid cannot be separated from amphibolite in a geologically reasonable time interval.

Granulites may be produced by the dehydration of amphibolites, and the vapor-absent, partial dehydration-melting of amphibolite may be an important part of the process (Fyfe 1973). Powell (1983) concluded that fluid loss under amphibolite/granulite-facies conditions is achieved most effectively by the formation and separation of a silicate liquid. If the H_2O-undersaturated liquid could escape, then it would contribute to the dehydration of the amphibolite source region, leaving granulite-facies rocks behind. Amphibolite in the deep crust at 850°C may contain a few percent of liquid that may be interconnected but too viscous to move far. The infiltration of H_2O into amphibolites may actually help promote regional dehydration. Infiltrating H_2O would dissolve into the liquid, and the addition of just a few weight percent H_2O would lower the liquid viscosity considerably. The degree to which this H_2O-enriched liquid could separate from its matrix depends on the amount of H_2O-influx. According to McKenzie's (1985) calculations, H_2O-undersaturated liquid is too viscous for segregation by compaction. At temperatures near 875°C, however, an influx of H_2O is not needed to generate an H_2O-saturated liquid during amphibolite anatexis. From the application of these new experimental results to McKenzie's equations, it appears that a hydrous granitoid melt may be able to escape from amphibolite, but only within a rather narrow temperature interval, 850-900°C, coincident with the wide-spread dehydration of hornblende.

Whether or not the calculated values are geologically relevant, the point remains that, in an amphibolite, liquid segregation in fact may be promoted at moderate temperatures by the generation of smaller rather than larger quantities of liquid, because the H_2O activity decreases (and thus viscosity increases) as the liquid fraction increases (with no H_2O-influx). Separation of liquid may not occur in a high-potassium rock, which could

produce sufficient initial liquid that it remains H_2O-undersaturated even with the transient H_2O vapor from dehydrating hornblende. If the viscosity of the granitoid melt is not lowered enough for segregation in this temperature interval, then magma migration, including entrained residual minerals, will not occur until the critical melt fraction is reached, at about 975°C.

What actually happens deep within the crust depends critically on the relationship between temperature and time – the heat flux. If the temperature increases too slowly below about 875°C, amphibolite may partially dehydrate without producing any liquid until relatively high temperatures are attained. If the temperature increases too fast above about 875°C, the increasing liquid fraction would have an increased viscosity as the H_2O content in the liquid decreased (Table 4.3). In these cases, the rate of liquid segregation would first be inhibited and then effectively terminated, until the critical melt fraction is reached.

Too many factors are involved to predict the actual quantity of liquid that may escape a source region undergoing dehydration-melting. However, these new experimental results and calculations indicate that it is possible that the quantity may be small. Although this relatively low temperature process may not produce large bodies of magma from partially melted amphibolites, it may be important in determining the trace element signatures of both the segregated liquid and the source region residuum (e.g., Arth and Barker 1976; Hanson 1980; Green and Pearson 1985; Burton and O'Nions 1990). The segregation of a small amount of hydrous liquid will effectively remove incompatible trace elements, causing a depletion of large ion lithophile elements (LILE) in the rock and giving the rock the LILE-depleted characteristic of many granulite terranes (e.g., Rudnick et al. 1985).

Using geochemical techniques, Sawyer (1990, 1991) has documented the occurrence of disequilibrium melting during migmatization of mafic rocks by hornblende dehydration-melting. The data indicate that segregation of the wet liquid (with 6 wt.% H_2O) took less than 100 years, and in a less likely scenario, dry liquid segregation still

took less than 10^5 years. Syntectonic, non-hydrostatic stresses may have contributed to segregation (Sawyer 1990, 1991). These results indicate that the rate of segregation calculations based on the amphibolite melting experiments may be reasonable.

5.11 Recycling Nominally Anhydrous Minerals Back into the Mantle

Dehydration and dehydration-melting are effective processes for partially removing H_2O from hydrated, subducted oceanic crust. Much of the lost H_2O migrates upwards in fluids or hydrous liquids and is associated with arc magmatism, but some of the H_2O may be recycled back into the mantle along with the subducting crust (e.g., Jambon and Zimmermann 1990). Mass balance calculations from the solid amphibolite melting experiments indicate that a transient H_2O-saturated liquid is produced between 875°C and 925°C at 10 kbar. The occurrence of this transient H_2O-saturated liquid could aid in the delivery of any H_2O that is added to the mantle.

Small amounts of H_2O can be incorporated into the structures of minerals typically regarded as anhydrous (G. Rossman, pers. comm., 12/1990). Clinopyroxene and garnet are the relevant minerals in a dehydrating and melting slab. Greater amounts of H_2O may be incorporated into these minerals if they grow under H_2O-richer conditions (D. Bell, pers. comm., 12/1990). Thus, clinopyroxene and garnet that grow in the presence of the transient H_2O-saturated liquid may contain more H_2O than they might have contained if H_2O-saturated conditions were not achieved. Loss of H_2O from these minerals is much slower than incorporation during growth, so the minerals probably do not dehydrate readily when H_2O-undersaturated conditions are attained. Therefore, due to the transient H_2O-saturated conditions, these minerals may carry more H_2O into the mantle that otherwise would have been expelled to the overlying arc.

This process also can be applied to the restitic material that may form at the base of the crust. As previously discussed, the density of this garnet pyroxenite restite is high enough (3.5 g/cm^3) to cause this mass to detach from the crust and to sink into the

underlieing mantle (Fig. 5.2). As the mass sinks and heats up, the density decreases as the garnet reacts out, and some H_2O is released into the mantle. Much of the structurally-bound water, incorporated during transient, high H_2O activities, could be retained in the foundering clinopyroxenite mass in the subcontinental lithosphere (Fig. 5.3).

5.12 Mechanical Effects of a Transient H_2O-Saturated Liquid

High H_2O pressures ($=P_{total}$) may aid in deformation. Relatively low temperature cataclastic deformation is dramatically enhanced by an increase in P_{H_2O} due to dehydration (Brodie and Rutter 1985). This dehydration-enhanced deformability may be important in amphibolites comprising subducting oceanic crust (e.g., Raleigh and Paterson 1965). I have shown that dehydration-melting of amphibolite can occur at relatively low temperatures (750°C). Thus dehydration-melting-enhanced deformation may be important in amphibolites. The formation of a transient H_2O-saturated liquid may facilitate deformation, although the nature of deformation may not be cataclastic because of the relatively high temperature, intracrystalline plasticity and presence of a silicate liquid. However, in deformation experiments on natural amphibolite (650-950°C temperatures, 5-15 kbar confining pressures, 10^{-4}-10^{-7} s^{-1} strain rates), Hacker and Christie (1990) observe cataclastic deformation and faulting along microshear zones under hypersolidus conditions. Wilks and Carter (1990) speculate that rock strength may be a function of texture. Dell'Angelo and Tullis (1988) conclude that the nature of deformation depends on the relative rates of strain and liquid extraction, and that high liquid pressure leads to cataclasis but not discrete macroscopic fracturing. The amphibole crystal chemistry may also influence mineral and thus rock strength (Phillips et al. 1988).

The deformation along the shear zones may enhance the kinetics of reactions (Brodie and Rutter 1985). If these reactions produce free H_2O, a positive-feedback cycle may be induced that accelerates both dehydration and deformation, as well as melting.

These processes may be focussed in the low-angle shear zones within the layer 3 amphibolitized gabbros of oceanic crust.

Walther and Orville (1982) suggest that hydraulic fracturing may be a major dehydration mechanism. The presence of veins implies that P_{H_2O} can be $\geq P_{total}$ (at least instantaneously) even under high pressure (20 kbar) conditions (Selverstone et al. 1990). The transient H_2O-saturated liquid also may be a catalyst for hydraulic fracturing – but of a partially melted system. During this fracturing, liquid segregation and migration may occur to some extent, in the form of dikes. As fluid or liquid pressure approaches P_{total}, magma injection by extensional fracture can occur at any depth (Shaw 1980). Fracturing under a deviatoric stress can occur even if $P_{H_2O} < P_{total}$ (Yardley 1986). Dikes oriented normal to the mineral lineation (σ_3) in crust undergoing lateral extension may enable liquid to migrate to the upper portions of the crust.

Using the hydrofracturing model of Nicolas (1990), $\Delta P = g\ \Delta\rho\ h$, I calculate a liquid overpressure (ΔP) to be about 10 bars in a 100 m thick partially melted region (where g is the gravitational constant, $\Delta\rho$ is the matrix-liquid density contrast [1.1 g/cm^3], and h is the liquid column height [100 m]). Hydrofracturing can occur if the liquid pressure reaches the yield strength of the rock in question. The yield strength of partially melted basalt (with a very low liquid fraction) is about 10 bars (Shaw 1980), so hydrofracturing is possible in this system. This quick calculation does not take into account the additional transient overpressure due to $P_{H_2O} = P_{total}$. This hydrofracturing and subsequent pressure depression may be very efficient at segregating a liquid from its source (Nicolas 1990).

Fracturing also may play a part in subducted oceanic crust seismicity (e.g., Raleigh 1977). The dehydration and dehydration-melting reactions can induce rock failures (Shaw 1980). If the initial hydration is confined to deep low angle shear zones, then subsequent dehydration and dehydration-melting along these shear zones will produce earthquakes.

The solid amphibolite experiments show that the anisotropic structure of hornblende may result in liquid pockets with flat-faced surfaces. It is unclear whether the morphology of these liquid-filled pockets and tubules in rocks mainly composed of anisotropic minerals will be dominantly crystallographically-controlled over geological time, but if this is the case, then it may have geophysical consequences. Seismic wave velocities are attenuated more if liquid-filled tubules are flattened (e.g., Watson et al. 1990). Thus less liquid is needed in these flattened (crystallographically-controlled) pockets to dampen seismic waves, or, conversely, the percentage of liquid in a partially melted region may be over-estimated if a round-walled (θ-controlled) model is used.

Table 5.1. High-Alumina Basalts (normalized to 100).

	1	2	3	4	5	6	7	8	9	10	11	**12**
SiO2	50.9	50.8	49.5	51.0	54.1	54.3	51.5	50.6	49.3	55.4	49.8	**51.82**
TiO2	0.97	0.91	0.92	1.04	0.71	0.74	0.63	1.30	1.03	0.80	1.67	**0.51**
Al2O3	19.8	20.9	18.9	17.8	18.2	19.0	18.0	19.8	19.1	18.9	20.3	**20.91**
FeO*	9.25	9.29	9.74	11.17	9.19	9.61	8.48	9.12	9.52	8.00	9.70	**7.09**
MnO	0.18	--	0.19	0.24	0.23	0.28	0.17	0.28	0.21	0.31	0.18	**0.23**
MgO	4.52	3.71	5.74	5.81	3.95	3.29	7.20	5.07	6.21	3.33	3.62	**6.36**
CaO	10.40	10.32	10.64	9.85	8.94	8.35	11.70	9.63	11.46	8.06	10.49	**11.50**
Na2O	3.14	3.28	3.34	2.56	3.41	3.15	2.04	3.43	2.57	4.15	3.20	**1.40**
K2O	0.88	0.71	0.98	0.58	1.23	1.32	0.29	0.79	0.65	1.00	0.56	**0.17**

1. Avg. of 117, Myers 1988
2. Myers et al. 1986
3. Avg. of 33, Brophy and Marsh 1986
4. Avg. of 3, Kuno 1960
5, 6. Brophy 1989
7. Johnston 1986
8-10. Baker and Eggler 1987
11. Fournelle and Marsh 1991
12. Liquid, run #134, 1000°C, This study

Table 5.2. Calculated bulk restite composition from powder experiments					
run #	106	113	103	119	134
Temp (°C)	900	925	950	975	1000
SiO2	47.84	46.65	45.25	46.97	48.75
TiO2	0.29	0.40	0.46	0.34	0.33
Al2O3	15.70	14.66	15.98	13.43	11.28
FeO	9.30	9.38	10.96	9.12	7.14
MnO	0.26	0.25	0.31	0.27	0.20
MgO	11.17	12.07	12.79	13.00	12.04
CaO	15.04	16.48	14.51	16.99	20.08
Na2O	0.30	0.19	0.13	0.08	0.13
K2O	0.06	0.03	0.02	0.02	0.02
Restite Density	3.13	3.33	3.50	3.37	3.25

Restite density calculated using the following mineral densities: Hb=3.20; Pl=2.76; Cpx=3.30; Ca-Hb=3.20; Al-Hb=3.20; Opx=3.40; Ga=3.9-3.8 (compositionally dependent)

Table 5.3. Amphibole-plagioclase thermometer of Blundy and Holland (1990) applied to hornblende compositions from amphibolite melting experiments.

T (°C)	n	Si	K	T_c (°C)
Hb				
---	14	7.165	0.2274	634
Al-Hb				
875	2	6.470	0.0969	908
925	5	6.443	0.0941	920
945	4	6.344	0.0849	966
990	1	6.152	0.0699	1062
Ca-Hb				
925	1	7.023	0.1856	687
945	1	7.099	0.2064	658
975	2	6.841	0.1471	756

T = temperature of experiment.
T_c = calculated temperature, where:

$$T_c = \frac{0.677\,P - 48.98 + Y}{-0.0429 - 0.008314 \ln K}$$

$$K = \left(\frac{Si - 4}{8 - Si}\right) X_{Ab}^{Pl}$$

$$Y = -8.06 + 25.5\,(1 - X_{Ab})^2$$

with P in kbar, T in K.

Table 5.4. Calculated run temperatures from four garnet-pyroxene geothermometers.

Run #	120	120	115	115	108	108	108	109	109	110	110	110
Temp (°C)	850	850	900	900	925	925	925	925	925	925	925	925
time (d)	8	8	4	4	1	1	1	2	2	4	4	4
mineral	Ga rim avg	Cpx avg	Ga rim avg	Cpx avg	Ga rim	Cpx	Opx	Ga rim avg	Opx avg	Ga rim	Cpx	Opx
n=	2	2	2	2	1	1	1	2	2	1	1	1
X_{Ca}^{Ga}	0.25		0.23		0.21			0.22		0.20		
K_D	2.731		2.981		2.315	2.529		2.036		1.706	1.480	
T_{calc} (°C) EG79	1069		1017		1112					1273		
T_{calc} (°C) P85	1064		1008		1110					1281		
T_{calc} (°C) GB87	1018		986		1083					1223		
T_{calc} (°C) H84						849		995			1279	

Run #	113	113	117	117	103	103	138	138	138
Temp (°C)	925	925	950	950	950	950	990	990	990
time (d)	8	8	1	1	2	2	1	1	1
mineral	Ga rim	Cpx avg	Ga rim	Cpx avg	Ga rim avg	Cpx	Ga rim avg	Cpx avg	Opx
n=	1	2	1	3	2	1	2	3	1
X_{Ca}^{Ga}	0.24		0.21		0.21		0.23		
K_D	3.064		1.892		1.456		2.009	1.777	
T_{calc} (°C) EG79	1008		1219		1381		1205		
T_{calc} (°C) P85	999		1224		1398		1208		
T_{calc} (°C) GB87	976		1173		1308		1145		
T_{calc} (°C) H84								1109	

Where:

$$K_D = \frac{\left(\frac{Fe}{Mg}\right)^{Ga}}{\left(\frac{Fe}{Mg}\right)^{Px}} \qquad X_{Ca}^{Ga} = \frac{Ca}{(Ca + Mg + Fe)}$$

where Ca, Mg and Fe are the number of atoms per formula unit

Table 5.4 (cont). Calculated run temperatures from garnet-hornblende geothermometer (Powell 1985).

Run #	108	108	109	109	110	110	113	113	103	103	138	138
Temp (°C)	925	925	925	925	925	925	925	925	950	950	990	990
time (d)	1	1	2	2	4	4	8	8	2	2	1	1
mineral	Ga rim	Al-Hb	Ga rim	Al-Hb	Ga rim	Al-Hb	Ga rim.	Al-Hb	Ga rim	Al-Hb	Ga rim	Al-Hb
X_{Ca}^{Ga}	0.21		0.22		0.20		0.24		0.21		0.23	
K_D	2.041		2.182		1.499		2.489		1.218		1.762	
T_{calc} (°C) P85	857		839		978		810		1094		934	

EG79: Ellis and Green (1979); Ga-Cpx

$$T_{calc} = \left(\frac{3104\, X_{Ca}^{Ga} + 3030 + 10.86\, P\ (kbar)}{\ln K_D + 1.9034}\right) - 273$$

P85: Powell (1985); Ga-Cpx

$$T_{calc} = \left(\frac{2790 + 10\, P\ (kbar) + 3140\, X_{Ca}^{Ga}}{1.735 + \ln K_D}\right) - 273$$

GB87: Ganguly and Bhattacharya (1987); Ga-Cpx

$$T_{calc} = \left(\frac{4307 + 11.07\, P\ (kbar)}{\ln K_D + 2.418}\right) - 273$$

H84: Harley (1984); Ga-Opx

$$T_{calc} = \left(\frac{3740 + 1400\, X_{Ca}^{Ga} + 22.86\, P\ (kbar)}{1.987 \ln K_D + 1.96}\right) - 273$$

P85: Powell (1985); Ga-Hb

$$T_{calc} = \left(\frac{2580 + 3340\, X_{Ca}^{Ga}}{\ln K_D + 2.20}\right) - 273$$

Table 5.4 (cont.). Calculated powder run temperatures from two-pyroxene geothermometer: solvus surface and Mg-Fe K_D (Kretz 1982).

Run #	126	126	108	108	110	110	141	141	138	138	134	134
Temp (°C)	875	875	925	925	925	925	945	945	990	990	1000	1000
time (d)	14	14	1	1	4	4	5	5	1	1	4	4
mineral	Cpx	Opx	Cpx	Opx	Cpx	Opx	Cpx avg	Opx avg	Cpx avg	Opx	Cpx avg	Opx avg
n =	1	1	1	1	1	1	4	4	3	1	3	3
X_{Fe}^{Px}	0.270	0.296	0.260	0.243	0.267	0.295	0.312	0.272	0.280	0.306	0.200	0.222
X_{Ca}^{Px}	0.479	0.022	0.414	0.022	0.453	0.035	0.493	0.029	0.448	0.030	0.429	0.034
K_D	1.134		0.916		1.152		0.823		1.131		1.137	
$T_{SS.calc}$ (°C) K82	577		1063		793		383		823		1024	
$T_{MF.calc}$ (°C) K82	1517		2439		1474		3364		1527		1512	

Where: (SS: solvus surface; MF: Mg-Fe K_D)

$$T_{SS.calc} = \left(\frac{1000}{\left(0.054 + 0.608\, X_{Fe}^{Cpx} - 0.304 \ln\left(1 - 2\, X_{Ca}^{Cpx}\right)\right)} \right) - 273$$

$$T_{MF.calc} = \left(\frac{1130}{\left(\ln K_D + 0.505\right)} \right) - 273$$

$$K_D = \frac{\left(\frac{X_{Fe}^{Opx}}{\left(1 - X_{Fe}^{Opx}\right)} \right)}{\left(\frac{X_{Fe}^{Cpx}}{\left(1 - X_{Fe}^{Cpx}\right)} \right)}$$

$$X_{Fe}^{Cpx} = \frac{Fe^{2+}}{\left(Mg + Fe^{2+}\right)} \qquad X_{Ca}^{Cpx} = \frac{Ca}{\left(Ca + Mg + Fe^{2+}\right)}$$

Calculated solid run temperatures.

Run #	133	133
Temp (°C)	1000	1000
time (d)	4	4
mineral	Cpx avg	Opx avg
n =	3	2
X_{Fe}^{Px}	0.228	0.228
X_{Ca}^{Px}	0.385	0.033
K_D	1.000	
$T_{SS.calc}$ (°C) K82	1291	
$T_{MF.calc}$ (°C) K82	1965	

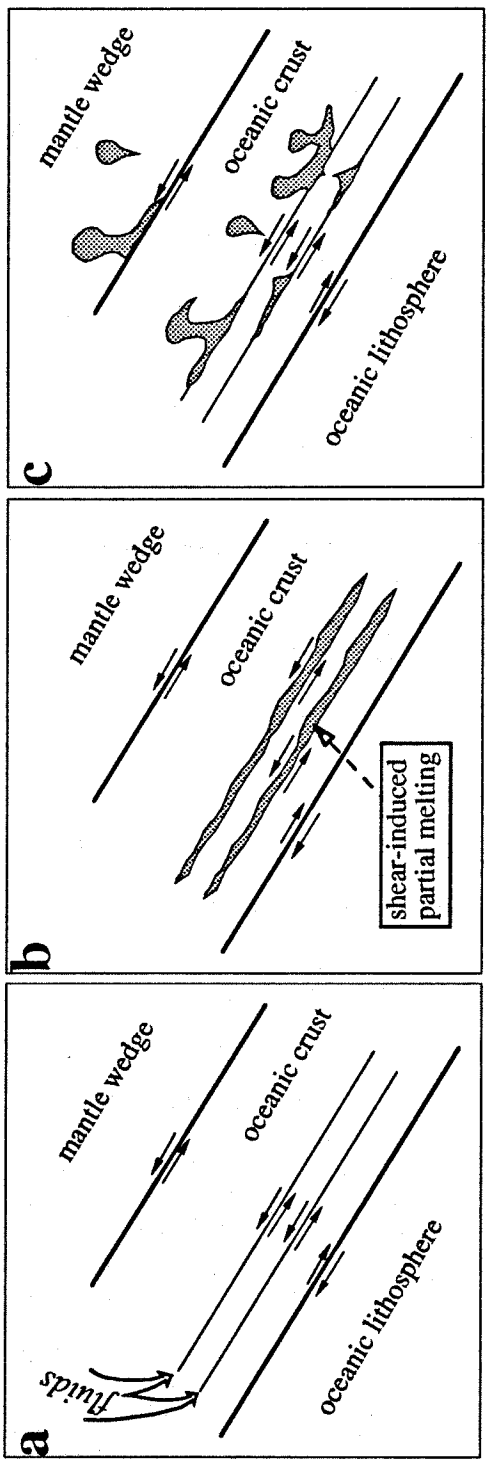

Fig. 5.1a-c. Schematic diagrams of low-angle, anatectic shear zones at the base of subducting oceanic crust (layer 3 gabbros) (based on Flagler and Spray 1991): [a] fluid infiltration; [b] subsequent amphibolitization and shear-induced anatexis; [c] coalescence and upward migration.

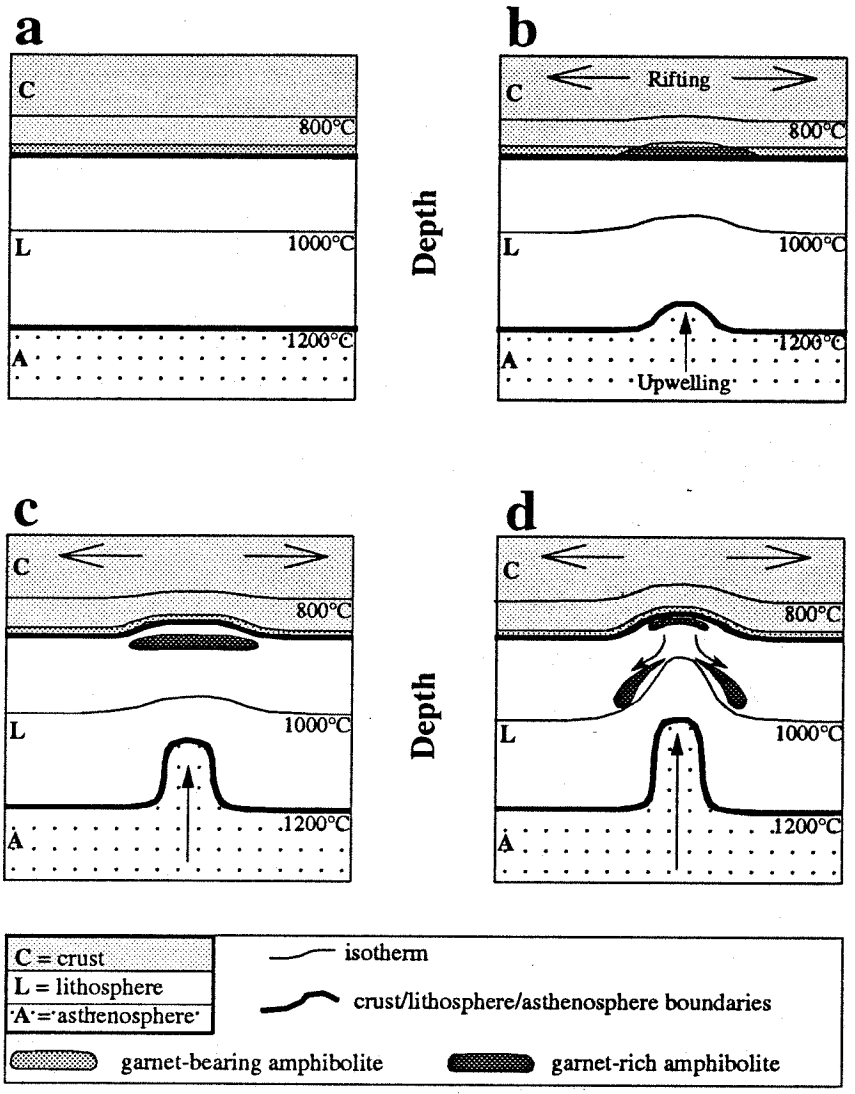

Fig. 5.2a-d. Schematic diagrams showing rift-induced asthenospheric upwelling and resultant upward shifts in isotherms. [a] Before rifting. [b] Anatexis and garnet growth in amphibolites at the base the continental crust occurs as the isotherms penetrate upward. [c] Garnet-rich amphibolite has a high density (3.3-3.5 gm/cm^3) and may delaminate from the crust and sink. [d] Garnet-out reaction at high temperature (1000°C) may result in a thinning of the central portion of the sinking restite followed by fragmentation of the mass. Further asthenospheric upwelling induces more garnet growth in deep crustal amphibolites with appropriate compositions.

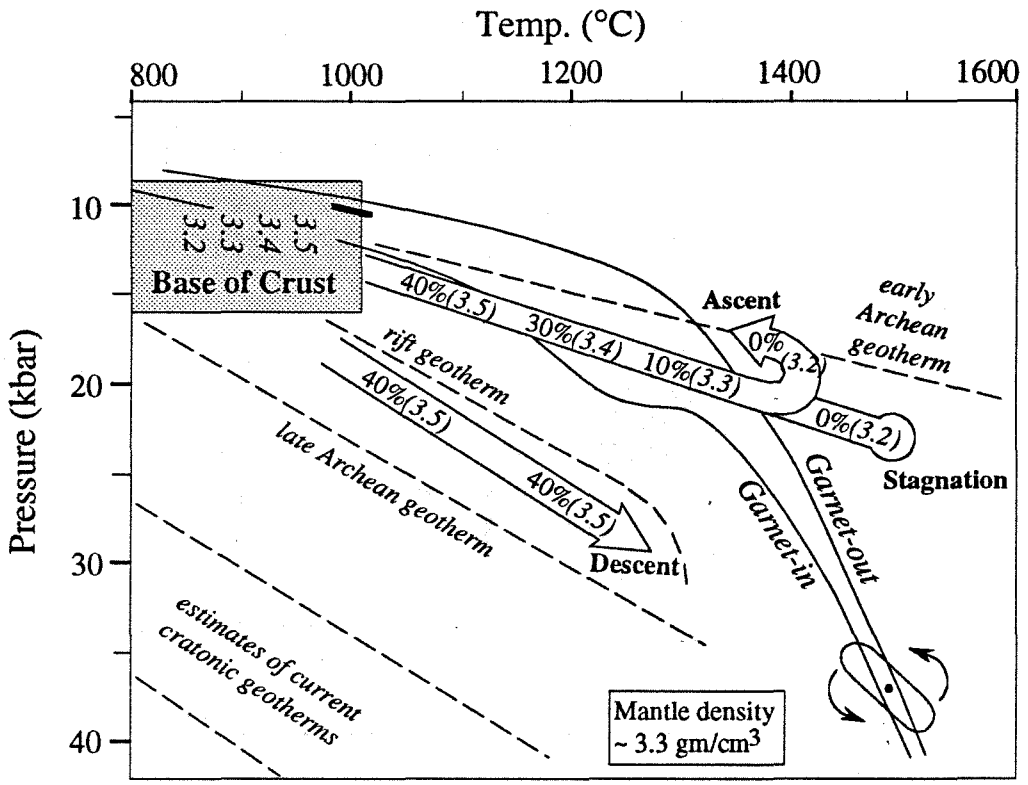

Fig. 5.3. Schematic diagram illustrating the relationships between garnet mode (number in front of parentheses) and restite density (italicized number in parentheses; restite composed of garnet and clinopyroxene) based on the results from this study. The delamination and sinking of restitic masses might follow one of the three paths shown, depending on body size and thermal structure of lithosphere and mantle. Intersection with the garnet-out curve decreases the restite density as garnet reacts out. The restite may stagnate or rise back up. "Pinwheeling" may occur if a mass only partially penetrates the region of garnet-out reaction. Lower portion of mass will become less dense than garnet-bearing upper portion, and the entire unstable body may flip over. Geotherms after those in Fig. 4.16.

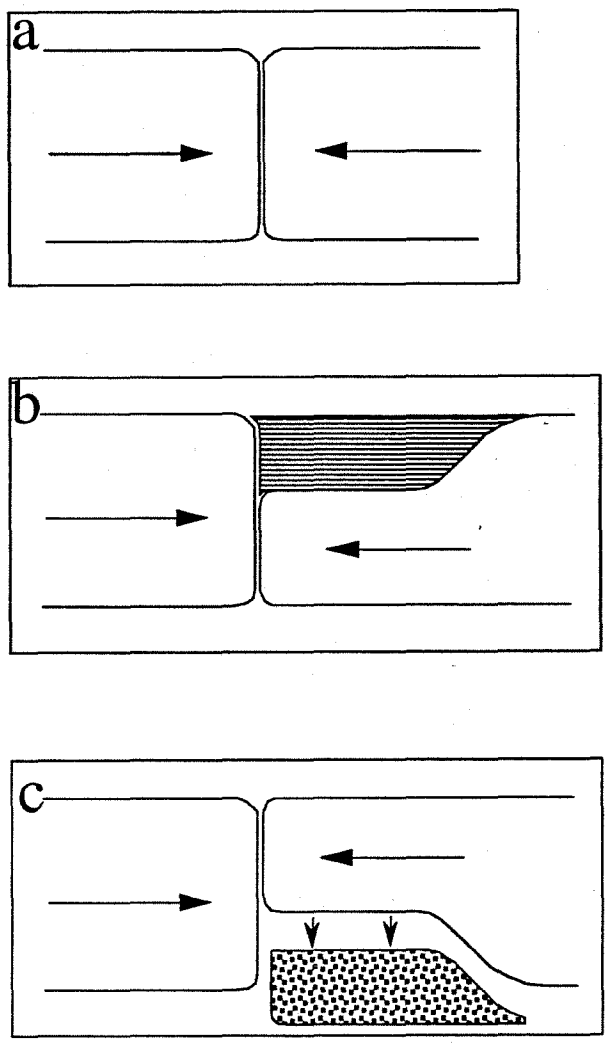

Fig. 5.4a-c. Schematic diagrams showing continent-continent collisions. [a] continents of equal thickness and thus equal strength. [b] one continental borderland thinned and weakened by a deep, sedimentary basin in the upper crust. [c] one continental borderland thinned and weakened by delamination of the garnet-rich lower crust. Thus, the composition of lower crust and related mineralogical and physical changes may influence the styles of tectonism during subsequent periods of collision and deformation.

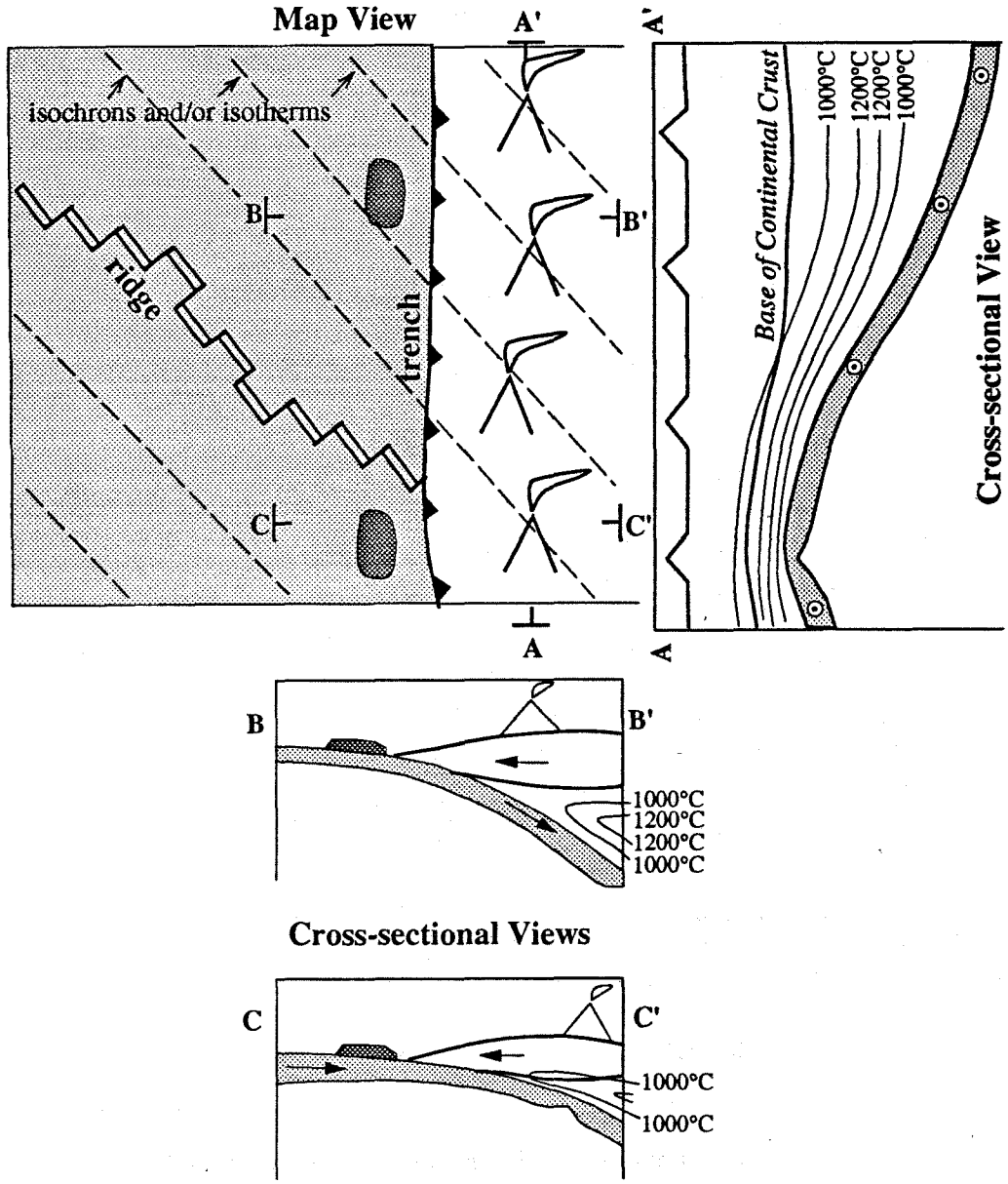

Fig. 5.5. Schematic diagrams showing the possible consequences of subduction of oceanic crust of different ages and temperatures on the basal thermal structure of the overriding plate. Map view depicts the oblique subduction of a ridge. Dashed lines record regions of similar age and temperature on the unsubducted and subducted portions of the oceanic crust (light shading). The darker shaded masses are seamounts. The volcanic arc is represented by triangles. Cross-sectional views show depth and thermal structures due to oblique subduction. Isotherms are shifted upward into the base of the upper plate as the hotter, shallower ridge passes beneath. Garnet growth and subsequent delamination of garnet-rich amphibolitic crust may result in thinning of the arc base. Significant lengths of the lower arc might be thinned during triple junction migration.

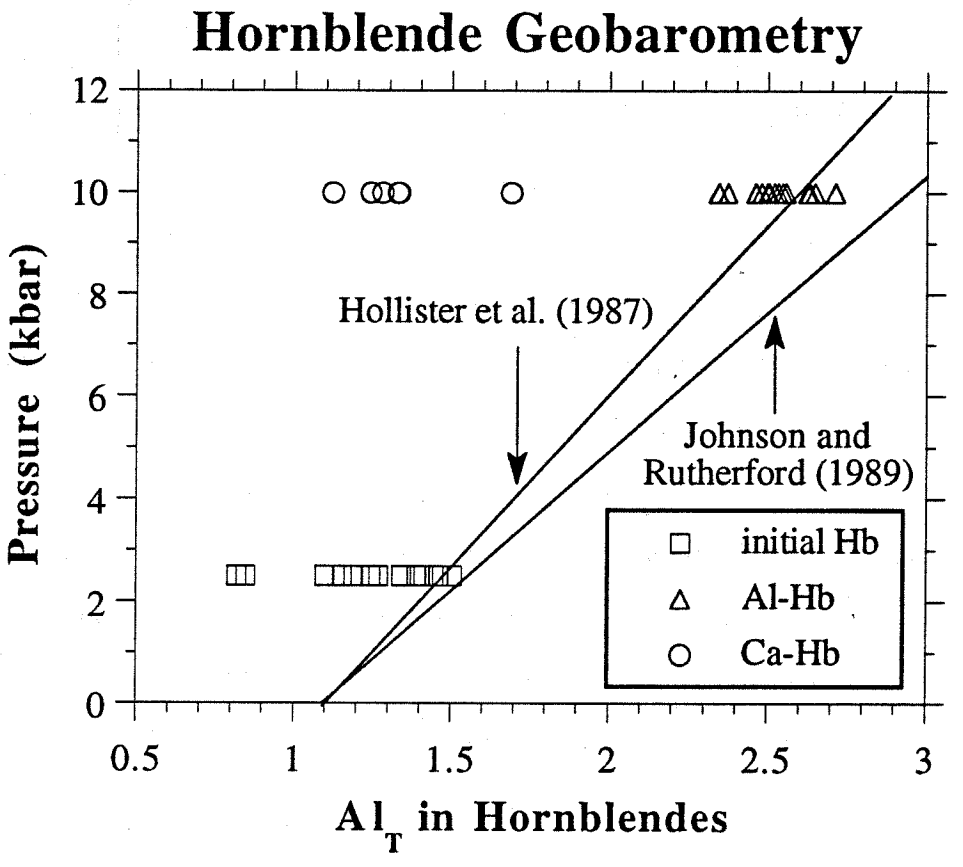

Fig. 5.6. Total alumina (Al_T) in hornblendes as a function of pressure, extended to high pressures (after Hammarstrom and Zen 1986; Hollister et al. 1987; and Johnson and Rutherford 1989). Initial hornblende compositions plotted at 2.5 kbar based on field relationships of amphibolite and hornblende geobarometry (Wolf and Saleeby 1990, 1991). The new hornblendes (Ca-Hb and Al-Hb) that were grown in the 10 kbar amphibolite dehydration-melting runs are plotted at 10 kbar. Total alumina in Al-Hb agrees with the geobarometer of Hollister et al. (1987) even though the mineral assemblage in the amphibolite melting experiments does not include many of the thermodynamically critical phases. Ca-Hb appears to be a metastable product.

REFERENCES

Aldiss DT (1978) Granitic rocks of ophiolites. Ph.D. Thesis, Earth Sciences, the Open University, 135 p

Allen JC, Boettcher AL (1978) Amphiboles in andesite and basalt: II. Stability as a function of P-T-$f(H_2O)$-f_{O_2}. Am Mineral 63:1074-1087

Allen JC, Boettcher AL (1983) The stability of amphibole in andesite and basalt at high pressures. Am Mineral 68:307-314

Armstrong JT (1988) Quantitative analysis of silicate and oxide materials: comparison of Monte Carlo, ZAF, and $\phi(\rho z)$ procedures. Microbeam Analysis 239-246

Arth JG (1979) Some trace elements in trondhjemites – their implications to magma genesis and paleotectonic setting. In: Barker F (ed) Trondhjemites, dacites, and related rocks. Elsevier, Amsterdam, pp 123-132

Arth JG, Barker F (1976) Rare-earth partitioning between hornblende and dacitic liquid and implications for the genesis of trondhjemitic-tonalitic magmas. Geology 4:534-536

Arth JG, Hanson GN (1972) Quartz diorites derived by partial melting of eclogite or amphibolite at mantle depths. Contrib Mineral Petrol 37:161-174

Arzi AA (1978) Critical phenomena in the rheology of partially melted rocks. Tectonophysics 44:173-84

Baker DR, Eggler DH (1987) Compositions of anhydrous and hydrous melts coexisting with plagioclase, augite, and olivine or low-Ca pyroxene from 1 atm to 8 kbar: application to the Aleutian volcanic center of Atka. Am Mineral 72:12-28

Barker F (1979) Trondhjemite: definition, environment and hypotheses of origin. In: Barker F (ed) Trondhjemites, dacites and related rocks. Elsevier, Amsterdam, pp 1-12

Barker F, Arth JG (1976) Generation of trondhjemitic-tonalitic liquids and Archean bimodel trondhjemite-basalt suites. Geology 4:596-600

Barker F, Arth JG, Millard HT Jr (1979a) Archean trondhjemites of the southwestern Big Horn Mountains, Wyoming: a preliminary report. In: Barker F (ed) Trondhjemites, dacites, and related rocks. Elsevier, Amsterdam, pp 401-414

Barker F, Millard HT Jr, Lipman PW (1979b) Four low-K siliceous rocks of the western U.S.A.. In: Barker F (ed) Trondhjemites, dacites, and related rocks. Elsevier, Amsterdam, pp 415-433

Barnicoat AC, O'Hara MJ (1979) High temperature pyroxenes from ironstones at Scourie, Sutherland. Mineral Mag 43:371-375

Beard JS (1990) Partial melting of metabasites in the contact aureoles of gabbroic plutons in the Smartville complex, Sierra Nevada, California. In: Anderson JL (ed) The nature and origin of cordilleran magmatism, Geol Soc Am Memoir 174, pp 303-313

Beard JS, Borgia A (1989) Temporal variation of mineralogy and petrology in cognate gabbroic enclaves at Arenal volcano, Costa Rica. Contrib Mineral Petrol 103:110-122

Beard JS, Lofgren GE (1989) Effect of water on the composition of partial melts of greenstone and amphibolite. Science 244:195-197

Beard JS, Lofgren GE (1991) Dehydration melting and water-saturated melting of basaltic and andesitic greenstones and amphibolites at 1, 3 and 6.9 kb. J Petrol 32:365-401

Beard JS, Rushmer T (1990) Significance of the hornblende hornfels to pyroxene hornfels transition in metamorphosed subalkaline basalts and andesites: experimental constraints. Geol Soc Am Abstracts with Prog 22:124

Beere W (1975) A unifying theory of the stability of penetrating liquid phases and sintering pores. Acta Metall 23:131-138

Bence AE, Albee AL (1968) Correction factors for electron probe microanalysis of silicates and oxides. J Geology 76:382-403

Bergantz GW (1990) Melt fraction diagrams: the link between chemical and transport models. In: Nicholls J, Russell JK (eds) Modern methods of igneous petrology. Mineral Soc Am, Reviews Mineral 24:239-257

Bird P (1979) Continental delamination and the Colorado Plateau. J Geophys Res 84:7561-7571

Blundy JD, Holland TJB (1990) Calcic amphibole equilibria and a new amphibole-plagioclase geothermometer. Contrib Mineral Petrol 104:208-224

Boettcher AL (1973) Volcanism and orogenic belts – the origin of andesites. Tectonophysics 17:204-233

Boettcher AL, Wyllie PJ (1968) The quartz-coesite transition measured in the presence of a silicate liquid and calibration of piston-cylinder apparatus. Contrib Mineral Petrol 17:224-232

Bohlen SR (1991) On the formation of granulites. J Metamorphic Geol 9:223-229

Bohlen SR, Mezger K (1989) Origin of granulite terranes and the formation of the lowermost continental crust. Science 244:326-329

Boudier F, Nicolas A (1977) Structural controls on partial melting in the Lanzo peridotites. Oregon Dept Geol Mineral Indust, Bull 96:63-78

Boyd FR, England JL (1960) Apparatus for phase-equilibrium measurements at pressures to 50 kilobars and temperatures up to 1750°C. J Geophys Res 65:741-748

Boyd FR, Bell PM, England JL, Gilbert MC (1967) Pressure measurement in single-stage apparatus. Carnegie Inst Washington, Yearbook 65:410-414

Boyd FR, Gurney JJ (1986) Diamonds and the African lithosphere. Science 232:472-477

Brearley AJ (1987) An experimental and kinetic study of the breakdown of aluminous biotite at 800°C: reaction microstructures and mineral chemistry. Bull Mineral 110:513-532

Brodie KH, Rutter EH (1985) On the relationship between deformation and metamorphism, with special reference to the behavior of basic rocks. In: Thompson AB and Rubie DC (eds) Metamorphic reactions, Adv Phys Geochem, vol 4. Springer-Verlag, New York pp 138-179

Brophy JG (1989) Can high-alumina arc basalt be derived from low-alumina arc basalt? Evidence from Kanaga Island, Aleutian arc, Alaska. Geology 17:333-336

Brophy JG, Marsh BD (1986) On the origin of high-alumina arc basalt and the mechanic of melt extraction. J Petrol 27:763-789

Brown GC, Fyfe WS (1970) The production of granitic melts during ultrametamorphism. Contrib Mineral Petrol 28:310-318

Bulau JR, Waff HS, Tyburczy JA (1979) Mechanical and thermodynamic constraints on fluid distribution in partial melts. J Geophys Res 84:6102-6108

Burnham CW (1979) Magmas and Hydrothermal Fluids. In: Barnes HL (ed) Geochemistry of hydrothermal ore deposits. 2nd ed, Wiley Interscience, New York, pp 71-136

Burns LE (1985) The Border Ranges ultramafic and mafic complex, south-central Alaska: cumulate fractionates and island arc volcanics. Can J Earth Sci 22:1028-1038

Burton KW, O'Nions RK (1990) The timescale and mechanism of granulite formation at Kurunegala, Sri Lanka. Contrib Mineral Petrol 106:66-89

Büsch W, Schneider G, Mehnert KR (1974) Initial melting at grain boundaries. Part II: Melting in rocks of granodioritic, quartzdioritic and tonalitic composition. N Jb Miner Mh 8:345-370

Bussod GYA, Williams DR (1991) Thermal and kinematic model of the southern Rio Grande rift: inferences from crustal and mantle xenoliths from Kilbourne Hole, New Mexico. Tectonophys 197:373-389

Carroll M, Wyllie PJ (1990) The system tonalite-H_2O at 15 kbar and the genesis of calc-alkaline magmas. Am Mineral 75:345-357

Cashman KV (1990) Textural constraints on the kinetics of crystallization of igneous rocks. In: Nicholls J, Russell JK (eds) Modern methods of igneous petrology. Mineral Soc Am, Reviews Mineral 24:259-314

Cashman KV, Marsh BD (1988) Crystal size distribution (CSD) in rocks and the kinetics and dynamics of crystallization: II. Makaopuhi lava lake. Contrib Mineral Petrol 99:292-305

Cawthorn RG, O'Hara MJ (1976) Amphibole fractionation in calc-alkaline magma genesis. Am J Sci 276:309-329

Clemens JD (1984) Water contents of silicic to intermediate magmas. Lithos 17:273-287

Clemens JD (1989) Granulites still being formed. Nature 342:228-229

Clemens JD, Vielzeuf D (1987) Constraints on melting and magma production in the crust. Earth Planet Sci Letts 86:287-306

Coleman RG, Peterman ZE (1975) Oceanic plagiogranite. J Geophys Res 80:1099-1108

Cooper RF, Kohlstedt DL (1984) Solution-precipitation enhanced diffusional creep of partially molten olivine-basalt aggregates during hot-pressing. Tectonophysics 107:207-233

Dasgupta S, Sengupta P, Fukuoka M, Bhattacharya PK (1991) Mafic granulites from the Eastern Ghats, India: further evidence for extremely high temperature crustal metamorphism. J Geology 99:124-133

DeBari SM, Sleep NH (1991) High-Mg, low-Al composition of the Talkeetna island arc, Alaska: implications for primary magmas and the nature of arc crust. Geol Soc Am Bull 103:37-47

Deer WA, Howie RA, Zussman J (1983) An introduction to the rock forming minerals. Longman, Essex, 528 p

Defant MJ, Drummond MS (1990) Derivation of some modern arc magmas by melting of young subducted lithosphere. Nature 347:662-665

Dell'Angelo LN, Tullis J (1988) Experimental deformation of partially melted granitic aggregates. J Metamorphic Geol 6:495-515

Dewey JF (1986) Diversity in the lower continental crust. In: Dawson JB, Carswell DA, Hall J, Wedepohl KH (eds) The nature of the lower continental crust. Geol Soc Spec Pub 24:71-78

DeVore GW (1981) The role of partial melting of oxidized and leached basalts on the origin of continents. Indian J Earth Sci 8:87-98

DeVore GW (1982) A note on the role of submarine alterations of basalt on generating trondhjemitic partial melts. Indian J Earth Sci 9:29-36

Drummond MS, Defant MJ (1990) Trondhjemite-tonalite-dacite (TTD) genesis via partial melting of the subducting slab: a uniformitarianism model for crustal growth. Trans Am Geophys Union (EOS) 71:1715

Eggler DH (1972) Amphibole stability in H_2O-undersaturated calc-alkaline melts. Earth Planet Sci Letts 15:28-34

Eggler DH (1973) Principles of melting of hydrous phases in silicate melt. Carnegie Inst Washington, Yearb 72:491-495

Ellis DJ (1983) The Napier and Rayner Complexes of Enderby Land, Antarctica: contrasting styles of metamorphism and tectonism. In: Oliver RL, James PR, Jago JB (eds) Antarctic geoscience. Cambridge Univ Press, Cambridge, pp 20-24

Ellis DJ (1986) Garnet-liquid Fe^{2+}-Mg equilibria and implications for the beginning of melting in the crust and subduction zones. Am J Sci 286:765-791

Ellis DJ (1987) Origin and evolution of granulites in normal and thickened crust. Geology 15:167-170

Ellis DJ, Green DH (1979) An experimental study of the effect of Ca upon garnet-clinopyroxene Fe-Mg exchange equilibria. Contrib Mineral Petrol 71:13-22

Ellis DJ, Thompson AB (1986) Subsolidus and partial melting reactions in the quartz-excess $CaO+MgO+Al_2O_3+SiO_2+H_2O$ system under water-excess and water-deficient conditions to 10 kb: some implications for the origin of peraluminous melts from mafic rocks. J Petrol 27:91-121

Faul UH, Waff HS, Chambers J (1990) Refined experimental determination of wetting angles in olivine-basalt partial melts. Trans Am Geophys Union (EOS) 71:1720

Flagler PA, Spray JG (1991) Generation of plagiogranite by amphibolite anatexis in oceanic shear zones. Geology 19:70-73

Fournelle J, Marsh BD (1991) Shishaldin Volcano: Aleutian high-alumina basalts and the question of plagioclase accumulation. Geology 19:234-237

Franz G, Thomas S, Selverstone J (1989) Fluid in eclogites: evidence from high-pressure veins in the Australian Alps. Trans Am Geophys Union (EOS) 70:1377

Fujii N, Osamura K, Takahashi E (1986) Effect of water saturation on the distribution of partial melt in the olivine-pyroxene-plagioclase system. J Geophys Res 91:9253-9259

Fukuyama H (1985) Gabbroic inclusions of Ichinomegata tuff cone: bulk chemical composition. J Fac Sci Univ Tokyo, Sect II, 22:67-80

Fyfe WS (1971) Some thoughts on granitic magmas. In: Newall G, Rast N (eds) Mechanisms of Igneous Intrusions. Geol J Spec Iss 2:201-216

Fyfe WS (1973) The granulite facies, partial melting and the Archaean crust. Phil Trans R Soc London A273:457-462

Ganguly J, Bhattacharya PK (1987) Xenoliths in Proterozoic kimberlites from southern India: petrology and geophysical implications. In: Nixon PH (ed) Mantle xenoliths. Wiley, Chichester, pp 249-265

George RP (1977) Subsolidus deformation mechanisms and hypersolidus creep of peridotite. Oregon Dept Geol Mineral Indust, Bull 96:233-262

German RM (1985) Liquid phase sintering. Plenum, New York

Gill J (1981) Orogenic andesites and plate tectonics. Springer-Verlag, New York, 390 p

Giret A, Bonin B, Leger JM (1980) Amphibole compositional trends in oversaturated and undersaturated alkaline plutonic ring-complexes. Can Mineral 18:481-495

Green TH (1977) Garnet in silicic liquids and its possible use as a P-T indicator. Contrib Mineral Petrol 65:59-67

Green TH (1982) Anatexis of mafic crust and high pressure crystallization of andesite. In: Thorpe RS (ed) Andesites: orogenic andesites and related rocks. Wiley, Chichester, pp 465-487

Green TH, Adam J (1991) Assessment of the garnet-clinopyroxene Fe-Mg exchange thermometer using new experimental data. J Metamorphic Geol 9:341-347

Green TH, Pearson NJ (1985) Experimental determination of REE partition coefficients between amphibole and basaltic to andesitic liquids at high pressure. Geochim Cosmochim Acta 49:1465-1468

Green TH, Ringwood AE (1968) Genesis of the calc-alkaline igneous rock suite. Contrib Mineral Petrol 18:105-162

Griffin WL, O'Reilly SY (1987) The composition of the lower crust and the nature of the continental Moho. In: Nixon PH (ed) Mantle xenoliths. Wiley, London, pp 413-430

Hacker BR (1990) Amphibolite-facies-to-granulite-facies reactions in experimentally deformed, unpowdered amphibolite. Am Mineral 75:1349-1361

Hacker BR, Christie JM (1990) Brittle/ductile and plastic/cataclastic transitions in experimentally deformed and metamorphosed amphibolite. The brittle-ductile transition in rocks, Am Geophys Union Monograph 56:127-147

Hammarstrom JM, Zen E-An (1986) Aluminum in hornblende: an empirical igneous geobarometer. Am Mineral 71:1297-1313

Hanson GN (1980) Rare earth elements in petrogenetic studies of igneous systems. Ann Rev Earth Planet Sci 8:371-406

Hanson GN (1981) Geochemical constraints on the evolution of the early continental crust. Phil Trans R Soc London A301:423-442

Harley SL (1984) An experimental study of the partitioning of Fe and Mg between garnet and orthopyroxene. Contrib Mineral Petrol 86:359-373

Harley SL (1989) The origins of granulites: a metamorphic perspective. Geol Mag 126:215-247

Hayob JL, Essene EJ, Ruiz J, Ortega-Gutierrez F, Aranda-Gómez JJ (1989) Young high-temperature granulites from the base of the crust in Mexico. Nature 342:265-268

Helz RT (1973) Phase relations of basalts in their melting range at P_{H_2O}=5 kb as a function of oxygen fugacity: Part I. mafic phases. J Petrol 14:249-302

Helz RT (1976) Phase relations of basalts in their melting range at P_{H_2O}=5 kb: Part II. melt compositions. J Petrol 17:139-193

Helz RT (1982) Phase relations and compositions of amphiboles produced in studies of the melting behavior of rocks. In: Veblen DR, Ribbe PH (eds) Amphiboles: petrology and experimental phase relations. Mineral Soc Am, Reviews Mineral 9B:279-347

Herring C (1951) Theorems on the free energies of crystal surfaces. Phys Rev 82:87-93

Hildreth W (1981) Gradients in silicic magma chambers; implications for lithospheric magmatism. J Geophys Res 86:10153-10192

Hollister LS, Grissom GC, Peters EK, Stowell HH, Sisson VB (1987) Confirmation of the empirical correlation of Al in hornblende with pressure of solidification of calc-alkaline plutons. Am Mineral 72:231-239

Hollocher K (1991) Prograde amphibole dehydration reactions during high-grade regional metamorphism, central Massachusetts, U.S.A. Am Mineral 76:956-970

Holloway JR (1971) Composition of fluid phase solutes in a basalt-H_2O-CO_2 system. Geol Soc Am Bull 82:233-238

Holloway JR, Burnham CW (1972) Melting relations of basalt with equilibrium water pressure less than total pressure. J Petrol 13:1-29

Huang WL, Wyllie PJ (1973) Melting relations of muscovite-granite to 35 kbar as a model for fusion of metamorphosed subducted oceanic sediments. Contrib Mineral Petrol 42:1-14

Huang WL, Wyllie PJ (1975) Melting reactions in the system $NaAlSi_3O_8$-$KAlSi_3O_8$-SiO_2 to 35 kilobars, dry and with excess water. J Geology 83:737-748

Huang WL, Wyllie PJ (1981) Phase relationships of S-type granite with H_2O to 35 kbar: muscovite granite from Harney Peak, South Dakota. J Geophys Res 86:1015-1029

Huang WL, Wyllie PJ (1986) Phase relationships of gabbro-tonalite-granite-water at 15 kbar with applications to differentiation and anatexis. Am Mineral 71:301-316

Isacks BL, Oliver J, Sykes LR (1968) Seismology and the new global tectonics. J Geophys Res 73:5855-5899

Jackson I, Arculus RJ (1984) Laboratory wave velocity measurements on lower crustal xenoliths from Calcutteroo, South Australia. Tectonophysics 101:185-197

Jahn B-M, Vidal P, Kröner A (1984) Multi-chronometric ages and origin of Archaean tonalitic gneisses in Finnish Lapland: a case for long crustal residence time. Contrib Mineral Petrol 86:398-408

Jambon A, Zimmermann JL (1990) Water in oceanic basalts: evidence for dehydration of recycled crust. Earth Planet Sci Letts 101:323-331

Jiang JX, Lasaga AC (1990) The effect of post growth thermal events on growth-zoned garnet – implications for metamorphic P-T history calculations. Contrib Mineral Petrol 105:454-459

Johannes W (1983) Metastable melting in granite and related systems. In: MP Atherton and CD Gribble (eds) Migmatites, melting and metamorphism. Shiva, Cheshire, pp 27-36

Johnson MC, Rutherford MJ (1989) Experimental calibration of the aluminum-in-hornblende geobarometer with application to Long Valley caldera (California) volcanic rocks. Geology 17:837-841

Johnston AD (1986) Anhydrous P-T phase relations of near-primary high-alumina basalt from the South Sandwich Islands. Contrib Mineral Petrol 92:368-382

Jurewicz SR, Jurewicz AJG (1986) Distribution of apparent angles on random sections with emphasis on dihedral angle measurements. J Geophys Res 91:9277-9282

Jurewicz SR, Watson EB (1984) Distribution of partial melt in a felsic system: the importance of surface energy. Contrib Mineral Petrol 85:25-29

Jurewicz SR, Watson EB (1985) The distribution of partial melt in a granitic system: the application of liquid phase sintering theory. Geochim Cosmochim Acta 49:1109-1121

Kamineni DC, Rao AT (1988) Sapphrine-bearing quartzite from the Eastern Ghats granulite terrane, Vizianagram, India. J Geology 96:209-220

Kars H, Jansen JBH, Tobi AC, Poorter RPE (1980) The metamorphic rocks of the polymetamorphic Precambrian of Rogaland, SW Norway (II). Contrib Mineral Petrol 75:235-244

Kay RW, Kay SM (1980) Chemistry of the lower crust: inferences from magmas and xenoliths. In: Continental tectonics, National Academy of Sciences (Geophysics Study Committee), Washington, D.C., pp 139-159

Kay SM, Kay RW (1985) Role of crystal cumulates and the oceanic crust in the formation of the lower crust of the Aleutian arc. Geology 13:461-464

Kempton PD, Harmon RS, Hawkesworth CJ, Moorbath S (1990) Petrology and geochemistry of lower crustal granulites from the Geronimo Vocanic Field, southeastern Arizona. Geochim Cosmochim Acta 54:3401-3426

Konnikov EG, Tsygankov AA, Zaguzin GN (1990) Find of garnet pyroxenites in the northern Baikal region: geological consequences. Soviet Geol Geophys 31:78-84

Kretz R (1966) Interpretation of the shape of mineral grains in metamorphic rocks. J Petrol 7:68-94

Kretz R (1982) Transfer and exchange equilibria in a portion of the pyroxene quadrilateral as deduced from natural and experimental data. Geochim Cosmochim Acta 46:411-421

Kröner A (1985) Evolution of the Archean continental crust. Ann Rev Earth Planet Sci 13:49-74

Kuno H (1960) High-alumina basalt. J Petrol 1:121-145

Kushiro I (1974) Melting of a hydrous upper mantle and possible generation of andesitic magma: an approach from synthetic systems. Earth Planet Sci Lett 2:294-299

Kushiro I (1990) Partial melting of mantle wedge and evolution of island arc crust. J Geophys Res 95:15929-15939

Kushiro I, Yoder HS (1972) Origin of calc-alkaline peraluminous andesite and dacites. Carnegie Inst Washington, Yearb 71:411-413

Laird J (1980) Phase equilibria in mafic schist from Vermont. J Petrol 21:1-38

Lambert IB, Wyllie PJ (1972) Melting of gabbroic (quartz eclogite) with excess water to 35 kilobars, with geological applications. J Geol 80:693-708

Leake BE (1971) On aluminous and edenitic hornblendes. Mineral Mag 38:389-407

Le Breton N, Thompson AB (1988) Fluid-absent (dehydration) melting of biotite in metapelites in the early stages of crustal anatexis. Contrib Mineral Petrol 99:226-237

Lindsley DH (1983) Pyroxene thermometry. Am Mineral 68:477-493

Lofgren GE (1980) Experimental studies on the dynamic crystallization of silicate melts. In: Hargraves RB (ed) Physics of magmatic processes. University Press, Princton, pp 487-549

Lofgren GE (1983) Effect of heterogeneous nucleation on basaltic textures: a dynamic crystallization study. J Petrol 24:229-255

Mack S, Russell K, Bishop JC, Sholes DA, Augugliaro FR (1986) Lithologic and structural variations in Cretaceous amphibole-rich gabbros in the Sierra Nevada foothills near Fresno. Calif Geology 39:108-113

Malpas J (1977) Petrology and tectonic significance of Newfoundland ophiolites, with examples from the Bay of Islands. Oregon Dept Geol Mineral Indust, Bull 95:13-23

Marsh BD, Fournelle J, Myers JD, Chou I-M (1990) On plagioclase thermometry in island-arc rocks: experiments and theory. In: Spencer RJ and Chou I-M (eds) Geochem Soc Spec Pub 2, pp 65-83

Martin H (1986) Effect of steeper Archean geothermal gradient on geochemistry of subduction-zone magmas. Geology 14:753-756

Martin H (1987) Petrogenesis of Archaean trondhjemites, tonalites, and granodiorites from eastern Finland: major and trace element geochemistry. J Petrol 28:921-953

Mason R (1978) Petrology of the metamorphic rocks. George Allen & Unwin, London, 254 p

Mazzone P, Stewart DC, Hughes JM (1987) Sub-solidus dehydration of amphiboles in an andesitic magma. Contrib Mineral Petrol 97:292-296

McKenzie DP (1984) The generation and compaction of partially molten rock. J Petrol 25:713-765

McKenzie DP (1985) The extraction of magma from the crust and mantle. Earth Planet Sci Lett 74:81-91

McKenzie DP (1987) The compaction of igneous and sedimentary rocks. J Geol Soc London 144:299-307

Mehnert KR, Büsch W, Schneider G (1973) Initial melting at grain boundaries of quartz and feldspar in gneisses and granulites. N Jb Miner Mh 4:165-183

Merrill RB, Robertson JK, Wyllie PJ (1970) Melting relations in the system $NaAlSi_3O_8$-$KAlSi_3O_8$-SiO_2-H_2O to 20 kilobars compared with results for other feldspar-quartz-H_2O and rock-H_2O systems. J Geology 78:558-569

Miller CF, Watson EB, Harrison TM (1988) Perspectives on the source, segregation and transport of granitoid magmas. Trans Royal Soc Edinburgh 79:135-156

Miyashiro A (1973) Metamorphism and metamorphic belts. George Allen & Unwin, London, 492 p

Moment RL, Gordon RB (1964) Energy of grain boundaries in halite. J Am Ceram Soc 47:570-573

Morgan BA (1977) The Baltimore Complex, Maryland, Pennsylvania, and Virginia. Oregon Dept Geol Mineral Indust, Bull 95:41-49

Morse SA, Talley JH (1971) Sapphrine reactions in deep-seated granulites near Wilson Lake, Central Labrador, Canada. Earth Planet Sci Letts 10:325-328

Mukhopadhyay B (1991) Garnet-clinopyroxene geobarometry: the problems, a prospect, and an approximate solution with some applications. Am Mineral 76:512-529

Myers JD (1988) Possible petrogenetic relations between low- and high-MgO Aleutian basalts. Geol Soc Am Bull 100:1040-1053

Myers JD, Frost CD, Angevine CL (1986) A test of a quartz eclogite source for parental Aleutian magmas: a mass balance approach. J Geology 94:811-828

Mysen BO (1982) The role of mantle anatexis. In: Thorpe RS (ed) Andesites: orogenic andesites and related rocks. Wiley, New York, pp 489-522

Nelson SA, Carmichael ISE (1979) Partial molar volumes of oxide components in silicate liquids. Contrib Mineral Petrol 71:117-124

Newton RC (1990) Fluids and shear zones in the deep crust. Tectonophysics 182:21-37

Newton RC, Smith JV, Windley BF (1980) Carbonic metamorphism, granulites and crustal growth. Nature 288:45-50

Nicholls IA (1974) Liquids in equilibrium with peridotitic mineral assemblages at high pressure. Contrib Mineral Petrol 45:289-316

Nicolas A (1990) Melt extraction from mantle peridotites: hydrofracturing and porous flow, with consequences for oceanic ridge activity. In: Ryan MP (ed) Magma transport and storage. Wiley, New York pp 159-173

O'Hara MJ (1976) Data reduction and projection schemes for complex compositions. Prog Exper Petrol NERC London 3:103-126

O'Reilly SY, Griffin WL (1985) A xenolith-derived geotherm for southeastern Australia and its geophysical implications. Tectonophys 111:41-63

Paquet J, Francois P (1980) Experimental deformation of partially melted granitic rocks at 600-900°C and 250 MPa confining pressure. Tectonophysics 68:131-146

Patiño Douce AE, Humphreys ED, Johnston AD (1990) Anatexis and metamorphism in tectonically thickened continental crust exemplified by the Sevier hinterland, western North America. Earth Planet Sci Letts 97:290-315

Patiño Douce AE, Johnston AD (1991) Phase equilibria and melt productivity in the pelitic system: implications for the origin of peraluminous granitoids and aluminous granulites. Contrib Mineral Petrol 107:202-218

Pattison DRM (1991) Infiltration-driven dehydration and anatexis in granulite facies metagabbro, Grenville Province, Ontario, Canada. J Metamorphic Geol 9:315-332

Peacock SM (1990a) Fluid processes in subduction zones. Science 248:329-337

Peacock SM (1990b) Numerical simulation of pressure-temperature-time paths in subduction zones: constraints on slab devolatilization and the origin of arc magmas. Geol Soc Am, Abstracts with Prog 22:A29

Pedersen RB, Malpas J (1984) The origin of oceanic plagiogranites from the Karmoy ophiolite, Western Norway. Contrib Mineral Petrol 88:36-52

Percival JA (1983) High-grade metamorphism in the Chapleau-Foleyet, Ontario. Am Mineral 68:667-686

Peterson JW, Newton RC (1990) Experimental biotite-quartz melting in the KMASH-CO_2 system and the role of CO_2 in the petrogenesis of granites and related rocks. Am Mineral 75:1029-1042

Phillips MW, Popp RK, Clowe CA (1988) Structural adjustments accompanying oxidation-dehydrogenation in amphiboles. Am Mineral 73:500-506

Powell R (1983) Processes in granulite-facies metamorphism. In: MP Atherton and CD Gribble (eds) Migmatites, melting and metamorphism. Shiva, Cheshire, pp 127-139

Powell R (1985) Regression diagnostics and robust regression in geothermobarometer-geobarometer calibration: the garnet-clinopyroxene geothermometer revisited. J Metamorphic Geol 3:231-243

Putnis A, McConnell JD (1980) Principles of mineral behaviour. Blackwell, Oxford, 257 p

Raase P (1974) Al and Ti contents of hornblende, indicators of pressure and temperature of regional metamorphism. Contrib Mineral Petrol 45:231-236

Raleigh CB, Paterson MS (1965) Experimental deformation of serpentinite and its tectonic implications. J Geophys Res 70:3965-3985

Rapp RP (1990) Partial melting of metabasalt at low water contents, and the origin of the Archean continental crust: a summary of experimental evidence. Trans Am Geophys Union (EOS) 71:1714

Rapp RP (1991) Origin of Archean granitoids and continental evolution. Trans Am Geophys Union (EOS) 72:225

Rapp RP, Watson EB, Miller CF (1991) Partial melting of amphibolite/eclogite and the origin of Archean trondhjemites and tonalites. Precambrian Res 51:1-25

Reymer A, Schubert G (1984) Phanerozoic addition rates to the continental crust and crustal growth. Tectonics 3:63-78

Richter FM, McKenzie DP (1984) Dynamical models for melt segregation from a deformable matrix. J Geol 92:729-740

Ringwood AE (1974) The petrological evolution of island arc systems. J Geol Soc London 130:183-204

Ringwood AE, Green DH (1966) An experimental investigation of the gabbro-eclogite transformation and some geophysical implications. Tectonophysics 3:383-427

Robertson JK, Wyllie PJ (1971) Rock-water systems, with special reference to the water-deficient region. Am J Sci 271:252-277

Robinson P (1982) Metamorphosed igneous rocks at high temperature: the breakdown of amphiboles. In: Veblen DR, Ribbe PH (eds) Amphiboles: petrology and experimental phase relations. Mineral Soc Am, Reviews Mineral 9B:182-210

Rock NMS, Leake BE (1984) The international mineralogical association amphibole nomenclature scheme: computerization and its consequences. Mineral Mag 48:211-227

Rubie DC, Brearley AJ (1987) Metastable melting during the breakdown of muscovite + quartz at 1 kbar. Bull Mineral 110:533-549

Rubie DC, Thompson AB (1985) Kinetics of metamorphic reactions at elevated temperatures and pressures: an appraisal of available experimental data. In: Thompson AB, Rubie (eds) Metamorphic reactions, Adv Phys Geochem, vol 4. Springer-Verlag, New York pp 27-79

Rudnick RL, McLennan SM, Taylor SR (1985) Large ion lithophile elements in rocks from high-pressure granulite facies terrains. Geochim Cosmochim Acta 49:1645-1655

Rudnick RL, Taylor SR (1986) Geochemical constraints on the origin of Archaean tonalitic-trondhjemitic rocks and implications for lower crustal composition. In: Dawson JB, Carswell DA, Hall J, Wedepohl KH (eds) The nature of the lower continental crust, Geol Soc Spec Pub 24:179-191

Rudnick RL, Taylor SR (1987) The composition and petrogenesis of the lower crust: a xenolith study. J Geophys Res 92:13981-14055

Rushmer T (1987) Fluid-absent melting of amphibolite: experimental results at 8 kbar. Terra Cognita 7:286

Rushmer T (1991) Partial melting of two amphibolites: contrasting experimental results under fluid-absent conditions. Contrib Mineral Petrol 107:41-59

Rutter EH, Brodie KH (1985) The permeation of water into hydrating shear zones. In: Thompson AB and Rubie DC (eds) Metamorphic reactions, Adv Phys Geochem, vol 4. Springer-Verlag, New York pp 242-250

Rutter MJ, Wyllie PJ (1988) Melting of vapour-absent tonalite at 10 kbar to simulate dehydration-melting in the deep crust. Nature 331:159-160

Rutter MJ, Van der Laan SR, Wyllie PJ (1989) Experimental data for a proposed empirical igneous geobarometer: aluminum in hornblende at 10 kbar pressure. Geology 17:897-900

Sandiford MA (1985) Metamorphic evolution of granulites at Fyfe Hills: implications for Archaean crustal thickness. J Metamorphic Geol 3:155-178

Sandiford MA, Powell R (1986) Pyroxene exsolution in granulites from Fyfe Hills, Enderby Land, Antarctica: evidence for 1000°C temperatures in Archaean continental crust. Am Mineral 71:946-954

Sandiford MA, Neall FB, Powell R (1987) Metamorphic evolution of aluminous granulites from Labrador Hills, Uganda. Contrib Mineral Petrol 95:217-225

Sawyer EW (1990) Disequilibrium melting and the melt-residuum separation time in migmatites. Goldschmidt Conf, Baltimore, p 79

Sawyer EW (1991) Disequilibrium melting and rate of melt-residuum separation during migmatization of mafic rocks from the Grenville Front, Quebec. J Petrol 32:701-738

Selverstone J, Franz G, Thomas S (1990) Fluids at high pressure: inferences from 20 kbar eclogites and associated veins in the Tauern Window, Austria. Goldschmidt Conf, Baltimore, p 81

Selverstone J, Spear FS, Franz G, Morteani G (1984) High pressure metamorphism in the SW Tauern Window, Austria: P-T paths from hornblende-kyanite-staurolite-schists. J Petrol 25:501-531

Shaw HR (1972) Viscosities of magmatic silicate liquids: an empirical method of prediction. Am J Sci 272:870-893

Shaw HR (1980) The fracture mechanisms of magma transport from the mantle to the surface. In: Hargraves RB (ed) Physics of magmatic processes, Princeton Univ Press, Princeton, 201-264 pp

Silver L, Stolper E (1985) A thermodynamic model for hydrous silicate melts. J Geol 93:161-178

Sleep NH (1974) Segregation of magma from a mostly crystalline mush. Geol Soc Am Bull 85:1225-1232

Smith CS (1964) Some elementary principles of polycrystalline microstructure. Metall Rev 9:1-47

Smith HD (1974) An experimental study of the diffusion of Na, K, and Rb in magmatic silicate liquids. Ph.D. dissertation, Univ. Oregon

Spear FS (1981) An experimental study of hornblende stability and composition variability in amphibolite. Am J Sci 281:697-734

Spear FS (1982) Phase equilibria of amphibolites from the Post Pond volcanics, Mt. Cube quadrangle, Vermont. J Petrol 23:383-426

Spray JG (1988) Generation and crystallization of an amphibolite shear melt: an investigation using radial friction welding apparatus. Contrib Mineral Petrol 99:464-475

Spry A (1969) Metamorphic textures. Pergamon Press, Oxford, 350 pp

Spulber SD, Rutherford MJ (1983) The origin of rhyolite and plagiogranite in oceanic crust: an experimental study. J Petrol 24:1-25

Stern CR, Wyllie PJ (1978) Phase compositions through crystallization intervals in basalt-andesite-H_2O at 30 kbar with implications for subduction zone magmas. Am Mineral 63:641-663

Streckeisen A (1976) To each plutonic rock its proper name. Earth Sci Rev 12:1-33

Sun S-S (1984) Geochemical characteristics of Archaean ultramafic and mafic volcanic rocks: implications for mantle composition and evolution. In: Kröner A, Hanson GN, Goodwin AM (eds) Archaean geochemistry. Springer-Verlag, Berlin, pp 25-47

Swalin RA (1972) Thermodynamics of solids. Wiley, New York, 387 pp

Taylor HP (1980) Stable isotope studies of spreading centers and their bearing on the origin of granophyres and plagiogranites, in, Colloques Internationaux du C.N.R.S. 272, Orogenic mafic-ultramafic association, pp 149-165

Taylor SR, McLennan SM (1985) The continental crust: its composition and evolution. Blackwell, Oxford, 312 p

Thompson AB (1982) Dehydration melting of pelitic rocks and the generation of H_2O-undersaturated granitic liquids. Am J Sci 282:1567-1595

Thompson AB (1988) Dehydration melting of crustal rocks. Rendiconti Soc Min Pet Italia 43:41-60

Thompson AB (1990) Heat, fluids, and melting in the granulite facies. In: Vielzeuf D and Vidal P (eds) Granulites and crustal evolution. NATO ASI series, vol 311. Kluwer, Dordrecht, pp 37-57

Thompson JB, Laird J, Thompson AB (1982) Reactions in amphibolite, greenschist and blueschist. J Petrol 23:1-27

Toramaru A, Fujii N (1986) Connectivity of melt phase in a partially molten peridotite. J Geophys Res 91:9239-9252

Tuttle OF, Bowen NL (1958) Origin of granite in the light of experimental studies in the system $NaAlSi_3O_8$-$KAlSi_3O_8$-SiO_2-H_2O. Mem Geol Soc Am 74

Van der Molen I, Paterson MS (1979) Experimental deformation of partially-melted granite. Contrib Mineral Petrol 70:299-318

Vernon RH (1970) Comparative grain-boundary studies of some basic and ultrabasic granulites, nodules and cumulates. Scott J Geol 6:337-351

Vernon RH (1976) Metamorphic processes. George Allen & Unwin, London, 247 pp

Vielzeuf D, Holloway JR (1988) Experimental determination of the fluid-absent melting relations in the pelitic system. Contrib Mineral Petrol 98:257-276

von Bargen N, Waff HS (1986) Permeabilities, interfacial areas and curvatures of partially molten systems: Results of numerical computations of equilibrium microstructures. J Geophys Res 91:9261-9276

Waff HS, Bulau JR (1979) Equilibrium fluid distribution in an ultramafic partial melt under hydrostatic stress conditions. J Geophys Res 84:6109-6114

Waff HS, Bulau JR (1982) Experimental studies of near-equilibrium textures in partially molten silicates at high pressures. Adv Earth Planet Sci 12:229-236

Walther JV, Orville PM (1982) Volatile production and transport in regional metamorphism. Contrib Mineral Petrol 79:133-145

Wang Z, Karato S, Fujino K (1991) High temperature creep of garnet. Trans Am Geophys Union (EOS) 72:287

Waters DJ (1988) Partial melting and the formation of granulite facies assemblages in Namaqualand, South Africa. J Metamorphic Geol 6:387-404

Watson EB (1982) Melt infiltration and magma evolution. Geology 10:236-240

Watson EB, Brenan JM (1987) Fluids in the lithosphere, 1. Experimentally-determined wetting characteristics of CO_2-H_2O fluids and their implications for fluid transport, host-rock physical properties, and fluid inclusion formation. Earth Planet Sci Letts 85:497-515

Watson EB, Brenan JM, Baker DR (1990) Distribution of fluids in the continental mantle. In: Menzies M (ed.) Continental Mantle. Clarendon Press, Oxford, pp 111-125

Weber C, Barbey P, Cuney M, Martin H, (1985) Trace element behaviour during migmatization. Evidence for a complex melt-residuum-fluid interaction in the St. Malo migmatitic dome (France). Contrib Mineral Petrol 90:52-62

White AJR, Chappell BW (1977) Ultrametamorphism and granitoid genesis. Tectonophysics 43:7-22

Wickham SM (1987) The segregation and emplacement of granitic magmas. J Geol Soc London 144:281-297

Wickham SM, Oxburgh ER (1987) Low pressure regional metamorphism in the Pyrenees and its implications for the thermal evolution of rifted continental crust. Phil Trans R Soc London A321:219-243

Wilkinson JFG (1982) The genesis of mid-ocean ridge basalt. Earth Sci Rev 18:1-57

Wilks KR, Carter NL (1990) Rheology of some continental lower crustal rocks. Tectonophys 182:57-77

Winther KT (1990) Experimental melting of basalt under high H_2O and CO_2 pressures. unpublished Ph.D. thesis, Univ. Chicago, 266 p

Winther KT, Newton RC (1990) Experimental melting of hydrous low-K tholeiite: evidence on the origin of Archaean cratons. Proceedings Nicholas Steno Symposium, Copenhagen

Winther KT, Steele IM, Newton RC (1989) Experimental melting of high Al, low K-tholeiite at 8-22 kbar H_2O pressures. Trans Am Geophys Union (EOS) 70:506

Wolf MB, Saleeby JB (1990) Crustal extension during the Nevadan orogeny in the southwestern Sierra Nevada Foothills terrane (FT), California. Geol Soc Am Abst with Progms 22:275

Wolf MB, Wyllie PJ (1986) Crystal settling in hydrous syenite melt at 15 kbar. Geol Soc Am Abst with Progms 18:200

Wolf MB, Wyllie PJ (1989) The formation of tonalitic liquids during the vapor-absent partial melting of amphibolite at 10 kb. Trans Am Geophys Union (EOS) 70:506

Wolf MB, Wyllie PJ (1990) Liquid morphology and interconnectivity in solid amphibolite during dehydration-melting at 10 kb. Trans Am Geophys Union (EOS) 71:1714

Wolf MB, Wyllie PJ (1991) Dehydration-melting of solid amphibolite at 10 kbar: textural development, liquid interconnectivity and applications to the segregation of magmas. Mineral and Petrol 44:151-179

Wyllie PJ (1977) Crustal Anatexis: an experimental review. Tectonophysics 43:41-71

Wyllie PJ (1987) Volcanic rocks: boundaries from experimental petrology. Fortschr Mineral 65:249-284

Yardley BWD (1977) An empirical study of diffusion in garnet. Am Mineral 62:793-800

Yardley BWD (1986) Fluid migration and veining in the Connemara schists, Ireland. In: Walther JV and Wood BJ (eds) Fluid-rock interactions during metamorphism, Adv Phys Geochem, vol 5. Springer-Verlag, New York, pp 109-131

Yoder HS (1976) Generation of basaltic magma. Nat Acad Sci, Washington, D.C., 265 p

Yoder HS, Tilley CE (1962) Origin of basalt magmas: an experimental study of natural and synthetic rock systems. J Petrol 3:342-532

Zen E-An (1986) Aluminum enrichment in silicate melts by fractional crystallization: some mineralogic and petrographic constraints. J Petrol 27:1095-1117

Appendix 1. Comparison of normalized glass compositions from SEM-EDS and EMP-WDS analyses.

Run #	SEM 119	sdom:3	EMP 119	sdom:3	SEM 118	sdom:4	EMP 118	sdom:3
SiO2	57.54	0.08	57.48	0.07	65.09	0.10	65.15	0.59
TiO2	0.47	0.03	0.46	0.05	0.30	0.04	0.29	0.02
Al2O3	20.93	0.21	20.39	0.08	19.27	0.17	18.38	0.44
FeO	5.99	0.11	5.90	0.06	3.69	0.09	3.69	0.01
MnO	n.a.	--	0.09	0.01	n.a.	--	0.02	0.01
MgO	3.48	0.09	3.65	0.03	1.99	0.08	2.32	0.28
CaO	9.24	0.13	9.12	0.08	7.91	0.09	8.48	0.46
Na2O	2.07	0.06	2.59	0.03	1.36	0.09	1.31	0.29
K2O	0.28	0.04	0.30	0.00	0.38	0.01	0.33	0.01

Appendix 2. Range in oxide compositions from SEM used to define limits for EMP-ARPA mineral identification

Mineral	Range from/fo	SiO2	Al2O3	FeO	MgO	CaO
Al-Hb	SEM	44-48	14-16	7-12	14-17	10-12
	EMP-ARP	42-50	13-17	6-13	13-18	9-13
Opx	SEM	49-53	2-8	15-19	23-27	1-2
	EMP-ARP	47-55	1-9	14-20	22-28	0-3
Hb	SEM	49-54	5-9	10-13	14-18	12-14
	EMP-ARP	47-56	3-12	9-14	13-19	10-15.5
Ca-Hb	SEM	47-50	6-10	10-12	14-16	15-18
	EMP-ARP	45-52	5-11	9-13	13-17	15.5-19
Cpx	SEM	48-52	3-10	5-10	11-16	19-23
	EMP-ARP	46-54	2-11	4-11	10-17	18-24
Ga	SEM	38-41	20-23	13-20	9-15	7-10
	EMP-ARP	36-43	19-24	12-21	8-16	6-11
Glass	SEM	57-68	18-22	3-7	1-4	7-10
	EMP-ARP	none	14-24	1-9	0-6	2-12
Pl	SEM	43-48	33-36	0-1	0-1	17-20
	EMP-ARP	41-50	32-37	0-2	0-2	16-21

Appendix 3. Average Garnet Compositions from Powder Runs (EMP-ARP)

Run #	118	115	106	109	110	113	117	103	121	119
Temp (C)	875	900	900	925	925	925	950	950	975	975
Time (d)	8	4	9	2	4	8	1	2	1	4
SiO2	40.24	41.44	40.49	40.88	40.65	39.34	41.18	41.45	39.66	40.02
Al2O3	21.73	21.39	20.32	21.54	21.48	21.66	21.81	21.23	22.46	21.44
FeO*	16.65	17.25	18.39	16.67	15.31	14.92	14.46	14.33	14.48	13.62
MgO	11.58	10.79	10.69	11.39	13.04	11.93	13.47	13.47	13.22	14.40
CaO	9.19	9.37	8.79	9.57	8.86	9.30	8.80	9.44	8.03	8.67
Total	99.39	100.25	98.67	100.04	99.34	97.16	99.73	99.92	97.84	98.14
n =	17	5	10	6	30	12	24	51	3	14
mole. %										
Alm	33.9	35.6	37.8	33.9	30.7	31.0	29.1	28.4	30.0	27.0
Pyr	42.1	39.7	39.1	41.2	46.6	44.2	48.3	47.6	48.8	50.9
Gross	24.0	24.8	23.1	24.9	22.8	24.8	22.7	24.0	21.3	22.0

Appendix 4. Electron microprobe analyses (EMP-WDS) of phases.

Mineral	Hb	Hb	Hb	Hb	Hb	Hb	Hb	Hb	Al-Hb	Al-Hb	Al-Hb	Pl	Pl	Pl	Pl
Run #	124s	124s	120	120	118	118	106	106	106	108	113	124s	120	120	118
Temp.(°C)	850	850	850	850	875	875	900	900	900	925	925	850	850	850	875
Time (d)	21	21	8	8	8	8	9	9	9	1	8	21	8	8	8
SiO2	47.71	48.82	48.15	50.46	47.79	48.86	53.48	50.16	51.55	44.23	45.77	45.38	45.87	46.26	44.10
TiO2	0.35	0.16	0.60	0.35	0.51	0.37	0.27	0.31	0.26	0.89	0.58	0.00	0.04	0.02	0.00
Al2O3	10.21	12.05	10.78	7.68	11.37	8.35	9.89	7.73	13.25	14.55	14.19	33.40	32.40	34.60	35.11
FeO	11.30	9.49	10.33	11.53	10.25	11.87	6.93	11.19	11.64	10.63	8.03	0.26	0.90	0.51	0.33
MnO	0.22	0.16	0.23	0.25	0.15	0.25	0.15	0.26	0.28	0.16	0.07	0.01	0.03	0.03	0.00
MgO	13.25	11.38	13.69	15.26	15.51	14.67	8.73	15.45	15.63	14.28	15.49	0.02	0.70	0.03	0.01
CaO	11.50	10.83	13.55	12.54	11.68	13.04	14.64	12.55	8.57	10.79	10.98	18.03	18.46	18.42	19.59
Na2O	1.05	1.28	1.02	1.07	1.77	1.25	0.72	1.18	0.27	2.14	2.16	1.24	0.84	1.37	0.54
K2O	0.17	0.18	0.09	0.12	0.12	0.13	0.18	0.11	0.07	0.15	0.13	0.01	0.04	0.02	0.00
Total	95.80	94.37	98.47	99.25	99.17	98.80	95.02	98.94	101.51	97.83	97.39	98.38	99.30	101.25	99.69
Ions/ X (O)	23	23	23	23	23	23	23	23	23	23	23	32	32	32	32
Si	6.997	7.144	6.876	7.156	6.761	7.010	7.674	7.134	6.988	6.375	6.526	8.513	8.558	8.445	8.201
Al4	1.003	0.856	1.124	0.844	1.239	0.990	0.326	0.866	1.012	1.625	1.474	7.385	7.125	7.445	7.696
Al6	0.762	1.222	0.690	0.440	0.657	0.422	1.347	0.429	1.105	0.847	0.911	--	--	--	--
Ti	0.039	0.018	0.064	0.037	0.054	0.040	0.029	0.033	0.027	0.096	0.062	0.000	0.006	0.003	0.000
Fe	1.386	1.161	1.234	1.367	1.213	1.424	0.832	1.331	1.320	1.281	0.958	0.041	0.140	0.078	0.051
Mn	0.027	0.020	0.028	0.030	0.018	0.030	0.018	0.031	0.032	0.020	0.008	0.002	0.005	0.005	0.000
Mg	2.897	2.482	2.914	3.226	3.271	3.138	1.867	3.276	3.158	3.069	3.293	0.006	0.195	0.008	0.003
Ca	1.807	1.698	2.073	1.905	1.770	2.004	2.251	1.912	1.245	1.666	1.677	3.624	3.690	3.603	3.903
Na	0.299	0.363	0.282	0.294	0.486	0.348	0.200	0.325	0.071	0.598	0.597	0.451	0.304	0.485	0.195
K	0.032	0.034	0.016	0.022	0.022	0.024	0.033	0.020	0.012	0.028	0.024	0.002	0.010	0.005	0.000

EMP-WDS = electron microprobe using wave-length dispersive spectrometers: 15 keV, 5 nA, spot (~2 microns dia.) beam for minerals, 10 micron diameter beam for glass analyses. Counting times were 60 seconds. Na2O and K2O were analyzed first.

Appendix 4 (cont.). Electron microprobe analyses (EMP-WDS) of phases.

Mineral	Pl	Pl	Pl	Pl	Cpx	Cpx	Cpx	Cpx	Opx	Opx	Opx	Ga	Ga	Ga	Ga
Run #	106	108	113	119	120	118	113	119	108	108	108	120	120	118	106
Temp.(°C)	900	925	925	975	850	875	925	975	925	925	925	850	850	875	900
Time (d)	9	1	8	4	8	8	8	4	1	1	1	8	8	8	9
SiO2	47.66	45.37	46.83	46.37	51.60	51.35	51.31	49.97	48.64	49.88	48.79	40.60	40.20	40.77	40.93
TiO2	0.00	0.01	0.00	0.04	0.29	0.29	0.23	0.35	0.14	0.16	0.14	0.72	0.59	0.46	0.50
Al2O3	33.43	33.88	33.41	34.24	5.03	5.95	5.88	8.58	9.53	7.53	9.38	22.22	21.94	22.33	21.75
FeO	0.29	0.27	0.40	0.45	9.62	7.51	7.12	9.20	16.57	16.31	15.87	19.12	18.67	16.78	18.95
MnO	0.00	0.02	0.02	0.02	0.32	0.19	0.16	0.27	0.35	0.35	0.30	1.06	0.94	0.50	0.90
MgO	0.01	0.00	0.01	0.04	14.30	14.03	14.02	13.82	23.42	23.68	22.28	10.08	10.07	11.31	10.01
CaO	17.38	18.46	17.83	18.57	20.34	21.62	21.40	18.78	1.14	2.03	3.01	8.62	8.97	9.28	9.02
Na2O	2.07	1.29	1.74	1.20	0.30	0.33	0.34	0.46	0.02	0.06	0.21	0.02	0.01	0.01	0.02
K2O	0.00	0.01	0.01	0.02	0.00	0.00	0.00	0.00	0.01	0.00	0.02	0.00	0.00	0.01	0.00
Total	100.85	99.31	100.24	100.97	101.82	101.27	100.46	101.44	99.82	99.08	99.62	102.44	101.38	101.44	102.08
Ions/ X (O)	32	32	32	32	6	6	6	6	6	6	6	24	24	24	24
Si	8.700	8.444	8.618	8.486	1.885	1.873	1.882	1.820	1.772	1.816	1.779	5.988	5.988	6.004	6.053
Al4	7.192	7.432	7.247	7.385	0.115	0.127	0.118	0.180	0.228	0.184	0.221	0.012	0.012	0.000	0.000
Al6	--	--	--	--	0.102	0.129	0.136	0.188	0.182	0.139	0.182	3.850	3.840	3.876	3.791
Ti	0.000	0.001	0.000	0.006	0.008	0.008	0.006	0.010	0.004	0.004	0.004	0.080	0.066	0.051	0.056
Fe	0.044	0.042	0.062	0.069	0.294	0.229	0.218	0.280	0.505	0.497	0.484	2.358	2.326	2.066	2.344
Mn	0.000	0.003	0.003	0.003	0.010	0.006	0.005	0.008	0.011	0.011	0.009	0.132	0.119	0.062	0.113
Mg	0.003	0.000	0.003	0.011	0.779	0.763	0.766	0.750	1.272	1.285	1.211	2.216	2.236	2.483	2.207
Ca	3.399	3.681	3.516	3.641	0.796	0.845	0.841	0.733	0.045	0.079	0.118	1.362	1.432	1.464	1.429
Na	0.733	0.466	0.621	0.426	0.021	0.023	0.024	0.032	0.001	0.004	0.015	0.006	0.003	0.003	0.006
K	0.000	0.002	0.002	0.005	0.000	0.000	0.000	0.000	0.000	0.000	0.001	0.000	0.000	0.002	0.000

Appendix 4 (cont.). EMP-WDS analyses of phases. Liquid oxides normalized to 100.

Mineral	Ga	Ga	Ga
Run #	108	113	119
Temp.(°C)	925	925	975
Time (d)	1	8	4
SiO2	40.19	40.99	42.29
TiO2	0.58	0.27	0.32
Al2O3	21.72	22.17	23.08
FeO	17.64	17.58	13.60
MnO	0.74	0.54	0.33
MgO	11.23	12.10	15.15
CaO	8.48	7.18	7.40
Na2O	0.00	0.01	0.01
K2O	0.00	0.00	0.00
Total	100.59	100.84	102.18
Ions/ X (O)	24	24	24
Si	5.996	6.055	6.040
Al4	0.004	0.000	0.000
Al6	3.816	3.860	3.885
Ti	0.065	0.030	0.034
Fe	2.201	2.172	1.624
Mn	0.094	0.068	0.040
Mg	2.498	2.664	3.226
Ca	1.356	1.136	1.132
Na	0.000	0.003	0.003
K	0.000	0.000	0.000

Run #	124s	118	sdm:3	113	sdm:3	119
Temp. (°C)	850	875		925		975
time (days)	21	8		8		4
SiO2	68.78	65.15	0.73	57.33	0.73	57.48
TiO2	0.09	0.29	0.02	0.42	0.02	0.46
Al2O3	17.59	18.38	0.54	20.15	0.54	20.39
FeO	3.61	3.69	0.02	5.61	0.14	5.90
MnO	0.13	0.02	0.01	0.13	0.03	0.09
MgO	1.05	2.32	0.34	3.93	0.60	3.65
CaO	6.77	8.48	0.56	9.61	0.70	9.12
Na2O	1.42	1.31	0.36	2.50	0.17	2.59
K2O	0.54	0.33	0.01	0.30	0.02	0.30
Cl	0.03	0.02	0.01	0.03	0.00	0.02
Total*	87.57	86.24	1.18	92.65	0.54	92.34
CIPW Norm						
Q	39.3	31.8		11.7		12.1
or	3.2	2.0		1.8		1.8
ab	12.0	11.1		21.2		21.9
an	33.6	42.1		42.9		43.1
C	2.4	0.5		0.0		0.0
di	0.0	0.0		4.0		1.8
hy	9.3	12.1		17.7		18.5
il	0.2	0.6		0.8		0.9

sdm:# = standard deviation of the mean of n=# analyses. (124s is a single analysis).
Total* = unnormalized total

PART II. INTRODUCTION

The western Sierra Nevada metamorphic belt in California is composed of Paleozoic and Mesozoic volcanic and sedimentary sequences that generally are older and of greater continental margin affinity toward the east. The belt has been subdivided into different sub-belts (e.g., structural blocks, terranes) based on different criteria (Clark, 1964; Saleeby, 1981, 1990b; Schweickert et al., 1984; Day et al., 1985; Edelman and Sharp, 1989). Rocks throughout the metamorphic belt have been folded and faulted during the Late Jurassic Nevadan orogeny and have a north-northwest-trending regional fabric. Steeply dipping, north-northwest-trending fault boundaries, such as the Bear Mountains and Melones fault zones – commonly containing blocks of serpentinized, Paleozoic, ophiolitic melange – divide or separate most of the terranes in the northern half of the metamorphic belt, north of ~37°30'. To the south, extensive intrusion of Cretaceous plutons of the Sierra Nevada batholith has left remaining only isolated fragments, or pendants, of the pre-Cretaceous rocks.

Studies of all aspects of these terranes, especially those that focused on the interrelationship of the magmatic and tectonic histories, have given us an understanding of the petrotectonic environment along the western edge of North America. The presence of dike swarms throughout these terranes records complex spatial and temporal patterns of extension and compression with significant tangential components of motion along the metamorphic belt, and is a testament to the coupling of magmatic and tectonic events. Such alternating phases of tectonism have been referred to as cycles of transtension and transpression (Saleeby, 1981) and are now recognized as important Cordilleran-wide phenomena (Saleeby, 1983; Beck, 1983; Oldow et al., 1989). The regional tectonics of six California Cordilleran dike swarms (Preston Peak, Smartville, Folsom, Sonora, Owens Mountain - Santa Cruz Mountain and Independence; Fig. 1) and the

transtensional-transpressional cycles may be related to the absolute motion of North America through paleomagnetic apparent polar wander analysis (e.g., May and Butler, 1986). The previously unrecognized Owens Mountain dike swarm/shear zone is the focus of this paper.

The nature of dike emplacement and the composition of the dikes are a function of the petrotectonic environment. Dikes emplaced within ophiolite sequences are predominantly mafic and can make up 100% of regionally extensive areas in which new lithosphere is generated (e.g., Moores, 1982). In contrast, a significant portion of the dikes emplaced within rifted arcs, along transforms at the margins of spreading basins or into continental crust can be felsic. The extent of sheeted structure in these environments may be greatly reduced because the dikes intrude into preexisting crustal basement. The magmas can be modified by the wallrocks, but the felsic composition is mostly the result of a greater degree of differentiation within the thicker or slower-rifting crust. Distinguishing between host and dike material can be problematic, especially if subsequent metamorphism and deformation takes place. As part of an intra- or fore-arc rift environment, the Cordilleran dike swarms span these structural and compositional ranges: from ~100% mafic dikes (Folsom) – through predominantly mafic dikes emplaced within older crust (Sonora) – to new felsic and mafic dikes emplaced within older crust (Owens Mountain).

West of the Sierran metamorphic belt, the late Middle Jurassic Coast Range ophiolite probably underlies much of the Great Valley and crops out in the Coast Ranges (Cady, 1975; Hopson et al., 1981). The related Josephine ophiolite lies to the north, in the Klamath Mountains. These ophiolites floored a regionally extensive, rifted fore-arc and/or intra-arc basin (Karig, 1971; Saleeby et al., 1992). Some of the Sierran dike swarms may have been related to these ophiolites as marginal sequences within the rifting fore-arc and arc (Folsom and Smartville dikes). The younger, Late Jurassic dike swarms post-dated the late Middle Jurassic ophiolite formation but were synchronous with its

basin collapse during the Nevadan orogeny. With a change from a transtensional to a transpressional regime, the dike swarms (Sonora, Owens Mountain - Santa Cruz Mountain and Independence dikes) intruded previously disrupted Paleozoic ophiolitic melange, lower Paleozoic continental rise strata, mid-Paleozoic arc rocks, upper Paleozoic to lower Mesozoic chert-argillite melange, Lower to Upper Jurassic arc rocks and overlapping flysch, and, to the southeast, Proterozoic crystalline basement.

Within this Late Jurassic transpressional-transtensional tectonoplutonic regime, lateral motion had a sinistral sense, as North America moved rapidly to the northwest (Oldow et al., 1984; May and Butler, 1986; Saleeby et al., 1992). Motion occurred along regional scale faults such as the Bear Mountains, Melones, Pine Nut, and Mojave-Sonora megashear (Tobisch et al., 1989; Oldow, 1983, Silver and Anderson, 1974; Silver, 1983). Intra-arc fault zones may have been prime hosts for dike emplacement. Dike orientation may have been controlled by fault orientation or preexisting rock fabric (e.g., Owens Mountain - Santa Cruz Mountain and Sonora dikes). Intra-fault, syntectonic dikes should have recorded the episodes of motion within the shear zone, as is the case with the Owens Mountain dikes.

In the present study, mapping, structural, petrographic, geochemical, and geochronologic techniques were employed to better understand the history of the Owens Mountain area and to place it in a regional context. Mapping, structural, petrographic, petrologic, geochemical (whole rock), and geochronologic (U-Pb zircon) techniques were employed to better understand the history of this area and its regional significance. Owens Mountain had been previously mapped by Primrose (1980), but the presence and thus significance of the dikes and the shear zone was unrecognized. In a regional study, MacDonald (1941) assigned all igneous rocks to elements of the Cretaceous plutons. The mapping in the present study was based in part on unpublished reconnaissance work done by Bill Power (1980).

The Owens Mountain area is petrotectonically important in both spatial and temporal senses. The coeval and cogenetic, felsic and mafic dikes formed in a rifting and collapsing fore-arc - arc environment during a major Late Jurassic plate motion change. The timing of dike emplacement at Owens Mountain and the sense of motion within the shear zone are pertinent to understanding the Late Jurassic Nevadan orogeny. The interrelationship between latest Jurassic magmatism and deformation exemplified by these dikes is directly related to the complex plate interactions along the western margin of North America.

GEOLOGICAL SETTING

The westernmost part of the western metamorphic belt is the Foothills terrane, which is further subdivided into western, central and eastern belts – separated by the Bear Mountains and Melones fault zones, respectively (Clark, 1964). Throughout the Foothills terrane, Paleozoic ophiolitic melange bodies crop out along the Bear Mountains and Melones fault zones (e.g., the Tuolumne River complex) and in the cores of the regional-scale anticlines. The Kings River ophiolite comprises a large pendant to the east and southeast of the study area (Saleeby, 1978, 1982). Disrupted Paleozoic ophiolitic melange probably forms the basement of much of the western metamorphic belt (Saleeby, 1981; Saleeby et al., 1992). Stratigraphically above the buried melange basement lie thick sequences of metavolcanic rocks, the Lower Jurassic Peñon Blanco Formation and the similar but younger Logtown Ridge, Copper Hill and Gopher Ridge Formations (Clark, 1964; Bogen, 1985). Slaty flysch of the Upper Jurassic Mariposa and the similar Salt Spring Formations overlies and interfingers with the younger metavolcanic units. The regionally extensive tight folds that expose the various units throughout the belt developed during the Late Jurassic Nevadan orogeny. These folded strata were subsequently intruded by Late Jurassic mafic and felsic magmas, such as the Guadalupe

igneous complex, the Santa Cruz Mountain and Hornitos plutons and associated dikes, and the Owens Mountain dikes and tabular plutons (Tobisch et al., 1989; Saleeby et al., 1989a; Wolf and Saleeby, 1990, 1991). In the Cretaceous period, voluminous plutonism of the Sierra Nevada batholith disrupted the southern portion of the Foothills terrane.

Owens Mountain is located in the west-central foothills of the Sierra Nevada, northeast of Fresno, California (Fig. 1). It is part of the westernmost belt of the Foothills terrane, but separated from most of the Foothills terrane to the northwest by Cretaceous plutons of what has been called the Fresno reentrant of the Sierra Nevada batholith (Saleeby, 1990a). The Owens Mountain study area is of roughly triangular shape about 25 mi^2, surrounded by Cretaceous tonalitic and granitic plutons to the north and east and by Tertiary and Quaternary sediments of the upper Great Valley sequence to the southwest. Mafic and ultramafic rocks of the Kings River ophiolite may extend into the Owens Mountain area as high-grade screens within the dike complex. The area was previously mapped by Primrose (1980), but the presence and thus significance of the dikes and the shear zone was unrecognized. In a regional study, MacDonald (1941) assigned all igneous rocks to elements of the Cretaceous plutons.

The Cretaceous plutons surrounding Owens Mountain consist of the Bass Lake and Academy plutons. The Bass Lake pluton (formerly the Blue Canyon tonalite) is a huge composite pluton comprising over 600 mi^2 of hornblende-biotite tonalite, stretching from east of Owens Mountain to the Foothills terrane and the Guadalupe igneous complex to the northwest (Bateman and Clark, 1974; Stern et al., 1981). The Academy pluton bounds the eastern margin of the Owens Mountain area. It is a arcuate-shaped, multiple intrusion of tonalites, quartz diorites and norites (Mack et al., 1979).

The felsic and mafic dikes of Owens Mountain intruded near-vertically dipping strata of both metavolcanic and metasedimentary rocks. The metavolcanic and metasedimentary rocks are tentatively correlated with the silicic Gopher Ridge volcanics and the Salt Spring slate (slaty flysch) of Clark (1964), which lie to the northwest

(Greenamyer, 1974; Primrose, 1980; Ruiz, 1982). The fossil age of the Salt Spring Formation (equivalent to the Mariposa Formation) is late Oxfordian to early Kimmeridgian, and the lower part of the interfingering Gopher Ridge Formation may be as old as Callovian (Clark, 1964). Deposition of the Mariposa Formation occurred between 160 and 154 Ma (Clark, 1964; Palmer, 1983; Tobisch et al., 1989).

The general structure of the area is a flat-lying, slightly domed, central region of fine-grained, felsic rocks surrounded by vertically dipping metavolcanic, metasedimentary, and mafic and felsic hypabyssal and plutonic rocks, striking E-W in the northeastern area and NNW-SSE in the southwestern area (Fig. 2). The dike swarm comprises the southwestern region, which rises ~1000 ft above the valleys as the Owens Mountain proper. The area has been mapped as an anticline (MacDonald, 1941; Primrose, 1980), but the evidence for such a structure in this area is equivocal, as discussed below.

LITHOLOGY AND PETROGRAPHY

Figure 2 is the geological map of the Owens Mountain area. Designation of the lithologic units based on single lithologies is not wholly satisfactory, because of the interlayered nature of rock types on the meso- and macroscopic scale. The units in Fig. 2 thus are composites of different lithologic layers, and the unit labels denote the predominant lithology, corresponding to an arbitrarily chosen >70% of the unit. Unit boundaries are drawn between large changes in the relative abundances of lithologies and the appearance or disappearance of a particular lithology. The rocks are grouped into fine-grained felsic and mafic units, two metasedimentary units, a metatonalite unit, and a mixed unit, as well as Cretaceous gabbros and granitoids, Quaternary alluvium, and small bodies of ultramafic rocks (not shown).

Ultramafic Rocks

A small number of metamorphosed ultramafic slivers crop out in the northeastern part of the Owens Mountain area and can be traced around the northern border of the Academy pluton. They are fragments of the Paleozoic ophiolitic melange basement that underlie the Foothills terrane and crop out extensively as the Kings River ophiolite just to the east-southeast of the Owens Mountain area (Saleeby, 1977, 1978, 1982). The ultramafic rocks are composed of pods of spinel, chlorite schist, talc and ophicalcite.

Metasedimentary Units

The Biotite Schist unit in the northern part of the Owens Mountain area consists of subequal portions of biotite, muscovite, plagioclase, and quartz (Fig. 2). The foliation is defined by the alignment of fine-grained micas. The rare occurrence of sericitized plagioclase phenocrysts may indicate a volcanic component to these metasediments. Some outcrops contain up to ~50 vol.% coarse-grained leucocratic material that may be partial melts derived by *in situ* melting of the schists or by injection of magma from external sources. A biotite, muscovite (± garnet) phyllite is present on the southwestern side of Owens Mountain (Phyllite unit in Fig. 2).

Mafic Unit

The northern and northeastern parts of the Owens Mountain area are predominantly amphibolites (>70%) interlayered with biotite-muscovite schists and fine-grained felsic rocks (Mafic unit in Fig. 2). Compositional layering is 10-200 cm thick. Mafic layers are also prominent within the Mixed unit (see below). Based on petrographic and compositional data (Wolf, 1992), the amphibolite protoliths probably were hornblende diorites and gabbros and herein are generically designated as mafic rocks.

Metamorphism and deformation have erased many primary features, especially near the Academy pluton, and identifying layers as either flows or dikes is difficult. A few of the mafic layers have fine-grained margins that bound coarser-grained, phenocryst-rich centers – a textural relationship possibly indicative of chilled dike margins. Rare structures somewhat reminiscent of pillows may indicate that a few of the mafic layers are pillow flows. One layer of pillow breccia near the contact with the Biotite Schist unit, though, is well-preserved. In the less deformed areas, there are abrupt but continuous changes between fine-grained amphibolitic and coarse-grained gabbroic textures, characteristic of intrusive diorites (Williams et al., 1982). Most of the mafic rocks have blastoporphyritic textures, containing euhedral phenocrysts of plagioclase (2-6 mm lengths), varying from 5 to 30 vol.%. Textural variation appears to be dependent on the degree of deformation (discussed below). The groundmasses are approximately 50-50 mixes (±10%) of green hornblende and plagioclase, with minor opaque and other accessory minerals. Twinning in the hornblendes and twinning and zoning in the plagioclases are common and are characteristic of an igneous origin (Williams et al., 1982). The plagioclase compositional range is large (oligoclase to anorthite). Clinopyroxene is not common; it is usually found as aggregates of small fragmented pieces, probably the remains of larger phenocrysts. Retrograde alteration in the mafic rocks is minimal.

Based in part on the basaltic compositions (see below) and structural relationships, most of the mafic layers probably are intrusive in origin (rather than a paraamphibolitic origin). This conclusion is most strongly supported within the Mixed unit of the dike swarm (where the mafic layers clearly intrude coarse-grained, tonalitic dikes) as well as the fine-scale layering (cm - m) of very silicic (~74 wt.% SiO_2) and very mafic rocks (~51 wt.% SiO_2) over a structural thickness in excess of 3 km.

Felsic Unit

Very fine-grained silicic rocks, also interlayered with the amphibolites and schists, are predominant in the low-lying, central part of the Owens Mountain area (Felsic unit in Fig. 2). Layering is 10-100 cm thick along the northern contact with the mafic unit, 1-100 cm thick along the southern contact with the Mixed unit of the dike complex, and 100 cm to massive (> a few meters) in the central part of the area. These silicic rocks are composed of recrystallized plagioclase (oligoclase-andesine) and quartz with minor amounts of hornblende, biotite, muscovite, epidote, clinopyroxene, sphene, and oxides. They are buff in color and have a granular texture. Some are rich in pyrite (a few vol.%). Small (2 mm long) sericitized phenocrysts of plagioclase are present in some of the layers. Most of these rocks probably are silicic hypabyssal domes or dikes, but some may be silicic volcanic flows. Compositionally, they are andesitic to rhyolitic. Some silicification has occurred, giving some of the rocks the appearance of quartzite or chert.

Mixed Unit

In the central and southwestern parts of the Owens Mountain area, variably deformed bodies of hornblende metatonalite form much of the resistant layers that form Owens Mountain proper, along with fine-grained, mafic and felsic layers. Where interlayering is in subequal portions of these three lithologies, the rocks are grouped together in a Mixed unit (Fig. 2). More than half of the rocks within the Mixed unit are felsic intrusive rocks (metatonalites). The metatonalites contain subequal portions of quartz and intermediate to calcic plagioclase (andesine-bytownite), and variable amounts of green hornblende (2-20%), clinopyroxene (0-7%), epidote (0-5%), brown biotite (0-3%), sphene (0-3%), orthopyroxene (0-1%), and opaque minerals (0-1%).

Metatonalite Unit

Where identifiable on the scale of the map, larger bodies of metaleucotonalite are distinguished (Metatonalite unit in Fig. 2). The metatonalitic masses range in thickness from a few centimeters to over 100 meters. They are interlayered with fine-grained, mafic and felsic layers centimeters to meters thick. The layers have sharply defined edges. All of these layers can be followed along their lengths for distances of a few meters to a few kilometers. On the southwestern side of Owens Mountain, large bodies of metatonalite (10-100 m thick) crop out between thinly interlayered regions. These larger bodies are composed of zones varying in grain size and degree of deformation. Zones of clearly intrusive rocks gradually grade into zones of rocks with questionable intrusive origins – with textures similar to fine-grained or porphyritic volcanic rocks. Protolith identification would be difficult in these cases if it were not for the obvious relationship with the metatonalites. This subtle textural variation between intrusive and extrusive rocks also have been described in similar rocks to the northwest by Tobisch et al. (1989). In addition to these complications, in some places it is clear that intense deformation has greatly reduced the grain size of tonalitic layers from coarse-grained to very fine-grained. These very fine-grained felsic layers look identical to the rocks of the Felsic unit. Over a period of time, felsic and mafic dikes probably were emplaced into both the older feeder dikes and the folded volcanic strata of similar compositions.

Deformation was moderate to intense. Fabrics vary from slightly foliated through augen gneissic to mylonitic. Some metatonalitic layers are boudinaged or disrupted. Mesoscopic igneous features are present in the moderately deformed bodies (e.g., cross-cutting relationships, presence of xenoliths and evidence for assimilation of proximal layers). Intense deformation in some layers has transposed many of these features.

Mafic Plutons

A number of Cretaceous mafic plutons crop out within the Owens Mountain area. Outcrop sizes range from ~100 m^2 to over 1 km^2, but some outcrops probably belong to the same partially buried body. The predominant rock type is hornblende gabbro, but all outcrops are highly variable in mineralogy, mode, grain size, and texture. Lithologies include hornblendites, olivine to quartz gabbros, norites (±quartz), and diorites (±quartz). There appears to be two general suites, defined by the relative abundances of hornblende and orthopyroxene and clinopyroxene. However, the abundance of primary green hornblende and very calcic plagioclase (andesine to anorthite) is common to most bodies in this area. These types of mafic bodies are common to this foothills region (e.g., Bishop, 1979; Mack et al., 1979, 1986; Saleeby and Sharp, 1980; Snoke et al., 1982; Russell, 1982; Sholes, 1982; Wolf and Saleeby, 1990; Clemens Knott et al., 1990). They are important in the context of the evolution of Owens Mountain because of their mineralogies, cross-cutting relationships and non-deformed textures (Wolf, 1992).

ROCK AND MINERAL COMPOSITIONS

Whole Rock Compositions

Whole rock chemistry previously has been used to provide useful information about magma genesis and paleotectonic settings for rocks in which the original mineralogy and texture have been altered or destroyed by metamorphism (e.g., Pearce, 1975; Menzies et al., 1980; Misra and Conte, 1991). In the present study, lithologic identification by petrographic means was difficult for many of the very fine-grained rocks. Identification was aided by the whole rock analyses. For instance, the fine-grained rocks previously described as quartzites and quartz-rich meta-arkoses (Primrose, 1980) are compositionally too poor in silica and are classified herein as felsic rocks.

Whole rock analyses of a representative sampling of the major lithologies from the Owens Mountain area are listed in Table 1. All measurements were obtained using a Beckman SpectraSpan VB direct current plasma spectrometer (DCP) with a multiple element cassette and external, natural rock standards of basaltic and granitic compositions. Weighed samples and standards initially were fused with a $LiBO_2$ flux (1:4 ratio) in graphite crucibles and then dissolved in 4% HNO_3. The dilution factor was 250:1 for trace element analysis. For major element analysis, this solution was further diluted 24:1 in a Ge-spiked (~10 ppm) Li_2CO_3 solution. Standard solutions (non- and partially-diluted) and blanks were repeatedly analyzed, after every 5 to 10 samples, in order to correct for systematic machine drifts, which, in most cases, was unnecessary. Plots of standard concentrations versus absorbances yield straight lines with R value fits >0.95. Measurements are reported with a precision of ±0.1.

Figures 3a and 3b are normative plots of the Owens Mountain whole rock compositions. Most of the felsic rocks plot in the tonalite fields. Slight classification discrepancies exist because initial lithologic designation was made on a modal basis. The tonalite field of Fig. 3a is subdivided into tonalite and trondhjemite fields in Fig. 3b. The finer-grained felsic rocks plot at the more sodic end within the larger field containing the coarser-grained tonalites.

Figures 4a-c are more plots of the whole rock compositions. An average hornblende composition calculated from Table 2 also is shown. On an AFM diagram, the geochemical evolution of the Owens Mountain mafic and felsic dikes follows a transitional tholeiitic to calc-alkalic trend (Fig. 4a). The gabbro-diorite-tonalite association is characteristic of ensimatic volcanic island arcs (Gill, 1981; Beard and Day, 1987). Fractionation of hornblende can account for only part of the trend. Fractionation of iron oxide must have occurred early during crystallization, although some FeO- and TiO_2-enrichment did occur in the mafic rocks.

Figure 4b is a plot of $1/4SiO_2$ - CaO - FeO+MgO. The line represents the compositional trend of calc-alkaline rocks from the Sierra Nevada (Stern and Wyllie, 1978). The rocks from Owens Mountain fall fairly close to this line. Fractionation of hornblende and iron oxide alone cannot produce this trend. Fractionation of a calcic mineral in addition is needed, possibly calcic plagioclase or clinopyroxene.

Figure 4c is an ACF-deluxe projection of the Owens Mountain rocks (after Thompson, 1982). Most of the rocks are diopside-normative, but the more aluminous schists and granites are corundum-normative. One iron-rich, garnetiferous felsic rock composition (#63 in Table 1) falls closer to the biotite schist compositions. The protolith of this rock probably was sedimentary. It resides within the mixed unit as a screen between mafic and felsic dikes. The diopside-normative rocks of igneous protolith form a well-defined trend that extends from plagioclase to compositions between hornblende and diopside. This slightly curved trend may indicate that clinopyroxene was in the supersolidus assemblage, though physical evidence suggests only a minor presence. However, any remaining, unfractionated clinopyroxene in the magma may have been subsequently converted into hornblende.

Figure 5 comprises a series of variation diagrams. In general, a trend is evident only by the inclusion of the mafic rock data, because the felsic rock data are widely dispersed along the oxide and Mg# axes. The felsic rock compositions fall in the Mg-poor end of the range of tonalite compositions. The mafic rocks form a fairly linear trend in all of the diagrams, but this trend is colinear to the overall compositional trend only for half of the oxides. These distinct trends suggest that different processes may have affected the mafic and felsic rocks. In the TiO_2-Mg# and FeO-Mg# plots of Fig. 5, the TiO_2 and FeO are negatively correlated with Mg# in the mafic rocks and positively correlated with Mg# in the felsic rocks (also see Fig. 4a). These trends indicate that fractionation of Fe-Ti oxides probably was not extensive in the mafic magmas.

Plots of elements considered to be relatively immobile during metasomatism or metamorphism are used to characterized magmas and distinguish tectonic settings (e.g., Pearce, 1982). TiO_2 is plotted against various elements and elemental ratios in Figs. 6a-d and 7a,b. The minor element dispersal patterns (Figs. 6a-d) mimic those of the major elements (Fig. 5) in that no clear distinction can be made between the fine-grained felsic rocks and the tonalites. In the TiO_2-Zr plot, most of the rocks fall within the arc field of Pearce (1982). However, a larger mafic rock data set reveals MORB- and low-Ti-like characteristics when plotted on Al_2O_3/TiO_2-TiO_2 or CaO/TiO_2-TiO_2 diagrams (after Sun and Nesbitt, 1978; Misra and Conte, 1991).

Figures 3-7 reveal the similarities in the whole rock compositions of the fine-grained and coarse-grained felsic (tonalitic) rocks. Some of the subtle differences can be accounted for by the lesser amount of mafic minerals in the fine-grained felsic rocks. In addition to field and isotopic evidence (discussed below), this likeness may indicate that these two rock-types are genetically related, possibly as penecontemporaneous flows and intrusive bodies, or as texturally different members of variably-deformed, similarly-composed hypabyssal rocks. A comparison of mineral compositions strengthens the link.

Mineral Compositions

Minerals generally were identified using standard optical microscopy procedures, but quantitative identification of very fine-grained minerals was accomplished using the energy-dispersive spectrometer (EDS) system of a Camscan scanning electron microscope (SEM) and Tracor Northern software. The software uses external mineral and oxide standards and Bence-Albee and Armstrong correction procedures (Bence and Albee, 1968; Armstrong, 1988a). Counting times were 60 s, and beam parameters in spot mode (~5 μm diameter) were 15 kV and 0.1 nA. All of the mineral compositions have been normalized to 100 on an anhydrous basis (Table 2).

The usefulness of the SEM became apparent while studying the fine-grained rocks, especially the felsic rocks. Modal estimates from the optical microscope yield very high quartz contents (~80 vol.%), but estimates of the quartz/plagioclase ratio based on SEM back-scattered electron imaging are closer to 1:1. In sample #51, for instance, the rock is composed of fine quartz grains (40 vol.%) surrounded by very fine grains of plagioclase (40 vol.%) – grains that were not detected optically. These textures and modes are corroborated by the whole rock chemical data.

Most of the rocks in the Owens Mountain area are composed predominantly of hornblende, plagioclase and quartz. Figures 8 and 9 show the compositional variations in plagioclases and hornblendes in a variety of the rocks. Although there is a wide range in plagioclase and hornblende compositions, there is a large overlap in the mineral compositions from different rock types. In general, the plagioclases in the mafic dikes and gabbros are more calcic than those in the metatonalites and felsic rocks, but both groups span almost the entire compositional range (Fig. 8). Most of the plagioclase in the metatonalites is oligoclase-andesine, but the plagioclase in some of the metatonalitic bodies is bytownite-anorthite. A plagioclase compositional gap exists in Fig. 8, but it is not known whether this is a reflection of the true plagioclase compositions or is due to a sampling problem.

The hornblendes in the mafic rocks fall within the upper part of the felsic rock – hornblende field in Mg#-Si compositional space (Fig. 9a). Some of the hornblendes in metatonalites are compositionally similar to those in the mafic layers and gabbros. The hornblendes in mafic dikes also are compositionally indistinguishable from those in the gabbros. Figure 9b shows that most of the amphiboles from most rock types can be classified as hornblendes.

The ranges in mineral compositions in the mafic and felsic dikes are nearly covered by the ranges in mineral compositions in the gabbros. The compositional similarities between both the hornblendes and plagioclases in the gabbros and mafic dikes

indicate that the dike mineralogies probably are primary (dioritic) – not metamorphosed, amphibolitized basalts. In a few mafic dikes, pristine euhedral plagioclase and hornblende phenocrysts within a groundmass of hornblende and plagioclase also attest to the primary nature of the mineralogy. There is little evidence of clinopyroxene → hornblende retrograde reactions. Thus, the mafic rocks are mineralogically equivalent to the younger hornblende gabbro plutons that crop out in the Owens Mountain area and throughout this part of the foothills.

The wide range in mineralogy within each of the rock types suggests that they were produced from a number of compositionally distinct magmas, each which underwent fractional crystallization at much deeper levels than what is now exposed. A much more detailed geochemical and isotopic study is necessary to firmly establish the genetic links and source regions.

The total alumina in hornblende (Al_T) geobarometer (Hammarstrom and Zen, 1986; Hollister et al., 1987; Johnson and Rutherford, 1989; Rutter et al., 1989) has been applied to both felsic and mafic dike rocks from Owens Mountain. The barometer was empirically calibrated using rocks containing plagioclase, K-feldspar, amphibole, biotite, quartz, sphene, and iron-titanium oxides. Most of the felsic rocks contain the requisite minerals, although K-feldspar is not common in some. The average Al_T value of ten of the felsic rocks is 1.5 f.u. (formula units). The mafic rocks do not contain the proper assemblage, but it is noteworthy that the average Al_T value of 10 mafic rocks is 1.4 f.u. Wolf (unpub. data) has found good experimental agreement between Al_T and crystallization pressure for a natural mafic rock without the requisite assemblage. These values give a 2-3 kbar crystallization pressure estimate, equal to 8-11 km. The actual Al_T values of rocks, however, reflect the bulk magma compositions in addition to the crystallization pressures.

Ague and Brimhall (1988a,b) tabulated Al_T values for amphiboles throughout the Sierra Nevada batholith. They found a general decrease in Al_T, and thus in calculated pressures, from west to east. Although they collected samples from neither the western-most part of the central Sierra Nevada batholith (the Fresno reentrant of Saleeby, 1990a) nor the Owens Mountain area, the data collected just to the east suggest relatively high crystallization pressures (3-5 kbar) and deep levels (11-19 km) for the now exposed rocks in the reentrant. The data from Owens Mountain change the local pressure/depth estimates but are not incompatible with the finer, more complex, calculated pressure variations within the batholith that were described by Ague and Brimhall (1988a,b). Alternatively, the 2-3 kbar pressure difference between the data sets may be a function of the temporal differences between the crystallization ages of the Jurassic Owens Mountain dikes and the Cretaceous Sierra Nevada batholith plutons. In the 30-70 m.y. intervening time span, depths of magma emplacement certainly could have changed. In addition, the styles of emplacement point to different crystallization depths, with the presence of dikes generally characterizing higher levels of emplacement than more equant plutons. Because the levels of present-day exposure are roughly the same, these differences imply that the western margin of the Sierra Nevada was carried down to greater depths, between the Late Jurassic and the mid-Cretaceous.

Zircon was separated from rock samples for U-Pb geochronologic analysis. The zircon crystals in all samples were invariably euhedral, clear, core-free, and generally free of inclusions. Rounded, anhedral morphologies and variably-colored size fractions typical of a Proterozoic, cratonic, detrital zircon component (Miller and Saleeby, 1987) are not evident in the Owens Mountain tonalites. Zircon samples of the fine-grained, felsic rocks gave the same morphological results, although the yields were so small (< 0.1 mg) that geochronologic analysis was not possible with the technique available.

STRUCTURES

Prior to a description of mesoscopic relationships between rock types, details of the macroscopic structural framework are given. The Owens Mountain area is divided into three structural domains, based on distinct differences in orientation of large-scale structures. Figure 10 contains lower hemisphere, equal-area projections of poles to foliation of the three domains. The foliation in the southwestern domain dips nearly vertically and generally strikes NNW-SSE (Fig. 10b). In the central domain, the foliation is nearly horizontal and slightly domal (Fig. 10c). The foliation in the northeastern domain dips nearly vertically and strikes E-W (Fig. 10d). The transitional zones between domains are a few hundred meters wide.

Owens Mountain has previously been interpreted to be the core of a large anticline, similar to the anticlines exposed in the Foothills terrane to the northwest (MacDonald, 1941; Primrose, 1980). These regional anticline/syncline structures may have extended far southward. While, there is some evidence to support this hypothesis at Owens Mountain, much of the data is equivocal due to subsequent intrusion and deformation.

The metasedimentary rocks in the southwestern and northeastern domains have been correlated with one another and, thus, became the limbs of the anticline, with the felsic rocks of the flat-lying central domain lying in the core (Primrose, 1980). However, it is not clear that the phyllite and schist are part of the same folded unit. The mineralogical and textural differences between these units could be due to differences in metamorphic grade of the rocks. However, the rocks at the northern edge of the Phyllite unit, near the Cretaceous pluton, do not show signs of increasing metamorphic grade, such as grain size coarsening and mineralogical changes. Thus the observed differences may be due to bulk compositional differences which could imply that these units are not part the same metasedimentary unit.

The steeply dipping southwestern and northeastern domains, adjacent to the shallowly dipping central domain, have been interpreted as the limbs of an anticline (MacDonald, 1941; Primrose, 1980). However, the structural data do not support this anticline hypothesis because of the domal structure of the central domain (stereoplot (c); Fig. 10). The presence of the dome is not consistent with a singly-folded anticlinal structure.

In addition, the axes of folds in the southwestern domain plunge steeply to the southeast (stereoplot (a); Fig. 10). This orientation is not consistent with the proposal (Primrose, 1980) that Owens Mountain is the core of a gently south-plunging anticline, but is consistent with the regional pattern of post-folding, ductile deformation (e.g., Newton, 1986; Paterson et al., 1987; Tobisch et al., 1989). The cross-sections in Fig. 11 are based on Fig. 10 and additional unpublished data (Wolf, 1992).

The deflections of the orientation of the structures in the central and northeastern domains (away from the NNW-SSE regional trend exposed in the southwestern domain) can be attributed to the intrusion of both mafic and felsic Cretaceous plutons. The intrusion of the Cretaceous Academy pluton clearly has strongly deformed the fringing Jurassic metamorphic rocks (Greenamayer, 1974) and probably has had the major impact on the current orientation of the structures in the area, as can be seen in Figs. 2 and 10 by the orientation of the foliation near the contacts (Wolf and Saleeby, 1990, 1991).

Numerous mafic bodies crop out within the central domain. The relative proximity of some outcrops may indicate that many of the bodies are interconnected. The shallow dips in the layers between mafic outcrops suggest that these areas are saddles above buried mafic rock. Paterson and Tobisch (1985) have used similar structural data to argue for the interconnectedness of isolated outcrops of intrusive rocks. Thus the shallow dips in the central domain may be due to underlying intrusive bodies, possibly but not necessarily of similar composition to the exposed mafic plutons in the area. In essence, the shallow, domal dips may indicate that the felsic rocks are presently capping a

partially exposed or unexposed pluton. Alternatively, the felsic rocks themselves may be part of a sequence of hypabyssal domes, and have behaved like a megaboudin, deflecting the foliation around the area. In this view, the vertical foliation around the domed area should have continued to the southeast with a vertical dip, but was subsequently flattened by Cretaceous Academy deformation (Figs. 10 and 11).

I do not intend to imply that the Owens Mountain area could not have been part of an anticline, but just that the data that may have supported this hypothesis have been obscured by subsequent intrusion and deformation. In fact, the Foothills terrane to the northwest is a fold belt composed of a number of anticline/syncline sets of regional extent (Clark, 1964; Bogen, 1985; Tobisch et al., 1989), and these structures probably extended far southward.

The E-W trend of the foliation in the northeastern domain probably is a result of rotation in the Cretaceous due to intrusion of the Academy pluton (Fig. 10). The NNW-SSE structural trend in the southwestern domain probably reflects the regional foothills fabrics previously inherited from the Paleozoic ophiolitic melange fabric but further developed during the Nevadan orogeny (Saleeby, 1977, 1982; Behrman, 1978). However, the fabric of the rocks in this southwestern domain cannot be wholly attributed to the folding that formed the regional scale Nevadan folds in the Foothills terrane to the northwest of the Owens Mountain area. Although the NNW-SSE trend is dominant, there is a distribution of foliation orientations that follows a discernable, curved pattern within this domain. This westward curvature is high-lighted by the outcrop pattern of the large, tabular pluton (Fig. 10). Thus, some aspects of the fabric may have been imposed by the forcible intrusion of the larger felsic bodies during dike emplacement. The shapes of these bodies are consistent with a sinistral sense of shear within this area.

Mack et al. (1979) proposed that the arcuate shape of the Academy pluton was caused by the inflation of the body out into the easily deformable mafic and felsic rocks (of the northeastern domain) and that the southern border was straighter because less

deformable country rocks in this area inhibited the outward bowing. This southern edge of the Academy pluton may have impinged against but did not greatly deform either the tonalitic dike rocks similar to those exposed in the southwestern domain of Owens Mountain or the Early Cretaceous gabbros that crop out throughout the Foothills region.

The mesoscopic structural relationships between different compositional layers are governed by intrusive and tectonic factors. Compositional layering of very silicic (~74 wt.% SiO_2) and very mafic rocks (~51 wt.% SiO_2) throughout the Owens Mountain area probably does not represent a primary, volcanic or volcaniclastic depositional stratigraphy but a coeval, deformed dike sequence characteristic of hypabyssal conditions.

Most of the metamorphosed rocks in the Owens Mountain area have a strong tectonite fabric. The foliation, a continuous cleavage, is parallel to the compositional layering and is defined by alignment of grains of biotite (± muscovite) in the schists, hornblende in the mafic and felsic rocks, and hornblende and quartz ribbons in the metatonalites. Crenulation cleavages are very rare. Some mafic layers have strong linear shape fabrics, with lineations plunging steeply to the southeast. Within some of the vertically dipping mafic layers, felsic layers that appear to have been formed by metamorphic differentiation are composed of steeply plunging, 1 cm-thick, rod-shaped segments connected along strike with 2-4 mm-thick planar segments. This foliated and lineated fabric may be indicative not of a true stretching lineation but of a layer-parallel shearing that began to buckle, boudinage and disrupt these layers. However, other mafic layers have strong constrictional shape fabrics that appear to have been formed during stretching.

Early features, such as bedding, layering and folds, have been strongly transposed parallel to the foliation, and the axial planes of folds are parallel to the nearly vertical foliation. Folds are not common, but where found are small (amplitudes less than a few

meters, generally a few centimeters), tight, plunge steeply to the southeast (Fig. 10), and, viewed down-plunge, generally have an asymmetric, S-fold (sinistral) geometry.

Some of the structural features found in the area are illustrated in Figs. 12a-d. Figure 12a shows a fine-grained, felsic dike cross-cutting both mafic and coarse-grained, felsic (tonalitic) dikes. This relationship indicates that many of the layers composed of fine-grained felsic material may, in fact, be intrusive – not extrusive – and their textures not necessarily related to grain-size reduction during deformation of coarser-grained tonalite.

Figure 12b depicts the intrusion of a coarse-grained tonalite into a thick, mafic dike. Complex, cross-cutting, mafic and fine- and coarse-grained felsic dike sequences appear flattened and may have been partially transposed into the plane of the foliation, which nearly parallels the original dike orientations. The mesoscopic structure shows little deformation of the intrusive contact. However, microscopic analysis reveals that the tonalite is moderately to strongly deformed, having a well-developed gneissic texture. This tonalite is zircon sample 3 (see below).

Many tonalite dikes contain fragments of mafic layers. Many of the smaller xenoliths (<15 cm diameters) are elliptical and may have been mixed into the tonalitic magmas as coeval partial melts. The ellipses generally have been flattened by subsequent deformation – deformation that could have taken place at either super- or subsolidus temperatures. In some cases, the xenoliths are elongated and have jagged ends, which indicates that they were incorporated into the tonalitic magmas as solidified fragments (Fig. 12c). These xenoliths have retained vestiges of their primary shapes; they have not been flattened substantially by deformation. However, the host tonalites have have a well-defined foliation and, thus, have been deformed at near-solidus temperatures. Deformation appears to have had a strong microscopic but a weak macroscopic effect, so deformation in some of the tonalites probably was not too intense. Both the foliation and fragment orientations are parallel to the dike edges. The alignment of the xenoliths may

be indicative of magmatic flow or passive emplacement with minimal layer disruption and no xenolith rotation. Macroscopic data for magmatic flow are supported by microscopic data of plagioclase fragments with twins aligned parallel to solid-state foliation. Evidence for magmatic to solid-state flow transitions may be indicative of syntectonic emplacement (Paterson et al., 1989; Vernon et al., 1989; Krohe 1991). Thus, the data suggest that many of the tonalite intrusions, mafic layer disruptions and preferential xenolith and xenocryst alignment (parallel to the foliation) were synchronous with foliation development, i.e., that intrusions were syntectonic.

The fabric in Fig. 12d has been strongly influenced by tectonic processes. The cross-cutting nature of the mafic dikes may be due, in part, to the initial intrusion pattern but has been subsequently partially transposed into the plane of the foliation, which parallels the overall layering. The felsic layers contain both fine- and coarse-grained rocks.

Figures 12a-d illustrate the variability in mesoscopic structures found in Owens Mountain. Some of the features which are present indicate that highly deformed rocks make up much of the area, such as subparallel layers and foliation and unusually regular layering of constant thickness (Fig. 13a) (Passchier et al., 1990). Layers range from <1 cm to just >1 m. Within the mixed unit of the southwestern domain, the thicknesses and compositions of the alternating layers vary randomly. Intense deformation in some layers has transposed some of the mesoscopic igneous features clearly present in the moderately deformed layers (e.g., cross-cutting relationships, presence of xenoliths and evidence for assimilation of proximal layers). Some metatonalitic layers are boudinaged or disrupted (Fig. 13b). Chilled dike margins are rarely preserved, which is an indication of the elevated temperatures within the area during intrusion. Subsequent transposition also may have destroyed the evidence of chilled margins.

In addition to the transposition of separate, compositionally distinct layers (dikes and dikelets), metamorphic differentiation within layers has occurred, expressed within

tonalitic layers as quartz ribbons and within mafic layers as alternating, 1-5 mm thick, plagioclase-hornblende lineations and foliations (Fig. 13c). These layers have more diffused edges than do the compositionally distinct layers. Metamorphic differentiation can occur in the absence of deformation (e.g., Passchier et al., 1990), but at Owens Mountain, it probably was greatly enhanced by the transposition process.

Rare mafic layers show signs of post-tectonic migmatization, with very coarse-grained, plagioclase-rich, anastomosing leucosomes directly surrounded by black, hornblende-rich melanosomes that, in turn, are surrounded by typical, unmelted hornblende plus plagioclase amphibolitic palaeosomes (Fig. 13d). Anatexis may have been more wide-spread, with intense deformation and transposition destroying the signs of earlier phases of segregation.

Figure 13a shows the high degree of transposition of mafic and felsic dikes. Transposition, though, has not destroyed all evidence of noncoaxial deformation. Although folds are not common throughout most of the Owens Mountain area, they are common in an area within the southwestern domain (west of station 4, in Fig. 10). Most fold sets are less than a meter in amplitude. Centimeter-scale rootless folds are common. All of the dozens of folds found in this area have an S-fold geometry, with axial folds plunging steeply to the southeast (Figs. 10 and 13b,e-g). This geometry implies a left-lateral sense of motion within this part of the Owens Mountain shear zone. Scattered folds within other parts of the Owens Mountain area do not show a consistent outcrop pattern indicative of map-scale folding. The strong linear shape fabrics in some of the mafic layers do indicate that some degree of vertical motion may have occurred as well.

The microscopic structures corroborate the variability in both degree and location of deformation that the rocks in the area have experienced. Meso- and microscopic mylonitic textures are apparent, such as ribbon quartz and greatly reduced grain size. The very fine-grained matrices of some of the tonalites developed by grain size reduction, which is indicative of syntectonic recrystallization. Annealing recrystallization also took

place in the quartz-rich rocks after deformation ceased, as shown by the granoblastic texture of the felsic rocks (Kerrich et al., 1980; Simpson and DePaor, 1991). Most quartz has completely recrystallized, but some larger grains show a little strain (e.g., undulose extinction and subgrain formation). S-C fabrics are poorly developed in these rocks, as they are in many of the Jurassic granitoids in this region (Tobisch et al., 1989). Figures 14a-f are photomicrographs of thin-sections (under crossed-polars) of rocks from the dike swarm/shear zone of the southwestern structural domain of Owens Mountain. Microtextural terms are after Williams et al. (1982), Wise et al. (1984) and Bard (1986).

Figure 14a shows the boundary between a tonalitic and a mafic dike. The mafic dike has a nematoblastic texture of hornblende needles aligned parallel to the dike edge. The tonalitic dike is composed of aligned laths of plagioclase, with the long axes and twinning generally parallel to the dike edge. Some of the larger plagioclase grains are framed by tiny grains, indicative of rotational recrystallization (Simpson and DePaor, 1991). These three textural features together (especially the aligned plagioclase laths) are suggestive of syn-kinematic magmatic flow.

The rock in Fig. 14b is from a mafic dike. It has a blastoporphyritic texture with relict hornblende and plagioclase phenocrysts in a nematoblastic matrix of very fine-grained hornblende and plagioclase.

Figures 14c-f show the tectonite textures of some of the tonalitic dikes and tabular bodies that were sampled for U-Pb zircon geochronological analysis (see below). Figures 14c-f are ordered from less to most deformed. Figure 14c (zircon sample 2) reveals a granoblastic heterogranular (blastoporphyritic) texture composed of xenomorphic plagioclase and quartz. Figures 14d and 14e (samples 4 and 3) show granoblastic heterogranular polygonal textures. Ribbon quartz is present (with undulose extinction and subgrain boundaries). The rocks are orthomylonites. Figure 14f (sample 7) shows a granoblastic heterogranular texture with extreme grain size reduction of the plagioclase and quartz matrix. The rock is an ultramylonite.

The tonalitic rocks do not have microscopically observable foliations. Anisotropic minerals (e.g., biotite and hornblende) are common but not in large enough quantities to affect the microtextures. The mesoscopic rock fabrics clearly indicate a past episode of strong deformation, but the microscopic textures generally lack this evidence because of pervasive annealing – both syn- and post-kinematic.

The tonalitic bodies are variably deformed. Deformation was moderate to intense; fabrics vary from slightly foliated through augen gneissic to mylonitic. This textural variation may have been caused by strain partitioning (discretized shearing) as a result of grain size, body size or compositional variations. If strain is partitioned homogeneously through time throughout a region, the bodies emplaced earlier will be more strained. Thus, the degree of deformation may be a function of emplacement age. Although resolving these different possibilities is very difficult, there does appear to be a correlation between crystallization age and the degree of strain, which implies that intrusion of the dike swarm as a whole was syntectonic (see geochronologic discussion below).

Other workers have documented similar ductile features along and southeast of the Bear Mountains fault zone in the Foothills terrane to the northwest of Owens Mountain (Clark, 1960; Newton, 1986; Paterson et al., 1987; Tobisch et al., 1989; Vernon et al., 1989). Owens Mountain lies roughly along strike with the Bear Mountains fault zone, and I suggest that the Owens Mountain shear zone is the southern extension and possibly deeper level of this fault zone.

The large scale structure of the Owens Mountain area reveals important information about the style of intrusion of the tonalitic masses and thus about the regional tectonics. Were the tonalites intruded as subhorizontal sills and later steeply rotated during Late Jurassic Nevadan folding, or were they intruded as subvertical dikes after

folding? Was ductile deformation synchronous with or subsequent to dike emplacement? The absolute timing of intrusion, determined by U-Pb zircon geochronology, is critical to understanding these events and is discussed below.

METAMORPHISM

Most of the rocks in the Owens Mountain area are amphibolite-facies grade, generally characterized by assemblages of andesine - oligoclase + hornblende ± quartz ± epidote ± biotite ± almandine, although plagioclase of bytownite-anorthite composition also is common in some rock types. Rare mafic layers show signs of limited anatexis. However, the phyllite unit to the southwest of Owens Mountain is of greenschist-facies grade, with garnet present in the higher grade areas closer to Owens Mountain.

There is little evidence for pervasive low-temperature, retrograde metamorphism throughout the Owens Mountain area. Some plagioclase is sericitized. Epidote-rich layers (0.5-5 cm thick) are present within some of the felsic layers. Many of these layers may have formed during spatially-restricted fluid infiltration related to post-plutonic, shear zone hydrodynamics. However, within the shear zone, concordantly folded epidote-rich layers indicate that at least some pre- or syntectonic epidote mineralization occurred. Because magmatism also was syntectonic, the accompanying syntectonic epidotization probably was a high-temperature phenomenon.

The proximity of the cross-cutting Cretaceous plutons cannot account for the amphibolite-facies grade nature of these rocks, because there is little evidence for contact metamorphism – even along the contacts with the Cretaceous plutons. There is no aureole or systematic variation in metamorphic grade away from the contacts. Neither pyroxene nor hornblende hornfelses have been identified, although hornblende hornfelses may be difficult to discern from the regional amphibolite-facies grade metamorphism.

None of the rocks has a static (hornfelsic) metamorphic overprint, so metamorphism was synchronous with development of the ductile structures. The intrusion of the Cretaceous plutons clearly post-dates the ductile deformation within the dike complex of Owens Mountain (southwestern domain), so deformation, metamorphism and annealing were pre-mid-Cretaceous. Thus, the localized amphibolite-facies grade metamorphism within the dike complex probably was of an autometamorphic nature. This thermal maximum was the result of syntectonic plutonism within the shear zone.

However, metamorphism during a later phase of deformation occurred in the eastern parts of the Owens Mountain area as a result of the forcible intrusion of the Cretaceous Academy pluton. This forcible intrusion rotated the layering in the southeastern part of Owens Mountain to a N-S orientation with little transposition. The layering in the northeastern-most part of Owens Mountain, north of the Academy pluton, may have been rotated slightly to an E-W orientation and also may have been attenuated along strike. No hornfelsic overprinting is evident in these rocks.

U-Pb ZIRCON GEOCHRONOLOGY

U-Pb Zircon Techniques

U-Pb zircon techniques were similar to those of Saleeby et al. (1989a). Sample lithologies and coordinates are given in Table 3, and locations are plotted in Fig. 2. The U-Pb results are listed in Table 4. Zircon was separated from 10-80 kg of rock by standard crushing, grinding, H_2O and heavy liquid density contrast, and magnetic susceptibility techniques. The magnetic separation technique (Frantz isodynamic magnetic separator) was adjusted to deliver maximum sample purity. Zircon concentrates were washed in concentrated HNO_3 for 30 minutes before splitting into size fractions (nylon mesh sieves). Fractions were hand picked under ethanol to >99.9% purity prior to

weighing and loading into teflon (TFE) bombs or microbombs. Samples were washed again in hot, ultrapure, concentrated HNO_3 for 15 minutes within the bombs. Dissolution techniques were modified after those of Krogh (1973) and Parrish (1987). After dissolution in ultrapure, concentrated HF, the HF was evaporated, and the samples were reheated overnight in 6N HCl. Samples weighing <3 mg were spiked with a mixed $^{205}Pb/^{235}U$ tracer, and samples weighing >3 mg were aliquoted and spiked with a mixed $^{208}Pb/^{235}U$ tracer. Spike equilibration was achieved overnight in the hot, 6N HCl within sealed teflon (PFA) vials. The 6N HCl was then evaporated, and the sample was redissolved in hot, 3N HCl. The samples were eluted through 50 µl ion-exchange columns using HCl and H_2O-HBr chemical extraction techniques similar to those of Krogh (1973).

A total of six fractions from five samples were leached prior to final dissolution in an attempt to remove the discordance from the fractions (Mattinson, 1984; 1987). Samples were washed in hot, ultrapure, concentrated HNO_3 within sealed teflon (PFA) vials and then left in ultrapure, concentrated HF for seven days at 100±5°C. Following complete evaporation of the HF, ~0.5 ml of 6N HCl was added to the vials, which were sealed and reheated overnight. The 6N HCl subsequently was pipetted off. The samples were rinsed in 6N HCl and H_2O and then transferred by pipet to the teflon (TFE) microbombs in concentrated HNO_3. The HNO_3 was pipetted off, and ultrapure, concentrated HF was added for the final dissolution step. Further steps were similar to those for the nonleached fractions, except that a mixed $^{205}Pb/^{235}U$ tracer was used regardless of fraction size.

Mass spectrometry was done on a 35 cm, 90° extended geometry, VG Sector multicollector instrument. Pb and U were run on outgassed single Re filaments with H_3PO_4 and silica gel (Cameron et al., 1969) or graphite loads, respectively. Pb was ionized at ~1450°C and U at ~2000°C, which yielded typical ion beam currents of ~10^{-11} A. A mass fractionation factor of 0.3±0.3 ‰/a.m.u. was obtained from periodic runs of

National Bureau of Standards reference Pb (983) and U (500) standards. Stabilities at the 10 ppm level over several hours were determined from regular intercalibration of the multiple detector system, so Pb and U were run in a static multicollector mode. Large $^{206}Pb^*/^{204}Pb$ ratios were obtained with the ^{204}Pb beam directed into a Daly deflection knob-photomultiplier system, with a gain factor stable to within 5 ‰.

Analytical uncertainties are represented as uncertainties in the radiogenic $^{206}Pb^*/^{238}U$ and $^{207}Pb^*/^{206}Pb^*$ ratios calculated independently for each analysis (Table 4). The $^{206}Pb^*/^{238}U$ uncertainties are bounded by a long-term reproducibility which is better than ±0.8% (Saleeby et al., 1989a). Initial Pb compositions used for nonradiogenic corrections are based on data from similar rocks from this general region (Saleeby and Chen, 1978; Chen and Tilton, 1991).

The assignment of igneous ages commonly is based on the concordance, or equivalence of the Pb/U and Pb/Pb ages, in a given analysis (internal concordance). Concordance is obtained statistically by the overlap of the analytical uncertainties of the internal ages, i.e., when the error bars of an analysis intersect the concordia line on a $^{207}Pb^*/^{206}Pb^*$ versus $^{238}U/^{206}Pb^*$ concordia diagram (Tera and Wasserburg, 1972). The near linearity of concordia for ages younger than mid-Paleozoic allows system disturbances to nearly follow concordia. Thus, internal concordance alone has been referred to as "apparent concordance" by Saleeby (1982). "True" or external concordance is achieved with the agreement of internally concordant ages from multiple fractions of a zircon population separated into physically different groups. The effects of multi-stage processes commonly vary with the physical properties of zircon fractions, so external concordance implies single-stage isotopic evolution, with the concordant age representing an accurate approximation of the igneous age (Saleeby et al., 1989a). Interpretation of the isotopic data requires the application of discordance mechanism models that are best constructed using the geologic context of the samples in addition to the details of the isotopic systematics (Saleeby et al., 1989a).

U-Pb Zircon Age Data

U-Pb zircon ages were determined from twelve samples, eleven from the Owens Mountain area and one from the Santa Cruz Mountain (SCM) area to the northwest (Figs. 1 and 2, Tables 3 and 4). Crystallization ages are correlated with emplacement ages, because of the relatively small body sizes and, thus, rapid cooling times. Stacked segments of concordia that facilitate comparisons between samples and the associated errors are shown in Figs. 15 and 16 a,b. The clear, euhedral zircon morphology and U-Pb systematics may indicate little or no detrital contribution from the Paleozoic craton of North America (e.g., Miller and Saleeby, 1987). Figure 15 shows the improvements in the data as a result of the leaching step described above. Application of the leaching technique described above results in smaller degrees of age discordance, and the improvements in the data are shown. Figure 16a combines the data from the leached and non-leached fractions.

Samples 1-7 are tonalitic dikes and tabular plutons from the Owens Mountain area. They were collected to determine the time span of dike emplacement. Sample 1 is strongly deformed and has a highly variable texture, from gneissic to mylonitic. Emplacement of the adjacent Cretaceous Academy pluton probably deformed the sample considerably, in addition to probable Late Jurassic deformation. The 4 m.y. difference in Pb^*/U ages between the finest and the two coarser zircon fractions of sample 1 indicates radiogenic Pb loss from the fine (45-62 μm) zircon population (Table 4). Figures 15 and 16a show that this age discrepancy is completely removed by the leaching technique. The two coarser fractions (>62 μm) and 45-62 μm leached fraction are both internally and externally concordant and yield an emplacement age of 148 Ma (Fig. 16a).

Samples 2-7 are tonalites from the dike complex of Owens Mountain, located in the southwestern domain. Sample 2 is moderately deformed – its foliation defined by ribbon quartz (with undulose extinction) and hornblende crystals. The five fractions of

sample 2 are externally discordant. The five non-leached fractions form a ~horizontal array off of concordia, that is indicative of radiogenic Pb loss, especially from the finest- and coarsest-grained fractions, <45 and 100-120 μm, respectively (Fig. 16a). The intersection of this array projects back to 160 Ma, and this could be interpreted as the true crystallization age. However, the leaching data permit a better interpretation. The most discordant fraction (<45 μm) and the least discordant fraction (80-100 μm) were leached. The <45 μm fraction moves from 134 to 151 Ma, but still remains internally discordant (Fig. 15). The older $^{207}Pb^*/^{206}Pb^*$ age indicates a small addition of older zircon. If the true age of crystallization was 160 Ma, the 80-100 μm fraction would have shifted toward an older age after leaching. However, the leached 80-100 μm fraction became internally concordant at 151 Ma instead of at 160 Ma (Fig. 15). The behaviors of these two leached fractions strongly suggest a 151 Ma emplacement and crystallization age, even with the superimposed characteristics of both inherited zircon and radiogenic Pb loss in the fractions (Fig. 16a).

Sample 3 is moderately to strongly deformed and has a gneissic mesoscopic texture. The four fractions of sample 3 are slightly discordant and cluster around a Pb^*/U age of 147-148 Ma. The slightly older $^{207}Pb^*/^{206}Pb^*$ ages suggest a minor addition of older zircon. However, the leached fraction clearly shows that the major factor in the discordance is Pb loss, not zircon inheritance (Fig. 15). The Pb^*/U ages shift from 147 to 152 Ma. The other, nonleached fractions exhibit Pb loss with a very small component of inherited zircon (Fig. 16a). The age of this sample is interpreted to be 152 Ma.

Samples 4 and 5 may come from different parts of the same large tabular pluton, in that they are on strike with each other (Fig 2). Mesoscopically, they are strongly deformed, tonalitic gneisses. The three fractions of sample 4 are internally concordant, but the 3.5 m.y. difference in the Pb^*/U ages between fractions indicates radiogenic Pb loss from the 62-80 μm fraction. The leaching of this 62-80 μm fraction removes much of the external discordance (Fig. 15). Further leaching may remove the rest of the

discordance and shift the age of this fraction back to 154 Ma age of the other two fractions. The data suggest that the age of this sample is 154 Ma (Fig. 16a). The two fractions of sample 5 are internally slightly discordant, and radiogenic Pb loss is indicated by the 6 m.y. Pb*/U age difference between fractions. Leaching of the 45-72 μm fraction shifts the age back from 148 to 152 Ma, part of the way to the 155 Ma age of the other fraction (Figs. 15 and 16a). The data suggest that the age of this sample is 155 Ma. Thus, taken as a whole, this pluton has an age of 154-155 Ma, but the two zircon samples also may record different magma pulses of slightly different ages.

Sample 6 is from a medium- to fine-grained, felsic, 1.5 m wide dike. It has a blastoporphyritic texture, with subhedral phenocrysts of plagioclase in a fine-grained, recrystallized matrix of plagioclase and quartz. It contains hornblende and garnet. It has been moderately to strongly deformed. The single fraction is internally concordant and has an age of 151 Ma (Fig. 16a).

Sample 7 is a strongly deformed (ultramylonitic) tonalite. The one fraction is slightly discordant and falls just below concordia. In the light of the leaching data from the other samples, this rock is tentatively assigned an age of 154 Ma (Fig. 16a).

Sample 8 was collected 2 km south of the Santa Cruz Mountain pluton, 60 km to the northwest of Owens Mountain. It was taken to establish a better understanding of the timing and emplacement relationships between the Santa Cruz Mountain - Guadalupe igneous complex area and the Owens Mountain area. The rock has a mylonitic texture, with areas of coarse-grained, euhedral, drusy plagioclase and fine-grained, recrystallized quartz clots separated by zones of very fine-grained, recrystallized plagioclase and quartz. Only one of the four fractions is internally concordant, with a Pb*/U age of 140 Ma that has a relatively large error. The $^{207}Pb^*/^{206}Pb^*$ ages of two of the fractions may indicate either old zircon inheritance or radiogenic Pb loss, but they probably are a result of the combination of these two processes (compare with sample 2). The uncertainties relating

to the discordance patterns and the large error on the apparently concordant fraction only permit an igneous age assignment of 145±7 Ma (Fig. 16a).

Figure 16b shows stacked segments of concordia for the Cretaceous igneous rocks in the Owens Mountain area. Sample 9 is an undeformed, non-foliated biotite-hornblende tonalite, from just to the north of the Jurassic rocks of Owens Mountain (Fig. 2). It is part of the Bass Lake plutonic suite – the huge composite pluton comprising over 600 mi^2 and stretching from east of Owens Mountain to the Foothills terrane and the Guadalupe igneous complex to the northwest (Bateman and Clark, 1974; Stern et al., 1981). The three fractions of this sample are internally and externally concordant, with an age of 118 Ma (Fig. 16b).

Samples 10, 11 and 12 are from dikes within Owens Mountain that cross-cut the Jurassic structures of Owens Mountain. Sample 10 cuts the hornblendite-gabbro pluton in the southeast area. The dike from which sample 11 was taken is part of a series of common dikes in the central and northeastern domains that follow the steep foliation in the west but curve northward and cut the foliation in the east. The sample 12 dike cuts the flat-lying felsic unit in the central area. These samples were collected to place a lower limit on the age of the main phase of deformation. They are nondeformed or very slightly deformed and show some signs of recrystallization.

Sample 10 is a pegmatitic biotite-muscovite granite. Deformation is minimal, present only as a slight undulose extinction in the quartz. The four fractions of sample 10 are discordant and clearly show the effects of progressive radiogenic Pb loss (Fig. 16b). The Pb^*/U ages project back to an emplacement age of ~123 Ma

Unfortunately, nothing definitive is revealed by the U-Pb data in samples 11 and 12, except their probable Cretaceous age. Sample 11 is an aplitic biotite-muscovite-garnet granite with a xenoblastic texture. Sample 12 is an undeformed, fine-grained, biotite dacite. Its subhedral, slightly recrystallized plagioclase laths are aligned due to

magmatic flow. The igneous ages probably are 120±7 Ma, but both an inherited zircon component and radiogenic Pb loss are indicated by the discordance of the fractions (Fig. 16b).

The U-Pb data from the Owens Mountain tonalitic dikes and tabular plutons indicate a 155-148 Ma emplacement age for the dike swarm (Fig. 16a). Mutually cross-cutting field relationships show that the cogenetic mafic dikes also must have been emplaced during this same period. Many of the Jurassic and Cretaceous samples are contaminated with a very minor amount of inherited zircon (Figs. 16a,b). This older zircon component may have been derived from a combination of the Paleozoic ophiolitic basement, remnants of the Early and Middle Jurassic arc and detritus from the Oxfordian-Kimmeridgian flysch. The data also indicate that some amount of Pb has been lost from most of the zircon fractions. The nature of this disturbance may imply that the zircons remained partially open for an extended period of time under syntectonic, hot subsolidus conditions in the Late Jurassic. Subsequent Cretaceous pluton emplacement also probably enhanced Pb mobility and loss. In addition, some Pb loss may be due to relatively young, near-surface heating events; remnants of Tertiary mafic flows (10 m.y.) crop out just to the north of Owens Mountain. These flows covered an area of at least 95 km^2 to a depth of as much as 60 m (Huber, 1981), and may have heated the near-surface topography of the Owens Mountain. However, Huber (1981) estimated that the flows did not engulf Owens Mountain. Sample 10, though, clearly shows a recent Pb loss (Fig. 16b).

Zeitler et al. (1990) found that ~micron-thick overgrowths of zircon were significantly younger than the xenocrystic cores and were precipated onto the cores by vein fluids during high-grade metamorphism. This same process may have occurred in the Owens Mountain zircons. A high-U overgrowth would suffer more radiation damage which could lead to more Pb loss. The leaching technique appears to have dissolved the

damaged regions, whether they were rim overgrowths or internal regions. Figure 17 shows that there is the expected negative correlation between U concentration and $^{206}Pb/^{238}U$ ages between the nonleached and leached fractions, which indicates that the high-U, lattice-damaged zircon which dissolved in the leaching step had suffered Pb loss.

DISCUSSION

Paleotectonic Setting

The gabbro-diorite-tonalite association is characteristic of ensimatic volcanic arcs (Gill, 1981; Beard and Day, 1987). Isotopic studies indicate an absence or a minimum of continental crustal material in the Sierra Nevada western-margin plutons (Saleeby and Chen, 1978; DePaolo, 1981; Clemens Knott et al., 1990; Chen and Tilton, 1991). The Late Jurassic arc was built on much older, genetically unrelated ophiolitic basement. In a TiO_2 - Zr plot, the rock compositions fall within the field for island arcs (Fig. 6). Although sparse, the plots of the amphibolite data indicate the coexistence of low-Ti (<0.5% TiO_2) and high-Ti (>0.5% TiO_2) mafic rocks, which is thought to be indicative of ophiolite sequences in back-arc (Misra and Conte, 1991) or fore-arc basin settings.

In the Owens Mountain area, genetic links between the hornblende gabbro plutons, mafic dikes, tonalites, and volcanic rocks are indicated by the close spatial and temporal association and similarities in mineral compositions (e.g., Wright and Fahan, 1988). The geochemical evolution of the Owens Mountain dikes follows a transitional tholeiitic to calc-alkalic trend (Wolf, 1992) – a trend similar to the Smartville dikes in the northern Sierran foothills (Day, 1977; Menzies et al., 1980; Xenophontos, 1984; Beard and Day, 1987). The rifting of the southern part of this arc produced the predominantly tonalitic Owens Mountain dike swarm but did not progress to the stage of ocean crust-formation.

The common problem of classifying the silicic volcaniclastic rocks as primary pyroclastic or epiclastic debris is intensified if the rocks have been extensively deformed,

as they have been in the Owens Mountain area. The compositional and mineralogical similarities and especially the coeval nature (spatially and temporally) of the the intrusive complex indicate that the volcaniclastic rocks are the products of active volcanism (e.g., Wright and Fahan, 1988).

The felsic metavolcanic and metasedimentary rocks in Owens Mountain are tentatively correlated with the silicic Gopher Ridge volcanics and the Salt Spring slate that are exposed in the Foothills terrane to the northwest (Clark, 1964; Greenamyer, 1974; Primrose, 1980; Ruiz, 1982). In the Foothills terrane, the Peñon Blanco, Logtown Ridge, Copper Hill and Gopher Ridge Formations form thick sequences of metavolcanic rocks which attest to the presence of a Jurassic active volcanic arc throughout the region (Clark, 1964; Bogen, 1985). The almost-synchronous deposition and folding of these strata and intrusion by mafic and felsic magmas (Guadalupe igneous complex, the Santa Cruz Mountain - Hornitos plutons and associated dikes, and the Owens Mountain dikes and tabular plutons) strongly suggest the rifting of the volcanic arc at the end of the Jurassic.

Tight folding just prior to rifting must have subtantially thickened the flysch strata. The total alumina in hornblende (Al_T) geobarometer (Hammarstrom and Zen, 1986; Hollister et al., 1987; Johnson and Rutherford, 1989; Rutter et al., 1989) has been applied to both felsic and mafic dike rocks from Owens Mountain. The barometer was empirically calibrated using rocks containing plagioclase, K-feldspar, amphibole, biotite, quartz, sphene, and iron-titanium oxides. Most of the felsic rocks contain the requisite minerals, although K-feldspar is not common in some. The average Al_T value of ten of the felsic rocks is 1.5 f.u. (formula units). The mafic rocks do not contain the proper assemblage, but it is noteworthy that the average Al_T value of 10 mafic rocks is 1.4 f.u. Wolf (1992) has found good experimental agreement between Al_T and crystallization pressure for a natural mafic rock without the requisite assemblage. These values give a 2-3 kbar crystallization pressure estimate, equal to 8-11 km. The actual Al_T values of

rocks, however, reflect the bulk magma compositions in addition to the crystallization pressures.

Ague and Brimhall (1988a, 1988b) tabulated Al_T values for amphiboles throughout the Sierra Nevada batholith. They found a general decrease in Al_T, and thus in calculated pressures, from west to east. Although they collected samples from neither the western-most part of the central Sierra Nevada batholith (the Fresno reentrant of Saleeby, 1990a) nor the Owens Mountain area, the data collected just to the east suggest relatively high crystallization pressures (3-5 kbar) and deep levels (11-19 km) for the now exposed rocks in the reentrant. The data from Owens Mountain (8-11 km depths) change the local pressure/depth estimates but are not incompatible with the finer, more complex, calculated pressure variations within the batholith that were described by Ague and Brimhall (1988a, 1988b).

Alternatively, the 2-3 kbar pressure difference between the data sets may be a function of the temporal differences between the crystallization ages of the Jurassic Owens Mountain dikes and the Cretaceous Sierra Nevada batholith plutons. In the 30-70 m.y. intervening time span, depths of magma emplacement certainly could have changed. In addition, the styles of emplacement point to different crystallization depths, with the presence of dikes generally characterizing higher levels of emplacement than more equant plutons. Because the levels of present-day exposure are roughly the same, these differences imply that the western margin of the Sierra Nevada was carried down to greater depths, between the Late Jurassic and the mid-Cretaceous.

Metamorphism and Metasomatism

Northwest of Owens Mountain, the Foothills terrane has been regionally metamorphosed mostly to greenschist-facies grade, although a few regionally extensive, higher-grade belts exist within the westernmost belt (Knopf, 1929; Taliaferro, 1942; Best, 1963; Clark, 1964; Ehrreich, 1965; Bogen, 1984; Paterson et al., 1987; Tobisch et al.,

1989). The rocks in the Owens Mountain area are amphibolite-facies grade, generally characterized by assemblages of andesine-oligoclase + hornblende ± quartz ± epidote ± biotite ± almandine. This area is along strike with and may correspond to the higher-grade, belt 2, of Tobisch et al. (1989).

Metamorphism was coeval with development of the ductile structures, though some annealing recrystallization took place in the quartz-rich rocks after deformation ceased. The intrusion of the Cretaceous plutons clearly post-dates the ductile deformation within the dike complex of Owens Mountain (southwestern domain), so deformation, metamorphism and annealing were pre-mid-Cretaceous. Amphibolite-facies grade metamorphism within the dike complex probably was of an autometamorphic nature, related to the syntectonic plutonism within the shear zone. The heat and fluids driven off of the magmas intruding the shear zone, as well as the magmas themselves, may have facilitated synplutonic ductile deformation. A later phase of deformation, and probably metamorphism, occurred in the eastern parts of the Owens Mountain area as a result of the forcible intrusion of the Cretaceous Academy pluton.

The whole rock chemistry data indicates that pervasive metasomatism has not occurred in this area. All of the rocks contain little potassium, with the exception of the biotite schists and the Cretaceous tonalites. This potassium-poor nature of the igneous rocks probably is inherited from the source region and not a result of shallow level metasomatism, because the amounts of sodium in the rocks are highly variable and do not mimic the potassium behavior. Sodium-rich tonalitic and amphibolitic layers are located adjacent to sodium-poor tonalitic and amphibolitic layers, and these compositional variations can be accounted for in the primary plagioclase compositions comprising the various layers.

Some of the felsic layers contain over 20 vol.% metamorphic epidote, indicating possible metasomatic calcium enrichment (and concomitant alkali loss?) or retrograde reactions associated with the dynamic metamorphism of the mafic layers that occurs

under shear stresses (Deer et al., 1966). Dilek (1989) suggests that epidosite lenses associated with sheared diabases in the Smartville complex formed by extensive hydrothermal activity during an extensional phase. The epidote-rich layers in the Owens Mountain area also may record extensive, though spatially restricted, hydrothermal activity.

Timing

The emplacement ages of the tonalitic tabular plutons and felsic and mafic dikes reveal important information about the style of intrusion and the large scale structure of the Owens Mountain area. The sedimentary and volcaniclastic strata (Salt Spring and Gopher Ridge Formations) into which the dike complex was emplaced were deposited between 160 and 154 Ma (Clark, 1964; Tobisch et al., 1989). In the Santa Cruz Mountain - Guadalupe igneous complex area, rotation and folding of these strata during the Nevadan orogeny occurred concomitantly with and subsequent to deposition, and prior to ductile deformation, from 160 to 151 Ma (Bogen, 1985; Tobisch et al., 1989). Thus, it seems likely that most of the Owens Mountain dike complex was emplaced into already steeply dipping strata as subvertical dikes, from 155 to 148 Ma (Table 4). The intrusion as dikes (in contrast to sills) better explains the limited areal extent of the tonalitic bodies, because folded tonalitic sills would be present throughout the area – not just in the southwestern domain – if an antiformal structure at Owens Mountain post-dated sill emplacement.

The coarse-grained tonalitic rocks generally are restricted to the southwestern domain, but the mafic rocks are found throughout the Owens Mountain area. Some of the mafic layers may be metavolcanic material that formed the country rock into which the dikes were intruded. Alternatively, the larger areal extent of the mafic dikes (over that of the tonalitic dikes) may be due to the lower viscosities that the mafic magmas probably

had. The lateral spread of magma away from the main source, and the infiltration along the country rock foliation would occur more readily with magmas with lower viscosities.

The emplacement ages of the felsic and mafic dike swarm also reveal important information about the regional tectonics during the Late Jurassic. In the strict definition of the timing of Nevadan orogenesis – 155±3 Ma (Bateman and Clark, 1974; Schweickert et al., 1984) – ductile deformation along the Bear Mountains fault zone and, subsequently, throughout the Foothills terrane was post-Nevadan (151 to 123 Ma) (Newton, 1986; Paterson et al., 1987; Tobisch et al., 1989). However, the onset of ductile deformation in the Santa Cruz Mountain - Guadalupe igneous complex area may have been earlier than 151 Ma (e.g., Vernon et al., 1989), but no older age can be assigned due to the lack of older, datable igneous rocks in the area.

In the Santa Cruz Mountain - Guadalupe igneous complex area (Fig. 1), a mafic-felsic, intrusive-extrusive (dike swarm?) assemblage similar to the Owens Mountain complex crops out (Tobisch et al., 1989). Saleeby et al. (1989a) have assigned a 147 Ma age to a deformed tonalite from the Santa Cruz Mountain pluton. Although most emplacement ages fall within a 151 to 145 Ma time span, the nearby Courthouse Rock tonalite (pervasively foliated) has a 138 Ma age (Saleeby et al., 1989a). My Santa Cruz Mountain zircon sample (8) was collected to establish a better understanding of the timing relationships between the different rock types in the Santa Cruz Mountain area and also with the Owens Mountain area. The hope was to find an intrusive rock that is older than 151 Ma and thus better constrain the age of deformation. Sample 8 is a highly deformed tonalite, probably a sheared dike. The 145±7 Ma age determined in this study falls within the period of emplacement of the other rocks in the area as determined by Saleeby et al. (1989a).

Magmatism in the Owens Mountain area (155 to 148 Ma) slightly preceded that in the Santa Cruz Mountain - Guadalupe igneous complex area (151 to 138 Ma). Thus, late

to post-Nevadan, syntectonic plutonism occurred throughout the central and southern parts of the Foothills terrane, from 155 to 138 Ma.

The igneous rocks in the Owens Mountain area are regionally significant because they span the traditional Nevadan - post-Nevadan period. The moderately to strongly deformed rocks of the Owens Mountain dike complex are tentatively identified as the southern extension of the Bear Mountains fault zone. Correlation with the Bear Mountains fault zone to the north gives a minimum age of 151 Ma for the initiation of Owens Mountain ductile deformation – during the midst of dike emplacement. However, the 155 to 151 Ma dikes (especially samples 2-5; Fig. 16a) exhibit an age - degree of deformation relationship in which the older dikes are more deformed. This relationship indicates synplutonic deformation within this time span (155 to 151 Ma). Thus, ductile deformation probably occurred before 151 Ma, at least in the Owens Mountain area. The structural and geochronologic data from Owens Mountain, therefore, reveal that ductile deformation probably was initiated during the late Nevadan orogeny (sensu stricto). Other workers have demonstrated that this phase of ductile deformation continued well into the Cretaceous. It seems logical not to attempt to separate Nevadan non-ductile structures and Nevadan - post-Nevadan ductile structures into two separate events. These different structures probably should be thought of as resulting from a continuous evolution of the same, protracted, transtensional-transpressional, Nevadan orogeny.

Three of the zircon samples (10-12) are from three different types of nondeformed, Cretaceous dikes that cut the Owens Mountain structures (Fig. 16b). The ~123 Ma granitic pegmatite dike (sample 10) cuts the hornblendite-gabbro pluton in the southeast area. Nothing definitive is revealed by the U-Pb data from samples 11 and 12, except their probable Cretaceous age.

Unfortunately, the ages of these dikes do not tightly constrain the timing of Owens Mountain deformation. The undeformed hornblendite-gabbro pluton must be older than the pegmatite dike that cuts it. Thus, its emplacement age must lie between

148 and 123 Ma, but no more accurate age can be assigned. Ductile deformation ceased sometime before 123 Ma. Ductile deformation also is constrained to have ceased by 123 Ma in the Santa Cruz Mountain - Guadalupe igneous complex area (Tobisch et al., 1989).

Enormous quantities of granitoid magma began to be emplaced at ~125 Ma – the beginning of the main phase of Cretaceous, Sierra Nevada plutonism (Bateman and Clark, 1974; Saleeby and Sharp, 1980; Stern et al., 1981; Armstrong, 1988b). The Bass Lake pluton was emplaced just to the north of Owens Mountain at 118 Ma (sample 9). In the Santa Cruz Mountain - Guadalupe igneous complex vicinity, the Bass Lake pluton has been dated at 115 Ma (date recalculated by Saleeby from the data of Stern et al., 1981). Just to the east of Owens Mountain, different phases of the Academy pluton were emplaced between 121 and 114 Ma (Saleeby, 1975; Mack et al., 1979). An overview of the Late Jurassic to mid-Cretaceous tectonoplutonic chronology of the Owens Mountain area is schematically represented in Fig. 18.

Implications for Regional Tectonics

The Owens Mountain and Santa Cruz Mountain dike swarms record a complex tectonic regime of transtension and transpression along the Cordilleran margin during the Late Jurassic period. Five other distinct swarms of mafic and associated felsic dikes also were emplaced into a variety of accreted ensimatic terranes as well as the adjacent North American sialic edge in late Middle and Late Jurassic time: [1] In the Rattlesnake Creek terrane (the Preston Peak and Seiad Valley areas) of the Klamath Mountains, late-stage and sheeted plagiogranite dikes within the ophiolitic melange basement and overlying hypabyssal complex have 164±1 and 172±2 Ma ages (Snoke, 1977; Saleeby et al., 1982, in press; Hill, 1985; Harper et al., in press). [2] In the northwest Sierran foothills, the north-northwest-trending Folsom mafic dike swarm and associated layered diorite-gabbro-pyroxenite plutons intruded previously disrupted Paleozoic ophiolitic melange at 164±1 Ma (Springer, 1980; Saleeby, 1982; Saleeby et al., 1989b; Saleeby, 1990b). [3]

North of and along strike with the Folsom dikes, the north-northwest-trending Smartville basaltic and tonalitic dike swarm and associated tonalitic and gabbroic tabular plutons were emplaced into a well-preserved, Lower and Middle Jurassic island-arc volcanic sequence at 162±1 Ma (Day, 1977; Xenophontos and Bond, 1978; Menzies et al., 1980; Day et al., 1985; Beard and Day, 1987; Saleeby et al., 1989b; Dilek, 1989). [4] At ~158 Ma, the east-west-trending Sonora mafic dike swarm (central Sierran foothills) intruded polydeformed lower Paleozoic continental rise strata, mid-Paleozoic arc rocks, upper Paleozoic to lower Mesozoic chert-argillite melange, and Lower to Middle Jurassic arc rocks (Sharp, 1980; Merguerian, 1986; Schweickert et al., 1988). [5] At ~148 Ma, the northwest-trending, mafic to felsic, Independence dike swarm (eastern Sierra) intruded Proterozoic crystalline rocks, Paleozoic strata and lower Mesozoic arc rocks that were deposited along the margin of North America (Moore and Hopson, 1961; Chen and Moore, 1979; James, 1989).

The relative timing of magmatism and tectonism varied along the arc length and did not follow a consistent geographic pattern, but, in general, Jurassic dike emplacement occurred earlier in the north than in the south. The Santa Cruz Mountain dikes are inconsistent with this timing-location pattern. Dating of variably deformed tonalitic dikes and plutons from the Owens Mountain swarm suggests Nevadan-aged, syntectonic emplacement over an ~7 m.y. period, possibly along a regional zone of weakness, such as the Bear Mountain fault zone. However, the Bear Mountains fault zone was not necessarily the only locus of transtension or extension in the region, as shown by the emplacement of the dike swarm of the more westerly Santa Cruz Mountain pluton and, possibly, the tabular bodies of the more easterly Guadalupe igneous complex.

Late Middle and Late Jurassic plutonism was not confined to shear zones. Although the Smartville dike complex pre-dated the Nevadan orogeny, it may only have experienced static autometamorphism, with only localized ductile deformation (Beiersdorfer and Day, 1983; Beard and Day, 1987). Nevadan ductile reverse faulting

occurred along the western margin of the Smartville complex, and occurred in association with the intrusion of the 158 Ma Yuba River pluton (Saleeby et al., 1989b). Synplutonic deformation is recorded (at ~164 Ma) along the northern end of the Bear Mountains ophiolite belt (Folsom dikes) (Springer, 1980; Saleeby, 1982, 1990b) and in the west-central Klamath Mountains (Donato, 1987; Coleman et al., 1988). A small degree of synplutonic deformation also occurred to the south, in some of the Sonora and Independence dikes (Merguerian, 1986; James, 1989).

Figures 19a-d schematically illustrate the tectonoplutonic environment along the southwest Cordillera for two sequential time periods – [a and c]: the late Middle to middle Late Jurassic, and [b and d]: the middle Late to latest Late Jurassic (modified from Saleeby, 1981 and Saleeby et al., 1992). Figures 19a,b generalize the information from the block diagrams (Figs. 19c,d).

During the late Middle Jurassic, the magnitude and direction of North American absolute motion was ~45 km/m.y. toward the north-northeast (May and Butler, 1986). Subduction was orthogonal to the plate margin and may have been subparallel to the North American vector (Figs. 19a,c). This subparallelism may have promoted the formation of the suprasubduction zone extensional environment in which the Coast Range and Josephine ophiolites developed.

During the middle Late Jurassic, the magnitude and direction of North American absolute motion changed to 150-230 km/m.y. to the northwest (May and Butler, 1986). Oblique subduction became dominant, because the North American margin was subparallel to the direction of relative motion (Figs. 19b,d). The margin was cut by a series of left-lateral transform faults. The intra- and fore-arc basins were deformed, closed and folded, and some of the marginal basin basement was obducted along thrust faults. Complex cycles of transtension and transpression occurred for a 5-10 m.y. period, during which syntectonic dike swarms were emplaced. This period of deformation is called the Nevadan orogeny.

Figure 20 illustrates the latitudinal changes in the position and orientation of North America during the Late Jurassic through Early Cretaceous. The 160, 150 and 140 Ma time slices were calculated using the hotspot and pole reconstructions of Morgan (1981) [Greenland-Antarctica] and Anderson and Schmidt (1983) [North America-Central America], and the paleomagnetic euler pole data (J1-J2 and J2-K tracks) of May and Butler (1986). The views are Mercator projections from the equator (0°) to N80° latitude. The data do not constrain longitude well, but in these views, the reference frame is fixed. Although the same amount of time elapses between views (10 m.y.), there is a much larger spatial displacement during the later time segment (150-140 Ma) due to the increased velocity to the northwest of North America at the J2 cusp (150 Ma), from 0.6 °/m.y. to 2.8 °/m.y. (May and Butler, 1986). This vector is represented by the arrow in the 150 Ma view.

The regional tectonics of the Cordilleran dike swarms may be related in a broad dynamic sense to the absolute motion of North America by using the apparent polar wander (APW) analysis (e.g., Gordon et al., 1984; May and Butler, 1986; May et al., 1989). The Preston Peak, Folsom and Smartville swarms intruded along a preexisting fabric in a broad extensional environment synchronous with suprasubduction ophiolite formation in the 162 to 164 Ma Josephine and 167 to 156 Ma Coast Range ophiolite belts (Hopson et al., 1981; Sharp and Evarts, 1982; Saleeby, 1990b). This extensional phase may have resulted from the retreat of North America relative to the plate edge. Evidence of synplutonic deformation in the Folsom and Preston Peak dikes (Saleeby, 1982; Yule et al., 1992), however, suggests some component of transform motion.

The late Nevadan Sonora, Owens Mountain - Santa Cruz Mountain and Independence dike swarms record a complex pattern of sinistral sense transtension-transpression. The orientation of the Sonora dikes – perpendicular to the plate margin – suggests margin-parallel extension, possibly related to intra-arc transform motion (Harper et al., 1985; Merguerian, 1986). The Owens Mountain dikes are especially important

because of their unique and critical emplacement ages and structural data; they reveal that plutonism and sinistral shearing occurred during the same period. Figure 21 schematically illustrates the relationship between Sonora and Owens Mountain dike orientations and the stress regime along the Cordilleran margin. The east-west orientation of the Sonora dikes may be related to tensional weaknesses within the margin, oriented 45° from the northwest direction of North American absolute motion and transform faulting (as shown by the opening of a tension gash in the strain ellipse). The north-northwest - south-southeast orientation of the Owens Mountain dikes may be related to their emplacement within the intra-arc Bear Mountains fault zone.

Contractile deformation appears to have been weaker to the east of the deforming arc, so Independence dike intrusion probably occurred in a transtensional-dominated environment, which may account for the northwest-southeast trend. However, Moore and Hopson (1961) found indications of left-lateral motion even here, expressed as an oblique schistosity in many of the dikes.

The Late Jurassic Cordilleran dike swarms developed in response to a period of left-oblique convergence that best fits the model of May and Butler (1986) and May et al. (1989) for the J2 APW cusp and the subsequent, rapid northward acceleration of North America. Left-lateral motion also may have been accommodated along the intra-arc Bear Mountains and Melones fault zones (Newton, 1986; Paterson et al., 1987; Tobisch et al., 1989; Gefell et al., 1989; Jayko, 1991). Although Miller and Paterson (1991) and Paterson and Wainger (1991) found little evidence for strike-slip motion along these fault zones, westward thrusting may have obscured earlier lateral motion. Left-lateral motion may have been better preserved at Owens Mountain because of the abundance of intrusive rocks in the dike swarm/shear zone. Alternatively, the differences in styles of displacement between the Owens Mountain and the more northern segments of the Bear Mountains fault zones may be due to a decoupling of motion between the lower and

upper regions of the fault. The emplacement of dikes may solve the space problem at the location of decoupling.

East of the Jurassic Sierran arc, sinistral slip along the Pine Nut fault system may have partially decoupled the rifting, collapsing arc to the west from the northward-moving North American craton to the east (Oldow, 1983; Oldow et al., 1984). Sinistral movement along the Mojave-Sonora megashear may have had a similar decoupling effect (e.g., Silver and Anderson, 1974; Silver, 1983; Anderson and Schmidt, 1983), and fragments of the Sierran western Foothills terrane may have been displaced southward as far as the pre-San Andreas position of the Transverse Ranges (Saleeby, 1991).

The syntectonic emplacement ages of the deformed Owens Mountain tonalitic tabular plutons and felsic and mafic dikes give important clues about the relationship between tectonism and plutonism in oblique subduction zone environments. May et al. (1989) calculated the northward component of absolute motion of western North America to be in excess of 150 km/m.y. and possibly as high as 230 km/m.y., between 150 and 135 Ma. Thus, the tangential component of subduction in the latest Jurassic - earliest Cretaceous rifting arc must have been very large and probably greater than the normal component of subduction. This result is in contrast to that reached by Glazner (1991), using hotspot-based data from Engebretson et al. (1985), that the tangential component was much less than the normal component, and declined from ~30 to ~20 km/m.y. during this time period. May et al. (1989) consider the significant differences between their paleomagnetic data and the hotspot data to be the result of poorly constrained Jurassic hotspot tracks and an inconsistent reference frame. Glazner's (1991) model correlates major episodes of Sierran plutonism with oblique convergence and lulls in plutonism (but not volcanism) with trench-normal convergence. However, the correlations weaken considerably when the more (?) reliable paleomagnetic data set of May et al. (1989) is used. In fact, the J2-K increased velocity of North America (with concomitant oblique convergence) is accompanied by a lull in plutonism within the Sierra and Klamath ranges

(Saleeby et al., 1982; Harper et al., 1985). Our geochronologic and structural data indicate that latest Jurassic plutonism (and volcanism) and left-oblique convergence were coeval but that sinistral motion along the Bear Mountains fault zone probably persisted into the earliest Cretaceous, without continued addition of magma. This tectonoplutonic chronology is illustrated in Fig. 18. This conclusion supports the evidence for high rates of tangential motion along the western margin of North America during the latest Jurassic - earliest Cretaceous.

CONCLUSIONS

Much of Owens Mountain comprises tonalitic dikes and tabular plutons and cogenetic mafic dikes. U-Pb zircon geochronological analysis of the tonalites indicates a 155 to 148 Ma time span for emplacement. The tonalitic and mafic dikes show mutually cross-cutting relationships and thus are coeval. The dike swarm was variably sheared and mylonitized with a sinistral sense of motion. Fabrics indicative of supersolidus deformation and a positive correlation between tonalite crystallization age and degree of deformation are suggestive of synplutonic ductile deformation.

The Owens Mountain shear zone may be the southern extension of the Bear Mountains fault (shear) zone. Evidence of sinistral motion, generally overprinted along the Bear Mountain fault zone, is well-preserved at Owens Mountain. These regional ductile deformational structures probably should be thought of as resulting from a continuous evolution of the same, long-lived, transtensional-transpressional, Nevadan orogeny, with an initial, relatively brief (<5 m.y.) phase of rigid bed rotation, from <160 to >155 Ma, followed by a later, extended phase of ductility, from 155 to 137 Ma, and possibly as late as 123 Ma.

Owens Mountain is just one of a number of dike swarms that records a complex pattern of alternating transtension and transpression along the length of the late Middle to

Late Jurassic arc off the western margin of North America. The regional tectonics of these dike swarms may be related to the absolute motion of North America. Pre-Nevadan dikes (Preston Peak, Folsom and Smartville) intruded during an extensional phase resulting from the retreat of North America relative to the plate edge. Late Nevadan dikes (Sonora, Owens Mountain - Santa Cruz Mountain and Independence) were emplaced into a sinistral sense transtensional-transpressional environment that developed at the J2 APW cusp and during later, rapid northwestward acceleration of North America.

Table 1. Owens Mountain Whole Rock Analyses from DCP Spectrometry

Sample #	W4	24	25	28	9	2	57	61A	3	4	73	77	79	82A	120-1
Rock type	ton	ton	ton	ton	ton	ton	ton	hb ton	ton	ton	hb ton	ton	bi ton	ton	hb ton
SiO2	74.9	73.2	74.3	75.9	64.8	72.6	67.7	70.6	74.2	76.1	76.0	76.7	72.8	68.0	71.6
TiO2	0.4	0.4	0.4	0.3	0.7	0.5	0.5	0.5	0.4	0.3	0.3	0.0	0.1	0.4	0.5
Al2O3	13.0	12.4	12.7	12.1	16.4	13.4	14.4	14.2	13.8	12.2	12.5	13.4	14.4	15.5	14.6
FeO	2.4	2.5	2.1	2.4	4.5	3.5	4.0	3.3	1.8	2.1	1.3	0.2	1.0	2.7	3.5
MnO	0.1	0.1	0.0	0.1	0.1	0.1	0.1	0.1	0.0	0.0	0.0	0.0	0.0	0.0	0.1
MgO	0.4	0.5	0.6	0.4	2.2	1.0	2.5	1.1	0.8	0.4	0.7	0.0	0.3	1.3	1.0
CaO	8.0	5.3	7.2	2.3	5.7	4.2	6.0	4.8	4.3	1.6	4.0	0.7	1.6	4.1	4.1
Na2O	1.7	3.0	1.6	4.8	3.7	4.2	3.6	4.0	4.5	5.9	3.9	6.0	5.0	4.1	4.1
K2O	0.2	0.2	0.5	0.1	1.5	0.2	0.1	0.2	0.2	0.8	0.3	1.8	2.4	1.6	0.5
P2O5	0.1	0.1	0.1	0.1	0.2	0.1	n.a.	n.a.	0.1	0.1	0.2	n.a.	0.1	0.2	n.a.
Total	101.1	97.6	99.2	98.4	99.6	99.7	98.9	98.8	100.0	99.4	99.0	98.8	97.6	97.7	100.0
(ppm):															
Ni	696	777	795	763	769	752	n.a.	n.a.	747	711	751	n.a.	736	783	n.a.
Cu	11	12	3	5	18	4	n.a.	n.a.	11	5	3	n.a.	2	3	n.a.
Zn	21	40	26	33	81	37	n.a.	n.a.	33	18	24	n.a.	52	65	n.a.
Sr	231	214	313	108	399	132	n.a.	n.a.	247	70	150	n.a.	183	324	n.a.
Zr	123	156	147	141	118	112	n.a.	n.a.	175	146	152	n.a.	57	79	n.a.
CIPW norm															
Q	46.9	43.5	47.7	40.9	19.8	35.2	28.5	33.4	36.6	34.1	43.0	33.6	30.6	26.2	33.0
or	1.2	1.2	3.0	0.6	8.9	1.2	0.5	1.4	1.2	4.8	1.8	10.8	14.5	9.7	3.0
ab	14.2	26.0	13.6	41.3	31.4	35.7	30.8	34.1	38.1	50.2	33.3	51.4	43.4	35.5	34.7
an	27.0	20.3	26.2	11.4	23.8	17.2	23.2	20.4	16.9	4.5	15.9	3.5	8.1	19.6	20.0
ne	0.0	0.0	0.0	0.0	0.0	0.0	0.0	0.0	0.0	0.0	0.0	0.0	0.0	0.0	0.0
C	0.0	0.0	0.0	0.0	0.0	0.0	0.0	0.0	0.0	0.0	0.0	0.3	0.7	0.0	0.0
di	9.4	5.7	8.3	0.2	3.8	3.2	5.7	3.2	3.7	3.0	3.5	0.0	0.0	1.0	0.3
hy	0.0	2.5	0.5	5.1	10.9	6.7	10.3	6.5	2.8	2.8	2.0	0.4	2.5	7.2	8.1
ol	0.0	0.0	0.0	0.0	0.0	0.0	0.0	0.0	0.0	0.0	0.0	0.0	0.0	0.0	0.0
il	0.8	0.8	0.8	0.6	1.3	1.0	0.9	1.0	0.8	0.6	0.6	0.0	0.2	0.8	1.0

ton = tonalite; felsic = felsic rock; grnt = granite; mafic = mafic rock; sch = schist; hb = hornblende; bi = biotite; ms = muscovite; n.a. = not analysed.

Table 1 (cont.). Owens Mountain Whole Rock Analyses from DCP Spectrometry

Sample #	W6	45	50-A	51	61C	63	69	120-6	120-7	21	10	76	82	90-A	56
Rock type	felsic	felsic	felsic	felsic	felsic	felsic	felsic	felsic	felsic	grnt	bi grnt	grnt	ms grnt	grnt	dacite
SiO2	74.4	78.5	78.2	68.0	77.1	63.7	82.2	78.3	67.0	78.6	76.5	75.0	76.9	70.4	61.2
TiO2	0.4	0.0	0.2	0.9	0.4	0.7	0.2	0.3	1.1	0.0	0.0	0.0	0.0	0.3	0.8
Al2O3	13.1	13.2	12.8	13.7	12.5	14.1	11.8	13.2	14.9	13.4	14.3	13.1	14.1	15.2	14.4
FeO	4.6	0.3	0.6	4.9	2.3	14.9	0.8	2.0	6.0	0.4	0.9	0.5	0.5	3.8	7.2
MnO	0.1	0.0	0.0	0.1	0.0	0.5	0.0	0.0	0.2	0.0	0.0	0.0	0.1	0.1	0.2
MgO	0.5	0.1	0.1	1.8	0.8	2.0	0.1	0.3	1.8	0.2	0.1	0.1	0.2	0.9	3.8
CaO	4.1	0.4	1.8	4.6	3.9	1.8	1.8	2.1	5.5	1.4	1.4	0.9	0.8	2.3	8.7
Na2O	3.7	6.8	5.8	4.2	4.1	1.8	4.6	4.9	3.8	3.9	4.6	3.8	2.3	3.4	3.3
K2O	0.2	1.1	0.8	0.2	0.1	1.1	0.3	0.4	0.8	3.8	4.0	5.0	2.6	2.2	0.3
P2O5	0.1	n.a.	n.a.	0.4	n.a.	0.2	n.a.	n.a.	n.a.	0.1	0.1	0.0	n.a.	n.a.	0.1
Total	101.1	100.4	100.3	98.4	101.2	100.6	101.8	101.4	101.1	101.7	101.8	98.4	97.5	98.6	99.9
(ppm):															
Ni	745	n.a.	n.a.	767	n.a.	783	n.a.	n.a.	n.a.	749	752	737	n.a.	n.a.	845
Cu	17	n.a.	n.a.	6	n.a.	16	n.a.	n.a.	n.a.	6	22	2	n.a.	n.a.	4
Zn	48	n.a.	n.a.	53	n.a.	105	n.a.	n.a.	n.a.	25	29	21	n.a.	n.a.	74
Sr	165	n.a.	n.a.	201	n.a.	68	n.a.	n.a.	n.a.	86	84	48	n.a.	n.a.	265
Zr	136	n.a.	n.a.	135	n.a.	124	n.a.	n.a.	n.a.	12	38	32	n.a.	n.a.	101
CIPW norm															
Q	38.9	33.3	37.4	28.3	42.0	29.6	48.9	41.2	24.0	37.1	30.1	31.9	52.4	33.4	15.2
or	1.2	6.5	4.7	1.2	0.6	6.5	1.7	2.3	4.7	22.1	23.2	30.0	15.8	13.2	1.8
ab	31.0	57.3	48.9	36.1	34.3	15.1	38.2	40.8	31.8	32.4	38.2	32.7	20.0	29.2	28.0
an	18.3	2.0	6.5	16.2	15.2	8.9	8.8	10.3	21.0	6.8	6.4	4.0	4.1	11.6	23.6
ne	0.0	0.0	0.0	0.0	0.0	0.0	0.0	0.0	0.0	0.0	0.0	0.0	0.0	0.0	0.0
C	0.0	0.1	0.0	0.0	0.0	6.6	0.6	0.9	0.0	0.3	0.0	0.0	6.2	3.1	0.0
di	1.6	0.0	2.0	4.2	3.3	0.0	0.0	0.0	5.1	0.0	0.3	0.5	0.0	0.0	16.4
hy	8.3	0.8	0.0	10.3	3.8	31.9	1.4	3.9	11.3	1.2	1.7	0.9	1.6	9.0	13.6
ol	0.0	0.0	0.0	0.0	0.0	0.0	0.0	0.0	0.0	0.0	0.0	0.0	0.0	0.0	0.0
il	0.8	0.0	0.4	1.7	0.8	1.3	0.4	0.6	2.1	0.0	0.0	0.0	0.0	0.6	1.5

Table 1 (cont.). Owens Mountain Whole Rock Analyses from DCP Spectrometry

Sample #	59-A	12	31	61B	120-2	120-5	459	422	90-D	101	136
Rock type	dacite	dacite	mafic	mafic	mafic	mafic	mafic	mafic	bi sch	bi sch	bi sch
SiO2	61.2	68.2	48.1	54.4	52.7	51.8	48.5	51.5	71.9	62.1	69.9
TiO2	1.2	0.5	1.0	0.8	1.7	1.1	0.4	0.9	0.5	1.1	0.8
Al2O3	15.0	15.7	17.7	15.3	17.1	16.9	14.4	15.4	12.8	19.4	15.2
FeO	6.7	4.1	9.0	8.9	11.9	10.6	8.5	9.2	3.8	8.7	5.3
MnO	0.2	0.1	0.1	0.2	0.3	0.2	0.2	0.2	0.0	0.1	0.0
MgO	2.3	0.9	7.1	6.8	4.5	6.3	10.8	7.0	1.4	3.2	2.4
CaO	5.6	3.4	13.9	8.7	8.5	10.6	14.8	9.9	2.2	1.3	1.2
Na2O	4.8	4.5	1.5	3.8	3.9	3.2	1.7	3.5	2.6	1.4	1.9
K2O	0.1	1.0	0.8	0.3	0.4	0.4	0.2	0.2	2.4	3.6	3.6
P2O5	n.a.	n.a.	n.a.	n.a.	n.a.	n.a.	0.1	n.a.	n.a.	n.a.	n.a.
Total	97.1	98.4	99.2	99.2	100.9	101.0	99.5	97.7	97.6	100.9	100.4
(ppm):											
Ni	n.a.	n.a.	n.a.	n.a.	n.a.	n.a.	1410	n.a.	n.a.	n.a.	n.a.
Cu	n.a.	n.a.	n.a.	n.a.	n.a.	n.a.	80	n.a.	n.a.	n.a.	n.a.
Zn	n.a.	n.a.	n.a.	n.a.	n.a.	n.a.	105	n.a.	n.a.	n.a.	n.a.
Sr	n.a.	n.a.	n.a.	n.a.	n.a.	n.a.	194	n.a.	n.a.	n.a.	n.a.
Zr	n.a.	n.a.	n.a.	n.a.	n.a.	n.a.	27	n.a.	n.a.	n.a.	n.a.
CIPW norm											
Q	14.9	27.2	0.0	0.0	0.0	0.0	0.0	0.0	38.9	26.1	34.8
or	0.6	5.9	4.8	1.7	2.3	2.3	1.2	1.0	14.5	21.0	21.1
ab	41.8	38.6	12.8	32.5	32.7	26.8	12.6	30.5	22.5	11.5	16.1
an	19.7	17.0	39.5	24.0	27.7	30.2	31.2	26.3	11.2	6.4	6.0
ne	0.0	0.0	0.0	0.0	0.0	0.0	1.0	0.0	0.0	0.0	0.0
C	0.0	1.2	0.0	0.0	0.0	0.0	0.0	0.0	2.0	10.8	6.0
di	7.6	0.0	24.7	16.1	11.8	18.1	34.6	19.6	0.0	0.0	0.0
hy	13.1	9.2	3.8	23.0	15.5	9.5	0.0	11.5	9.9	22.1	14.6
ol	0.0	0.0	12.5	1.1	6.7	10.9	18.6	9.4	0.0	0.0	0.0
il	2.4	1.0	1.9	1.6	3.2	2.1	0.8	1.9	1.0	2.1	1.4

Table 2. Owens Mountain amphibole compositions from SEM-EDS (normalized to 100).

Rock Type	Ton	Ton	Ton	Ton	Ton	Ton	Ton	Ton	Mafic	Mafic	Mafic	Ton
Sample #	9	57	2	4	6	3f	3f	3f	3m	3m	68A m	68A f
SiO2	44.76	46.68	46.40	50.29	42.68	46.48	49.66	45.19	48.38	47.60	52.47	50.32
TiO2	1.38	0.33	0.34	0.15	0.59	0.57	0.29	0.22	0.55	0.69	0.28	0.74
Al2O3	10.19	10.85	5.88	4.37	14.06	9.90	7.19	10.31	8.65	8.91	5.69	7.17
FeO	19.55	14.87	25.79	15.59	19.23	15.27	15.03	16.98	14.43	14.84	10.50	10.99
MnO	0.29	0.28	0.76	0.59	0.80	0.38	0.22	0.17	0.20	0.00	0.13	0.23
MgO	10.14	13.52	12.24	15.22	9.84	13.68	15.53	12.84	14.66	14.58	16.59	16.41
Cr2O3	0.00	0.14	0.00	0.00	0.00	0.00	0.12	0.00	0.00	0.00	0.20	0.00
P2O5	0.00	0.20	0.00	0.00	0.00	0.00	0.00	0.00	0.00	0.00	0.00	0.00
CaO	11.28	10.98	7.09	11.71	10.52	11.25	10.51	11.98	11.49	11.58	12.74	12.41
Na2O	1.84	2.01	1.39	1.89	2.06	2.19	1.30	2.09	1.50	1.63	1.40	1.54
K2O	0.57	0.13	0.11	0.19	0.22	0.27	0.15	0.21	0.14	0.17	0.00	0.18
Ions/23 oxygens												
Si	6.618	6.718	6.967	7.263	6.295	6.717	7.092	6.602	6.919	6.832	7.353	7.093
Al 4	1.382	1.282	1.033	0.737	1.705	1.283	0.908	1.398	1.081	1.168	0.647	0.907
Al 6	0.394	0.559	0.007	0.006	0.740	0.403	0.302	0.378	0.376	0.339	0.292	0.283
Ti	0.153	0.036	0.038	0.016	0.065	0.062	0.031	0.024	0.059	0.074	0.030	0.078
Fe	2.417	1.790	3.239	1.883	2.372	1.845	1.796	2.074	1.726	1.782	1.231	1.296
Mn	0.036	0.034	0.097	0.072	0.100	0.046	0.027	0.021	0.024	0.000	0.015	0.027
Mg	2.236	2.901	2.740	3.278	2.163	2.947	3.307	2.797	3.126	3.121	3.467	3.448
Cr	0.000	0.005	0.000	0.000	0.000	0.000	0.005	0.000	0.000	0.000	0.008	0.000
P	0.000	0.005	0.000	0.000	0.000	0.000	0.000	0.000	0.000	0.000	0.000	0.000
Ca	1.787	1.694	1.140	1.811	1.663	1.742	1.609	1.876	1.761	1.782	1.913	1.875
Na	0.527	0.561	0.404	0.529	0.589	0.613	0.360	0.592	0.416	0.453	0.380	0.421
K	0.107	0.024	0.021	0.035	0.041	0.050	0.027	0.039	0.026	0.031	0.000	0.032

Ton = tonalite; gbro = gabbro; Hbdite = hornblendite; Ophicalc = ophicalcite; Calc-sil = calc-silicate; Chl Sch = chlorite schist

n.d. = not determined; n = number of averaged analyses.

Table 2 (cont.). Owens Mountain amphibole compositions from SEM-EDS (normalized to 100).

Rock Type	Dacite	Dacite	Mafic	Mafic	Ton	Mafic	Mafic	Hb gbro	Hb gbro	Hbdite	Hbdite	Mafic
Sample #	56	56	58 m	58 m	58 f	W3 m	W3 m	67	67	89	89	62
SiO2	44.84	45.17	46.95	46.15	48.41	48.88	48.55	44.11	43.53	51.00	52.08	49.49
TiO2	0.56	0.77	0.64	0.52	0.28	0.41	0.67	1.01	1.47	0.54	0.66	0.71
Al2O3	11.00	11.32	9.88	10.78	8.54	7.90	8.97	13.45	13.53	6.90	3.97	6.86
FeO	18.81	16.90	14.24	14.48	14.17	13.82	13.67	13.72	14.13	10.82	11.15	14.17
MnO	0.47	0.34	0.27	0.47	0.14	0.35	0.24	0.36	0.45	0.10	0.24	0.00
MgO	10.40	11.53	13.84	13.84	14.50	14.53	14.93	13.46	13.21	17.54	17.97	14.99
Cr2O3	0.00	0.00	0.00	0.00	0.00	0.38	0.00	0.13	0.00	0.00	0.13	0.00
P2O5	0.00	0.00	0.00	0.00	0.00	0.00	0.15	0.00	0.00	0.00	0.00	0.00
CaO	11.59	11.04	12.02	11.50	12.35	12.48	11.32	11.48	11.26	12.38	12.59	12.84
Na2O	1.92	2.62	1.86	2.08	1.51	1.07	1.31	2.13	2.20	0.61	1.11	0.93
K2O	0.40	0.30	0.30	0.18	0.10	0.18	0.19	0.14	0.21	0.10	0.10	0.00
Ions/23 oxygens												
Si	6.604	6.588	6.750	6.645	6.929	7.003	6.917	6.345	6.280	7.143	7.341	7.068
Al 4	1.396	1.412	1.250	1.355	1.071	0.997	1.083	1.655	1.720	0.857	0.659	0.932
Al 6	0.515	0.535	0.424	0.474	0.369	0.337	0.423	0.626	0.581	0.282	0.000	0.223
Ti	0.062	0.084	0.069	0.056	0.030	0.044	0.072	0.109	0.159	0.057	0.070	0.076
Fe	2.317	2.061	1.713	1.744	1.697	1.656	1.629	1.651	1.705	1.268	1.314	1.693
Mn	0.059	0.042	0.033	0.057	0.017	0.042	0.029	0.044	0.055	0.012	0.028	0.000
Mg	2.285	2.508	2.967	2.972	3.095	3.103	3.171	2.887	2.842	3.662	3.776	3.192
Cr	0.000	0.000	0.000	0.000	0.000	0.014	0.000	0.005	0.000	0.000	0.005	0.000
P	0.000	0.000	0.000	0.000	0.000	0.000	0.004	0.000	0.000	0.000	0.000	0.000
Ca	1.830	1.726	1.851	1.773	1.895	1.916	1.728	1.770	1.741	1.858	1.902	1.966
Na	0.548	0.740	0.518	0.580	0.419	0.297	0.362	0.594	0.615	0.166	0.304	0.257
K	0.075	0.056	0.055	0.033	0.018	0.033	0.035	0.026	0.039	0.018	0.019	0.000

Table 2 (cont.). Amphibole compositions.

Rock Type	Mafic	Felsic	Ophicalc	Mafic
Sample #	62	83	41	459 avg
SiO2	49.66	53.65	43.75	50.39
TiO2	0.69	0.00	0.84	0.36
Al2O3	6.82	5.73	14.65	7.92
FeO	13.93	13.78	11.02	12.33
MnO	0.24	0.73	0.00	0.27
MgO	15.26	14.79	13.07	15.32
Cr2O3	0.00	n.d.	n.d.	0.06
P2O5	0.00	n.d.	n.d.	n.d.
CaO	12.26	11.32	13.97	13.10
Na2O	1.15	0.00	2.10	0.12
K2O	0.00	0.00	0.60	0.12
				n = 23
Ions/23 oxygens				
Si	7.083	7.536	6.260	7.108
Al 4	0.917	0.464	1.740	0.892
Al 6	0.229	0.484	0.730	0.426
Ti	0.074	0.000	0.090	0.038
Fe	1.661	1.619	1.319	1.455
Mn	0.029	0.087	0.000	0.032
Mg	3.245	3.097	2.788	3.219
Cr	0.000	n.d.	n.d.	0.007
P	0.000	n.d.	n.d.	n.d.
Ca	1.874	1.704	2.142	1.980
Na	0.317	0.000	0.583	0.032
K	0.000	0.000	0.110	0.021

Table 2 (cont.). Owens Mountain plagioclase compositions from SEM-EDS (normalized to 100).

Rock Type	Ton	Ton	Ton	Ton	Ton	Ton	Ton	Ton	Ton	Ton	Ton	Ton
Plagioclase	Olig	Olig	Olig	Olig	Bytown	Bytown	And	And	And	And	And	Alb
Sample #	1	1	28	28	25	25	9	9	57	57	2	4
SiO2	63.58	63.70	61.50	61.84	47.12	45.68	56.83	51.43	57.22	57.61	58.22	64.38
TiO2	0.21	0.18	0.00	0.00	0.10	0.00	0.16	0.12	0.00	0.00	0.00	0.00
Al2O3	22.29	22.31	23.60	23.51	33.48	34.94	27.58	30.03	26.62	26.70	26.08	22.17
FeO	0.16	0.37	0.00	0.00	0.28	0.22	0.00	0.00	0.00	0.00	0.14	0.00
MnO	0.00	0.00	0.15	0.00	0.00	0.14	0.00	0.00	0.00	0.00	0.00	0.00
MgO	0.00	0.00	0.00	0.00	0.00	0.00	0.00	0.00	0.00	0.00	0.00	0.00
Cr2O3	0.00	0.00	0.00	0.00	0.00	0.21	0.15	0.00	0.00	0.00	0.00	0.00
P2O5	0.00	0.00	0.00	0.00	0.00	0.00	0.00	0.00	0.00	0.00	0.00	0.00
CaO	2.84	2.76	4.25	3.80	16.02	16.27	9.06	9.86	8.04	7.67	6.92	2.18
Na2O	10.78	10.37	10.40	10.86	2.87	2.54	6.12	8.36	8.12	7.91	8.51	11.02
K2O	0.14	0.31	0.10	0.00	0.13	0.00	0.10	0.19	0.00	0.11	0.13	0.25
Ions/32 oxygens												
Si	11.266	11.285	10.961	11.004	8.674	8.430	10.193	9.408	10.287	10.335	10.443	11.374
Ti	0.028	0.024	0.000	0.000	0.014	0.000	0.022	0.017	0.000	0.000	0.000	0.000
Al	4.655	4.658	4.958	4.930	7.263	7.599	5.830	6.476	5.642	5.646	5.514	4.617
Fe	0.024	0.055	0.000	0.000	0.043	0.034	0.000	0.000	0.000	0.000	0.021	0.000
Mn	0.000	0.000	0.023	0.000	0.000	0.022	0.000	0.000	0.000	0.000	0.000	0.000
Mg	0.000	0.000	0.000	0.000	0.000	0.000	0.000	0.000	0.000	0.000	0.000	0.000
Cr	0.000	0.000	0.000	0.000	0.000	0.010	0.007	0.000	0.000	0.000	0.000	0.000
P	0.000	0.000	0.000	0.000	0.000	0.000	0.000	0.000	0.000	0.000	0.000	0.000
Ca	0.539	0.524	0.811	0.724	3.160	3.217	1.740	1.933	1.548	1.474	1.329	0.413
Na	3.702	3.564	3.593	3.746	1.024	0.908	2.127	2.966	2.830	2.750	2.958	3.774
K	0.032	0.070	0.023	0.000	0.031	0.000	0.023	0.044	0.000	0.025	0.030	0.056
An mol.%	13	13	18	16	76	78	45	39	35	35	31	10

Olig = oligoclase; Bytown = bytownite; And = andesine; Alb = albite; An = anorthite

Table 2 (cont.). Owens Mountain plagioclase compositions from SEM-EDS (normalized to 100).

Rock Type	Ton	Ton	Ton	Ton	Ton	Ton	Ton	Ton	Ton	Mafic	Mafic	Mafic
Plagioclase	Olig	Olig	And	And	Bytown	An	And	Olig	Olig	Olig	Olig	And
Sample #	4	73	6	6	W4	53	3 f	3 f	3 f	3 m	3 m	68A m
SiO2	63.80	59.21	56.51	56.54	46.70	45.45	59.11	61.27	60.73	59.96	60.93	57.42
TiO2	0.00	0.00	0.00	0.00	0.54	0.00	0.00	0.00	0.00	0.00	0.00	0.00
Al2O3	22.02	25.45	25.23	27.74	32.75	33.90	26.35	24.52	24.39	24.67	24.29	26.63
FeO	0.00	0.27	1.85	0.00	1.12	0.00	0.00	0.00	0.17	0.37	0.00	0.22
MnO	0.00	0.00	0.00	0.00	0.00	0.00	0.00	0.00	0.00	0.00	0.00	0.00
MgO	0.00	0.00	0.88	0.00	0.00	0.00	0.00	0.00	0.00	0.00	0.00	0.00
Cr2O3	0.00	0.00	0.13	0.13	n.d.	n.d.	0.00	0.00	0.00	0.00	0.00	0.00
P2O5	0.00	0.00	0.00	0.00	n.d.	n.d.	0.00	0.00	0.00	0.00	0.00	0.00
CaO	2.47	6.33	7.94	9.03	16.17	20.09	7.16	5.41	5.00	5.20	5.39	8.54
Na2O	11.50	8.39	7.37	6.56	2.72	0.00	7.29	8.66	9.62	9.71	9.27	7.01
K2O	0.21	0.35	0.10	0.00	0.00	0.56	0.09	0.14	0.09	0.09	0.12	0.18
Ions/32 oxygens												
Si	11.313	10.598	10.261	10.152	8.638	8.421	10.532	10.882	10.829	10.726	10.854	10.314
Ti	0.000	0.000	0.000	0.000	0.075	0.000	0.000	0.000	0.000	0.000	0.000	0.000
Al	4.603	5.370	5.399	5.872	7.140	7.403	5.534	5.133	5.126	5.202	5.100	5.638
Fe	0.000	0.040	0.281	0.000	0.173	0.000	0.000	0.000	0.025	0.055	0.000	0.033
Mn	0.000	0.000	0.000	0.000	0.000	0.000	0.000	0.000	0.000	0.000	0.000	0.000
Mg	0.000	0.000	0.238	0.000	0.000	0.000	0.000	0.000	0.000	0.000	0.000	0.000
Cr	0.000	0.000	0.006	0.006	n.d.	n.d.	0.000	0.000	0.000	0.000	0.000	0.000
P	0.000	0.000	0.000	0.000	n.d.	n.d.	0.000	0.000	0.000	0.000	0.000	0.000
Ca	0.469	1.214	1.544	1.737	3.204	3.988	1.366	1.029	0.955	0.996	1.028	1.643
Na	3.953	2.911	2.593	2.283	0.975	0.000	2.518	2.981	3.325	3.367	3.201	2.440
K	0.047	0.080	0.023	0.000	0.000	0.132	0.020	0.032	0.020	0.021	0.027	0.041
An mol.%	11	29	37	43	77	100	35	26	22	23	24	40

Table 2 (cont.). Owens Mountain plagioclase compositions from SEM-EDS (normalized to 100).

Rock Type	Ton	Dacite	Dacite	Ton	Mafic	Mafic	Ton	Mafic	Mafic	Mafic	Hb gbro	Hb gbro
Plagioclase	And	Olig	And	An	And	Olig	And	And	And	And	Bytown	Bytown
Sample #	68A f	56	56	70	58 m	58 dk	58 f	W3 f	W3 m	W3 m	67	67
SiO2	59.23	58.84	57.31	44.42	57.41	58.81	58.42	57.38	55.53	56.20	46.38	44.91
TiO2	0.15	0.00	0.00	0.00	0.00	0.17	0.20	0.12	0.00	0.00	0.00	0.00
Al2O3	25.44	25.59	27.05	34.39	26.32	25.34	25.63	26.56	27.96	27.25	34.51	34.83
FeO	0.00	0.13	0.15	1.42	0.00	0.30	0.00	0.28	0.23	0.17	0.00	0.26
MnO	0.00	0.00	0.00	0.62	0.18	0.00	0.09	0.00	0.00	0.00	0.00	0.00
MgO	0.00	0.00	0.00	0.00	0.00	0.00	0.00	0.00	0.00	0.00	0.00	0.00
Cr2O3	0.26	0.00	0.00	n.d.	0.39	0.00	0.00	0.00	0.00	0.00	0.00	0.00
P2O5	0.00	0.00	0.00	n.d.	0.00	0.00	0.15	0.00	0.00	0.15	0.00	0.00
CaO	6.74	5.90	8.80	19.15	8.85	6.34	6.88	7.60	9.48	8.08	16.72	17.98
Na2O	8.18	9.48	6.57	0.00	6.79	8.95	8.43	8.01	6.72	7.96	2.34	1.90
K2O	0.00	0.07	0.13	0.00	0.07	0.10	0.20	0.06	0.08	0.18	0.06	0.12
Ions/32 oxygens												
Si	10.594	10.544	10.277	8.271	10.335	10.546	10.487	10.311	10.017	10.145	8.530	8.317
Ti	0.020	0.000	0.000	0.000	0.000	0.023	0.027	0.016	0.000	0.000	0.000	0.000
Al	5.363	5.405	5.718	7.547	5.585	5.356	5.423	5.626	5.944	5.797	7.481	7.602
Fe	0.000	0.019	0.022	0.221	0.000	0.045	0.000	0.042	0.035	0.026	0.000	0.040
Mn	0.000	0.000	0.000	0.098	0.027	0.000	0.014	0.000	0.000	0.000	0.000	0.000
Mg	0.000	0.000	0.000	0.000	0.000	0.000	0.000	0.000	0.000	0.000	0.000	0.000
Cr	0.012	0.000	0.000	n.d.	0.018	0.000	0.000	0.000	0.000	0.000	0.000	0.000
P	0.000	0.000	0.000	n.d.	0.000	0.000	0.005	0.000	0.000	0.005	0.000	0.000
Ca	1.291	1.132	1.690	3.820	1.706	1.218	1.323	1.463	1.832	1.564	3.295	3.568
Na	2.836	3.292	2.284	0.000	2.369	3.111	2.933	2.790	2.349	2.787	0.834	0.681
K	0.000	0.016	0.030	0.000	0.016	0.023	0.046	0.014	0.018	0.041	0.014	0.028
An mol.%	31	26	43	100	42	28	31	34	44	36	80	84

Table 2 (cont.). Owens Mountain plagioclase compositions from SEM-EDS (normalized to 100).

Rock Type	Hbdite	Mafic	Mafic	Felsic	Felsic	Felsic	Felsic	Ophicalc	Mafic
Plagioclase	And	Bytown	Bytown	Olig	And	And	And	An	An
Sample #	89	62	62	83	51	W6	63	41	459 avg
SiO2	54.72	47.11	45.54	63.77	61.21	57.84	58.29	44.21	45.55
TiO2	0.00	0.00	0.00	0.00	0.55	0.00	1.09	0.00	0.00
Al2O3	28.26	33.46	34.86	23.98	24.83	28.24	25.85	35.52	34.60
FeO	0.00	0.28	0.00	0.00	0.00	0.00	0.00	0.00	0.25
MnO	0.00	0.16	0.00	0.00	0.00	0.00	0.00	0.00	0.00
MgO	0.00	0.00	0.00	0.00	0.00	0.00	0.00	0.00	0.00
Cr2O3	0.00	0.18	0.00	n.d.	n.d.	n.d.	n.d.	n.d.	n.d.
P2O5	0.00	0.00	0.00	n.d.	n.d.	n.d.	n.d.	n.d.	n.d.
CaO	10.38	15.27	17.15	5.06	6.64	8.75	8.92	20.27	18.40
Na2O	6.56	3.55	2.39	7.19	6.77	5.17	5.85	0.00	1.19
K2O	0.08	0.00	0.06	0.00	0.00	0.00	0.00	0.00	0.02
									n = 6
Ions/32 oxygens									
Si	9.897	8.683	8.402	11.192	10.832	10.283	10.412	8.181	8.409
Ti	0.000	0.000	0.000	0.000	0.073	0.000	0.146	0.000	0.000
Al	6.024	7.269	7.581	4.961	5.179	5.918	5.442	7.747	7.528
Fe	0.000	0.043	0.000	0.000	0.000	0.000	0.000	0.000	0.038
Mn	0.000	0.025	0.000	0.000	0.000	0.000	0.000	0.000	0.000
Mg	0.000	0.000	0.000	0.000	0.000	0.000	0.000	0.000	0.000
Cr	0.000	0.009	0.000	n.d.	n.d.	n.d.	n.d.	n.d.	n.d.
P	0.000	0.000	0.000	n.d.	n.d.	n.d.	n.d.	n.d.	n.d.
Ca	2.011	3.015	3.391	0.952	1.259	1.667	1.707	4.019	3.638
Na	2.300	1.268	0.855	2.447	2.323	1.782	2.026	0.000	0.426
K	0.018	0.000	0.014	0.000	0.000	0.000	0.000	0.000	0.004
An mol.%	47	70	80	28	35	48	46	100	90

Table 2 (cont.). Other Owens Mountain mineral compositions from SEM-EDS (normalized to 100).

Rock Type	Ton	Ton	Ton	Ton	Ton	Ton	Ton	Mafic	Hb gbro	Hb gbro
Mineral	Epid	Hyp	Mt	Epid	Epid	Epid	Biot	Sphn	Mt	Ilm
Sample #	1	28	25	25	25	25	9	W3 f	67	67
SiO2	38.73	52.08	0.47	38.51	37.97	37.58	34.10	30.29	0.29	0.30
TiO2	0.00	0.00	0.31	0.00	0.00	0.11	4.32	39.02	0.17	47.64
Al2O3	25.95	0.96	0.63	24.40	23.44	25.09	14.78	0.61	0.25	0.16
FeO	11.14	30.18	97.90	13.15	14.54	12.50	26.42	0.46	98.44	49.72
MnO	0.10	1.48	0.35	0.00	0.00	0.00	0.00	0.00	0.17	1.25
MgO	0.00	13.98	0.22	0.00	0.30	0.17	8.78	0.00	0.43	0.30
Cr2O3	0.20	0.21	0.00	0.00	0.00	0.17	0.00	0.16	0.25	0.00
P2O5	0.00	0.00	0.00	0.26	0.22	0.00	0.00	0.16	0.00	0.00
CaO	23.88	0.34	0.12	22.89	23.11	24.38	0.00	28.87	0.00	0.07
Na2O	0.00	0.69	0.00	0.71	0.42	0.00	0.79	0.43	0.00	0.56
K2O	0.00	0.08	0.00	0.08	0.00	0.00	10.82	0.00	0.00	0.00

Rock Type	Calc-sil	Calc-sil	Chl Sch	Chl Sch	Ophicalc	Felsic	Ton	Ton
Mineral	Chl	Cpx	Sp	Chl	Cpx	Chl	Epid	Epid
Sample #	80-A1	80-A1	80-A	80-A	41	63	W4	53
SiO2	34.26	53.01	0.00	31.68	53.29	30.42	38.91	40.07
TiO2	0.00	0.00	0.00	0.66	0.00	0.66	0.00	0.00
Al2O3	27.76	3.55	63.38	26.04	1.73	23.26	24.26	23.38
FeO	4.64	2.39	16.61	6.42	8.14	28.68	10.09	12.11
MnO	0.00	0.00	0.00	0.00	0.00	0.00	0.00	0.00
MgO	33.34	15.45	19.36	35.20	12.92	16.09	0.00	0.00
CaO	0.00	25.60	0.38	0.00	23.59	0.89	26.74	24.44
Na2O	0.00	0.00	0.00	0.00	0.00	0.00	0.00	0.00
K2O	0.00	0.00	0.27	0.00	0.33	0.00	0.00	0.00

Epid = epidote; Hyp = hypersthene; Biot = biotite; Sphn = sphene; Mt = magnetite; Ilm = ilmenite; Chl = chlorite; Cpx = clinopyroxene; Sp = spinel.

Table 3. Owens Mountain Zircon Geochronology Sample Locations, Interpreted Ages and Petrographic Overview

Sample #	Latitude (N)	Longitude (W)	Interpreted Age (Ma)	Petrography
1	36°56'05"	119°35'35"	148	moderately to strongly deformed tonalite
2	36°56'10"	119°38'00"	151	moderately deformed hornblende-biotite tonalite
3	36°55'55"	119°38'45"	152	moderately to strongly deformed hornblende tonalite
4	36°55'45"	119°39'05"	154	strongly deformed tonalite
5	36°55'05"	119°38'50"	155	strongly deformed tonalite
6	36°55'40"	119°37'37"	151	moderately deformed hornblende-garnet tonalite
7	36°55'50"	119°38'30"	154	moderately deformed tonalite
8	37°25'46"	120°12'25"	145±7	stongly deformed tonalite
9	36°57'45"	119°37'07"	118	undeformed biotite-hornblende tonalite
10	36°55'27"	119°36'12"	123	undeformed pegmatitic biotite-muscovite granite
11	36°56'45"	119°36'45"	120±7	undeformed aplitic biotite-muscovite-garnet granite
12	36°56'16"	119°36'55"	120±7	undeformed, fine-grained, biotite dacite

Table 4. ZIRCON ISOTOPIC AGE DATA

Sample #	Magnetic Properties§	Fraction Size§§ (μm)	Amount Analyzed (mg)	Concentration‡ ^{238}U (ppm)	Concentration‡ $^{206}Pb^*$ (ppm)	Atomic Ratios $^{206}Pb/^{204}Pb$	Atomic Ratios $^{206}Pb^*/^{238}U$	Atomic Ratios $^{207}Pb^*/^{235}U$	Atomic Ratios $^{207}Pb^*/^{206}Pb^*$	Isotopic Ages (Ma)‡‡ $^{206}Pb^*/^{238}U$	Isotopic Ages (Ma)‡‡ $^{207}Pb^*/^{235}U$	Isotopic Ages (Ma)‡‡ $^{207}Pb^*/^{206}Pb^*$
1	1/20	45-62	2.5	165	3.2	5977	0.02258(12)	0.15263	0.04904(19)	144.0	144.2	150±9
		45-62 L	5.7	136	2.7	7007	0.02325(13)	0.15714	0.04905(10)	148.2	148.2	150±5
		62-80	6.9	141	2.8	6368	0.02324(16)	0.15699	0.04902(11)	148.1	148.1	148±5
		80-100	5.8	72	1.4	3579	0.02325(16)	0.15723	0.04908(19)	148.2	148.3	151±9
2	2/20	<45	2.0	168	3.0	1714	0.02092(12)	0.14166	0.04912(11)	133.5	134.5	153±5
		<45 L	7.0	104	2.1	8351	0.02364(12)	0.16120	0.04948(12)	150.6	151.8	170±6
		45-62	3.8	198	4.0	5132	0.02332(16)	0.15869	0.04937(05)	148.7	149.6	165±3
		62-80	8.5	166	3.3	5568	0.02308(15)	0.15655	0.04921(06)	147.1	147.7	157±4
		80-100	9.1	139	2.8	6293	0.02369(16)	0.16088	0.04927(09)	151.0	151.5	160±5
		80-100 L	4.6	116	2.4	6388	0.02364(13)	0.16001	0.04912(12)	150.6	150.7	153±6
		100-120	2.4	178	3.4	1487	0.02219(12)	0.15014	0.04910(21)	141.5	142.0	152±10
3	2/20	<45	2.8	314	6.3	1090	0.02309(14)	0.15552	0.04887(14)	147.2	146.8	142±6
		<45 L	6.8	214	4.4	23818	0.02383(13)	0.16142	0.04914(28)	151.9	152.0	154±14
		45-62	3.5	256	5.1	1951	0.02296(14)	0.15587	0.04957(13)	146.3	147.1	160±6
		62-80	6.3	194	3.9	9394	0.02313(16)	0.15702	0.04927(16)	147.4	148.1	160±8
		80-100	6.4	186	3.7	9892	0.02321(16)	0.15752	0.04924(20)	148.0	148.5	159±10
4	2/20	45-62	4.4	267	5.6	5048	0.02409(16)	0.16315	0.04914(20)	153.5	153.5	154±9
		62-80	5.5	242	4.9	5383	0.02349(16)	0.15894	0.04909(13)	149.7	149.8	152±6
		62-80 L	4.8	140	2.9	9072	0.02393(13)	0.16224	0.04920(17)	152.5	152.7	157±8
		80-100	6.1	189	3.9	852	0.02410(18)	0.16318	0.04913(18)	153.6	153.5	154±9
5	1.5/20	45-72	6.1	236	4.8	10069	0.02327(16)	0.15765	0.04916(13)	148.3	148.6	155±7
		45-72 L	5.5	181	3.7	11224	0.02389(13)	0.16180	0.04913(19)	152.2	152.3	154±9
		72-100	5.8	242	5.1	2350	0.02428(17)	0.16472	0.04923(19)	154.7	154.8	158±9
6	1/20	<80	2.2	223	4.6	920	0.02372(14)	0.16018	0.04901(12)	151.1	150.9	148±5
7	10/20	80-100	0.2	38	0.8	1102	0.02419(14)	0.16288	0.04886(24)	154.1	153.2	141±12

Table 4 (cont.). ZIRCON ISOTOPIC AGE DATA

Sample #	Magnetic Properties§	Fraction Size§§ (μm)	Amount Analyzed (mg)	Concentration‡ ^{238}U (ppm)	Concentration‡ $^{206}Pb^*$ (ppm)	Atomic Ratios $^{206}Pb/^{204}Pb$	Atomic Ratios $^{206}Pb^*/^{238}U$	Atomic Ratios $^{207}Pb^*/^{235}U$	Atomic Ratios $^{207}Pb^*/^{206}Pb^*$	Isotopic Ages (m.y.)‡‡ $^{206}Pb^*/^{238}U$	Isotopic Ages (m.y.)‡‡ $^{207}Pb^*/^{235}U$	Isotopic Ages (m.y.)‡‡ $^{207}Pb^*/^{206}Pb^*$
8	2/20	<45	0.3	460	8.7	334	0.02193(15)	0.14772	0.04887(28)	139.9	139.9	141±13
		45-62	0.8	485	9.2	1407	0.02184(12)	0.14763	0.04905(10)	139.3	139.8	150±5
		62-80	1.9	421	8.0	1227	0.02188(13)	0.14804	0.04909(11)	139.5	140.2	152±5
		>80	2.0	397	7.7	1000	0.02256(13)	0.15297	0.04920(14)	143.8	144.5	157±7
9	2/20	45-62	6.0	290	4.6	6122	0.01856(12)	0.12387	0.04843(16)	118.6	118.6	120±8
		62-80	6.1	339	5.4	5583	0.01834(12)	0.12223	0.04838(09)	117.2	117.1	117±5
		80-100	5.6	320	5.1	5100	0.01852(12)	0.12360	0.04843(10)	118.3	118.3	120±5
10	5/20	<45	0.7	2732	30.3	3867	0.01282(08)	0.08567	0.04851(09)	82.1	83.5	124±4
		45-62	1.0	6775	99.0	4467	0.01688(20)	0.11291	0.04852(06)	108.0	108.6	124±3
		62-80	1.0	3118	36.3	2622	0.01346(10)	0.08987	0.04846(08)	86.2	87.4	121±2
		>80	0.6	6582	81.0	3188	0.01422(12)	0.09515	0.04855(09)	91.0	92.3	126±4
11	2/20	<80	0.4	898	14.2	648	0.01832(11)	0.12514	0.04957(16)	117.0	119.7	175±7
		>80	1.0	982	15.8	415	0.01862(13)	0.12495	0.04870(19)	118.9	119.6	133±9
12	2/20	<80	1.8	378	5.8	4198	0.01772(10)	0.12016	0.04921(12)	113.2	115.2	157±6
		>80	1.3	394	6.1	5030	0.01788(10)	0.12076	0.04900(07)	114.3	115.8	148±3

* denotes radiogenic Pb. Nonradiogenic correction based upon a 40 picogram Pb blank (1:18.78:15.61:38.50) and approximate initial Pb ratios of: 206/204 = 18.6; 207/204 = 15.6; 208/204 = 38.0 (Saleeby and Chen, 1978).

§ Magnetic properties are given as nonmagnetic split at side/front slopes for 1.7 A on a Frantz isodynamic magnetic separator.

§§ Samples are sieved with new plastic screens into size fractions and then hand picked under ethanol to >99.9% purity before dissolution. Dissolution and ion-exchange elution techniques modified from Krogh (1973). "L" denotes fractions leached in HF for 7 days at 100°C prior to complete dissolution step.

‡ Due to the uncertainties in sample weight, U and Pb concentrations may not be accurate, but use of a $^{205}Pb/^{235}U$ or a $^{208}Pb^{235}U$ spike insures a correct age.

‡‡ Decay constants used in age calculations: $\lambda\ ^{238}U = 1.55125E\text{-}10\ yrs^{-1}$, $\lambda\ ^{235}U = 9.8485E\text{-}10\ yrs^{-1}$ (Jaffey and others, 1971); $^{238}U/^{235}U$ atom = 137.88. Uncertainty in last two numbers of $^{206}Pb^*/^{238}U$ is given in parentheses; two-sigma uncertainty in $^{207}Pb^*/^{206}Pb^*$ is given as "±." Uncertainties calculated by quadratic sum of total derivatives of ^{238}U and ^{206}Pb concentrations and $^{207}Pb^*/^{206}Pb^*$ equations with error differntials defined as: [1] isotope ratio determinations from standard errors ($\sigma/\sqrt{n}$) of mass spectrometer runs plus uncertainties in fractionation corrections based on multiple runs of NBS 981, 982, 983, and U500 standards; [2] spike concentrations from range of deviations in multiple calibrations with normal solutions; [3] spike compositions from external precisions of multiple isotope ratio determinations; [4] uncertainty in natural $^{238}U/^{235}U$ from Chen and Wasserburg (1981); and [5] nonradiogenic Pb isotopic compositions from uncertainties in isotope ratio determinations of blank Pb and uncertainties in composition of initial Pb from estimates of regional variations based on Saleeby and Chen (1978) and consideration of rock type.

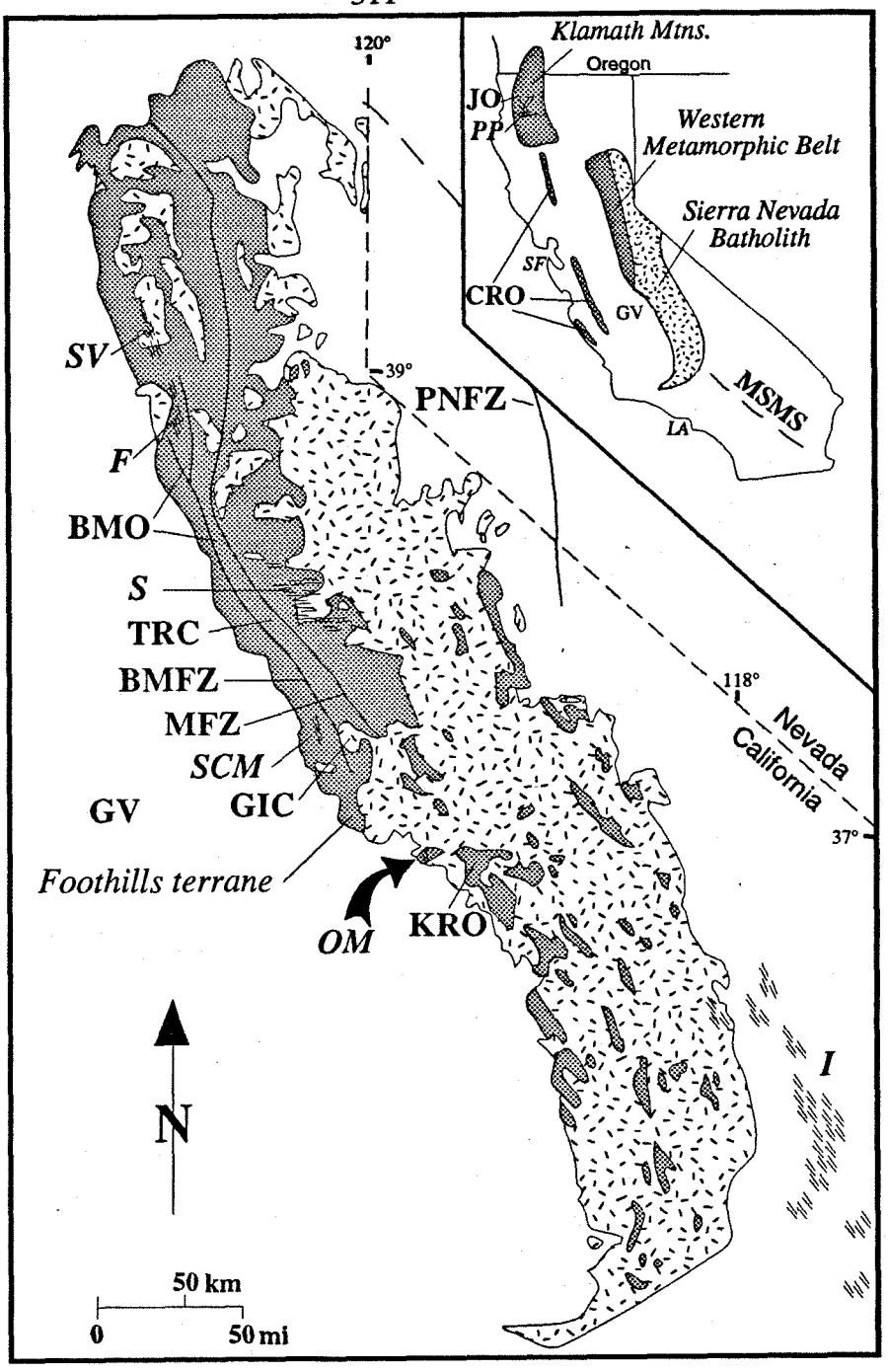

Fig. 1. Generalized geological map of California showing the location of selected fault zones, ophiolite and igneous complexes and Late Jurassic dike swarms in the Sierra Nevada and Klamath Ranges. Hatchured pattern: igneous rocks of the Sierra Nevada; shaded pattern: undifferentiated metamorphic and igneous rocks. Lettering as follows: BMFZ: Bear Mountains fault zone; MFZ: Melones fault zone; PNFZ: Pine Nut fault zone; MSMS: Mojave-Sonora megashear; JO: Josephine ophiolite; CRO: Coast Range ophiolite; BMO: Bear Mountain ophiolite; KRO: Kings River ophioite; TRC: Tuolumne River complex; GIC: Guadalupe igneous complex; PP: Preston Peak dikes; SV: Smartville dikes; F: Folsom dikes; S: Sonora dikes; SCM: Santa Cruz Mountain dikes; I: Independence dikes; OM: Owens Mountain dikes; GV: Great Valley. General orientation of the dike swarms is shown by the orientation of the pairs of short lines.

Fig. 2. Geological map of the Owens Mountain area, located 10 km northeast of Fresno, CA, in the foothills of the Sierra Nevada. Numbers inside squares refer to zircon samples collected for U-Pb geochronology. Sample 8, not on this map, was collected from the Santa Cruz Mountain area, 60 km to the northwest. The foliation symbols represent the strike and dip of both mineral foliations and layering.

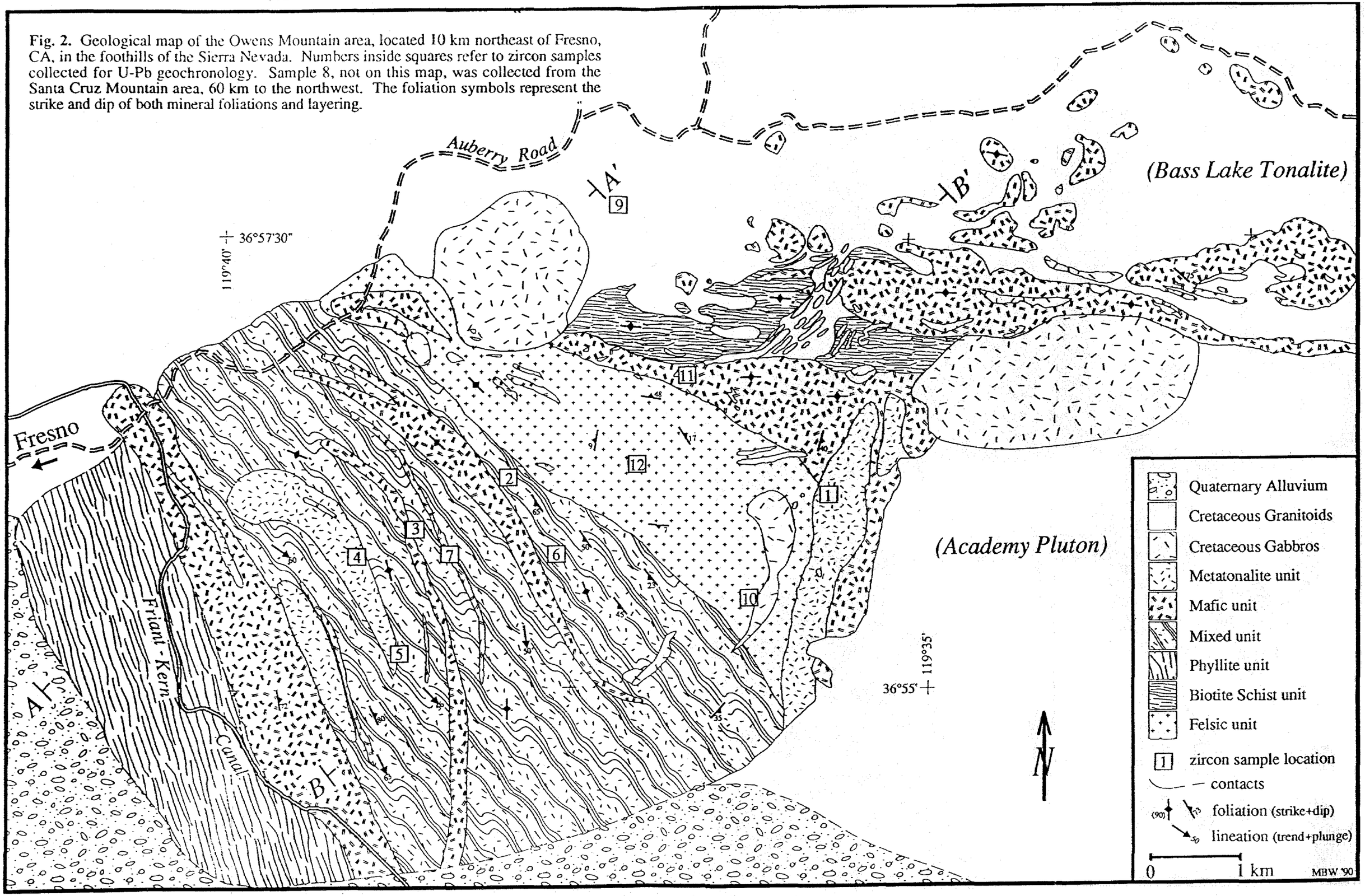

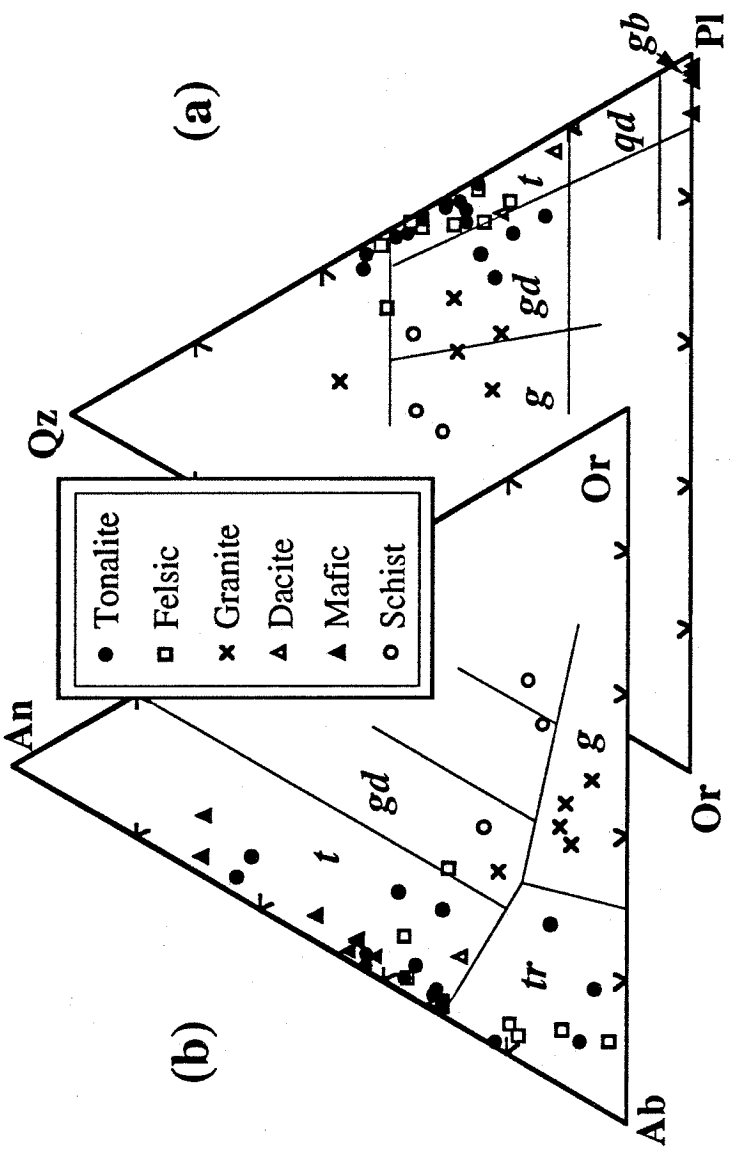

Fig. 3. Normative plots of Owens Mountain whole rock compositions. Analysis done by DCP spectrometry (see Table 1). [a] Normative quartz-orthoclase-plagioclase (Qz-Or-Pl) plot, classification after Streckeisen (1976); [b] Normative anorthite-albite-orthoclase (An-Ab-Or) plot, classification after Barker (1979). Rock field labels: t: tonalite; tr: trondhjemite; gd: granodiorite; g: granite; qd: quartz diorite; gb: gabbro.

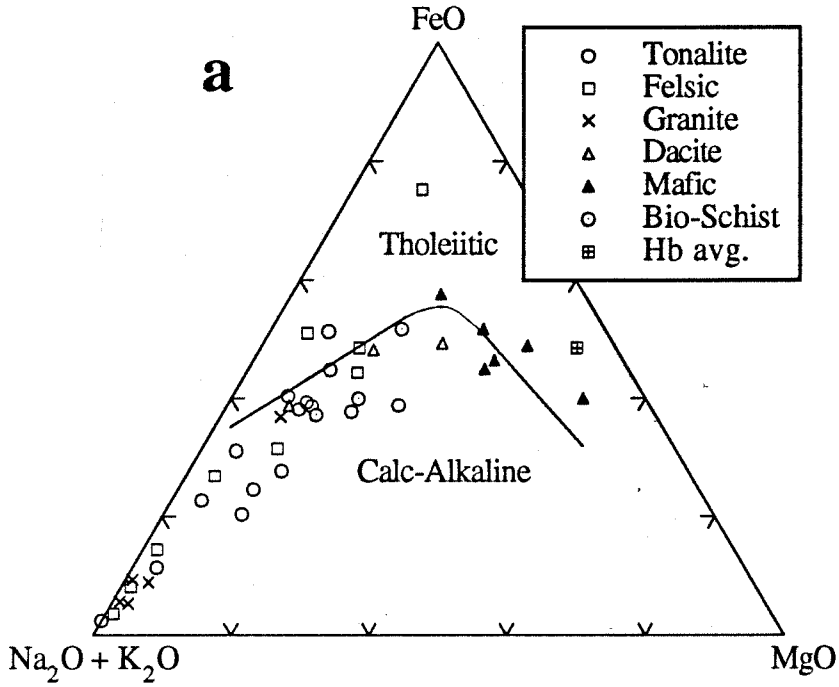

Fig. 4. Plots of Owens Mountain whole rock compositions. Average composition of Owens Mountain hornblende also plotted as a crossed square (from Table 2). [a] AFM diagram (wt.%) with boundary between tholeiitic and calc-alkaline rocks (after Irvine and Baragar, 1971). Owens Mountain rocks exhibit a calc-alkaline trend. [b] Plot of $1/4SiO_2$ - CaO - FeO+MgO (wt.%). The line represents the compositional trend of calc-alkaline rocks from the Sierra Nevada (Stern and Wyllie, 1978). [c] ACF-deluxe diagram (mol.%) (after Thompson, 1982). Rock compositions extend from subaluminous (diopside-norm.) to peraluminous (corundum-norm.) fields.

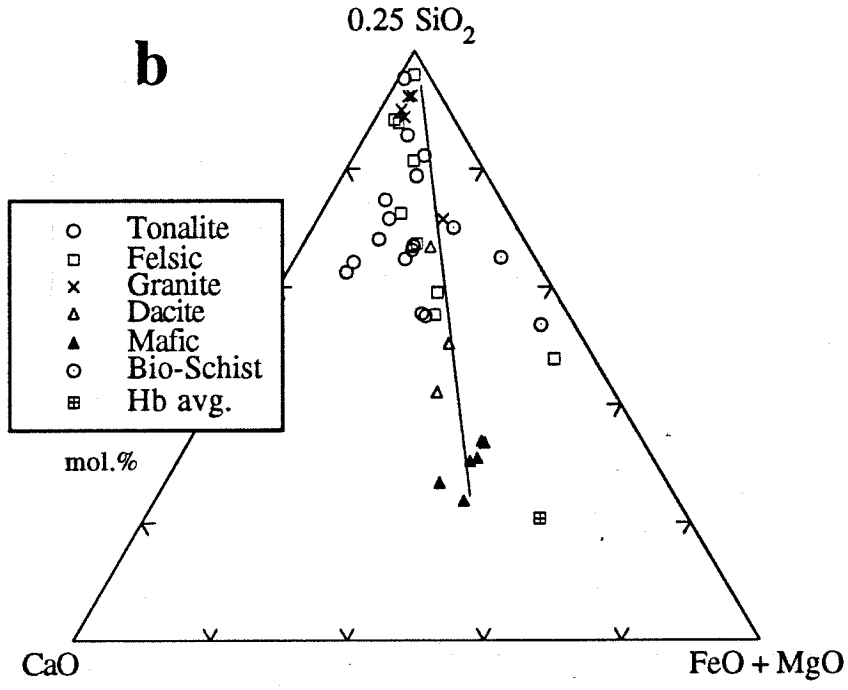
b
0.25 SiO2
Tonalite
Felsic
Granite
Dacite
Mafic
Bio-Schist
Hb avg.
mol.%
CaO
FeO + MgO

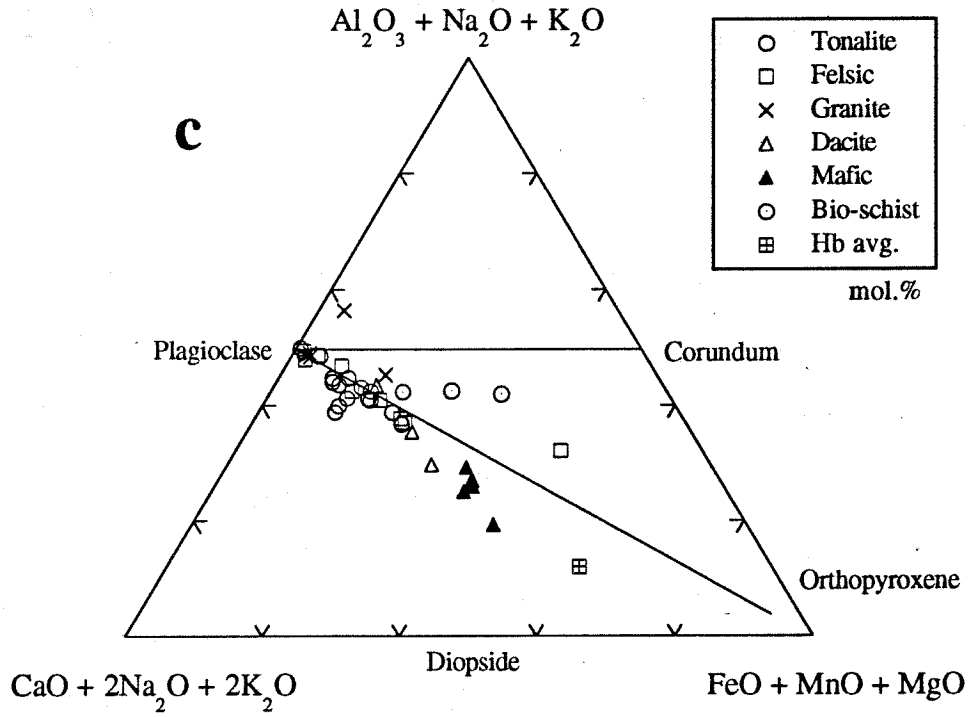
c
Al2O3 + Na2O + K2O
Tonalite
Felsic
Granite
Dacite
Mafic
Bio-schist
Hb avg.
mol.%
Plagioclase
Corundum
Orthopyroxene
Diopside
CaO + 2Na2O + 2K2O
FeO + MnO + MgO

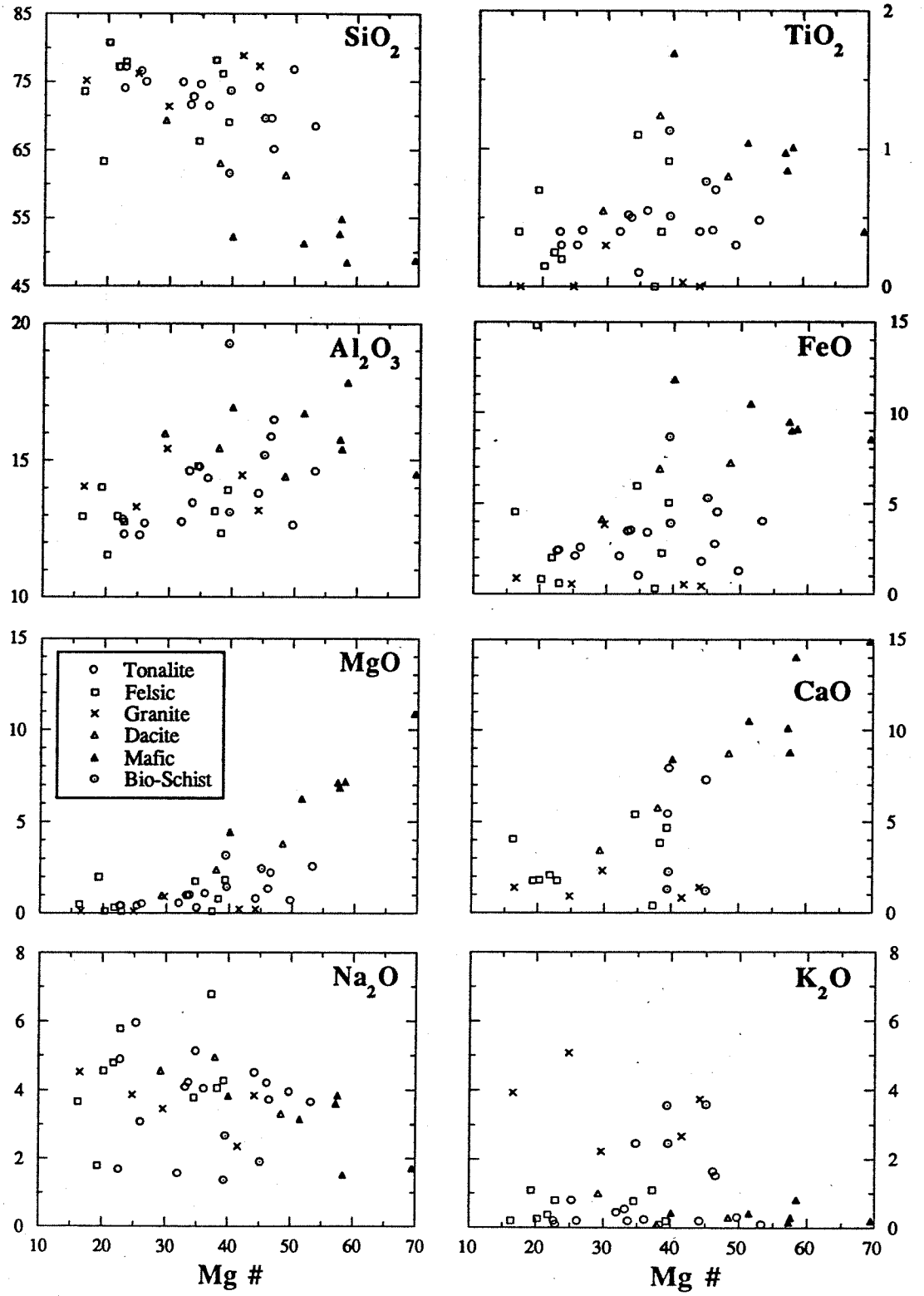

Fig. 5. Variation diagrams (wt.%) as a function of Mg# for Owens Mountain whole rock compositions.

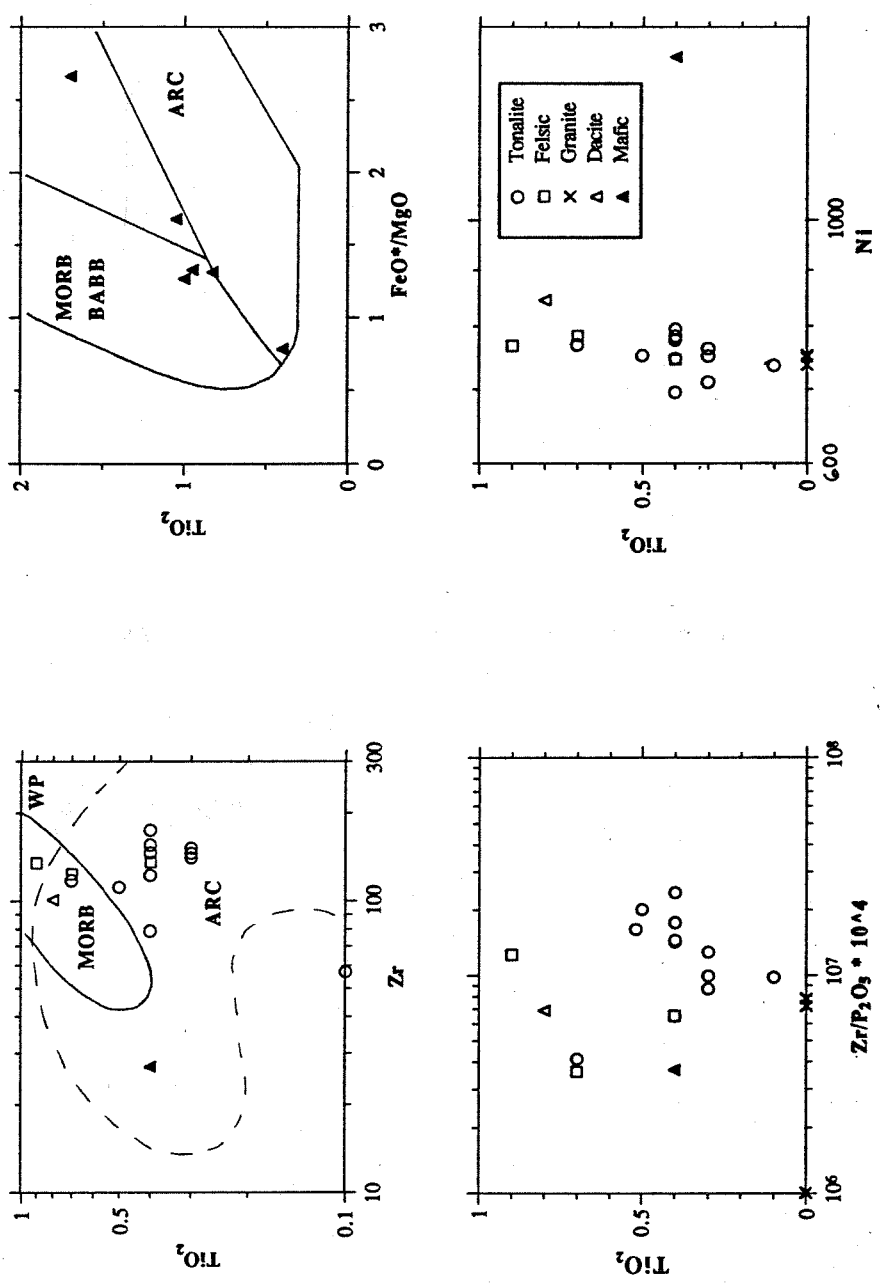

Fig. 6. Variation diagrams (wt.% or ppm) as a function of TiO_2 for Owens Mountain whole rock compositions. Field boundaries in TiO_2-Zr plot after Pearce (1975; 1982); MORB: mid-ocean ridge basalts; WP: within plate; ARC: island-arc; BABB: back-arc basin basalts.

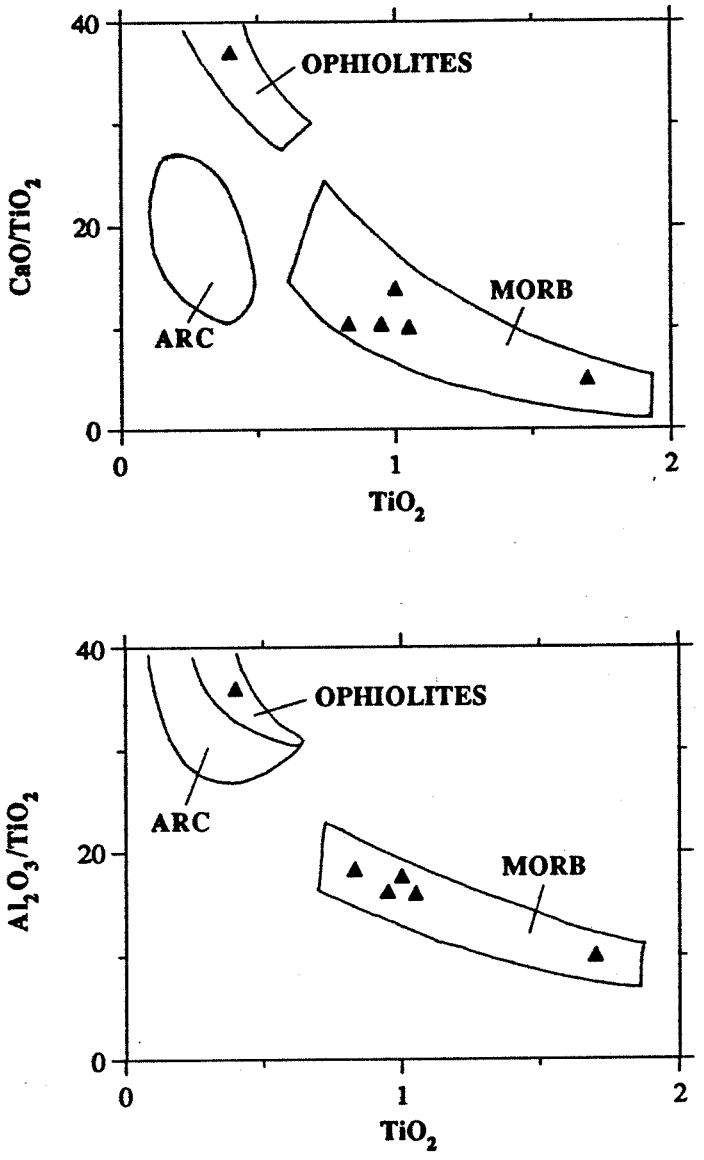

Fig. 7. Plots of TiO_2 versus CaO/TiO_2 and Al_2O_3/TiO_2. Field boundaries after Sun and Nesbitt (1978); MORB: mid-ocean ridge basalts; ARC: island-arc basalts; OPHIOLITES: low-TiO_2 ophiolites.

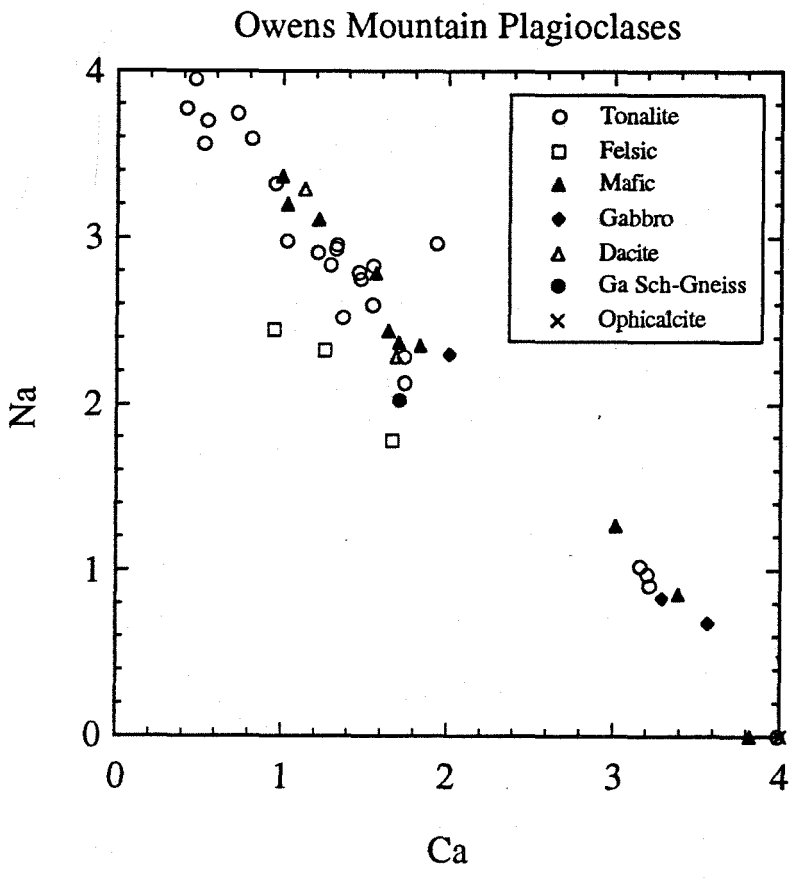

Fig. 8. Plot of Na versus Ca (# of ions) of Owens Mountain plagioclases. Compositions determined from SEM-EDS.

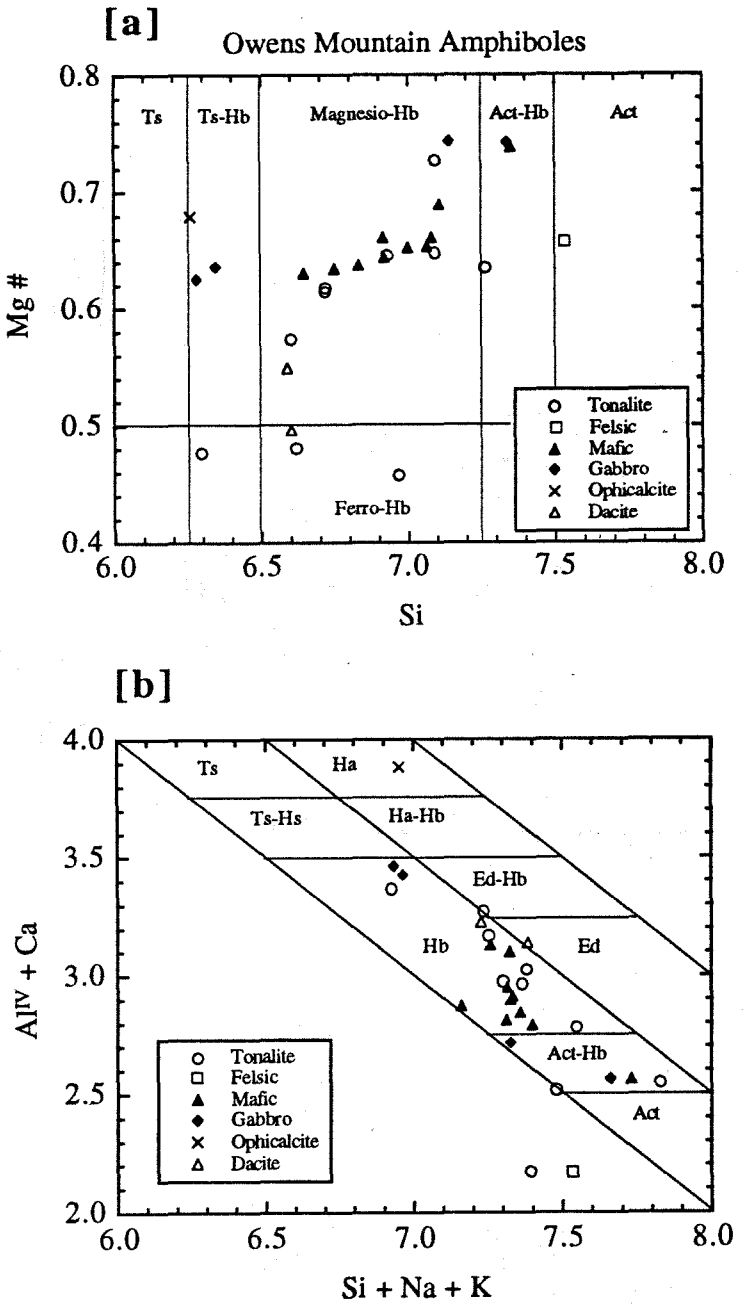

Fig. 9. Compositions of Owens Mountain amphiboles, determined from SEM-EDS. Classification schemes for amphiboles after: [a] Rock and Leake (1984) and [b] Giret and others (1980). Most amphiboles are classified as hornblendes. Amphibole abbreviations: Hb: hornblende; Act: actinolite; Ed: edenite; Ha: hastingsite; Ts: tschermakite.

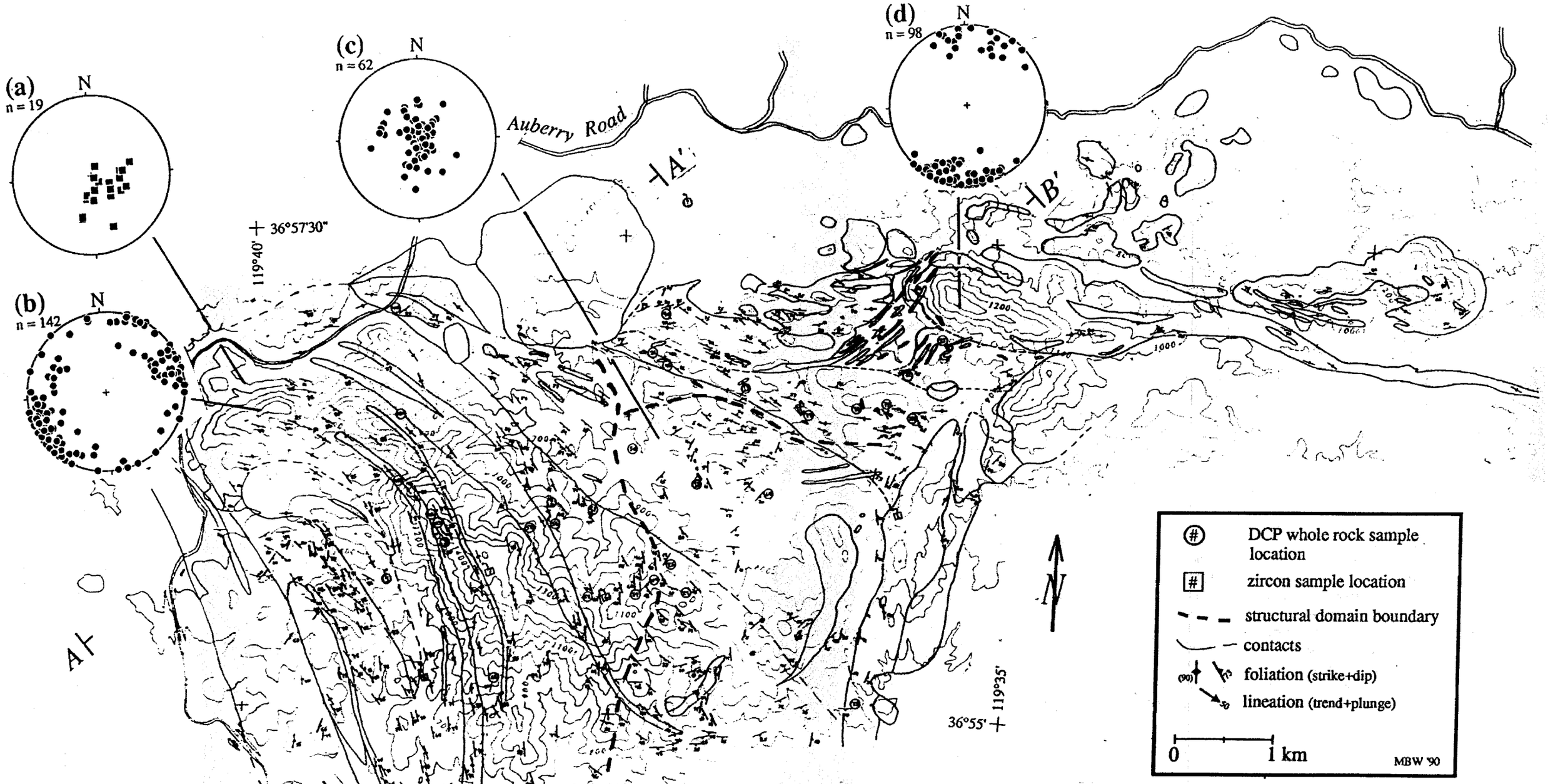

Fig. 10. Topographic map of Owens Mountain area, with structural data and unit boundaries. Stereoplots are equal area, lower hemisphere plots. Plot (a) is of fold axes. Plots (b)-(d) are of poles to foliation. Owens Mountain is divided into three structural domains: stereoplots (a) and (b) from the southwestern domain; stereoplot (c) is from the central domain; stereoplot (d) is from the northeastern domain.

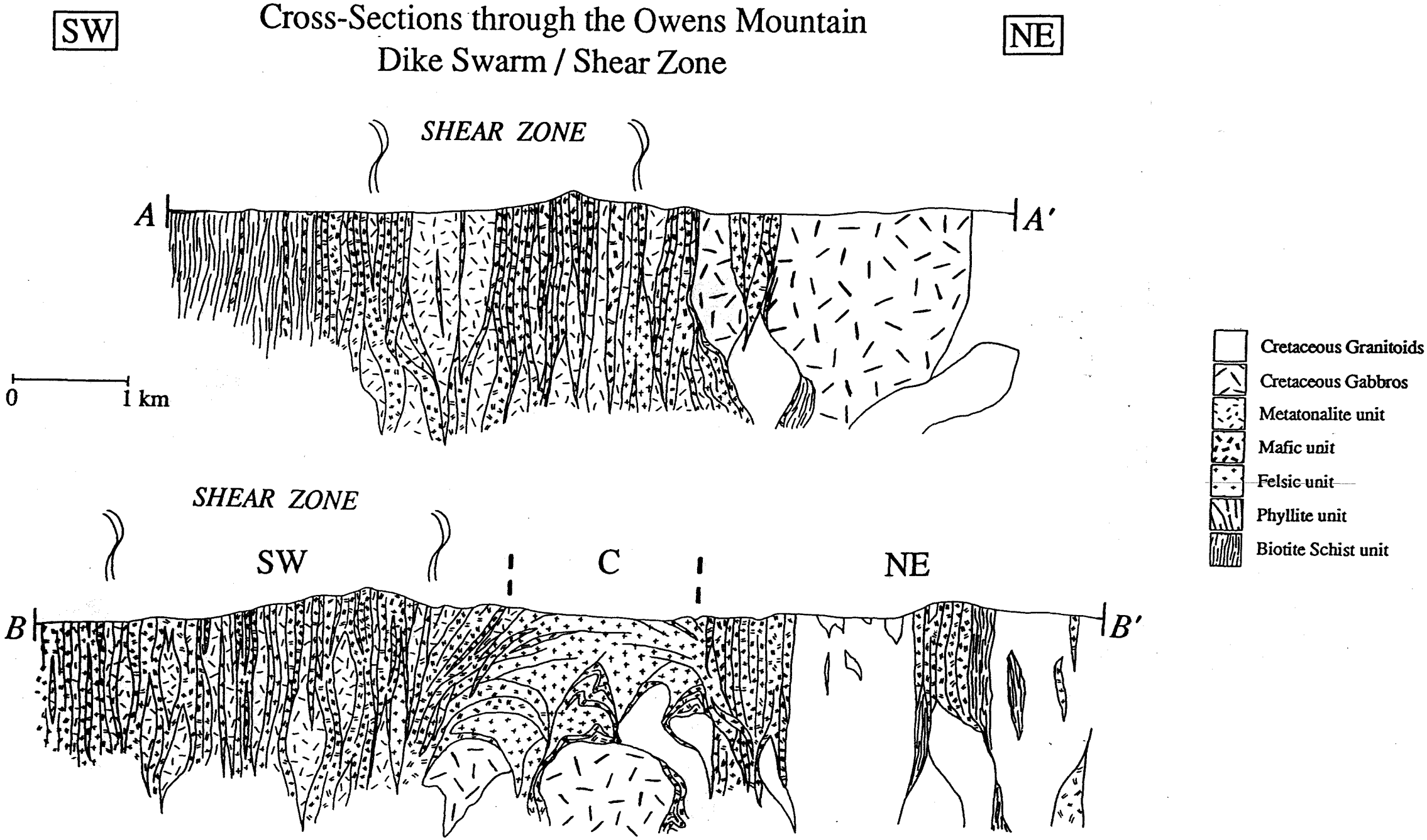

Fig. 11. Two SW-NE-trending cross-sections through the Owens Mountain area, along lines A-A' and B-B' (see Figs. 2 and 10 for lithologic and structural keys). Thick dashed lines bound the structural domains (SW: southwestern; C: central; NE: northeastern). Curved lines bound the areas containing evidence of a shear zone (mylonitic textures, intrafolial folds, etc.). Horizontal scale = vertical scale.

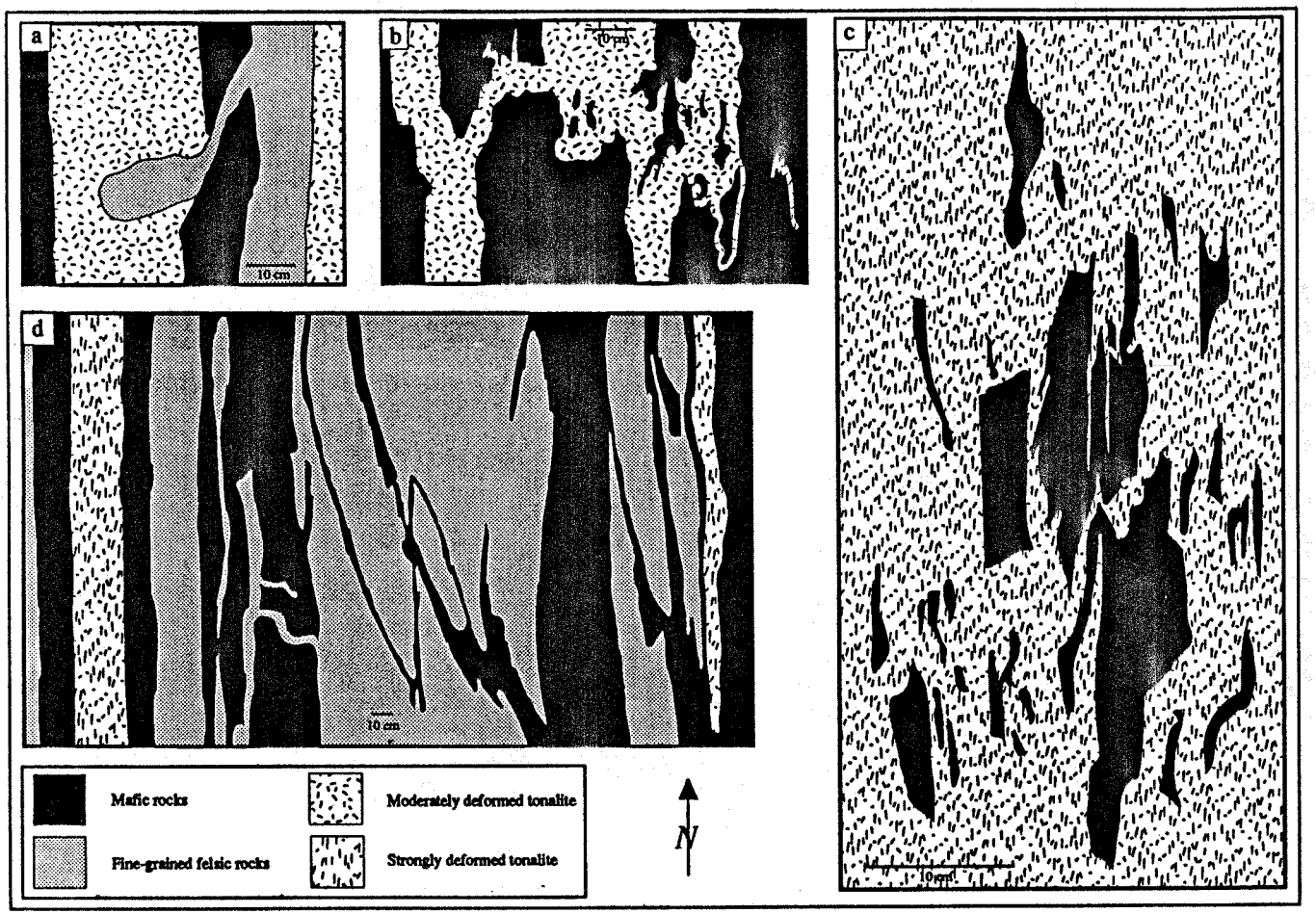

Fig. 12. Drawings of characteristic mesoscopic structural relationships: [a] strongly deformed, cross-cutting mafic and felsic dikes; [b] moderately deformed tonalite intruded into thick mafic layer; [c] fragments of mafic layers within strongly deformed tonalite dike; [d] interlayered, transposed felsic and mafic dikes, evidence of folds may be present in the sequence. Scale bars are 10 cm.

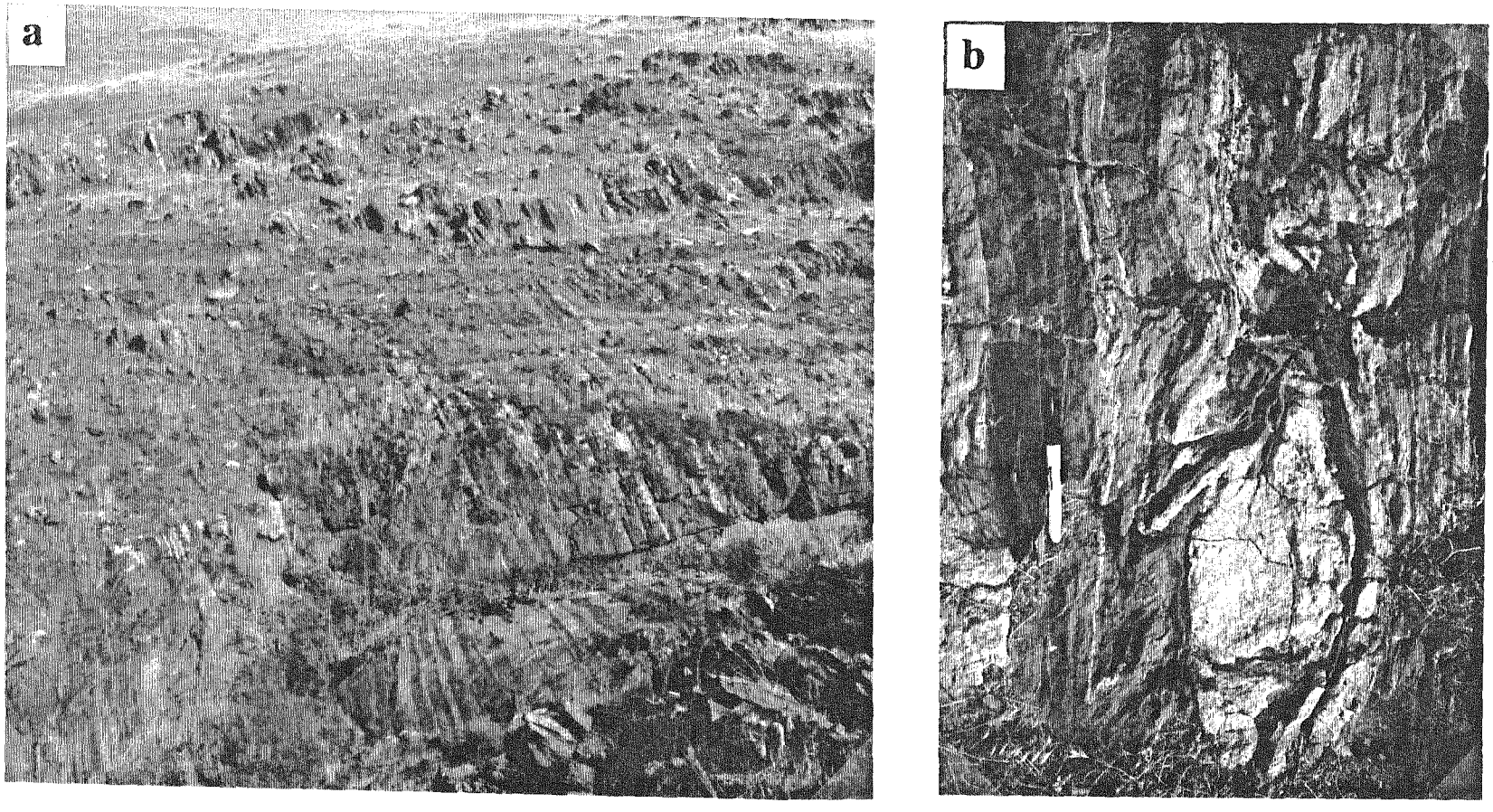

Fig. 13. Photographs and drawings of mesoscopic structural relationships in Owens Mountain rocks from the southwestern domain such as: [a] transposed mafic and felsic dikes (view looking north); [b] boudinaged and folded tonalite dikes; [c] metamorphic differentiation of mafic dikes; [d] migmatization of mafic dikes; and [e-g] folds displaying S-fold geometry with steeply-plunging fold axes indicative of left-lateral motion. In drawings, the scale bars = 10 cm, except where indicated; black layers = mafic layers; black lines = foliation and layering in felsic layers. The 5 cm-long black pen cap points to north in the photographs.

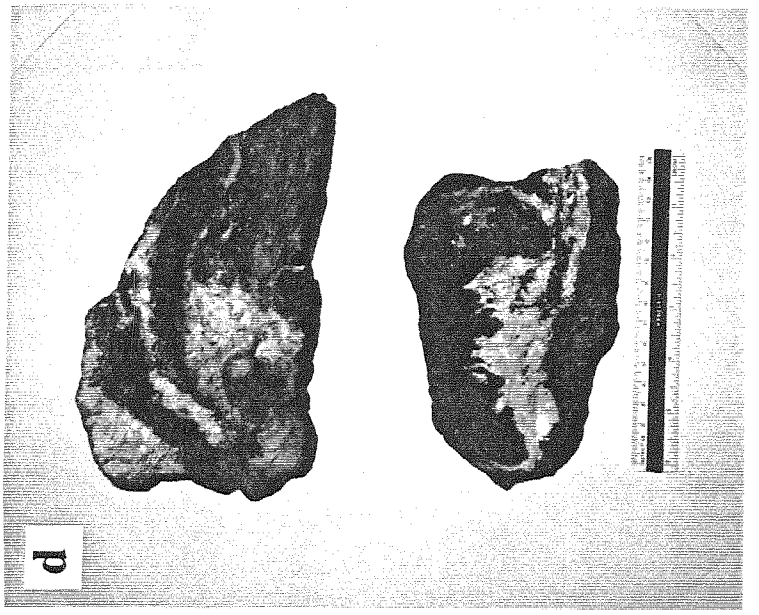
d

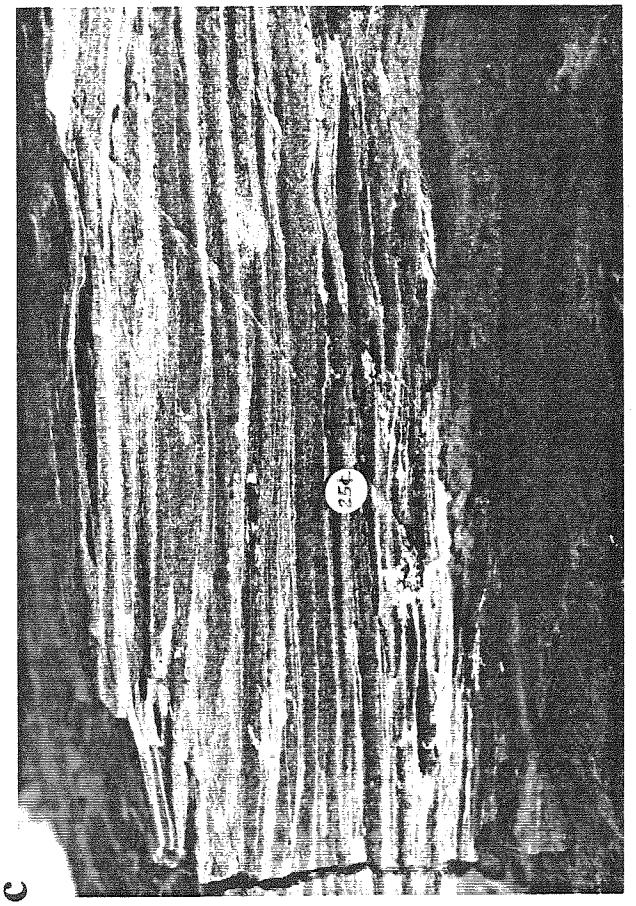
c
2.5t
2

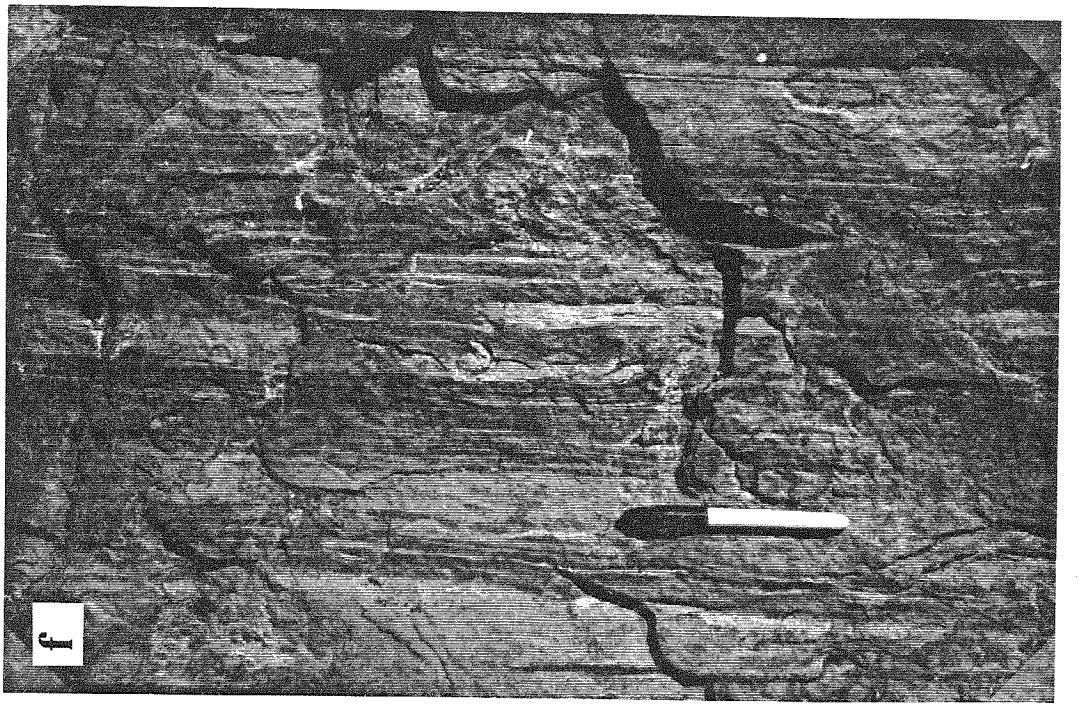
f


e

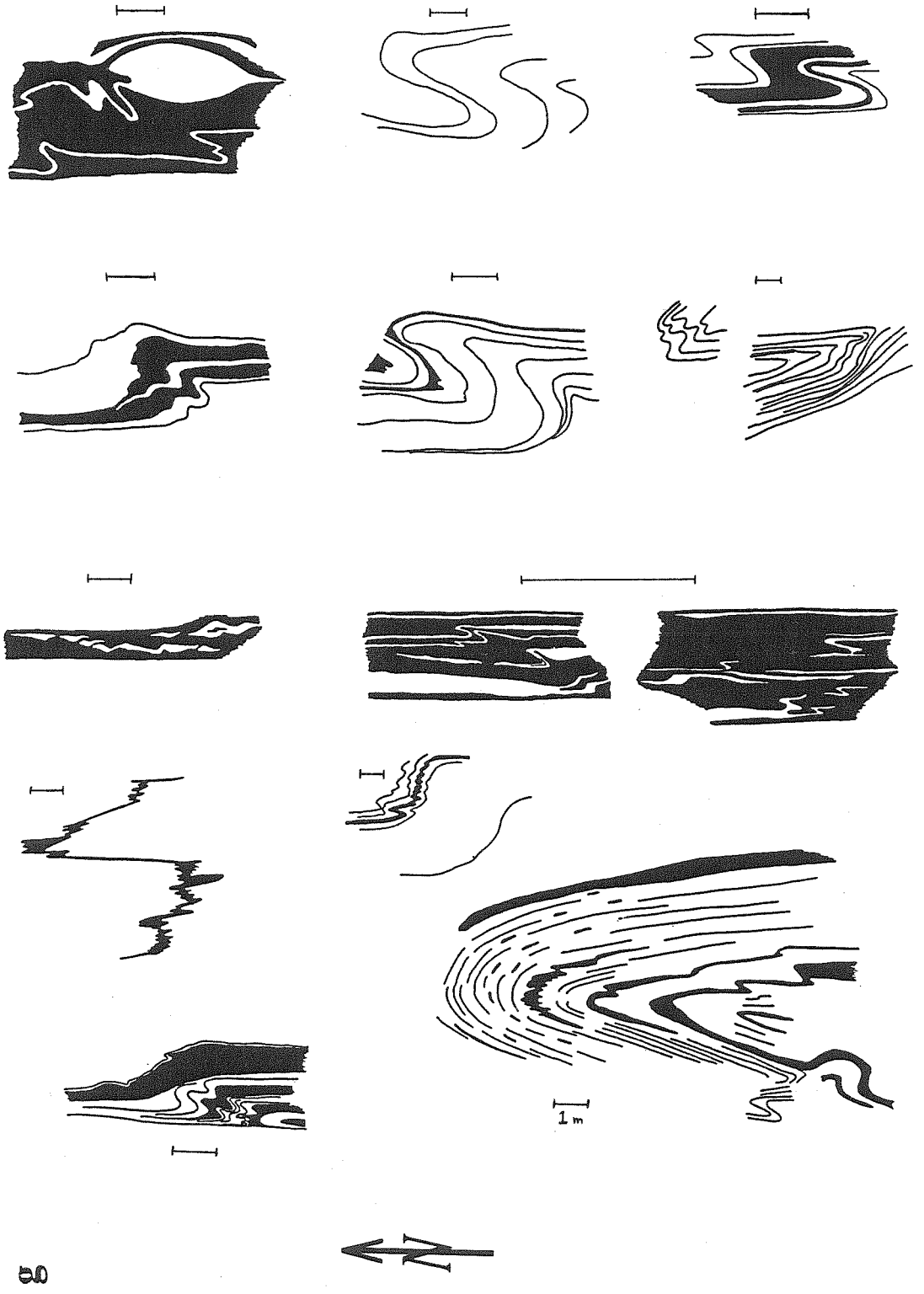
1 m

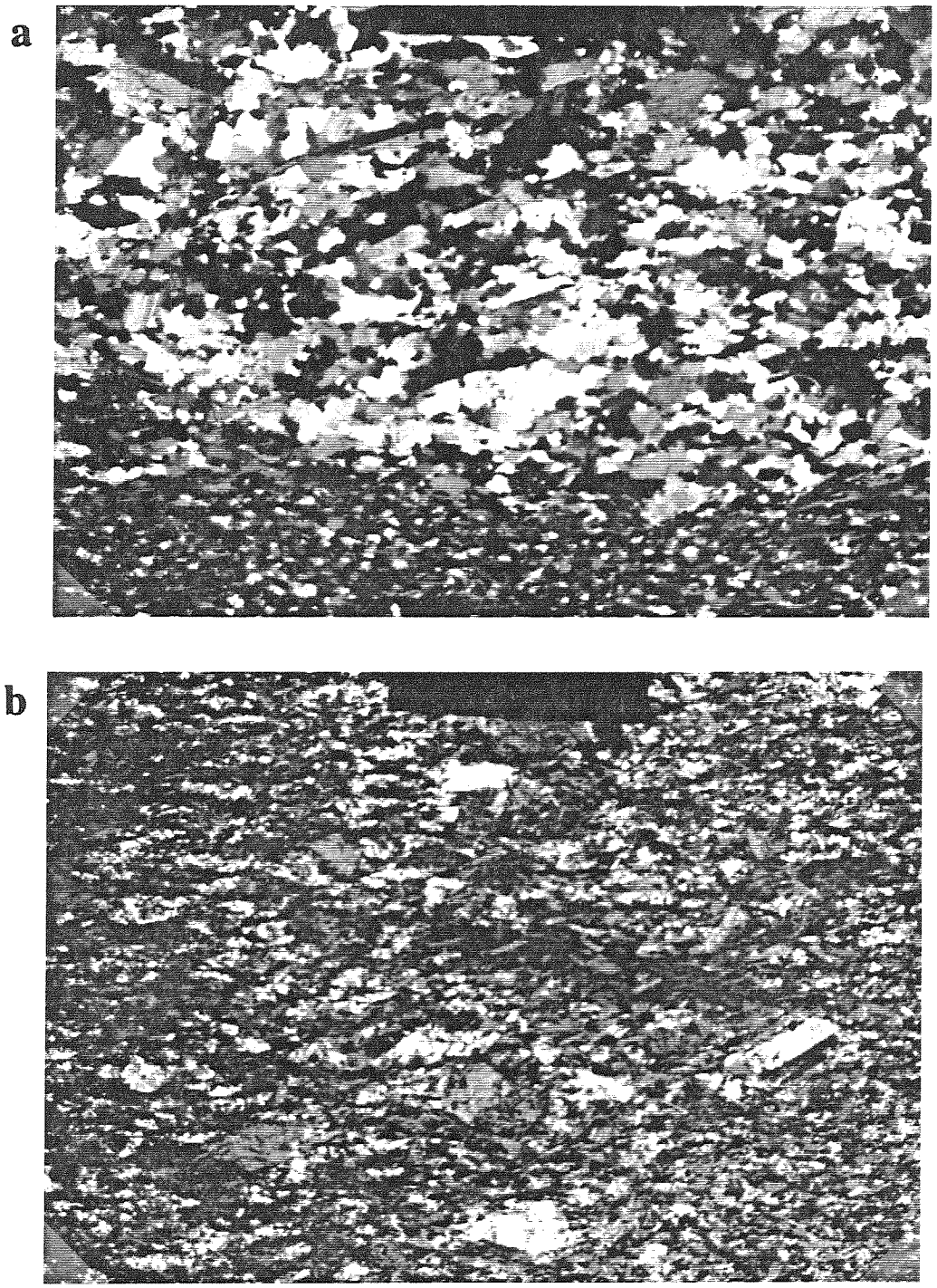

Fig. 14. Photomicrographs of thin-sections of tonalitic and mafic dikes showing tectonite textures (under crossed-polars). The black scale bars are all 5 mm long. [a] tonalite-mafic dike boundary. Plagioclase crystals aligned parallel to dike edge indicates synkinematic magmatic flow; [b] a mafic dike with a blastoporphyritic texture containing relict hornblende and plagioclase phenocrysts; [c-f] photomicrographs of tonalites (from geochronological study) arranged in order of increasing degrees of deformation and recrystallization: [c]: sample 2; [d]: sample 4; [e]: sample 3; [f]: sample 7.

c

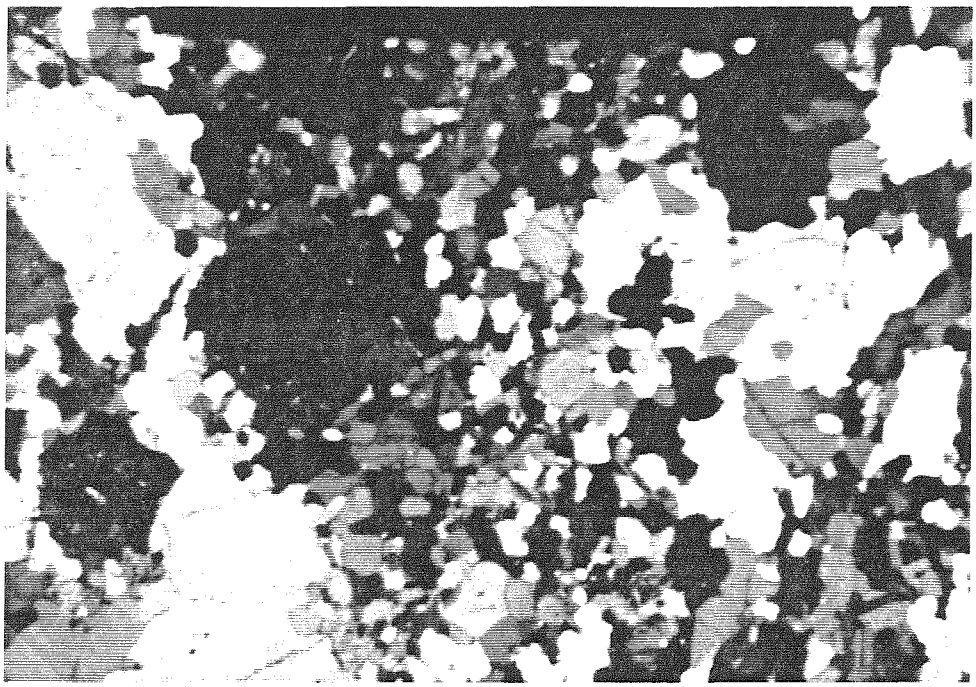

d

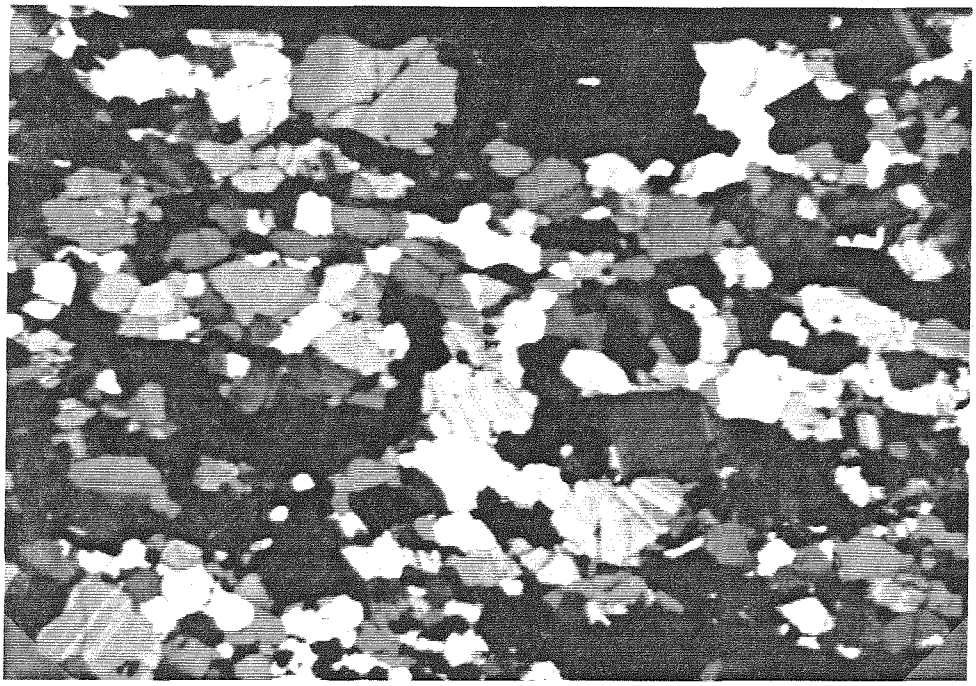

e

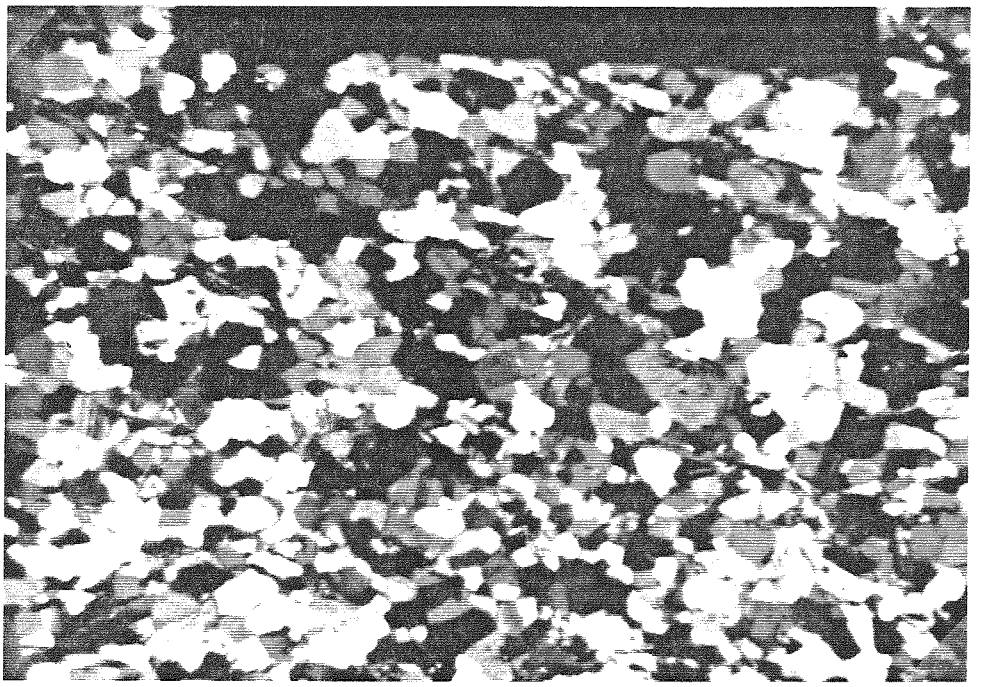

f

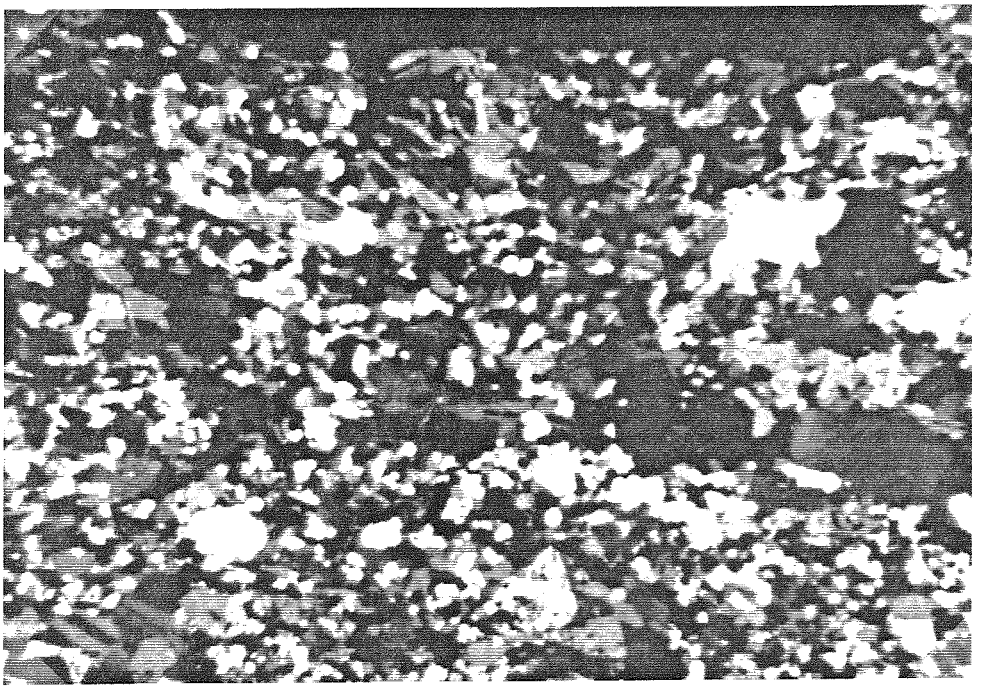

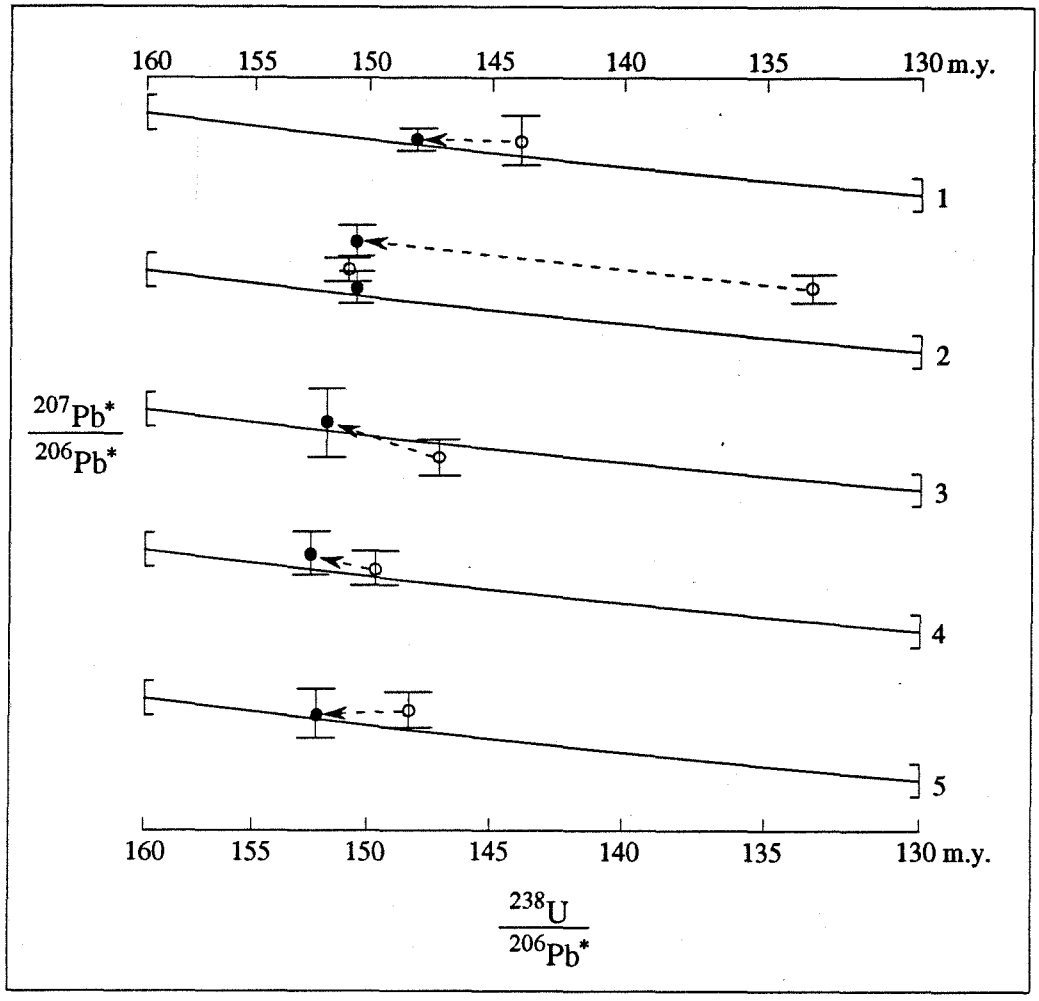

Fig. 15. Stacked segments of concordia plotted as $^{207}Pb^*/^{206}Pb^*$ versus $^{238}U/^{206}Pb^*$. Concordia diagrams arranged for sample comparisons of error bar relationships with concordia. Diagram shows the effect of the HF-leaching step in diminishing discordance (arrows link same-sized fractions). Open circles are nonleached fractions. Solid circles are leached fractions. Bars at ends of concordia segments show uncertainty in values of $^{207}Pb^*/^{206}Pb^*$ for concordia based on uncertainties in ^{235}U and ^{238}U decay constants based on Mattinson's (1987) use of Jaffey and others' (1971) data.

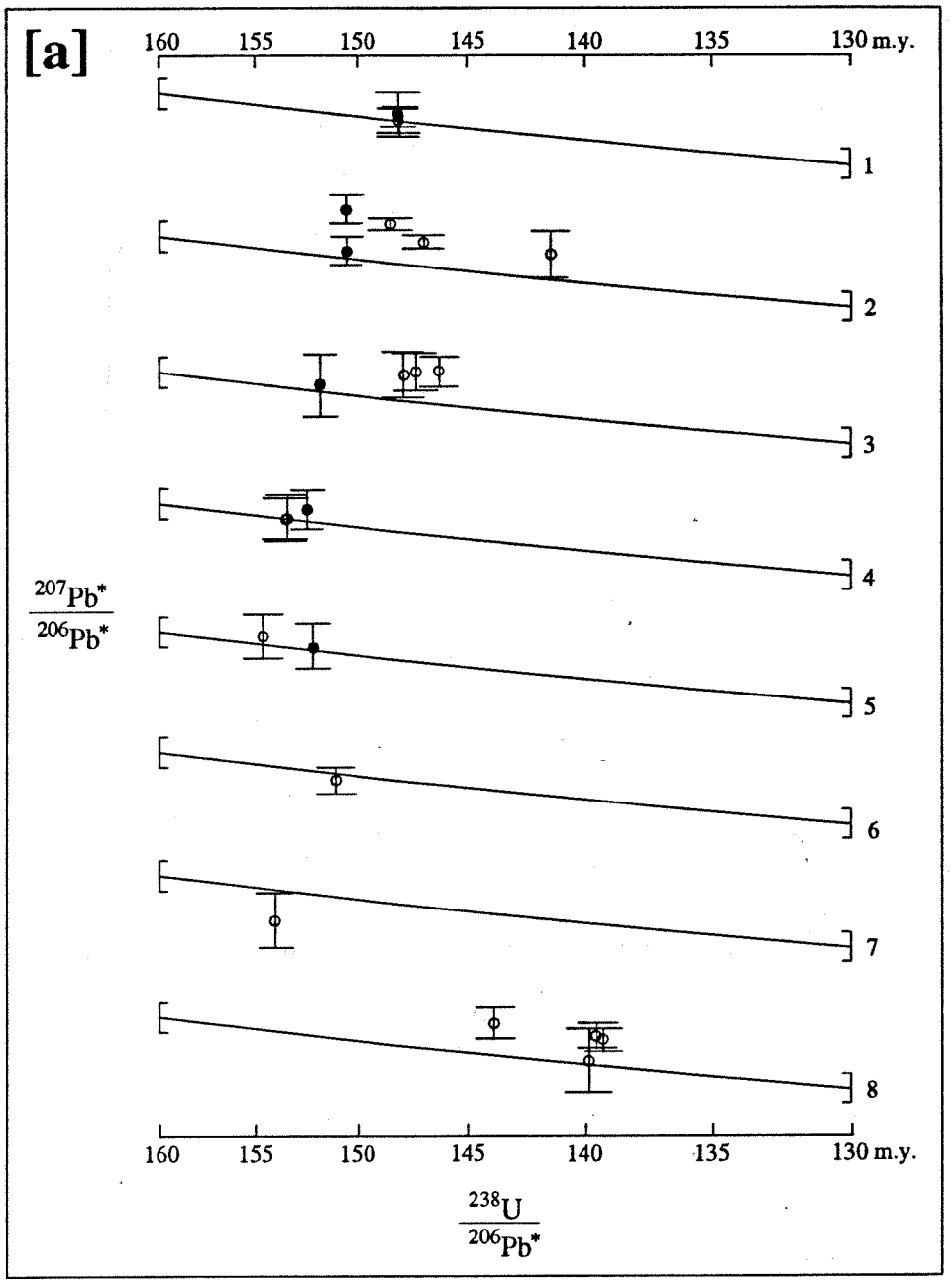

Fig. 16. Stacked segments of concordia plotted as $^{207}Pb^*/^{206}Pb^*$ versus $^{238}U/^{206}Pb^*$. Concordia diagrams arranged for sample comparisons of error bar relationships with concordia. Leached fractions (solid) compiled with nonleached (open), different-sized fractions from the same samples. [a] Jurassic granitoids; 1-7 from Owens Mountain, 8 from Santa Cruz Mountain; [b] Cretaceous granitoids.

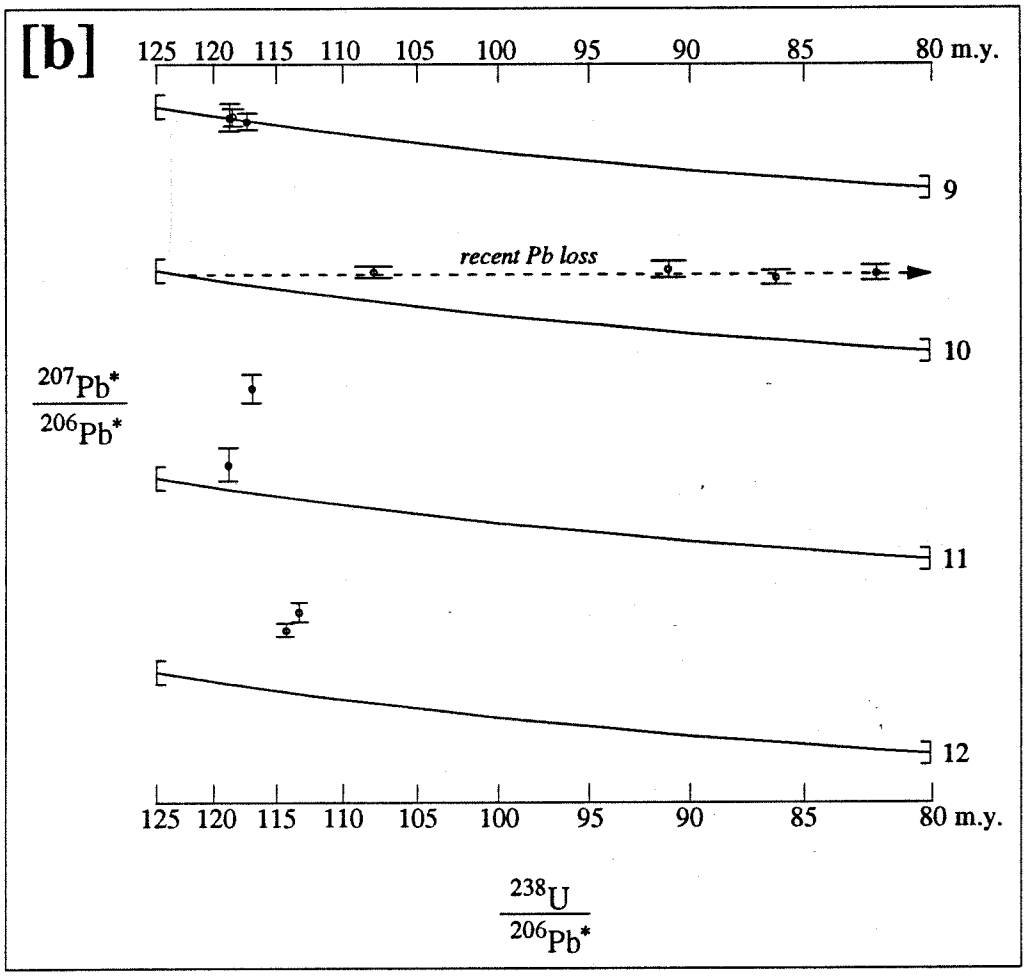
[b]
125 120 115 110 105 100 95 90 85 80 m.y.
9
recent Pb loss
10
$\frac{^{207}Pb^*}{^{206}Pb^*}$
11
12
125 120 115 110 105 100 95 90 85 80 m.y.
$\frac{^{238}U}{^{206}Pb^*}$

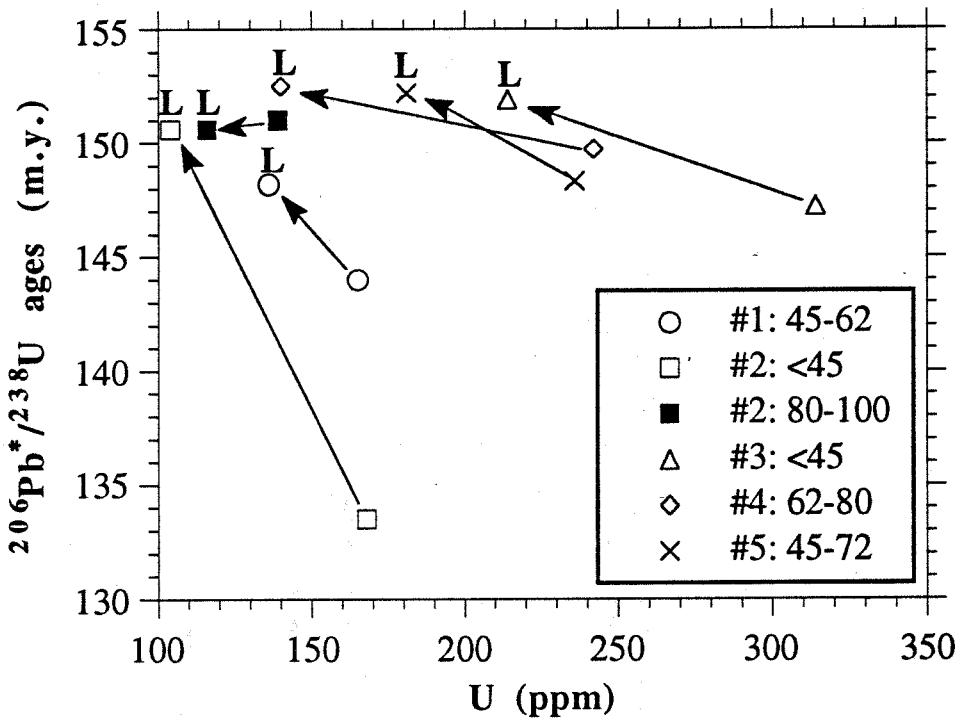

Fig. 17. Plot of $^{206}Pb^*/^{238}U$ versus U concentration. Negative correlation between leached and nonleached fractions indicates that high-U, radiation-damaged lattices which had experienced Pb loss comprised the dissolved parts of the leached zircon fractions.

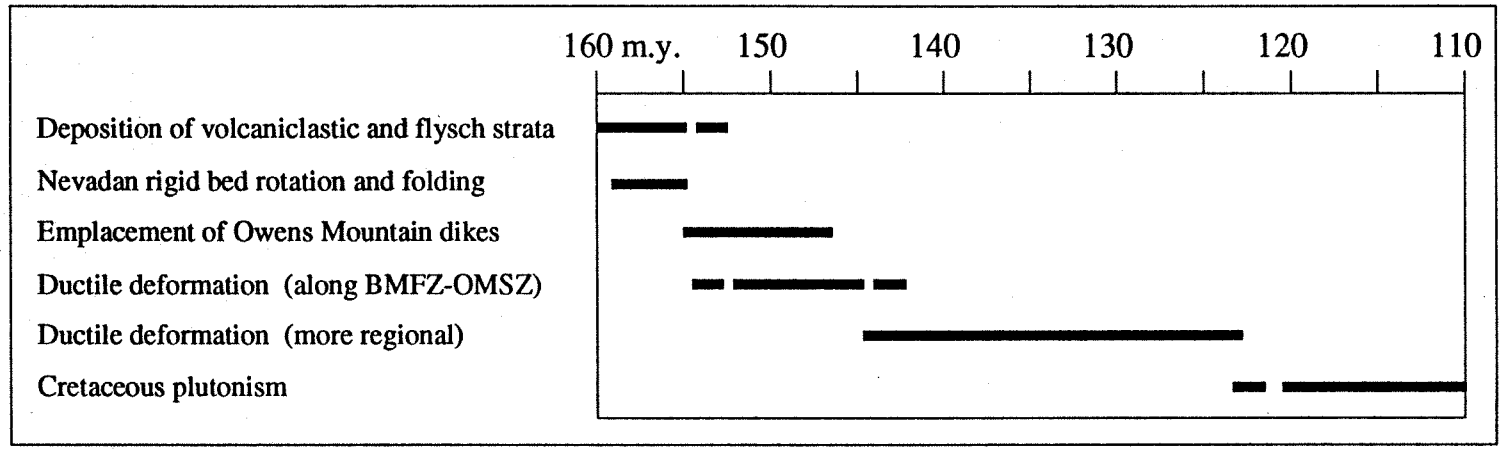

Fig. 18. Tectonoplutonic chronological summary of the Owens Mountain area. Dashed segments represent uncertainties, not known gaps in tectonoplutonic processes.

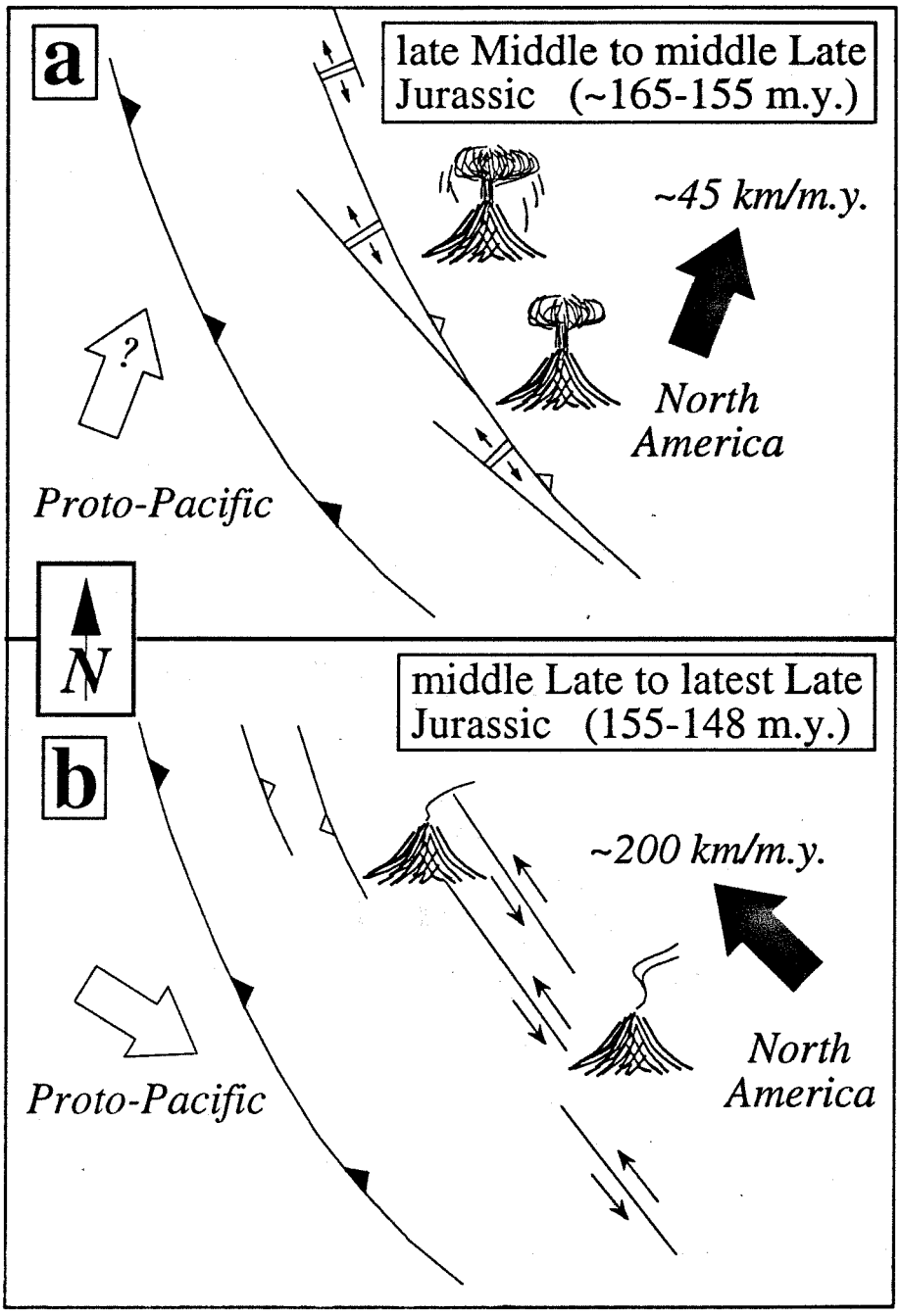

Fig. 19. Schematic diagrams of the California Cordillera during the late Middle to latest Late Jurassic illustrating tectonic processes related to changes in North American plate motion (modified after Saleeby, 1981; May and Butler, 1986; Saleeby and others, 1991). [a,c]: the late Middle to middle Late Jurassic, and [b,d]: the middle Late to latest Jurassic. [a,b] generalize the information from the block diagrams with cross-sections of [c,d]. The two time slices show inferred changes in the evolving tectonoplutonic environment, from subduction zone-dominated to transform-dominated. Some dike swarms within the rifting arc may have been localized in deforming pull-apart basins. Absolute angular velocity and direction of North America shown by numbered arrows (also see Fig. 20).

late Middle to middle Late Jurassic (~165-155 m.y.)

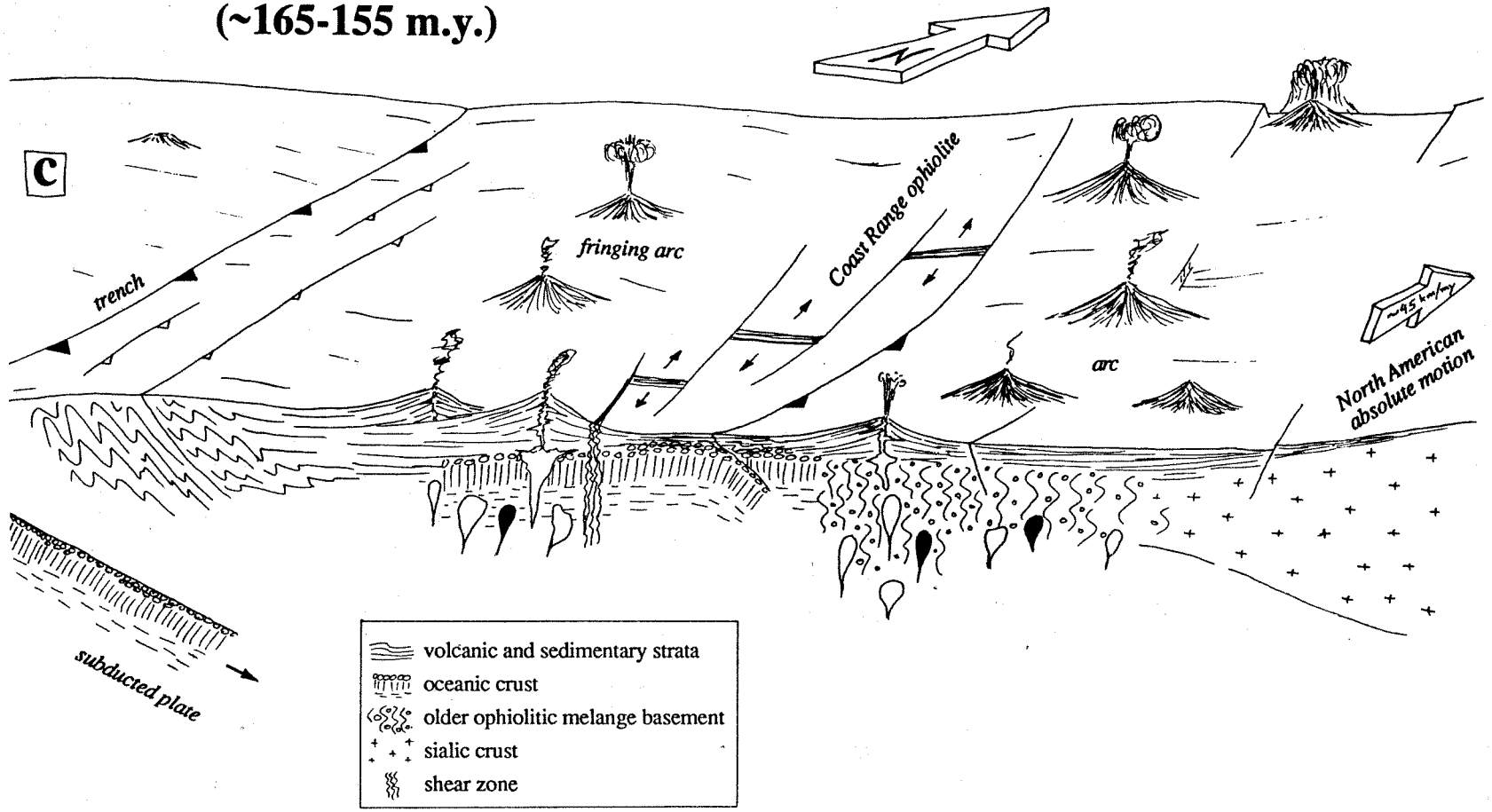

middle Late to latest Jurassic
(155-147 m.y.)

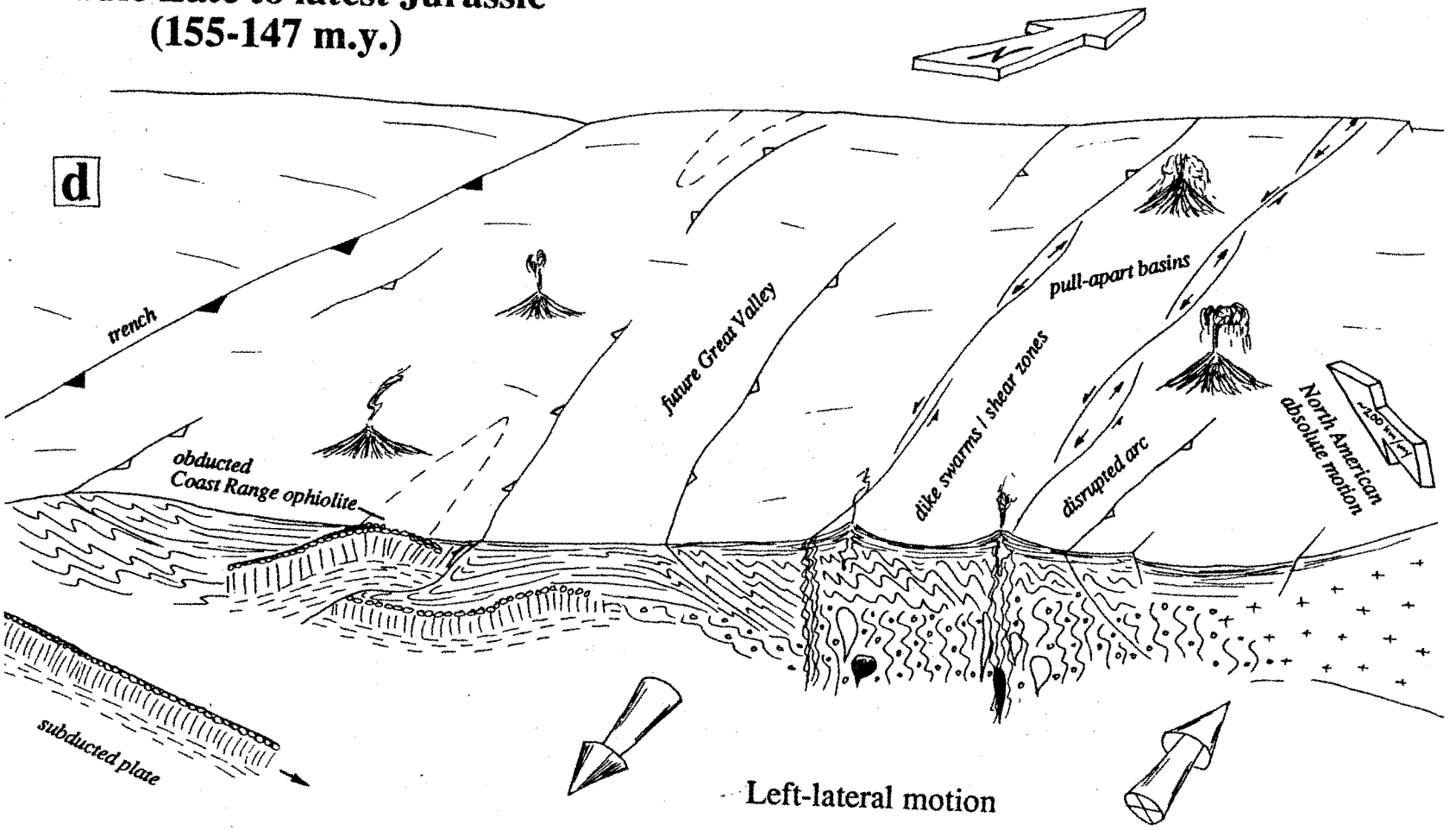

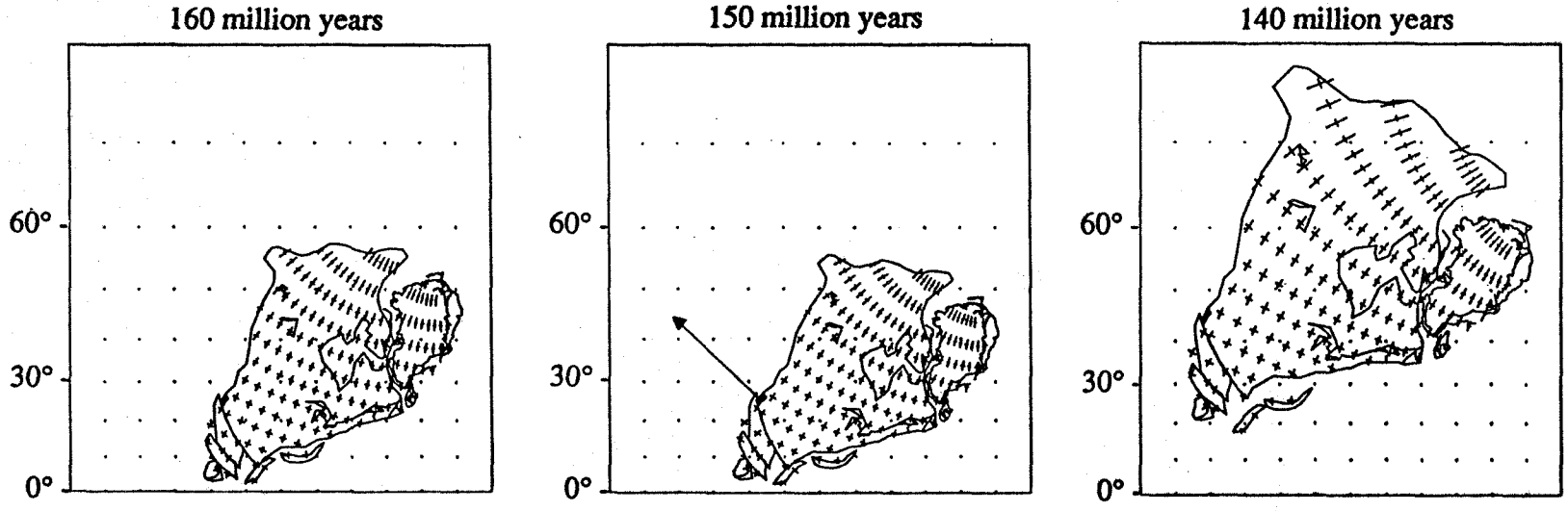

Fig. 20. Mercator projections of time slices showing the changes in the position and orientation of North America at 160, 150 and 140 m.y. (calculated from APW paths of May and Butler (1986) and pole reconstructions of Morgan (1981) and Anderson and Schmidt (1983)). At 150 m.y. (the J2 cusp), North America accelerated from ~45 km/m.y. to the NNE to ~150-230 km/m.y. to the NW. The arrow in the 150 m.y. view is the 150-140 m.y. vector. California is the small, blackened region. 10° separate each tick mark. The crosses represent current-day latitude/longitude intersections.

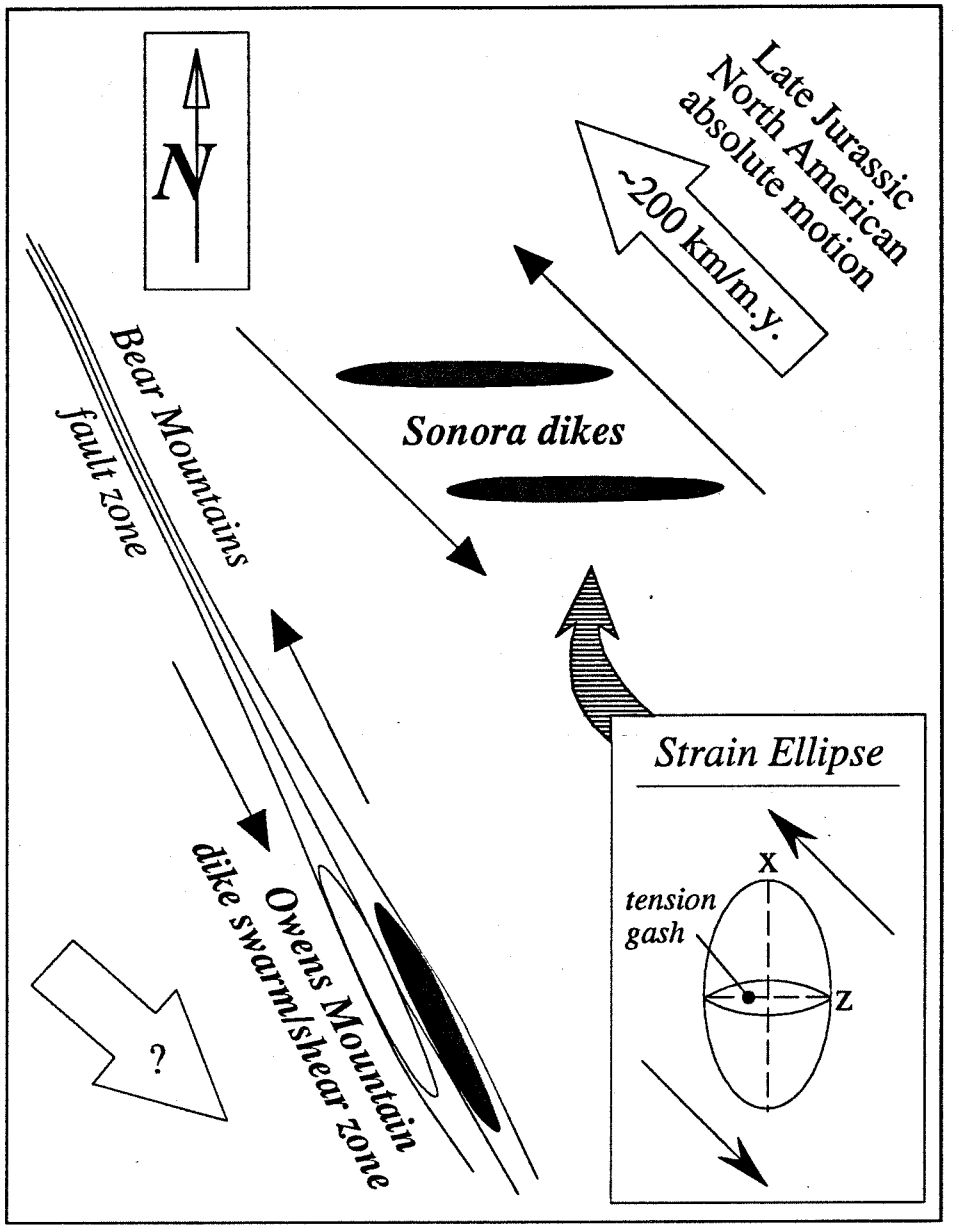

Fig. 21. Schematic diagram of the Sonora and Owens Mountain swarms showing the relationship between dike orientations and sinistral stress regime caused by rapid northwest motion of North America. Sonora dike orientation may be related to tensional weakness in margin. Owens Mountain dike swarm/shear zone orientation may be correlated with north-northwest trend of the regional Bear Mountains fault zone.

REFERENCES

Ague, J.J., and Brimhall, G.H., 1988a, Regional variations in bulk chemistry, mineralogy, and the compositions of mafic and accessory minerals in the batholiths of California: Geological Society of America Bulletin, v. 100, p. 891-911.

Ague, J.J., and Brimhall, G.H., 1988b, Magmatic arc asymmetry and distribution of anomalous plutonic belts in the batholiths of California: effects of assimilation, crustal thickness, and depth of crystallization: Geological Society of America Bulletin, v. 100, p. 912-927.

Anderson, T.H., and Schmidt, V.A., 1983, The evolution of middle America and the Gulf of Mexico-Caribbean Sea region during Mesozoic time: Geological Society of America Bulletin, v. 94, p. 941-966.

Armstrong, J.T., 1988a, Quantitative analysis of silicate and oxide materials: comparison of Monte Carlo, ZAF, and $\phi(\rho z)$ procedures: Microbeam Analysis, p. 239-246.

Armstrong, R.L., 1988b, Mesozoic and early Cenozoic magmatic evolution of the Canadian Cordillera, *in* Clark, S.P., Jr., Burchfiel, B.C., and Suppe, J., eds., Processes in continental lithosphere deformation: Geological Society of America Special Paper 218, p. 55-92.

Bard, J.P., 1986, Microtextures of igneous and metamorphic rocks: Dordrecht, Reidel, 264 p.

Barker, F., 1979, Trondhjemite: definition, environment and hypotheses of origin, *in* Barker, F., ed., Trondhjemites, dacites and related rocks: Amsterdam, Elsevier, p. 1-12.

Bateman, P.C., and Clark, L.D., 1974, Stratigraphic and structural setting of the Sierra Nevada batholith, California: Pacific Geology, v. 8, p. 78-89.

Beard, J.S., and Day, H.W., 1987, The Smartville intrusive complex, Sierra Nevada, California: the core of a rifted volcanic arc: Geological Society of America Bulletin, v. 99, p. 779-791.

Beck, M.E., Jr., 1983, On the mechanism of tectonic transport in zones of oblique subduction: Tectonophysics, v. 93, p. 1-11.

Behrman, P.G., 1978, Pre-Callovian rocks west of the Melones Fault Zone, central Sierra Nevada Foothills, *in* Howell, D.E., and McDougall, K.A., eds., Mesozoic paleogeography of the western United States: Pacific Section, Society of Economic Paleontologists and Mineralogists, Pacific Coast Paleogeography Symposium, 2nd, p. 337-348.

Beiersdorfer, R.E., and Day, H.W., 1983, Pumpellyite-actinolite facies metamorphism in the Smartville ophiolite complex, northern Sierra Nevada: Geological Society of America Abstracts with Programs, v. 15, p. 436.

Bence, A.E., and Albee, A.L., 1968, Correction factors for electron probe microanalysis of silicates and oxides: Journal of Geology, v. 76, p. 382-403.

Best, M.G., 1963, Petrology and structural analysis of metamorphic rocks in the southwestern Sierra Nevada foothills, California: University of California Publications in Geological Sciences, v. 42, p. 111-150.

Bishop, J.C., Jr., 1979, Petrology of the Blasingame gabbro, Fresno County, California [M.A. thesis]: Fresno, California, California State University, 88 p.

Bogen, N.L., 1984, Stratigraphy and sedimentary petrology of the Upper Jurassic Mariposa Formation, western Sierra Nevada, California, *in* Crouch, J.K., and Bachman, S.B., eds., Tectonics and sedimentation along the California margin: Society of Economic Paleontologists and Mineralogists, Pacific Section, v. 38, p. 119-134.

Bogen, N.L., 1985, Stratigraphic and sedimentologic evidence of a submarine island-arc volcano in the lower Mesozoic Peñon Blanco and Jaspar Point Formations, Mariposa County, California: Geological Society of America Bulletin, v. 96, p. 1322-1331.

Cady, J.W., 1975, Magnetic and gravity anomalies in the Great Valley and western Sierra Nevada metamorphic belt, California: Geological Society of America Special Paper 168, 56 p.

Cameron, A.E., Smith, D.H., and Walker, R.L., 1969, Mass spectrometry of nanogram-size samples of lead: Analytical Chemistry, v. 41, p. 525-526.

Chen, J.H., and Moore, J.G., 1979, Late Jurassic Independence dike swarm in eastern California: Geology, v. 7, p. 129-133.

Chen, J.H., and Tilton, G.R., 1978, Lead and strontium isotopic studies of the southern Sierra Nevada batholith, California: Geological Society of America Abstracts with Programs, v. 8, p. 99.

Chen, J.H., and Tilton, G.R., 1991, Applications of lead and strontium isotopic relationships to the petrogenesis of granitoid rocks, central Sierra Nevada batholith, California: Geological Society of America Bulletin, v. 103, p. 439-447.

Chen, J.H., and Wasserburg, G.J., 1981, Isotopic determination of uranium in picomole and subpicomole quantities: Analytical Chemistry, v. 53, p. 2060-2067.

Clark, L.D., 1960, Foothills fault system, western Sierra Nevada, California: Geological Society of America Bulletin, v. 71, p. 483-496.

Clark, L.D., 1964, Stratigraphy and structure of part of the western Sierra Nevada metamorphic belt, California: U.S. Geological Survey Professional Paper 923, 26 p.

Clemens Knott, D., Saleeby, J.B., Taylor, H.P., Jr., and Chappell, B.W., 1990, Petrology of the Early Cretaceous Sierra Nevada batholith: the Stokes Mountain region, CA: Eos, Transactions, American Geophysical Union, v. 71, p. 1576.

Coleman, R.G., Manning, C.E., Mortimer, N., Donato, M.M., and Hill, L.B., 1988, Tectonic and regional metamorphic framework of the Klamath Mountains and adjacent Coast Ranges, California and Oregon, *in* Ernst, W.G., ed., Metamorphism and crustal evolution of the western United States; Rubey Volume 7: Englewood Cliffs, Prentice-Hall, p. 1061-1097.

Day, S.D., 1977, The petrology of a mafic dike complex near Smartville, Yuba County, California [M.S. thesis]: Davis, California, University of California, 113 p.

Day, H.W., Moores, E.M., and Tuminas, A.C., 1985, Structure and tectonics of the northern Sierra Nevada: Geological Society of America Bulletin, v. 96, p. 436-450.

Deer, W.A, Howie, R.A., and Zussman, J., 1966, An introduction to the rock forming minerals: Essex, Longman, 528 p.

DePaolo, D.J., 1981, A neodymium and strontium isotopic study of the Mesozoic calc-alkaline granitic batholiths of the Sierra Nevada and Peninsular Ranges, California: Journal of Geophysical Research, v. 86, p. 10470-10488.

Dilek, Y., 1989, Tectonic significance of post-accretion rifting of a Mesozoic island-arc terrane in the northern Sierra Nevada, California: Journal of Geology, v. 97, p. 503-518.

Doe, B.R., and Zartman, R.E., 1979, Plumbotectonics, the Phanerozoic, *in* Barnes, H.L., ed., Geochemistry of hydrothermal ore deposits: New York, Wiley Interscience, p. 22-70.

Donato, M.M., 1987, Evolution of an ophiolitic tectonic melange, Marble Mountains, northern California Klamath Mountains: Geological Society of America Bulletin, v. 98, p. 448-464.

Duncan, R.A., and Green, D.H., 1980, The role of multistage melting in the formation of ocean crust: Geology, v. 18, p. 22-28.

Edelman, S.H., and Sharp, W.D., 1989, Terranes, early faults, and pre-Late Jurassic amalgamation of the western Sierra Nevada metamorphic belt, California: Geological Society of America Bulletin, v. 101, p. 1420-1433.

Edelman, S.H., Day, H.W., and Bickford, M.E., 1989, Implications of U-Pb zircon ages for the tectonic settings of the Smartville and Slate Creek complexes, northern Sierra Nevada, California: Geology, v. 17, p. 1032-1035.

Ehrreich, A.L., 1965, Metamorphism, migmatization, and intrusion in the foothills of the Sierra Nevada, Madera, Mariposa, and Merced counties [Ph.D. thesis]: Los Angeles, California, University of California, 320 p.

Engebretson, D.C., Cox, A., and Gordon, R.G., 1985, Relative motions between oceanic and continental plates in the Pacific Basin: Geological Society of America Special Paper 206, 59 p.

Gefell, M.J., Twiss, R.J., and Moores, E.M., 1989, Ductile and brittle shear sense for the "melones fault zone," northern Sierra Nevada, California: Geological Society of America Abstracts with Programs, v. 21, p. 83.

Gill, J., 1981, Orogenic andesites and plate tectonics: New York, Springer-Verlag, 385 p.

Giret, A., Bonin, B., and Leger, J.M., 1980, Amphibole compositional trends in oversaturated and undersaturated alkaline plutonic ring-complexes: Canadian Mineralogist, v. 18, p. 481-495.

Glazner, A.F., 1991, Plutonism, oblique subduction, and continental growth: an example from the Mesozoic of California: Geology, v. 19, p. 784-786.

Gordon, R.G., Cox, A., O'Hare, S., 1984, Paleomagnetic Euler poles and the apparent polar wander and absolute motion of North America since the Carboniferous: Tectonics, v. 3, p. 499-537.

Greenamyer, R.A., 1974, Marginal geology Academy pluton: a study of the bedrock marginal to the Academy pluton, California [M.A. thesis]: Fresno, California, California State University.

Hammarstrom, J.M., and Zen, E-An, 1986, Aluminum in hornblende: an empirical igneous geobarometer: American Mineralogist, v. 71, p. 1297-1313.

Harper, G.D., and Wright, J.E., 1984, Middle to Late Jurassic tectonic evolution of the Klamath Mountains, California-Oregon: Tectonics, v. 3, p. 759-772.

Harper, G.D., Saleeby, J.B., and Norman, E.A.S, 1985, Geometry and tectonic setting of sea-floor spreading for the Josephine ophiolite, and implications for Jurassic

accretionary events along the California margin, *in* Howell, D.B., ed., Tectonostratigraphic terranes of the circum-Pacific region: American Association of Petroleum Geologists Earth Science Series 1, p. 239-257.

Harper, G.D., Saleeby, J.B., and Heizler, M., 1990, Isotopic age of emplacement of the Josephine Ophiolite and overlying flysch during the Late Jurassic Nevadan orogeny, Klamath Mountains, Oregon-California: Journal of Geophysical Research (in press).

Hill, L.B., 1985, Metamorphic, deformational, and temporal constraints on terrane assembly, northern Klamath Mountain, California, *in* Howell, D.B., ed., Tectonostratigraphic terranes of the circum-Pacific region: American Association of Petroleum Geologists Earth Science Series 1, p. 173-186.

Hollister, L.S., Grissom, G.C., Peters, E.K., Stowell, H.H., Sisson, V.B., 1987, Confirmation of the empirical correlation of Al in hornblende with pressure of solidification of calc-alkaline plutons: American Mineralogist, v. 72, p. 231-239.

Hopson, C.A., Mattinson, J.M., and Pessagno, E.A., Jr., 1981, Coast Range ophiolite, western California, in Ernst, W.G., ed., The geotectonic development of California, Rubey Volume 1: Englewood Cliffs, New Jersey, Prentice-Hall, p. 418-510.

Huber, N.K., 1981, Amount and timeing of Late Cenozoic uplift and tilt of the central Sierra Nevada, California – evidence from the upper San Joaquin River basin: U.S. Geological Survey Professional Paper 1197, 28 p.

Irvine,T.N., and Baragar, W.R.A., 1971, A guide to the chemical classification of the common volcanic rocks: Canadian Journal of Earth Sciences, v. 8, p. 523-546.

Jaffey, A.H., Flynn, K.F., Glendenin, L.E., Bentley, W.C., and Essling, A.M., 1971, Precision measurement of half-lives and specific activities of ^{235}U and ^{238}U: Physical Reviews, v. C4, p. 1889-1906.

James, E.W., 1989, Southern extension of the Independence dike swarm of eastern California: Geology, v. 17, p. 587-590.

Jayko, A.S., 1990, Stratigraphy and tectonics of Paleozoic arc-related rocks of the northernmost Sierra Nevada, California; the eastern Klamath and northern Sierra terranes, *in* Harwood, D.S., and Miller, M.M., eds., Paleozoic and early Mesozoic paleogeographic relations; Sierra Nevada, Klamath Mountains, and related terranes: Boulder, Colorado, Geological Society of America Special Paper 255.

Johnson, M.C., and Rutherford, M.J., 1989, Experimental calibration of the aluminum-in-hornblende geobarometer with application to Long Valley caldera (California) volcanic rocks: Geology, v. 17, p. 837-841.

Karig, D.E., 1971, Origin and development of marginal basins in the western Pacific: Journal of Geophysical Research, v. 76, p. 2542-2561.

Kerrich, R., Allison, I., Barnett, R.L., Moss, S., and Starkey, J., 1980, Microstructural and chemical transformations accompanying deformation of granite in a shear zone at Miéville, Switzerland; with implications for stress corrosion cracking and superplastic flow: Contributions to Mineralogy and Petrology, v. 73, p. 221-242.

Knopf, A., 1929, The Mother Lode system of California: U.S. Geological Survey Professional Paper 157, 88 p.

Krogh, T.E., 1973, A low-contamination method for hydrothermal decomposition of zircon and extraction of U and Pb for isotopic age determinations: Geochimica Cosmochimica Acta, v. 37, p. 485-494.

Krohe, A., 1991, Emplacement of synkinematic plutons in the Variscan Odenwald (Germany) controlled by transtensional tectonics: Geologische Rundschau, v. 80, p. 391-409.

MacDonald, G.A., 1941, Geology of the western Sierra Nevada between the Kings and San Joaquin Rivers, California: University of California Publications in Geological Sciences, v. 26, p. 215-286.

Mack, S., Russell, K., Bishop, J.C., Jr., Sholes, D.A., and Augugliaro, F.R., 1986, Lithologic and structural variations in Cretaceous amphibole-rich gabbros in the Sierra

Nevada foothills near Fresno, Fresno County: California Geology, May volume, p. 108-113.

Mack, S., Saleeby, J.B., and Ferrell, J.G., 1979, Origin and emplacement of the Academy pluton, Fresno County, California: Geological Society of America Bulletin, Part II, v. 90, p. 633-694.

Mattinson, J.M., 1987, U-Pb ages of zircon: a basic examination of error propagation: Chemical Geology, v. 66, p. 151-162.

May, S.R., and Butler, R.F., 1986, North American Jurassic apparent polar wander: implications for plate motion, paleography and cordilleran tectonics: Journal of Geophysical Research, v. 91, p. 11519-11544.

May, S.R., Beck, M.E., Jr., and Butler, R.F., 1989, North American apparent polar wander, plate motion, and left-oblique convergence: Late Jurassic - Early Cretaceous orogenic consequences: Tectonics, v. 8, p. 443-451.

Menzies, M.D., Blanchard, D., and Xenophontos, C., 1980, Genesis of the Smartville arc-ophiolite, Sierra Nevada foothills, California: American Journal of Science, v. 280A, p. 329-344.

Merguerian, C., 1986, Geology of the Sonora dike swarm, Sierra Nevada foothills, California: Geological Society of America Abstract with Program, v. 18, p. 157.

Miller, M.M., and Saleeby, J.B., 1987, Detrital zircon studies of the Galice Formation: common provenance of strata overlying the Josephine ophiolite and Rogue Island arc, western Klamath Mountains terrane: Geological Society of America Abstract with Program, v. 19, p. 772-772.

Miller, R.B., and Paterson, S.R., 1991, Geology and tectonic evolution of the Bear Mountains fault zone, Foothills terrane, central Sierra Nevada, California: Tectonics, v. 10, p. 995-1006.

Misra, K.C., and Conte, J.A., 1991, Amphibolites of the Ashe and Alligator Back Formations, North Carolina: samples of Late Proterozoic-early Paleozoic oceanic crust: Geological Society of America Bulletin, v. 103, p. 737-750.

Moore, J.G., and Hopson, C.A., 1961, The Independence dike swarm in eastern California: American Journal of Science, v. 259, p. 241-259.

Moores, E.M., 1982, Origin and emplacement of ophiolites: Reviews of Geophysics and Space Physics, v. 20, p. 735-760.

Morgan, W.J., 1981, Hotspot tracks and the opening of the Atlantic and Indian Oceans, *in* Emiliani, C., ed., The Sea, Vol. 7, New York, Wiley, p. 443-487.

Newton, M.C., 1986, The southern part of the Bear Mountains fault zone, Foothills terrane, western Sierra Nevada, California: Geological Society of America Abstract with Program, v. 18, p. 164.

Oldow, J.S., 1983, Tectonic implications of a late Mesozoic fold and thrust belt in northwestern Nevada: Geology, v. 11, p. 542-546.

Oldow, J.S., Avé Lallemant, H.G., and Schmidt, W.J., 1984, Kinematics of plate convergence deduced from Mesozoic structures in the western Cordillera: Tectonics, v. 3, p. 201-227.

Oldow, J.S., Bally, A.W., Avé Lallemant, H.G., Leeman, W.P., 1989, Phanerozoic evolution of the North American Cordillera; United States and Canada, *in* Bally, A.W., and Palmer, A.R., eds., The Geology of North America – An overview: Geological Society of America, The Geology of North America, v. A, p. 139-232.

Parrish, R.R., 1987, An improved mirco-capsule for zircon dissolution in U-Pb geochronology: Chemical Geology, v. 66, p. 99-102.

Passchier, C.W., Myers, J.S., and Kröner, A., 1990, Field geology of high-grade gneiss terrains: Berlin, Springer-Verlag, p. 150.

Paterson, S.R., and Tobisch, O.T., 1985, Regional relations between metamorphism, pluton emplacement, and deformations in southern portions of the Foothills belt, Sierra

Nevada, Calfiornia: Geological Society of America Abstract with Program, v. 17, p. 399.

Paterson, S.R., Tobisch, O.T., and Radloff, J.K., 1987, Post-Nevadan deformation along the Bear Mountains fault zone: implications for the Foothills terrane, central Sierra Nevada, California: Geology, v. 15, p. 513-516.

Paterson, S.R., Vernon, R.H., and Tobisch, O.T., 1989, A review of criteria for the identification of magmatic and tectonic foliations in granitoids: Journal of Structural Geology, v. 11, p. 349-363.

Paterson, S.R., and Wainger L., 1991, Strains and structures associated with a terrane bounding stretching fault: the Melones fault zone, central Sierra Nevada, California: Tectonophysics, v. 194, p. 69-90.

Pearce, J.A., 1975, Basalt geochemistry used to investigate past tectonic environment in Cyprus: Tectonophysics, v. 25, p. 41-67.

Pearce, J.A., 1982, Trace element characteristics of lavas from destructive boundaries, *in* Thorpe, R.S., ed., Andesites, orogenic andesites and related rocks: Wiley, New York, p. 525-547.

Primrose, A., 1980, Geology of the Owens Mountain area, Fresno County, California [M.A. thesis]: Fresno, California, California State University, 46 p.

Rock, N.M.S., and Leake, B.E., 1984, The international mineralogical association amphibole nomenclature scheme: computerization and its consequences: Mineralogy Magazine, v. 48, p. 211-227.

Ruiz, J.T., 1982, Geology of the Copper King mine and surrounding area: Fresno County, California [M.A. thesis]: Fresno, California, California State University, 62 p.

Russell, K., 1982, Geology of the Campbell Mountain pluton, southern Fresno County, California [M.A. thesis]: Fresno, California, California State University, 119 p.

Rutter, M.J., Van der Laan, S.R., and Wyllie, P.J., 1989, Experimental data for a proposed empirical igneous geobarometer: aluminum in hornblende at 10 kbar pressure: Geology, v. 17, p. 897-900.

Saleeby, J.B., 1975, Structure, petrology and geochronology of the Kings-Kaweah mafic-ultramafic belt, southwestern Sierra Nevada foothills, California [Ph.D. thesis]: Santa Barbara, California, University of California, 286 p.

Saleeby, J.B., 1977, Fracture zone tectonics, continental margin fragmentation, and emplacement of the Kings-Kaweah ophiolite belt, southwest Sierra Nevada, California, *in* Coleman, R.G., and others, eds., North American ophiolites: Oregon Department of Geological and Mineralogical Industries Bulletin, v. 95, p. 141-159.

Saleeby, J.B., 1978, Kings River ophiolite, southwest Sierra Nevada foothills, California: Geological Society of America Bulletin, v. 89, p. 617-636.

Saleeby, J.B., 1981, Ocean floor accretion and volcano-plutonic arc evolution of the Mesozoic Sierra Nevada, California, *in* Ernst, W.G., ed., The geotectonic development of California; Rubey Vol. 1: Englewood Cliffs, Prentice-Hall, p. 132-181.

Saleeby, J.B., 1982, Polygenetic ophiolite belt of the California Sierra Nevada; geochronological and tectonostratigraphic development: Journal of Geophysical Research, v. 87, p. 1803-1824.

Saleeby, J.B., 1983, Accretionary tectonics of the North American Cordillera: Annual Reviews in Earth and Planetary Sciences, v. 15, p. 45-73.

Saleeby, J.B., 1990a, Progress in tectonic and petrogenetic studies in an exposed cross-section of young (~100 Ma) continental crust, southern Sierra Nevada, California, *in* Salisbury, M.H. and Fountain D.M., eds., Exposed cross-sections of the continental crust: Dordrecht, Kluwer, p. 137-158.

Saleeby, J.B., 1990b, Geochronological and tectonostratigraphic framework of Sierra-Klamath ophiolitic assemblages: Geological Society of America Special Paper 255, p. 93-114.

Saleeby, J.B., and Chen, J.H., 1978, Preliminary report on initial lead and strontium isotopes from ophiolitic and batholitic rocks, southwestern foothills, Sierra Nevada, California: U.S. Geological Survey Open File Report 78-701, p. 375-376.

Saleeby, J.B., Harper, G.D., Sharp, W.D., and Snoke, A.W., 1982, Time relations and structural-stratigraphic patterns in ophiolite accretion, west-central Klamath Mountains, California: Journal of Geophysical Research, v. 87, p. 3831-3848.

Saleeby, J.B., Geary, E.E., Paterson, S.R., Tobisch, O.T., 1989a, Isotopic systematics of Pb/U (zircon) and $^{40}Ar/^{39}Ar$ (biotite/hornblende) from rocks of the Central Foothills terrane, Sierra Nevada, California: Geological Society of America Bulletin, v. 101, p. 1481-1492.

Saleeby, J.B., Shaw, H.F., Niemeyer, S., and Moores, E.M., 1989b, U/Pb, Sm/Nd, and Rb/Sr geochronological and isotopic study of northern Sierra Nevada ophiolitic assemblage, California: Contributions to Mineralogy and Petrology, v. 102, p. 205-220.

Saleeby, J.B., and Sharp, W.D., 1980, Chronology of the structural and petrologic development of the southwest Sierra Nevada foothills, California: Geological Society of America Bulletin, Part II, v. 91, p. 1416-1535.

Saleeby, J.B., and seven others, 1991, Early Mesozoic tectonic evolution of the western U.S. Cordillera: The Geology of North America, v. G-3, The Cordilleran Orogen; Conterminous U.S.: Geological Society of America, (in press).

Schweickert, R.A., Bogen, N.L., Girty, G.H., Hanson, R.E., and Merguerian, C., 1984, Timing and structural expression of the Nevadan orogeny, Sierra Nevada, California: Geological Society of America Bulletin, v. 95, p. 967-979.

Schweickert, R.A., Merguerian, C., and Bogen, N.L., 1988, Deformational and metamorphic history of Paleozoic and Mesozoic basement terranes in the western Sierra Nevada metamorphic belt, *in* Ernst, W.G., ed., Metamorphism and crustal evolution of

the western United States; Rubey Volume 7: Englewood Cliffs, Prentice-Hall, p. 789-822.

Sharp, W.D., 1980, Ophiolite accretion in the northern Sierra: Eos, Transactions, American Geophysical Union, v. 61, p. 1122.

Sharp, W.D., and Evarts, R.C., 1982, New constraints on the environment of formation of the Coast Range ophiolite at Del Puerto Canyon, California: Geological Society of America Abstracts with Programs, v. 14, p. 233.

Sholes, D.A., 1982, The origin and emplacement of three Cretaceous gabbroic bodies in the Sierran foothills east of Fresno, California [M.A. thesis]: Fresno, California, California State University, 105 p.

Silver, L.T., 1983, Further evidence and analysis of the role of the Mojave-Sonora megashear (s) in Mesozoic Cordilleran tectonics: Geological Society of America Abstracts with Programs, v. 15, p. 273.

Silver, L.T., and Anderson, T.H., 1974, Possible left-lateral early to middle Mesozoic disruption of the southwestern North American craton margin: Geological Society of America Abstracts with Programs, v. 6, p. 955-956.

Simpson, C., and De Paor, D., 1991, Deformation and kinematics of high strain zones: Geological Society of America Short Course, San Diego, 116 p.

Snoke, A.W., 1977, A thrust plate of ophiolitic rocks in the Preston Peak area, Klamath Mountains, California: Geological Society of America Bulletin, v. 88, p. 1641-1659.

Snoke, A.W., Sharp, W.D., Wright, J.E., and Saleeby, J.B., 1982, Significance of mid-Mesozoic peridotitic to dioritic intrusive complexes, Klamath Mountains - western Sierra Nevada, California: Geology, v. 10, p. 160-166.

Springer, R.K., 1980, Geology of the Pine Hill intrusive complex; a layered gabbroic body in the western Sierra Nevada foothills, California, Summary I: Geological Society of America Bulletin, v. 91, p. 381-385.

Steiger, R.H., and Jager, E., 1977, Subcommission on geochronology: convention on the use of decay constants in geo- and cosmochemistry: Earth and Planetary Science Letters, v. 36, p. 350-362.

Stern, T.W., Bateman, P.C., Morgan, B.A., Newell, M.F., and Peck, D.L., 1981, Isotopic U-Pb ages of zircon from the granitoids of the central Sierra Nevada: U.S. Geological Survey Professional Paper 185, 17 p.

Stern, C.R., and Wyllie, P.J., 1978, Phase compositions through crystallization intervals in basalt-andesite-H2O at 30 kb with implications for subduction zone magmas: American Mineralogist, v. 63, p. 641-663.

Streckeisen, A., 1976, To each plutonic rock its proper name: Earth Science Reviews, v. 12, p. 1-33.

Sun, S.S., and Nesbitt, R.W., 1978, Geochemical regularities and genetic significance of ophiolitic basalts: Geology, v. 6, p. 689-693.

Taliaferro, N.L., 1942, Geologic history and correlation of the Jurassic of southwestern Oregon and California: Geological Society of America Bulletin, v. 53, p. 71-112.

Tera, F., and Wasserburg, G.S., 1972, U-Th-Pb systematics in three Apollo 14 basalts and the problems of the initial Pb in lunar rocks: Earth and Planetary Science Letters, v. 14, p. 281-304.

Thompson, A.B., 1982, Dehydration melting of pelitic rocks and the generation of H_2O-undersaturated granitic liquids: American Journal of Science, v. 282, p. 1567-1595.

Tobisch, O.T., Paterson, S.R., Saleeby, J.B., and Geary, E.E., 1989, Nature and timing of deformation in the Foothills terrane, central Sierra Nevada, California: its bearing on orogenesis: Geological Society of America Bulletin, v. 101, p. 401-413.

Vernon, R.H., Paterson, S.R., and Geary, E.E., 1989, Evidence for syntectonic intrusion of plutons in the Bear Mountains fault zone, California: Geology, v. 17, p. 723-726.

Williams, H., Turner, F.J., and Gilbert, C.M., 1982, Petrography: an introduction to the study of rocks in thin sections, 2nd ed.: New York, Freeman, 626 p.

Wise, D.U., and seven others, 1984, Fault-related rocks: suggestions for terminology: Geology, v. 12, p. 391-394.

Wolf, M.B., and Saleeby, J.B., 1990, Crustal extension during the Nevadan orogeny in the southwestern Sierra Nevada Foothills terrane (FT), California: Geological Society of America Abstracts with Programs, v. 22, p. 275.

Wolf, M.B., and Saleeby, J.B., 1991, Tectonics of Late Jurassic dike emplacement in the Sierra Nevada region: Geological Society of America Abstracts with Programs, v. 23, p. 248.

Wright, J.E., and Fahan, M.R., 1988, An expanded view of Jurassic orogenesis in the western United States Cordillera: Middle Jurassic (pre-Nevadan) regional metamorphism and thrust faulting within an active arc environment, Klamath Mountains, California: Geological Society of America Bulletin, v. 100, p. 859-876.

Xenophontos, C., 1984, Geology, petrology, and geochemistry of part of the Smartville complex, northern Sierra Nevada foothills, California [Ph.D. thesis]: Davis, California, University of California, 446 p.

Xenophontos, C., and Bond, G.C., 1978, Petrology, sedimentation and paleogeography of the Smartville terrane (Jurassic) – bearing on the genesis of the Smartville ophiolite, *in* Howell, D.E., and McDougall, K.A., eds., Mesozoic paleogeography of the western United States: Pacific Section, Society of Economic Paleontologists and Mineralogists, Pacific Coast Paleogeography Symposium, 2nd, p. 291-302.

York, D., 1969, Least-squares fitting of a straight line with correlated errors: Earth and Planetary Science Letters, v. 5, p. 320-324.

Yule, D.J., Saleeby, J.B., Jones, D.L., and Silk, M., 1992, Correlation of basement terranes across the Late Jurassic Josephine interarc basin, southwestern Oregon and northern California: Geological Society of America Abstracts with Programs, v. 24, p. 93.

Zeitler, P.K., Barreiro B., Chamberlain, C.P., and Rumble, D., 1990, Ion-microprobe dating of zircon from quartz-graphite veins at the Bristol, New Hampshire, metamorphic hot spot: Geology, v. 18, p. 626-629.

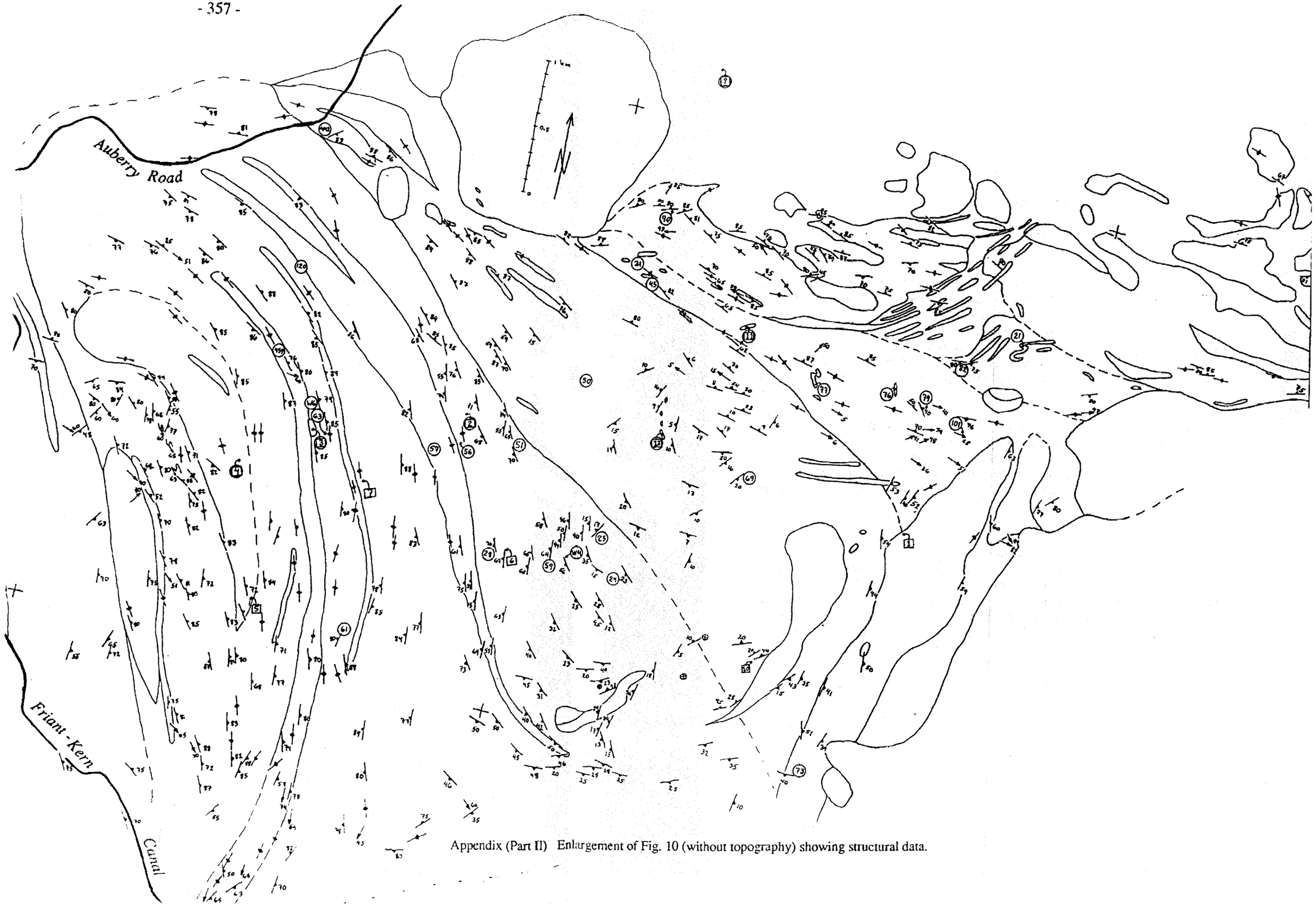

Appendix (Part II) Enlargement of Fig. 10 (without topography) showing structural data.